Technical Report: 026511-2-T

MODELING MICROWAVE BACKSCATTER FROM DISCONTINUOUS TREE CANOPIES

Kyle C. McDonald
Fawwaz T. Ulaby

JPL Contract C-958437 (NASA Prime)
Principal Investigator: Fawwaz T. Ulaby

June, 1991

ABSTRACT

Forest ecosystems represent a significant portion of Earth's vegetation cover. While playing an important role in the global carbon cycle, the areal extent of forests, the rate of global deforestation and the amount of forest biomass remain key unknown parameters in understanding atmospheric carbon dioxide flux from these biomes. Spaceborne microwave imaging systems have been proposed as a means of assessing biophysical parameters of vegetation canopies. Such systems can monitor regions of the globe where environmental conditions render optical techniques ineffective. Scattering models that accurately simulate forest canopy backscatter allow measured radar data to be coupled to canopy parameters and significantly aid in applying remotely sensed data to understanding canopy physiological state.

The goal of this work is to develop a robust microwave scattering model for forested areas. A tree canopy is characterized as an inhomogeneous medium comprised of discrete scatterers that represent the trunks, branches, stems, needles and leaves. Radiative transfer theory is applied to derive a first-order fully-polarimetric solution for backscatter. The fundamental contribution of this thesis is the development of a model that accounts for backscatter from forest canopies that have discontinuous crown layer geometries. By treating parameters describing the size, shape and location of individual tree crowns as random variables, a statistical approach is taken that defines the expected value of canopy backscatter.

Application of the radiative transfer equations to the discontinuous canopy geometry is reviewed. The application of random variables defining the crown geometry and the incorporation of these variables into the radiative transfer solution is discussed. The resulting model is valid for microwave frequencies over a wide range of radar incidence angles. Model simulations are compared to results derived with the

continuous canopy model. The effect of the open crown geometry is found to be most significant at shallow incidence angles and at high frequencies for trees with well-developed crowns. The model successfully couples canopy biophysical parameters to radar backscatter measurements. When compared to measured radar data, variations in backscatter that occur because of changing environmental conditions that cause changes in canopy water status are accurately predicted.

TABLE OF CONTENTS

LIST OF FIGURES

LIST OF TABLES

LIST OF APPENDICES

Appendix

CHAPTER I

INTRODUCTION

Microwave radar has been used in remote sensing applications since the early 1960s and is becoming a major tool for observing Earth's biosphere (Ulaby *et al.*,[70]; Ulaby and Elachi, [62]). By exploiting their ability to provide an independent source of illumination and their capability to penetrate clouds, space-borne microwave imaging systems can provide long and short term terrain monitoring in areas of the globe where environmental conditions render optical techniques ineffective. Microwave remote sensing has proven useful in studying properties of the ocean surface, polar ice, land cover, and in some cases subsurface terrain features.

Another advantageous property of microwaves is their ability to penetrate more deeply into vegetation canopies than optical waves. The extent of this penetration depends on several factors, including canopy moisture content, radar frequency and radar incidence angle. In general, many canopy characteristics strongly influence the radar signature. Along with the moisture content of the vegetation itself, these include such properties as soil moisture content, total vegetation biomass, physical location and structure of the vegetation constituents, ground surface state (bare soil, snow cover, vegetation cover, flooded) and canopy phenological and biophysical state.

Forest ecosystems represent a significant portion of Earth's vegetation cover.

While playing an important role in the global carbon cycle, the areal extent of forests, the rate of global deforestation and the amount of biomass in existing forests remain key unknown parameters in understanding atmospheric carbon dioxide flux from these biomes. Because of their aforementioned capabilities, microwave imaging systems have been proposed as a means of assessing these parameters. The development of scattering models that accurately simulate backscatter from such canopies allows measured data to be mathematically coupled to canopy parameters and significantly aids in understanding the physiological state of the canopy.

The goal of this work is to develop a robust microwave scattering model for forested areas. A tree canopy may be characterized as an inhomogeneous medium comprised of discrete scatterers that represent the trunks, branches, stems, needles and leaves. Most models for radar scattering from vegetation treat the canopy as a uniform layer of some specified height containing a random distribution of scatterers (Attema and Ulaby,[2]; Eom and Fung,[19]; Fung and Ulaby, [22]; Karam and Fung, [31]; Lang and Sidhu, [35]; Richards *et al.*, [48]; Tsang and Kong, [59]). Models based on the field approach (Fung and Ulaby,[22]; Tsang and Kong,[59]) account for the inhomogeneity of the medium through the correlation function characterizing the fluctuating component of the dielectric constant of the medium whereas models based on the radiative transfer intensity approach (Durden *et al.*,[17]; Eom and Fung,[19]; Tsang *et al.*,[60]; Ulaby *et al.*,[70]) account for the inhomogeneity by averaging the Stokes matrix over the statistical distributions characterizing the sizes, shapes, and orientations of the canopy elements. In general, the field approach is appropriate for weakly scattering media in which the ratio of the fluctuating component of the dielectric constant to the mean value for the medium is small (Lee and Kong, [36]; Ulaby *et al.*,[70]). For a medium such as vegetation in which the individual scatterers

have discrete configurations and have dielectric constants that are much larger than that of the background (air), the radiative transfer approach is more appropriate.

A first-order radiative transfer model for simulating backscatter from tree canopies has been under development at The University of Michigan Radiation Laboratory for some time (Ulaby *et al.*, [67], [68],[69]). This model, known as the Michigan Microwave Canopy Scattering (MIMICS) model, is fully polarimetric and is designed to function for a frequency range extending from 0.5 to 10 GHz and over a wide range of incidence angles. Several variations of MIMICS have been under development. The first-generation model, MIMICS I, models tree canopies that have continuous or closed crown layer geometries. The second generation model, MIMICS II, models canopies with discontinuous or open crown layer geometries.

The fundamental contribution of this thesis is the introduction of MIMICS II. To this end, Chapter II begins with a presentation of the definitions used in describing tree canopy parameters. Sizes and orientations of the canopy elements are defined in terms of random variables with specified probability density functions (PDFs). Brief reviews of the fundamentals of radiative transfer theory and radar polarimetry are also presented.

Chapter III presents the development of the closed-crown canopy model. The radiative transfer equations are applied to the continuous canopy geometry and an iterative technique is used to find for the first-order solution. A technique is then introduced by which ground vegetation or snow cover may be modeled.

Chapter IV presents the development of the open-crown canopy model. In developing MIMICS II, the same radiative transfer approach that was applied in developing MIMICS I is used except that now the scattering and extinction properties of the crown layer are specified in a statistical fashion, in terms of random variables

that depend on the location, size and shape of individual tree crowns. The resulting expression is then in terms of the expected value of the Canopy Backscattering Transformation matrix. Statistical parameters that define the structure of the crown layer are introduced and polarimetric and scalar expressions for canopy backscatter are derived.

Chapter V presents the derivation of the crown layer shape statistics for several types of canopy architectures. Parameters are considered on the individual crown level as well as for collections of crowns. It is necessary to introduce these statistics into the MIMICS II radiative transfer solution in order to compute backscatter for a particular canopy geometry.

Chapter VI then presents several modeling analyses and applications of both the closed-crown and open-crown canopy models. These analyses include sets of measured radar data obtained with truck-mounted scatterometer systems and with aircraft-mounted synthetic aperture radars (SAR).

CHAPTER II

BACKGROUND

2.1 Tree Canopy Parameters

For modeling purposes, a tree canopy may be characterized by two layers of vegetation distributed over a ground surface. Figure 2.1(a) shows the geometry of a tree canopy with a continuous or closed crown layer, and Figure 2.1(b) shows the geometry of a canopy with a discontinuous or open crown layer. In both cases, the canopy vegetation is distributed between two regions. The upper region has vertical extent d and contains the foliage that comprises the tree crowns. The lower region contains the tree trunks and has a height equivalent to the average trunk height H_t. The closed canopy geometry is characterized by a crown layer whose elements are distributed within a layer of uniform thickness d whereas the open canopy geometry has a crown layer of total vertical extent d whose constituents are contained within individual tree crown volumes. In general, the crown and trunk layers may overlap such that the total canopy height is $H \leq H_t + d$.

Two classes of parameters are relevant for model development. These are: (1) the dielectric parameters that specify the electrical properties of canopy constituents and (2) the geometric parameters that specify the shapes, sizes and spatial distributions of the canopy constituents. The dielectric parameters, which are summarized

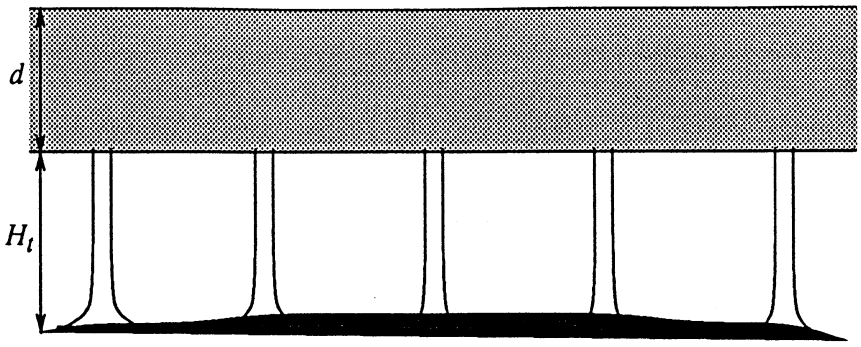

(a) Continuous Crown Layer

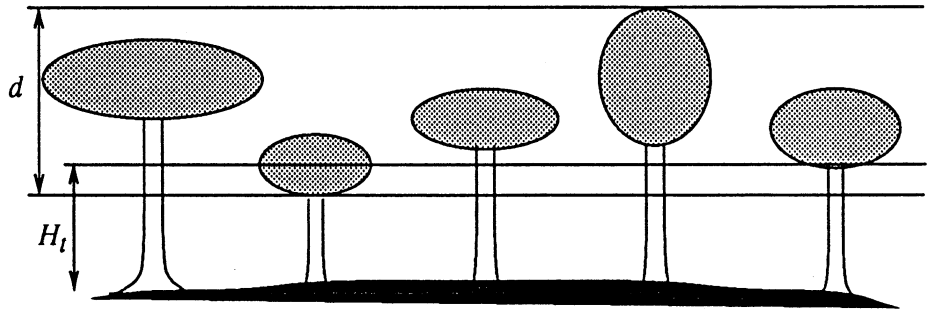

(b) Discontinuous Crown Layer

Figure 2.1: Geometry of a tree canopy with (a) a continuous (closed) crown layer and (b) a discontinuous (open) crown layer.

in Table 2.1, may be used as direct inputs to the model or may be inferred from the appropriate constituent parameters listed in the table. These parameters include moisture content, constituent temperature, vegetation bulk density, and soil textural composition. Models that link these parameters to the dielectric constants are reviewed in Appendix A.

Table 2.2 summarizes the canopy geometric parameters. Two types of random variables are used to define the statistical properties of the canopy geometry. The tree-level random variables define geometrical parameters within individual trees

Table 2.1: Canopy dielectric parameters.

Constituent Dielectric	Relevant Constituent Parameters
Vegetation Dielectrics:	
Trunk ϵ_r	Moisture content
Branch ϵ_r	Temperature (freeze/thaw state)
Needle ϵ_r	Bulk density ρ
Leaf ϵ_r	
Surface Dielectric	Surface composition (soil,snow,standing water)
	Moisture content
	Temperature (freeze/thaw state)
	Soil textural components (sand, silt, clay)

Table 2.2: Canopy geometric parameters.

Tree-level Random Variables	Canopy-level Random Variables
Branches and Needles:	Canopy height parameters:
Cylinder PDF: $f_c(l_c, d_c; \theta_c, \phi_c)$	Trunk layer height: H_t
Number Density: N_c	Crown layer height: d
(cylinders per unit volume)	Crown parameters:
Leaves:	Crown shape factor
Disk PDF: $f_d(d_d, t_d; \theta_d, \phi_d)$	Crown size PDF: $f_{cr}(\cdots)$
Number Density: N_d	Area density: N_t
(disks per unit volume)	(trees per unit area)
Trunks:	Ground Surface Roughness:
Cylinder PDF: $f_t(l_t, d_t; \theta_t, \phi_t)$	l_s, m

and allow for determination of the microwave scattering characteristics of individual canopy components. Canopy-level random variables, on the other hand, define parameters on the scale of the total canopy and thus describe the gross canopy structure. Both sets of random variables are assumed to be statistically homogeneous over the region of interest. In addition, the tree-level random variables are assumed to have identical distributions throughout all tree crown volumes and are therefore independent of the canopy-level random variables. This property will be referred to as local statistical homogeneity.

The size and orientation of each class of vegetation constituent is defined in terms of a probability density function (PDF). In general, the crown layer consists of K

constituent classes such as primary and secondary branches, leaves, and needles, each with a corresponding number density of N_k particles per unit volume. The joint probability density function $f_k(\mathsf{s}_k; \theta_k, \phi_k)$ describes the distribution in size and orientation of constituent class k. The vector s_k consists of the size parameters that are relevant to class k. Branches and needles are described in terms of the length l_c and diameter d_c of an equivalent cylinder so that $(l_c, d_c) \in \mathsf{s}_c$. Leaves are described in terms of the diameter d_d and thickness t_d of an equivalent circular disk so that $(d_d, t_d) \in \mathsf{s}_d$. The parameters (θ_k, ϕ_k) describe the orientation of class k in inclination and azimuth. Trunk size and orientation are defined in terms of similar random variables $(l_t, d_t; \theta_t, \phi_t)$. Each of these classes may be divided further into sub-classes as appropriate for the canopy being considered. A given canopy may, for example, include two or three classes of branches representing primary, secondary and tertiary branching structures.

Canopy-level random variables include the crown shape factor and PDF describing the size distribution of crowns. These shape parameters are relevant only for canopies with open crown layer geometries. Equations (2.1) and (2.2) conveniently describe a wide variety of crown shape factors in Cartesian coordinates with the z-axis directed in the zenith direction:

$$\left(\frac{2x}{a}\right)^{\alpha} + \left(\frac{2y}{b}\right)^{\beta} + \left(\frac{2z}{c}\right)^{\gamma} = 1, \tag{2.1}$$

$$\left(\frac{2x}{a}\right)^{\alpha} + \left(\frac{2y}{b}\right)^{\beta} - \left(1 - \frac{z}{c}\right) = 0. \tag{2.2}$$

Equation (2.1) describes crowns with ellipsoidal shapes while (2.2) describes those with conical shapes. By choosing appropriate values for the shape factor constants a, b, c, α, β and γ, it is possible to simulate many different crown shapes. Table 2.3 lists values of the constants for a few of the simple shapes. The constants a or b

and the constant c represent the maximum diameter and height of the crown. More complex shapes may be simulated by allowing values for these constants to vary with quadrant or by combining the two equations (Horn, [26]). The crown shape PDF, $f_{cr}(a, b, c; \alpha, \beta, \gamma)$, is defined over the domain of the shape factor constants, allowing for a convenient statistical description of the shape and size of tree crowns within a canopy.

Table 2.3: Values of Shape Factor Constants for Simple Crown Shapes.

Crown Shape	Shape Factor Constants	
Equation 2.1:		
Spherical	$a = b = c;$	$\alpha = \beta = \gamma = 2$
Oblate Spheroid	$a = b, c < a;$	$\alpha = \beta = \gamma = 2$
Prolate Spheroid	$a = b, c > a;$	$\alpha = \beta = \gamma = 2$
Square	$a = b = c;$	$\alpha = \beta = \gamma \rightarrow \infty$
Oblate Square Column	$a = b, c < a;$	$\alpha = \beta = \gamma \rightarrow \infty$
Prolate Square Column	$a = b, c > a;$	$\alpha = \beta = \gamma \rightarrow \infty$
Equation 2.2:		
Circular Cone	$a = b;$	$\alpha = \beta = 2$

2.2 Radiative Transfer Theory

Radiative transfer theory deals with the transport of energy through a medium containing particles that absorb, emit and scatter radiation (Chandrasekhar [4]; Ishimaru [27]; Tsang *et al.*, [60]; Ulaby and Elachi, [62]; Ulaby *et al.*, [70]). At microwave frequencies, the intensity that propagates through a vegetation medium will in general exhibit some degree of polarization. Therefore, this discussion defines quantities that are applicable to the solution of the vector radiative transfer equation, which accounts for the polarization state of the intensity.

The vector radiative transfer equation is formulated in terms of the vector specific intensity $\mathbf{I}(\mathbf{r}, \hat{\mathbf{p}})$ where $\mathbf{r}$ is a position vector and $\hat{\mathbf{p}}$ denotes the direction of prop-

agation. The electric field of an elliptically polarized monochromatic plane wave propagating in the direction $\hat{\mathbf{k}}$ in a medium with intrinsic impedance η may be described as

$$\mathbf{E} = \left(E_v \hat{\mathbf{v}} + E_h \hat{\mathbf{h}}\right) e^{i\mathbf{k}\cdot\mathbf{r}}, \tag{2.3}$$

where $\hat{\mathbf{v}}$ and $\hat{\mathbf{h}}$ are the unit vertical and horizontal polarization vectors. The corresponding vector specific intensity $\mathbf{I}$ is defined in terms of the modified Stokes vector $\mathbf{F}_m$ by the relation:

$$\mathbf{I} = \mathbf{F}_m \,/\eta = \begin{bmatrix} I_v \\ I_h \\ U \\ V \end{bmatrix} /\eta = \begin{bmatrix} |\, E_v \,|^2 \\ |\, E_h \,|^2 \\ 2\,\mathrm{Re}(E_v\, E_h^*) \\ 2\,\mathrm{Im}(E_v\, E_h^*) \end{bmatrix} / \eta \ . \tag{2.4}$$

The specific intensity $\mathbf{I}^s$ scattered by a single particle is related to the incident specific intensity $\mathbf{I}^i$ by

$$\mathbf{I}^s(\theta_s, \phi_s) \ = \ \frac{1}{r^2}\, \mathcal{L}_m(\theta_s, \phi_s; \theta_i, \phi_i; \theta_j, \phi_j)\ \mathbf{I}^i(\theta_i, \phi_i)\,, \tag{2.5}$$

where (θ_s, ϕ_s) defines the scattered direction in inclination and azimuth, (θ_i, ϕ_i) defines the incident direction, (θ_j, ϕ_j) defines the particle orientation, and

$$\mathcal{L}_m = \begin{bmatrix} |S_{vv}|^2 & |S_{vh}|^2 & \mathrm{Re}(S_{vh}^* S_{vv}) & -\mathrm{Im}(S_{vh}^* S_{vv}) \\ |S_{hv}|^2 & |S_{hh}|^2 & \mathrm{Re}(S_{hh}^* S_{hv}) & -\mathrm{Im}(S_{hv} S_{hh}^*) \\ 2\mathrm{Re}(S_{vv} S_{hv}^*) & 2\mathrm{Re}(S_{vh} S_{hh}^*) & \mathrm{Re}(S_{vv} S_{hh}^* + S_{vh} S_{hv}^*) & -\mathrm{Im}(S_{vv} S_{hh}^* - S_{vh} S_{hv}^*) \\ 2\mathrm{Im}(S_{vv} S_{hv}^*) & 2\mathrm{Im}(S_{vh} S_{hh}^*) & \mathrm{Im}(S_{vv} S_{hh}^* + S_{vh} S_{hv}^*) & \mathrm{Re}(S_{vv} S_{hh}^* - S_{vh} S_{hv}^*) \end{bmatrix} \tag{2.6}$$

is the modified Mueller matrix, defined in terms of the elements of the particle scattering matrix $\mathcal{S}$ that relate the incident and scattered electric fields $\mathbf{E}^i$ and $\mathbf{E}^s$ as follows:

$$\begin{bmatrix} E_v^s \\ E_h^s \end{bmatrix} = \frac{e^{ikr}}{r} \begin{bmatrix} S_{vv} & S_{vh} \\ S_{hv} & S_{hh} \end{bmatrix} \begin{bmatrix} E_v^i \\ E_h^i \end{bmatrix} \ . \tag{2.7}$$

For a distributed target, the scattered specific intensity must be defined in terms of the net electric field $\mathbf{E}^s$, representing the vector sum of all fields scattered from

an illuminated area A subtending a solid angle $\mathrm{d}\Omega = A\cos\theta_s/r^2$ at the range r from the surface. The angle θ_s is the angle between the outward normal to A and the scattering direction. In this case,

$$\mathbf{I}^s\,\mathrm{d}\Omega = \begin{bmatrix} I_v^s \\ I_h^s \\ U^s \\ V^s \end{bmatrix} \mathrm{d}\Omega\,/\eta = \begin{bmatrix} |\,E_v^s\,|^2 \\ |\,E_h^s\,|^2 \\ 2\mathrm{Re}(E_v^s E_h^{s*}) \\ 2\mathrm{Im}(E_v^s E_h^{s*}) \end{bmatrix} / \eta\ . \tag{2.8}$$

The integral form of the vector radiative transfer equation for a medium in a free space background is (Chandrasekhar [4]):

$$\mathbf{I}(\mu,\phi,z) = e^{-\boldsymbol{\kappa}z/\mu}\mathbf{I}(\mu,\phi,0) + \int_0^z e^{-\boldsymbol{\kappa}(z-z')/\mu}\mathbf{F}(\mu,\phi,z')\mathrm{d}z', \tag{2.9}$$

where $\boldsymbol{\kappa}$ is the 4×4 extinction matrix of the medium, $\mathbf{F}$ is the source function, $\mu = \cos\theta$ and $z \geq 0$. The first term accounts for extinction of the intensity as it propagates through the distance z/μ in the direction (μ,ϕ). The source function

$$\mathbf{F}(\mu,\phi,z') = \int \mathcal{P}\,(\theta_s,\phi_s;\theta_i,\phi_i)\,\mathbf{I}\,(\mu_i,\phi_i)\,\mathrm{d}\Omega_i \tag{2.10}$$

with $\mathrm{d}\Omega_i = \mathrm{d}\mu_i\mathrm{d}\phi_i = \sin\theta_i\mathrm{d}\theta_i\mathrm{d}\phi_i$ accounts for the scattering of energy propagating in the direction (θ_i,ϕ_i) into the direction (θ_s,ϕ_s) *via* the phase matrix $\mathcal{P}\,(\theta_s,\phi_s;\theta_i,\phi_i)$. The effect of self emission has been ignored here because in radar remote sensing its contribution is negligibly small in comparison to the other terms in the equation.

One of the fundamental assumptions of radiative transfer theory is that in a medium containing a random distribution of particles, the waves scattered from the particles are random in phase, thereby allowing the addition of the waves to be performed incoherently. That is, the Stokes parameters of the mixture are the sum of the respective Stokes parameters of the separate waves (Tsang *et al.*, [60]; p. 127).

If the medium contains N_k particles per unit volume that are distributed over the size and orientation parameters s_k and (θ_k, ϕ_k), then

$$\begin{aligned} \mathcal{P}_k\ (\theta_s, \phi_s; \theta_i, \phi_i) &= N_k \left\langle\ \mathcal{L}_k\left(\theta_s, \phi_s; \theta_i, \phi_i; \mathrm{s}_k; \theta_k, \phi_k\right)\right\rangle \\ &= N_k \int\int\int f_k\left(\mathrm{s}_k; \theta_k, \phi_k\right) \\ &\quad \cdot \mathcal{L}_k\left(\theta_s, \phi_s; \theta_i, \phi_i; \mathrm{s}_k; \theta_k, \phi_k\right) \mathrm{d}\mathrm{s}_k \mathrm{d}\theta_k \mathrm{d}\phi_k \end{aligned} \tag{2.11}$$

where $f_k\left(\mathrm{s}_k; \theta_k, \phi_k\right)$ is the joint probability density function over the shape, size, and orientation parameters $(\mathrm{s}_k; \theta_k, \phi_k)$ of the particles. If the medium contains K classes of particles, the total phase matrix is

$$\mathcal{P}\ (\theta_s,\ \phi_s;\ \theta_i,\ \phi_i) = \sum_{k=1}^{K} \mathcal{P}_k\ (\theta_s,\ \phi_s;\ \theta_i,\ \phi_i) \tag{2.12}$$

where the summation over k represents an addition over all of the K constituent classes.

For a medium containing arbitrary particles, the extinction matrix is given by (Ishimaru and Cheung [28]):

$$\boldsymbol{\kappa} = \begin{bmatrix} -2\mathrm{Re}(M_{vv}) & 0 & -\mathrm{Re}(M_{vh}) & -\mathrm{Im}(M_{vh}) \\ 0 & -2\mathrm{Re}(M_{hh}) & -\mathrm{Re}(M_{hv}) & \mathrm{Im}(M_{hv}) \\ -2\mathrm{Re}(M_{hv}) & -2\mathrm{Re}(M_{vh}) & -\mathrm{Re}(M_{vv}+M_{hh}) & \mathrm{Im}(M_{vv}-M_{hh}) \\ 2\mathrm{Im}(M_{hv}) & -2\mathrm{Im}(M_{vh}) & -\mathrm{Im}(M_{vv}-M_{hh}) & -\mathrm{Re}(M_{vv}+M_{hh}) \end{bmatrix} \tag{2.13}$$

where

$$\mathcal{M}_{mn} = \sum_{k=1}^{K} \frac{i2\pi N_k}{k_0} \langle S_{mnk}(\theta_i, \phi_i; \theta_i, \phi_i; \theta_j, \phi_j)\rangle_k; \qquad m, n = v, h. \tag{2.14}$$

The summation over k represents an addition over the K particle classes, N_k is the number density per unit volume of each class, $\langle\ \ \rangle_k$ represents statistical averages over the size and orientation distributions of class k, and S_{mnk} is the scattering amplitude for forward scattering corresponding to polarization mn for class k.

The quantity $e^{-\kappa z/\mu}$ is defined by

$$e^{\kappa z/\mu} = \mathcal{E}(\mu,\phi)\mathcal{D}(\mu,\phi;-z/\mu)\mathcal{E}^{-1}(\mu,\phi), \tag{2.15}$$

with the 4×4 eigenmatrix $\mathcal{E}(\mu,\phi)$ given by

$$\mathcal{E}(\theta,\phi) = \begin{bmatrix} 1 & b_2^* & b_2 & |\, b_2 \,|^2 \\ |\, b_1 \,|^2 & b_1 & b_1^* & 1 \\ 2\mathrm{Re}(b_1) & 1+b_1 b_2^* & 1+b_1^* b_2 & 2\mathrm{Re}(b_2) \\ -2\mathrm{Im}(b_1) & -i(1-b_1 b_2^*) & i(1-b_1^* b_2) & 2\mathrm{Im}(b_2) \end{bmatrix}, \tag{2.16}$$

where

$$b_1 = \frac{2M_{hv}}{M_{vv}-M_{hh}+r}, \tag{2.17}$$

$$b_2 = \frac{2M_{vh}}{-M_{vv}+M_{hh}-r}, \tag{2.18}$$

$$r = \{(M_{vv}-M_{hh})^2 + 4M_{hv}M_{vh}\}^{1/2}. \tag{2.19}$$

$\mathcal{D}(\mu,\phi;-z/\mu)$ is a diagonal matrix with elements:

$$[\mathcal{D}(\mu,\phi;-z/\mu)]_{ii} = e^{-\beta_i(\mu,\phi)z/\mu} \tag{2.20}$$

where $\beta_i(\mu,\phi)$ represents the ith eigenvalue of $\kappa(\mu,\phi)$. The eigenvalues are given by

$$\beta(\hat{\mathrm{s}}) = \begin{bmatrix} \beta_1(\theta,\phi) \\ \beta_2(\theta,\phi) \\ \beta_3(\theta,\phi) \\ \beta_4(\theta,\phi) \end{bmatrix} = -\mathrm{Re}(M_{vv}+M_{hh}) + \frac{1}{2}\begin{bmatrix} -r-r^* \\ -r+r^* \\ r-r^* \\ r+r^* \end{bmatrix} \tag{2.21}$$

$$= \begin{bmatrix} 2\mathrm{Im}K_1 \\ iK_2^* - iK_1 \\ iK_1^* - iK_2 \\ 2\mathrm{Im}K_2 \end{bmatrix}, \tag{2.22}$$

where

$$K_1 = k_0 - \frac{i}{2}[M_{vv} + M_{hh} + r] \tag{2.23}$$

$$K_2 = k_0 - \frac{i}{2}[M_{vv} + M_{hh} - r]. \tag{2.24}$$

For particles that do not depolarize, $M_{hv} = M_{vh} = 0$ and $\mathcal{E}$ becomes

$$\mathcal{E} = \begin{bmatrix} 1 & 0 & 0 & 0 \\ 0 & 0 & 0 & 1 \\ 0 & 1 & 1 & 0 \\ 0 & -i & i & 0 \end{bmatrix}. \tag{2.25}$$

In solving (2.9) in a vegetation canopy, an expression is sought that relates the vector specific intensity $\mathbf{I}^i$ incident on the canopy to that which is scattered from the canopy $\mathbf{I}^s$. As will be seen in Chapter III, this is achieved through a 4×4 transformation matrix $\mathcal{T}$ such that $\mathbf{I}^s = \mathcal{T}\ \mathbf{I}^i$. $\mathcal{T}$ may be used to compute the linearly polarized canopy backscattering coefficients:

$$\sigma^0_{vv} = 4\pi \cos\theta_0 [\mathcal{T}]_{11} \tag{2.26}$$

$$\sigma^0_{hh} = 4\pi \cos\theta_0 [\mathcal{T}]_{22} \tag{2.27}$$

$$\sigma^0_{hv} = 4\pi \cos\theta_0 [\mathcal{T}]_{21} \tag{2.28}$$

$$\sigma^0_{vh} = 4\pi \cos\theta_0 [\mathcal{T}]_{12} \tag{2.29}$$

or, by applying wave synthesis techniques, the matrix may be used to compute the backscattering coefficient for any transmitting and receiving polarization combination. The techniques involved in doing this are discussed in Section 2.3.

2.3 Radar Polarimetry

The specific intensity scattered by a medium may be related to the intensity incident upon the medium by

$$\mathbf{I}^s = \mathcal{T}\,\mathbf{I}^i \tag{2.30}$$

where $\mathcal{T}$ is a 4×4 transformation matrix. Given $\mathcal{T}$, the received power may be computed for any possible combination of transmitting and receiving polarizations. The process is called polarization synthesis (van Zyl *et al.*,[75]; Zebker *et al.*, [85]; Ulaby and Elachi [62]). This section reviews some of the principles of radar polarimetry as they apply to polarization synthesis and to the radiative transfer problem.

The polarization state of an electromagnetic wave propagating in the $\hat{\mathbf{k}}$ direction may be defined in terms of the ellipse shown in Figure 2.2. The electric field for such a wave is described by

$$\mathbf{E} = \left(E_v \hat{\mathbf{v}} + E_h\, \hat{\mathbf{h}}\right) e^{ik\hat{\mathbf{k}}\cdot\mathbf{r}} \tag{2.31}$$

where the electric field components E_v and E_h are complex quantities, $\hat{\mathbf{v}}$ and $\hat{\mathbf{h}}$ are the polarization basis vectors and the wave travels in the $\hat{\mathbf{k}}$ direction (out of the page). The unit vectors $\hat{\mathbf{v}}$ and $\hat{\mathbf{h}}$ have been defined such that they are oriented in a direction consistent with scattering in a standard spherical coordinate system. The polarization ellipse represents the locus of points that the tip of the electric field vector traces out as a function of time. In the general case, the ellipse axes ξ and ζ are rotated with respect to the polarization basis vectors through a rotation angle ψ measured clockwise from the $\hat{\mathbf{v}}$ axis. The degree of ellipticity is defined by the ellipticity angle χ measured clockwise from the ξ axis. The limits of ψ are $-90^o \geq \psi \leq 90^o$ and the limits of χ are $-45^o \geq \chi \leq 45^o$. The sense of rotation of the electric field vector around the ellipse corresponds to the handedness of the wave.

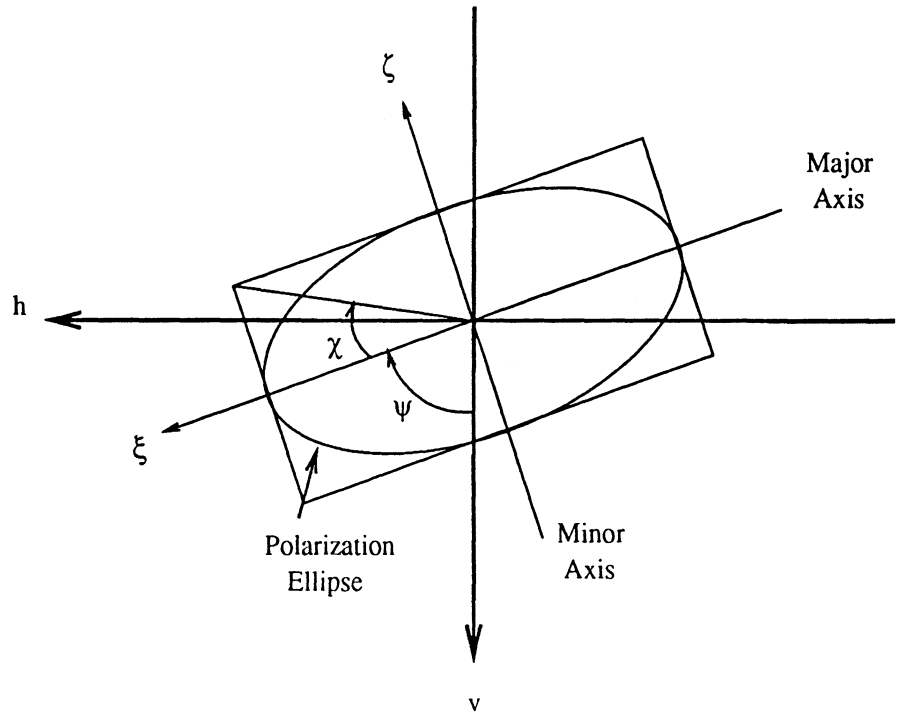

Figure 2.2: Polarization ellipse illustrating the polarization state of an electromagnetic wave traveling in the $\hat{\mathbf{k}}$ direction (out of the page). The angles χ and ψ are measured clockwise.

The wave is left-handed if $\chi > 0$ and right-handed if $\chi < 0$. The wave is linearly polarized for $\chi = 0$ and circularly polarized for $\chi = 45°$.

The polarization state of the wave may be expressed in terms of the modified Stokes vector

$$\mathbf{F}_m = \begin{bmatrix} I_v \\ I_h \\ U \\ V \end{bmatrix} = \begin{bmatrix} |\, E_v \,|^2 \\ |\, E_h \,|^2 \\ 2\,\mathrm{Re}\,(E_v\, E_h^*) \\ 2\,\mathrm{Im}\,(E_v\, E_h^*) \end{bmatrix} = \begin{bmatrix} \frac{1}{2}\,(1 + \cos 2\psi \cos 2\chi) \\ \frac{1}{2}\,(1 - \cos 2\psi \cos 2\chi) \\ \sin 2\psi \cos 2\chi \\ \sin 2\chi \end{bmatrix} I_0 \qquad (2.32)$$

where $I_0 = |E_v|^2 + |E_h|^2$ is proportional to the total intensity of the wave. For a completely polarized wave, the elements of the Stokes vector are related by $I_0^2 =$

$(I_v - I_h)^2 + U^2 + V^2$.

Given the polarization angles (ψ_t, χ_t) of a particular transmitted wave and (ψ_r, χ_r) for a received wave, the scattering cross section of the target is given by

$$\sigma_{rt}(\psi_r, \chi_r, \psi_t, \chi_t) = 4\pi \, \mathbf{A}_m^r(\psi_r, \chi_r) \cdot \mathcal{M}_m \mathbf{A}_m^t(\psi_t, \chi_t) \tag{2.33}$$

where $\mathbf{A}_m^t(\psi_t, \chi_t) = \mathbf{F}_m^t(\psi_t, \chi_t)/I_0$ and $\mathbf{A}_m^r(\psi_r, \chi_r) = \mathbf{F}_m^r(\psi_r, \chi_r)/I_0$ are the normalized modified Stokes vectors for the transmit and receive waves and $\mathcal{M}_m$ is the modified Stokes scattering operator of the target. For a point target

$$\mathcal{M}_m = \mathcal{Q}\mathcal{L}_m \tag{2.34}$$

where $\mathcal{L}_m$ is the modified Mueller matrix given by Equation (2.6) and

$$\mathcal{Q} = \begin{bmatrix} 1 & 0 & 0 & 0 \\ 0 & 1 & 0 & 0 \\ 0 & 0 & \frac{1}{2} & 0 \\ 0 & 0 & 0 & -\frac{1}{2} \end{bmatrix} . \tag{2.35}$$

The modified Stokes scattering operator $\mathcal{M}_m$ for a distributed medium illuminated over an area A is

$$\mathcal{M}_m = A \cos \theta_s \mathcal{Q}\mathcal{T} \tag{2.36}$$

where $\mathcal{T}$ is the transformation matrix of the medium and θ_s is the angle between the surface normal and the scattered direction. For a distributed target, the scattering cross section is

$$\sigma_{rt}^0 = 4\pi \cos\theta_s \mathbf{A}_m^r \cdot \mathcal{Q} \, \mathcal{T} \, \mathbf{A}_m^t \ . \tag{2.37}$$

The polarization signature or polarization response (Agrawal, A. P., and W. M. Boerner, [1]; Ulaby and Elachi, [62]; van Zyl,[74]; van Zyl *et al.*, [75]; Zebker *et al.*, [85]) of a point or distributed target is a convenient graphical representation of

(2.33) or (2.37) that consists of a plot of the synthesized scattering cross section as a function of the polarization angles (ψ_t, χ_t) of the transmitted wave. Three types of responses will be presented in this study. The co-polarized response represents the scattering cross section synthesized for receive and transmit antennas having identical polarization $(\psi_r = \psi_t, \chi_r = \chi_t)$. The cross-polarized response corresponds to the case in which the receive antenna is polarized orthogonal to the transmit antenna $(\psi_r = \psi_t + 90^o, \chi_r = -\chi_t)$. The linear-polarized response corresponds to the synthesized scattering cross section for all combinations of linear polarization. This response is synthesized by setting $\chi_r = \chi_t = 0$ and $\psi_r = \psi_t + \delta$ where $0 \leq \delta \leq 90^o$ is defined as the linear polarization angle. The condition $\delta = 0$ represents like-polarized cross section and $\delta = 90^o$ represents cross-polarized cross section. All polarization responses presented here for a given target will be normalized to the maximum scattering cross section synthesized for that target.

As an example, the modified Stokes scattering operator of a short, thin conducting cylinder of radius a and length l oriented parallel to the v axis is (Ulaby and Elachi,[62]):

$$\mathcal{M}_m = \frac{k_0^4 l^6}{9\left[\ln(4l/a) - 1\right]^2} \begin{pmatrix} 1 & 0 & 0 & 0 \\ 0 & 0 & 0 & 0 \\ 0 & 0 & 0 & 0 \\ 0 & 0 & 0 & 0 \end{pmatrix} . \tag{2.38}$$

The polarization response may be synthesized from (2.33) and is presented in Figure 2.3. The co-polarized response shows a maximum value at σ_{vv} $(\psi = 0, \chi = 0)$ and a minimum at σ_{hh} $(\psi = \pm 90°, \chi = 0)$. The cross-polarized response shows minima at σ_{vv} and σ_{hh}. The linear-polarized response illustrates the behavior of σ_{rt} as a function of the linear polarization angle δ.

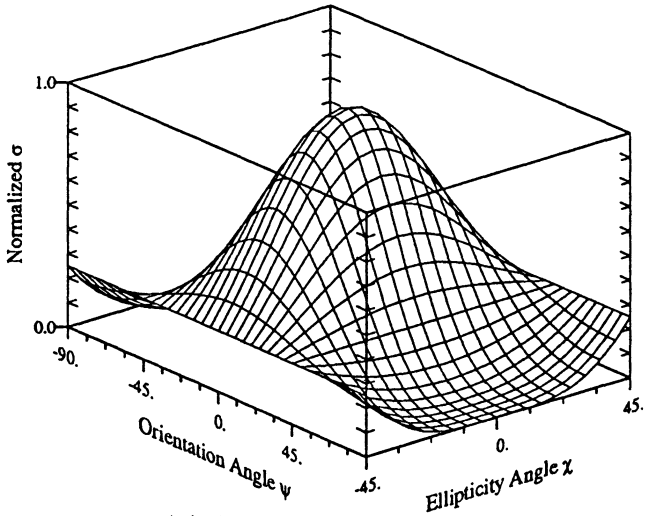

(a) Co-polarized response.

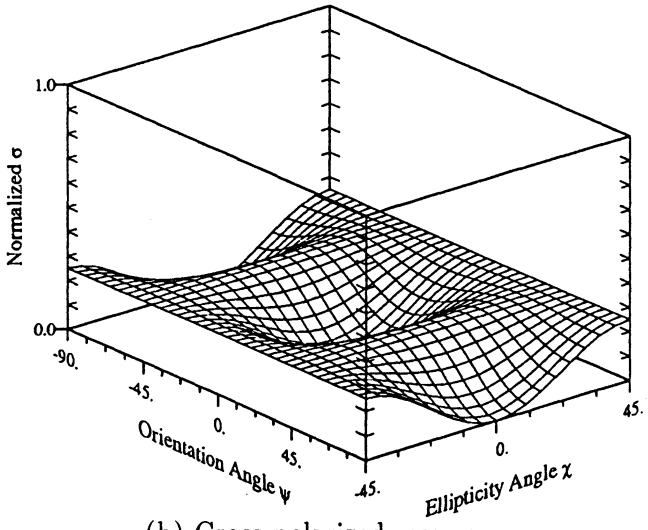

(b) Cross-polarized response.

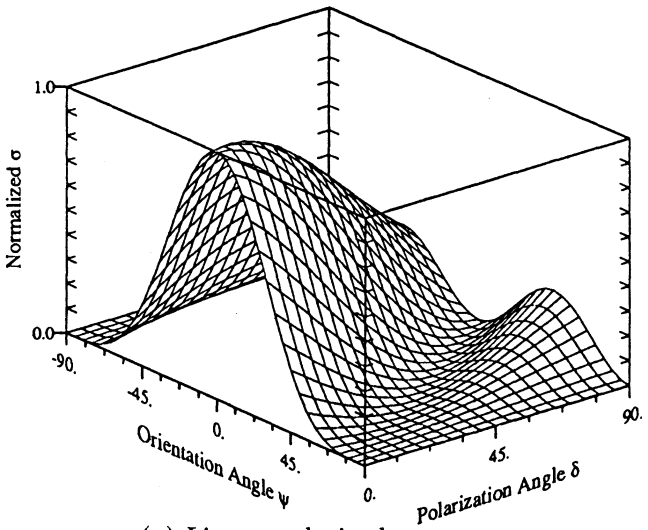

(c) Linear-polarized response.

Figure 2.3: Polarization response of a short, thin conducting cylinder oriented vertically.

CHAPTER III

RADAR BACKSCATTER MODEL FOR A CLOSED-CROWN TREE CANOPY

A first-order solution for the radiative transfer equation useful in simulating microwave backscatter from tree canopies with continuous (closed) crown layer geometries has been developed at The University of Michigan and is presented by Ulaby *et al.,* [67],[68], [69], Ulaby and Elachi, [62] and Sarabandi [50]. This model, which represents the first version of the Michigan Microwave Canopy Scattering model (MIMICS I) has been developed specifically for modeling microwave backscatter from tree canopies but is also useful for a variety of other applications in studying remote sensing of vegetation. MIMICS I is a fully polarimetric model and is valid over a wide range of incidence angles. The first section of this chapter presents the derivation of MIMICS I. Then, Section 3.2 introduces a technique that is useful in accounting for various types of ground surface states, including the case of a snow-covered ground surface or a foliar canopy understory. Section 3.3 briefly discusses some applications of this model. Detailed modeling analysis and applications will be presented in Chapter VI.

3.1 MIMICS I Solution for the Radiative Transfer Equations

For purposes of solving the radiative transfer equations, a forest canopy is modeled as shown in Figure 3.1. The canopy consists of two distinct horizontal vegetation layers over a dielectric ground surface. The top (crown) layer consists of the tree crowns and is comprised of an appropriate combination of leaves, needles, and branches. This layer has height d, is statistically homogeneous, and is continuous in the horizontal direction. The bottom (trunk) layer has height H_t and consists of the tree trunks.

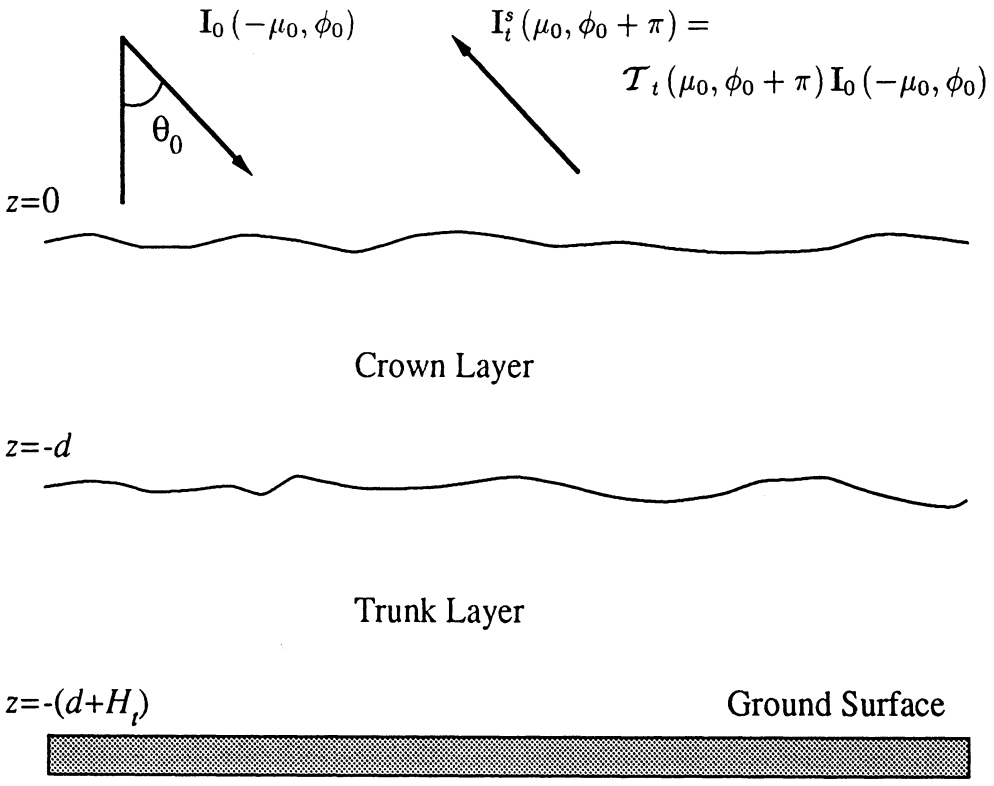

Figure 3.1: Forest Canopy Model.

The total backscattered intensity $\mathbf{I}_t^s(\mu_0, \phi_0 + \pi)$ may be related to the intensity

$\mathbf{I}_0$ incident upon the canopy through the transformation matrix $\mathcal{T}_t(\mu_0, \phi_0 + \pi)$ by

$$\mathbf{I}_t^s(\mu_0, \phi_0 + \pi) = \mathcal{T}_t(\mu_0, \phi_0 + \pi)\mathbf{I}_0(-\mu_0, \phi_0). \tag{3.1}$$

The 4×4 matrix $\mathcal{T}_t(\mu_0, \phi_0 + \pi)$ will be called the total canopy backscattering transformation matrix.

To solve for $\mathcal{T}_t(\mu_0, \phi_0 + \pi)$, the problem is divided into two parts. First, a solution is found with the ground surface treated as a specular dielectric interface. This assumption is reasonable as long as the intensity scattered by this surface is dominated by its coherent component in the specular direction. If the surface is very rough or its mean slope is not zero relative to the vertical direction, this assumption will not hold. The scattered intensity for a vegetation layer over a specular surface is

$$\mathbf{I}^s(\mu_0, \phi_0 + \pi) = \mathcal{T}_c(\mu_0, \phi_0 + \pi)\mathbf{I}_0(-\mu_0, \phi_0), \tag{3.2}$$

where $\mathcal{T}_c(\mu_0, \phi_0)$ is the canopy transformation matrix relating the incident and scattered intensities in the absence of direct backscatter from the ground surface.

In the second part of the problem, direct backscatter from the ground surface is accounted for by expressing the backscattered intensity as

$$\mathbf{I}_g^s(\mu_0, \phi_0 + \pi) = \mathcal{T}_g(\mu_0, \phi_0 + \pi)\mathbf{I}_0(-\mu_0, \phi_0), \tag{3.3}$$

where $\mathcal{T}_g(\mu_0, \phi_0 + \pi)$ is the transformation matrix that accounts for propagation through the canopy down to the ground surface, backscatter by the ground surface, and propagation again through the canopy back to the radar. Combining (3.2) and (3.3) yields the total backscattered intensity in terms of the total canopy backscattering transformation matrix $\mathcal{T}_t$:

$$\mathbf{I}_t^s(\mu_0, \phi_0 + \pi) = [\mathcal{T}_c(\mu_0, \phi_0 + \pi) + \mathcal{T}_g(\mu_0, \phi_0 + \pi)]\,\mathbf{I}_0(-\mu_0, \phi_0) \tag{3.4}$$

$$= \mathcal{T}_t(\mu_0, \phi_0 + \pi)\mathbf{I}_0(-\mu_0, \phi_0). \tag{3.5}$$

Consider first the problem of two homogeneous layers over a specular surface. To solve for $\mathcal{T}_c(\mu_0, \phi_0)$, the integral form of the radiative transfer equation is set up separately in the crown and trunk layers. Boundary conditions are applied at the layer interfaces and the equations are solved iteratively to obtain the zero- and first-order solutions. This technique is applicable for weakly scattering media in which the scattering albedo is small.

The geometry of this problem is illustrated in Figure 3.2. The specific intensity in each layer is separated into upward-going $\mathbf{I}^+(\mu, \phi, z)$ and downward-going $\mathbf{I}^-(-\mu, \phi, z)$ components, noting that $\mu = \cos\theta$ and θ varies between 0 and $\pi/2$. The radiative transfer equation will then be expressed as a set of coupled equations in each layer.

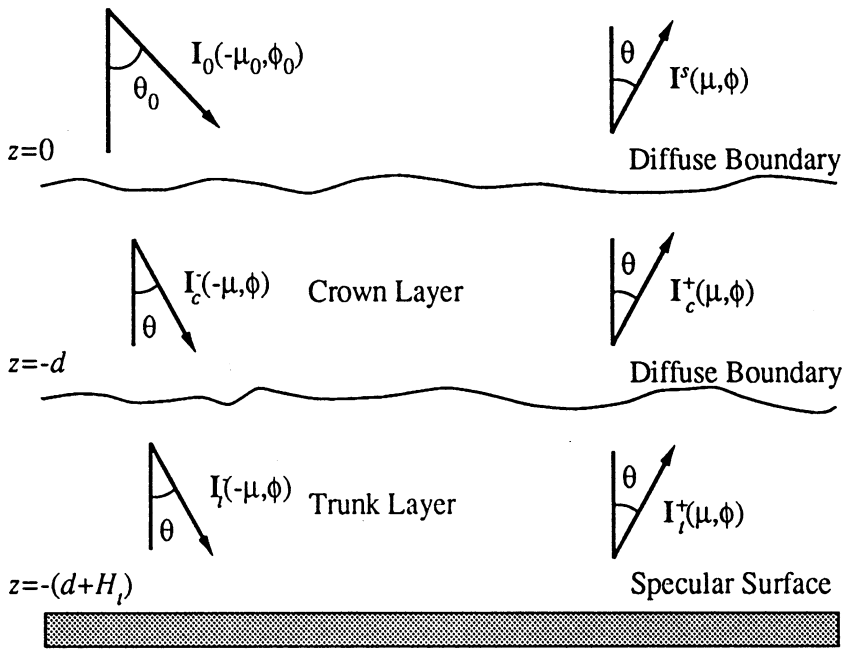

Figure 3.2: Problem Geometry showing the positive- and negative-going intensities in the crown and trunk layers.

In the crown layer, the coupled radiative transfer equations are

$$\mathbf{I}_c^+(\mu,\phi,z) = \mathrm{e}^{-\boldsymbol{\kappa}_c^+(z+d)/\mu}\mathbf{I}_c^+(\mu,\phi,-d) + \int_{-d}^{z}\mathrm{e}^{-\boldsymbol{\kappa}_c^+(z-z')/\mu}\boldsymbol{\mathcal{F}}_c^+(\mu,\phi,z')\,\mathrm{d}z' \tag{3.6}$$

$$\mathbf{I}_c^-(-\mu,\phi,z) = \mathrm{e}^{\boldsymbol{\kappa}_c^- z/\mu}\mathbf{I}_c^-(-\mu,\phi,0) + \int_{z}^{0}\mathrm{e}^{\boldsymbol{\kappa}_c^-(z-z')/\mu}\boldsymbol{\mathcal{F}}_c^-(-\mu,\phi,z')\,\mathrm{d}z' \tag{3.7}$$

where the subscript c has been used to denote quantities specific to the crown layer. Similarly, the equations:

$$\begin{aligned}\mathbf{I}_t^+(\mu,\phi,z) &= \mathrm{e}^{-\boldsymbol{\kappa}_t^+[z+(d+H_t)]/\mu}\mathbf{I}_t^+[\mu,\phi,-(d+H_t)] \\ &\quad + \int_{-(d+H_t)}^{z}\mathrm{e}^{-\boldsymbol{\kappa}_t^+(z-z')/\mu}\boldsymbol{\mathcal{F}}_t^+(\mu,\phi,z')\,\mathrm{d}z' \qquad (3.8)\\ \mathbf{I}_t^-(-\mu,\phi,z) &= \mathrm{e}^{\boldsymbol{\kappa}_t^-(z+d)/\mu}\mathbf{I}_t^-(-\mu,\phi,-d) \\ &\quad + \int_{z}^{-d}\mathrm{e}^{\boldsymbol{\kappa}_t^-(z-z')/\mu}\boldsymbol{\mathcal{F}}_t^-(-\mu,\phi,z')\,\mathrm{d}z' \qquad (3.9)\end{aligned}$$

apply in the trunk layer.

In the trunk layer, for cylindrical trunks oriented near-vertical with length greater than the propagating wavelength ($H_t \gg \lambda$), only two types of scattering will be considered. These are forward scattering from the trunks that gives rise to extinction of the forward propagating field and specular scattering from the trunks that gives rise to a ground-trunk interaction contribution to the field backscattered from the canopy. This means that the phase matrix in the trunk layer is significant only in the forward and specular scatter directions and that direct backscatter form the trunk layer may be neglected. The source functions in the crown and trunk layers are then

$$\begin{aligned}\mathbf{F}_c^+(\mu,\phi,z) = \frac{1}{\mu}\Bigg[&\int_0^{2\pi}\int_0^1 \boldsymbol{\mathcal{P}}_c(\mu,\phi;\mu',\phi')\mathbf{I}_c^+(\mu',\phi',z)\,\mathrm{d}\Omega' \\ &+ \int_0^{2\pi}\int_0^1 \boldsymbol{\mathcal{P}}_c(\mu,\phi;-\mu',\phi')\mathbf{I}_c^-(-\mu',\phi',z)\,\mathrm{d}\Omega'\Bigg]\end{aligned} \tag{3.10}$$

$$\mathbf{F}_c^-(-\mu,\phi,z)=\frac{1}{\mu}\left[\int_0^{2\pi}\int_0^1 \mathcal{P}_c(-\mu,\phi;\mu',\phi')\mathbf{I}_c^+(\mu',\phi',z)\,\mathrm{d}\Omega'\right.$$
$$\left.+\int_0^{2\pi}\int_0^1 \mathcal{P}_c(-\mu,\phi;-\mu',\phi')\mathbf{I}_c^-(-\mu',\phi',z)\,\mathrm{d}\Omega'\right] \tag{3.11}$$

and

$$\mathbf{F}_t^+(\mu,\phi,z)=\frac{1}{\mu}\int_0^{2\pi}\int_0^1 \mathcal{P}_t(\mu,\phi;\mu',\phi')\mathbf{I}_t^+(\mu',\phi',z)\delta_k(\mu-\mu')\,\mathrm{d}\Omega' \tag{3.12}$$

$$\mathbf{F}_t^-(-\mu,\phi,z)=\frac{1}{\mu}\int_0^{2\pi}\int_0^1 \mathcal{P}_t(-\mu,\phi;-\mu',\phi')\mathbf{I}_t^-(-\mu',\phi',z)\delta_k(\mu-\mu')\,\mathrm{d}\Omega' \tag{3.13}$$

where $\delta_k(\mu-\mu')$ is the Kronecker delta function defined by

$$\delta_k(\mu-\mu')=\begin{cases}1; & \mu=\mu'\\ 0; & \text{otherwise.}\end{cases} \tag{3.14}$$

The air-crown interface ($z=0$) and the crown-trunk interface ($z=-d$) may be treated as diffuse boundaries, in which case the intensities across these interfaces become continuous. This assumption yields the boundary conditions:

$$\mathbf{I}_c^-(-\mu,\phi,0) = \mathbf{I}_0(-\mu_0,\phi_0)\,\delta(\mu-\mu_0)\,\delta(\phi-\phi_0) \tag{3.15}$$

$$\mathbf{I}_c^+(\mu,\phi,-d) = \mathbf{I}_t^+(\mu,\phi,-d) \tag{3.16}$$

$$\mathbf{I}_t^-(-\mu,\phi,-d) = \mathbf{I}_c^-(-\mu,\phi,-d) \tag{3.17}$$

$$\mathbf{I}^s(\mu,\phi) = \mathbf{I}_c^+(\mu,\phi,0). \tag{3.18}$$

At the trunk-ground interface where $z=-(d+H_t)$, we have

$$\mathbf{I}_t^+[\mu,\phi,-(d+H_t)] = \mathcal{R}(\mu)\,\mathbf{I}_t^-[-\mu,\phi,-(d+H_t)], \tag{3.19}$$

where $\mathcal{R}(\mu)$ is the reflectivity matrix of the specular surface:

$$\mathcal{R}(\mu)=\begin{bmatrix} |r_v|^2 & 0 & 0 & 0\\ 0 & |r_h|^2 & 0 & 0\\ 0 & 0 & \mathrm{Re}(r_v r_h^*) & -\mathrm{Im}(r_v r_h^*)\\ 0 & 0 & \mathrm{Im}(r_v r_h^*) & \mathrm{Re}(r_v r_h^*)\end{bmatrix} \tag{3.20}$$

where r_v and r_h are the Fresnel reflectivity coefficients for the specular surface at vertical and horizontal polarizations, respectively.

To solve for the specific intensities in each layer, these boundary conditions are applied to (3.6) through (3.9) yielding:

$$\begin{aligned}
\mathbf{I}_c^-(-\mu,\phi,z) &= \mathrm{e}^{\boldsymbol{\kappa}_c^- z/\mu}\mathbf{I}_0(-\mu_0,\phi_0)\,\delta(\mu-\mu_0)\,\delta(\phi-\phi_0) \\
&\quad + \int_z^0 \mathrm{e}^{\boldsymbol{\kappa}_c^-(z-z')/\mu}\boldsymbol{\mathcal{F}}_c^-(-\mu,\phi,z')\,\mathrm{d}z' \qquad (3.21)
\end{aligned}$$

$$\begin{aligned}
\mathbf{I}_t^-(-\mu,\phi,z) &= \mathrm{e}^{\boldsymbol{\kappa}_t^-(z+d)/\mu}\mathbf{I}_c^-(-\mu,\phi,-d) + \int_z^{-d} \mathrm{e}^{\boldsymbol{\kappa}_t^-(z-z')/\mu}\boldsymbol{\mathcal{F}}_t^-(-\mu,\phi,z')\,\mathrm{d}z' \\
&= \mathrm{e}^{\boldsymbol{\kappa}_t^-(z+d)/\mu}\mathrm{e}^{-\boldsymbol{\kappa}_c^- d/\mu}\mathbf{I}_0(-\mu_0,\phi_0)\,\delta(\mu-\mu_0)\,\delta(\phi-\phi_0) \\
&\quad + \mathrm{e}^{\boldsymbol{\kappa}_t^-(z+d)/\mu}\int_{-d}^0 \mathrm{e}^{\boldsymbol{\kappa}_c^-(-d-z')/\mu}\boldsymbol{\mathcal{F}}_c^-(-\mu,\phi,z')\,\mathrm{d}z' \\
&\quad + \int_z^{-d} \mathrm{e}^{\boldsymbol{\kappa}_t^-(z-z')/\mu}\boldsymbol{\mathcal{F}}_t^-(-\mu,\phi,z')\,\mathrm{d}z' \qquad (3.22)
\end{aligned}$$

$$\begin{aligned}
\mathbf{I}_t^+(\mu,\phi,z) &= \mathrm{e}^{-\boldsymbol{\kappa}_t^+[z+(d+H_t)]/\mu}\boldsymbol{\mathcal{R}}(\mu)\,\mathbf{I}_t^-[-\mu,\phi,-(d+H_t)] \\
&\quad + \int_{-(d+H_t)}^z \mathrm{e}^{-\boldsymbol{\kappa}_t^+(z-z')/\mu}\boldsymbol{\mathcal{F}}_t^+(\mu,\phi,z')\,\mathrm{d}z' \\
&= \mathrm{e}^{-\boldsymbol{\kappa}_t^+[z+(d+H_t)]/\mu}\boldsymbol{\mathcal{R}}(\mu)\,\mathrm{e}^{-\boldsymbol{\kappa}_t^- H_t/\mu}\mathrm{e}^{-\boldsymbol{\kappa}_c^- d/\mu} \\
&\qquad \cdot\mathbf{I}_0(-\mu_0,\phi_0)\,\delta(\mu-\mu_0)\,\delta(\phi-\phi_0) \\
&\quad + \mathrm{e}^{-\boldsymbol{\kappa}_t^+[z+(d+H_t)]/\mu}\boldsymbol{\mathcal{R}}(\mu)\,\mathrm{e}^{-\boldsymbol{\kappa}_t^- H_t/\mu} \\
&\qquad \int_{-d}^0 \mathrm{e}^{\boldsymbol{\kappa}_c^-(-d-z')/\mu}\boldsymbol{\mathcal{F}}_c^-(-\mu,\phi,z')\,\mathrm{d}z' \\
&\quad + \mathrm{e}^{-\boldsymbol{\kappa}_t^+[z+(d+H_t)]/\mu}\boldsymbol{\mathcal{R}}(\mu) \\
&\qquad \int_{-(d+H_t)}^{-d} \mathrm{e}^{\boldsymbol{\kappa}_t^-(-(d+H_t)-z')/\mu}\boldsymbol{\mathcal{F}}_t^-(-\mu,\phi,z')\,\mathrm{d}z' \\
&\quad + \int_{-(d+H_t)}^z \mathrm{e}^{-\boldsymbol{\kappa}_t^+(z-z')/\mu}\boldsymbol{\mathcal{F}}_t^+(\mu,\phi,z')\,\mathrm{d}z' \qquad (3.23)
\end{aligned}$$

$$
\begin{aligned}
\mathbf{I}_c^+(\mu,\phi,z) &= e^{-\boldsymbol{\kappa}_c^+(z+d)/\mu}\mathbf{I}_t^+(\mu,\phi,-d) + \int_{-d}^{z} e^{-\boldsymbol{\kappa}_c^+(z-z')/\mu}\boldsymbol{\mathcal{F}}_c^+(\mu,\phi,z')\,dz' \\
&= e^{-\boldsymbol{\kappa}_c^+(z+d)/\mu} e^{-\boldsymbol{\kappa}_t^+ H_t/\mu}\boldsymbol{\mathcal{R}}(\mu)\, e^{-\boldsymbol{\kappa}_t^- H_t/\mu} e^{-\boldsymbol{\kappa}_c^- d/\mu} \\
&\qquad \cdot \mathbf{I}_0(-\mu_0,\phi_0)\,\delta(\mu-\mu_0)\,\delta(\phi-\phi_0) \\
&+ e^{-\boldsymbol{\kappa}_c^+(z+d)/\mu} e^{-\boldsymbol{\kappa}_t^+ H_t/\mu}\boldsymbol{\mathcal{R}}(\mu)\, e^{-\boldsymbol{\kappa}_t^- H_t/\mu} \\
&\qquad \int_{-d}^{0} e^{\boldsymbol{\kappa}_c^-(-d-z')/\mu}\boldsymbol{\mathcal{F}}_c^-(-\mu,\phi,z')\,dz' \\
&+ e^{-\boldsymbol{\kappa}_c^+(z+d)/\mu} e^{-\boldsymbol{\kappa}_t^+ H_t/\mu}\boldsymbol{\mathcal{R}}(\mu) \\
&\qquad \int_{-(d+H_t)}^{-d} e^{\boldsymbol{\kappa}_t^-(-(d+H_t)-z')/\mu}\boldsymbol{\mathcal{F}}_t^-(-\mu,\phi,z')\,dz' \\
&+ e^{-\boldsymbol{\kappa}_c^+(z+d)/\mu} \int_{-(d+H_t)}^{-d} e^{\boldsymbol{\kappa}_t^+(d+z')/\mu}\boldsymbol{\mathcal{F}}_t^+(\mu,\phi,z')\,dz' \\
&+ \int_{-d}^{z} e^{-\boldsymbol{\kappa}_c^+(z-z')/\mu}\boldsymbol{\mathcal{F}}_c^+(\mu,\phi,z')\,dz' \qquad (3.24)
\end{aligned}
$$

In the bistatic case, the intensity scattered from the canopy is:

$$
\begin{aligned}
\mathbf{I}^s(\mu,\phi) &= \mathbf{I}_c^+(\mu,\phi,0) \qquad (3.25) \\
&= e^{-\boldsymbol{\kappa}_c^+ d/\mu} e^{-\boldsymbol{\kappa}_t^+ H_t/\mu}\boldsymbol{\mathcal{R}}(\mu)\, e^{-\boldsymbol{\kappa}_t^- H_t/\mu} e^{-\boldsymbol{\kappa}_c^- d/\mu} \\
&\qquad \cdot \mathbf{I}_0(-\mu_0,\phi_0)\,\delta(\mu-\mu_0)\,\delta(\phi-\phi_0) \\
&+ e^{-\boldsymbol{\kappa}_c^+ d/\mu} e^{-\boldsymbol{\kappa}_t^+ H_t/\mu}\boldsymbol{\mathcal{R}}(\mu)\, e^{-\boldsymbol{\kappa}_t^- H_t/\mu} \\
&\qquad \cdot \int_{-d}^{0} e^{\boldsymbol{\kappa}_c^-(-d-z')/\mu}\boldsymbol{\mathcal{F}}_c^-(-\mu,\phi,z')\,dz' \\
&+ e^{-\boldsymbol{\kappa}_c^+ d/\mu} e^{-\boldsymbol{\kappa}_t^+ H_t/\mu}\boldsymbol{\mathcal{R}}(\mu) \\
&\qquad \cdot \int_{-(d+H_t)}^{-d} e^{\boldsymbol{\kappa}_t^-(-(d+H_t)-z')/\mu}\boldsymbol{\mathcal{F}}_t^-(-\mu,\phi,z')\,dz' \\
&+ e^{-\boldsymbol{\kappa}_c^+ d/\mu} \int_{-(d+H_t)}^{-d} e^{\boldsymbol{\kappa}_t^+(d+z')/\mu}\boldsymbol{\mathcal{F}}_t^+(\mu,\phi,z')\,dz' \\
&+ \int_{-d}^{0} e^{\boldsymbol{\kappa}_c^+ z'/\mu}\boldsymbol{\mathcal{F}}_c^+(\mu,\phi,z')\,dz' \qquad (3.26)
\end{aligned}
$$

Solving (3.21) through (3.24) with $\boldsymbol{\mathcal{F}}_t^{\pm} = \boldsymbol{\mathcal{F}}_c^{\pm} = 0$ gives the zero-order solution at any depth z:

$$
\mathbf{I}_c^{(0)+}(\mu,\phi,z) = e^{-\boldsymbol{\kappa}_c^+(z+d)/\mu} e^{-\boldsymbol{\kappa}_t^+ H_t/\mu}\boldsymbol{\mathcal{R}}(\mu)\, e^{-\boldsymbol{\kappa}_t^- H_t/\mu} e^{-\boldsymbol{\kappa}_c^- d/\mu}
$$

$$\cdot \mathbf{I}_0\left(-\mu_0,\phi_0\right)\delta(\mu-\mu_0)\delta(\phi-\phi_0) \tag{3.27}$$

$$\mathbf{I}_c^{(0)-}(-\mu,\phi,z) = \mathrm{e}^{\boldsymbol{\kappa}_c^- z/\mu}\mathbf{I}_0\left(-\mu_0,\phi_0\right)\delta(\mu-\mu_0)\delta(\phi-\phi_0) \tag{3.28}$$

$$\mathbf{I}_t^{(0)+}(\mu,\phi,z) = \mathrm{e}^{-\boldsymbol{\kappa}_t^+(z+(d+H_t))/\mu}\boldsymbol{\mathcal{R}}\left(\mu\right)\mathrm{e}^{-\boldsymbol{\kappa}_t^- H_t/\mu}\mathrm{e}^{-\boldsymbol{\kappa}_c^- d/\mu}$$

$$\cdot \mathbf{I}_0\left(-\mu_0,\phi_0\right)\delta(\mu-\mu_0)\delta(\phi-\phi_0) \tag{3.29}$$

$$\mathbf{I}_t^{(0)-}(-\mu,\phi,z) = \mathrm{e}^{\boldsymbol{\kappa}_t^-(z+d)/\mu}\mathrm{e}^{-\boldsymbol{\kappa}_c^- d/\mu}\mathbf{I}_0\left(-\mu_0,\phi_0\right)\delta(\mu-\mu_0)\delta(\phi-\phi_0). \tag{3.30}$$

These zero-order intensities are now substituted into (3.10) through (3.13), yielding the zero-order source functions:

$$\begin{aligned}\mathbf{F}_c^{(0)+}(\mu,\phi,z) &= \frac{1}{\mu}\left[\int_0^{2\pi}\int_0^1 \boldsymbol{\mathcal{P}}_c(\mu,\phi;\mu',\phi')\mathbf{I}_c^{(0)+}(\mu',\phi',z)\,\mathrm{d}\Omega'\right.\\ &\quad\left.+\int_0^{2\pi}\int_0^1 \boldsymbol{\mathcal{P}}_c(\mu,\phi;-\mu',\phi')\mathbf{I}_c^{(0)-}(-\mu',\phi',z)\,\mathrm{d}\Omega'\right]\\ &= \frac{1}{\mu}\left[\boldsymbol{\mathcal{P}}_c(\mu,\phi;\mu_0,\phi_0)\mathrm{e}^{-\boldsymbol{\kappa}_c^+(z+d)/\mu_0}\mathrm{e}^{-\boldsymbol{\kappa}_t^+ H_t/\mu_0}\boldsymbol{\mathcal{R}}\left(\mu_0\right)\mathrm{e}^{-\boldsymbol{\kappa}_t^- H_t/\mu_0}\right.\\ &\quad\left.\cdot\mathrm{e}^{-\boldsymbol{\kappa}_c^- d/\mu_0}+\boldsymbol{\mathcal{P}}_c(\mu,\phi;-\mu_0,\phi_0)\mathrm{e}^{\boldsymbol{\kappa}_c^- z/\mu_0}\right]\mathbf{I}_0\left(-\mu_0,\phi_0\right)\end{aligned} \tag{3.31}$$

$$\begin{aligned}\mathbf{F}_c^{(0)-}(-\mu,\phi,z) &= \frac{1}{\mu}\left[\int_0^{2\pi}\int_0^1 \boldsymbol{\mathcal{P}}_c(-\mu,\phi;\mu',\phi')\mathbf{I}_c^{(0)+}(\mu',\phi',z)\,\mathrm{d}\Omega'\right.\\ &\quad\left.+\int_0^{2\pi}\int_0^1 \boldsymbol{\mathcal{P}}_c(-\mu,\phi;-\mu',\phi')\mathbf{I}_c^{(0)-}(-\mu',\phi',z)\,\mathrm{d}\Omega'\right]\\ &= \frac{1}{\mu}\left[\boldsymbol{\mathcal{P}}_c(-\mu,\phi;\mu_0,\phi_0)\mathrm{e}^{-\boldsymbol{\kappa}_c^+(z+d)/\mu_0}\mathrm{e}^{-\boldsymbol{\kappa}_t^+ H_t/\mu_0}\boldsymbol{\mathcal{R}}\left(\mu_0\right)\mathrm{e}^{-\boldsymbol{\kappa}_t^- H_t/\mu_0}\right.\\ &\quad\left.\cdot\mathrm{e}^{-\boldsymbol{\kappa}_c^- d/\mu_0}+\boldsymbol{\mathcal{P}}_c(-\mu,\phi;-\mu_0,\phi_0)\mathrm{e}^{\boldsymbol{\kappa}_c^- z/\mu_0}\right]\mathbf{I}_0\left(-\mu_0,\phi_0\right)\end{aligned} \tag{3.32}$$

$$\begin{aligned}\mathbf{F}_t^{(0)+}(\mu,\phi,z) &= \frac{1}{\mu}\int_0^{2\pi}\int_0^1 \boldsymbol{\mathcal{P}}_t(\mu,\phi;\mu',\phi')\mathbf{I}_t^{(0)+}(\mu',\phi',z)\delta_k\left(\mu-\mu'\right)\,\mathrm{d}\Omega'\\ &= \frac{1}{\mu}\boldsymbol{\mathcal{P}}_t(\mu,\phi;\mu_0,\phi_0)\mathrm{e}^{-\boldsymbol{\kappa}_t^+(z+(d+H_t))/\mu_0}\boldsymbol{\mathcal{R}}\left(\mu_0\right)\mathrm{e}^{-\boldsymbol{\kappa}_t^- H_t/\mu_0}\\ &\quad\cdot\mathrm{e}^{-\boldsymbol{\kappa}_c^- d/\mu_0}\mathbf{I}_0\left(-\mu_0,\phi_0\right)\delta_k\left(\mu-\mu_0\right)\end{aligned} \tag{3.33}$$

$$\begin{aligned}\mathbf{F}_t^{(0)-}(-\mu,\phi,z) &= \frac{1}{\mu}\int_0^{2\pi}\int_0^1 \boldsymbol{\mathcal{P}}_t(-\mu,\phi;-\mu',\phi')\mathbf{I}_t^{(0)-}(-\mu',\phi',z)\delta_k\left(\mu-\mu_0\right)\,\mathrm{d}\Omega'\\ &= \frac{1}{\mu}\boldsymbol{\mathcal{P}}_t(-\mu,\phi;-\mu_0,\phi_0)\mathrm{e}^{\boldsymbol{\kappa}_t^-(z+d)/\mu_0}\\ &\quad\cdot\mathrm{e}^{-\boldsymbol{\kappa}_c^- d/\mu_0}\mathbf{I}_0\left(-\mu_0,\phi_0\right)\delta_k\left(\mu-\mu_0\right)\end{aligned} \tag{3.34}$$

where $\boldsymbol{\kappa}^{\pm}/\mu = \boldsymbol{\kappa}(\pm\mu,\phi)/\mu$ and $\boldsymbol{\kappa}^{\pm}/\mu_0 = \boldsymbol{\kappa}(\pm\mu_0,\phi_0)/\mu_0$.

Substituting these source functions into (3.21) through (3.24) and separating terms gives the first-order solution for the specific intensities:

$$\begin{aligned}
\mathbf{I}_c^{(1)-}(-\mu,\phi,z) &= \Bigg\{ e^{\boldsymbol{\kappa}_c^- z/\mu}\delta(\mu-\mu_0)\,\delta(\phi-\phi_0) \\
&\quad + \frac{1}{\mu}\left[\int_z^0 e^{\boldsymbol{\kappa}_c^-(z-z')/\mu}\boldsymbol{\mathcal{P}}_c(-\mu,\phi;\mu_0,\phi_0)e^{-\boldsymbol{\kappa}_c^+(z'+d)/\mu_0}\,dz'\right] \\
&\qquad \cdot e^{-\boldsymbol{\kappa}_t^+ H_t/\mu_0}\boldsymbol{\mathcal{R}}(\mu_0)\,e^{-\boldsymbol{\kappa}_t^- H_t/\mu_0}e^{-\boldsymbol{\kappa}_c^- d/\mu_0} \\
&\quad + \frac{1}{\mu}\left[\int_z^0 e^{\boldsymbol{\kappa}_c^-(z-z')/\mu}\boldsymbol{\mathcal{P}}_c(-\mu,\phi;-\mu_0,\phi_0)e^{\boldsymbol{\kappa}_c^- z'/\mu_0}\,dz'\right]\Bigg\} \\
&\quad \cdot \mathbf{I}_0(-\mu_0,\phi_0) \qquad (3.35)
\end{aligned}$$

$$\begin{aligned}
\mathbf{I}_t^{(1)-}(-\mu,\phi,z) &= \Bigg\{ e^{\boldsymbol{\kappa}_t^-(z+d)/\mu}e^{-\boldsymbol{\kappa}_c^- d/\mu}\delta(\mu-\mu_0)\,\delta(\phi-\phi_0) \\
&\quad + e^{\boldsymbol{\kappa}_t^-(z+d)/\mu} \\
&\qquad \cdot\frac{1}{\mu}\left[\int_{-d}^0 e^{\boldsymbol{\kappa}_c^-(-d-z')/\mu}\boldsymbol{\mathcal{P}}_c(-\mu,\phi;\mu_0,\phi_0)e^{-\boldsymbol{\kappa}_c^+(z'+d)/\mu_0}\,dz'\right] \\
&\qquad \cdot e^{-\boldsymbol{\kappa}_t^+ H_t/\mu_0}\boldsymbol{\mathcal{R}}(\mu_0)\,e^{-\boldsymbol{\kappa}_t^- H_t/\mu_0}e^{-\boldsymbol{\kappa}_c^- d/\mu_0} \\
&\quad + e^{\boldsymbol{\kappa}_t^-(z+d)/\mu} \\
&\qquad \cdot\frac{1}{\mu}\left[\int_{-d}^0 e^{\boldsymbol{\kappa}_c^-(-d-z')/\mu}\boldsymbol{\mathcal{P}}_c(-\mu,\phi;-\mu_0,\phi_0)e^{\boldsymbol{\kappa}_c^- z'/\mu_0}\,dz'\right] \\
&\quad + \frac{1}{\mu}\left[\int_z^{-d} e^{\boldsymbol{\kappa}_t^-(z-z')/\mu}\boldsymbol{\mathcal{P}}_t(-\mu,\phi;-\mu_0,\phi_0)e^{\boldsymbol{\kappa}_t^-(z'+d)/\mu_0}\,dz'\right] \\
&\qquad \cdot e^{-\boldsymbol{\kappa}_c^- d/\mu_0}\delta_k(\mu-\mu_0)\Bigg\}\mathbf{I}_0(-\mu_0,\phi_0) \qquad (3.36)
\end{aligned}$$

$$\begin{aligned}
\mathbf{I}_t^{(1)+}(\mu,\phi,z) &= \Bigg\{ e^{-\boldsymbol{\kappa}_t^+[z+(d+H_t)]/\mu}\boldsymbol{\mathcal{R}}(\mu)\,e^{-\boldsymbol{\kappa}_t^- H_t/\mu}e^{-\boldsymbol{\kappa}_c^- d/\mu}\delta(\mu-\mu_0)\,\delta(\phi-\phi_0) \\
&\quad + e^{-\boldsymbol{\kappa}_t^+[z+(d+H_t)]/\mu}\boldsymbol{\mathcal{R}}(\mu)\,e^{-\boldsymbol{\kappa}_t^- H_t/\mu} \\
&\qquad \cdot\frac{1}{\mu}\left[\int_{-d}^0 e^{\boldsymbol{\kappa}_c^-(-d-z')/\mu}\boldsymbol{\mathcal{P}}_c(-\mu,\phi;\mu_0,\phi_0)e^{-\boldsymbol{\kappa}_c^+(z'+d)/\mu_0}\,dz'\right] \\
&\qquad \cdot e^{-\boldsymbol{\kappa}_t^+ H_t/\mu_0}\boldsymbol{\mathcal{R}}(\mu_0)\,e^{-\boldsymbol{\kappa}_t^- H_t/\mu_0}e^{-\boldsymbol{\kappa}_c^- d/\mu_0} \\
&\quad + e^{-\boldsymbol{\kappa}_t^+[z+(d+H_t)]/\mu}\boldsymbol{\mathcal{R}}(\mu)\,e^{-\boldsymbol{\kappa}_t^- H_t/\mu}
\end{aligned}$$

$$\cdot\frac{1}{\mu}\left[\int_{-d}^{0} e^{\kappa_c^-(-d-z')/\mu}\mathcal{P}_c(-\mu,\phi;-\mu_0,\phi_0)e^{\kappa_c^- z'/\mu_0}\,dz'\right]$$

$$+\ e^{-\kappa_t^+[z+(d+H_t)]/\mu}\mathcal{R}(\mu)$$

$$\cdot\frac{1}{\mu}\left[\int_{-(d+H_t)}^{-d} e^{\kappa_t^-(-(d+H_t)-z')/\mu}\mathcal{P}_t(-\mu,\phi;-\mu_0,\phi_0)\right.$$

$$\left.\cdot e^{\kappa_t^-(z'+d)/\mu_0}\,dz'\right]e^{-\kappa_c^- d/\mu_0}\delta_k(\mu-\mu_0)$$

$$+\ \frac{1}{\mu}\left[\int_{-(d+H_t)}^{z} e^{-\kappa_t^+(z-z')/\mu}\mathcal{P}_t(\mu,\phi;\mu_0,\phi_0)e^{-\kappa_t^+(z'+(d+H_t))/\mu_0}\,dz'\right]$$

$$\left.\cdot\mathcal{R}(\mu_0)\,e^{-\kappa_t^- H_t/\mu_0}e^{-\kappa_c^- d/\mu_0}\delta_k(\mu-\mu_0)\right\}\mathbf{I}_0(-\mu_0,\phi_0)$$

(3.37)

$$\mathbf{I}_c^{(1)+}(\mu,\phi,z) = \left\{e^{-\kappa_c^+(z+d)/\mu}e^{-\kappa_t^+ H_t/\mu}\mathcal{R}(\mu)\,e^{-\kappa_t^- H_t/\mu}e^{-\kappa_c^- d/\mu}\right.$$

$$\cdot\delta(\mu-\mu_0)\,\delta(\phi-\phi_0)$$

$$+\ e^{-\kappa_c^+(z+d)/\mu}e^{-\kappa_t^+ H_t/\mu}\mathcal{R}(\mu)\,e^{-\kappa_t^- H_t/\mu}$$

$$\cdot\frac{1}{\mu}\left[\int_{-d}^{0} e^{\kappa_c^-(-d-z')/\mu}\mathcal{P}_c(-\mu,\phi;\mu_0,\phi_0)e^{-\kappa_c^+(z'+d)/\mu_0}\,dz'\right]$$

$$\cdot e^{-\kappa_t^+ H_t/\mu_0}\mathcal{R}(\mu_0)\,e^{-\kappa_t^- H_t/\mu_0}e^{-\kappa_c^- d/\mu_0}$$

$$+\ e^{-\kappa_c^+(z+d)/\mu}e^{-\kappa_t^+ H_t/\mu}\mathcal{R}(\mu)\,e^{-\kappa_t^- H_t/\mu}$$

$$\cdot\frac{1}{\mu}\left[\int_{-d}^{0} e^{\kappa_c^-(-d-z')/\mu}\mathcal{P}_c(-\mu,\phi;-\mu_0,\phi_0)e^{\kappa_c^- z'/\mu_0}\,dz'\right]$$

$$+\ \frac{1}{\mu}\left[\int_{-d}^{z} e^{-\kappa_c^+(z-z')/\mu}\mathcal{P}_c(\mu,\phi;\mu_0,\phi_0)e^{-\kappa_c^+(z'+d)/\mu_0}\,dz'\right]$$

$$\cdot e^{-\kappa_t^+ H_t/\mu_0}\mathcal{R}(\mu_0)\,e^{-\kappa_t^- H_t/\mu_0}e^{-\kappa_c^- d/\mu_0}$$

$$+\ e^{-\kappa_c^+(z+d)/\mu}e^{-\kappa_t^+ H_t/\mu}\mathcal{R}(\mu)$$

$$\cdot\frac{1}{\mu}\left[\int_{-(d+H_t)}^{-d} e^{\kappa_t^-(-(d+H_t)-z')/\mu}\mathcal{P}_t(-\mu,\phi;-\mu_0,\phi_0)\right.$$

$$\left.\cdot e^{\kappa_t^-(z'+d)/\mu_0}\,dz'\right]e^{-\kappa_c^- d/\mu_0}\delta_k(\mu-\mu_0)$$

$$+\ e^{-\kappa_c^+(z+d)/\mu}$$

$$\cdot\frac{1}{\mu}\left[\int_{-(d+H_t)}^{-d} e^{\kappa_t^+(d+z')/\mu}\mathcal{P}_t(\mu,\phi;\mu_0,\phi_0)\right.$$

$$\cdot e^{-\kappa_t^+(z'+(d+H_t))/\mu_0}\,dz'\Big]$$

$$\cdot\mathcal{R}(\mu_0)\,e^{-\kappa_t^- H_t/\mu_0}e^{-\kappa_c^- d/\mu_0}\delta_k(\mu-\mu_0)$$

$$+\ \frac{1}{\mu}\left[\int_{-d}^{z} e^{-\kappa_c^+(z-z')/\mu}\mathcal{P}_c(\mu,\phi;-\mu_0,\phi_0)e^{\kappa_c^- z'/\mu_0}\,dz'\right]\Bigg\}$$

$$\cdot\mathbf{I}_0(-\mu_0,\phi_0)\,. \tag{3.38}$$

The first-order solution for the bistatically scattered intensity emerging from the canopy is

$$\mathbf{I}^s(\mu,\phi) = \mathbf{I}_c^{(1)+}(\mu,\phi,0) \tag{3.39}$$

$$= \mathcal{T}_c(\mu,\phi)\ \mathbf{I}_0(-\mu_0,\phi_0) \tag{3.40}$$

where

$$\begin{aligned}
\mathcal{T}_c(\mu,\phi) &= e^{-\kappa_c^+ d/\mu}e^{-\kappa_t^+ H_t/\mu}\mathcal{R}(\mu)\,e^{-\kappa_t^- H_t/\mu}e^{-\kappa_c^- d/\mu}\delta(\mu-\mu_0)\,\delta(\phi-\phi_0)\\
&+\ \frac{1}{\mu}e^{-\kappa_c^+ d/\mu}e^{-\kappa_t^+ H_t/\mu}\mathcal{R}(\mu)\,e^{-\kappa_t^- H_t/\mu}\mathcal{A}_1(\mu,\phi;\mu_0,\phi_0)\\
&\qquad\cdot e^{-\kappa_t^+ H_t/\mu_0}\mathcal{R}(\mu_0)\,e^{-\kappa_t^- H_t/\mu_0}e^{-\kappa_c^- d/\mu_0}\\
&+\ \frac{1}{\mu}e^{-\kappa_c^+ d/\mu}e^{-\kappa_t^+ H_t/\mu}\mathcal{R}(\mu)\,e^{-\kappa_t^- H_t/\mu}\mathcal{A}_2(\mu,\phi;\mu_0,\phi_0)\\
&+\ \frac{1}{\mu}\mathcal{A}_3(\mu,\phi;\mu_0,\phi_0)\,e^{-\kappa_t^+ H_t/\mu_0}\mathcal{R}(\mu_0)\,e^{-\kappa_t^- H_t/\mu_0}e^{-\kappa_c^- d/\mu_0}\\
&+\ \frac{1}{\mu}e^{-\kappa_c^+ d/\mu}e^{-\kappa_t^+ H_t/\mu}\mathcal{R}(\mu)\,\mathcal{A}_4(\mu,\phi;\mu_0,\phi_0)\,e^{-\kappa_c^- d/\mu_0}\delta_k(\mu-\mu_0)\\
&+\ \frac{1}{\mu}e^{-\kappa_c^+ d/\mu}\mathcal{A}_5(\mu,\phi;\mu_0,\phi_0)\,\mathcal{R}(\mu_0)\,e^{-\kappa_t^- H_t/\mu_0}e^{-\kappa_c^- d/\mu_0}\delta_k(\mu-\mu_0)\\
&+\ \frac{1}{\mu}\mathcal{A}_6(\mu,\phi;\mu_0,\phi_0)
\end{aligned} \tag{3.41}$$

with

$$\mathcal{A}_1(\mu,\phi;\mu_0,\phi_0) = \int_{-d}^{0} e^{-\kappa_c^-(d+z')/\mu}\mathcal{P}_c(-\mu,\phi;\mu_0,\phi_0)e^{-\kappa_c^+(z'+d)/\mu_0}\,dz' \tag{3.42}$$

$$\mathcal{A}_2(\mu,\phi;\mu_0,\phi_0) = \int_{-d}^{0} e^{-\kappa_c^-(d+z')/\mu}\mathcal{P}_c(-\mu,\phi;-\mu_0,\phi_0)e^{\kappa_c^- z'/\mu_0}\,dz' \tag{3.43}$$

$$\mathcal{A}_3(\mu,\phi;\mu_0,\phi_0) = \int_{-d}^{0} e^{\kappa_c^+ z'/\mu}\mathcal{P}_c(\mu,\phi;\mu_0,\phi_0)e^{-\kappa_c^+(z'+d)/\mu_0}\,dz' \tag{3.44}$$

$$\mathcal{A}_4(\mu,\phi;\mu_0,\phi_0) = \int_{-(d+H_t)}^{-d} e^{-\kappa_t^-(d+H_t+z')/\mu}\mathcal{P}_t(-\mu,\phi;-\mu_0,\phi_0)e^{\kappa_t^-(z'+d)/\mu_0}\,dz' \quad (3.45)$$

$$\mathcal{A}_5(\mu,\phi;\mu_0,\phi_0) = \int_{-(d+H_t)}^{-d} e^{\kappa_t^+(d+z')/\mu}\mathcal{P}_t(\mu,\phi;\mu_0,\phi_0)e^{-\kappa_t^+(z'+d+H_t)/\mu_0}\,dz' \quad (3.46)$$

$$\mathcal{A}_6(\mu,\phi;\mu_0,\phi_0) = \int_{-d}^{0} e^{\kappa_c^+ z'/\mu}\mathcal{P}_c(\mu,\phi;-\mu_0,\phi_0)e^{\kappa_c^- z'/\mu_0}\,dz' \,. \quad (3.47)$$

$\mathcal{T}_c(\mu,\phi)$ is the canopy bistatic transformation matrix and relates the incident and scattered intensities for the bistatic scattering case. Each of the seven terms in (3.41) corresponds to one of the scattering processes illustrated in Figure 3.3. These mechanisms are now examined in order of their appearance in (3.41):

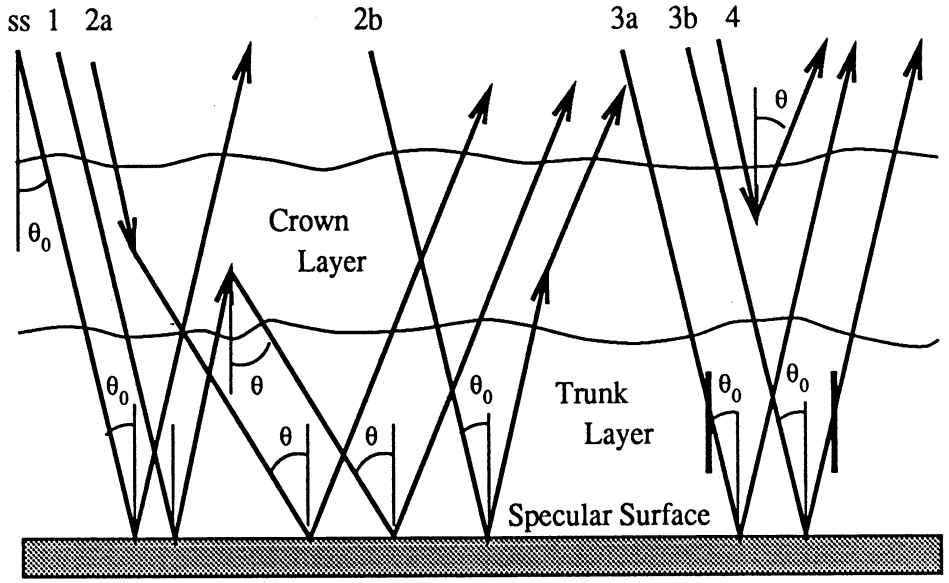

Figure 3.3: First-order contributions to bistatic scatter.

Term ss This term represents propagation of the incident intensity down through the crown and trunk layers to the ground surface, specular scatter by the ground surface at the angle θ_0, and propagation back up through the trunk and crown layers. This terms exists only in the specular direction $(\theta,\phi) = (\theta_0,\phi_0)$.

Term 1 This term represents propagation of the incident intensity down through the crown and trunk layers to the ground surface, specular scatter by the ground surface at an angle θ_0, propagation up through the trunk layer, scatter by the crown layer back down to the ground in a direction $(\pi - \theta, \phi)$, specular scatter again by the ground layer at an angle θ and propagation back up through the trunk and crown layers in a direction (θ, ϕ).

Term 2a This term represents propagation of the incident intensity down into the crown layer, scatter by the crown layer into the direction $(\pi - \theta, \phi)$ such that, after specular scatter by the ground surface at an angle θ, the scattered intensity propagates in a direction (θ, ϕ) up through the trunk and crown layers.

Term 2b This term in the compliment of term 2a. It represents propagation down through the crown and trunk layers in a direction $(\pi - \theta_0, \phi_0)$, specular scatter by the ground surface at an angle θ_0, propagation in a direction (θ_0, ϕ_0) up into the crown layer and scatter by the crown layer into the direction (θ, ϕ).

Term 3a This is a trunk-ground interaction mechanism that represents propagation of the incident intensity into the trunk layer, scatter by the trunk layer into the direction $(\pi - \theta_0, \phi)$, specular scatter by the ground layer at the angle θ_0 followed by propagation up through the trunk and crown layers in the direction (θ_0, ϕ).

Term 3b This is the complement of term 3a. It represents propagation down through the crown and trunk layers in a direction $(\pi - \theta_0, \phi_0)$, specular scatter by the ground surface at an angle θ_0, scatter by the trunk layer into the direction (θ, ϕ), followed by propagation crown layer in the direction (θ, ϕ).

Term 4 This term represents direct scatter by the crown layer of the incident

intensity into the direction (θ, ϕ).

Note that the only contribution to $\mathcal{T}_c(\mu, \phi)$ from direct ground scatter comes from a term that is specularly scattered by the ground surface (term ss). Taking $\mu = \mu_0$ and $\phi = \phi_0 + \pi$ in $\mathcal{T}_c(\mu, \phi)$ yields the canopy backscatter in the absence of direct ground backscatter.

To obtain the contribution from direct ground backscatter, the second part of the canopy scattering problem is now considered. Direct backscatter from the ground is described by propagation down through the crown and trunk layers in a direction $(-\mu_0, \phi_0)$, backscatter by the ground surface, and propagation back up through the trunk and crown layers in the direction $(\mu_0, \phi_0 + \pi)$. Then in (3.3),

$$\mathcal{T}_g(\mu_0, \phi_0 + \pi) = e^{-\kappa_c^+ d/\mu_0} e^{-\kappa_t^+ H_t/\mu_0} \mathcal{G}(\theta_0) e^{-\kappa_t^- H_t/\mu_0} e^{-\kappa_c^- d/\mu_0} \tag{3.48}$$

where $\mathcal{G}(\theta_0)$ is the ground backscattering matrix that accounts for direct backscatter by a rough surface at an angle θ_0. The form chosen for this matrix depends on the roughness parameters of the ground surface. Techniques used to model $\mathcal{G}(\theta_0)$ for different surface roughness states are presented in Appendix B.

The total canopy backscattering transformation matrix is obtained by adding $\mathcal{T}_g(\mu_0, \phi_0 + \pi)$ to $\mathcal{T}_c(\mu_0, \phi_0 + \pi)$:

$$\begin{aligned}
\mathcal{T}_t(\mu_0, \phi_0 + \pi) = & \frac{1}{\mu_0} e^{-\kappa_c^+ d/\mu_0} e^{-\kappa_t^+ H_t/\mu_0} \mathcal{R}(\mu_0) e^{-\kappa_t^- H_t/\mu_0} \mathcal{A}_1(\mu_0, \phi_0 + \pi; \mu_0, \phi_0) \\
& \cdot e^{-\kappa_t^+ H_t/\mu_0} \mathcal{R}(\mu_0) e^{-\kappa_t^- H_t/\mu_0} e^{-\kappa_c^- d/\mu_0} \\
& + \frac{1}{\mu_0} e^{-\kappa_c^+ d/\mu_0} e^{-\kappa_t^+ H_t/\mu_0} \mathcal{R}(\mu_0) e^{-\kappa_t^- H_t/\mu_0} \mathcal{A}_2(\mu_0, \phi_0 + \pi; \mu_0, \phi_0) \\
& + \frac{1}{\mu_0} \mathcal{A}_3(\mu_0, \phi_0 + \pi; \mu_0, \phi_0) e^{-\kappa_t^+ H_t/\mu_0} \mathcal{R}(\mu_0) e^{-\kappa_t^- H_t/\mu_0} e^{-\kappa_c^- d/\mu_0} \\
& + \frac{1}{\mu_0} e^{-\kappa_c^+ d/\mu_0} e^{-\kappa_t^+ H_t/\mu_0} \mathcal{R}(\mu_0) \mathcal{A}_4(\mu_0, \phi_0 + \pi; \mu_0, \phi_0) e^{-\kappa_c^- d/\mu_0}
\end{aligned}$$

$$+ \frac{1}{\mu_0} e^{-\kappa_c^+ d/\mu_0} \mathcal{A}_5 (\mu_0, \phi_0 + \pi; \mu_0, \phi_0) \mathcal{R} (\mu_0) e^{-\kappa_t^- H_t/\mu_0} e^{-\kappa_c^- d/\mu_0}$$
$$+ \frac{1}{\mu_0} \mathcal{A}_6 (\mu_0, \phi_0 + \pi; \mu_0, \phi_0)$$
$$+ e^{-\kappa_c^+ d/\mu_0} e^{-\kappa_t^+ H_t/\mu_0} \mathcal{G} (\theta_0) e^{-\kappa_t^- H_t/\mu_0} e^{-\kappa_c^- d/\mu_0} . \quad (3.49)$$

Figure 3.4 shows the seven contributions to the backscattered specific intensity. Combining term 2a with its complement 2b and term 3a with 3b yields an effec-

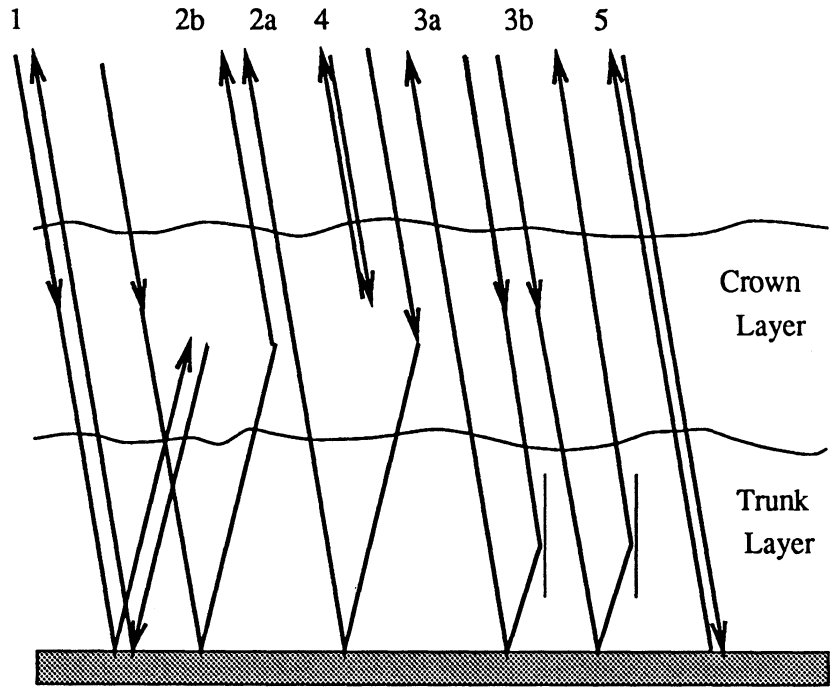

Figure 3.4: First-order contributions to canopy backscatter.

tive number of 5 contributions. These terms will be referred to by the mechanism names listed in Table 3.1.

The integrals defined by (3.42) through (3.47) may be computed by applying (2.15). In the backscatter case:

$$\mathcal{A}_1 (\mu_0, \phi_0 + \pi; \mu_0, \phi_0) \quad =$$

Table 3.1: Terms contributing to canopy backscatter.

Mechanism Number	Mechanism Name	Relationship to Listed Term
1	Ground-Crown-Ground multiple bounce	Term 1
2	Crown-Ground interaction	Terms 2a + 2b
3	Trunk-Ground interaction	Terms 3a + 3b
4	Direct Crown backscatter	Term 4
5	Direct Ground backscatter	Term 5

$$\int_{-d}^{0} \mathcal{E}_c(-\mu_0, \phi_0 + \pi)\mathcal{D}_c(-\mu_0, \phi_0 + \pi; -(d + z')/\mu_0)\mathcal{E}_c^{-1}(-\mu_0, \phi_0 + \pi)$$
$$\cdot\mathcal{P}_c(-\mu_0, \phi_0 + \pi; \mu_0, \phi_0)\mathcal{E}_c(\mu_0, \phi_0)\mathcal{D}_c(\mu_0, \phi_0; -(d + z')/\mu_0)\mathcal{E}_c^{-1}(\mu_0, \phi_0)\,\mathrm{d}z' \tag{3.50}$$

$$\mathcal{A}_2(\mu_0, \phi_0 + \pi; \mu_0, \phi_0) =$$
$$\int_{-d}^{0} \mathcal{E}_c(-\mu_0, \phi_0 + \pi)\mathcal{D}_c(-\mu_0, \phi_0 + \pi; -(d + z')/\mu_0)\mathcal{E}_c^{-1}(-\mu_0, \phi_0 + \pi)$$
$$\cdot\mathcal{P}_c(-\mu_0, \phi_0 + \pi; -\mu_0, \phi_0)\mathcal{E}_c(-\mu_0, \phi_0)\mathcal{D}_c(-\mu_0, \phi_0; z'/\mu_0)\mathcal{E}_c^{-1}(-\mu_0, \phi_0)\,\mathrm{d}z' \tag{3.51}$$

$$\mathcal{A}_3(\mu_0, \phi_0 + \pi; \mu_0, \phi_0) =$$
$$\int_{-d}^{0} \mathcal{E}_c(\mu_0, \phi_0 + \pi)\mathcal{D}_c(\mu_0, \phi_0 + \pi; z'/\mu_0)\mathcal{E}_c^{-1}(\mu_0, \phi_0 + \pi)$$
$$\cdot\mathcal{P}_c(\mu_0, \phi_0 + \pi; \mu_0, \phi_0)\mathcal{E}_c(\mu_0, \phi_0)\mathcal{D}_c(\mu_0, \phi_0; -(z' + d)/\mu_0)\mathcal{E}_c^{-1}(\mu_0, \phi_0)\,\mathrm{d}z' \tag{3.52}$$

$$\mathcal{A}_4(\mu_0, \phi_0 + \pi; \mu_0, \phi_0) =$$
$$\int_{-(d+H_t)}^{-d} \mathcal{E}_t(-\mu_0, \phi_0 + \pi)\mathcal{D}_t(-\mu_0, \phi_0 + \pi; -(d + H_t + z')/\mu_0)\mathcal{E}_t^{-1}(-\mu_0, \phi_0 + \pi)$$
$$\cdot\mathcal{P}_t(-\mu_0, \phi_0 + \pi; -\mu_0, \phi_0)\mathcal{E}_t(-\mu_0, \phi_0)\mathcal{D}_t(-\mu_0, \phi_0; (z' + d)/\mu_0)\mathcal{E}_t^{-1}(-\mu_0, \phi_0)\,\mathrm{d}z' \tag{3.53}$$

$$\mathcal{A}_5(\mu_0, \phi_0 + \pi; \mu_0, \phi_0) =$$
$$\int_{-(d+H_t)}^{-d} \mathcal{E}_t(\mu_0, \phi_0 + \pi)\mathcal{D}_t(\mu, \phi; (d + z')/\mu_0)\mathcal{E}_t^{-1}(\mu_0, \phi_0 + \pi)$$

$$\cdot\mathcal{P}_t(\mu_0,\phi_0+\pi;\mu_0,\phi_0)\mathcal{E}_t(\mu_0,\phi_0)\mathcal{D}_t(\mu_0,\phi_0;-(z'+d+H_t)/\mu_0)\mathcal{E}_t^{-1}(\mu_0,\phi_0)\,\mathrm{d}z' \tag{3.54}$$

$$\begin{aligned}\mathcal{A}_6(\mu_0,\phi_0+\pi;\mu_0,\phi_0) \;=\; & \\ \int_{-d}^{0}&\mathcal{E}_c(\mu_0,\phi_0+\pi)\mathcal{D}_c(\mu_0,\phi_0+\pi;z'/\mu_0)\mathcal{E}_c^{-1}(\mu_0,\phi_0+\pi) \\ \cdot&\mathcal{P}_c(\mu_0,\phi_0+\pi;-\mu_0,\phi_0)\mathcal{E}_c(-\mu_0,\phi_0)\mathcal{D}_c(-\mu_0,\phi_0;z'/\mu_0)\mathcal{E}_c^{-1}(-\mu_0,\phi_0)\,\mathrm{d}z'\end{aligned} \tag{3.55}$$

For a canopy symmetric in ϕ, $\kappa_c^+ = \kappa_c^-$, $\kappa_t^+ = \kappa_t^-$ and the 4×4 $\mathcal{A}_n$ matrices are given by

$$\mathcal{A}_1(\mu_0,\phi_0+\pi;\mu_0,\phi_0) = \mathcal{E}_c(-\mu_0,\phi_0+\pi)\mathcal{B}_1(\mu_0,\phi_0+\pi;\mu_0,\phi_0)\mathcal{E}_c^{-1}(\mu_0,\phi_0)$$

$$\begin{aligned}[\mathcal{B}_1(\mu_0,\phi_0+\pi;\mu_0,\phi_0)]_{ij} = & \\ &\frac{1-\exp[-(\beta_i^c(-\mu_0,\phi_0+\pi)/\mu_0+\beta_j^c(\mu_0,\phi_0)/\mu_0)d]}{\beta_i^c(-\mu_0,\phi_0+\pi)/\mu_0+\beta_j^c(\mu_0,\phi_0)/\mu_0} \\ &\cdot[\mathcal{E}_c^{-1}(-\mu_0,\phi_0+\pi)\mathcal{P}_c(-\mu_0,\phi_0+\pi;\mu_0,\phi_0)\mathcal{E}_c(\mu_0,\phi_0)]_{ij}\end{aligned} \tag{3.56}$$

$$\mathcal{A}_2(\mu_0,\phi_0+\pi;\mu_0,\phi_0) = \mathcal{E}_c(-\mu_0,\phi_0+\pi)\mathcal{B}_2(\mu_0,\phi_0+\pi;\mu_0,\phi_0)\mathcal{E}_c^{-1}(-\mu_0,\phi_0)$$

$$[\mathcal{B}_2(\mu_0,\phi_0+\pi;\mu_0,\phi_0)]_{ij} =$$

$$\begin{cases} d\mathrm{e}^{-\beta_i^c(\mu_0)d/\mu_0}\cdot\left[\mathcal{E}_c^{-1}(-\mu_0,\phi_0+\pi)\right. & \\ \left.\cdot\mathcal{P}_c(-\mu_0,\phi_0+\pi;-\mu_0,\phi_0)\mathcal{E}_c(-\mu_0,\phi_0)\right]_{ii} & i=j \\ \dfrac{\exp[-\beta_i^c(-\mu_0,\phi_0+\pi)d/\mu_0]-\exp[-\beta_j^c(-\mu_0,\phi_0)d/\mu_0]}{-\beta_i^c(-\mu_0,\phi_0+\pi)/\mu_0+\beta_j^c(-\mu_0,\phi_0)/\mu_0} & \\ \cdot[\mathcal{E}_c^{-1}(-\mu_0,\phi_0+\pi)\mathcal{P}_c(-\mu_0,\phi_0+\pi;-\mu_0,\phi_0)\mathcal{E}_c(-\mu_0,\phi_0)]_{ij} & i\neq j \end{cases} \tag{3.57}$$

$$\mathcal{A}_3(\mu_0,\phi_0+\pi;\mu_0,\phi_0) = \mathcal{E}_c(\mu_0,\phi_0+\pi)\mathcal{B}_3(\mu_0,\phi_0+\pi;\mu_0,\phi_0)\mathcal{E}_c^{-1}(\mu_0,\phi_0)$$

$$[\mathcal{B}_3(\mu_0, \phi_0 + \pi; \mu_0, \phi_0)]_{ij} =$$

$$\begin{cases} \left.\begin{array}{l} d\mathrm{e}^{-\beta_i^c(\mu_0)d/\mu_0} \cdot \left[\mathcal{E}_c^{-1}(\mu_0, \phi_0 + \pi)\right. \\ \left. \cdot \mathcal{P}_c(\mu_0, \phi_0 + \pi; \mu_0, \phi_0)\mathcal{E}_c(\mu_0, \phi_0)\right]_{ii} \end{array}\right\} & i = j \\ \left.\begin{array}{l} \dfrac{\exp[-\beta_j^c(\mu_0, \phi_0)d/\mu_0] - \exp[-\beta_i^c(\mu_0, \phi_0 + \pi)d/\mu]}{\beta_i^c(\mu_0, \phi_0 + \pi)/\mu_0 - \beta_j^c(\mu_0, \phi_0)/\mu_0} \\ \cdot[\mathcal{E}_c^{-1}(\mu_0, \phi_0 + \pi)\mathcal{P}_c(\mu_0, \phi_0 + \pi; \mu_0, \phi_0)\mathcal{E}_c(\mu_0, \phi_0)]_{ij} \end{array}\right\} & i \neq j \end{cases} \tag{3.58}$$

$$\mathcal{A}_4(\mu_0, \phi_0 + \pi; \mu_0, \phi_0) = \mathcal{E}_t(-\mu_0, \phi_0 + \pi)\mathcal{B}_4(\mu_0, \phi_0 + \pi; \mu_0, \phi_0)\mathcal{E}_t^{-1}(-\mu_0, \phi_0)$$

$$[\mathcal{B}_4(\mu_0, \phi_0 + \pi; \mu_0, \phi_0)]_{ij} =$$

$$\begin{cases} \left.\begin{array}{l} H_t\mathrm{e}^{-\beta_i^t(\mu_0)H_z/\mu_0} \cdot \left[\mathcal{E}_t^{-1}(-\mu_0, \phi_0 + \pi)\right. \\ \left. \cdot \mathcal{P}_t(-\mu_0, \phi_0 + \pi; -\mu_0, \phi_0)\mathcal{E}_t(-\mu_0, \phi_0)\right]_{ii} \end{array}\right\} & i = j \\ \left.\begin{array}{l} \dfrac{\exp[-\beta_i^t(-\mu_0, \phi_0 + \pi)H_t/\mu_0] - \exp[-\beta_j^t(-\mu_0, \phi_0)H_t/\mu_0]}{-\beta_i^t(-\mu_0, \phi_0 + \pi)/\mu_0 + \beta_j^t(-\mu_0, \phi_0)/\mu_0} \\ \cdot[\mathcal{E}_t^{-1}(-\mu_0, \phi_0 + \pi)\mathcal{P}_t(-\mu_0, \phi_0 + \pi; -\mu_0, \phi_0)\mathcal{E}_t(-\mu_0, \phi_0)]_{ij} \end{array}\right\} & i \neq j \end{cases} \tag{3.59}$$

$$\mathcal{A}_5(\mu_0, \phi_0 + \pi; \mu_0, \phi_0) = \mathcal{E}_t(\mu_0, \phi_0 + \pi)\mathcal{B}_5(\mu_0, \phi_0 + \pi; \mu_0, \phi_0)\mathcal{E}_t^{-1}(\mu_0, \phi_0)$$

$$[\mathcal{B}_5(\mu_0, \phi_0 + \pi; \mu_0, \phi_0)]_{ij} =$$

$$\begin{cases} \left.\begin{array}{l} H_t\mathrm{e}^{-\beta_i^t(\mu_0)H_z/\mu_0} \cdot \left[\mathcal{E}_t^{-1}(\mu_0, \phi_0 + \pi)\right. \\ \left. \cdot \mathcal{P}_t(\mu_0, \phi_0 + \pi; \mu_0, \phi_0)\mathcal{E}_t(\mu_0, \phi_0)\right]_{ii} \end{array}\right\} & i = j \\ \left.\begin{array}{l} \dfrac{\exp[-\beta_j^t(\mu_0, \phi_0)H_t/\mu_0] - \exp[-\beta_i^t(\mu_0, \phi_0 + \pi)H_t/\mu_0]}{\beta_i^t(\mu_0, \phi_0 + \pi)/\mu_0 - \beta_j^t(\mu_0, \phi_0)/\mu_0} \\ \cdot[\mathcal{E}_t^{-1}(\mu_0, \phi_0 + \pi)\mathcal{P}_t(\mu_0, \phi_0 + \pi; \mu_0, \phi_0)\mathcal{E}_t(\mu_0, \phi_0)]_{ij} \end{array}\right\} & i \neq j \end{cases} \tag{3.60}$$

$$\mathcal{A}_6(\mu_0, \phi_0 + \pi; \mu_0, \phi_0) = \mathcal{E}_c(\mu_0, \phi_0 + \pi)\mathcal{B}_6(\mu_0, \phi_0 + \pi; \mu_0, \phi_0)\mathcal{E}_c^{-1}(-\mu_0, \phi_0)$$

$$[\mathcal{B}_6(\mu_0, \phi_0 + \pi; \mu_0, \phi_0)]_{ij} =$$
$$\frac{1 - \exp[-(\beta_i^c(\mu_0, \phi_0 + \pi)/\mu_0 + \beta_j^c(-\mu_0, \phi_0)/\mu_0)d]}{\beta_i^c(\mu_0, \phi_0 + \pi)/\mu_0 + \beta_j^c(-\mu_0, \phi_0)/\mu_0}$$
$$\cdot[\mathcal{E}_c^{-1}(\mu_0, \phi_0 + \pi)\mathcal{P}_c(\mu_0, \phi_0 + \pi; -\mu_0, \phi_0)\mathcal{E}_c(-\mu_0, \phi_0)]_{ij} \tag{3.61}$$

where β_m^t and β_m^c are the nth eigenvalues of $\boldsymbol{\kappa}_t^{\pm}$ and $\boldsymbol{\kappa}_c^{\pm}$, respectively. The phase and extinction matrices, $\mathcal{P}$ and $\boldsymbol{\kappa}^{\pm}$, may be computed by applying (2.12) and (2.13) together with appropriate scattering models for the individual vegetation constituents. The choice of which scattering models to apply for a given canopy depends on the shapes of the scattering constituents present in the canopy, as well as on their sizes relative to the radar wavelength. Constituent scattering models that are applicable to a wide variety of canopy architectures are presented in Appendices C and D.

$\mathcal{T}_t(\mu_0, \phi_0 + \pi)$ represents a first-order solution for canopy backscatter. This first-order approximation is reasonable at lower frequencies in cases where the scattering albedo of the medium is small. At higher frequencies, the effects of multiple scatter become more important and this approximation may break down (Ulaby *et al.*,[65]; McDonald *et al.* [43],[44]). In such cases, it may be appropriate to examine a second- or higher-order solution for backscatter. A second-order MIMICS solution may be derived by using the first-order intensities as new source functions in the radiative transfer equations and continuing with the iterative technique. Appendix E presents such a solution for direct crown backscatter. Although straightforward to derive, in the general case determination of the second-order backscatter contribution becomes computationally prohibitive and will not be examined in this study.

3.2 Modeling Ground Surface Cover

The model discussed in Section 3.1 works well for modeling many types of closed crown canopies situated on level ground if the ground surface may be accurately modeled by a specular surface for purposes of describing its forward scatter, and if the direct ground backscatter may be accurately modeled by applying an appropriate rough surface scattering model for $\mathcal{G}(\theta_0)$. As seen in some MIMICS I modeling analyses (Dobson *et al.*,[13]), ground surface cover can have a substantial effect on the canopy backscatter. If the ground is covered with snow or with a dense foliar understory, the accuracy of the specular forward scatter approximation and of the ground surface backscattering matrix comes into question. This section discusses techniques in which underlying ground cover may be accounted for in MIMICS.

Two basic approaches may be considered for modifying MIMICS I to account for ground cover. In one approach, an additional layer representing the ground cover may be added to the forest geometry and the radiative transfer equations solved for a three-layer forest medium over a dielectric half-space. In the other approach, the ground backscattering matrix $\mathcal{G}(\theta)$ and the ground reflectivity matrix $\mathcal{R}(\mu)$ may be modified to account for differences in the backscattered and specular scattered intensities from the ground surface. In this section, the latter approach is employed. This technique allows for a straightforward modification to the solution derived in Section 3.1 that still accounts for the first-order interaction mechanisms that occur between the canopy overstory and the underlying surface. Section 3.2.1 presents an approach for modeling a ground surface covered by a vegetation understory and Section 3.2.2 discusses an approach for modeling a ground surface covered by a snow layer.

3.2.1 Ground Surface Covered by a Foliar Understory

Canopy understory may be modeled as a single layer of vegetation over a ground surface. Figure 3.5 shows the scattering processes applicable to this problem. The understory layer has height H_u, a diffuse upper boundary, and is azimuthally symmetric. Figure 3.5(a) illustrates the scattering processes that modify the canopy direct ground backscatter. The specific intensity backscattered by the understory,

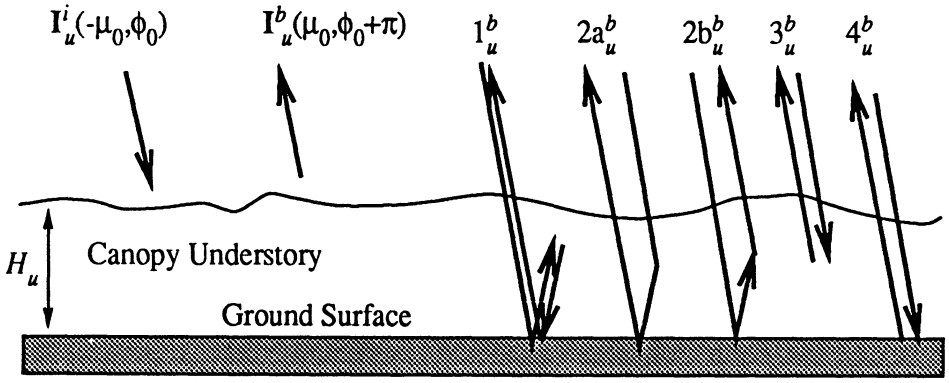

(a) Terms affecting the direct ground backscatter.

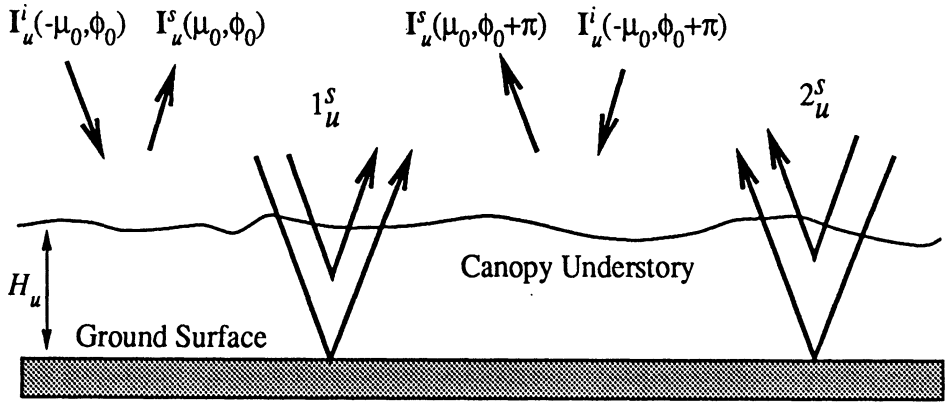

(b) Terms affecting ground specular scatter.

Figure 3.5: Contributions to canopy backscatter from the canopy understory.

$\mathbf{I}^b_u(-\mu_0, \phi_0 + \pi)$, is related to the intensity incident on the understory, $\mathbf{I}^i_u(-\mu_0, \phi_0)$,

through an effective ground backscattering matrix $\mathcal{G}_u(\theta_0)$ by the relationship

$$\mathbf{I}_u^b(-\mu_0, \phi_0 + \pi) = \mathcal{G}_u(\theta_0)\,\mathbf{I}_u^i(-\mu_0, \phi_0) \tag{3.62}$$

where the subscript u has been used to denote ground backscatter in the presence of a canopy understory.

$\mathcal{G}_u(\theta_0)$ is found by solving the radiative transfer problem for a single vegetation layer of height H_u over a ground surface (Ulaby and Elachi, [62]). This may be accomplished by employing (3.49) with no trunk layer ($H_t = 0$) and with the crown layer height d set equal to H_u:

$$\begin{aligned}
\mathcal{G}_u(\theta_0) \;=\;& \frac{1}{\mu_0} e^{-\boldsymbol{\kappa}_u^+ H_u/\mu_0} \mathcal{R}(\mu_0)\, \mathcal{A}_1(\mu_0, \phi_0 + \pi; \mu_0, \phi_0)\, \mathcal{R}(\mu_0)\, e^{-\boldsymbol{\kappa}_u^- H_u/\mu_0} \\
&+ \frac{1}{\mu_0} e^{-\boldsymbol{\kappa}_u^+ H_u/\mu_0} \mathcal{R}(\mu_0)\, \mathcal{A}_2(\mu_0, \phi_0 + \pi; \mu_0, \phi_0) \\
&+ \frac{1}{\mu_0} \mathcal{A}_3(\mu_0, \phi_0 + \pi; \mu_0, \phi_0)\, \mathcal{R}(\mu_0)\, e^{-\boldsymbol{\kappa}_u^- H_u/\mu_0} \\
&+ \frac{1}{\mu_0} \mathcal{A}_6(\mu_0, \phi_0 + \pi; \mu_0, \phi_0) \\
&+ e^{-\boldsymbol{\kappa}_u^+ H_u/\mu_0} \mathcal{G}(\theta_0)\, e^{-\boldsymbol{\kappa}_u^- H_u/\mu_0}
\end{aligned} \tag{3.63}$$

where $\boldsymbol{\kappa}_u^+ = \boldsymbol{\kappa}_u^-$ is the understory extinction matrix and the $\mathcal{A}_n$ values are computed by applying (3.56) through (3.61) to the understory layer.

The five terms in (3.63) correspond to terms 1_u^b, $2a_u^b$, $2b_u^b$, 3_u^b and 4_u^b, respectively, in Figure 3.5(a). The direct ground backscatter transformation matrix becomes

$$\mathcal{T}_g(\mu_0, \phi_0 + \pi) = e^{-\boldsymbol{\kappa}_c^+ d/\mu_0} e^{-\boldsymbol{\kappa}_t^+ H_t/\mu_0} \mathcal{G}_u(\theta_0)\, e^{-\boldsymbol{\kappa}_t^- H_t/\mu_0} e^{-\boldsymbol{\kappa}_c^- d/\mu_0} \tag{3.64}$$

where $\mathcal{G}(\theta_0)$ has been replaced by $\mathcal{G}_u(\theta_0)$ in (3.49).

Figure 3.5(b) illustrates the effect of the canopy understory on the ground specular scatter. This effect modifies the trunk-ground and crown-ground interaction scattering mechanisms, along with the ground-crown-ground multiple bounce term.

The intensity scattered by the understory $\mathbf{I}_u^s(\mu_0, \phi_0)$ is related to the incident intensity $\mathbf{I}_u^i(-\mu_0, \phi_0)$ through the two specular scattering mechanisms shown as part of term 1_u^s. Similarly, $\mathbf{I}_u^s(\mu_0, \phi_0 + \pi)$ is related to $\mathbf{I}_u^i(-\mu_0, \phi_0 + \pi)$ through the mechanisms shown as part of term 2_u^s. Terms 1_u^s and 2_u^s are identical for an azimuthally symmetric understory. Each of the two terms consists of two components. These represent an intensity scattered by the ground surface attenuated by two-way propagation through the understory layer and an intensity scattered by the vegetation itself. These components comprise the effective ground reflectivity matrix $\mathcal{R}_u(\mu_0)$ which relates the incident and scattered intensities as

$$\mathbf{I}_u^s(-\mu_0, \phi_0) = \mathcal{R}_u(\mu_0)\,\mathbf{I}_u^i(-\mu_0, \phi_0) \tag{3.65}$$

and

$$\mathbf{I}_u^s(-\mu_0, \phi_0 + \pi) = \mathcal{R}_u(\mu_0)\,\mathbf{I}_u^i(-\mu_0, \phi_0 + \pi) \tag{3.66}$$

where the subscript u denotes reflection by the ground layer in the presence of a canopy understory.

To solve for $\mathcal{R}_u(\mu_0)$, the radiative transfer equations are applied to a single vegetation layer over a specular ground surface. The solution is found by applying the canopy bistatic transformation matrix in (3.41) in the specular scatter direction ($\mu = \mu_0$ and $\phi = \phi_0$) with $H_t = 0$ and $d = H_u$. In addition, it is assumed that the component that is reflected from the ground is dominated by the zero-order intensity $\mathbf{I}^{(0)+}$, thereby neglecting terms 1 - 3 in Figure 3.3. Under these assumptions, $\mathcal{R}_u(\mu_0)$ becomes, in terms of (3.41),

$$\mathcal{R}_u(\mu_0) = e^{-\boldsymbol{\kappa}_u^+ H_u/\mu_0}\mathcal{R}(\mu_0)\,e^{-\boldsymbol{\kappa}_u^- H_u/\mu_0} + \frac{1}{\mu_0}\mathcal{A}_6(\mu_0, \phi_0; \mu_0, \phi_0) \tag{3.67}$$

where $\boldsymbol{\kappa}_u^+ = \boldsymbol{\kappa}_u^-$ is the understory extinction matrix and $\mathcal{A}_6$ is computed by applying

(3.47) to the understory layer. The effect on the ground specular scatter is then accounted for by setting $\mathcal{R}(\mu_0) = \mathcal{R}_u(\mu_0)$ in (3.49).

3.2.2 Ground Surface Covered by a Snow Layer

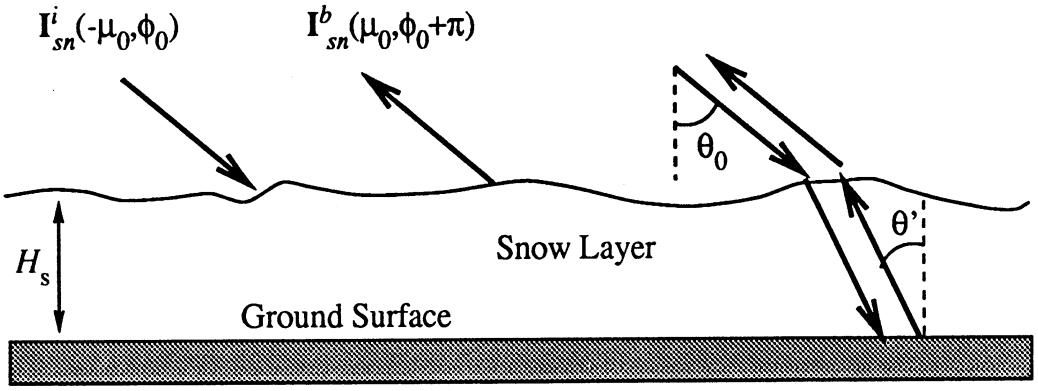

(a) Terms affecting the direct ground backscatter.

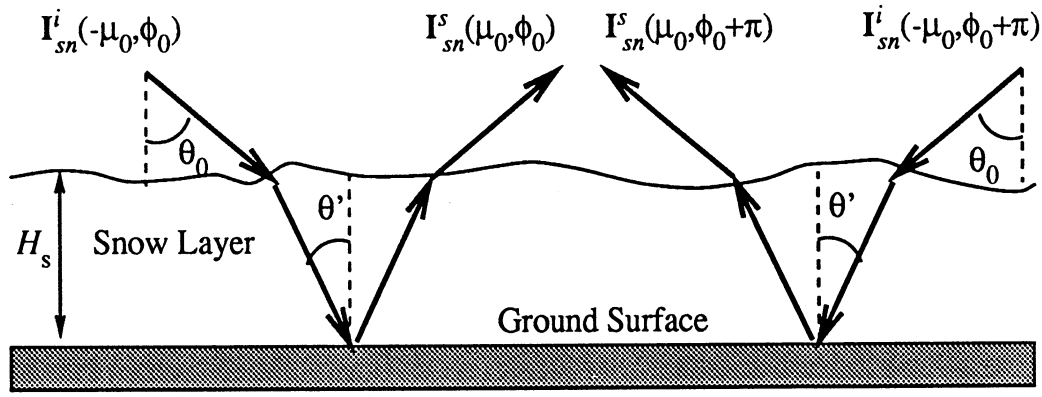

(b) Terms affecting ground specular scatter.

Figure 3.6: Contributions to canopy backscatter from an underlying snow layer.

At low frequencies, a snow layer may be modeled as an attenuating layer over a dielectric half space as shown in Figure 3.6. The snow layer has height H_s and relative dielectric ϵ_{sn}. The ground half-space has relative dielectric $\epsilon_r \gg \epsilon_{sn}$. Under this assumption, most scattering will occur at the snow-ground interface, thus allowing

any scattering from the snow surface and any volume scatter inside the snow layer to be neglected. This assumption works well at low frequencies (P- and L-bands) but may be inappropriate at higher frequencies where the contribution of volume scatter in the snow becomes more important.

Figure 3.6(a) illustrates the effect of the snow layer on direct ground backscatter. The intensity backscattered from the snow $\mathbf{I}^b_{sn}(\mu_0, \phi_0 + \pi)$ is related to the incident intensity $\mathbf{I}^i_{sn}(-\mu_0, \phi_0)$ through the effective ground backscattering matrix $\mathcal{G}_{sn}(\theta_0)$ as

$$\mathbf{I}^b_{sn}(-\mu_0, \phi_0 + \pi) = \mathcal{G}_{sn}(\theta_0)\, \mathbf{I}^i_{sn}(-\mu_0, \phi_0) \tag{3.68}$$

where the subscript sn in used to denote ground backscatter in the presence of a snow layer.

The angle of refraction in the snow layer θ' is related to the angle of incidence on the snow surface θ_0 through Snell's law. For a lossless layer in which ϵ_{sn} is a purely real number,

$$\sin\theta' \frac{1}{\sqrt{\epsilon_{sn}}} \sin\theta_0. \tag{3.69}$$

This relationship changes, however, for a layer in which $\epsilon_{r,s}$ is complex although Snell's law still holds in a purely formal way (Stratton, [56] pp. 500-505; Ulaby *et al.*, [70] pp. 76-78). In such a layer

$$\tan(\theta') = \frac{k_0 \sin\theta_0}{\frac{1}{\sqrt{2}}\sqrt{(p^2+q^2)^{1/2}+q}} \tag{3.70}$$

where

$$p = 2\alpha\beta \tag{3.71}$$

$$q = \beta^2 - \alpha^2 - k_0^2 \sin^2\theta_0 \tag{3.72}$$

$$\alpha = k_0 \left|\mathrm{Im}\sqrt{\epsilon_{sn}}\right| \tag{3.73}$$

$$\beta = k_0 \mathrm{Re}\sqrt{\epsilon_{sn}} \tag{3.74}$$

θ' is equivalent to the local angle of incidence on the ground surface. The snow layer therefore acts as a lens, focusing the incident intensity onto the ground surface.

The effective ground backscattering matrix is given by

$$\mathcal{G}_{sn}(\theta_0) = \mathrm{e}^{-\boldsymbol{\kappa}_{sn}H_s/\mu'}\mathcal{G}_{s\to g}(\theta')\mathrm{e}^{-\boldsymbol{\kappa}_{sn}H_s/\mu'} \tag{3.75}$$

where $\boldsymbol{\kappa}_{sn}$ is the snow extinction matrix, $\mathcal{G}_{s\to g}(\theta')$ is the ground backscattering matrix evaluated at θ' for the snow-ground interface and $\mu' = \cos\theta'$.

The extinction coefficient of the snow layer is related to the relative dielectric of the snow by

$$\kappa_{sn} = 2k_0\,|\mathrm{Im}\sqrt{\epsilon_{sn}}| \tag{3.76}$$

Since κ_{sn} is the same for both horizontal and vertical polarizations, the extinction matrix may be written in diagonal form:

$$\boldsymbol{\kappa}_{sn} = \begin{bmatrix} \kappa_{sn} & 0 & 0 & 0 \\ 0 & \kappa_{sn} & 0 & 0 \\ 0 & 0 & \kappa_{sn} & 0 \\ 0 & 0 & 0 & \kappa_{sn} \end{bmatrix} \tag{3.77}$$

so that the transmissivity of the snow layer is

$$\boldsymbol{\Upsilon}_{sn}(\mu') = \mathrm{e}^{-\boldsymbol{\kappa}_{sn}H_s/\mu'} \tag{3.78}$$

$$= \mathrm{e}^{-2\kappa_{sn}H_s/\mu'}\begin{bmatrix} 1 & 0 & 0 & 0 \\ 0 & 1 & 0 & 0 \\ 0 & 0 & 1 & 0 \\ 0 & 0 & 0 & 1 \end{bmatrix} \tag{3.79}$$

Equation (3.75) may then be written as

$$\mathcal{G}_{sn}(\theta_0) = \mathrm{e}^{-4\kappa_{sn}H_s/\mu'}\mathcal{G}_{s\to g}(\theta'). \tag{3.80}$$

Figure 3.6(b) illustrates the effect of the snow layer on the ground specular scatter. The intensity scattered from the snow $\mathbf{I}^s_{sn}(\mu_0, \phi_0)$ is related to the incident intensity $\mathbf{I}^i_{sn}(-\mu_0, \phi_0)$ through the effective ground reflectivity matrix $\mathcal{R}_{sn}(\mu_0)$. The scattered and incident intensities $\mathbf{I}^s_{sn}(\mu_0, \phi_0 + \pi)$ and $\mathbf{I}^i_{sn}(-\mu_0, \phi_0 + \pi)$ are similarly related. $\mathcal{R}_{sn}(\mu_0)$ is given by

$$\mathcal{R}_{sn}(\mu_0) = e^{-\kappa_{sn} H_s/\mu'} \mathcal{R}_{s\to g}(\mu') e^{-\kappa_{sn} H_s/\mu'} \tag{3.81}$$

$$= e^{-4\kappa_{sn} H_s/\mu'} \mathcal{R}_{s\to g}(\mu') \tag{3.82}$$

where $\mathcal{R}_{s\to g}(\mu')$ is the reflectivity matrix of the specular surface at the snow-ground interface, evaluated at the local angle of incidence θ'. Note that both $\mathcal{R}_{s\to g}(\mu')$ and $\mathcal{G}_{s\to g}(\theta')$ must be evaluated for scatter from an interface with a relative dielectric given by the ratio of the snow and ground dielectrics. The effect of the snow layer on the ground specular scatter is now accounted for by setting $\mathcal{R}(\mu_0) = \mathcal{R}_{sn}(\mu_0)$ in (3.49).

3.3 Applicability of MIMICS I

This chapter has presented the development of the MIMICS I model. MIMICS I represents the first in a planned series of radar backscatter models for use in modeling microwave backscatter from tree canopies. This model has been developed for application to azimuthally symmetric tree canopies on flat ground and with closed crown layer geometries. In this development, the canopy layers have been assumed to be statistically homogeneous. Thus, it cannot account for the effects of geometries such as row structure, as would be seen in many agricultural canopies.

MIMICS I has been found to function very well in a number of modeling studies. McDonald *et al.* [41], [42], [43], [44] and Dobson *et al.* [13] have used MIMICS I to model multi-angle and multi-temporal scatterometer measurements of a walnut

orchard. These analyses were performed as part of the EOS Synergism Study at the Kearney Agricultural Center in Fresno County, California during the summer of 1987 (Cimino *et al.* [9], Dobson *et al.* [15]). Here, MIMICS I has been shown to account for variations in canopy backscatter caused by changes in canopy water status as observed over a period of several days.

Dobson *et al.* [12], [13] and Kasischke *et al.* [32] have used MIMICS I to study multi-frequency, multi-polarization backscatter and extinction properties of several types of tree canopies in the Alaskan Boreal forest. In these analyses, the model has been shown to predict the behavior of canopy backscatter over changes in environmental conditions that caused the canopy to cycle between frozen and thawed states. This application is being extended by Way *et al.* [76], [78], [79], [80], for monitoring seasonal environmental and phenologic state of Alaskan forests.

The applicability of MIMICS I for predicting the sensitivity of microwave backscatter to changes in canopy biomass for Black Spruce stands has been examined by Skelly [53] and Skelly *et al.* [54], [55]. Data simulated in this study, although not compared directly with backscatter measurements, demonstrate how MIMICS may be applied to provide greater understanding of the use of SAR for estimating forest biomass.

Although developed primarily for application to tree canopies, MIMICS I may also be applied to model backscatter from many other types of vegetation canopies. For example, Ulaby and Elachi [62] p. 184 applied MIMICS in modeling like-polarized phase difference of backscatter from corn canopies (Ulaby *et al.*, [66]). These results have been extended in Chapter VI to illustrate a technique useful for monitoring soil moisture in corn canopies.

A major limitation of the MIMICS I model is that it was developed specifically for tree canopies with continuous crown layers. In order to more fully understand the

effect that discontinuous or open crown layer geometries have on canopy backscatter, a new version of MIMICS must be developed. To this end, the MIMICS II model is proposed in Chapter IV. Details of the statistics required for this model are examined in Chapter V. Chapter VI will then present specific modeling analyses and applications for both MIMICS I and II.

CHAPTER IV

RADAR BACKSCATTER MODEL FOR AN OPEN-CROWN CANOPY - MIMICS II

Although the closed-crown tree canopy model presented in Chapter III has been used successfully in many modeling applications, it does not account for the effects that discontinuities in the crown layer have on canopy backscatter. The purpose of this chapter is to introduce a radiative transfer-based model for tree canopies with discontinuous, or open, crown layer geometries, which shall be referred to as MIMICS II. In this case, backscatter mechanisms similar to those found for a closed crown canopy must be accounted for while allowing for opens areas, or gaps, in the crown layer. Figure 4.1 illustrates the types of backscattering mechanisms that must be considered. Terms 1 through 5 illustrate mechanisms which interact with the crown layer similar to those presented in Figure 3.4 while terms 6 through 10 illustrate the effects crown layer gaps have on these mechanisms.

A variety of work has been performed in modeling the interception of radiation with vegetation canopies that have discontinuous crown layers (Charles-Edward and Thorpe, [5]; Ferguson, [21]; Jackson and Palmer, [29]; Li, [37]; Li and Strahler, [38],[39]). Much of this work has been carried out for application to models describing processes at optical wavelengths. Typically, these analyses consider one of two

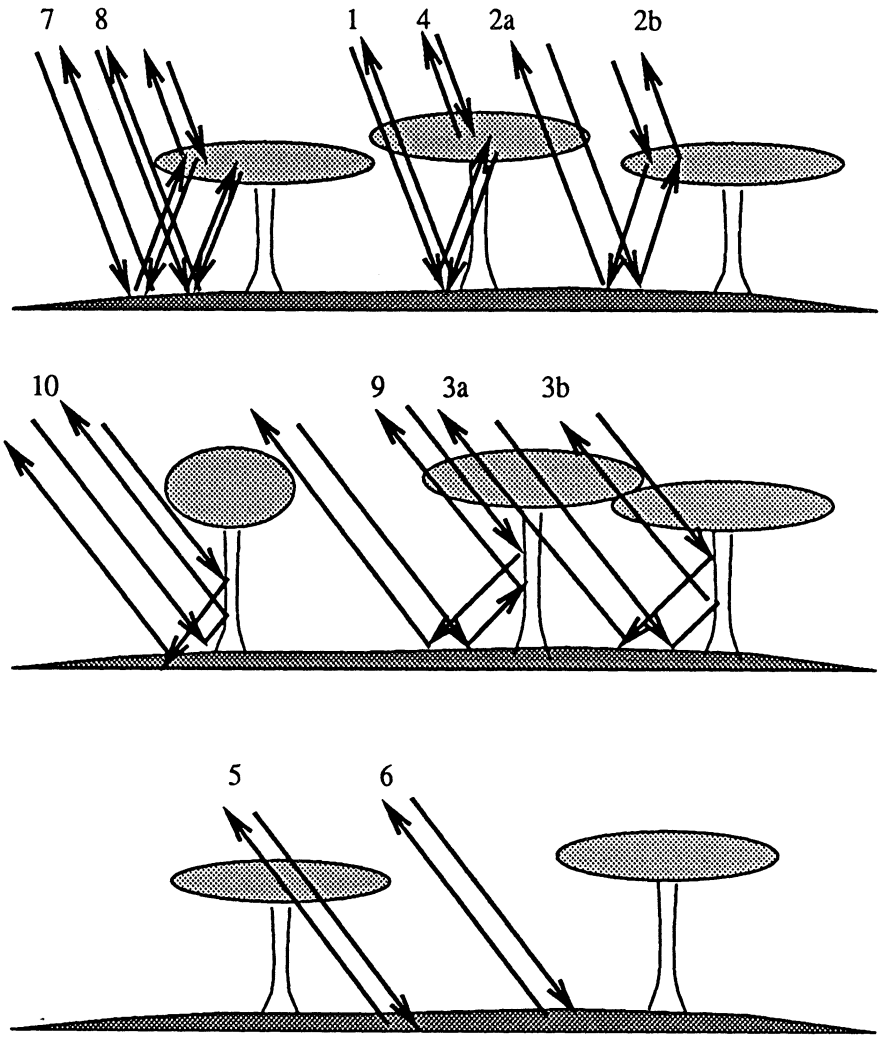

Figure 4.1: First-order backscatter terms for a discontinuous canopy.

general cases. These are the deterministic case, in which the shapes, sizes and locations of the tree crowns are precisely specified, and the statistical case in which these parameters are not precisely known but rather are specified in terms of probability distribution functions (PDFs). In general, deterministic modeling techniques may be applied to modeling radiation interception by canopies whose crown geometries and locations are well-specified, e.g. orchards, whereas statistical techniques may be applied when considering canopies whose crown geometries are not as well or-

dered. When considering natural forest stands, the latter approach is generally more appropriate.

Although several models have been proposed for continuous vegetation canopies (Attema and Ulaby, [2]; Durden *et al.*, [17]; Eom and Fung, [19]; Fung and Ulaby, [22]; Karam and Fung, [31]; Lang and Sidhu, [35]; Richards *et al.*, [48]; Tsang and Kong, [59]; Ulaby *et al.*, [69]), very little work has been done in developing models for canopies with discontinuous geometries at microwave frequencies. To date, Sun *et al.* [57] have proposed one such model for tree canopies. In this model, canopy-level statistics are used in the development of probability factors that describe the interception of radiation by the individual tree crowns. The MIMICS I solution is multiplied by these factors in order to account for the discontinuous nature of the crown layer. Essentially, this solution modifies the MIMICS I solution by a series of weighting factors.

This chapter proposes an approach to this problem that is based directly on the radiative transfer solution. This model represents the second version of the Michigan Microwave Canopy Scattering model, MIMICS II. Development of MIMICS II begins with the MIMICS I radiative transfer solution and proceeds by applying the canopy-level random variables to characterize an additional averaging process over and above that required in accounting for size and orientation on the level of the individual constituents.

First, Section 4.1 presents the form of the radiative transfer equations and transformation matrix for a canopy with a discontinuous crown layer. Given the form of these equations, a basic understanding of the statistics of open crown geometries must be developed. Section 4.2 develops these ideas by discussing the adaptation of canopy-level statistical parameters for application to the radiative transfer solution.

Two forms of the total canopy transformation matrix are then presented. Section 4.3 describes the fully polarimetric form and section 4.4 describes the scalar form. Detailed modeling examples will be presented in Chapter VI.

4.1 Radiative Transfer Solution for an Open-Crown Canopy

To determine the solution of the radiative transfer equations for a canopy with a discontinuous crown layer, a statistical method may be employed in which the gross crown layer geometry is described by a set of random variables with specified distribution functions. Once the radiative transfer solution is found for such a canopy, these canopy-level statistics may be introduced to estimate the canopy backscatter. To this end, a radiative transfer approach similar to that used in MIMICS I is applied with appropriate canopy-level statistical parameters introduced where necessary.

Again, the tree canopy is considered to have a three-layer structure as shown in Figure 4.2 with the crown and trunk layers each occupying distinct layers. The height of the trunk layer is defined by the average height of the trunks H_t and the height of the crown layer is defined by the maximum vertical distance d through which individual tree crowns are distributed. The total equivalent canopy height is $d' = H_t + d$.

As with MIMICS I, the problem is solved in two parts. First, the problem of backscatter from a two-layer canopy over a specular ground surface is addressed. Then, an appropriate term is added to account for backscatter directly from the ground surface. For the closed-crown geometry, the incident and scattered specific intensities are related through the total canopy backscattering transformation matrix $\mathcal{T}_t(\mu_0, \phi_0 + \pi)$, which is a function of the phase and extinction matrices of the crown and trunk layers. These quantities depend directly on an averaging process

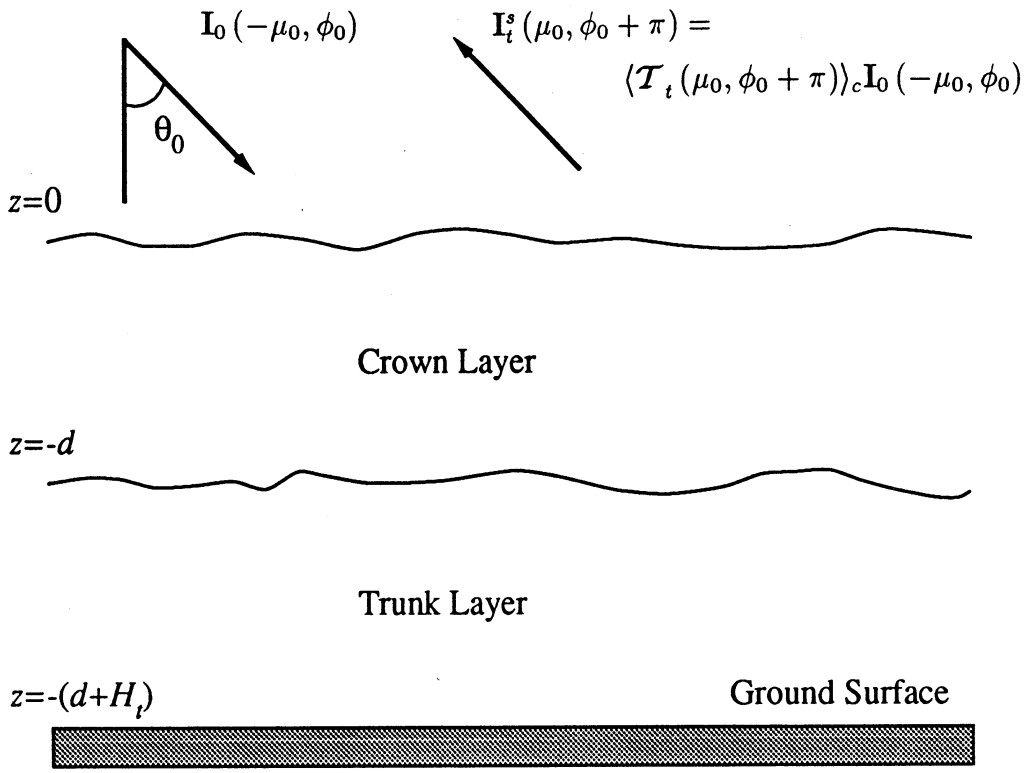

Figure 4.2: Model geometry for a canopy with a discontinuous crown layer.

performed over distribution functions that describe *tree-level* random variables defining constituent size and orientation. For the open crown layer case,

$$\langle \mathbf{I}_t^s(\mu_0, \phi_0 + \pi) \rangle_c = \langle \mathcal{T}_t(\mu_0, \phi_0 + \pi) \rangle_c \mathbf{I}_0(-\mu_0, \phi_0) \tag{4.1}$$

where crown layer discontinuities have been accounted for through an additional averaging process over the *canopy-level* random variables, as indicated by the notation $\langle \cdots \rangle_c$. This specifies the backscatter solution in terms of an extended set of parameters that includes the canopy-level random variables.

The function $\langle \mathcal{T}_t(\mu_0, \phi_0 + \pi) \rangle_c$, which represents the expected value of $\mathcal{T}_t$, is itself the sum of the expected values of the canopy and ground backscattering transformation matrices:

$$\langle \mathcal{T}_t(\mu_0, \phi_0 + \pi) \rangle_c = \langle \mathcal{T}(\mu_0, \phi_0 + \pi) \rangle_c + \langle \mathcal{T}_g(\mu_0, \phi_0 + \pi) \rangle_c . \tag{4.2}$$

where $\langle \mathcal{T}(\mu_0, \phi_0 + \pi) \rangle_c$ is the canopy backscattering transformation matrix relating incident and scattered intensities for the canopy over a specular ground surface:

$$\langle \mathbf{I}^s(\mu_0, \phi_0 + \pi) \rangle_c = \langle \mathcal{T}(\mu_0, \phi_0 + \pi) \rangle_c \mathbf{I}_0(-\mu_0, \phi_0) \tag{4.3}$$

and $\langle \mathcal{T}_g(\mu_0, \phi_0 + \pi) \rangle_c$ is the ground backscattering transformation matrix that accounts for the contribution of direct backscatter from the ground:

$$\left\langle \mathbf{I}_g^s(\mu_0, \phi_0 + \pi) \right\rangle_c = \langle \mathcal{T}_g(\mu_0, \phi_0 + \pi) \rangle_c \mathbf{I}_0(-\mu_0, \phi_0) \tag{4.4}$$

The effects of the open crown layer on the upward- and downward-propagating intensities in the crown and trunk layers may also be examined:

$$\begin{aligned}
\left\langle \mathbf{I}_c^+(\mu, \phi, z) \right\rangle_c &= \left\langle e^{-\boldsymbol{\kappa}_c^+(z+d)/\mu} \mathbf{I}_c^+(\mu, \phi, -d) \right\rangle_c \\
&\quad + \left\langle \int_{-d}^{z} e^{-\boldsymbol{\kappa}_c^+(z-z')/\mu} \mathbf{F}_c^+(\mu, \phi, z') \mathrm{d}z' \right\rangle_c \qquad (4.5) \\
\left\langle \mathbf{I}_c^-(-\mu, \phi, z) \right\rangle_c &= \left\langle e^{\boldsymbol{\kappa}_c^- z/\mu} \mathbf{I}_c^-(-\mu, \phi, 0) \right\rangle_c \\
&\quad + \left\langle \int_{z}^{0} e^{\boldsymbol{\kappa}_c^-(z-z')/\mu} \mathbf{F}_c^-(-\mu, \phi, z') \mathrm{d}z' \right\rangle_c \qquad (4.6) \\
\left\langle \mathbf{I}_t^+(\mu, \phi, z) \right\rangle_c &= e^{-\boldsymbol{\kappa}_t^+(z+d'))/\mu} \left\langle \mathbf{I}_t^+(\mu, \phi, -d') \right\rangle_c \\
&\quad + \left\langle \int_{-d'}^{z} e^{-\boldsymbol{\kappa}_t^+(z-z')/\mu} \mathbf{F}_t^+(\mu, \phi, z') \mathrm{d}z' \right\rangle_c \qquad (4.7) \\
\left\langle \mathbf{I}_t^-(-\mu, \phi, z) \right\rangle_c &= e^{\boldsymbol{\kappa}_t^-(z+d)/\mu} \left\langle \mathbf{I}_t^-(-\mu, \phi, -d) \right\rangle_c \\
&\quad + \left\langle \int_{z}^{-d} e^{\boldsymbol{\kappa}_t^-(z-z')/\mu} \mathbf{F}_t^-(-\mu, \phi, z') \mathrm{d}z' \right\rangle_c \qquad (4.8)
\end{aligned}$$

where $\langle \cdots \rangle_c$ denotes the expected value of the enclosed expression, indicating their dependence on the averaging process at the canopy level. Similarly, the source functions that account for coupling between the upward and downward propagating intensities are

$$\left\langle \mathbf{F}_c^+(\mu, \phi, z) \right\rangle_c = \left\langle \frac{1}{\mu} \int_0^{2\pi} \int_0^1 \mathcal{P}_c(\mu, \phi; \mu', \phi') \mathbf{I}_c^+(\mu', \phi', z) d\Omega' \right\rangle_c$$

$$+\left\langle \frac{1}{\mu}\int_0^{2\pi}\int_0^1 \mathcal{P}_c(\mu,\phi;-\mu',\phi')\mathbf{I}_c^-(-\mu',\phi',z)d\Omega' \right\rangle_c \tag{4.9}$$

$$\left\langle \mathbf{F}_c^-(-\mu,\phi,z)\right\rangle_c = \left\langle \frac{1}{\mu}[\int_0^{2\pi}\int_0^1 \mathcal{P}_c(-\mu,\phi;\mu',\phi')\mathbf{I}_c^+(\mu',\phi',z)d\Omega' \right\rangle_c$$
$$+\left\langle \frac{1}{\mu}\int_0^{2\pi}\int_0^1 \mathcal{P}_c(-\mu,\phi;-\mu',\phi')\mathbf{I}_c^-(-\mu',\phi',z)d\Omega' \right\rangle_c \tag{4.10}$$

$$\left\langle \mathbf{F}_t^+(\mu,\phi,z)\right\rangle_c = \left\langle \frac{1}{\mu}\int_0^{2\pi}\int_0^1 \mathcal{P}_t(\mu,\phi;\mu',\phi')\mathbf{I}_t^+(\mu',\phi',z)d\Omega'\delta_k(\mu-\mu') \right\rangle_c \tag{4.11}$$

$$\left\langle \mathbf{F}_t^-(-\mu,\phi,z)\right\rangle_c = \left\langle \frac{1}{\mu}\int_0^{2\pi}\int_0^1 \mathcal{P}_t(-\mu,\phi;-\mu',\phi')\mathbf{I}_t^-(-\mu',\phi',z)d\Omega'\delta_k(\mu-\mu') \right\rangle_c . \tag{4.12}$$

The iterative approach identical to that discussed in Chapter III is used to find the solution to (4.5) through (4.8), yielding

$$\begin{aligned}
&\langle \boldsymbol{\mathcal{T}}_t(\mu_0,\phi_0+\pi)\rangle_c \\
&\quad = \frac{1}{\mu_0}\langle e^{-\boldsymbol{\kappa}_c^+ d/\mu_0} e^{-\boldsymbol{\kappa}_t^+ H_t/\mu_0}\boldsymbol{\mathcal{R}}(\mu_0)\, e^{-\boldsymbol{\kappa}_t^- H_t/\mu_0}\boldsymbol{\mathcal{A}}_1(\mu_0,\phi_0+\pi;\mu_0,\phi_0) \\
&\qquad\qquad \cdot e^{-\boldsymbol{\kappa}_t^+ H_t/\mu_0}\boldsymbol{\mathcal{R}}(\mu_0)\, e^{-\boldsymbol{\kappa}_t^- H_t/\mu_0} e^{-\boldsymbol{\kappa}_c^- d/\mu_0}\rangle_c \\
&\quad + \frac{1}{\mu_0}\langle e^{-\boldsymbol{\kappa}_c^+ d/\mu_0} e^{-\boldsymbol{\kappa}_t^+ H_t/\mu_0}\boldsymbol{\mathcal{R}}(\mu_0)\, e^{-\boldsymbol{\kappa}_t^- H_t/\mu_0}\boldsymbol{\mathcal{A}}_2(\mu_0,\phi_0+\pi;\mu_0,\phi_0)\rangle_c \\
&\quad + \frac{1}{\mu_0}\langle \boldsymbol{\mathcal{A}}_3(\mu_0,\phi_0+\pi;\mu_0,\phi_0)\, e^{-\boldsymbol{\kappa}_t^+ H_t/\mu_0}\boldsymbol{\mathcal{R}}(\mu_0)\, e^{-\boldsymbol{\kappa}_t^- H_t/\mu_0} e^{-\boldsymbol{\kappa}_c^- d/\mu_0}\rangle_c \\
&\quad + \frac{1}{\mu_0}\langle e^{-\boldsymbol{\kappa}_c^+ d/\mu_0} e^{-\boldsymbol{\kappa}_t^+ H_t/\mu_0}\boldsymbol{\mathcal{R}}(\mu_0)\, \boldsymbol{\mathcal{A}}_4(\mu_0,\phi_0+\pi;\mu_0,\phi_0)\, e^{-\boldsymbol{\kappa}_c^- d/\mu_0}\rangle_c \\
&\quad + \frac{1}{\mu_0}\langle e^{-\boldsymbol{\kappa}_c^+ d/\mu_0}\boldsymbol{\mathcal{A}}_5(\mu_0,\phi_0+\pi;\mu_0,\phi_0)\,\boldsymbol{\mathcal{R}}(\mu_0)\, e^{-\boldsymbol{\kappa}_t^- H_t/\mu_0} e^{-\boldsymbol{\kappa}_c^- d/\mu_0}\rangle_c \\
&\quad + \frac{1}{\mu_0}\langle \boldsymbol{\mathcal{A}}_6(\mu_0,\phi_0+\pi;\mu_0,\phi_0)\rangle_c \\
&\quad + \langle e^{-\boldsymbol{\kappa}_c^+ d/\mu_0} e^{-\boldsymbol{\kappa}_t^+ H_t/\mu_0}\boldsymbol{\mathcal{G}}(\theta_0)\, e^{-\boldsymbol{\kappa}_t^- H_t/\mu_0} e^{-\boldsymbol{\kappa}_c^- d/\mu_0}\,.\rangle_c
\end{aligned} \tag{4.13}$$

where the $\boldsymbol{\mathcal{A}}_n$ matrices are given by (3.56) through (3.61).

Quantities describing trunk layer and ground surface scattering remain unchanged from the closed-crown layer case. Quantities in (4.13) that depend on the PDFs describing the canopy-level random variables include the crown layer phase matrices, $\mathcal{P}_c(\cdots)$, and the crown layer transmissivity matrix $e^{-\boldsymbol{\kappa}_c^{\pm} z}$.

4.2 Application of Canopy-level Statistical Parameters

In order to perform the averaging process over the canopy-level random variables, expressions relating the crown layer architecture to the parameters used in the radiative transfer solution must be developed. This section defines the attributes of the canopy-level statistical parameters necessary to describe crown-layer transmissivity and scattering properties.

4.2.1 Crown Layer Transmissivity

An important parameter in modeling the amount of radiation intercepted by a vegetation canopy is the *probability of gap*, or *gap probability*, P_{GAP} of the canopy (Li and Strahler,[39]). Historically, P_{GAP} has been used to describe transmissivity through canopies at optical frequencies. In these applications, the individual canopy constituents have infinite optical thickness and thus the gap probability represents the fraction of radiation that passes through a gap in the canopy. That is, P_{GAP} corresponds to the fraction of incident radiation not intercepted by any canopy constituent. In general, P_{GAP} may be defined as the probability that a portion of incident radiation will pass through a canopy unintercepted, i.e. the fraction of radiation that is unattenuated by the canopy. At microwave frequencies, this is equivalent to the canopy transmissivity. For a continuous crown layer (Li and Strahler,[39]),

$$P_{\mathrm{GAP}} = e^{-\tau s} \tag{4.14}$$

where τ is the extinction per unit length of the crown layer and s, the *within-crown propagation distance*, is the distance of propagation through the crown layer. Similarly, at microwave frequencies a continuous crown layer is characterized by an

extinction matrix $\boldsymbol{\kappa}_c$ and the transmissivity at a depth z in the crown layer is

$$\boldsymbol{\Upsilon}_c(z) = e^{\boldsymbol{\kappa}_c z/\mu} \tag{4.15}$$

where $\mu = \cos\theta$, z/μ is the total propagation distance in the crown layer and $z \leq 0$ represents the path length in the layer.

To find the transmissivity of a discontinuous crown layer, the geometry shown in Figure 4.3 is considered. In general, the distance s, which is a random variable

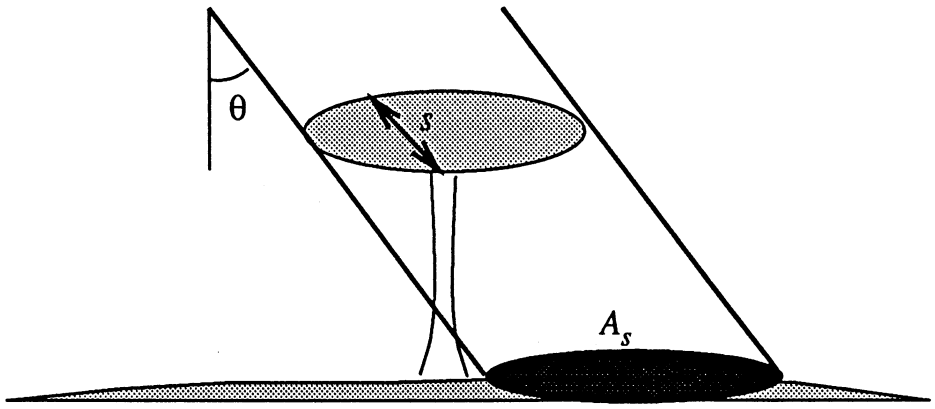

Figure 4.3: Illustration showing one individual tree crown, the within-crown propagation length s and the projected shadow area on the ground A_s for a view angle θ.

representing the total within-crown propagation distance for radiation incident at an angle θ, is a function of both θ and location (x, y) in the horizontal plane. If a PDF $p(s)$ describing $s(x, y, \theta)$ in the entire crown layer is known, then P_{GAP} may be expressed as an expected value:

$$P_{\mathrm{GAP}}(\theta) = \int_0^\infty p(s)\, e^{-\tau s} \mathrm{d}s. \tag{4.16}$$

Similarly, the expected value of transmissivity of the crown layer is

$$\langle \boldsymbol{\Upsilon}_c(\theta) \rangle_c = \int_0^\infty p(s)\, e^{-\boldsymbol{\kappa}_c s} \mathrm{d}s. \tag{4.17}$$

More generally, the expected value of the transmissivity for propagation l times through the same location in the crown layer is

$$\langle \Upsilon_c^l(\theta) \rangle_c = \int_0^\infty p(s)\, e^{-l\kappa_c s} ds. \tag{4.18}$$

The functional form of $p(s)$ depends on the shape and size of the tree crowns.

Li and Strahler, [39], have previously derived $p(s)$ for an entire crown layer and their approach is applied here. Consider a point on the ground (x, y). As illustrated in Figure 4.4, this point may be covered by no crown shadows, one shadow or any number n of shadows, where a shadow is defined from a radar-backscatter perspective. The probability that a ray passes through a given number of individual crowns

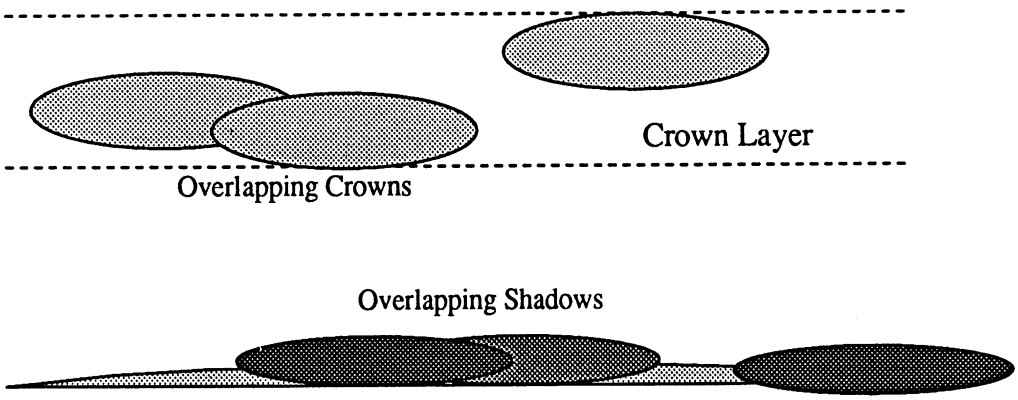

Figure 4.4: Canopy illumination geometry showing ovelapping crowns in th crown layer and the corresponding overlapping shadows on the ground. The number density of scatterers in the region where the two crowns overlap is twice that within one individual crown volume.

is equivalent to the probability of that number of shadows overlapping a point (x, y). For trees that are randomly spaced such that the crown shadows fall with equal likelihood anywhere on the ground, this probability is characterized by a Poisson PDF (Gedis and Jackson,[23]):

$$P(n) = (A_s N_t)^n \frac{e^{-(A_s N_t)}}{n!} \tag{4.19}$$

where N_t specifies the average number of trees per unit area in the canopy and A_s is the mean shadow size of the individual crowns. This distribution has a mean of $\overline{n} = A_s N_t$.

It is now assumed that the number density of scatterers within the overlapping portion of the tree crowns increases proportionally with the number of intersecting crowns. That is, the number of scatterers per unit volume is doubled, tripled, etc. corresponding to the number of crown volumes that overlap. If the propagation distance through the i^{th} crown is s_i and if n individual crowns are intersected, then the total within-crown pathlength is

$$s = \sum_{i=1}^{n} s_i. \tag{4.20}$$

The distribution of this within-crown pathlength given that the propagation is occuring through n crowns is

$$p(s|n) = p(s_1|1) * p(s_2|1) * \ldots * p(s_n|1) \tag{4.21}$$

where $*$ represents convolution. Then the PDF of s, taking into account all possibilities of multiple shadowing, and including the no-shadow case, is given by

$$p(s) = \sum_{n=0}^{\infty} P(n)\, p(s|n) \tag{4.22}$$

where $P(0)$ represesnts the no-shadow case. From (4.18), the average crown transmissivity becomes

$$\left\langle \Upsilon_c^l(\theta) \right\rangle_c = P(0) + \sum_{n=1}^{\infty} P(n) \int_0^{\infty} p(s|n)\, e^{-l\kappa_c s} ds \tag{4.23}$$

$$= P(0) + \sum_{n=1}^{\infty} P(n) \prod_{i=1}^{n} \int_0^{\infty} p(s_i|1)\, e^{-l\kappa_c s} ds \tag{4.24}$$

where $e^{-l\kappa_c s}$ has been treated as a Fourier kernel. If $p(s|1)$ is the same for all of the crowns, then

$$\left\langle \Upsilon_c^l(\theta) \right\rangle_c = P(0) + \sum_{n=1}^{\infty} P(n) \left[\int_0^{\infty} p(s|1)\, e^{-l\kappa_c s} ds \right]^n \tag{4.25}$$

where $l = 1$ for one-way transmissivity and $l = 2$ for the two-way case.

The probability $p(s|1)$ represents the distribution of s for propagation through a single crown and may be derived analytically or numerically for a wide variety of tree crowns. Derivation of $p(s|1)$ is discussed in Chapter V for various crown shapes. The transmissivity at any depth z in the crown layer may also be found from (4.25) by computing $p(s|1)$ for the partial crown shapes that result from slicing the crown layer at the depth z.

4.2.2 Crown Layer Phase Matrix

The crown layer phase matrix $\mathcal{P}_c$ is a random variable that depends on depth z in the crown layer. The expected value of $\mathcal{P}_c$ for an intensity incident in the (θ_i, ϕ_i) direction and scattered in the (θ_s, ϕ_s) direction is

$$\begin{aligned}
&\langle \mathcal{P}_c(\theta_s, \phi_s; \theta_i, \phi_i; z) \rangle_c \\
&= \sum_{k=1}^{K} \langle \mathcal{P}_k(\theta_s, \phi_s; \theta_i, \phi_i; z) \rangle_c \qquad (4.26) \\
&= \sum_{k=1}^{K} \left\langle N_k(z) \iiint f_k(\mathrm{s}_k; \theta_k, \phi_k)\, \mathcal{L}_k(\theta_s, \phi_s; \theta_i, \phi_i; \mathrm{s}_k; \theta_k, \phi_k)\, \mathrm{d}\mathrm{s}_k \mathrm{d}\theta_k \mathrm{d}\phi_k \right\rangle_c \qquad (4.27) \\
&= \sum_{k=1}^{K} \langle N_k(z) \rangle_c\, \overline{\mathcal{L}}_k(\theta_s, \phi_s; \theta_i, \phi_i; \mathrm{s}_k; \theta_k, \phi_k) \qquad (4.28)
\end{aligned}$$

where the summation over k represents an addition over the K constituent classes within the crown layer (branches, leaves, needles, etc.), $N_k(z)$ is the number density per unit volume of each class, $\mathcal{L}_k(\theta_s, \phi_s; \theta_i, \phi_i; \mathrm{s}_k; \theta_k, \phi_k)$ is the Mueller matrix for class k with size and orientation specified by s_k and (θ_k, ϕ_k), respectively, and $f_k(\mathrm{s}_k; \theta_k, \phi_k)$ is a distribution function over the size and orientation parameters. In general, for discontinuous crown layers, the number density of each constituent class is a random variable that depends on location in the crown layer. Thus, $N_k(z)$ at a particular depth z is an effective density that depends on the shapes and locations of

the individual crowns. In going from (4.27) to (4.28), the location of the scatterers in the crown layer is assumed to be independent of their scattering characteristics, thus imposing the condition of local statistical homogeneity.

4.2.3 Effective Scatterer Number Density

The expected value of the constituent number density $\langle N_k(z)\rangle_c$ is now considered. If number density increases proportionally with the number of intersecting crowns,

$$\langle N_k(z)\rangle_c = N_k \langle n(z)\rangle_c \tag{4.29}$$

where N_k is the number density of scatterers in class k within one individual crown volume and $\langle n(z)\rangle_c$ is the expected number of crowns overlapping at point (x, y) at depth z in the layer. For a canopy with density N_t trees per square meters that are randomly placed, the crown overlapping statistics are described by the Poisson distribution such that

$$\langle n(z)\rangle_c = \sum_0^\infty nP(n) \tag{4.30}$$

$$= \langle A_c(z)\rangle_c N_t \tag{4.31}$$

where $\langle A_c(z)\rangle_c$ is the expected value of cross sectional area of a single crown at depth z. Equation (4.31) is simply the expected value of the Poisson distribution $P(n)$.

As illustrated in Figure 4.5, the cross sectional area A_c of an individual crown is not only a function of z but also depends on random variables describing crown size and center location z_i. The expected value of the crown cross section is

$$\langle A_c(z)\rangle_c = \int_{\mathbf{t}}\int_{z_i} A_c(z, z_i, \mathbf{t})\, p_{z_i}(z_i)\, p_{\mathbf{t}}(\mathbf{t})\, dz_i d\mathbf{t} \tag{4.32}$$

where $p_{z_i}(z_i)$ and $p_{\mathbf{t}}(\mathbf{t})$ are the PDFs for the crown center location z_i and crown size parameters $\mathbf{t}$, and $A_c(z, z_i, \mathbf{t})$ is a function describing crown cross sectional area at

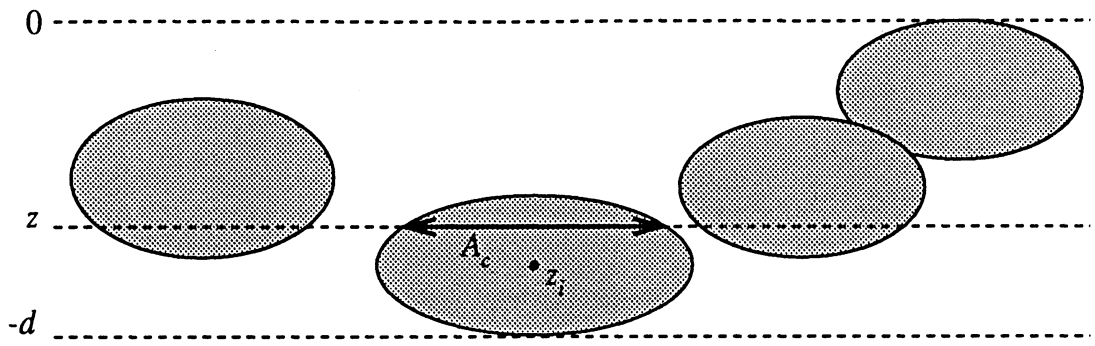

Figure 4.5: Cross-sectional area A_c at depth z of a crown centered at z_i.

a depth z for a crown characterized by size parameter t and whose center is at point z_i.

The quantity $\langle A_c(z)\rangle_c$ may be computed for a variety of combinations of crown shapes and center location distributions. Derivation of $\langle A_c(z)\rangle_c$ for a variety of crown shapes and crown layer geometries is presented in Chapter V. Given these expressions, the effective scatterer number density is

$$\langle N_k(z)\rangle_c = N_k N_t \langle A_c(z)\rangle_c . \tag{4.33}$$

4.3 Polarimetric Solution

When seeking a polarimetric solution for canopy backscatter, all of the boldface terms in (4.13) represent 4x4 matrices. Thus, since order of matrix multiplication is important, the trunk and crown layer transmissivities and phase matrices cannot be easily separated. To derive a solution, the matrix multiplications may be expanded and the canopy-level random variables applied to the individual elements. For example, to determine the elements of the crown-layer transmissivity matrix,

consider

$$\langle \boldsymbol{\Upsilon}_c(\theta_0)\rangle_c = \left\langle e^{-\boldsymbol{\kappa}_c s}\right\rangle_c \tag{4.34}$$

$$= \int_0^\infty p(s) e^{-\boldsymbol{\kappa}_c s} \mathrm{d}s \tag{4.35}$$

$$= \int_0^\infty p(s) \boldsymbol{\mathcal{E}}_c(\mu_0,\phi_0)\, \boldsymbol{\mathcal{D}}_c(\mu_0,\phi_0;s)\, \boldsymbol{\mathcal{E}}_c^{-1}(\mu_0,\phi_0)\, \mathrm{d}s \tag{4.36}$$

where

$$\boldsymbol{\mathcal{D}}_c(\mu_0,\phi_0;s) = \begin{bmatrix} e^{-\lambda_1(\mu_0,\phi_0)s} & 0 & 0 & 0 \\ 0 & e^{-\lambda_2(\mu_0,\phi_0)s} & 0 & 0 \\ 0 & 0 & e^{-\lambda_3(\mu_0,\phi_0)s} & 0 \\ 0 & 0 & 0 & e^{-\lambda_4(\mu_0,\phi_0)s} \end{bmatrix} \tag{4.37}$$

and the elements of $\boldsymbol{\mathcal{E}}_c$, which are defined in (2.16), are constant throughout the crown volumes. Expanding the matrix multiplications gives

$$\left\langle [\boldsymbol{\Upsilon}_c(\theta_0)]_{(i,j)}\right\rangle_c = \sum_{l=1}^{4} [\boldsymbol{\mathcal{E}}_c(\mu_0,\phi_0)]_{(i,l)} \left[\boldsymbol{\mathcal{E}}_c^{-1}(\mu_0,\phi_0)\right]_{(l,j)} \int_0^\infty p(s) e^{-\lambda_l s} \mathrm{d}s \tag{4.38}$$

where $p(s)$ is the PDF of within-crown propagation lengths. Each of the (i,j) elements of $\langle \boldsymbol{\Upsilon}_c(\theta_0)\rangle_c$ is seen to depend on the four eigenvalues defined by λ_l. Note that

$$\int_0^\infty p(s) e^{-\lambda_l s} \mathrm{d}s = P(0) + \sum_{n=1}^{\infty} P(n) \left[\int_0^\infty p(s|1)\, e^{-\lambda_l s} \mathrm{d}s\right]^n \tag{4.39}$$

and for complex λ_l:

$$\int_0^\infty p(s) e^{-\lambda_l s} \mathrm{d}s = P(0) + \sum_{n=1}^{\infty} P(n) \left\{ \int_0^\infty p(s|1)\, e^{-\mathrm{Re}(\lambda_l)s} \cos\left[\mathrm{Im}(\lambda_l)s\right] \mathrm{d}s \right.$$
$$\left. -i \int_0^\infty p(s|1)\, e^{-\mathrm{Re}(\lambda_l)s} \sin\left[\mathrm{Im}(\lambda_l)s\right] \mathrm{d}s \right\}^n \tag{4.40}$$

This matrix expansion technique may be applied to each of the scattering contributions in (4.13):

- Ground-Crown-Ground Multiple Bounce

$$\langle \mathcal{T}_{gcg}(\ \mu_0\ ,\phi_0+\pi)\rangle_c =$$

$$\frac{1}{\mu_0}\Big\langle e^{-\boldsymbol{\kappa}_c^+ d/\mu_0} e^{-\boldsymbol{\kappa}_t^+ H_t/\mu_0}\mathcal{R}(\mu_0)\, e^{-\boldsymbol{\kappa}_t^- H_t/\mu_0}$$
$$\cdot\left[\int_{-d}^{0} e^{-\boldsymbol{\kappa}_c^-(d+z')/\mu_0}\mathcal{P}_c(-\mu_0,\phi_0+\pi;\mu_0,\phi_0)\, e^{-\boldsymbol{\kappa}_c^-(z'+d)/\mu_0}\mathrm{d}z'\right]$$
$$\cdot e^{-\boldsymbol{\kappa}_t^+ H_t/\mu_0}\mathcal{R}(\mu_0)\, e^{-\boldsymbol{\kappa}_t^- H_t/\mu_0} e^{-\boldsymbol{\kappa}_c^- d/\mu_0}\Big\rangle_c \tag{4.41}$$

The paths of the upward and downward intensities, as they propagate completely through the crown layer, are assumed to be independent of the path of the intensity that is reflected upward by the ground and then backscattered by the crown down to the ground. First, let

$$\begin{aligned}\mathcal{M}_{gcg} &= \int_{-d}^{0} e^{-\boldsymbol{\kappa}_c^-(d+z')/\mu_0}\mathcal{P}_c(-\mu_0,\phi_0+\pi;\mu_0,\phi_0)\, e^{-\boldsymbol{\kappa}_c^-(z'+d)/\mu_0}\mathrm{d}z' \\ &= \int_{-d}^{0}\left[\mathcal{E}_c\cdot\mathcal{D}_c\left[-(d+z')/\mu_0\right]\cdot\mathcal{E}_c^{-1}\right]\cdot\mathcal{P}_c(-\mu_0,\phi_0+\pi;\mu_0,\phi_0) \\ &\quad\cdot\left[\mathcal{E}_c\cdot\mathcal{D}_c\left[-(z'+d)/\mu_0\right]\cdot\mathcal{E}_c^{-1}\right]\mathrm{d}z' \end{aligned}\tag{4.42}$$

so that for element (m,n) of $\mathcal{M}_{gcg}$,

$$\begin{aligned}[\mathcal{M}_{gcg}]_{(m,n)} &= \sum_{l=1}^{4}\sum_{k=1}^{4}\mathcal{E}_c(m,k)\,\mathcal{E}_c^{-1}(l,n) \\ &\quad \sum_{j=1}^{4}\sum_{i=1}^{4}\mathcal{P}_c(j,i)\,\mathcal{E}_c(i,l)\,\mathcal{E}_c^{-1}(k,j) \\ &\quad \cdot\int_{-d}^{0} e^{-(d+z')(\lambda_l+\lambda_k)/\mu_0}\mathrm{d}z' \qquad (4.43) \\ &= \sum_{l=1}^{4}\sum_{k=1}^{4}\mathcal{E}_c(m,k)\,\mathcal{E}_c^{-1}(l,n) \\ &\quad \cdot\ \sum_{j=1}^{4}\sum_{i=1}^{4}\frac{\mu_0\mathcal{P}_c(j,i)}{\lambda_l+\lambda_k}\mathcal{E}_c(i,l)\,\mathcal{E}_c^{-1}(k,j)\left[1-e^{-d(\lambda_l+\lambda_k)/\mu_0}\right]. \qquad (4.44)\end{aligned}$$

It then follows that

$$\left\langle[\mathcal{M}_{gcg}]_{(m,n)}\right\rangle_c = \sum_{l=1}^{4}\sum_{k=1}^{4}\mathcal{E}_c(m,k)\,\mathcal{E}_c^{-1}(l,n)$$

$$\cdot \sum_{j=1}^{4}\sum_{i=1}^{4}\left\langle \frac{\mu_0 \mathcal{P}_c(j,i)}{\lambda_l+\lambda_k}\right\rangle_c \mathcal{E}_c(i,l)\,\mathcal{E}_c^{-1}(k,j) \left[1-\int_0^\infty p(s)e^{-s(\lambda_l+\lambda_k)}ds\right]. \tag{4.45}$$

Now define

$$\mathcal{R}'(\mu_0) = \mathrm{e}^{-\kappa_t^+ H_t/\mu_0}\mathcal{R}(\mu_0)\,\mathrm{e}^{-\kappa_t^- H_t/\mu_0} \tag{4.46}$$

so

$$\begin{aligned}\langle \mathcal{T}_{gcg}(\ \mu_0\ ,\phi_0+\pi)\rangle_c &= \frac{1}{\mu_0}\left\langle\left[\mathcal{E}_c\cdot\mathcal{D}_c\cdot\mathcal{E}_c^{-1}\right]\cdot\left[\mathcal{R}'(\mu_0)\cdot\mathcal{M}_{gcg}\cdot\mathcal{R}'(\mu_0)\right]\right. \\ &\quad \left.\cdot\left[\mathcal{E}_c\cdot\mathcal{D}_c\cdot\mathcal{E}_c^{-1}\right]\right\rangle_c \qquad (4.47)\\ &= \frac{1}{\mu_0}\left\langle\left[\mathcal{E}_c\cdot\mathcal{D}_c\cdot\mathcal{E}_c^{-1}\right]\cdot\mathcal{M}_{gcg}^{(2)}\cdot\left[\mathcal{E}_c\cdot\mathcal{D}_c\cdot\mathcal{E}_c^{-1}\right]\right\rangle_c \qquad (4.48)\end{aligned}$$

where

$$\mathcal{M}_{gcg}^{(2)} = \mathcal{R}'(\mu_0)\cdot\mathcal{M}_{gcg}\cdot\mathcal{R}'(\mu_0). \tag{4.49}$$

Finally,

$$\begin{aligned}\left\langle[\mathcal{T}_{gcg}]_{(m,n)}\right\rangle_c &= \frac{1}{\mu_0}\sum_{l=1}^{4}\sum_{k=1}^{4}\mathcal{E}_c(m,k)\,\mathcal{E}_c^{-1}(l,n) \\ &\quad\cdot\sum_{j=1}^{4}\sum_{i=1}^{4}\mathcal{M}_{gcg}^{(2)}(j,i)\,\mathcal{E}_c(i,l)\,\mathcal{E}_c^{-1}(k,j)\left\langle e^{-s(\lambda_l+\lambda_k)}\right\rangle_c \qquad (4.50)\\ &= \frac{1}{\mu_0}\sum_{l=1}^{4}\sum_{k=1}^{4}\mathcal{E}_c(m,k)\,\mathcal{E}_c^{-1}(l,n) \\ &\quad\cdot\sum_{j=1}^{4}\sum_{i=1}^{4}\mathcal{M}_{gcg}^{(2)}(j,i)\,\mathcal{E}_c(i,l)\,\mathcal{E}_c^{-1}(k,j) \\ &\quad\cdot\left[\int_0^\infty p(s)e^{-s(\lambda_l+\lambda_k)}ds\right]. \qquad (4.51)\end{aligned}$$

This gives the expression for the (m,n) element of $\langle \mathcal{T}_{gcg}\rangle_c$.

- Crown-Ground Interaction

Here, the paths of the upward- and downward-propagating intensities are assumed to be independent, so

$$\begin{aligned}
&\langle \mathcal{T}_{cg}(\ \mu_0\ , \phi_0+\pi)\rangle_c \\
&\quad = \frac{1}{\mu_0}\Big\langle e^{-\boldsymbol{\kappa}_c^+ d/\mu_0} \mathrm{e}^{-\boldsymbol{\kappa}_t^+ H_t/\mu_0} \boldsymbol{\mathcal{R}}(\mu_0)\, \mathrm{e}^{-\boldsymbol{\kappa}_t^- H_t/\mu_0} \\
&\qquad \cdot \int_{-d}^{0} e^{-\boldsymbol{\kappa}_c^-(d+z')/\mu_0} \boldsymbol{\mathcal{P}}_c(-\mu_0, \phi_0+\pi; -\mu_0, \phi_0)\, e^{\boldsymbol{\kappa}_c^- z'/\mu_0} \mathrm{d}z' \Big\rangle_c \qquad (4.52) \\
&\quad = \frac{1}{\mu_0}\Big\langle e^{-\boldsymbol{\kappa}_c^+ d/\mu_0}\Big\rangle_c \boldsymbol{\mathcal{R}}'(\mu_0) \\
&\qquad \cdot \Big\langle \int_{-d}^{0} e^{-\boldsymbol{\kappa}_c^-(d+z')/\mu_0} \boldsymbol{\mathcal{P}}_c(-\mu_0, \phi_0+\pi; -\mu_0, \phi_0)\, e^{\boldsymbol{\kappa}_c^- z'/\mu_0} \mathrm{d}z' \Big\rangle_c \qquad (4.53) \\
&\quad = \frac{1}{\mu_0}\langle \boldsymbol{\Upsilon}_c(\theta_0)\rangle_c \boldsymbol{\mathcal{R}}'(\mu_0) \\
&\qquad \cdot \Big\langle \int_{-d}^{0} e^{-\boldsymbol{\kappa}_c^-(d+z')/\mu_0} \boldsymbol{\mathcal{P}}_c(-\mu_0, \phi_0+\pi; -\mu_0, \phi_0)\, e^{\boldsymbol{\kappa}_c^- z'/\mu_0} \mathrm{d}z' \Big\rangle_c \qquad (4.54)
\end{aligned}$$

Examine:

$$\begin{aligned}
\boldsymbol{\mathcal{M}}_{cg} &= \int_{-d}^{0} e^{-\boldsymbol{\kappa}_c^-(d+z')/\mu_0} \boldsymbol{\mathcal{P}}_c(-\mu_0, \phi_0+\pi; -\mu_0, \phi_0)\, e^{\boldsymbol{\kappa}_c^- z'/\mu_0} \mathrm{d}z' \qquad (4.55) \\
&= \int_{-d}^{0} \left[\boldsymbol{\mathcal{E}}_c \cdot \boldsymbol{\mathcal{D}}_c\left[-(d+z')/\mu_0\right] \cdot \boldsymbol{\mathcal{E}}_c^{-1}\right] \boldsymbol{\mathcal{P}}_c(-\mu_0, \phi_0+\pi; -\mu_0, \phi_0) \\
&\quad \cdot \left[\boldsymbol{\mathcal{E}}_c \cdot \boldsymbol{\mathcal{D}}_c\left[(z')/\mu_0\right] \cdot \boldsymbol{\mathcal{E}}_c^{-1}\right] \mathrm{d}z' \qquad (4.56)
\end{aligned}$$

Expanding gives

$$\begin{aligned}
[\boldsymbol{\mathcal{M}}_{cg}]_{(m,n)} &= \int_{-d}^{0} \sum_{l=1}^{4}\sum_{k=1}^{4} \boldsymbol{\mathcal{E}}_c(m,k)\, \boldsymbol{\mathcal{E}}_c^{-1}(l,n) \\
&\quad \cdot \sum_{j=1}^{4}\sum_{i=1}^{4} \boldsymbol{\mathcal{P}}_c(j,i)\, \boldsymbol{\mathcal{E}}_c(i,l)\, \boldsymbol{\mathcal{E}}_c^{-1}(k,j) \\
&\qquad \cdot e^{-(d+z')\lambda_k/\mu_0 + z'\lambda_l/\mu_0} \mathrm{d}z' \qquad (4.57) \\
&= \sum_{l=1}^{4}\sum_{k=1}^{4} \boldsymbol{\mathcal{E}}_c(m,k)\, \boldsymbol{\mathcal{E}}_c^{-1}(l,n) \\
&\quad \cdot \sum_{j=1}^{4}\sum_{i=1}^{4} \boldsymbol{\mathcal{P}}_c(j,i)\, \boldsymbol{\mathcal{E}}_c(i,l)\, \boldsymbol{\mathcal{E}}_c^{-1}(k,j) \\
&\quad \cdot \frac{\mu_0}{\lambda_l - \lambda_k}\left[e^{-d\lambda_k/\mu_0} - e^{-d\lambda_l/\mu_0}\right] \qquad (4.58)
\end{aligned}$$

$$= \sum_{l=1}^{4}\sum_{k=1}^{4} \mathcal{E}_c(m,k)\,\mathcal{E}_c^{-1}(l,n)$$
$$\cdot \sum_{j=1}^{4}\sum_{i=1}^{4} \mathcal{E}_c(i,l)\,\mathcal{E}_c^{-1}(k,j)\,\mathcal{Q}(l,k) \qquad (4.59)$$

where

$$\mathcal{Q}(l,k) = \begin{cases} \mu_0 d\mathcal{P}_c(j,i)\,e^{-d\lambda_k/\mu_0} & l=k \\ \frac{\mu_0\mathcal{P}_c(j,i)}{\lambda_l-\lambda_k}\left[e^{-d\lambda_k/\mu_0} - e^{-d\lambda_l/\mu_0}\right] & l\neq k \end{cases} \qquad (4.60)$$

so

$$\left\langle [\mathcal{M}_{cg}]_{(m,n)} \right\rangle_c = \sum_{l=1}^{4}\sum_{k=1}^{4} \mathcal{E}_c(m,k)\,\mathcal{E}_c^{-1}(l,n)$$
$$\sum_{j=1}^{4}\sum_{i=1}^{4} \mathcal{E}_c(i,l)\,\mathcal{E}_c^{-1}(k,j)\,\langle \mathcal{Q}(l,k)\rangle_c \qquad (4.61)$$

with

$$\langle \mathcal{Q}(l,k)\rangle_c = \begin{cases} \mu_0 d\,\langle \mathcal{P}_c(j,i)\rangle_c \int_0^\infty p(s)e^{-s\lambda_k}\mathrm{d}s & l=k \\ \mu_0 \left\langle \frac{\mathcal{P}_c(j,i)}{\lambda_l-\lambda_k}\right\rangle_c \int_0^\infty p(s)\left[e^{-s\lambda_k} - e^{-s\lambda_l}\right]\mathrm{d}s & l\neq k \end{cases} \qquad (4.62)$$

The entire term is then given by the product of three matrices:

$$\langle \mathcal{T}_{cg}(\ \mu_0\ , \phi_0+\pi)\rangle_c$$
$$= \frac{1}{\mu_0}\langle \Upsilon_c(\theta_0)\rangle_c\,\mathcal{R}'(\mu_0)\,\langle \mathcal{M}_{cg}\rangle_c . \qquad (4.63)$$

- Ground-Crown Interaction

Derivation of this term is very similar to that of the crown-ground interaction:

$$\langle \mathcal{T}_{gc}(\ \mu_0\ , \phi_0+\pi)\rangle_c$$
$$= \frac{1}{\mu_0}\left\langle \left[\int_{-d}^{0} e^{\kappa_c^+ z'/\mu_0}\mathcal{P}_c(\mu_0,\phi_0+\pi;\mu_0,\phi_0)\,e^{-\kappa_c^+(z'+d)/\mu_0}\mathrm{d}z'\right]\right.$$
$$\left.\cdot e^{-\kappa_t^+ H_t/\mu_0}\mathcal{R}(\mu_0)\,e^{-\kappa_t^- H_t/\mu_0}e^{-\kappa_c^- d/\mu_0}\right\rangle_c \qquad (4.64)$$
$$= \frac{1}{\mu_0}\left\langle \left[\int_{-d}^{0} e^{\kappa_c^+ z'/\mu_0}\mathcal{P}_c(\mu_0,\phi_0+\pi;\mu_0,\phi_0)\,e^{-\kappa_c^+(z'+d)/\mu_0}\mathrm{d}z'\right]\right\rangle_c$$
$$\cdot\mathcal{R}'(\mu_0)\,\langle \Upsilon_c(\theta_0)\rangle_c \qquad (4.65)$$

Letting

$$\mathcal{M}_{gc} = \int_{-d}^{0} e^{\kappa_c^+ z'/\mu_0} \mathcal{P}_c(\mu_0, \phi_0+\pi; \mu_0, \phi_0)\, e^{-\kappa_c^+ (z'+d)/\mu_0} \mathrm{d}z' \tag{4.66}$$

$$= \int_{-d}^{0} \left[\mathcal{E}_c \cdot \mathcal{D}_c[z'/\mu_0] \cdot \mathcal{E}_c^{-1}\right] \mathcal{P}_c(\mu_0, \phi_0+\pi; \mu_0, \phi_0) \left[\mathcal{E}_c \cdot \mathcal{D}_c[-(z'+d)/\mu_0] \cdot \mathcal{E}_c^{-1}\right] \mathrm{d}z' \tag{4.67}$$

where

$$[\mathcal{M}_{gc}]_{(m,n)} = \int_{-d}^{0} \sum_{l=1}^{4}\sum_{k=1}^{4} \mathcal{E}_c(m,k)\,\mathcal{E}_c^{-1}(l,n) \cdot \sum_{j=1}^{4}\sum_{i=1}^{4} \mathcal{P}_c(j,i)\,\mathcal{E}_c(i,l)\,\mathcal{E}_c^{-1}(k,j) \cdot e^{z'\lambda_k/\mu_0 - (z'+d)\lambda_l/\mu_0} \mathrm{d}z' \tag{4.68}$$

$$= \sum_{l=1}^{4}\sum_{k=1}^{4} \mathcal{E}_c(m,k)\,\mathcal{E}_c^{-1}(l,n) \cdot \sum_{j=1}^{4}\sum_{i=1}^{4} \mathcal{E}_c(i,l)\,\mathcal{E}_c^{-1}(k,j)\,\mathcal{Q}(l,k) \tag{4.69}$$

with

$$\mathcal{Q}(l,k) = \begin{cases} \mu_0 d \mathcal{P}_c(j,i)\, e^{-d\lambda_k/\mu_0} & l = k \\ \frac{\mu_0 \mathcal{P}_c(j,i)}{\lambda_k - \lambda_l}\left[e^{-d\lambda_l/\mu_0} - e^{-d\lambda_k/\mu_0}\right] & l \neq k, \end{cases} \tag{4.70}$$

we have

$$\left\langle [\mathcal{M}_{gc}]_{(m,n)} \right\rangle_c = \sum_{l=1}^{4}\sum_{k=1}^{4} \mathcal{E}_c(m,k)\,\mathcal{E}_c^{-1}(l,n) \cdot \sum_{j=1}^{4}\sum_{i=1}^{4} \mathcal{E}_c(i,l)\,\mathcal{E}_c^{-1}(k,j)\,\langle \mathcal{Q}(l,k)\rangle_c \tag{4.71}$$

where

$$\langle \mathcal{Q}(l,k)\rangle_c = \begin{cases} \mu_0 d \langle \mathcal{P}_c(j,i)\rangle_c \int_0^\infty p(s) e^{-s\lambda_k} \mathrm{d}s & l = k \\ \mu_0 \left\langle \frac{\mathcal{P}_c(j,i)}{\lambda_k - \lambda_l} \right\rangle_c \int_0^\infty p(s)\left[e^{-s\lambda_l} - e^{-s\lambda_k}\right] \mathrm{d}s & l \neq k. \end{cases} \tag{4.72}$$

Finally,

$$\langle \mathcal{T}_{gc}(\ \mu_0\ , \phi_0+\pi)\rangle_c = \frac{1}{\mu_0} \langle \mathcal{M}_{gc}\rangle_c\, \mathcal{R}'(\mu_0)\, \langle \mp_c(\theta_0)\rangle_c \tag{4.73}$$

yields the ground-crown interaction mechamism.

- Trunk-Ground Interaction

This mechanism is independent of the crown layer statistics except as they apply to crown layer transmissivity. The propagation paths in the crown layer for positive- and negative-going intensities are assumed to be independent. Hence,

$$\begin{aligned}\langle \mathcal{T}_{tg}(\ \mu_0\ , \phi_0+\pi)\rangle_c \doteq \\ \frac{1}{\mu_0}\ \Big\langle & e^{-\kappa_c^+ d/\mu_0} e^{-\kappa_t^+ H_t/\mu_0}\mathcal{R}(\mu_0) \\ \cdot\ & \left[\int_{-d'}^{-d} e^{-\kappa_t^-(d'+z')/\mu_0}\mathcal{P}_t(-\mu_0,\phi_0+\pi;-\mu_0,\phi_0)\, e^{\kappa_t^-(z'+d)/\mu_0}\mathrm{d}z'\right] \\ \cdot\ & e^{-\kappa_c^- d/\mu_0}\Big\rangle_c \end{aligned} \tag{4.74}$$

Noting that

$$\begin{aligned}\mathcal{M}_{tg} \ =\ & e^{-\kappa_t^+ H_t/\mu_0}\mathcal{R}(\mu_0) \\ & \left[\int_{-d'}^{-d} e^{-\kappa_t^-(d'+z')/\mu_0}\mathcal{P}_t(-\mu_0,\phi_0+\pi,;-\mu_0,\phi_0)\, e^{\kappa_t^-(z'+d)/\mu_0}\mathrm{d}z'\right]\end{aligned} \tag{4.75}$$

is identical to the MIMICS I solution for trunk-ground scattering in the absence of a crown layer, it follows that

$$\langle \mathcal{T}_{tg}\rangle_c = \frac{1}{\mu_0}\left\langle e^{-\kappa_c^+ d/\mu_0}\cdot\mathcal{M}_{tg}\cdot e^{-\kappa_c^- d/\mu_0}\right\rangle_c \tag{4.76}$$

$$= \frac{1}{\mu_0}\left\langle\left[\mathcal{E}_c\cdot\mathcal{D}_c\cdot\mathcal{E}_c^{-1}\right]\cdot\mathcal{M}_{tg}\cdot\left[\mathcal{E}_c\cdot\mathcal{D}_c\cdot\mathcal{E}_c^{-1}\right]\right\rangle_c \tag{4.77}$$

$$= \frac{1}{\mu_0}\left\langle\left[\mathcal{E}_c\cdot\mathcal{D}_c\cdot\mathcal{E}_c^{-1}\right]\right\rangle_c\cdot\mathcal{M}_{tg}\cdot\left\langle\left[\mathcal{E}_c\cdot\mathcal{D}_c\cdot\mathcal{E}_c^{-1}\right]\right\rangle_c \tag{4.78}$$

with elements (m,n) given by

$$\left\langle[\mathcal{T}_{tg}]_{(m,n)}\right\rangle_c = \frac{1}{\mu_0}\sum_{l=1}^{4}\sum_{k=1}^{4}\mathcal{E}_c(m,k)\,\mathcal{E}_c^{-1}(l,n)$$

$$\cdot \sum_{j=1}^{4}\sum_{i=1}^{4} \mathcal{M}_{tg}(j,i)\,\mathcal{E}_c(i,l)\,\mathcal{E}_c^{-1}(k,j)\left\langle e^{-s\lambda_l}\right\rangle_c \left\langle e^{-s\lambda_k}\right\rangle_c \quad (4.79)$$

$$= \frac{1}{\mu_0}\sum_{l=1}^{4}\sum_{k=1}^{4} \mathcal{E}_c(m,k)\,\mathcal{E}_c^{-1}(l,n)$$
$$\cdot \sum_{j=1}^{4}\sum_{i=1}^{4} \mathcal{M}_{tg}(j,i)\,\mathcal{E}_c(i,l)\,\mathcal{E}_c^{-1}(k,j)$$
$$\cdot \left[\int_0^\infty p(s)\,e^{-s\lambda_l}\mathrm{d}s\right]\left[\int_0^\infty p(s)\,e^{-s\lambda_k}\mathrm{d}s\right]. \quad (4.80)$$

- Ground-Trunk Interaction

Expansion of this mechanism follows in the same way:

$$\langle \mathcal{T}_{gt}(\ \mu_0\ ,\phi_0+\pi)\rangle_c =$$
$$\frac{1}{\mu_0}\left\langle e^{-\kappa_c^+ d/\mu_0}\left[\int_{-d'}^{d} e^{\kappa_t^+(d+z')/\mu_0}\mathcal{P}_t(\mu_0,\phi_0+\pi,;\mu_0,\phi_0)\,e^{-\kappa_t^+(d'+z')/\mu_0}\mathrm{d}z'\right]\right.$$
$$\left.\cdot\ \ \mathcal{R}(\mu_0)\,e^{-\kappa_t^- H_t/\mu_0}e^{-\kappa_c^- d/\mu_0}\right\rangle_c \quad (4.81)$$
$$= \frac{1}{\mu_0}\left\langle e^{-\kappa_c^+ d/\mu_0}\left[\mathcal{M}_{gt}\right]e^{-\kappa_c^- d/\mu_0}\right\rangle_c \quad (4.82)$$

where

$$\mathcal{M}_{gt} = \left[\int_{-d'}^{d} e^{\kappa_t^+(d+z')/\mu_0}\mathcal{P}_t(\mu_0,\phi_0+\pi,;\mu_0,\phi_0)\,e^{-\kappa_t^+(d'+z')/\mu_0}\mathrm{d}z'\right]$$
$$\cdot\mathcal{R}(\mu_0)\,e^{-\kappa_t^- H_t/\mu_0} \quad (4.83)$$

is identical to the MIMICS I case. Then

$$\langle \mathcal{T}_{gt}\rangle_c = \frac{1}{\mu_0}\left\langle e^{-\kappa_c^+ d/\mu_0}\cdot\mathcal{M}_{gt}\cdot e^{-\kappa_c^- d/\mu_0}\right\rangle_c \quad (4.84)$$
$$= \frac{1}{\mu_0}\left\langle\left[\mathcal{E}_c\cdot\mathcal{D}_c\cdot\mathcal{E}_c^{-1}\right]\cdot\mathcal{M}_{gt}\cdot\left[\mathcal{E}_c\cdot\mathcal{D}_c\cdot\mathcal{E}_c^{-1}\right]\right\rangle_c \quad (4.85)$$
$$= \frac{1}{\mu_0}\left\langle\left[\mathcal{E}_c\cdot\mathcal{D}_c\cdot\mathcal{E}_c^{-1}\right]\right\rangle_c\cdot\mathcal{M}_{gt}\cdot\left\langle\left[\mathcal{E}_c\cdot\mathcal{D}_c\cdot\mathcal{E}_c^{-1}\right]\right\rangle_c \quad (4.86)$$

and expanding gives:

$$\left\langle\left[\mathcal{T}_{gt}\right]_{(m,n)}\right\rangle_c = \frac{1}{\mu_0}\sum_{l=1}^{4}\sum_{k=1}^{4}\mathcal{E}_c(m,k)\,\mathcal{E}_c^{-1}(l,n)$$

$$\cdot \sum_{j=1}^{4}\sum_{i=1}^{4} \mathcal{M}_{gt}(j,i)\,\mathcal{E}_c(i,l)\,\mathcal{E}_c^{-1}(k,j)\left\langle e^{-s\lambda_l}\right\rangle_c \left\langle e^{-s\lambda_k}\right\rangle_c \quad (4.87)$$

$$= \frac{1}{\mu_0}\sum_{l=1}^{4}\sum_{k=1}^{4} \mathcal{E}_c(m,k)\,\mathcal{E}_c^{-1}(l,n)$$
$$\cdot \sum_{j=1}^{4}\sum_{i=1}^{4} \mathcal{M}_{gt}(j,i)\,\mathcal{E}_c(i,l)\,\mathcal{E}_c^{-1}(k,j)$$
$$\cdot \left[\int_0^\infty p(s)\,e^{-s\lambda_l}\mathrm{d}s\right]\left[\int_0^\infty p(s)\,e^{-s\lambda_k}\mathrm{d}s\right]. \quad (4.88)$$

- Direct Crown Backscatter

Here,

$$\langle \mathcal{T}_c(\ \mu_0\ ,\phi_0+\pi)\rangle_c$$
$$= \frac{1}{\mu_0}\left\langle \int_{-d}^{0} e^{\kappa_c^+ z'/\mu_0}\,\mathcal{P}_c(\mu_0,\phi_0+\pi,;-\mu_0,\phi_0)\,e^{\kappa_c^- z'/\mu_0}\mathrm{d}z'\right\rangle_c \quad (4.89)$$
$$= \frac{1}{\mu_0}\left\langle \int_{-d}^{0} \left[\mathcal{E}_c\cdot\mathcal{D}_c(z')\cdot\mathcal{E}_c^{-1}\right]\cdot\mathcal{P}_c(\mu_0,\phi_0+\pi,;-\mu_0,\phi_0)\right.$$
$$\left.\cdot\left[\mathcal{E}_c\cdot\mathcal{D}_c(z')\cdot\mathcal{E}_c^{-1}\right]\mathrm{d}z'\right\rangle_c \quad (4.90)$$

Expanding gives

$$\left\langle [\mathcal{T}_c]_{(m,n)}\right\rangle_c = \frac{1}{\mu_0}\left\langle \int_{-d}^{0}\sum_{l=1}^{4}\sum_{k=1}^{4} \mathcal{E}_c(m,k)\,\mathcal{E}_c^{-1}(l,n)\right.$$
$$\left.\cdot \sum_{j=1}^{4}\sum_{i=1}^{4} \mathcal{P}_c(j,i)\,\mathcal{E}_c(i,l)\,\mathcal{E}_c^{-1}(k,j)\,e^{z'(\lambda_l+\lambda_k)/\mu_0}\mathrm{d}z'\right\rangle_c \quad (4.91)$$
$$= \frac{1}{\mu_0}\sum_{l=1}^{4}\sum_{k=1}^{4} \mathcal{E}_c(m,k)\,\mathcal{E}_c^{-1}(l,n)$$
$$\cdot \sum_{j=1}^{4}\sum_{i=1}^{4} \mu_0\left\langle \frac{\mathcal{P}_c(j,i)}{\lambda_l+\lambda_k}\right\rangle_c \mathcal{E}_c(i,l)\,\mathcal{E}_c^{-1}(k,j)$$
$$\left[1-\int_0^\infty p(s)e^{-s(\lambda_l+\lambda_k)}\mathrm{d}s\right] \quad (4.92)$$

- Direct Ground Backscatter

In this case, the paths of the upward- and downward-propagating intensities in the crown layer are identical. Hence,

$$\langle \mathcal{T}_g(\ \mu_0\ ,\phi_0+\pi)\rangle_c =$$

$$\left\langle e^{-\kappa_c^+ d/\mu_0} e^{-\kappa_t^+ H_t/\mu_0} \mathcal{G}(\theta_0) e^{-\kappa_t^- H_t/\mu_0} e^{-\kappa_c^- d/\mu_0} \right\rangle . \quad (4.93)$$

Defining

$$\mathcal{M}_g = e^{-\kappa_t^+ H_t/\mu_0} \mathcal{G}(\theta_0) e^{-\kappa_t^- H_t/\mu_0} \quad (4.94)$$

so that

$$\langle \mathcal{T}_g \rangle_c = \left\langle e^{-\kappa_c^+ d/\mu_0} \mathcal{M}_g e^{-\kappa_c^- d/\mu_0} \right\rangle_c \quad (4.95)$$

$$= \frac{1}{\mu_0} \left\langle \left[\mathcal{E}_c \cdot \mathcal{D}_c \cdot \mathcal{E}_c^{-1} \right] \cdot \mathcal{M}_g \cdot \left[\mathcal{E}_c \cdot \mathcal{D}_c \cdot \mathcal{E}_c^{-1} \right] \right\rangle_c \quad (4.96)$$

gives

$$\left\langle [\mathcal{T}_g]_{(m,n)} \right\rangle_c = \frac{1}{\mu_0} \sum_{l=1}^{4} \sum_{k=1}^{4} \mathcal{E}_c(m,k) \mathcal{E}_c^{-1}(l,n)$$
$$\cdot \sum_{j=1}^{4} \sum_{i=1}^{4} \mathcal{M}_g(j,i) \mathcal{E}_c(i,l) \mathcal{E}_c^{-1}(k,j) \left\langle e^{-s(\lambda_l + \lambda_k)} \right\rangle_c \quad (4.97)$$

$$= \frac{1}{\mu_0} \sum_{l=1}^{4} \sum_{k=1}^{4} \mathcal{E}_c(m,k) \mathcal{E}_c^{-1}(l,n)$$
$$\cdot \sum_{j=1}^{4} \sum_{i=1}^{4} \mathcal{M}_g(j,i) \mathcal{E}_c(i,l) \mathcal{E}_c^{-1}(k,j)$$
$$\cdot \left[\int_0^\infty p(s) e^{-s(\lambda_l + \lambda_k)} ds \right] \quad (4.98)$$

These terms may now be combined to obtain an estimate of the total canopy backscatter. The canopy-level statistics come into play here in computing the average crown layer phase matrix $\langle \mathcal{P}_c \rangle_c$ and in integrating over exponentials that are dependent on the eigenvalues of the crown layer extinction matrix:

$$\int_0^\infty p(s) e^{-s\lambda_l} ds.$$

Quantities of the form

$$\left\langle \frac{\mathcal{P}(i,j)}{\lambda_l \pm \lambda_k} \right\rangle_c$$

represent ratios of phase matrix elements to eigenvalues of the extinction matrix. These quantities are constant throughout the crown volumes and thus do not depend on the canopy-level random variables.

4.4 Scalar Solution

When considering only HH and VV polarization configurations, the solution may be simplified considerably by considering the scalar solution for which the boldface terms in (4.13) become scalar quantities. This allows those variables that depend on trunk layer parameters to be factored out of terms that include the crown layer statistics. If the constituents in the crown and trunk layers are distributed uniformly in azimuth, then $\kappa_{t_c}^{\pm} = \kappa_{t_c}$. Making these simplifications to (4.13) leads to:

$$\begin{aligned}
\langle T_t(\mu_0, \phi_0 + \pi)\rangle_c &= \frac{1}{2}\left\langle \Upsilon_c^2(\theta_0)\right\rangle_c \left\langle \frac{P_c(-\mu_0, \phi_0 + \pi; \mu_0, \phi_0)}{\kappa_c}\right\rangle_c \left(1 - \left\langle \Upsilon_c^2(\theta_0)\right\rangle_c\right) \\
&\quad \cdot e^{-4\kappa_t H_t/\mu_0} [G(\theta_0)]^2 \\
&+ \frac{d}{\mu_0} \langle \Upsilon_c(\theta_0)\rangle_c^2 \langle P_c(-\mu_0, \phi_0 + \pi; -\mu_0, \phi_0)\rangle_c \\
&\quad \cdot e^{-2\kappa_t H_t/\mu_0} G(\theta_0) \\
&+ \frac{d}{\mu_0} \langle \Upsilon_c(\theta_0)\rangle_c^2 \langle P_c(\mu_0, \phi_0 + \pi; \mu_0, \phi_0)\rangle_c \\
&\quad \cdot e^{-2\kappa_t H_t/\mu_0} G(\theta_0) \\
&+ \frac{1}{\mu_0} \langle \Upsilon_c(\theta_0)\rangle_c^2 e^{-2\kappa_t H_t/\mu_0} R(\mu_0) H_t P_t(-\mu_0, \phi_0 + \pi; -\mu_0, \phi_0) \\
&+ \frac{1}{\mu_0} \langle \Upsilon_c(\theta_0)\rangle_c^2 e^{-2\kappa_t H_t/\mu_0} R(\mu_0) H_t P_t(\mu_0, \phi_0 + \pi; \mu_0, \phi_0) \\
&+ \frac{2}{\mu_0} \left\langle \frac{P_c(\mu_0, \phi_0 + \pi; -\mu_0, \phi_0)}{\kappa_c}\right\rangle_c \left(1 - \left\langle \Upsilon_c^2(\theta_0)\right\rangle_c\right) \\
&+ \left\langle \Upsilon_c^2(\theta_0)\right\rangle_c e^{-2\kappa_t H_t/\mu_0} G(\theta_0) \qquad (4.99)
\end{aligned}$$

where crown layer transmissivities have been separated into one- and two-way transmissivities, corresponding to propagation through differing or identical propagation

paths. The quantity

$$\frac{P_c(\mu_s, \phi_s; \mu_i, \phi_i)}{\kappa_c}$$

represents the ratio of scattering to extinction for intensity incident in the (μ_i, ϕ_i) direction and scattered in the (μ_s, ϕ_s) direction. This quantity, is constant throughout the crown volumes and therefore is not affected by the canopy-level random variables.

CHAPTER V

SHAPE STATISTICS FOR TREE CROWNS

This chapter presents the derivations of the statistics associated with specific crown shapes. These statistics are necessary for applying the radiative transfer solution derived in Chapter IV to particular canopy geometries. Section 5.1 presents the derivation of the probability density function $p(s|1)$ of the within-crown propagation length for various shapes of tree crowns. The derivation considers several classes of crown shapes for crowns that have a specified size. Section 5.2 then generalizes these results to account for crowns distributed in size and location throughout the crown layer. The derivation of the crown cross-sectional area is presented in Section 5.3. Again, several classes of crown shapes are considered and results are generalized for crowns distributed in size and location.

5.1 Calculation of Within-Crown Propagation Length PDF for Different Crown Shapes

The distribution of within-crown propagation pathlength for single tree crowns, $p(s|1)$, may be computed numerically for arbitrarily shaped crowns. However, some simple shapes allow for straightforward derivation of analytical expressions for $p(s|1)$. In either case, $p(s|1)$ is most easily derived for shapes that can be easily defined mathematically. Equations (5.1) and (5.2) allow for simple mathematical definition

of a wide variety of crown shapes in Cartesian coordinates (Horn [26]).

$$\left(\frac{2x}{a}\right)^{\alpha} + \left(\frac{2y}{b}\right)^{\beta} + \left(\frac{2z}{c}\right)^{\gamma} = 1, \tag{5.1}$$

$$\left(\frac{2x}{a}\right)^{\alpha} + \left(\frac{2y}{b}\right)^{\beta} - \left(1 - \frac{z}{c}\right) = 0. \tag{5.2}$$

Equation (5.1) describes crowns with ellipsoidal shapes while (5.2) describes those with conical shapes. The specific shapes considered in this section are (1) spheroid, (2) square column and (3) cone. In addition, examples are shown for a mixed spheroid for which the shape factor constants in (5.1) assume different values in the upper and lower half-spaces.

5.1.1 Spheroid

The spheroid is a natural choice for modeling the crown shape for many types of trees. This section presents the derivation of $p(s|1)$ for a sphere as well as for prolate and oblate spheroids. The derivation for a sphere is considered first and then the result is generalized to prolate and oblate spheroids.

Sphere

An analytical expression for $p(s|1)$ for a sphere has been derived by Li and Strahler, [39], and is reproduced here for completeness. Letting $a = b = c$ and $\alpha = \beta = \gamma = 2$ in (2.1) yields the equation of a sphere. Figure 5.1 diagrams a sphere and the within-crown path s at a distance r from the center of the sphere. For a given r, the sphere will contain a cylinder of length s along the illumination direction, as indicated by the shaded region in the figure. As r increases to $r + \mathrm{d}r$, s decreases to $s' = s - \mathrm{d}s$. The quantity $p(s|1)\mathrm{d}s$ represents the proportional rate of change of s at a distance r. This is the proportion of the area of the circle represented by the

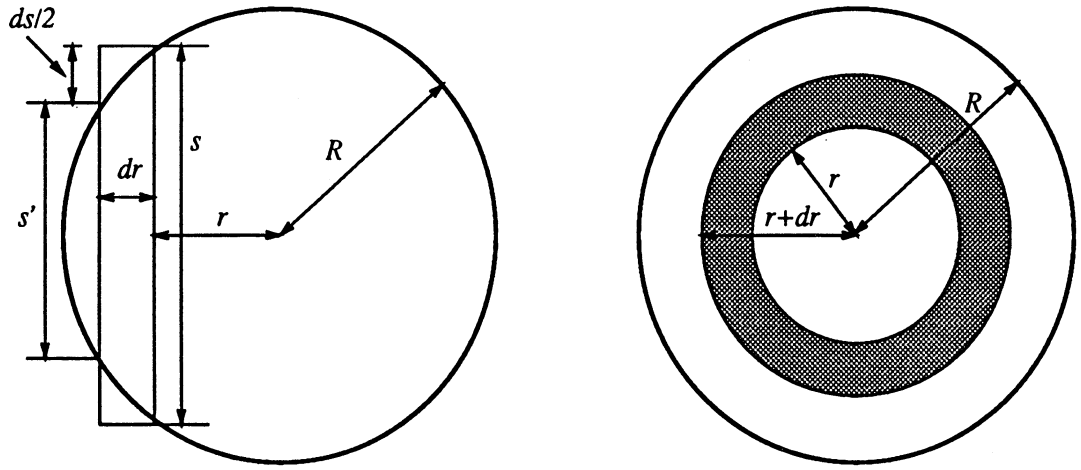

Figure 5.1: Geometry of a sphere of radius R showing a within-crown path length s at a distance r from the center of the sphere.

shaded annulus in the figure. The infinitesimal area in which s and r are constant is $2\pi r\mathrm{d}r$. Thus the proportion by which s changes at distance r is $-2\pi r\mathrm{d}r/\pi R^2$ so

$$p(s|1)\,\mathrm{d}s = \frac{-2\pi r}{\pi R^2}\mathrm{d}r. \tag{5.3}$$

Furthermore,

$$r = \sqrt{R^2 - \left(\frac{1}{2}s\right)^2} \tag{5.4}$$

so

$$\frac{\mathrm{d}r}{\mathrm{d}s} = \frac{-s}{4\sqrt{R^2 - \left(\frac{1}{2}s\right)^2}} \tag{5.5}$$

$$= -\frac{s}{4r}. \tag{5.6}$$

It follows that

$$p(s|1) = -\frac{2\pi r}{\pi R^2}\cdot\frac{\mathrm{d}r}{\mathrm{d}s} \tag{5.7}$$

$$= \frac{s}{2R^2}. \tag{5.8}$$

For a sphere with diameter $a = 2R$,

$$p(s|1) = \frac{2s}{a^2} \tag{5.9}$$

where $0 \leq s \leq a$. Equation (5.9) represents a ramp function rising from 0 to $2/a$ as s goes from 0 to a.

Generalization to prolate and oblate spheroids

Letting $a = b$ and $\alpha = \beta = \gamma = 2$ in (2.1) yields the general equation of a spheroid. The spheroid is prolate when $c > a$ and oblate when $c < a$. As illustrated in Figure 5.2, $p(s|1)$ for a spheroid is easily derived from (5.9) through a linear

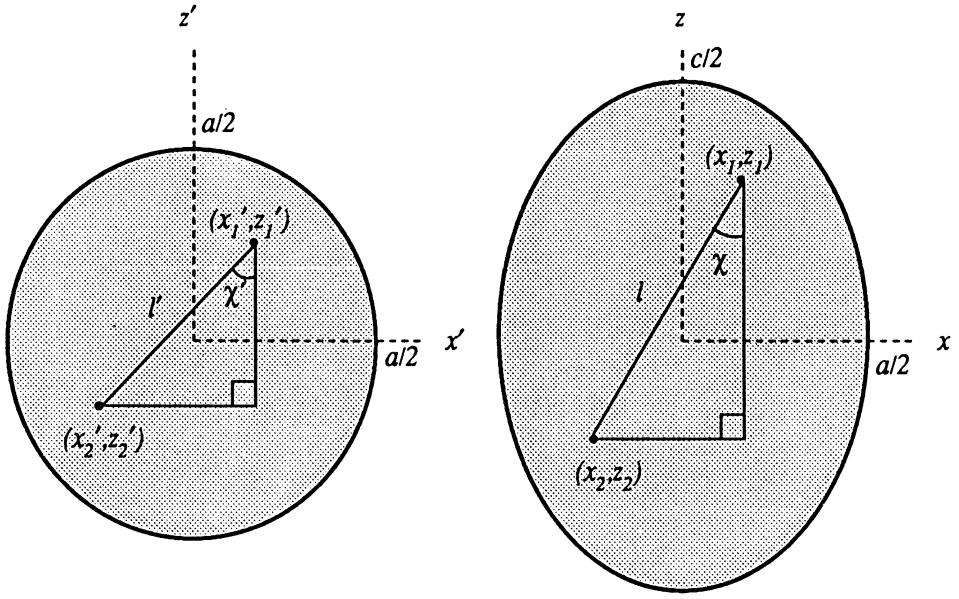

Figure 5.2: Transformation of a sphere to a prolate spheroi

transformation of the z axis. For example, a sphere of diameter a is transformed to a prolate spheroid with major axis c and minor axis a through a stretching of its z-axis. If the original axes are x' and z' and the transformed axes are x and z, then the points in the sphere (x_1', z_1') and (x_2', z_2') are transformed to the points (x_1, z_1)

and (x_2, z_2) in the prolate spheroid. If $f = c/a$ then $z_1 = f \cdot z_1'$ and $z_2 = f \cdot z_2'$ while $x_1 = x_1'$ and $x_2 = x_2'$. The difference values are defined as

$$\Delta x' = x_2' - x_1' \tag{5.10}$$

$$\Delta z' = z_2' - z_1' \tag{5.11}$$

$$\Delta x = x_2 - x_1 = f \cdot \Delta x' \tag{5.12}$$

$$\Delta z = z_2 - z_1 = f \cdot \Delta z' \tag{5.13}$$

Furthermore,

$$\tan \chi' = \frac{\Delta x'}{\Delta z'} = f \cdot \tan \chi \tag{5.14}$$

and the path lengths are

$$l' = \sqrt{(\Delta x')^2 + (\Delta z')^2} = \Delta z' \sqrt{1 + f^2 \tan^2 \chi} \tag{5.15}$$

$$l = \sqrt{(\Delta x)^2 + (\Delta z)^2} = \Delta z \sqrt{1 + \tan^2 \chi} \tag{5.16}$$

It follows that

$$\frac{l}{l'} = \frac{\Delta z \sqrt{1 + \tan^2 \chi}}{\Delta z' \sqrt{1 + f^2 \tan^2 \chi}} \tag{5.17}$$

so

$$l = l' \frac{\Delta z}{\Delta z'} \frac{\sqrt{1 + \tan^2 \chi}}{\sqrt{1 + f^2 \tan^2 \chi}} \tag{5.18}$$

$$= l' f \frac{\sqrt{1 + \tan^2 \chi}}{\sqrt{1 + f^2 \tan^2 \chi}} \tag{5.19}$$

$$= l' \Lambda(\chi) \tag{5.20}$$

is the new path length where

$$\Lambda(\chi) = \frac{c}{a} \frac{\sqrt{1 + \tan^2 \chi}}{\sqrt{1 + \left(\frac{c}{a}\right)^2 \tan^2 \chi}} \tag{5.21}$$

For a radar incidence angle θ, the sphere diameter a in (5.9) must be scaled by $\Lambda(\theta)$, giving

$$p(s|1) = \frac{2s}{[a\Lambda(\theta)]^2} \tag{5.22}$$

$$= \left[\frac{1+\left(\frac{c}{a}\right)^2\tan^2\theta}{1+\tan^2\theta}\right]\frac{2}{c^2}s \tag{5.23}$$

where $0 \leq s \leq a\Lambda(\theta)$. Since this process is a simple linear transformation, (5.23) represents a ramp function rising from 0 to $2/[a\Lambda(\theta)]$ as s goes from 0 to $a\Lambda(\theta)$.

The validity of (5.23) is easily verified by considering two special cases. First, let $\theta = 0$ so the spheroid is viewed along the z-axis. Here, $\Lambda(\theta) = c/a$ and

$$p(s|1)\Big|_{\theta=0} = \frac{2s}{c^2} \tag{5.24}$$

where $0 \leq s \leq c$. This is identical to $p(s|1)$ for a sphere with diameter c.

Now, let $\theta = \pi/2$ so the spheroid is viewed along the x-axis. Here, $\Lambda(\theta) \rightarrow 1$ and

$$p(s|1)\Big|_{\theta=\pi/2} = \frac{2s}{a^2} \tag{5.25}$$

where $0 \leq s \leq a$ and $p(s|1)$ is now identical to that in (5.9).

5.1.2 Square Column

The derivation of $p(s|1)$ for a rectangular solid is now presented. Mathematically, this shape is convenient to couple with the radiative transfer equations and therefore warrants some consideration.

Letting $a = b$ and allowing $\alpha = \beta = \gamma \rightarrow \infty$ in (2.1) yields a square column. $a = b < c$ gives an oblate square column, $a = b > c$ yields a prolate square column, and $a = b = c$ yields a cube. The radar look direction is assumed to be perpendicular to a face of the column, thereby simplifying the derivation of $p(s|1)$ significantly since

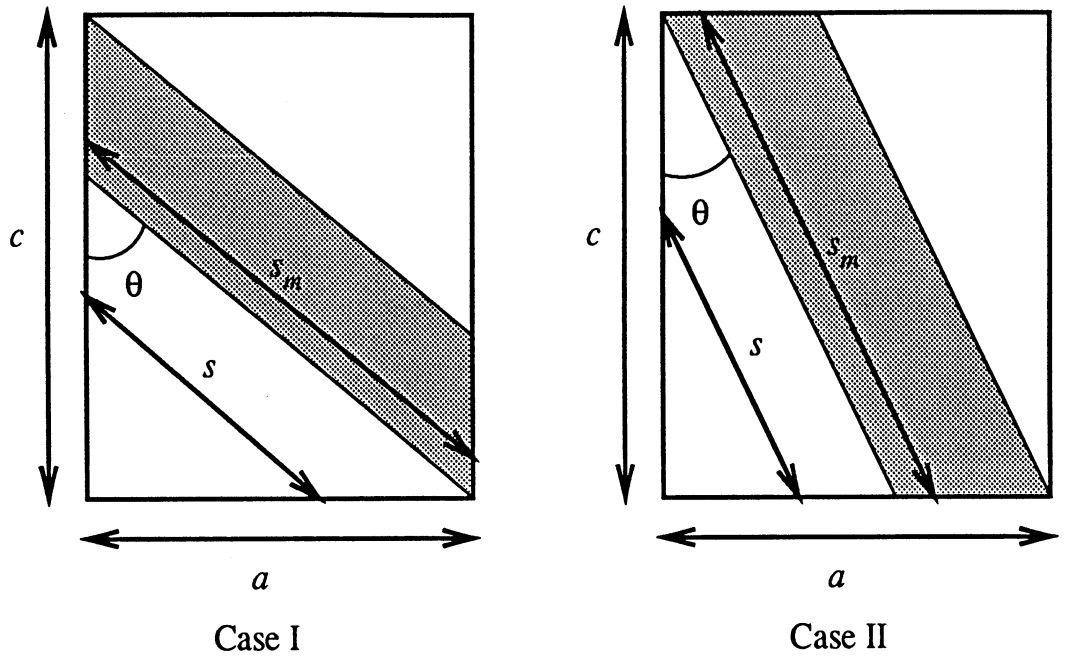

Figure 5.3: Illustration of the within-crown propagation length for a crown with a rectangular shape factor. Case I occurs for a radar look angle $\theta > \theta_c$. Case II occurs for a radar look angle $\theta < \theta_c$. The critical angle θ_c is determined from $\tan\theta_c = a/c$. s_m represents the maximum value of s for a given crown. The solids have depth b into the paper.

it may now be represented in two dimensions, as shown in Figure 5.3. Two cases must be considered in deriving $p(s|1)$. These cases are differentiated through the definition of a critical angle θ_c that is related to the crown dimensions by

$$\tan\theta_c = \frac{a}{c} \tag{5.26}$$

Case I arises when $\theta > \theta_c$, whereas Case II occurs when $\theta < \theta_c$

The PDF for the entire column may be expressed as an integral over the column volume:

$$p(s|1) = \frac{1}{V_T}\int_V p_v(s)\mathrm{d}V \tag{5.27}$$

where $p_v(s)$ is the PDF describing s within the differential volume $\mathrm{d}V$ and V_T is the total volume of the column. $p(s|1)$ is partitioned over three regions of interest within

which $p_v(s)$ varies only with s:

$$p(s|1) = \frac{1}{V_T}\left[\int_{V_1} p_{v1}(s)\mathrm{d}V_1 + \int_{V_2} p_{v2}(s)\mathrm{d}V_2 + \int_{V_3} p_{v3}(s)\mathrm{d}V_3\right] \quad (5.28)$$

$$= \frac{1}{V_T}\left[p_{v1}(s)\int_{V_1}\mathrm{d}V_1 + p_{v2}(s)\int_{V_2}\mathrm{d}V_2 + p_{v3}(s)\int_{V_3}\mathrm{d}V_3\right] \quad (5.29)$$

$$= \frac{1}{V_T}\left[p_{v1}(s)V_1 + p_{v2}(s)V_2 + p_{v3}(s)V_3\right] \quad (5.30)$$

The volumes V_1, V_2 and V_3 and their respective PDFs correspond to the regions shown in Figure 5.4.

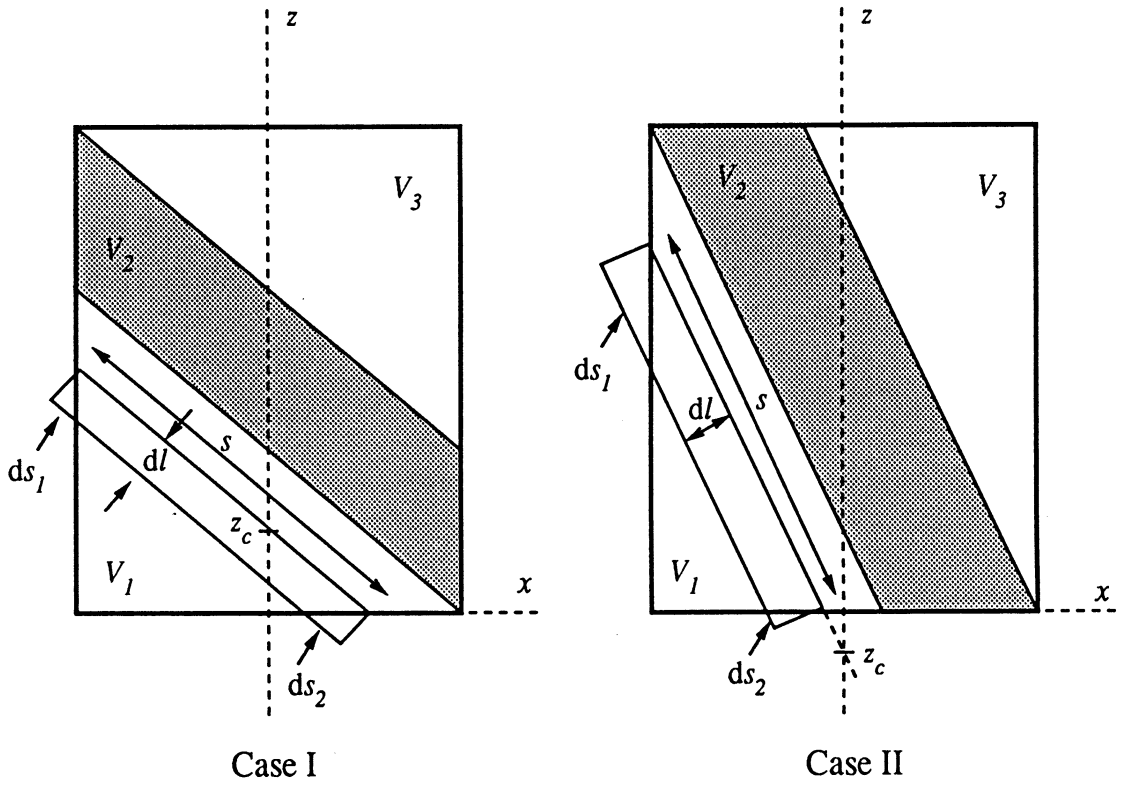

Figure 5.4: Geometry used for deriving $p(s|1)$ for a square column.

For Case I, the maximum value of the within-crown propagation length is $s_m = a/\sin\theta$. Examining the volume V_1, The equation of the line of length s is

$$z = -\cot\theta x + z_c \quad (5.31)$$

where z_c is the z-intercept and the length of this line is

$$s = \frac{a}{2\sin\theta} + \frac{z_c}{\cos\theta}. \tag{5.32}$$

Also, $\mathrm{d}s = \mathrm{d}z/\cos\theta$ where $\mathrm{d}s = \mathrm{d}s_1 + \mathrm{d}s_2$. Now, the infinitesimal volume in which s and z are constant is $(sb)\cdot \mathrm{d}l$ and $V_1 = \frac{1}{2}a^2 b\cot\theta$. The quantity $p(s)\mathrm{d}s$ represents the proportional rate of change of s at a given z. This is simply the ratio of the volume of the strip of thickness $\mathrm{d}l$ to the volume V_1:

$$p_{v_1}(s)\mathrm{d}s = \frac{2sb}{a^2 b\cot\theta}\mathrm{d}l. \tag{5.33}$$

Since $\mathrm{d}l = \mathrm{d}z\sin\theta$

$$\begin{aligned} p_{v_1}(s) &= \frac{2s\sin\theta\tan\theta}{a^2}\cdot\frac{\mathrm{d}z}{\mathrm{d}s} && (5.34)\\ &= \frac{2s\sin\theta\tan\theta}{a^2}\cos\theta && (5.35)\\ &= 2\left(\frac{\sin\theta}{a}\right)^2 s \qquad ;0 \le s \le s_m. && (5.36) \end{aligned}$$

Through a similar analysis, it can easily be shown that

$$p_{v_3}(s) = p_{v_1}(s). \tag{5.37}$$

Finally, it is seen straightaway

$$p_{v_2}(s) = \delta_k(s - s_m) \tag{5.38}$$

where

$$\delta_k(s - s_m) = \begin{cases} 1 & ; s = s_m \\ 0 & ; \text{otherwise.} \end{cases} \tag{5.39}$$

The volumes of interest are:

$$V_1 = \frac{a^2 b}{2\tan\theta} \tag{5.40}$$

$$V_2 = s_m(c - a/\tan\theta)b\sin\theta \tag{5.41}$$

$$V_3 = V_1 \tag{5.42}$$

$$V_T = V_1 + V_2 + V_3 = abc. \tag{5.43}$$

Applying (5.30) and simplifying gives

$$p(s|1)\Big|_{\theta\geq\theta_c} = \begin{cases} \frac{2\cos\theta\sin\theta}{ac}s + \left(1 - \frac{a}{c\tan\theta}\right)\delta_k(s - s_m) & ;0 \leq s \leq s_m \\ 0 & ;\text{otherwise} \end{cases} \tag{5.44}$$

where $s_m = a/\sin\theta$.

This same technique may be used to derive $p(s|1)$ for Case II. Here, $s_m = c/\cos\theta$ and

$$V_1 = \frac{c^2 b\tan\theta}{2} \tag{5.45}$$

$$V_2 = s_m(a - c\tan\theta)b\cos\theta \tag{5.46}$$

$$V_3 = V_1 \tag{5.47}$$

$$V_T = V_1 + V_2 + V_3 = abc. \tag{5.48}$$

Therefore

$$p_{v_1}(s)\mathrm{d}s = \frac{2sb}{c^2 b\tan\theta}\mathrm{d}l \tag{5.49}$$

so

$$p_{v_1}(s) = \frac{2sb\sin\theta}{c^2 b\tan\theta}\cdot\frac{\mathrm{d}z}{\mathrm{d}s} \tag{5.50}$$

$$= \frac{2s\sin\theta}{c^2\tan\theta}\cos\theta \tag{5.51}$$

$$= 2\left(\frac{\cos\theta}{c}\right)^2 s \tag{5.52}$$

$$= p_{v_3}(s). \tag{5.53}$$

Furthermore, as in Case I:

$$p_{v_2}(s) = \delta_k(s - s_m). \tag{5.54}$$

Again, following (5.30) and simplifying:

$$p(s|1)\Big|_{\theta\leq\theta_c} = \begin{cases} \frac{2\cos\theta\sin\theta}{ac}s + \left(1 - \frac{c\tan\theta}{a}\right)\delta_k(s - s_m) & ;0 \leq s \leq s_m \\ 0 & ;\text{otherwise} \end{cases} \tag{5.55}$$

where $s_m = c/\cos\theta$.

Equations (5.44) and (5.55) represent ramp functions rising from 0 to $\frac{2\cos\theta\sin\theta}{ac}s_m$ as s goes from 0 to s_m. At $s = s_m$, an additional contribution is added to $p(s|1)$ to account for the shaded regions in which $s = s_m$, a constant. Figure 5.5 shows $p(s|1)$

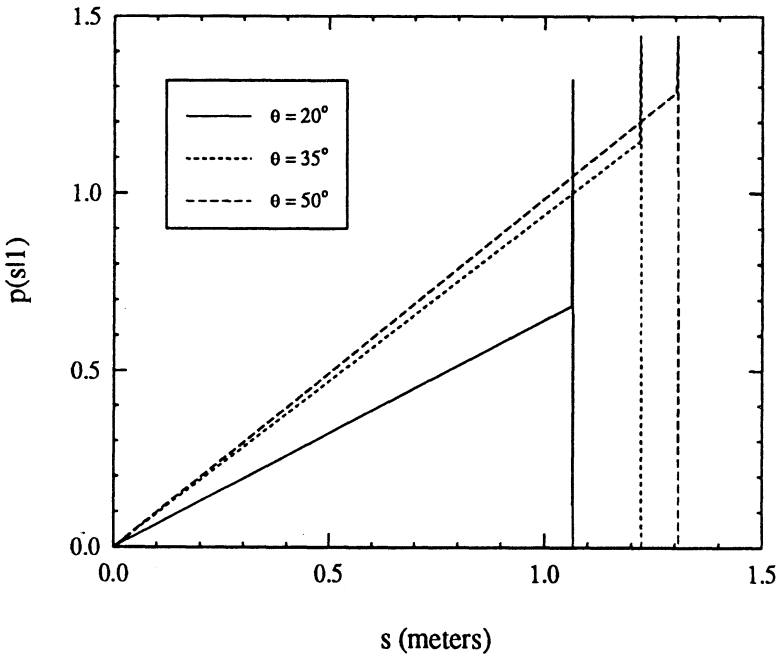

Figure 5.5: $p(s|1)$ for a square column with $a = b = c = 1$. Values are shown for three incidence angles.

for a square column with $a = b = c = 1$ at three angles of incidence. For this shape, $\theta_c = 45°$.

5.1.3 Cone

Setting $a = b$ and $\alpha = \beta = 2$ in (2.2) yields a right circular cone with apex at $z = c$, base at $z = 0$ and basal diameter a, as shown in Figure 5.6. The apex angle

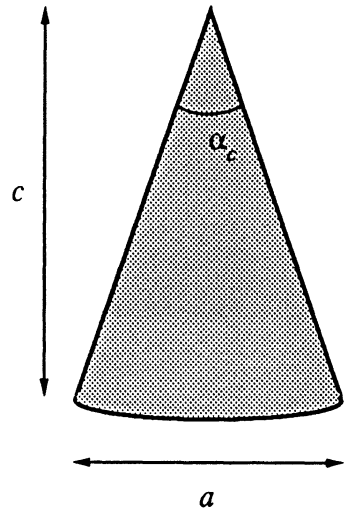

Figure 5.6: Geometry of a conical crown with height c, basal diameter a and apex angle α_c.

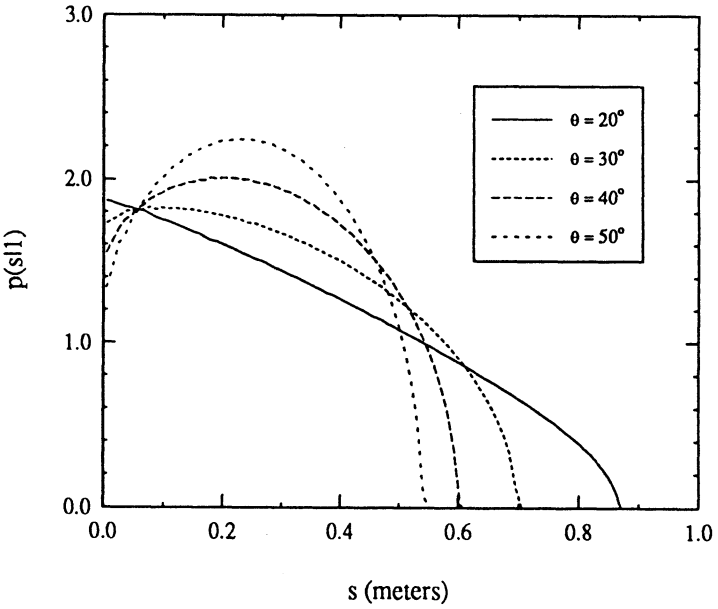

Figure 5.7: $p(s|1)$ for several incidence angles for a right circular cone with $a = b = 0.5$ and $c = 1$.

$\alpha_c = 2\tan^{-1}(a/2c)$. Derivation of an analytical expression for $p(s|1)$ for this shape is very difficult. Thus, numerical integration is a more straightforward technique for computing the distribution of s. Figure 5.7 was generated with such a technique. In this example, the cone dimensions are $a = b = 0.5$ and $c = 1$. The function $p(s|1)$ is shown for several incidence angles.

5.1.4 Partial Crown Shapes

When examining the specific intensity at an arbitrary depth in the crown layer, it becomes important to consider the within-crown propagation length for partial crown shapes. The PDF $p(s|1)$ is now examined as a function of penetration into individual crown shapes. For a square column crown, the partial shape formed by slicing the crown with a plane parallel to the $x - y$ plane is itself a square column. $p(s|1)$ for the sliced shape may therefore be computed by applying the appropriate parameters of the sliced crown to (5.44) and (5.55).

Other shapes exhibit more complicated behavior with respect to the depth of the slicing plane. Figure 5.8 illustrates the geometry of this problem for spheroidal shapes. The spheroid is sliced at a depth $z < 0$ where $z = 0$ represents the spheroid top. Figures 5.9 and 5.10 show $p(s|1)$ for a spheroid with $a = b = 2$ and $c = 10$.

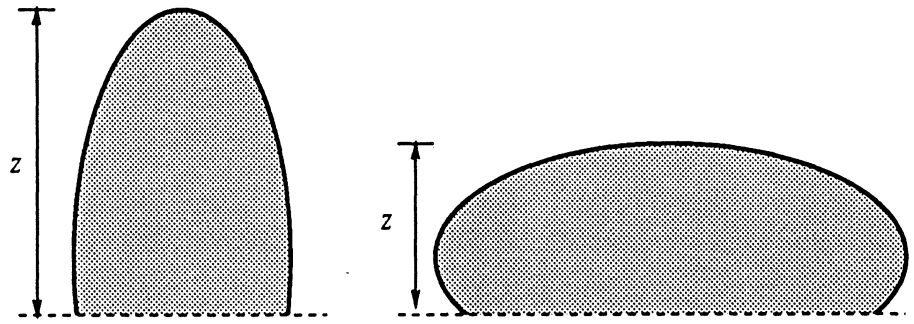

Figure 5.8: Geometry of spheroid crowns with propagation depth $|z| < c$.

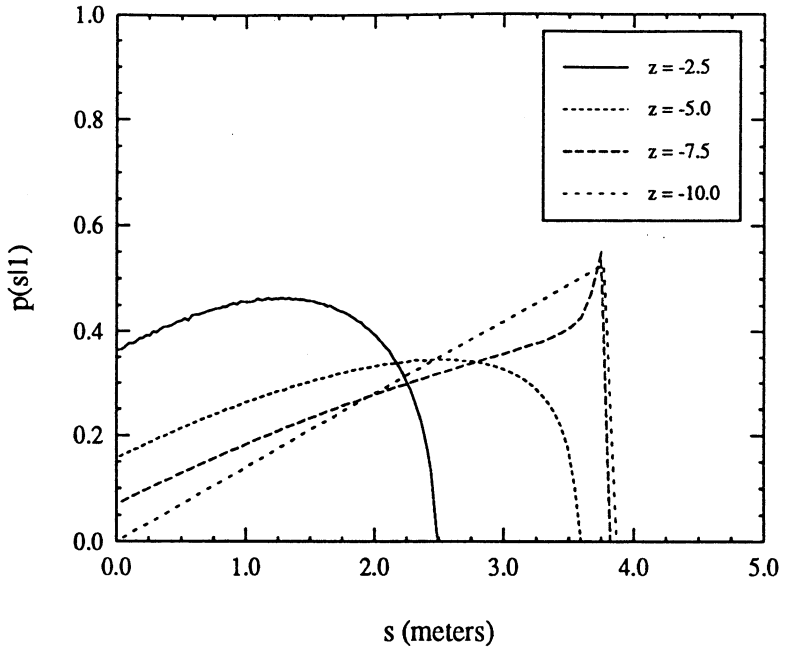

Figure 5.9: $p(s|1)$ of a spheroid with $a = b = 2$ and $c = 10$ for several penetration depths. The incidence angle $\theta = 30°$.

Figure 5.9 shows $p(s|1)$ at various depths z for an incidence angle $\theta = 30°$ and Figure 5.10 shows $p(s|1)$ at various incidence angles for $z = -c/2 = -5$. Note that for $z = -c = -10$, the resulting $p(s|1)$ is identical to that of the entire spheroid.

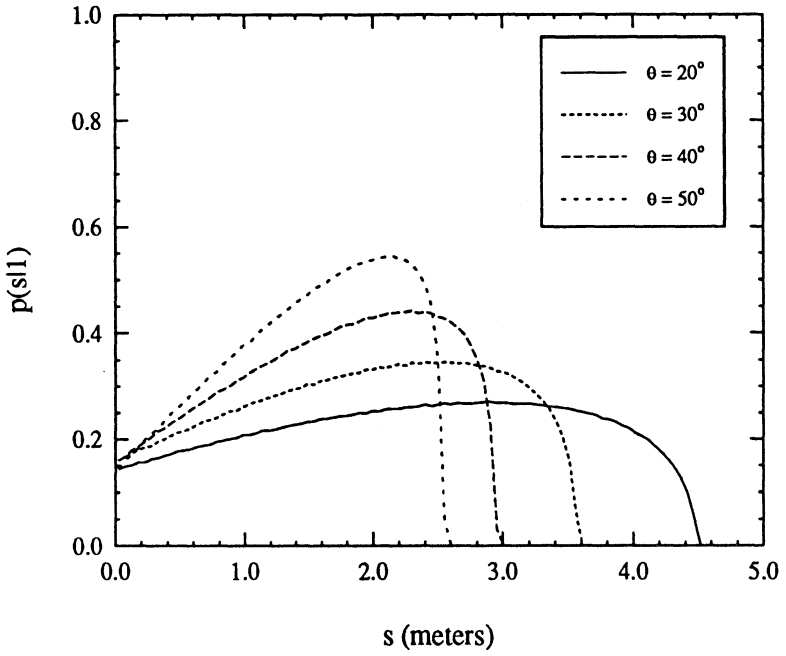

Figure 5.10: $p(s|1)$ for several incidence angles for an spheroid with propagation depth $z = -c/2$. The ellipsoid has $a = b = 2$ and $c = 10$.

In general, there are two partial crown shapes defined by the intersection of the slicing plane with the crown, one partial shape above the plane and one below. In the case of square columns, both of these partial shapes are themselves square columns. Similarly, in the case of spheroids, both partial shapes are spheroids. For a right circular cone, however, the slicing plane defines a right circular cone in the upper half-space and a frustum of a right circular cone in the lower half-space. $p(s|1)$ has already been handled for the former case. For the cone frustum, the geometry of Figure 5.11 may be considered. As before, the cone has a total height c and basal

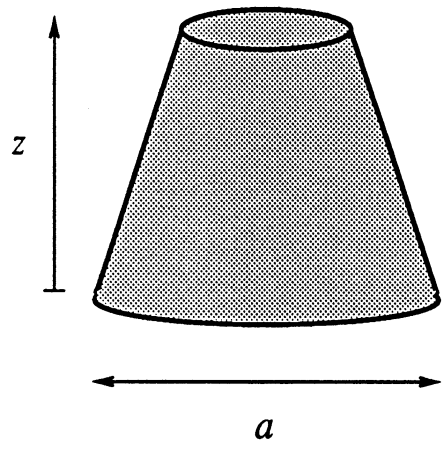

Figure 5.11: Geometry for computing $p(s|1)$ of a frustum of a right circular cone.

diameter a. The height of the frustum is designated by z (shown referenced to the cone base) and depends on the location of the slicing plane. Figure 5.12 shows the results of numerical computation of $p(s|1)$ for a cone frustum of several heights at $\theta = 30°$. This cone has $a = b = 0.5$ and $c = 1$. The delta function occurs at values of $s = z/\cos(\theta)$ which correspond to paths entering the top face of the frustum and exiting its base.

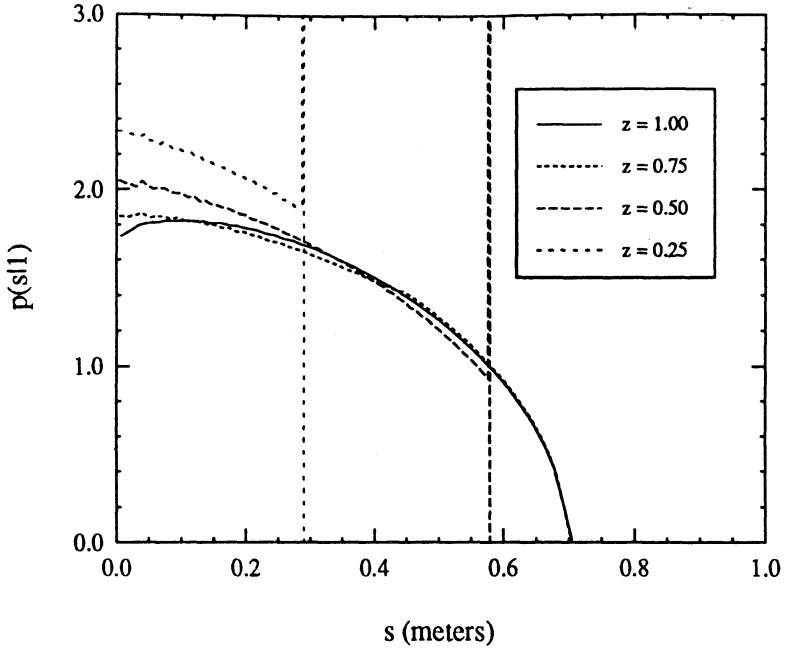

Figure 5.12: $p(s|1)$ of a cone frustum for several heights at an incidence angle $\theta = 30°$. The cone has $a = b = 0.5$ and $c = 1$.

5.1.5 General Shapes

By selecting appropriate values for α, β and γ and by letting a, b and c vary with quadrant, (2.1) and (2.2) may be used to define a wide variety of crown shapes. As a simple example, if $\alpha = \beta = \gamma = 2$ and $a = b = 2$ in (2.1) and letting $c = 10$ for $z > 0$ and $c = 4$ for $z < 0$ the mixed spheroid shown in Figure 5.13 is obtained. The corresponding $p(s|1)$ may be generated numerically and the result is shown in Figure 5.14 for several angles of incidence.

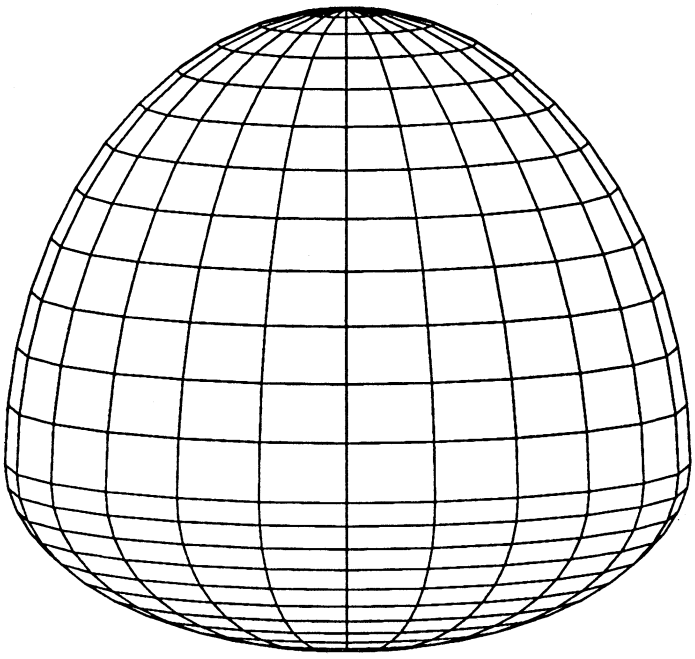

Figure 5.13: Geometry of a mixed spheroid. The upper spheroid has $a = b = 2$ and $c = 10$. The lower spheroid has $a = b = 2$ and $c = 4$.

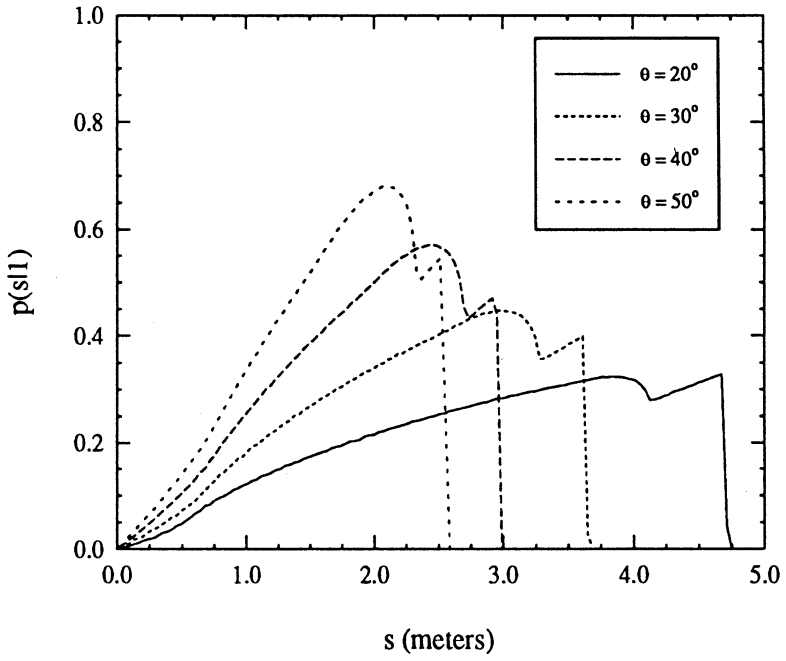

Figure 5.14: $p(s|1)$ of a mixed spheroid shape at several incidence angles.

5.2 Within-Crown Propagation Length PDF for Crowns Distributed in Size and Location

In order to model $p(s)$ for a wide variety of canopy architectures, the results of the previous section must be generalized to crowns distributed in size and location. Crowns within a given canopy are assumed to have identical shape classes and have specified distributions in center location and crown height. $p(s|1)$ will also be considered as a function of penetration depth into the crown layer.

The propagation length s through a single tree crown with a specified shape is described in terms of the PDF $p(s|1;z';c;z_i)$. As illustrated in Figure 5.15, c represents the height of the crown, z_i corresponds to the location of the crown center, and z' represents the depth in the crown layer where the value of the propagating intensity is to be estimated. For a collection of crowns distributed in c and z_i, the

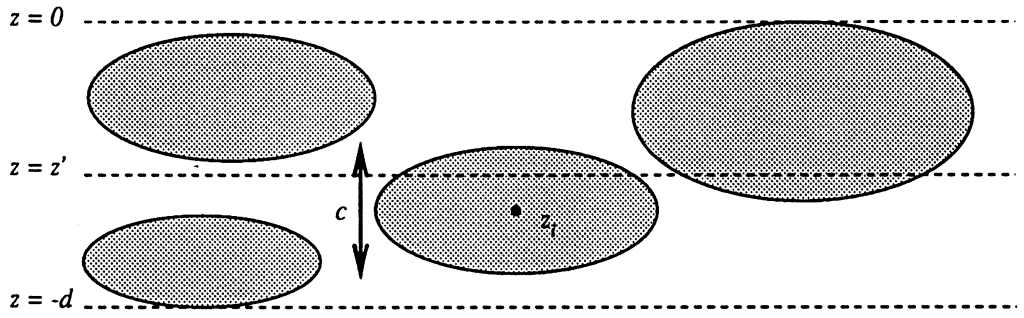

Figure 5.15: Illustration of ellipsoidal crowns in a crown layer of thickness d. the crowns are distributed in both height c and center location z_i. z' represents the depth in the layer at which the value of the propagating intensity is to be estimated.

PDF of within-crown propagation length for a single crown is

$$p(s|1;z') = \int\int p(s|1;z';c;z_i)p_c(c)p_{z_i}(z_i)\mathrm{d}c\mathrm{d}z_i \tag{5.56}$$

where $p_c(c)$ is the PDF of crown size defined in terms of the random variable c and

$p_{z_i}(z_i)$ is the PDF of crown center location defined by z_i. General analytic expressions for $p(s|1;z')$ are very tedious to derive for all but the most simple distributions over crown shape, size and location. Thus, it is more convenient to compute the PDF numerically. Some examples of $p(s|1;z')$ are now presented for crown layers consisting of spherical and conical crowns.

For crowns having identical center locations z_i and a distribution in height described by the PDF $p_c(c)$,

$$p(s|1;z';z_i) = \int p(s|1;z';c;z_i)p_c(c)\mathrm{d}c. \tag{5.57}$$

The crown height c and width a may be coupled through the width-to-height ratio $k = a/c$. For ellipsoidal crowns, $k = 1$ yields spherical shapes. Figure 5.16 shows $p(s)$

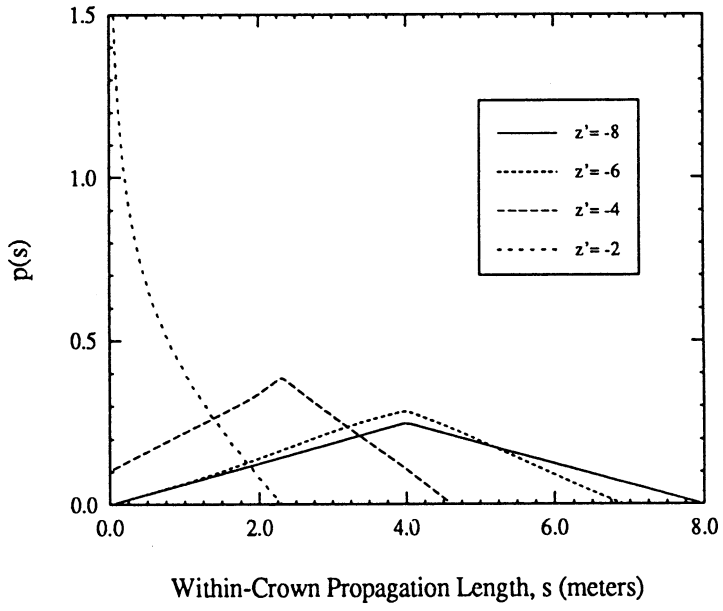

Figure 5.16: $p(s)$ at various depths z' in the crown layer for a spheri
centers located at $z_i = -4$ meters and size uniformly distributed between $4 \leq c \leq 8$ with $a/c = 1$ and $\theta = 30°$.

for an incidence angle $\theta = 30°$ at various depths z' in the crown layer for spherical crowns centered at $z_i = -4$ meters and with height uniformly distributed between $4\text{m} \leq c \leq 8\text{m}$. Note that the maximum propagation length increases directly with

z' up to a maximum value of $s = 8$ at $z' = -8$. This corresponds to the maximum crown diameter.

Figure 5.17 shows $p(s)$ at $\theta = 30°$ for conical crowns centered at $z_i = -4$ with

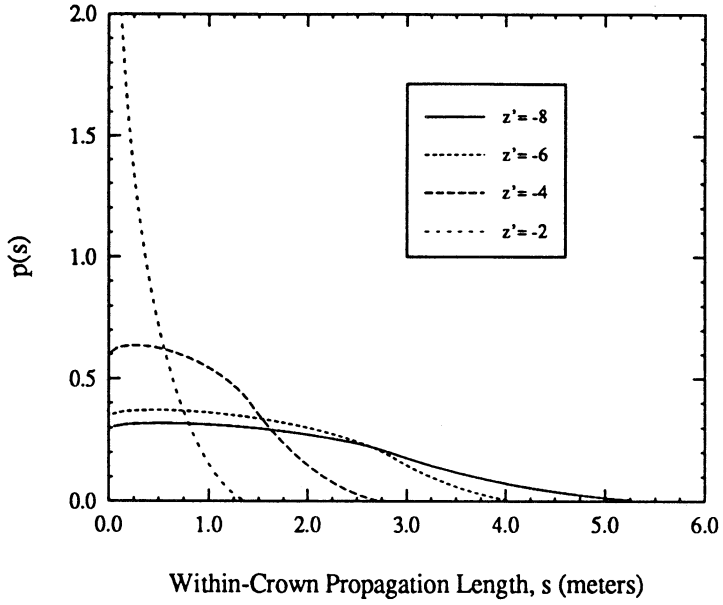

Figure 5.17: $p(s)$ at various depths z' in the crown layer for conical crowns with centers located at $z_i = -4$ meters and size uniformly distributed between $4 \leq c \leq 8$ with $a/c = 0.5$ and $\theta = 30°$.

height uniformly distributed over $4\text{m} \leq c \leq 8\text{m}$ and with $a/c = 0.5$. Comparison of Figures 5.16 and 5.17 indicates that the shorter within-crown pathlengths are slightly more important for conical shapes than for spherical shapes.

For crowns of identical size with a distribution in center location z_i described by the PDF $p_{z_i}(z_i)$ is given by:

$$p(s|1; z'; c) = \int p(s|1; z'; c; z_i) p_{z_i}(z_i) \mathrm{d}z_i. \tag{5.58}$$

Figures 5.18 and 5.19 show $p(s)$ at various values of z_i for spherical and conical crowns each with constant size $c = 6\text{m}$ and center location uniformly distributed with $-7\text{m} \leq z_i \leq -3\text{m}$.

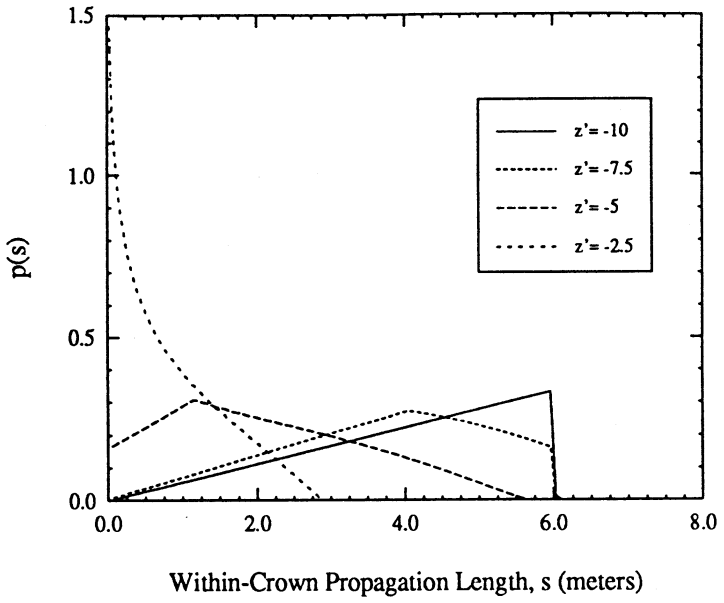

Figure 5.18: $p(s)$ at various depths z' in the crown layer for a spherical crown with size $c = 6$ meters, $a/c = 1$, center location uniformly distributed between $-7 \leq z_i \leq -3$ and $\theta = 30°$.

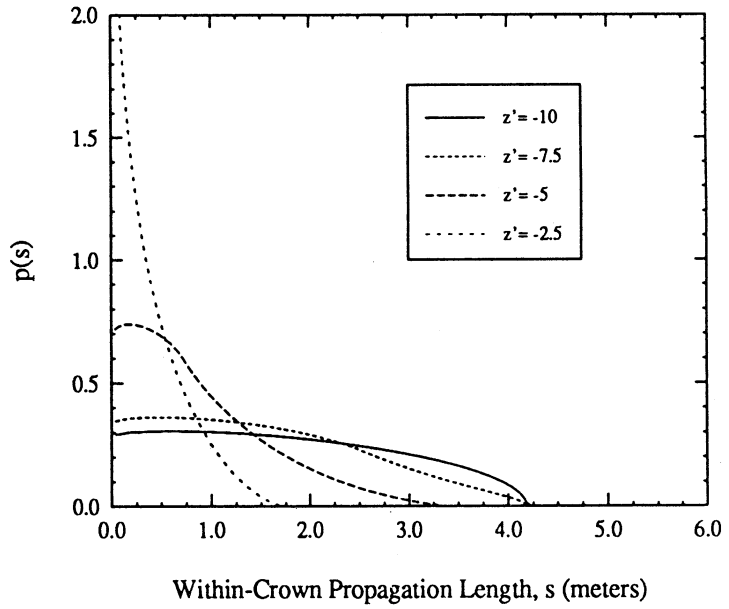

Figure 5.19: $p(s)$ at various depths z' in the crown layer for a conical crown with size $c = 6$ meters, $a/c = 0.5$, center location uniformly distributed between $-7 \leq z_i \leq -3$ and $\theta = 30°$.

To consider the effect of crowns distributed in both size and center location, these parameters may be coupled such that small crowns are located low in the crown layer and large crowns are high in the layer. This simulates crown placement in many natural canopies. If z_i is distributed between $-8 \leq z_i \leq -3$ and c is varied linearly with z_i as $c = z_i + 9$ then the smallest crowns have height $c = 1$ and are located at $z_i = -8$ and the largest crowns have height $c = 6$ and are located at $z_i = -3$. Figures 5.20 and 5.21 show $p(s)$ for spherical and conical crowns at various depths z' in the crown layer for such a case at $\theta = 30°$ with z_i uniformly distributed.

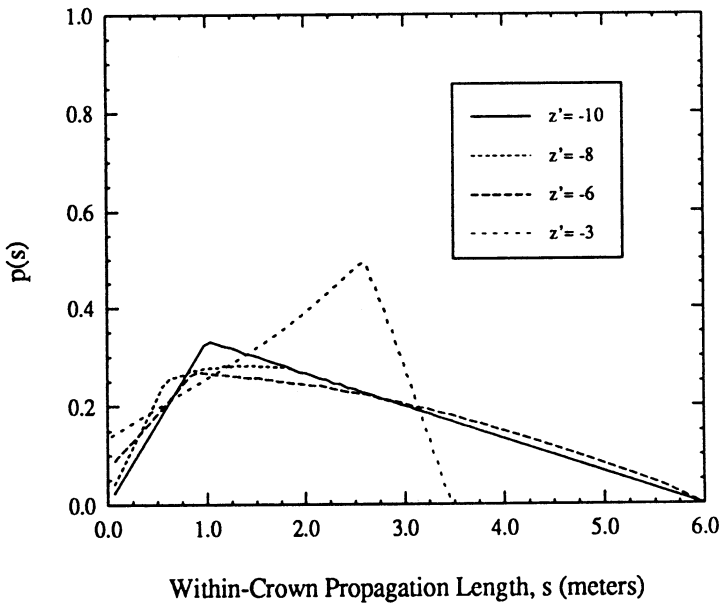

Figure 5.20: $p(s)$ at various depths z' in the crown layer for a spherical crown with crown center location uniformly distributed between $-8 \leq z_i \leq -3$ and size varying linearly with z_i between $1 \leq c \leq 6$ and $a/c = 1$ such that the smaller crowns are low in the canopy and the larger crowns are high in the canopy. The incidence angle $\theta = 30°$.

To this point, only uniform distributions in crown size and location have been considered. Another case of interest is crowns with center location lognormally dis-

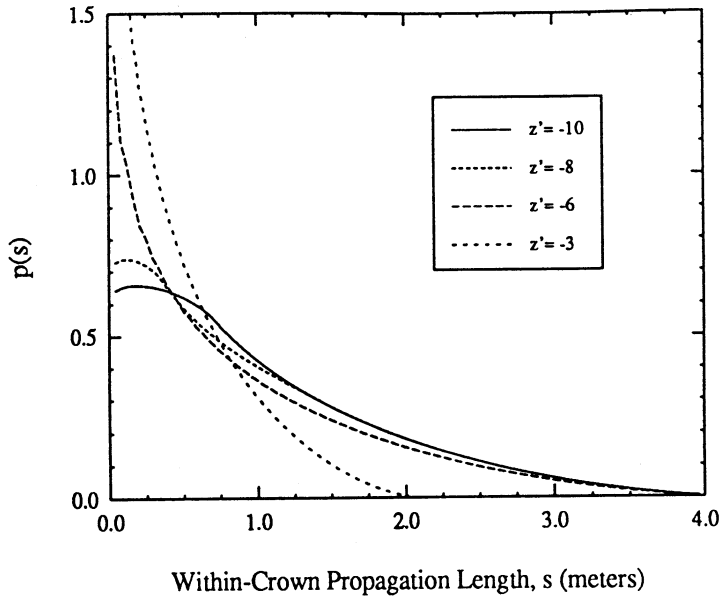

Figure 5.21: $p(s)$ at various depths z' in the crown layer for a conical crown with crown center location uniformly distributed between $-8 \leq z_i \leq -3$ and size varying linearly with z_i between $1 \leq c \leq 6$ and $a/c = 0.5$ such that the smaller crowns are low in the canopy and the larger crowns are high in the canopy. The incidence angle $\theta = 30°$.

tributed. A random variable x which is lognormally distributed has PDF

$$p_x(x) = \frac{1}{x\sigma\sqrt{2\pi}} \exp\left\{ \frac{-\left[\ln(\frac{x}{m})\right]^2}{2\sigma^2} \right\} \tag{5.59}$$

with median= m and mean= $m\exp(\sigma^2/2)$. It is clear that x is defined over the interval $0 \leq x \leq \infty$. To apply this distribution to a crown layer of finite height, $p_x(x)$ is offset to $-d$ (the lower boundary of the layer) and normalized so that

$$p_{z_i}(z_i) = \frac{p_x(z_i + d)}{\int_0^d p_x(x)\mathrm{d}x}. \tag{5.60}$$

Figure 5.22 compares the uniform distribution to lognormal distributions with $m = 1$ and $\sigma = 1$ and with $m = 2.5$ and $\sigma = 1$. In general, the lognormal distribution places more crowns in the lower portion of the crown layer and, when coupled with crown size that varies linearly with center location, accounts for a higher number density of small crowns in the canopy.

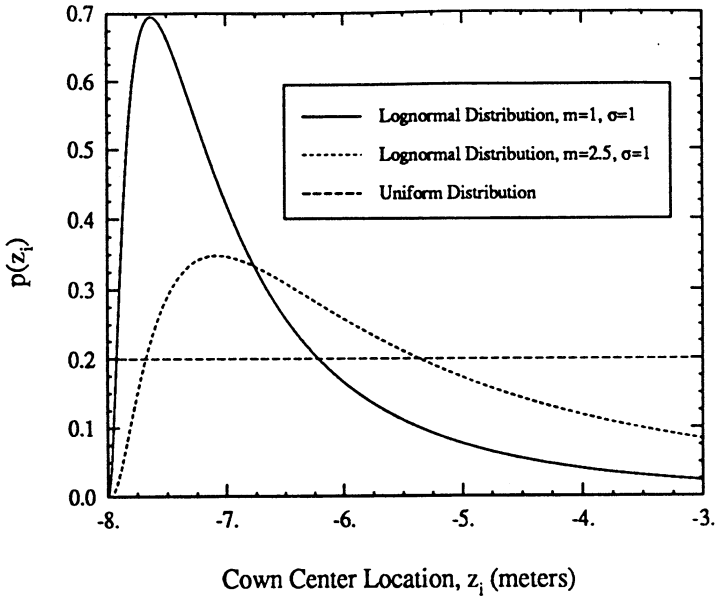

Figure 5.22: PDF of crown center height $p(z_i)$ for lognormal and uniform distributions.

Figures 5.23 and 5.24 show $p(s)$ at $\theta = 30°$ and $z' = -10$ meters for spherical and conical crowns with these three distributions in center location. The lognormal distributions yield $p(s)$ that peaks at lower values of s than the uniform distribution.

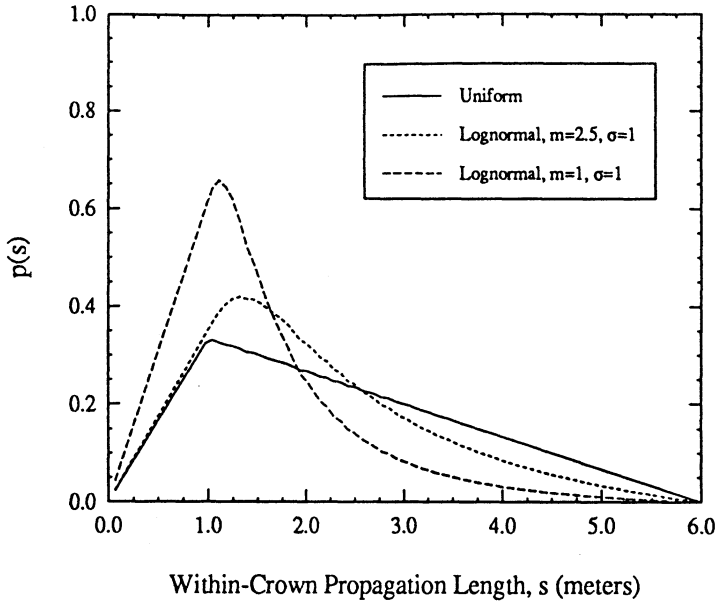

Figure 5.23: $p(s)$ at $z' = -10$ meters in the crown layer for a spherical crown with center location having three different distributions between $-8 \leq z_i \leq -3$ and size varying linearly with z_i between $1 \leq c \leq 6$ and $a = c$ such that the smaller crowns are low in the canopy and the larger crowns are high in the canopy. The incidence angle $\theta = 30°$.

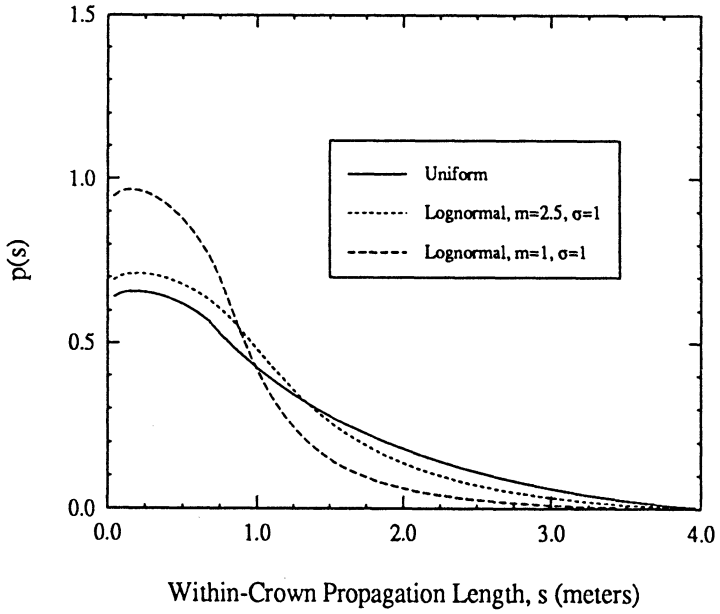

Figure 5.24: $p(s)$ at $z' = -10$ meters in the crown layer for a conical crown with center location having three different distributions between $-8 \leq z_i \leq -3$ and size varying linearly with z_i between $1 \leq c \leq 6$ and $a = 0.5c$ such that the smaller crowns are low in the canopy and the larger crowns are high in the canopy. The incidence angle $\theta = 30°$.

5.3 Calculation of Crown Cross-Sectional Area

The expected value of the crown cross sectional area as a function of depth z in a crown layer of thickness d must be considered in order to compute the expected value of the crown layer phase matrix. As illustrated in Figure 5.25, the cross section A_c of an individual crown sliced at depth z depends on the location of the crown

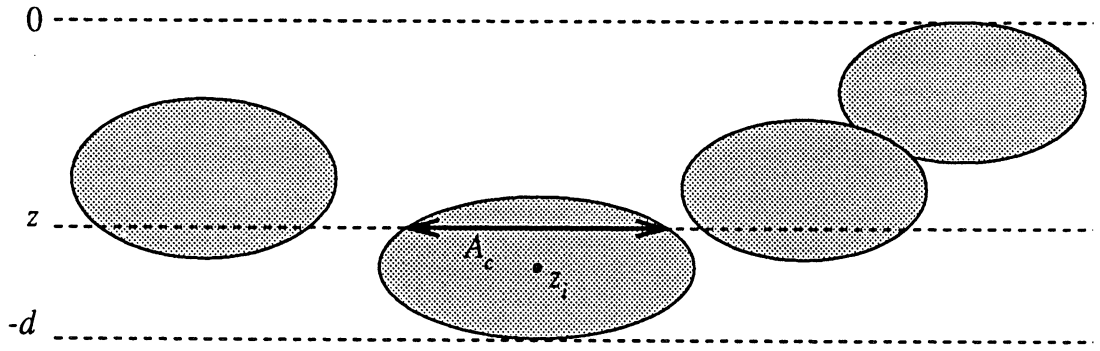

Figure 5.25: Cross-sectional area A_c at depth z of a crown centered at z_i.

center z_i along with the crown shape and size. For a given crown, if z_i and crown size are treated as random variables with specified distributions, the expected value of A_c is

$$\langle A_c(z)\rangle_c = \int_{\mathbf{t}}\int_{z_i} A_c(z, z_i, \mathbf{t})\, p_{z_i}(z_i)\, p_{\mathbf{t}}(\mathbf{t})\, \mathrm{d}z_i \mathrm{d}\mathbf{t} \tag{5.61}$$

where $p_{z_i}(z_i)$ and $p_{\mathbf{t}}(\mathbf{t})$ are the PDFs describing the distribution of the crown center location z_i and crown size parameters $\mathbf{t}$ and $A_c(z, z_i, \mathbf{t})$ is a function describing crown cross sectional area at depth z for a crown with center at z_i and size $\mathbf{t}$. Since, as evident from Equations (4.28), (4.29) and (4.31), the crown layer phase matrix is a linear function of crown cross-sectional area, the behavior of $\langle A_c(z)\rangle_c$ is a direct indicator of the behavior of the phase matrix as a function of z.

5.3.1 Cross-Sectional Area of Selected Crown Shapes with Specified Size and Location.

Given the shape, size and location of a specific crown, the cross-sectional area at a depth z may be determined explicitly by applying the crown shape equations. For a crown with a square column shape of base dimensions $a \times a$ and height c with center at z_i, the cross sectional area is

$$A_c(z, z_i, a, c) = \begin{cases} a^2 & ; z_i - \frac{c}{2} \leq z \leq z_i + \frac{c}{2} \\ 0 & ; \text{otherwise.} \end{cases} \tag{5.62}$$

For a spheroid crown with height c, width a, and center at z_i:

$$A_c(z, z_i, a, c) = \begin{cases} \frac{\pi a^2}{4}\left[1 - \left(\frac{z_i - z}{c/2}\right)^2\right] & ; z_i - \frac{c}{2} \leq z \leq z_i + \frac{c}{2} \\ 0 & ; \text{otherwise.} \end{cases} \tag{5.63}$$

A right circular cone with height c centered at z_i, basal diameter a has

$$A_c(z, z_i, a, c) = \begin{cases} \frac{\pi a^2}{4}\left[1 - \left(\frac{z - z_i + (c/2)}{c}\right)\right]^2 & ; z_i - \frac{c}{2} \leq z \leq z_i + \frac{c}{2} \\ 0 & ; \text{otherwise.} \end{cases} \tag{5.64}$$

Note that the size parameters $(a, c) \in \mathbf{t}$. Each of these shapes is non-zero only over the region $z_i - \frac{c}{2} \leq z \leq z_i + \frac{c}{2}$ and may therefore be expressed as an area factor A_f times a rectangular pulse function:

$$A_c(z, z_i, \mathbf{t}) = A_f(z, z_i, \mathbf{t}) \cdot \left\{u\left[z - (z_i - \frac{c}{2})\right] - u\left[z - (z_i + \frac{c}{2})\right]\right\} \tag{5.65}$$

$$= A_f(z, z_i, \mathbf{t}) \cdot \text{rect}\left[\frac{z - z_i}{c}\right] \tag{5.66}$$

where $(a, c) \in \mathbf{t}$, $u(z)$ is the unit step function defined by

$$u(z - z_o) = \begin{cases} 1 & ; z \geq z_o \\ 0 & ; z < z_o \end{cases} \tag{5.67}$$

and

$$\text{rect}(z) = \begin{cases} 1 & ;|z| \leq 1/2 \\ 0 & ;\text{otherwise} \end{cases} \tag{5.68}$$

If the crown parameters are known deterministically, (5.66) may be applied straightaway to find A_c. The problem of computing A_c for crowns with statistically specified parameters is examined next.

5.3.2 Cross-Sectional Area for Crowns Distributed in Height

If the crown center location has a distribution specified by the probability density function $p_{z_i}(z_i)$ then

$$\langle A_c(z,\mathbf{t})\rangle_c = \int_{z_i} A_c(z,z_i,\mathbf{t})\, p_{z_i}(z_i)\, \mathrm{d}z_i \tag{5.69}$$

$$= \int_{z_i} A_f(z,z_i,\mathbf{t})\, \text{rect}\left[\frac{z-z_i}{c}\right] p_{z_i}(z_i)\, \mathrm{d}z_i \tag{5.70}$$

where $p_{z_i}(z_i)$ is defined over the region $z_1 \leq z_i \leq z_2$ such that

$$p_{z_i}(z_i) = p_{z_i}(z_i) \cdot \text{rect}\left[\frac{z_i - \frac{1}{2}(z_1+z_2)}{z_2 - z_1}\right] \tag{5.71}$$

The quantity $\langle A_c(z,\mathbf{t})\rangle_c$ may then be written as

$$\langle A_c(z,\mathbf{t})\rangle_c = \int_{z_2}^{z_1} A_f(z,z_i,\mathbf{t})\, p_{z_i}(z_i)\, \text{rect}\left[\frac{z-z_i}{c}\right] \text{rect}\left[\frac{z_i - \frac{1}{2}(z_1+z_2)}{z_2 - z_1}\right] \mathrm{d}z_i. \tag{5.72}$$

Note that the crown centers must be located such that $-d + \frac{c}{2} \leq z_2 \leq z_1 \leq -\frac{c}{2}$ in order for all of the the crowns to be completely contained within the layer $-d \leq z \leq 0$.

Equation (5.72) is similar to a convolution integral and may be evaluated accordingly. Two cases must be considered. Case I applies when $z_1 - z_2 \geq c$ and Case II applies when $z_1 - z_2 \leq c$. In each case, the integral must be evaluated over three

regions. Equation (5.72) may be expressed as

$$\langle A_c(z,\mathbf{t})\rangle_c = \int_{z_l(z)}^{z_u(z)} A_f(z,z_i,\mathbf{t})\, p_{z_i}(z_i)\, \mathrm{d}z_i. \tag{5.73}$$

where $z_u(z)$ and $z_l(z)$ represent the upper and lower limits of integration for each of the three regions. These limits are summarized in Table 5.1. The function

Table 5.1: Integration limits for computing $\langle A_c(z,\mathbf{t})\rangle_c$.

Case I: $z_1 - z_2 \geq c$			
Range of z	$z_2 - \frac{c}{2} \leq z \leq z_2 + \frac{c}{2}$	$z_2 + \frac{c}{2} \leq z \leq z_1 - \frac{c}{2}$	$z_1 - \frac{c}{2} \leq z \leq z_1 + \frac{c}{2}$
$z_u(z)$	$z + \frac{c}{2}$	$z + \frac{c}{2}$	z_1
$z_l(z)$	z_2	$z - \frac{c}{2}$	$z - \frac{c}{2}$
Case II: $z_1 - z_2 \leq c$			
Range of z	$z_2 - \frac{c}{2} \leq z \leq z_1 - \frac{c}{2}$	$z_1 - \frac{c}{2} \leq z \leq z_2 + \frac{c}{2}$	$z_2 + \frac{c}{2} \leq z \leq z_1 + \frac{c}{2}$
$z_u(z)$	$z + \frac{c}{2}$	z_1	z_1
$z_l(z)$	z_2	z_2	$z - \frac{c}{2}$

$\langle A_c(z,\mathbf{t})\rangle_c$ may be evaluated for a given crown by applying (5.73) to the specified crown area factor A_f and center location PDF $p_{z_i}(z_i)$.

If the crown center is uniformly distributed in z_i then

$$p_{z_i}(z_i) = \frac{1}{z_1 - z_2} \cdot \mathrm{rect}\left[\frac{z_i - \frac{1}{2}(z_1 + z_2)}{z_2 - z_1}\right] \tag{5.74}$$

and Equation (5.73) may be solved analytically for crowns with areas specified in (5.62) - (5.64). Table 5.2 shows the solution for $\langle A_c(z,\mathbf{t})\rangle_c$ for square column, spheroid, and conical crowns as a function of depth z, crown center distribution limits z_1 and z_2, and crown size $(a,c) \in \mathbf{t}$. Figures 5.26 - 5.28 are graphs of $\langle A_c(z,\mathbf{t})\rangle_c$ for these crown shapes. Each figure shows cross section as a function of z for a single crown with center uniformly distributed between $z_2 \leq z_i \leq z_1$ and size $a = c = 2$. It is interesting to note that for each set of crown parameters

$$\int_{-d}^{0} \langle A_c(z,\mathbf{t})\rangle_c \, \mathrm{d}z = V \tag{5.75}$$

where V is the volume of the crown.

Table 5.2: Cross sectional area for crowns with centers uniformly distributed between z_1 and z_2.

CASE I: $z_1 - z_2 \geq c$		
Range of z	Square Column	Spheroid
$z_2 - \frac{c}{2} \leq z \leq z_2 + \frac{c}{2}$	$\frac{a^2(c+2z-2z_2)}{2(z_1-z_2)}$	$\frac{\pi a^2(c+2z-2z_2)^2(c-z+z_2)}{12c^2(z_1-z_2)}$
$z_2 + \frac{c}{2} \leq z \leq z_1 - \frac{c}{2}$	$\frac{a^2 c}{z_1-z_2}$	$\frac{\pi a^2 c}{6(z_1-z_2)}$
$z_1 - \frac{c}{2} \leq z \leq z_1 + \frac{c}{2}$	$\frac{a^2(c-2z+2z_1)}{2(z_1-z_2)}$	$\frac{\pi a^2(c+z-z_1)(c-2z+2z_1)^2}{12c^2(z_1-z_2)}$

Range of z	Cone
$z_2 - \frac{c}{2} \leq z \leq z_2 + \frac{c}{2}$	$\frac{\pi a^2(c+2z-2z_2)\left(7c^2-8cz+4z^2+8cz_2-8zz_2+4z_2^2\right)}{96c^2(z_1-z_2)}$
$z_2 + \frac{c}{2} \leq z \leq z_1 - \frac{c}{2}$	$\frac{\pi a^2 c}{12(z_1-z_2)}$
$z_1 - \frac{c}{2} \leq z \leq z_1 + \frac{c}{2}$	$\frac{\pi a^2(c-2z+2z_1)^3}{96c^2(z_1-z_2)}$

CASE II: $z_1 - z_2 \leq c$		
Range of z	Square Column	Spheroid
$z_2 - \frac{c}{2} \leq z \leq z_1 - \frac{c}{2}$	$\frac{a^2(c+2z-2z_2)}{2(z_1-z_2)}$	$\frac{\pi a^2(c+2z-2z_2)^2(c-z+z_2)}{12c^2(z_1-z_2)}$
$z_1 - \frac{c}{2} \leq z \leq z_2 + \frac{c}{2}$	a^2	$\frac{\pi a^2\left(3c^2-12z^2+12zz_1-4z_1{}^2+12zz_2-4z_1z_2-4z_2^2\right)}{12c^2}$
$z_2 + \frac{c}{2} \leq z \leq z_1 + \frac{c}{2}$	$\frac{a^2(c-2z+2z_1)}{2(z_1-z_2)}$	$\frac{\pi a^2(c+z-z_1)(c-2z+2z_1)^2}{12c^2(z_1-z_2)}$

Range of z	Cone
$z_2 - \frac{c}{2} \leq z \leq z_1 - \frac{c}{2}$	$\frac{\pi a^2(c+2z-2z_2)\left(7c^2-8cz+4z^2+8cz_2-8zz_2+4z_2^2\right)}{96c^2(z_1-z_2)}$
$z_1 - \frac{c}{2} \leq z \leq z_2 + \frac{c}{2}$	$\frac{\pi a^2\left(3c^2-12cz+12z^2+6cz_1-12zz_1+4z_1{}^2+6cz_2-12zz_2+4z_1z_2+4z_2^2\right)}{48c^2}$
$z_2 + \frac{c}{2} \leq z \leq z_1 + \frac{c}{2}$	$\frac{\pi a^2(c-2z+2z_1)^3}{96c^2(z_1-z_2)}$

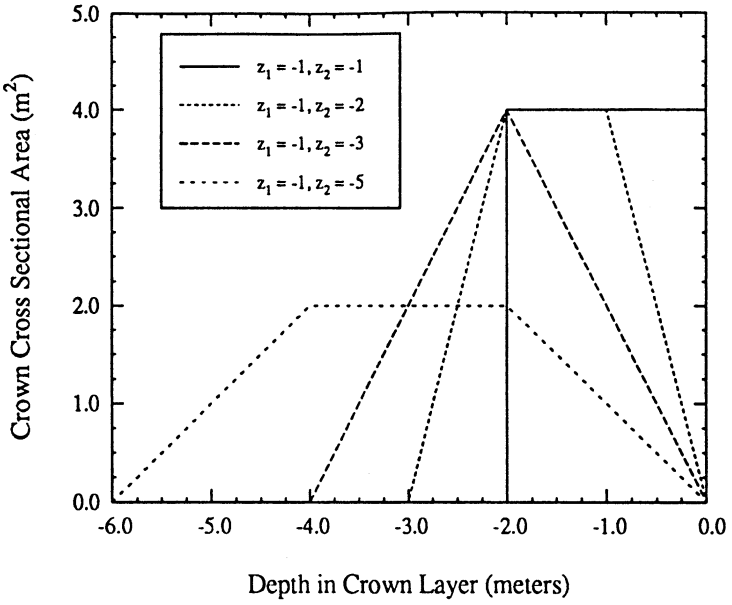

Figure 5.26: Expected value of crown cross-sectional area at depth z in a crown layer for a single square column crown with center uniformly distributed over $z_1 \leq z_i \leq z_2$ with $a = c = 2$.

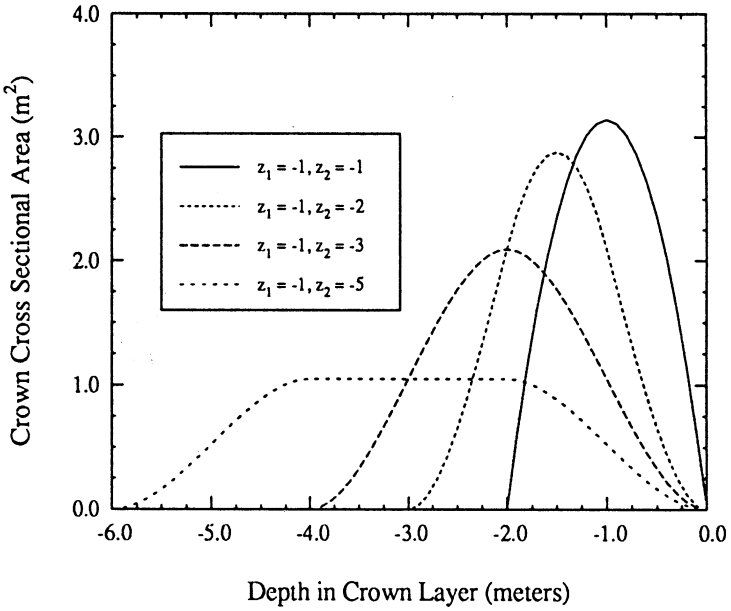

Figure 5.27: Expected value of crown cross-sectional area at depth z in a crown layer for a single spheroidal crown with center uniformly distributed over $z_1 \leq z_i \leq z_2$ with $a = c = 2$.

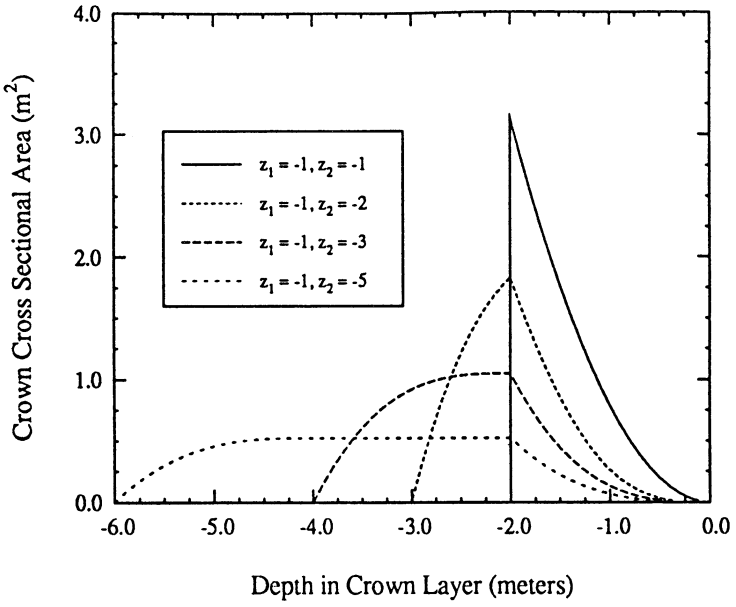

Figure 5.28: Expected value of crown cross-sectional area at depth z in a crown layer for a single conical crown with center uniformly distributed over $z_1 \leq z_i \leq z_2$ with $a = c = 2$.

5.3.3 Cross-Sectional Area for Crowns Distributed in Size

For a crown with specified center location (constant z_i) with a size distribution specified by the PDF $p_t(t)$ the expected cross section at a given depth z in the crown layer is

$$\langle A_c(z, z_i)\rangle_c = \int_s A_c(z, z_i, t)\, p_t(t)\, dt \tag{5.76}$$

$$= \int_s A_f(z, z_i, t)\, \text{rect}\left[\frac{z - z_i}{c}\right] p_t(t)\, dt. \tag{5.77}$$

Expressing the size PDF in terms of the crown height c as

$$p_t(t) = \begin{cases} p_c(c) & ; c_1 \leq c \leq c_2 \\ 0 & ;\text{otherwise} \end{cases} \tag{5.78}$$

$$= p_c(c) \cdot \text{rect}\left[\frac{c - \frac{1}{2}(c_1 + c_2)}{c_2 - c_1}\right] \tag{5.79}$$

where c_1 and c_2 are the lower and upper limits of crown height, respectively, yields

$$\langle A_c(z, z_i)\rangle_c = \int_{c_1}^{c_2} A_f(z, z_i, \mathrm{t}(c))\, p_c(c)\, \mathrm{rect}\left[\frac{z - z_i}{c}\right] \mathrm{rect}\left[\frac{c - \frac{1}{2}(c_1 + c_2)}{c_2 - c_1}\right] \mathrm{dc}. \quad (5.80)$$

To perform the integration over c, it is convenient to express

$$\langle A_c(z, c)\rangle_c = \int_{c_l(z)}^{c_u(z)} A_f(z, z_i, \mathrm{t}(c))\, p_c(c)\, \mathrm{dc} \quad (5.81)$$

where the $c_l(z)$ and $c_u(z)$ represent the lower and upper limits of integration as determined by the product of the pulses in (5.80). Table 5.3 summarizes these limits. The function $\langle A_c(z, z_i)\rangle_c$ may be evaluated by applying (5.81) to specified

Table 5.3: Integration limits for computing $\langle A_c(z, z_i)\rangle_c$.

Range	$z_i - \frac{c_2}{2} \le z \le z_i - \frac{c_1}{2}$	$z_i + \frac{c_1}{2} \le z \le z_i + \frac{c_1}{2}$	$z_i + \frac{c_1}{2} \le z \le z_i + \frac{c_2}{2}$
$z_u(z)$	c_2	c_2	c_2
$z_l(z)$	$-2(z - z_i)$	c_1	$2(z - z_i)$

crown area factor A_f and size PDF $p_c(c)$.

If the crown is uniformly distributed in c such that

$$p_c(c) = \frac{1}{c_2 - c_1}, \quad (5.82)$$

then the cross sections may be computed analytically for the crown areas specified in (5.62) - (5.64). Table 5.4 shows the solution for $\langle A_c(z, z_i)\rangle_c$ for square column, spheroid, and conical crowns as a function of depth in the crown layer z, crown center location z_i, and crown height limits c_1 and c_2. Here, the crown size was assumed to vary with height so that $a = c$ for all values of c. Figures 5.29 - 5.31 are graphs of $\langle A_c(z, z_i)\rangle_c$ for these crown shapes.

Table 5.4: Cross sectional area for crowns with height uniformly distributed such that $c_1 \leq c \leq c_2$ and $a = c$.

Range of z	Square Column	Spheroid
$z_i - \frac{c_2}{2} \leq z \leq z_1 - \frac{c_1}{2}$	$\frac{{c_2}^3}{3(c_2-c_1)} + \frac{8(z-z_i)^3}{3(c_2-c_1)}$	$\frac{\pi(c_2+2z-2z_i)^2(c_2-4z+4z_i)}{12(c_2-c_1)}$
$z_i - \frac{c_1}{2} \leq z \leq z_1 + \frac{c_1}{2}$	$\frac{{c_1}^2+c_1c_2+{c_2}^2}{3}$	$\frac{\pi\left({c_1}^2+c_1c_2+{c_2}^2-12z^2+24zz_i-12{z_i}^2\right)}{12}$
$z_i + \frac{c_1}{2} \leq z \leq z_1 + \frac{c_2}{2}$	$\frac{{c_2}^3}{3(c_2-c_1)} - \frac{8(z-z_i)^3}{3(c_2-c_1)}$	$\frac{\pi(c_2+4z-4z_i)(c_2-2z+2z_i)^2}{12(c_2-c_1)}$

Range of z	Cone
$z_i - \frac{c_2}{2} \leq z \leq z_1 - \frac{c_1}{2}$	$\frac{\pi(c_2+2z-2z_i)\left({c_2}^2-8c_2z+28z^2+8c_2z_i-56zz_i+28{z_i}^2\right)}{48(c_2-c_1)}$
$z_i - \frac{c_1}{2} \leq z \leq z_1 + \frac{c_1}{2}$	$\frac{\pi\left({c_1}^2+c_1c_2+{c_2}^2-6c_1z-6c_2z+12z^2+6c_1z_i+6c_2z_i-24zz_i+12{z_i}^2\right)}{48}$
$z_i + \frac{c_1}{2} \leq z \leq z_1 + \frac{c_2}{2}$	$\frac{\pi(c_2-2z+2z_i)^3}{48(c_2-c_1)}$

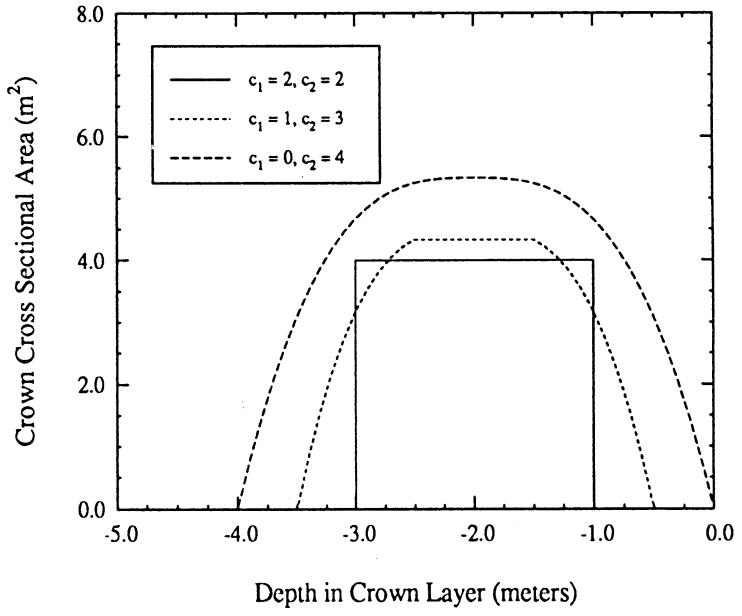

Figure 5.29: Expected value of crown cross-sectional area at depth z in a crown layer for a single square column crown with c uniformly distributed between c_1 and c_2, $a = c$ and $z_i = -2$.

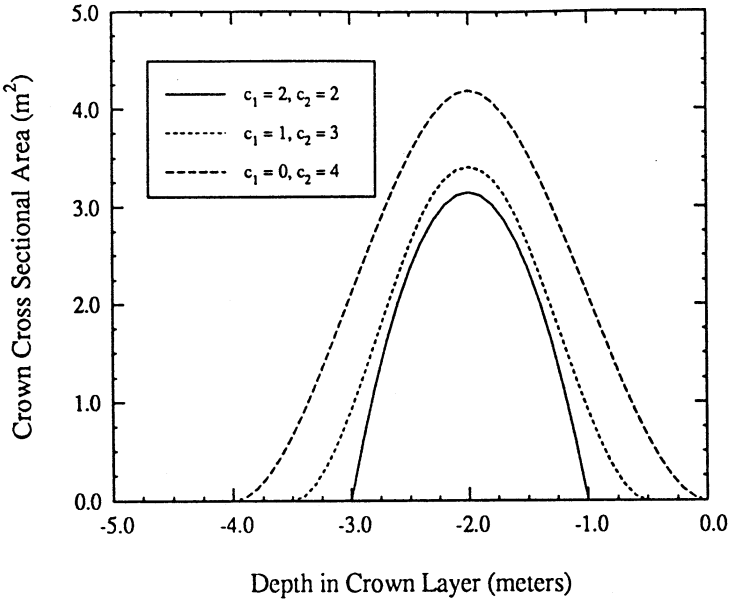

Figure 5.30: Expected value of crown cross-sectional area at depth z in a crown layer for a single spherical crown with c uniformly distributed between c_1 and c_2, $a = c$ and $z_i = -2$.

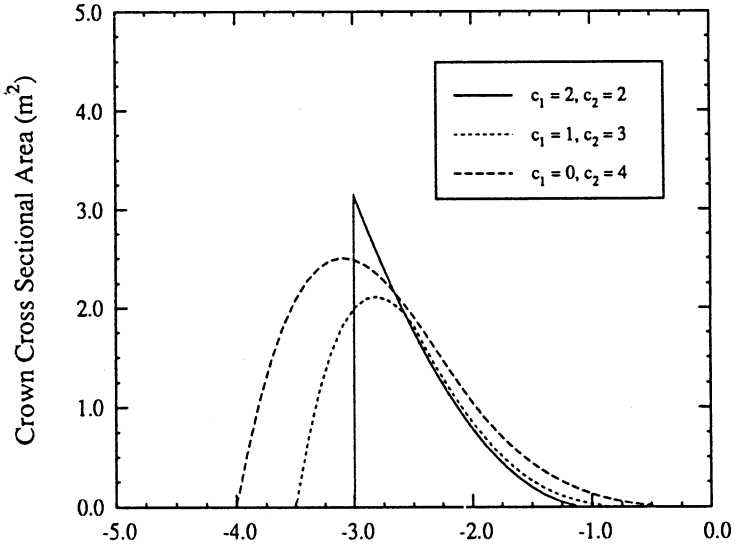

Figure 5.31: Expected value of crown cross-sectional area at depth z in a crown layer for a single conical crown with c uniformly distributed between c_1 and c_2, $a = c$ and $z_i = -2$.

Each figure shows the cross section as a function of z for a single crown with c uniformly distributed between $c_1 \leq c \leq c_2$, crown center at $z_i = -2$ and $a = c$. It is interesting to note that for each set of crown parameters

$$\int_{-d}^{0} \langle A_c(z, z_i) \rangle_c \, dz = \overline{V} \tag{5.83}$$

where $\overline{V}$ is the average volume of the crown.

5.3.4 Cross-Sectional Area for Crowns Distributed in Height and Size

For crowns with distributions specified in both s and z_i

$$\begin{aligned} \langle A_c(z) \rangle_c \; = \\ \int_{c_1}^{c_2} \int_{z_2}^{z_1} A_f(z, z_i, \mathrm{t}(c)) p_{z_i}(z_i) p_c(c) \\ \cdot \mathrm{rect}[\frac{z - z_i}{c}] \mathrm{rect}[\frac{z_i - \frac{1}{2}(z_1 + z_2)}{z_2 - z_1}] \mathrm{rect}[\frac{c - \frac{1}{2}(c_1 + c_2)}{c_2 - c_1}] dz_i dc. \end{aligned} \tag{5.84}$$

In this case, analytical solutions are more tedious to derive and numerical techniques become more efficient. Figures 5.32, 5.33 and 5.34 show $\langle A_c(z) \rangle_c$ for square column, spherical, and conical crowns, respectively. All crowns have been assigned a uniform size distribution with $1 \leq c \leq 3$ and $a = c$. The crown centers have been assigned a uniform distribution with $z_2 \leq z_i \leq z_1$. As seen in the cases for which $z_1 = -2$, $z_2 = -8$, the behavior of $\langle A_c(z) \rangle_c$ for all three shapes becomes similar for crowns whose centers are widely distributed throughout the crown layer.

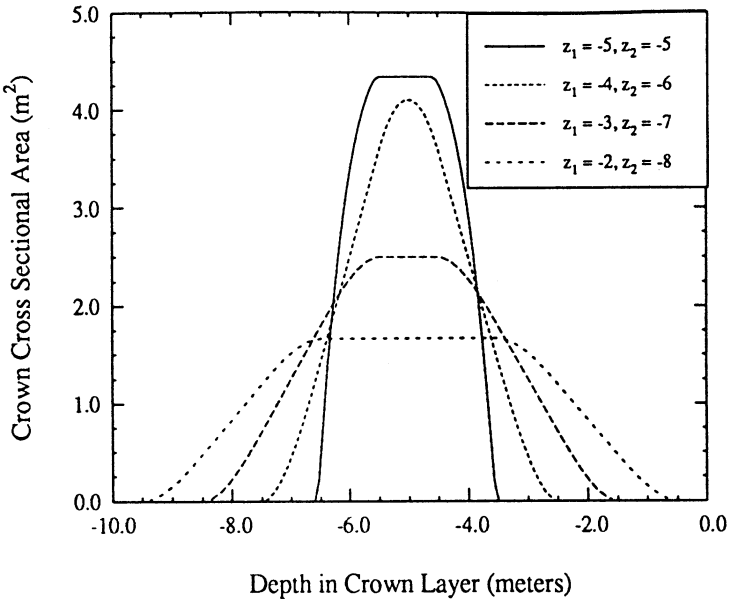

Figure 5.32: Expected value of crown cross-sectional area at depth z in a crown layer for a single square column crown with center uniformly distributed between z_1 and z_2 and c uniformly distributed between 1 and 3 meters with $a = c$.

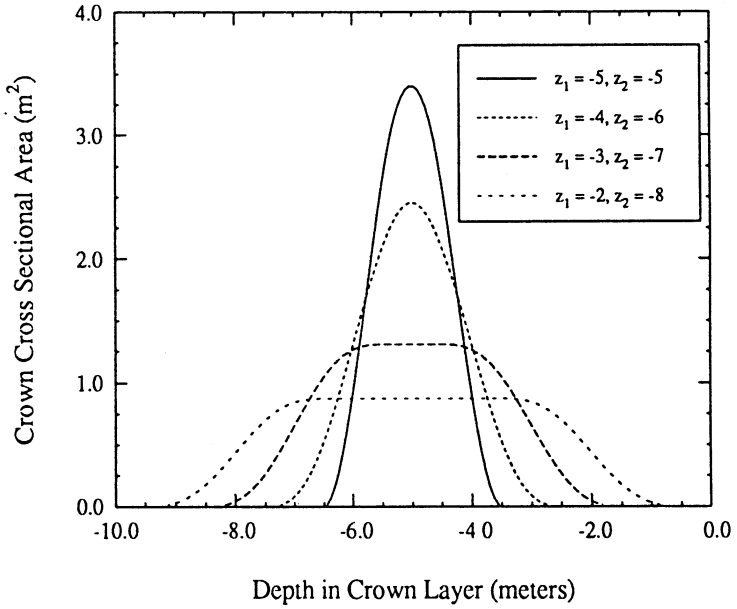

Figure 5.33: Expected value of crown cross-sectional area at depth z in a crown layer for a single spherical crown with center uniformly distributed between z_1 and z_2 and c uniformly distributed between 1 and 3 meters with $a = c$.

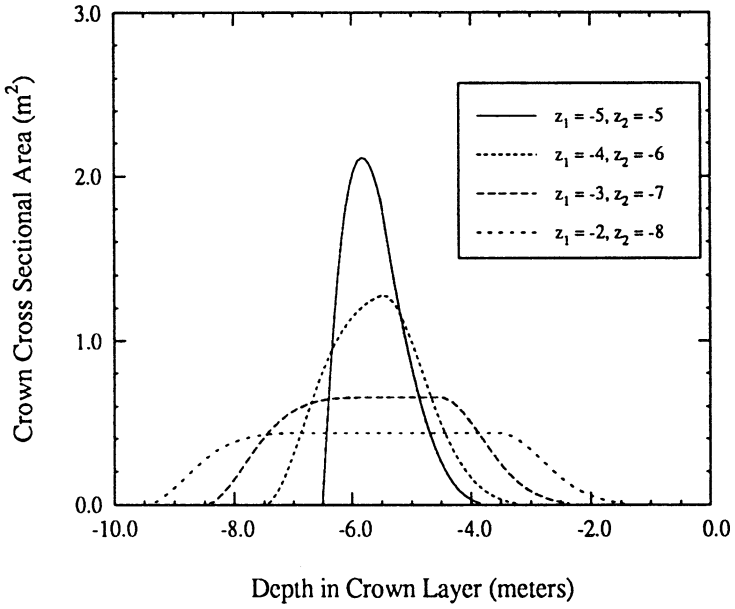

Figure 5.34: Expected value of crown cross-sectional area at depth z in a crown layer for a single conical crown with center uniformly distributed between z_1 and z_2 and c uniformly distributed between 1 and 3 meters with $a = c$.

In all of these cases,

$$\int_{-d}^{0} \langle A_c(z) \rangle_c \, dz = \overline{V} \tag{5.85}$$

where $\overline{V}$ is the average volume of the crown. Applying Equations (4.28), (4.29) and (4.31), the average crown layer phase matrix may be written as

$$\begin{aligned} \langle \mathcal{P}_c(\theta_s, \phi_s; \theta_i, \phi_i) \rangle_c &= \frac{1}{d} \int_{-d}^{0} \langle \mathcal{P}_c(\theta_s, \phi_s; \theta_i, \phi_i; z) \rangle_c \, dz & (5.86) \\ &= \frac{N_t}{d} \int_{-d}^{0} \langle A_c(z) \rangle_c \, dz \\ &\quad \cdot \sum_{k=1}^{K} N_k \overline{\mathcal{L}}_k(\theta_s, \phi_s; \theta_i, \phi_i; \mathrm{s}_k; \theta_k, \phi_k) & (5.87) \\ &= \frac{N_t \overline{V}}{d} \mathcal{P}_c^{(1)}(\theta_s, \phi_s; \theta_i, \phi_i) & (5.88) \end{aligned}$$

where N_t is the number density of trees per unit area and $\mathcal{P}_c^{(1)}(\theta_s, \phi_s; \theta_i, \phi_i)$ is the phase matrix for a unit volume contained in a single crown. For a continuous canopy, $\overline{V}/d = 1/N_t$ so

$$\langle \mathcal{P}_c(\theta_s, \phi_s; \theta_i, \phi_i) \rangle_c = \mathcal{P}_c^{(1)}(\theta_s, \phi_s; \theta_i, \phi_i) \tag{5.89}$$

5.4 Summary of Crown Shape Statistics

This chapter has presented the derivation of shape statistics for specified classes of tree crowns. Given the distribution for within-crown propagation length $p(s|1)$ for individual crowns from Section 5.1, the techniques discussed in Section 5.2 may be applied to compute $p(s|1)$ for distributions of crowns. The PDF $p(s|1)$, together with the cross-sectional area $A_c(z)$ discussed in Section 5.3, may be coupled to the radiative transfer solution for an open-crown canopy presented in Chapter IV to solve for backscatter from a particular canopy. This is done in Chapter VI.

CHAPTER VI

MODELING ANALYSES AND APPLICATIONS

This chapter presents some examples in which MIMICS is used to model the scattering characteristics of some vegetation canopies. The first three sections present analyses in which MIMICS I has been applied to model various types of canopies. Section 6.1 presents a modeling analysis in which MIMICS is used to model polarization phase difference for a selection of corn fields in Illinois. In Section 6.2, MIMICS is used to model multi-angle and multi-temporal backscatter from a walnut orchard in Fresno County, California. Section 6.3 presents an analysis of canopy transmissivity and backscatter from various forest stands in the Alaskan boreal forest. In each of these cases, the model is driven with ancillary ground measurements and the output is compared to radar data measured with truck-based or aircraft-mounted systems. Finally, in Section 6.4 MIMICS II is applied to simulate transmissivity and backscatter for several of these canopies and the results are compared with MIMICS I simulations.

6.1 MIMICS I Corn Canopy Modeling Using SIR-B Data

The second Shuttle Imaging Radar (SIR-B) flew aboard the Challenger on mission STS-41G in October of 1984 (Cimino *et al.*, [7]). This instrument provided

researchers with orbital L-band HH-polarized SAR imagery for various science objectives. One study conducted during the SIR-B flight is described by Dobson and Ulaby, [16] and Ulaby *et al.*, [66]. They used the SIR-B instrument together with aircraft SAR underflights to address such issues as land-cover classification and assessment of near-surface soil moisture content. The test site for this study comprised an area in west-central Illinois of roughly 250 km^2 within which approximately 400 agricultural fields were surveyed for ancillary ground measurements of canopy properties. As a first modeling example, MIMICS I is applied to model characteristics of the backscatter from a number of the corn canopies for which ground measurements and SAR data are available.

Polarization phase difference distributions were generated from the aircraft SAR data for over 80 different corn fields in the test site (Ulaby *et al.*, [66]). From these distributions, the mean like-polarized phase difference was estimated for each field. For a canopy with small like-to-cross polarized backscatter ratio, the mean like-polarized phase difference relative to VV-polarization, $\Delta\phi_{\text{HH-VV}}$, may be approximated by considering the quantities of the modified Mueller matrix defined in terms of the scattering matrix elements (Equation 2.6). If cross-polarized backscatter is small,

$$\Delta\phi_{\text{HH-VV}} = \text{Tan}^{-1}\left[\frac{\text{Im}(S_{vv}S_{hh}^*)}{\text{Re}(S_{vv}S_{hh}^*)}\right] \tag{6.1}$$

$$= \text{Tan}^{-1}\left|\frac{[\mathcal{T}]_{(4,3)}}{[\mathcal{T}]_{(3,3)}}\right| \tag{6.2}$$

where $[\mathcal{T}]_{(m,n)}$ represents the (m,n) element of the canopy transformation matrix.

From ancillary ground measurements, canopy characteristics representative of an effective average corn canopy were estimated. These characteristics are listed in Table 6.1. The stalks were assigned vertical orientations while the leaves were assigned an orientation distribution uniform in the incremental solid angle $d\Omega = \sin\theta d\theta d\phi$. Since

Table 6.1: Corn canopy parameters for fields observed by the aircraft SAR.

Canopy density = 8.77 stalks/m^2
Stalk height = 2.5 m
Stalk diameter = 2.5 cm
Stalk dielectric constant = 6.5 $+i$ 0.5
Soil dielectric constant = 15 $+i$ 2
Soil RMS height = 2 cm
Soil correlation length = 26 cm
Leaf gravimetric moisture = 0.1
Leaf number density = 200/m^3
Leaf diameter = 6.18 cm
Leaf thickness = 0.2 mm

this experiment occurred late in the growing season, the leaves were senescent and quite dry and therefore had minimal effect on the canopy backscatter. MIMICS I was run at an L-band frequency of 1.2 GHz as a function of incidence angle. Figure 6.1 compares the measured polarization phase difference to that predicted by MIMICS. The model agrees well with the data, predicting the sharp increase in $\Delta\phi$ observed for $25° \leq \theta \leq 35°$, which is caused by the effect of the Brewster angle on the reflection from the corn stalks. It is important to note that while each circle on this graph represents the observed $\Delta\phi$ for a single corn canopy, the model calculation represents the $\Delta\phi$ calculated by MIMICS for the average field conditions represented in Table 6.1, and therefore the results do not incorporate the natural field-to-field variability inherent in the scene.

Since a major objective of this study was to assess the ability of orbital SAR for use in soil moisture estimation, the response of the measured SIR-B backscatter to changes in this parameter is now examined (Dobson and Ulaby, [16]). Volumetric soil moisture has been estimated for many of the corn fields in the test site through analysis of soil samples extracted from three locations in each field. Table 6.2 lists the average canopy characteristics that correspond to these fields. Leaf parameters

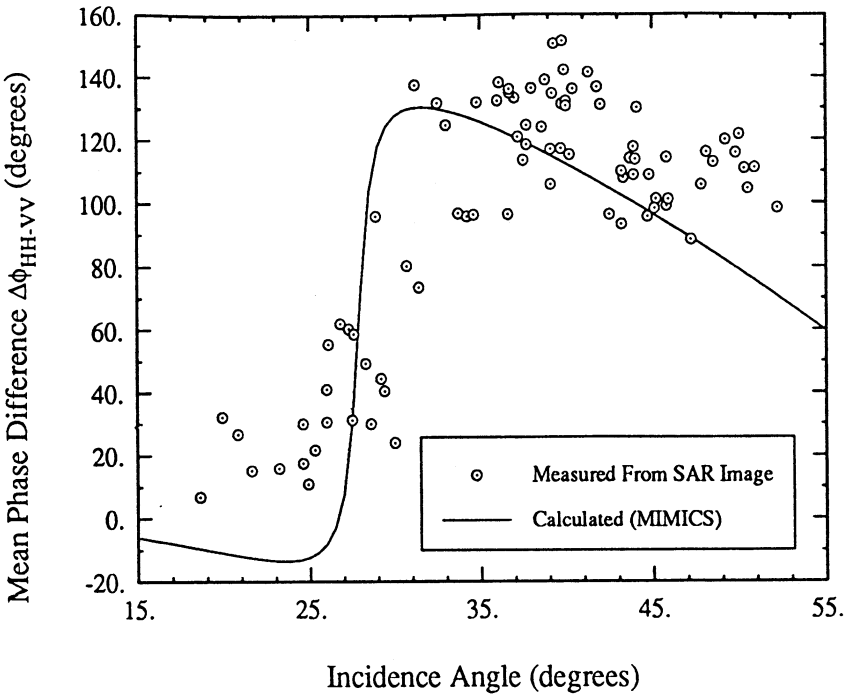

Figure 6.1: Comparison of the polarization phase difference calculated by MIMICS to that extracted from the aircraft SAR imagery.

Table 6.2: Corn canopy parameters for fields observed by the SIR-B SAR.

Canopy density = 6.58 stalks/m^2
Stalk height = 2.8 m
Stalk diameter = 2.5 cm
Soil RMS height = 2 cm
Soil correlation length = 26 cm

were the same as those given in Table 6.1.

Using the dielectric models described in Appendix A and assigning soil textural components of 10% sand, 30% clay and 60% silt, MIMICS was run as a function of volumetric soil moisture at a frequency of 1.2 GHz for an incidence angle $\theta = 30°$, corresponding to SIR-B SAR parameters. Figure 6.2 compares MIMICS predictions to data extracted from SIR-B imagery. Three MIMICS simulations are shown in this figure. Each of the first two simulations presents the MIMICS response to changing soil moisture with all other canopy parameters help constant. The uppermost curve

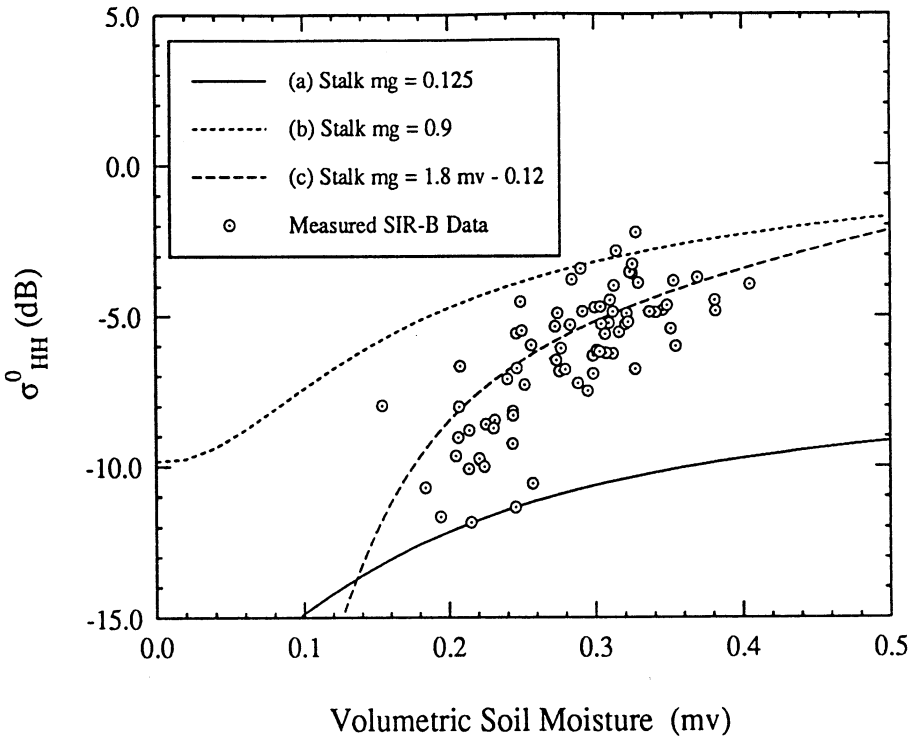

Figure 6.2: L-band σ^0 HH-polarized backscatter response to changes in volumetric soil moisture. Data measured by the SIR-B SAR are compared with MIMICS simulations for canopies with (a) dry stalks with gravimetric moisture = 0.125, (b) wet stalks with gravimetric moisture = 0.9, (c) stalks with gravimetric moisture coupled to the soil moisture via mg = 1.8 mv - 0.12.

depicts the σ^0 response for a canopy whose stalks have a gravimetric moisture (mg) of 0.9 (relatively wet) while the lowermost curve depicts σ^0 for a canopy with stalks of mg = 0.125 (relatively dry). It is seen that MIMICS predicts slightly less sensitivity of σ^0 to changes in soil moisture than was observed by SIR-B. A possible explanation for this phenomenon is that soil moisture may be coupled to other canopy biophysical parameters and, therefore, changes in soil moisture may be coupled to changes in other canopy properties. One such mechanism is illustrated by the third MIMICS simulation in Figure 6.2. While the wet and dry stalk moisture conditions present an upper and lower bound for the SAR data, coupling the stalk moisture (mg) to the soil moisture (mv) via the equation mg = 1.8 mv - 0.12 successfully predicts the

appropriate sensitivity of σ^0 to changes in moisture.

Unfortunately, the strategy applied in collecting canopy ground measurements involved using separate teams for measuring soil and vegetation parameters and thus there are very few corn fields for which there are coincident soil and stalk moisture measurements. The insignificant amount of these data make it impossible to verify any discernible relationship between stalk and soil moisture. However, it is instructional to examine the potential for using MIMICS together with SAR measurements to decouple canopy moisture parameters.

If one assumes that plant and soil moisture are coupled, the question arises of how to apply measured backscatter parameters together with MIMICS in order to separately estimate the moisture content of the plant and soil. Figure 6.3 shows the co-polarized backscatter response for a corn canopy under wet and dry moisture conditions with other parameters being identical. The polarization responses for these cases are very similar, indicating very little change in the polarization characteristics of the backscatter for the wet and dry conditions. Examination of Figure 6.4 gives a more direct indication of σ^0 response to changes in stalk and ground moisture content. Here, to assess the sensitivity of canopy backscatter to changes in stalk and soil moisture, MIMICS was run at $\theta = 20°$ varying both moisture parameters. Figure 6.4 (a), (b) and (c) show the response of σ^0_{HH}, σ^0_{VV} and $\Delta\phi_{\mathrm{HH\text{-}VV}}$ respectively. Roughly speaking, the HH-polarized backscatter exhibits about 4-5 dB of change over the displayed range of stalk moisture and about 10 dB of change over the range of soil moisture. VV-polarized backscatter exhibits about 13 dB of change over the range of stalk moisture while changing by about 10 dB with soil moisture. $\Delta\phi$ exhibits about 125° of change with stalk moisture but has virtually no dependence on soil moisture.

By combining these three responses, one may illustrate how to predict both moisture contents from a given set of SAR observations. Assuming all other canopy parameters are known, stalk moisture may be estimated from $\Delta\phi$. Then, σ^0_{HH} and σ^0_{VV} may be applied to estimate soil moisture. Given measured values of σ^0_{HH}, σ^0_{VV} and $\Delta\phi$ for the particular canopy structure, contours that represent families of constant backscatter and phase difference are generated from Figure 6.4. Each contour represents a solution set in stalk and soil moisture for that particular backscatter quantity. For a given canopy state, the intersection of contour families yields the desired moisture values.

Figure 6.5 illustrates two examples of this process. Figure 6.5(a) illustrates an example of the intersection of the contours for a canopy with wet conditions and Figure 6.5(b) shows an example for the same canopy with dry conditions. In both cases, $\Delta\phi$ is constant as a function of soil moisture, and therefore determines the stalk moisture. σ^0_{HH} and σ^0_{VV} then yield the solution for soil moisture. It is important to note that Figure 6.5 represents an ideal modeling case in which σ^0_{HH}, σ^0_{VV} and $\Delta\phi$ have been chosen to yield a unique intersection point. In applying this technique to determine canopy moisture status from an actual SAR image, it is highly unlikely that the three families will all intersect at the same point and further analysis involving estimation of canopy parameters would have to be applied for the model to converge on unique estimates of plant and soil moisture.

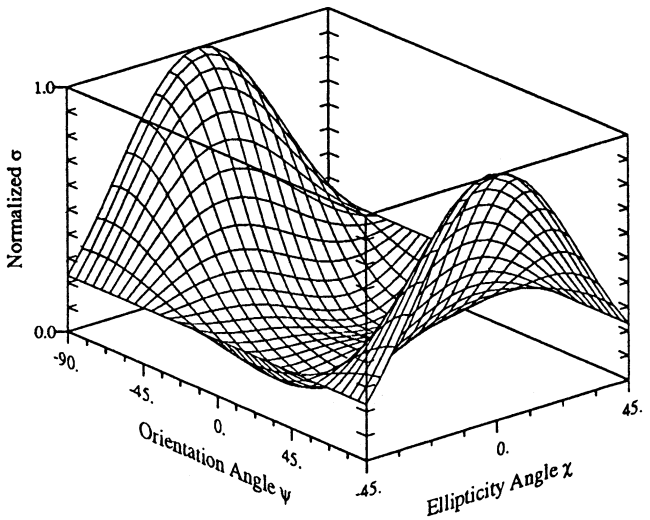

(a) Wet conditions

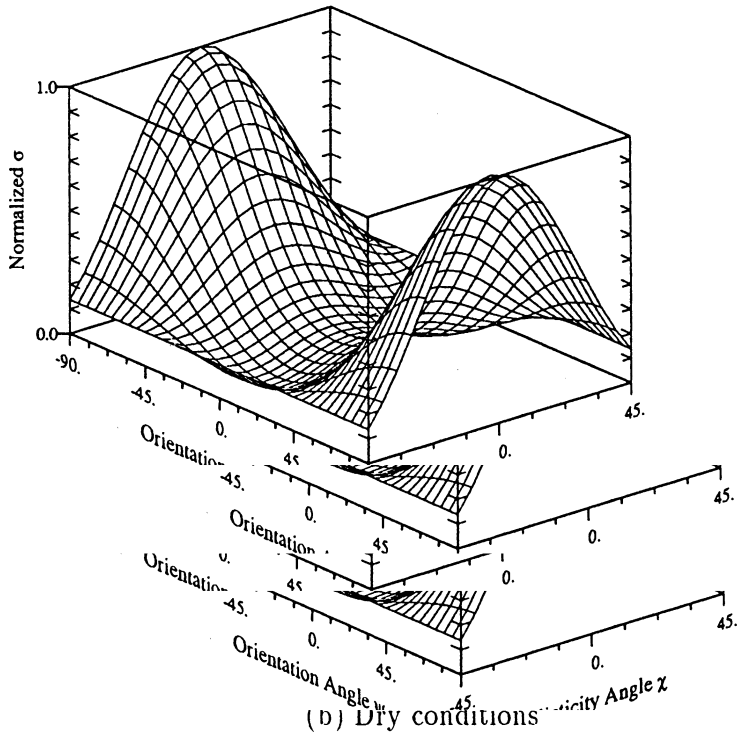

(b) Dry conditions

Figure 6.3: Co-polarized L-band response of a corn canopy at $\theta = 30°$ for (a) wet conditions with soil moisture = 0.3 and stalk moisture = 0.6 and (b) dry conditions with soil moisture = 0.08 and stalk moisture = 0.35.

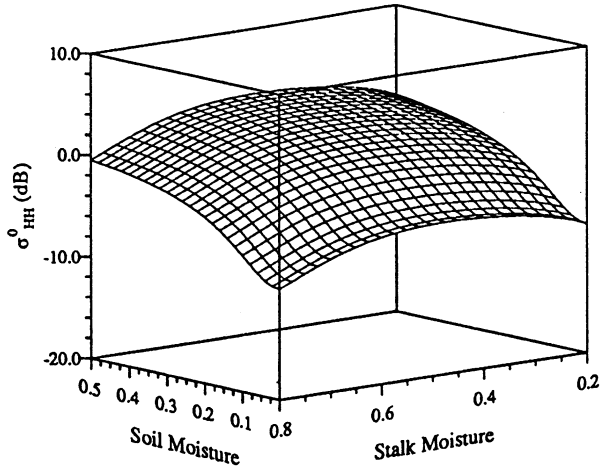

(a)

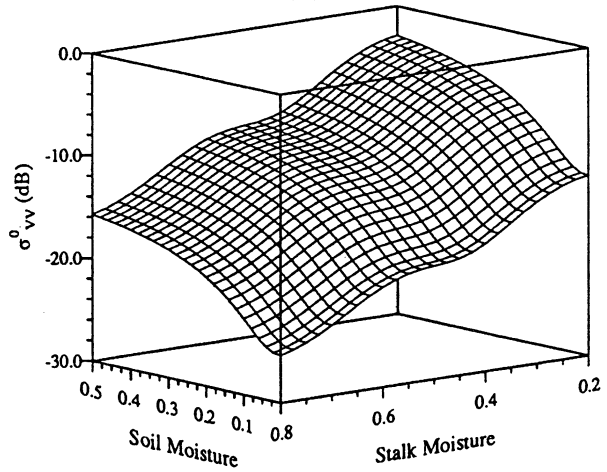

(b)

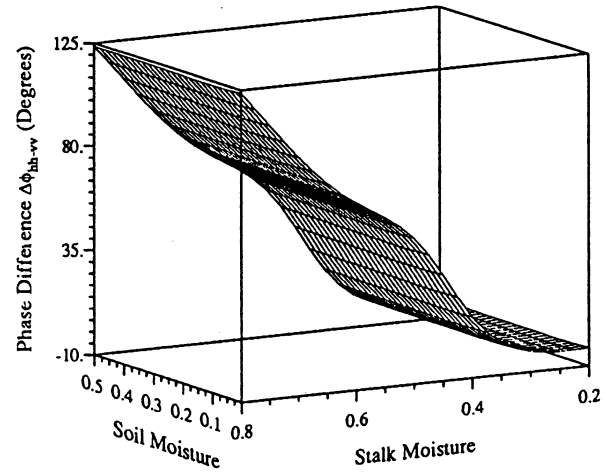

(c)

Figure 6.4: Corn canopy backscatter response to changes in volumetric soil moisture and gravimetric stalk moisture for an incidence angle $\theta = 20°$. (a) HH-polarized response, (b) VV-polarized response, (c) polarization phase difference response.

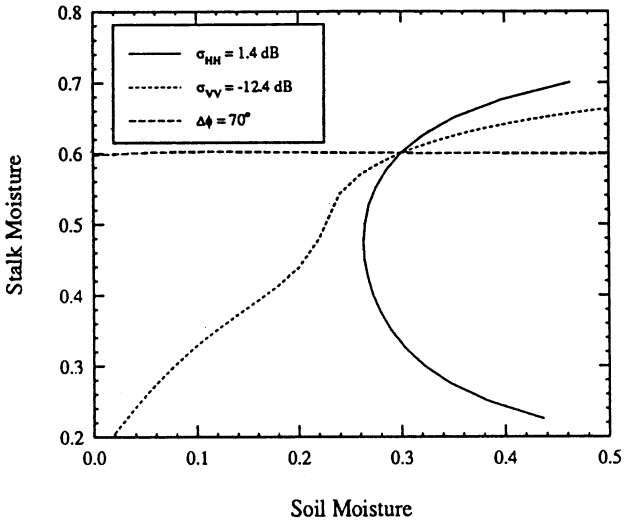

(a) Wet conditions

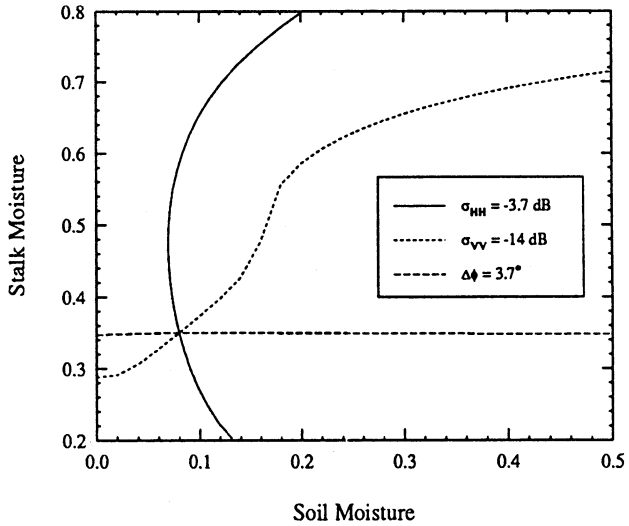

(b) Dry conditions

Figure 6.5: Solution set for estimation of canopy moisture conditions
(a) wet conditions with soil moisture = 0.3 and stalk moist
(b) dry conditions with soil moisture = 0.08 and stalk moisture = 0.35.

6.2 Eos Synergism Study

MIMICS I is now used to model microwave scatterometer data that were obtained during the August 1987 Eos Simultaneity Experiment (Cimino *et al.*,[9]; Dobson *et al.*,[15]; McDonald *et al.*,[41], [42],[43], [44]). During this experiment, truck-based scatterometers were used to measure radar backscatter from a walnut orchard in Fresno County, California. The modeling of two sets of L- and X-band measurements are discussed. The first set consists of a series of multiangle data for which a set of trees was observed at varying angles of incidence. The second set consists of a series of diurnal measurements in which this same set of trees was observed continuously over several 24 hour periods.

With *in situ* ancillary data describing canopy architecture and moisture conditions used as input, MIMICS is run at L-band and X-band frequencies of 1.5 GHz and 9.6 GHz. Measured scatterometer data are compared to theoretical data generated by MIMICS. MIMICS is seen to predict the diurnal variations that are observed on 24 hour cycles. Examinations of backscatter response to changes in canopy dielectric properties are performed to determine the causes of the changes observed in the short term trends and diurnal patterns. This section presents a brief overview of the modeling analysis. A more complete discussion is provided in Appendix G.

6.2.1 Orchard Canopy Characteristics

As part of the synergism study, an extensive set of ancillary data was collected in order to characterize the walnut orchard. Data describing canopy architecture (Ustin *et al.*,[71],[72]), dielectric properties (Dobson,[10]) and canopy water status (Weber and Ustin, [82],[83]) were analyzed to determine canopy density, branch and leaf orientation and size distribution, constituent dielectric properties, and other gross

canopy characteristics.

To adapt the branch geometry data for input to MIMICS, the orchard is divided into distinct crown and trunk layers with heights of 3.1 m and 1.7 m, respectively. The branches are then divided into the four size classes identified in Table 6.3. Figure 6.6 is a sketch of the geometry of an individual tree, showing the four branch classes and the leaves. The orientation functions are converted into probability distributions for use in MIMICS by dividing each by a normalizing factor given by $\int_0^{\pi} f(\theta)\,\mathrm{d}\theta$.

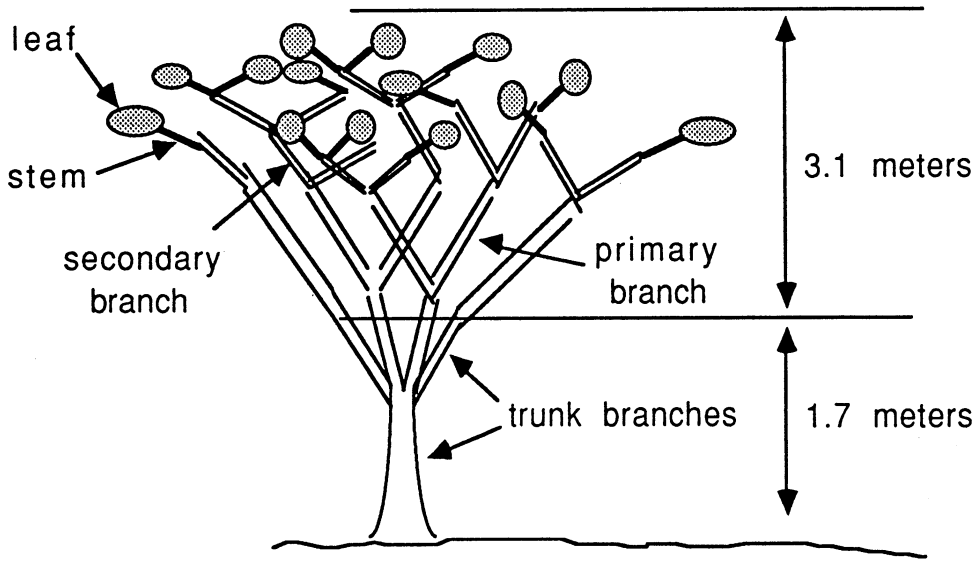

Figure 6.6: Illustration of a walnut tree showing the four branch classes and the leaves.

Characteristics of the leaves were determined from detailed leaf counts (Ustin *et al.*,[72]) and are summarized in Table 6.4. The leaves are modeled as thin circular dielectric disks with a specified diameter and thickness. The leaf number density together with the leaf diameter and crown height yield an equivalent canopy leaf area index (LAI) of 3.4.

Table 6.3: Canopy Branch Classes.

Constituent Class Characteristic	Branch Size Class			
	Trunk Branches	Crown Branches		
		primary	secondary	stems
Max. Diam. (cm)	-	4.0	0.9	0.4
Min. Diam. (cm)	4.0	0.9	0.4	-
Ave. Diam. (cm)	7.3	1.9	0.6	0.1
Ave. Length (cm)	92.8	35.8	10.9	5.0
Density ($\#/m^3$)	0.13	1.25	1.14	250
Orientation $f(\theta)$	$\cos^6\theta$	$\sin^4 2\theta$	$\sin\theta$	$\sin\theta$

Table 6.4: Leaf Characteristics.

Number density	250 leaves per cubic meter
Average diameter	7.47 cm
Average thickness	0.1 mm
Leaf area index	3.4
Orientation	$f(\theta) = \sin\theta$
Folding angle	$\chi = 152°$ along midrib
Radii of curvature	$\rho_1 = 7.7$ cm (along midrib)
	$\rho_2 = 10$ cm

The radii of curvature of the leaves were determined form measurements of the leaf folding angle (Appendix G). The effect of leaf curvature on canopy backscatter was accounted for through the equation (Sarabandi *et al.* [51]):

$$\frac{\sigma_c}{\sigma_f} = \left| \frac{1}{\gamma_1}\mathcal{F}(\gamma_1) \cdot \frac{1}{\gamma_2}\mathcal{F}(\gamma_2) \right|^2 \tag{6.3}$$

where

$$\mathcal{F}(\gamma) = \int_0^{\gamma} \exp\left(iu^2\right) du \tag{6.4}$$

is the finite range Fresnel integral,

$$\gamma_1 = \frac{a}{2}\sqrt{\frac{k_0}{\rho_1}}, \quad \gamma_2 = \frac{a}{2}\sqrt{\frac{k_0}{\rho_2}} \tag{6.5}$$

and k_0 is the free space wavenumber. This effect was approximated in MIMICS by using flat leaves with effective diameters that depend on the frequency under

consideration. Table 6.5 lists the normalized backscatter and corresponding effective diameters for L- and X-bands. At L-band, the effect of leaf curvature is essentially negligible.

Table 6.5: Effects of Leaf Curvature at L- and X-Bands.

	Normalized Backscatter (σ_c/σ_f)		Effective Diameter (cm)
L-Band	0.972	(-0.1 dB)	7.42
X-Band	0.297	(-5.3 dB)	5.52
Flat Leaf	1.000	(0.0 dB)	7.47

A correction factor that accounts for the difference between the actual canopy LAI and the LAI observed with the scatterometer system may be determined by considering the radar measurement volume together with the variation of leaf number density with height (Appendix G). This factor estimates the canopy LAI that is observed by the scatterometer, which is a slowly varying function that has a minimum of 0.35 at $\theta = 40°$, increasing to a maximum of 0.6 at 51°, and then tails off to 0.55 at 55°.

Canopy Dielectric Characteristics

Observations of the relative dielectric constant of soil and vegetation were made *in situ* at 1.2 GHz using a portable dielectric probe. Observations were made of the soil surface and tree trunks. Trunk measurements included both the exterior bark and the interior sapwood. A statistically insignificant amount of dielectric data were recorded for the vegetation in the crown layer. However, the dielectric behavior of these constituents may be inferred from observations of other canopy physiological parameters, and the models applied here to predict the relative dielectric constant do in fact agree with the few recorded observations.

The dielectric properties of the tree boles were seen to vary dramatically with time. Figure 6.7 shows a piecewise fit to the measured dielectric constant. This represents the best estimate of the trunk dielectric behavior at L-band. These data

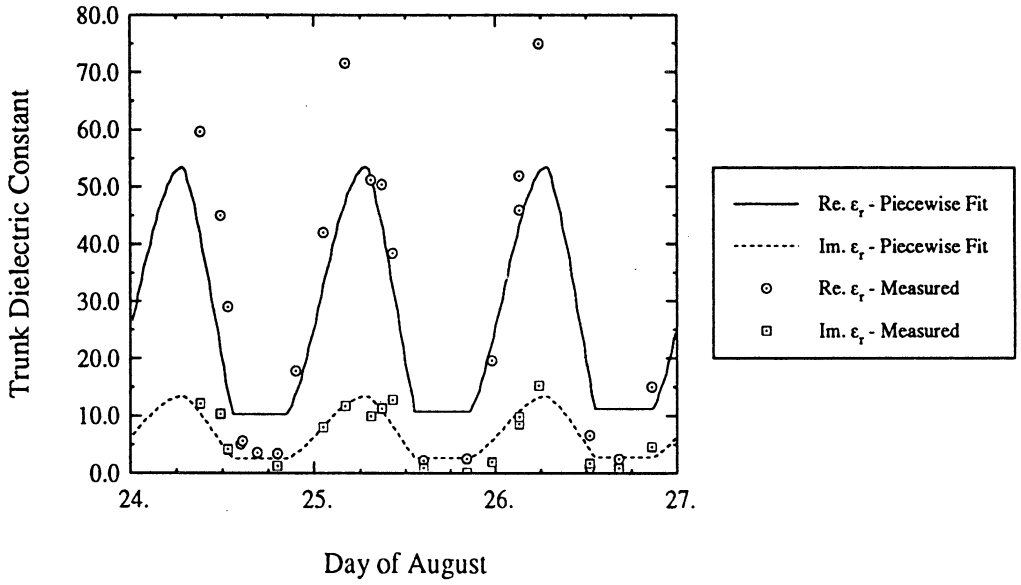

Figure 6.7: Comparison of a periodic piecewise fit to measured L-band trunk dielectric constant data for real and imaginary parts.

were recorded during the three day period that coincides with the time during which diurnal scatterometer data were recorded. The numbers on the time axis correspond to midnight on that day of August.

Figure 6.8 illustrates the best estimate of the soil dielectric behavior. During these three days, the orchard was irrigated 2.5 hours per day beginning at 6:00 each evening. The irrigation periods are manifest by the jumps in the dielectric constant that begin at 6 p.m. each day. The dielectric continues to increase until the irrigation shuts off. Then, ϵ_r decreases as the soil dries. The loss tangent of the soil dielectric was assigned a value of 0.1 at L-band, as was determined from the measured data.

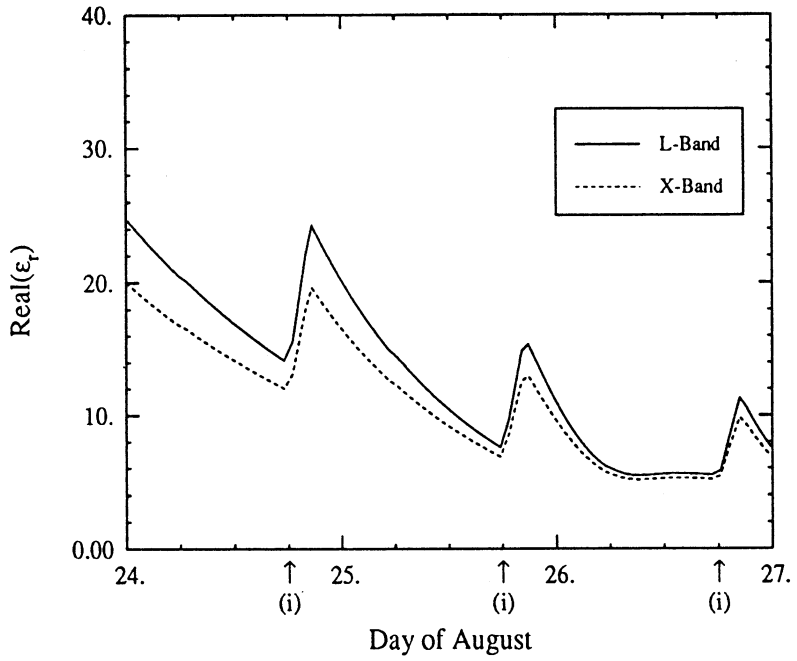

Figure 6.8: Behavior of the soil dielectric constant showing the estimated behavior of the L- and X-band dielectric constant. The symbol (i) indicates the beginning of a 2.5 hour irrigation period.

To determine the X-band soil dielectric, the dielectric model presented in Appendix A was inverted using the L-band data, thereby obtaining values for effective soil volumetric moisture. The dielectric model was then applied at 9.6 GHz to estimate the X-band dielectric.

Leaf gravimetric moisture content mg_l was used to determine the leaf dielectric constant. Analysis of wet and dry leaf weights indicate that the average leaf gravimetric moisture was approximately 0.7. Applying the vegetation dielectric model presented in Appendix A, the relative dielectric constant of leaves were found to be $28.3 + i8.5$ and $21.8 + i8.8$ at L- and X-bands, respectively. This value was also assigned to the dielectric of the higher order stems. No discernible variation of leaf gravimetric moisture with time was observed.

Canopy water status was analyzed to estimate the behavior of the branch dielectric constants. A periodic piecewise fit to the measured leaf water potential was scaled to obtain the branch dielectric behavior shown in Figure 6.9(a). This figure shows the real part of the piecewise fit to the L-band dielectric constant for the three classes of woody vegetation. All measured values of the branch dielectric that were recorded during this time are also shown. The X-band dielectrics were obtained through application of the vegetation dielectric model. This model was numerically inverted at L-band (1.2 GHz) using the dielectric functions shown in Figure 6.9(a), yielding effective values of branch moisture as a function of time. Given the effective moisture, the model was then applied at 9.6 GHz to obtain the real and imaginary parts of the X-band dielectrics. Figure 6.9(b) illustrates the real part of ϵ_r at X-band.

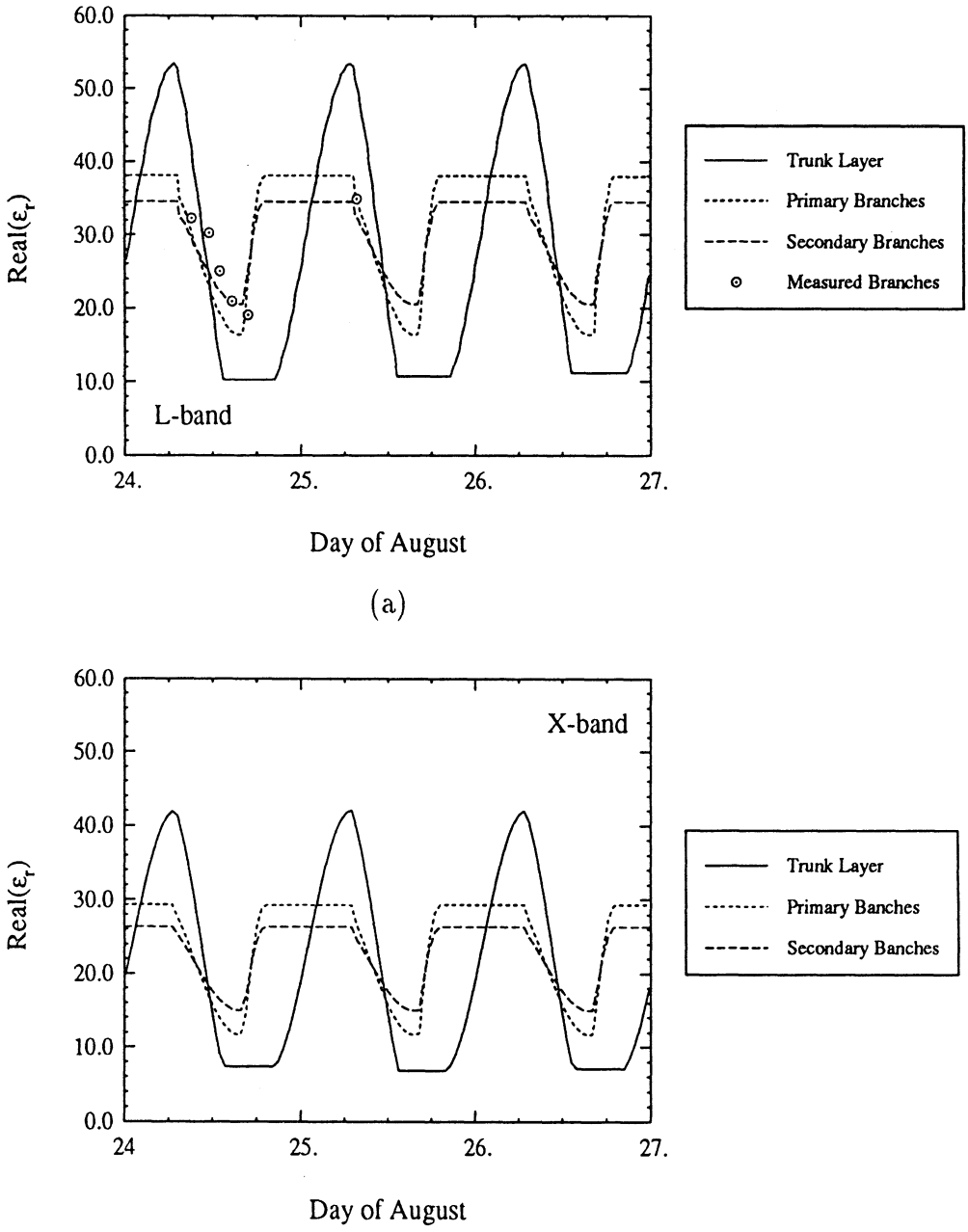

Figure 6.9: Dielectric constants of woody constituents for (a) L-band and (b) X-band.

6.2.2 Modeling Analysis

As a first step in the modeling analysis, MIMICS was run as a function of radar look angle at L- and X-bands. Table 6.6 lists the canopy dielectric parameters used in this analysis. These values correspond to measurements made at the approximate time that the multi-angle scatterometer data were recorded. Figure 6.10 shows a

Table 6.6: Canopy Dielectric Characteristics.

Constituent	L-Band	X-Band
Ground Surface	$25 + i2.5$	$20.2 + i7.6$
Trunk Branches	$45 + i11.2$	$35.0 + i14.8$
Primary Branches	$34 + i8.5$	$25.9 + i10.8$
Secondary Branches	$30 + i7.5$	$22.7 + i9.4$
Leaves and Stems	$28.3 + i8.5$	$21.8 + i8.8$

comparison of L- and X-band modeled and measured data over the range $40° \leq \theta \leq 55°$ for like- and cross-polarized backscatter. Figure 6.10(a) compares the predicted L-band backscatter with the scatterometer data. This figure demonstrates very good agreement between MIMICS-generated data and the measured values. The like-polarized backscatter exhibit similar amplitudes with HH being slightly higher than VV in both the measured and modeled data while the cross-polarized backscatter is about 5 dB lower than the like-polarized response.

The failure of the model to predict the cross-polarized backscatter at 40° is attributed to the inhomogeneous characteristics of the orchard canopy architecture. Whereas MIMICS I has been derived for a canopy that has a continuous crown layer, it is being used to model backscatter from a canopy with a crown layer that is discontinuous. As incidence angle becomes smaller, a larger proportion of the canopy area observed by the scatterometer consists of smooth, bare soil that is not covered by the orchard canopy. Since the model predicts backscatter for a canopy

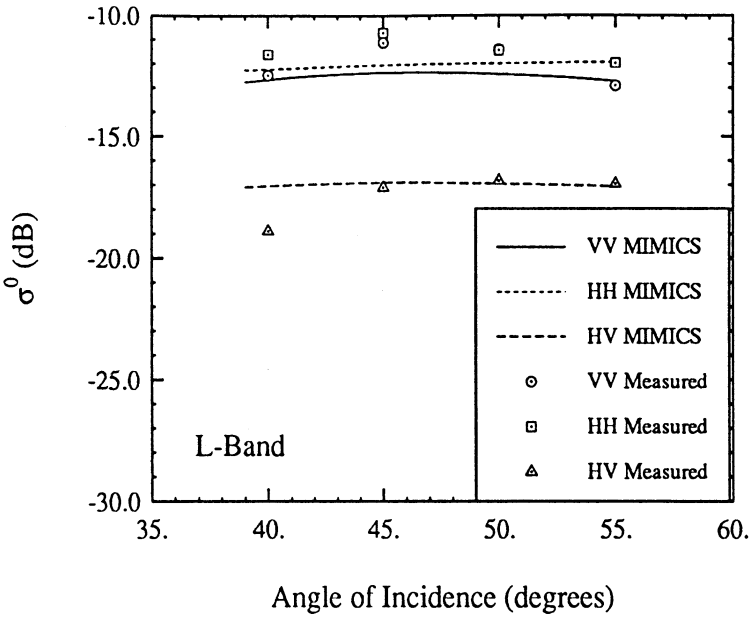

(a)

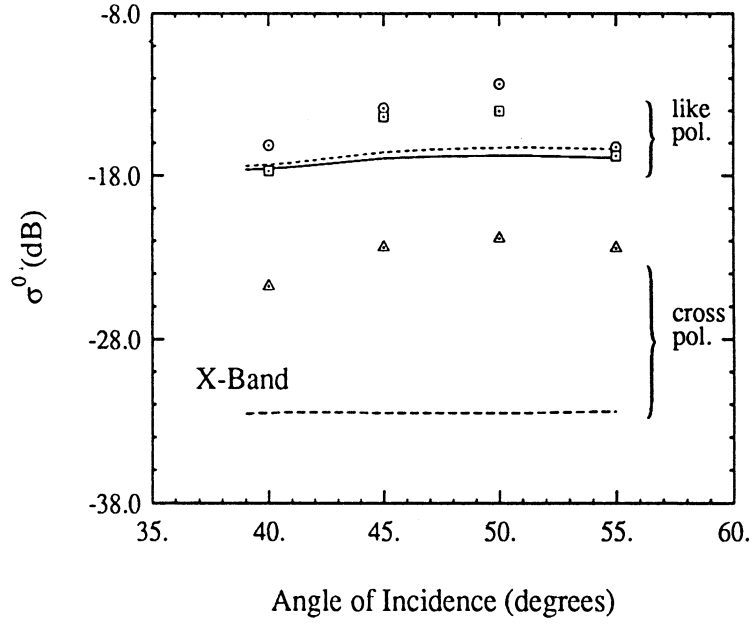

(b)

Figure 6.10: Comparison of MIMICS results with measured L- and X-band multi-angle data. (a) compares L-band modeled total canopy backscatter to the scatterometer measurements for like- and cross-polarized configurations (HH, VV, HV). (b) compares X-band modeled direct crown backscatter to the scatterometer measurements for these same polarizations.

that has a homogeneous crown layer, some error will be introduced in the modeled data. We expect that the model will be more successful in predicting backscatter from this orchard at higher angles of incidence since the scatterometer observes almost no bare soil at these angles. We also expect this effect to be more pronounced for cross-polarized configurations since a smooth soil surface generates very little cross-polarized backscatter compared to that generated by the crown layer.

As was found in more detailed analyses (Appendix G), the measured X-band backscatter consists primarily of the direct crown contribution to the total canopy backscatter. Figure 6.10(b) compares the predicted direct crown X-band backscatter with the scatterometer data. Here, MIMICS agrees with the level of the like-polarized backscatter but underestimates the cross-polarized response by as much as 10 dB. The failure of MIMICS to more accurately reproduce the angular dependence of the like-polarized backscatter at 45° and 50° may also be attributed to the inhomogeneous nature of the orchard canopy. The effective canopy geometry sampled by the scatterometer measurement volume changes with θ. As radar incidence angle changes, the canopy backscatter responds to these changes in the sampled canopy volume. The angular dependence of backscatter at X-band has been partially accounted for by applying the LAI correction factor in generating the multi-angle MIMICS data. However, crown layer discontinuities also affect the character of backscatter from the stems and branches. This effect is more prevalent at X-band in part because of the relatively narrow X-band beamwidth and also because the crown layer constituents that contribute most to this effect (leaves and smaller branches) contribute more to X-band scatter than to L-band.

As previously noted, the X-band cross-polarized backscatter is significantly underestimated by MIMICS. In general, the effect of higher-order multiple scattering on

radar backscatter becomes more important as frequency increases. Ulaby *et al.* [65] have shown that, at millimeter wave frequencies, a numerical solution to the radiative transfer equations in which higher-order scattering is accounted for may add more than 10 dB to the predicted first-order cross-polarized backscatter while having little effect on the like-polarized backscatter. Since the numerical solution for radiative transfer requires specifying the scattering phase matrix in all incident and scattering directions, determination of the higher-order scattering contribution becomes very computationally intensive. The phase matrix of the walnut orchard crown layer has a very complicated form and determination of the numerical solution is computationally prohibitive. Although an expression for the second-order scattering in the crown layer may be derived (Appendix E), analysis of these higher-order effects is beyond the scope of this study. While Ulaby *et al.* [65] derived their results at millimeter wave frequencies for which the scattering albedo for vegetation $\omega \simeq 0.6-0.9$, it is understood that ω usually increases with increasing frequency. In light of the study by Ulaby *et al.*,[65], it is expected that, as frequency increases, higher-order scattering would first be manifest in terms of its effect on the cross-polarized backscatter.

Having established that MIMICS successfully predicts canopy backscatter as a function of angle, the model is now run at a constant incidence angle, $\theta = 55°$, while varying the canopy dielectric parameters so as to simulate the variations seen over the three-day diurnal experiment (Figures 6.8 and 6.9). Figure 6.11 presents the resulting computed backscatter along with the measured values of canopy backscatter for the like- and cross-polarizations. At L-band, MIMICS successfully predicts the appropriate level of the measured data together with the decreasing trend in backscatter observed over the three day period for all three polarization configurations. Furthermore, MIMICS predicts the 1 to 2 dB dip seen in σ^0_{VV} and σ^0_{HV} in the

early afternoon of each day.

The X-band MIMICS data presented here represent the direct crown component of total canopy backscatter and have been produced for a canopy with an effective leaf area index of 1.0 in order to account for the variations in effective canopy geometry as a function of incidence angle. An offset of 8 dB has been added to the cross-polarized MIMICS data to approximate the effects of higher-order scattering. Although the measured X-band data exhibit significantly more scatter than does the L-band data, the early afternoon dip in backscatter is present for all three polarizations and is predicted by MIMICS.

The variation in the measured data that is associated with the scatterometer measurement process comes primarily from two sources. The first of these is fading that arises from the coherent nature of the scatterometer. Following the analysis in Ulaby et al. [70], pp.483–486., the uncertainty due to fading is about ± 0.2 dB. The other source of variation arises from statistical sampling of the inhomogeneous orchard canopy. This is caused in large part by the partially discontinuous properties of the crown layer. Because of the azimuth scanning technique used to account for the effects of fading, each measured data point represents an average of 30 samples recorded over a single azimuth sweep. The locations sampled within the canopy by each of these 30 samples do not correspond precisely to those observed during other azimuth sweeps. Therefore, some variation will exist simply because the values of σ^0 do not represent measurements of precisely the same canopy volume. In addition, factors such as wind speed contribute to a time-varying canopy geometry. This effect is readily observed in the measured diurnal data, especially at X-band. Modeling results shown here demonstrate extraordinarily good agreement between measured and predicted backscatter, especially when this measurement variability is taken into

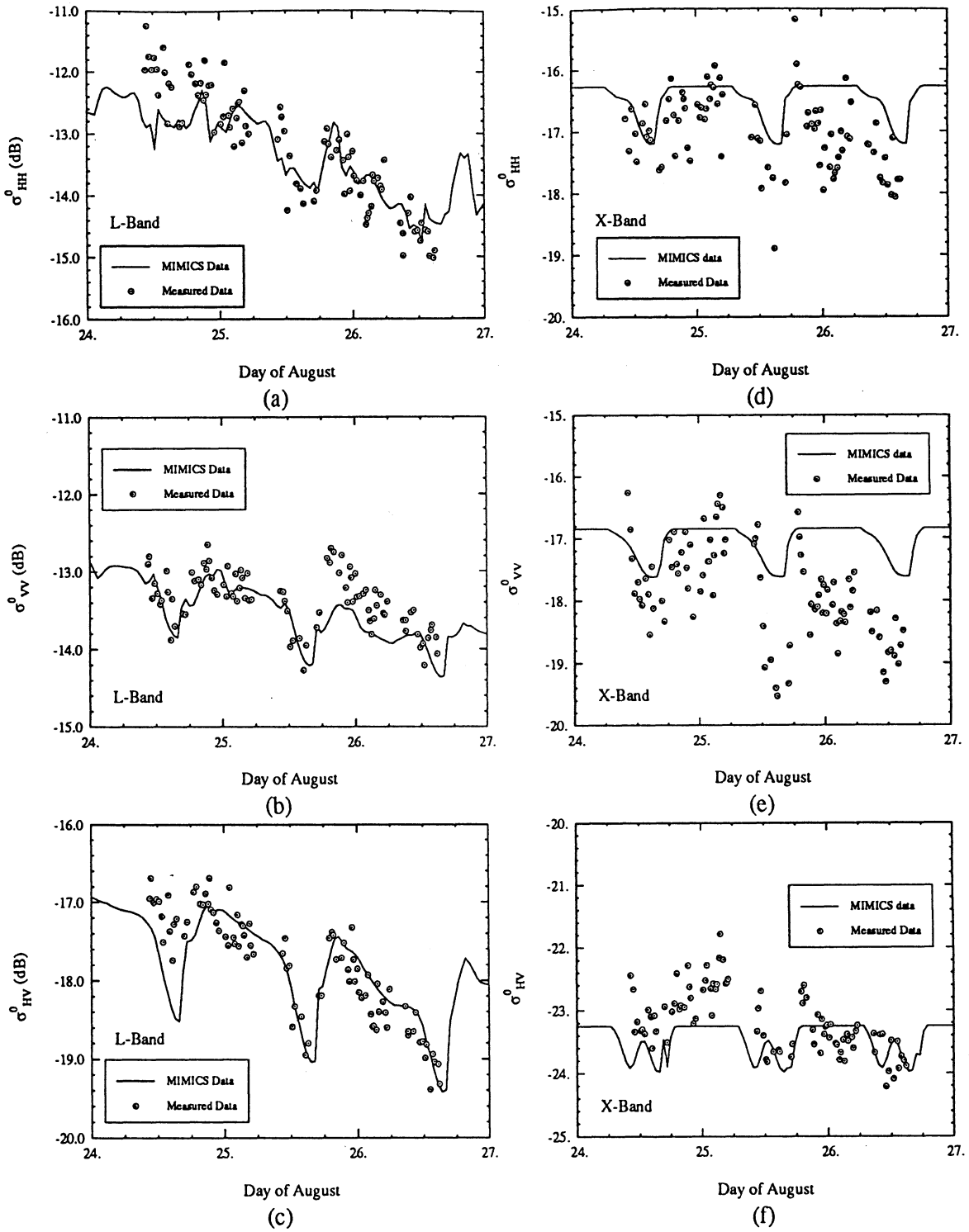

Figure 6.11: Comparison of MIMICS results with measured backscatter recorded during the three day diurnal experiment for (a) HH polarized L-band backscatter, (b) VV polarized L-band backscatter, (c) HV polarized L-band backscatter, (d) HH polarized X-band backscatter, (e) VV polarized X-band backscatter and (f) HV polarized X-band backscatter. The X-band HV MIMICS data has been offset 8 dB to account for multiple scatter.

account.

Figure 6.12 shows the MIMICS-predicted backscatter to changes in canopy biomass for the walnut orchard response for VV and VH polarizations. These data were generated by varying canopy height and generating σ^0 at each height. The models for canopy biophysical parameters presented in Appendix F were applied to compute the dry canopy biomass. Data are shown for P-band (0.5 GHz), L-band (1.5 GHz), C-band (5 GHz), and X-band (9.6 GHz). For low values of biomass, the backscatter at both like- and cross-polarizations is dominated by the direct-ground component of canopy backscatter whereas at high values the canopy itself dominates σ^0. Therefore, the σ^0 value observed at low values of biomass is determined solely from the estimate of direct ground backscatter for both polarizations. In order to achieve a reasonable estimate of both the like- and cross-polarized direct ground backscatter, measured values from Ulaby and Dobson [61] were used to simulate the direct ground backscatter. This approach was necessary because the first-order ground backscatter model implemented in MIMICS does not account for any cross-polarized return. It should also be noted that at high biomass values the X-band cross-polarized response is several dB lower than anticipated because MIMICS does not account for multiple scattering in the crown layer. This analysis demonstrates that the lower radar frequencies (P- and L-bands) are more sensitive to changes in total canopy biomass than are the higher frequencies (C- and X-bands).

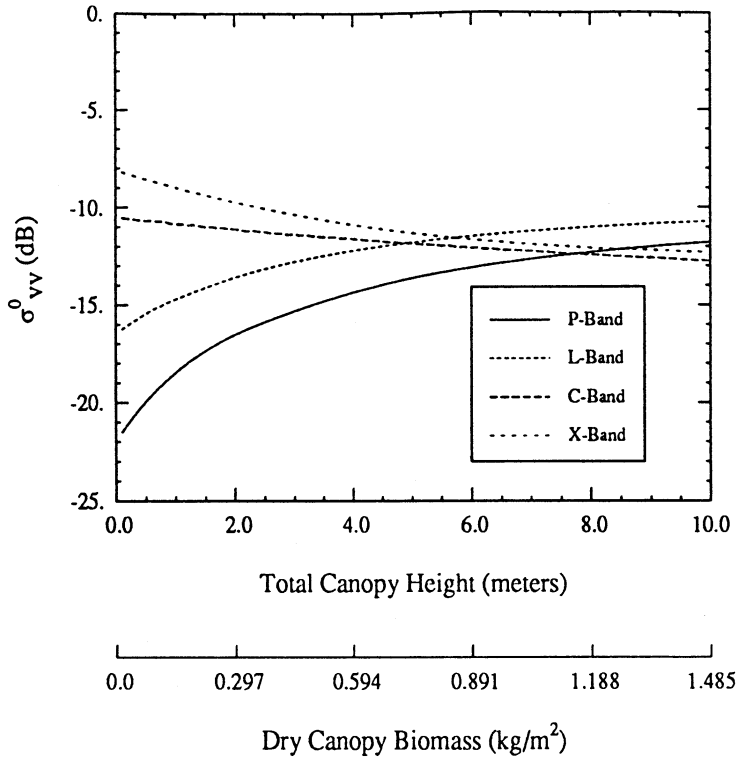

(a) VV-polarized response.

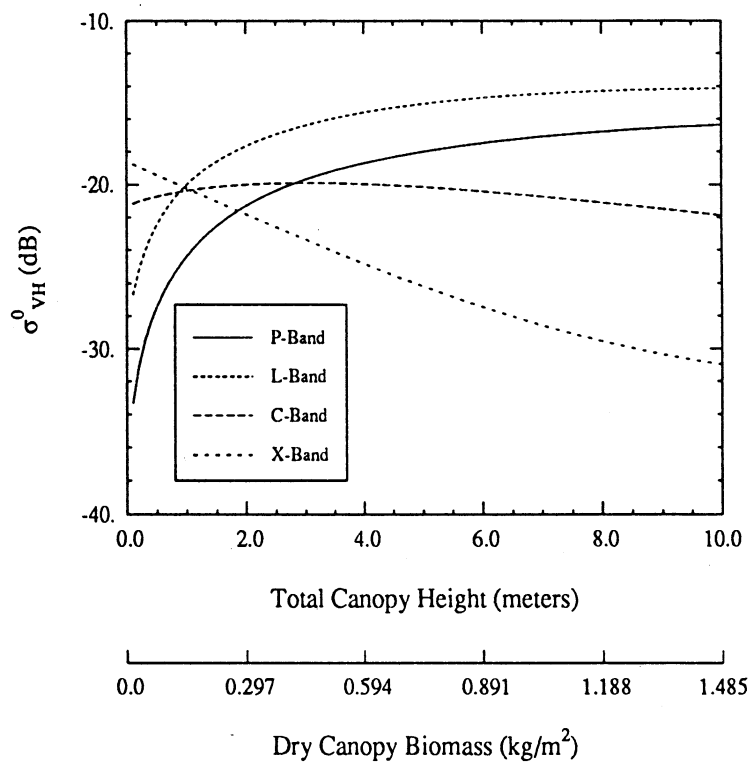

(b) VH-polarized response.

Figure 6.12: Walnut orchard backscatter response to changes in canopy biomass for (a) VV-polarization, (b) VH-polarization. The incidence angle $\theta = 30°$.

6.3 ERS-1 Alaskan Boreal Forest Study

In March 1988, a series of airborne SAR data was acquired over the Bonanza Creek Experimental Forest near Fairbanks, Alaska (Way *et al.,* [77], [76]; Dobson *et al.,* [13], [14]). This study was the first in a series of multi-season aircraft experiments flown over selected forest sites for the purpose of understanding the kinds of biophysical properties that may be detected with spaceborne SAR systems such as the C-band SAR to be flown aboard the European Space Agency's Earth Resources Satellite (ERS-1). The purpose of this experiment was to determine if changes in plant fluid status associated with thawing and freezing result in changes in radar backscatter which could be detected by SAR and to determine if theoretical backscatter models such as MIMICS could predict these changes.

This section provides a brief overview of the MIMICS modeling effort that accompanied this study. A more detailed analysis is provided in Appendix H. This analysis focuses on L- C, and X-band data obtained on March 13, March 19 and March 22, 1988. These dates were selected to encompass the range of environmental conditions that occurred over the duration of the experiment. An unseasonably warm period during which thawed conditions prevailed in the forest extended through the evening of March 13. This was followed by more normal subfreezing temperatures for the remainder of the experiment. As liquid water was frozen by the subfreezing temperatures, the dielectric properties of both the vegetation and of the 20-30 cm snow layer that covered the ground were modified, thereby changing the scattering and absorption properties of these constituents.

6.3.1 Test Site Description and Canopy Properties

Ground Surface Characteristics

The ground surface was covered with a snow layer 20-30 cm deep. Below the snow layer, the upper 20 cm of the mineral soil was frozen throughout the entire experiment. The early March thaw caused the snow layer to have a complex wetness structure that varied with stand species (Dobson *et al.*, [13]). Snow wetness varied considerably with spatial location, depth, and time. A Debye-like model presented by Hallikainen *et al.*, [24] was applied to estimate the dielectric properties of the snow. This model, which is reviewed in Appendix A, relates the snow dielectric to snow wetness (volume %), frequency and dry snow density. The modeled values of snow dielectric constant are listed in Table 6.7 at L-, C- and X-bands for frozen and thawed conditions.

Table 6.7: Modeled Dielectric Characteristics of Snow for Frozen and Thawed Conditions.

Frequency	Thawed Conditions (March 13)	Frozen Conditions (March 19-22)
L-Band	$1.58 + i0.024$	$1.37 + i0.0$
C-Band	$1.54 + i0.079$	$1.37 + i0.0$
X-Band	$1.49 + i0.09$	$1.37 + i0.0$

The dielectric of the frozen mineral soil was measured using portable dielectric probes in a trench cut into the permafrost. The average L-band dielectric constant of the soil was found to be $7.96 + i0.96$.

Stand Geometry

Ground surveys of seven stands were conducted to determine the number of trees per unit area by species and also record their respective diameters at breast height

(DBH) (Jaeger, [30]). To estimate above ground biomass for each stand, these data were coupled with allometric equations. The measured DBH, heights, and status of each tree were used to estimate the quantities listed in Table 6.8 on the basis of allometric expressions drawn from the literature for each species (Kirby,[33]; Manning *et al.*,[40]; Singh,[52]; Yarie and Van Cleve,[84]).

Table 6.8: Summary of Stand Biophysical Parameters.

Species	White Spruce				Black Spruce	Balsam Poplar
Stand Name	WS-1	WS-2	WS-5	WS-7	BS-1	BP-2
Density						
Mean (trunks/hectare)	1248	2073	1484	1123	1975	1615
Standard Deviation	342	576	618	654	1483	407
Basal Area						
Mean (m^2/hectare)	46	41	44	46	12	50
Standard Deviation	16.6	7.0	8.5	12.4	3.3	25.8
Basal Volume						
Mean (m^3/hectare)	442	332	392	442	51	344
Standard Deviation	169	60	100	115	12	190
Dry Biomass - Summer						
Mean (kg/m^2)	21.7	16.7	18.1	21.5	3.7	18.2
Standard Deviation	8.8	3.6	4.8	6.1	0.8	10.9
Dry Biomass - Winter						
Mean (kg/m^2)	21.7	16.7	18.1	21.5	3.7	17.9
Standard Deviation	8.8	3.6	4.8	6.1	0.8	10.7

In addition, trihedral corner reflectors were placed in several stands to estimate canopy transmissivity (Kasischke *et al.*,[32]). These stands were also characterized with respect to density, height and diameter (Jaeger,[30]). These stands included a single species of alder and mixed species stands of alder, balsam poplar and white spruce. Table 6.9 summarizes mean DBH, height and basal area for all stands.

To characterize the trunk layer geometry in terms of parameters required for MIMICS input, DBH histograms were generated from the ancillary ground measurements and coupled with the allometric height equations listed in Table 6.10.

Table 6.9: Summary of Mean DBH, Height and Basal Area for All Stands.

Stand Name	DBH (cm)	Height (m)	Basal Area (m^2/hectare)
WS-1	19.6	22.1	46
WS-2	14.5	20.1	41
WS-5	17.9	21.3	44
WS-7	21.4	24.5	46
BS-1	8.8	7.6	12
BP-2	18.0	17.6	50

Stands with trihedral reflectors:				
Stand Name	Species	DBH (cm)	Height (m)	Basal Area (m^2/hectare)
Alder	alder	6.0	6.3	66.5
Balsam Poplar	balsam poplar	11.0	12.7	22.9
	alder	6.0	6.3	3.1
White Spruce	white spruce	7.8	8.6	12.4
	balsam poplar	9.4	11.6	10.0
	alder	6.1	6.3	5.4

Table 6.10: Equations Defining Height-to-DBH Relationship.

Species	Equation
White Spruce	$H = -1.7096 + 1.4224(\text{DBH}) - 0.016(\text{DBH})^2$
Black Spruce	$H = 0.9494 + 0.7657(\text{DBH})$
Balsam Poplar	$H = 1.0526 + 1.143(\text{DBH}) - 0.0145(\text{DBH})^2$
Alder	$H = 2.871 + 0.5666(\text{DBH})$

H = height in meters

DBH = diameter in cm measured at breast height

Together, these data define the PDF in size required to compute the trunk layer phase matrix for a given stand. All trunks are assumed to have a vertical orientation for purposes of MIMICS simulations.

The size and orientations of crown layer constituents have been inferred through a combination of field observations and morphology data from Nelson *et al.*,[45]. Table 6.11 summarizes the geometry of the crown layer constituents. Each of the

Table 6.11: Geometry of Crown Layer Constituents.

Species	Constituent Class	Average Length (cm)	Average Diameter (cm)	Orientation Function
White Spruce	primary branches	113	2.24	$\sin^4\theta$
	secondary branches	57.16	1.04	$\sin^9\theta$
	needles	1.6	0.1	$\sin\theta$
Black Spruce	primary branches	81.3	2.37	$\sin^9(\theta - 30°)$
	secondary branches	51.17	1.06	$\sin^9\theta$
	needles	0.8	0.1	$\sin\theta$
Balsam Poplar	primary branches	200	1.5	$\sin^9(\theta + 60°)$
	secondary branches	100	0.75	$\sin^9(\theta + 60°)$
Alder	primary branches	200	1.5	$\sin^9(\theta + 60°)$
	secondary branches	100	0.75	$\sin^9(\theta + 60°)$

orientation functions is normalized to convert it to a PDF for implementation in MIMICS.

Table 6.12 lists the number density of each canopy constituent for each of the seven stands, assuming that each stand may be modeled as a continuous (closed) canopy. The biomass of a single element is computed from the size and dry density parameters of that element as presented in Appendix F.

Table 6.12: Number Density of Canopy Constituents.

Stand Name	Canopy Density (trees/m^2)	Primary Branches (#/m^3)	Secondary Branches (#/m^3)	Needles (#/m^3)
Alder	1.36	1.19	9.92	NA
BP-2	0.16	0.85	6.69	NA
WS-1	0.12	0.44	2.37	12,300
WS-2	0.12	0.48	2.57	13,310
WS-5	0.12	0.50	2.7	14,000
WS-7	0.12	0.48	2.6	13,490
BS-1	0.20	0.25	1.31	18,340

Stand Dielectric Characteristics

The dielectric properties of the trees vary as a function of frequency and canopy properties such as constituent dry density and freeze/thaw state. The dielectric properties of the stands were monitored with L- and C-band portable dielectric probes. The dielectrics listed in Table 6.13 were inferred by coupling dielectric measurements to the dielectric models (Dobson *et al.*, [13]).

Table 6.13: Relative Dielectric Constant for Tree Constituents.

Species	Frequency (GHz)	Relative Dielectric +5°C	Relative Dielectric −15°C
White Spruce	1.25	$36.47 + i10.99$	$5.19 + i1.09$
	5.3	$29.01 + i11.97$	$4.85 + i0.32$
	9.38	$22.78 + i13.20$	$4.81 + i0.18$
Black Spruce	1.25	$12.46 + i4.50$	$3.72 + i0.78$
	5.3	$9.30 + i3.33$	$3.47 + i0.23$
	9.38	$7.82 + i3.22$	$3.44 + i0.13$
Balsam Poplar and Alder	1.25	$30.71 + i9.56$	$4.95 + i1.07$
	5.3	$24.18 + i9.85$	$4.61 + i0.32$
	9.38	$19.16 + i10.69$	$4.57 + i0.17$

6.3.2 Boreal Forest Transmissivity Analysis

Data collected at C- and X-bands on March 22 have been applied to analyze canopy transmissivity (Dobson *et al.*, [13],[14]). To compute the one-way canopy propagation loss, the point target responses of trihedrals that were placed in the forest stands were compared to the response of trihedrals placed in an open area. Stands selected for this analysis included a single-species alder canopy, a balsam poplar stand that contained shorter alder trees, and a white spruce stand that also contained a mixture of balsam poplars and alders. Stand statistics measured in the neighborhood of the targets showed significant local variance in stand geometry, both locally within the neighborhood of individual targets and in comparing different target locations within the same stand. Not only does that within-stand variability affect the estimation of canopy extinction, but also there is an inherent bias toward values of low extinction due to the logistics of placing physically large reflectors in a canopy of large discrete scatterers. The measured extinction values represent realizations over only the few azimuth degrees required to construct the synthetic aperture. It would be best to have a set of infinitesimally small point targets that one could place at a statistically large number of random locations within a given stand.

Each set of stand statistics was used as input to MIMICS, applying the dielectric constants for frozen vegetation constituents (Table 6.13) and the trunk height *versus* DBH equations (Table 6.10). For the mixed-species stands, MIMICS was run separately for each constituent species and the resultant propagation losses were added together to estimate the total net loss. Since only gross estimates of crown biomass were available, and in order to expedite the transmissivity analysis, only extinction through the trunk layer was considered.

Figures 6.13 – 6.15 show MIMICS simulations of the maximum and minimum one-way propagation loss for each of the three stands together with the measured values as determined for each trihedral reflector. The maximum and minimum MIMICS simulations correspond to the maximum and minimum biomass conditions for each of the three stands. Figure 6.13 shows these data for the alder stand, Figure 6.14 shows data for the balsam poplar stand and Figure 6.15 presents the white spruce stand simulation. In all cases, the V-polarized extinction is greater than that at H-polarization with the difference being less than 1.5 dB.

Figure 6.16 is a plot of the MIMICS-simulated one-way propagation loss *versus* the measured loss at C-band. Data are shown for all three stands at both polarizations. Each set of stand data were fit with a straight line to help illustrate the combined effects of measurement and model error. Good correlations exist between measured data and model simulations for all three stands, with the correlation coefficient $\rho \geq 0.75$, however MIMICS never predicts 0 dB of loss which may be measured at low values of incidence angle because of placement of the reflectors in canopy gaps. This indicates that more reflectors should be used in this type of study and more careful attention should be paid to random placement of the targets in the canopy. Furthermore, this figure illustrates an underprediction of canopy extinction by MIMICS in the white spruce stand. This illustrates the importance of including the crown layer constituents in canopy transmissivity analyses, especially for foliated species.

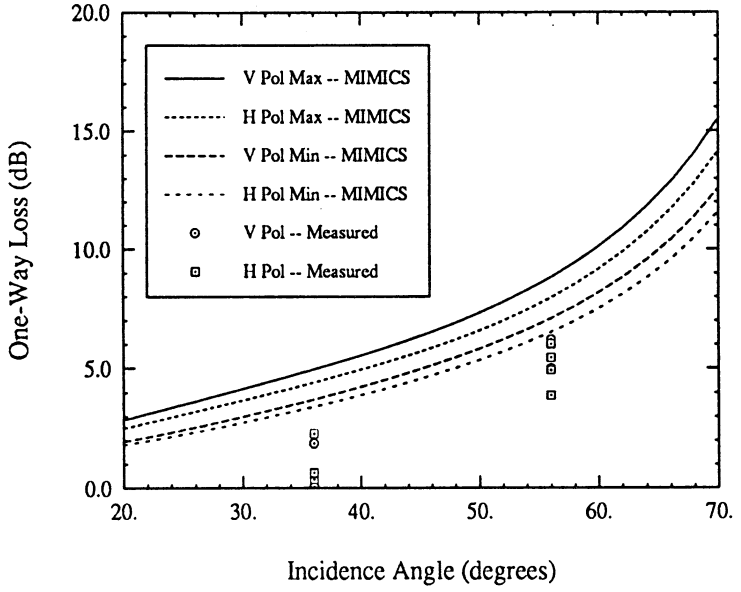

(a) C-band.

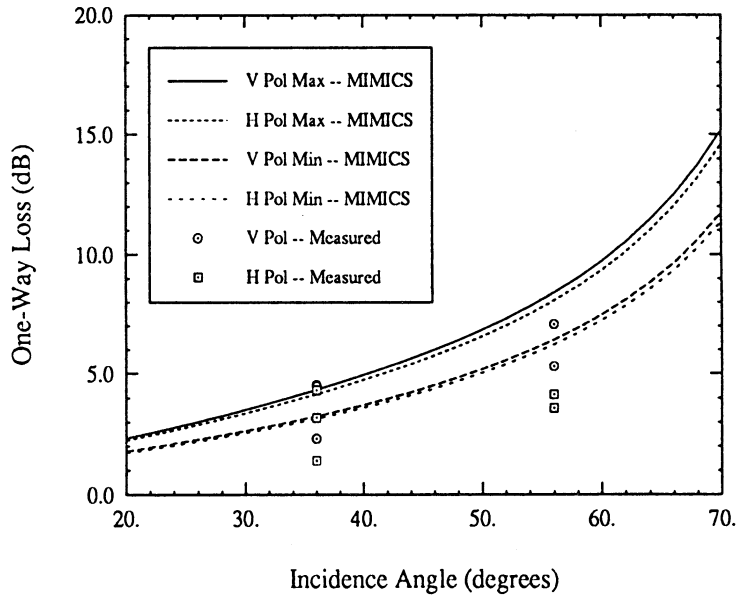

(b) X-band.

Figure 6.13: Transmission loss for one-way propagation through the alder canopy. Measurements are shown for four trihedral targets at (a) C-band and (b) X-band.

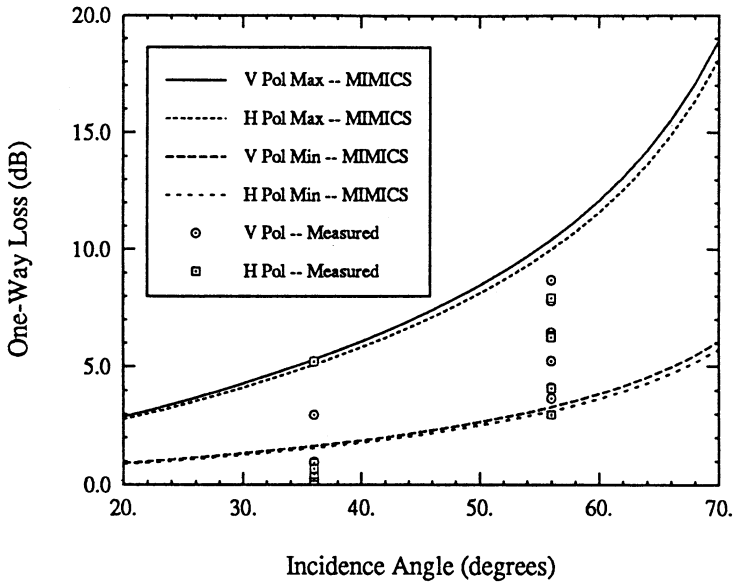

(a) C-band.

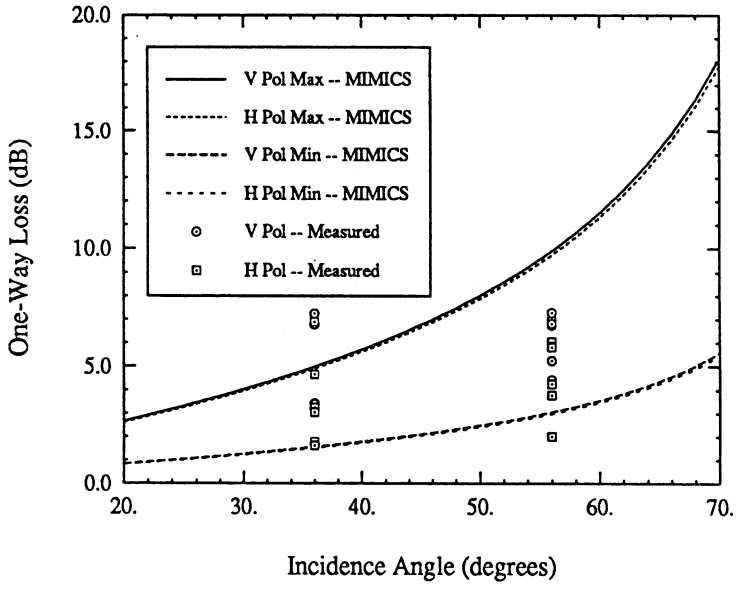

(b) X-band.

Figure 6.14: Transmission loss for one-way propagation through the mixed balsam poplar/alder canopy. Measurements are shown for seven trihedral targets at (a) C-band and (b) X-band.

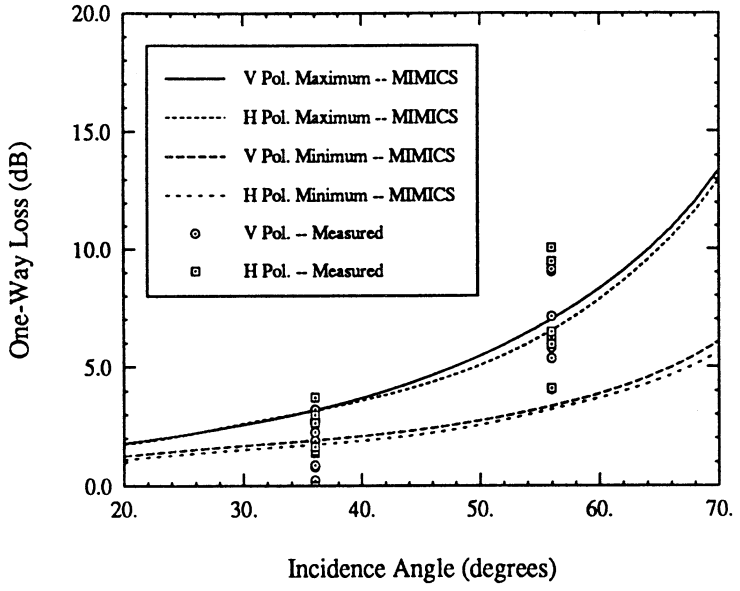

(a) C-band.

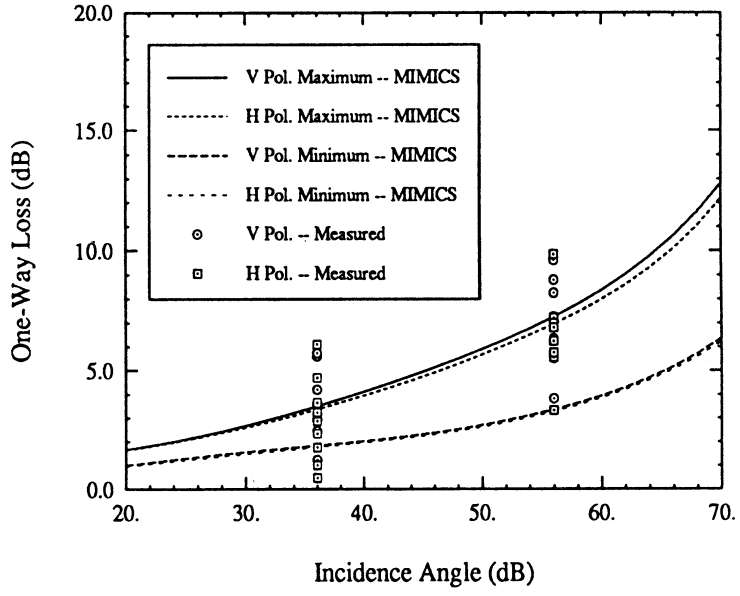

(b) X-band.

Figure 6.15: Transmission loss for one-way propagation through the mixed white spruce/balsam poplar/alder canopy. Measurements are shown for nine trihedral targets at (a) C-band and (b) X-band.

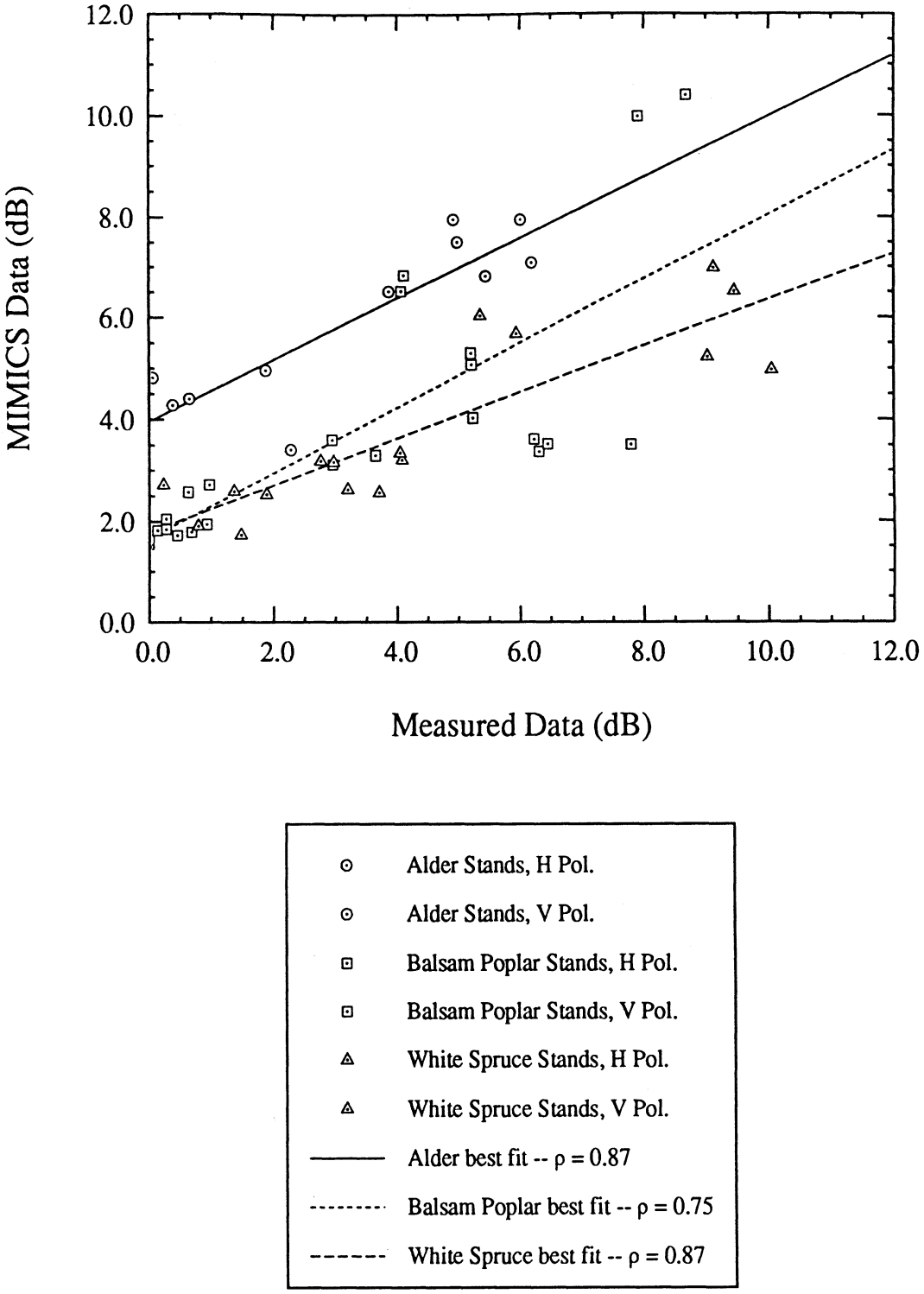

Figure 6.16: Comparison of MIMICS simulated and measured transmission loss for one-way propagation through the alder, balsam poplar and white spruce canopies at C-band. The best-fit straight lines are shown for each canopy, together with their respective correlation coefficients ρ.

6.3.3 Boreal Forest Backscatter Analysis

Data recorded at L-, C- and X-bands have been applied to analyze backscatter from several single-species stands (Dobson *et al.*, [13],[14]). Of these, only the L-band data has been calibrated to an absolute level. These data were collected on March 13 (frozen canopy conditions) and on March 19 (thawed canopy conditions) (Way *et al.*,[77]). Since the stands considered in this study were only partially characterized by on-site sampling, information on biomass apportionment and canopy constituent size and density characteristics is only approximate. Errors introduced in the biomass apportionment analysis will have an effect on the backscatter simulated by MIMICS.

The 20-30cm thick snow layer also significantly complicated the backscatter analysis. The roughness parameters and other characteristics of the snow-ground interface were not characterized. These parameters could only be estimated by fitting MIMICS to ground backscatter measurements of open areas on sandbars that were outside the tree canopies. Since the roughness of these regions do not correspond to the roughness of a forest floor, and since the goal of this study is to examine model performance without using parameter fitting, the snow substrate was modeled as a half-space of snow. This ignores scattering at the snow-ground interface completely and in some cases reduces the effectiveness of the MIMICS simulations. A simple technique that accounts for the snow-ground interface at L-band was introduced in Section 3.2.2. However, because of lack of adequate characterization of the ground surface, its effectiveness is also somewhat limited.

Comparison with Measured Data

Table 6.14 lists the MIMICS backscatter simulations together with the SAR observations for six stands. Measured data were recorded by the JPL SAR at L-band for

both frozen and thawed conditions. This table shows very good agreement for both frozen and thawed canopy states except for VV and VH polarizations for the stands BS-1, BP-2 and Alder under frozen conditions. Figure 6.17 graphically illustrates the

Table 6.14: Comparison of MIMICS Estimates to Measured L-band SAR Data (dB).

		March 13, 1988 Thawed Conditions		March 19, 1988 Frozen Conditions	
Stand	Polarization	SAR	MIMICS	SAR	MIMICS
WS-1	HH	-10.0	-9.2	-13.1	-12.2
	VV	-10.4	-12.1	-14.9	-15.6
	VH	-15.2	-14.9	-21.0	-22.8
WS-2	HH	-8.4	-9.1	-11.4	-12.8
	VV	-9.9	-12.3	-14.5	-16.4
	VH	-14.2	-15.0	-20.4	-23.6
WS-5	HH	-8.1	-9.1	-11.1	-12.2
	VV	-9.1	-12.0	-14.8	-15.5
BS-1	HH	-12.9	-10.7	-14.9	-16.9
	VV	-14.4	-15.1	-16.4	-23.2
	VH	-20.0	-19.5	-23.7	-32.5
BP-2	HH	-9.2	-11.7	-12.7	-14.4
	VV	-10.4	-11.6	-14.8	-22.0
Alder	HH	-8.7	-9.9	-11.3	-14.6
	VV	-9.7	-11.4	-14.0	-23.2

effectiveness of MIMICS in predicting the HH- and VV-polarized backscatter. The measured SAR data are plotted against that predicted by MIMICS. Data are shown for all six stands for both frozen and thawed conditions. From here it is seen that MIMICS tends to underpredict backscatter for all stands except for white spruce. The underprediction of VV backscatter for frozen conditions for all stands except white spruce is also evident. The general underestimation of σ^0 may be attributed to the modeling of the snow surface as an infinite half-space. It is expected that accounting for scatter at the snow-ground interface would increase σ^0 somewhat and may alleviate this problem.

Figures 6.18 and 6.19 present L-band polarization responses for frozen and thawed

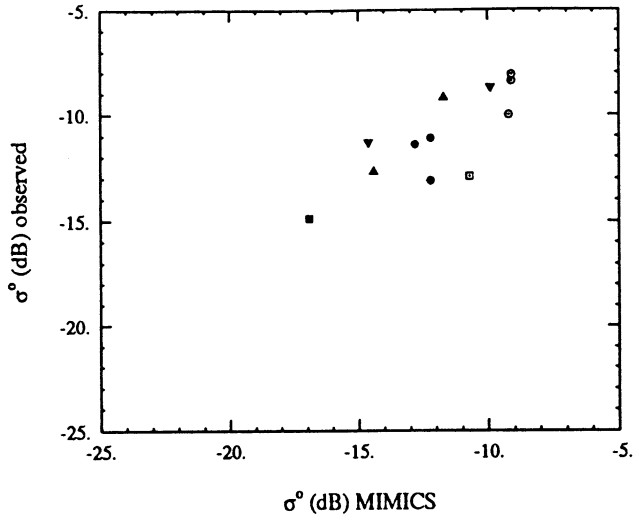

(a) HH-polarization.

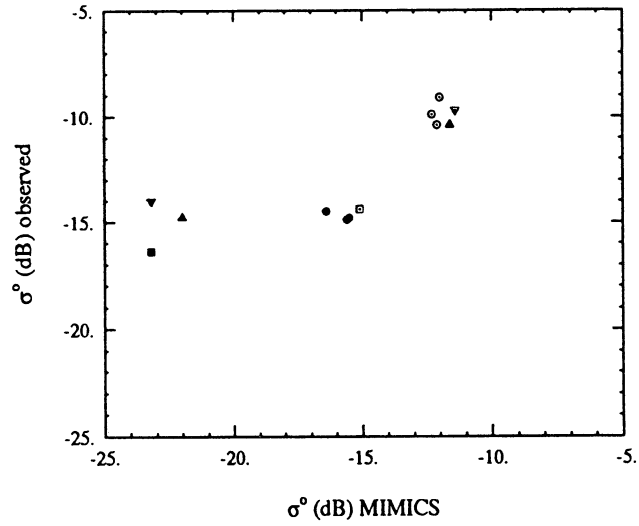

(b) VV-polarization.

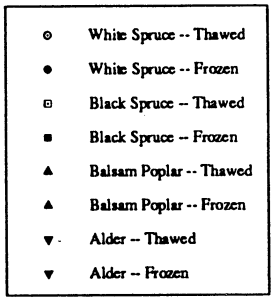

Figure 6.17: Comparison of measured canopy backscatter to
ter for (a) HH-polarization and (b) VV-polarization.

white spruce (WS-5), respectively. Responses are shown for co-polarized and cross-polarized configurations. Figures 6.20 and 6.21 present the measured frozen and thawed L-band responses. Again MIMICS successfully recreates the behavior of the measured data. MIMICS not only correctly reproduces the shapes of each of the surfaces, but MIMICS accounts for the increase in the pedestal observed in going from frozen to thawed states. These figures demonstrate that MIMICS has successfully modeled the backscatter response of this stand for all of these polarization states. Figure 6.22 shows the linear polarized response of this stand as simulated by MIMICS for frozen and thawed conditions. The character of the responses are very similar for the two environmental states, with the thawed conditions yielding slightly more cross-polarized backscatter.

Modeling at C- and X-bands has been complicated by the lack of available calibrated SAR data. Furthermore, data at these frequencies are available only for frozen canopy conditions. To deal with the uncalibrated data problem, the backscatter values were normalized to that of the white spruce stand WS-1 for each SAR pass. These normalized data are presented in Figure 6.23. For the most part, MIMICS predictions agree with the SAR measurements to within ± 1.5 dB. Exceptions to this include some VV-polarization observations of the balsam poplar, black spruce and alder stands. As was the case at L-band, this is probably caused by the method used to model the snow-soil interface.

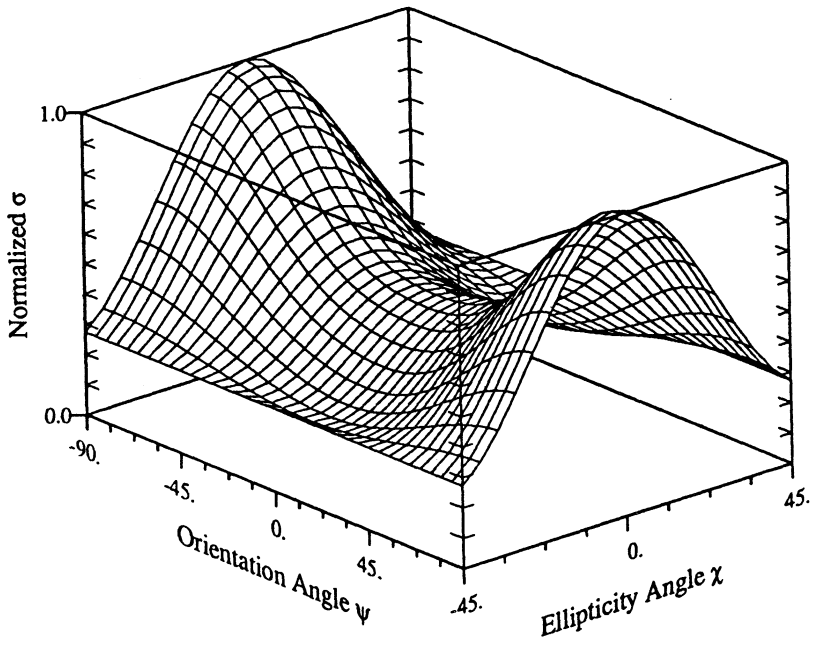

(a) Co-polarized response.

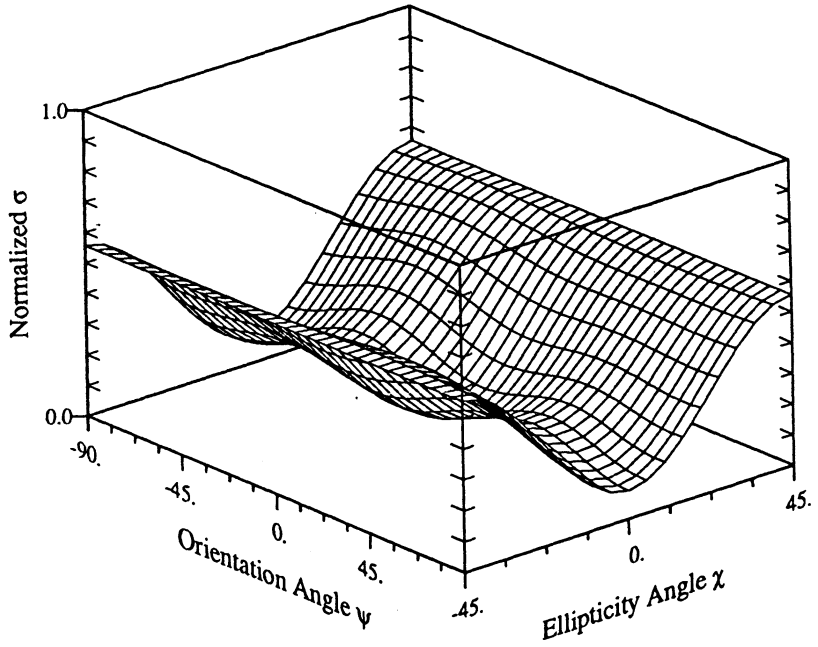

(b) Cross-polarized response.

Figure 6.18: MIMICS simulated L-band polarization response of frozen white spı
WS-5.

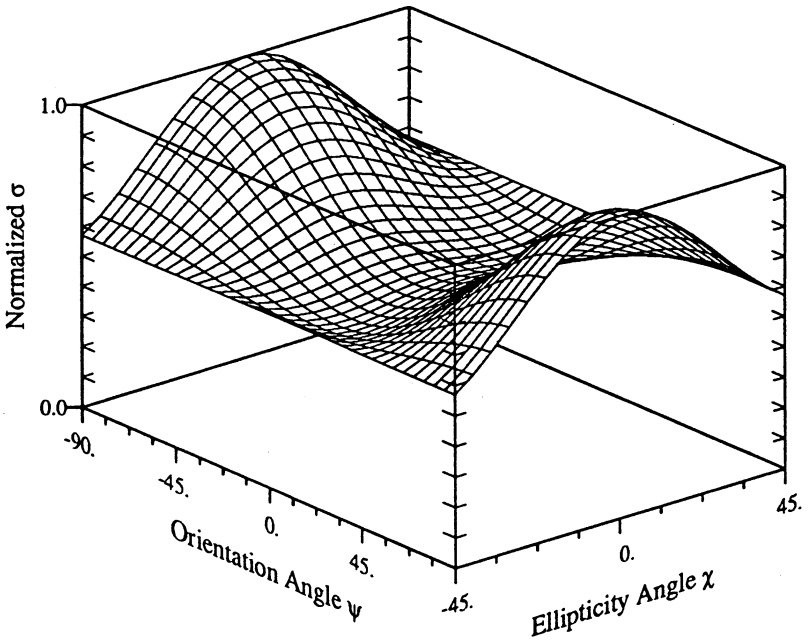

(a) Co-polarized response.

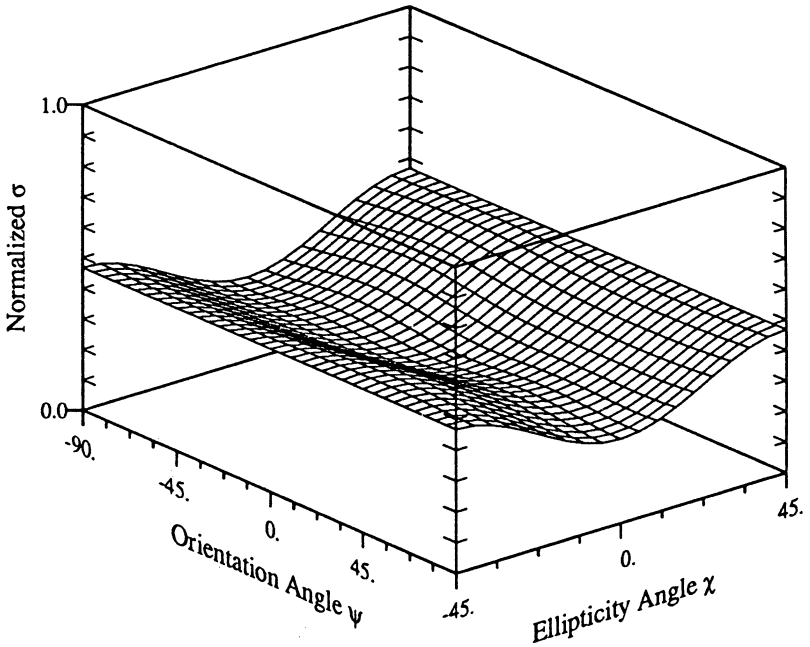

(b) Cross-polarized response.

Figure 6.19: MIMICS simulated L-band polarization response of thawed white spruce stand WS-5.

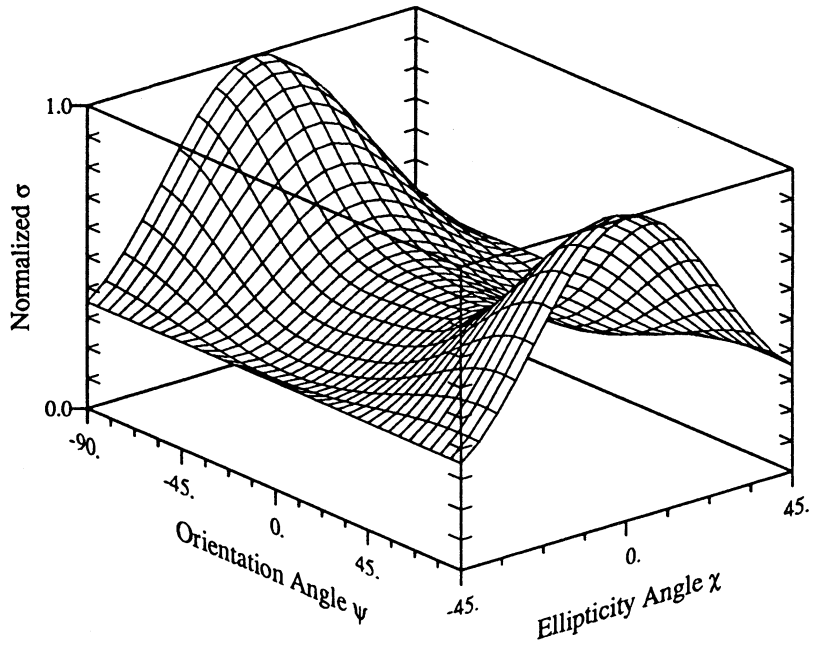

(a) Co-polarized response.

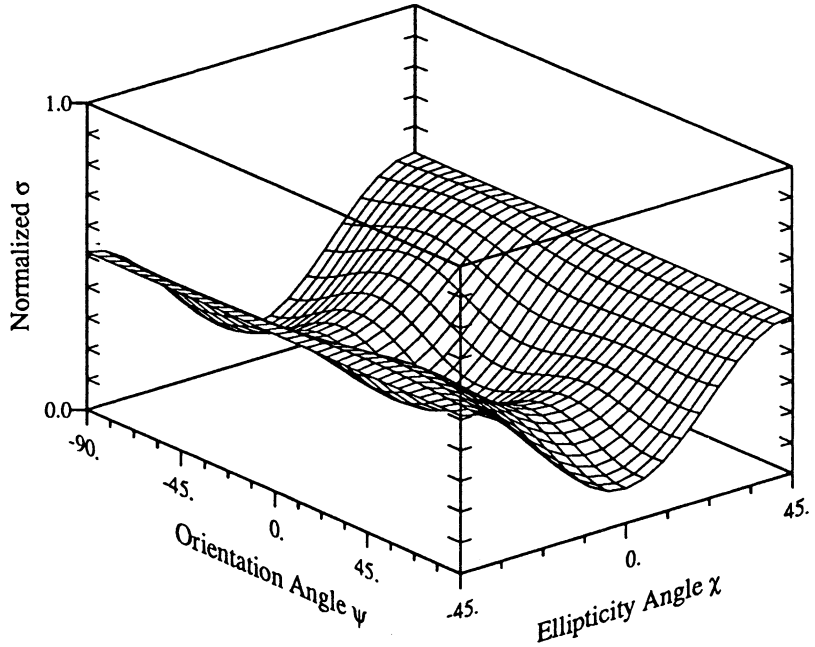

(b) Cross-polarized response.

Figure 6.20: Measured L-band polarization response of frozen white spruce stand WS-5.

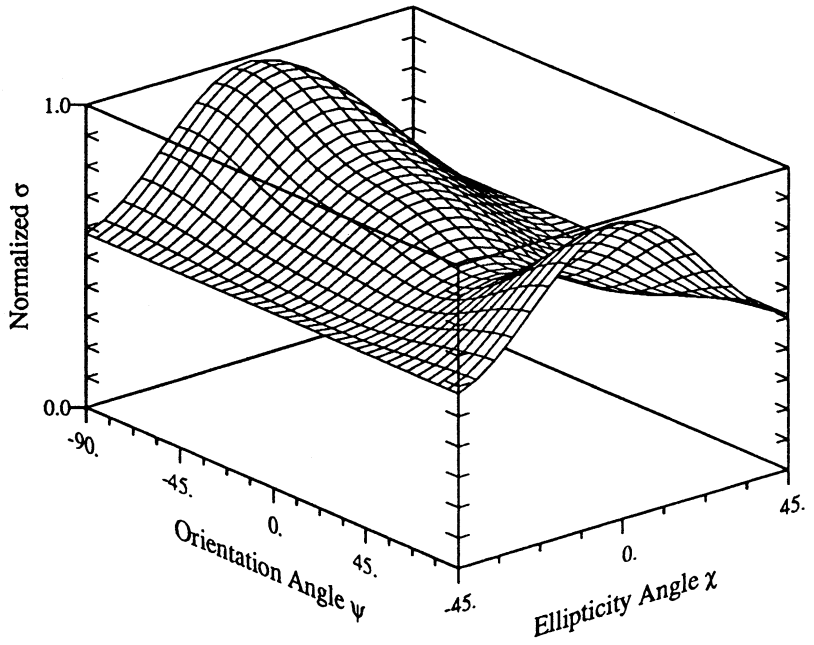

(a) Co-polarized response.

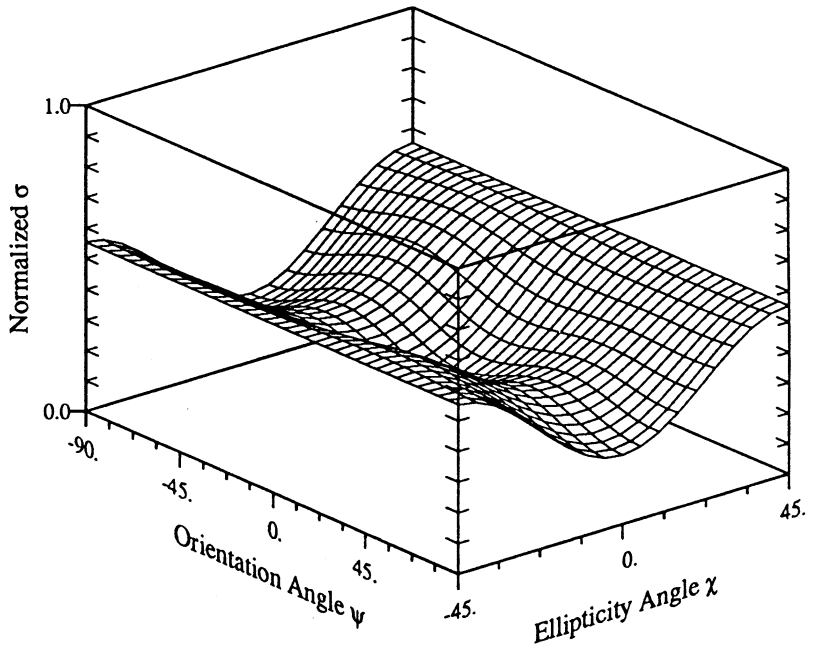

(b) Cross-polarized response.

Figure 6.21: Measured L-band polarization response of thawed white spruce stand WS-5.

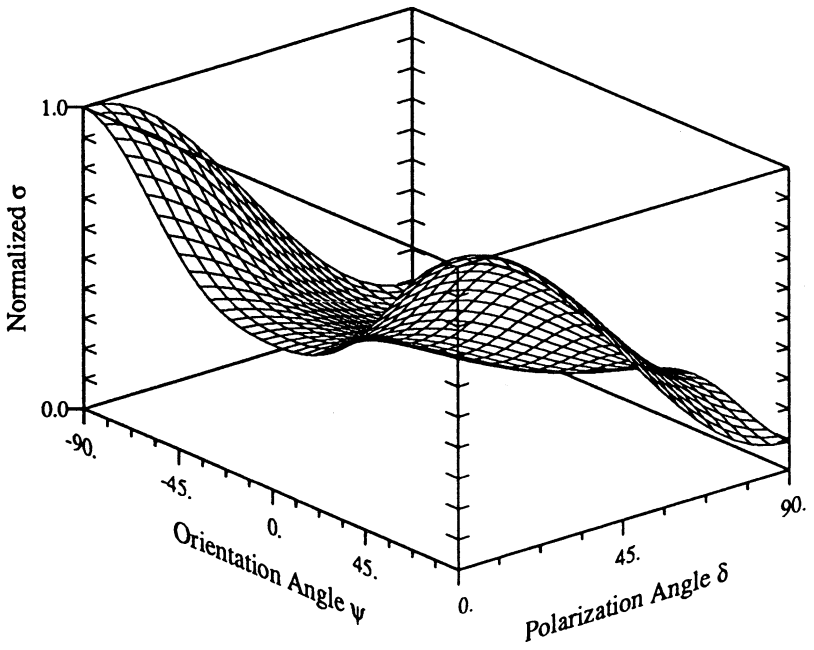

(a) Frozen Conditions.

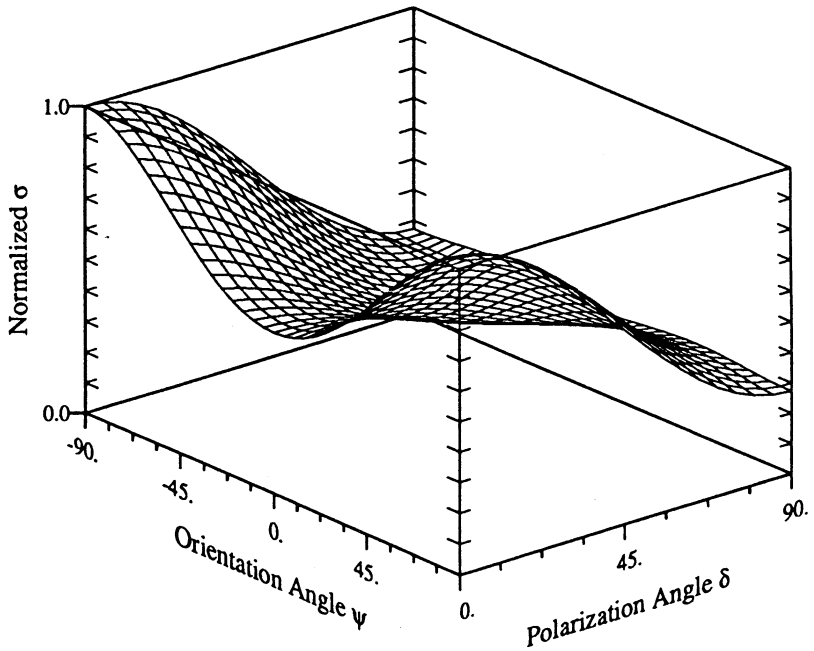

(b) Thawed Conditions.

Figure 6.22: MIMICS-simulated L-band linear polarization response of thawed white spruce stand WS-5.

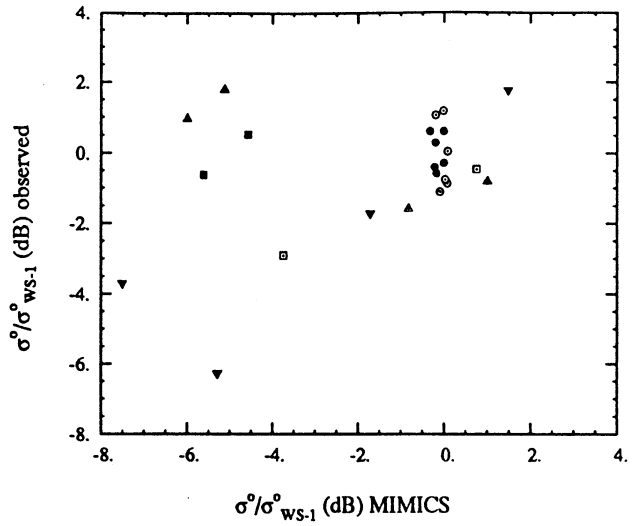

(a) C-Band.

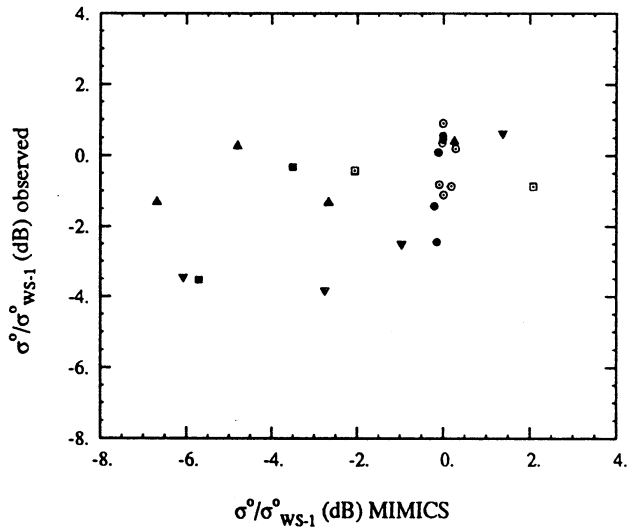

(b) X-Band.

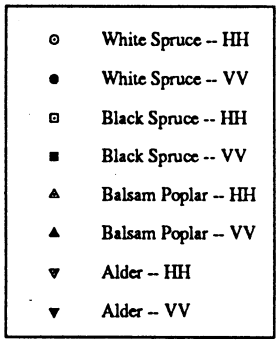

Figure 6.23: Comparison of measured canopy backscatter to MIMICS simulated backscatter for (a) C-band and (b) X-band. The data have been normalized to the backscatter from white spruce stand WS-1 for each SAR pass.

Black Spruce Simulations

Having established the ability to model backscatter from these forest stands, MIMICS may now be used to compute backscatter over a wider range of sensor parameters and the resulting simulated backscatter may be examined on a more detailed level. This allows examination of the relative contribution of each of the scattering mechanisms to the net canopy backscatter. Detailed analyses of this type tend to be lengthy and are presented in Appendix H for several of the Alaskan forest stands. However, to gain an understanding of the effect of the snow layer on net backscatter, the approach presented in Section 3.2.2 for modeling the scattering at the snow-soil interface is applied at L-band to the black spruce stand.

The black spruce stand (BS-1) is a much more sparsely populated stand than the other species. This stand, in fact, does not represent a closed canopy. However, to simplify this initial analysis, MIMICS I is applied to model σ^0 for the black spruce stand as if it were indeed a closed canopy.

Figures 6.24 and 6.25 compare backscatter from the canopy, with the ground layer modeled as a half-space of snow, with the backscatter for a canopy above a 20 cm thick snow layer over a frozen soil half-space. Figure 6.24 shows this simulation for frozen canopy conditions while Figure 6.25 shows these data for thawed canopy conditions. In both cases, σ^0 is higher for the snow-covered soil for all polarizations. The effect is more prevalent for like-polarized backscatter with σ^0_{vv} being responding slightly more than σ^0_{hh}. This demonstrates the effect that the snow layer has on modifying the local angle of incidence at the ground surface.

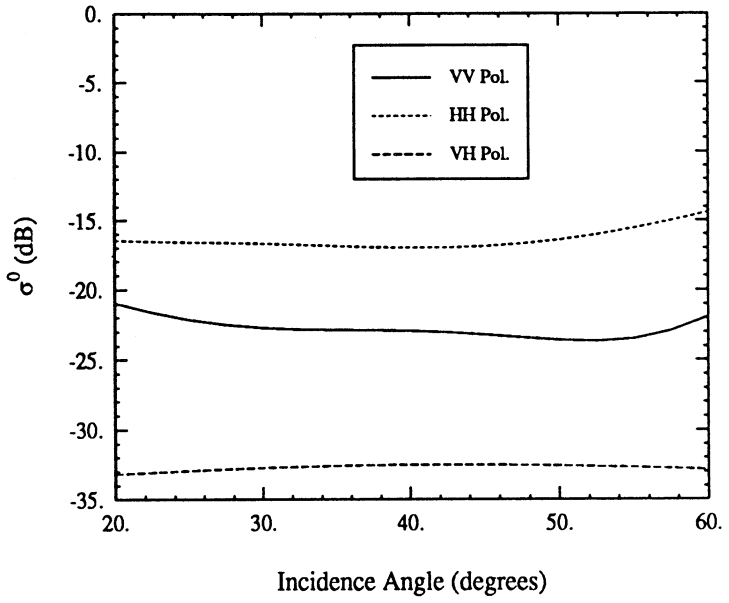

(a) Snow half-space.

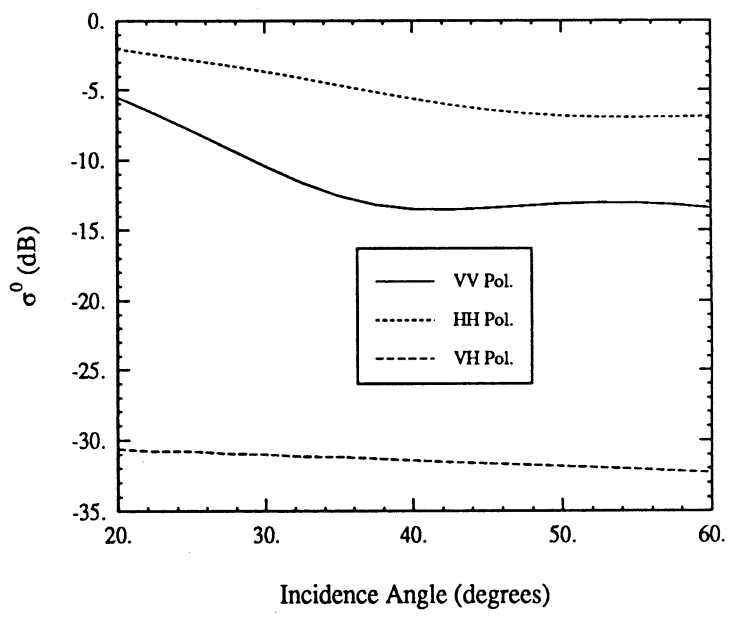

(b) Snow layer over soil half-space.

Figure 6.24: Total canopy backscatter for black spruce stand (BS-1) at L-band under frozen canopy conditions for (a) ground layer consisting of a snow half-space and (b) ground layer consisting of a snow layer on top of a soil half-space.

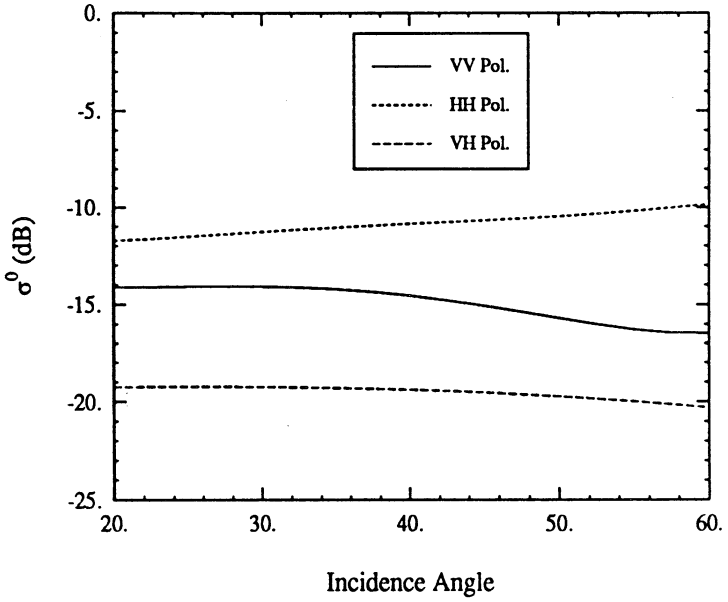

(a) Snow half-space.

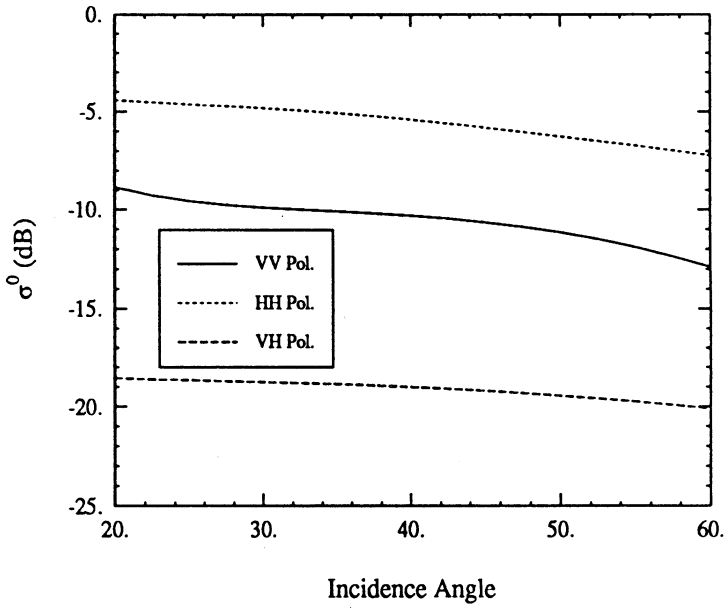

(b) Snow layer over soil half-space.

Figure 6.25: Total canopy backscatter for black spruce stand (BS-1) at L-band under thawed canopy conditions for (a) ground layer consisting of a snow half-space and (b) ground layer consisting of a snow layer on top of a soil half-space.

6.3.4 Boreal Forest Multi-Season Simulation

The European Space Agency's Earth Resources Satellite, ERS-1, is scheduled for launch on 16 July 1991. This satellite represents the first in a planned series of remote sensing satellites that will allow monitoring of seasonal phenologic and environmental change of forest ecosystems. ERS-1 includes a C-band, VV-polarized SAR that will operate at an incidence angle of approximately 23°. Since the boreal forest study was carried out in support of the ERS-1 mission, it is useful to consider the simulated backscatter response through an annual cycle for sensor parameters corresponding to the ERS-1 platform.

Simulated backscatter response to changing environmental conditions has been studied by Way *et al.*,[80]. Table 6.15 presents a list of environmental and phenologic conditions that exist throughout the course of a typical seasonal cycle. Canopy phenological state is strongly influenced by environmental conditions and may vary with species. The table lists 13 states that may occur through the coarse of a year. The conditions begin in winter with the canopy in a frozen state and progress through a spring thaw, budding, a wet rainy season, a dry season, a flooded period, and autumn freezing. Periods of water stress are manifest by a negative water potential.

Applying the dielectric models presented in Appendix A, MIMICS was used to simulate the backscatter from the stand presented in Table 6.15 as a function of phenologic state. The results of this analysis are presented in Figure 6.26. Keeping in mind that for snow-covered ground MIMICS predicted σ^0 to be slightly lower than SAR observations for both balsam poplar and black spruce, these data perform very much as one might expect. Except for one condition, balsam poplar exhibits the highest backscatter during that part of the season when it is foliated. The exception occurs during the spring thaw, before the leaves come out and when the soil is wet.

Table 6.15: Specified Environmental and Phenologic Conditions for MIMICS Simulation.

	Environment			Balsam Poplar		
Condition	Air Temp	Soil State	Snow State	Leaves	Bole	Water Potential
1	< 0	frozen	dry	none	frozen	0
2	> 0	frozen	wet	none	wet	0
3	> 0	frozen	none	none	wet	0
4	> 0	frozen	none	none	wet	0
5	> 0	wet	none	none	wet	0
6	> 0	wet	none	very wet	wet	0
7	> 0	wet	none	wet	wet	0
8	> 0	dry	none	wet	wet	neg
9	> 0	dry	none	dry	dry	neg
10	> 0	dry	none	dry	dry	neg
11	> 0	flooded	none	wet	wet	0
12	< 0	frozen	none	none	wet	0
13	< 0	frozen	none	none	frozen	0

	White Spruce			Black Spruce		
Condition	Needles	Bole	Water Potential	Needles	Bole	Water Potential
1	frozen	frozen	0	frozen	frozen	0
2	wet	wet	0	wet	wet	0
3	wet	wet	neg	wet	wet	neg
4	dry	dry	neg	dry	dry	neg
5	wet	wet	0	wet	wet	0
6	wet	wet	0	wet	wet	0
7	wet	wet	0	wet	wet	0
8	wet	wet	0	wet	wet	0
9	wet	wet	neg	wet	wet	neg
10	dry	dry	neg	dry	dry	neg
11	wet	wet	0	wet	wet	0
12	wet	wet	0	wet	wet	0
13	frozen	frozen	0	frozen	frozen	0

Notes:

(1) dry soil 10% sand; 30% clay; mvs = 0.1, 5° C

(2) wet soil 10% sand; 30% clay; mvs = 0.3, 5° C

(3) very wet leaves grav. moisture = 0.8

(4) wet leaves grav. moisture = 0.6

(5) dry leaves grav. moisture = 0.2

(6) dry and stressed woody vegetation dielectrics are assumed same as that of frozen woody vegetation

(7) ground surface corr. length = 6 cm, rms height = 0.5 cm,

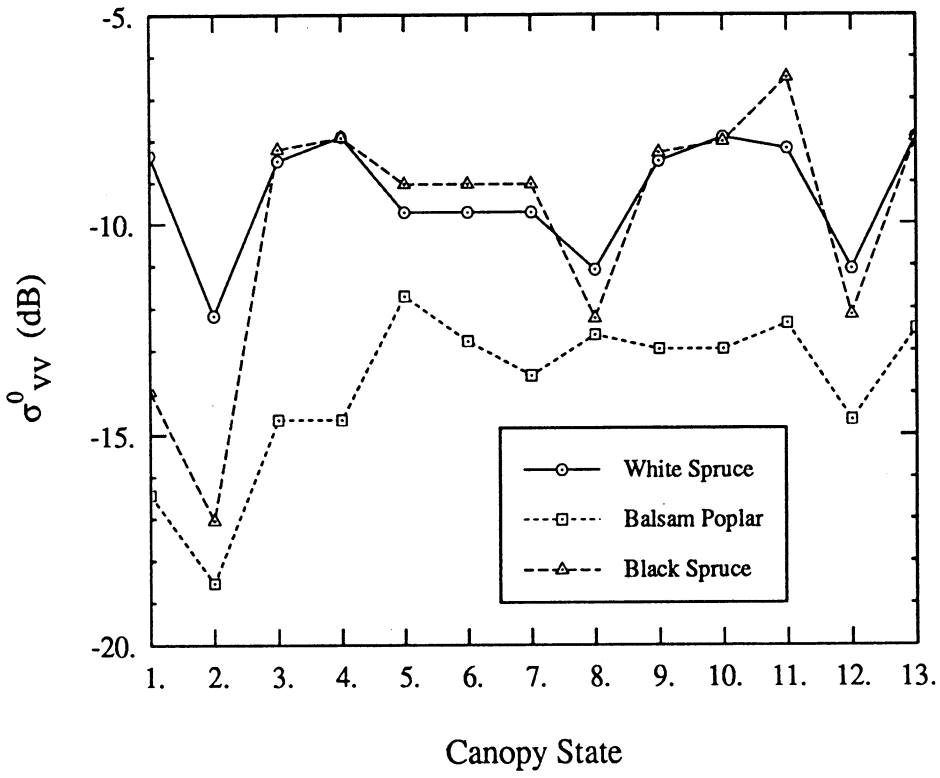

Figure 6.26: MIMICS simulated canopy backscatter response to environmental state for ERS-1 parameters (C-band, VV-polarization, $\theta = 23°$).

During this time, there is little attenuation through the crown layer and the wet soil leads to an accentuated ground-trunk interaction.

White spruce and black spruce backscatter respond alike throughout the cycle since both species are coniferous. Black spruce exhibits its highest backscatter when the ground surface is flooded. As with balsam poplar, this arises from an increased ground-trunk interaction. This is not observed in the white spruce or in the poplars because they are more densely populated stands (the poplars are foliated during this time) and C-band extinction through the crown layer is large enough to attenuate this term.

6.4 MIMICS II Simulations of Open-Crown Canopies

Now that an understanding of the function and behavior of the closed-crown canopy model has been developed, the simulations may be extended to include the discontinuous crown layer model. In doing this, the response of the models to changes in canopy parameters may be compared and the backscatter response to changes in parameters affecting the discontinuous nature of the canopy may be examined. Only the polarimetric model will be considered in these analyses so that cross-polarized backscatter may be simulated.

Three canopies are considered in this analysis. In all three cases, the tree-level parameters have been derived directly from those applied in the EOS synergism study and the ERS-1 Alaskan boreal forest study. The first canopy is a sparsely populated black spruce stand similar to that found in the Alaskan boreal forest. The second canopy is a more densely populated coniferous stand which closely resembles an Alaskan white spruce stand. Finally, a deciduous canopy with parameters derived from those of the the walnut orchard is considered.

Since backscatter coming directly from the ground surface is expected to contribute more to the net canopy backscatter in the discontinuous canopy case than in the continuous case, an effort has been made in the MIMICS II simulations to account for a stronger direct ground backscatter mechanism than is usually observed for bare soil. A statistical analysis of backscatter from short vegetation is presented by Ulaby and Dobson [61]. The rough surface parameters applied in the MIMICS II simulations have been inferred from these statistics and are summarized in Table 6.16. The model type, RMS surface roughness, and surface correlation length are

Table 6.16: Ground Surface Roughness Parameters for the MIMICS II Simulations.

	L-Band	C-Band	X-Band
Surface Scattering Model	Small Perturbation	Physical Optics	Geometrical Optics
RMS Surface Roughness	1.0 cm	0.5 cm	2.0 cm
Correlation Length	5.0 cm	2.0 cm	6.0 cm

allowed to vary with frequency so that the like-polarized surface backscatter from a moderately dry soil surface as a function of incidence angle roughly agrees with values measured for short vegetation.

6.4.1 Black Spruce Simulation

As mentioned in Section 6.3, the black spruce stand considered in the Alaskan boreal forest study was in fact a sparsely populated open-crown layer canopy. Therefore, this stand (BS-1) represents a reasonable test case for the MIMICS II model. Since the presence of an underlying snow layer complicates model behavior, this analysis will model the surface as a bare soil surface with the roughness parameters listed in Table 6.16.

The canopy is modeled as illustrated in Figure 6.27. The crowns are modeled as square columns of identical size with a height of 7.8 meters and side length 1.0

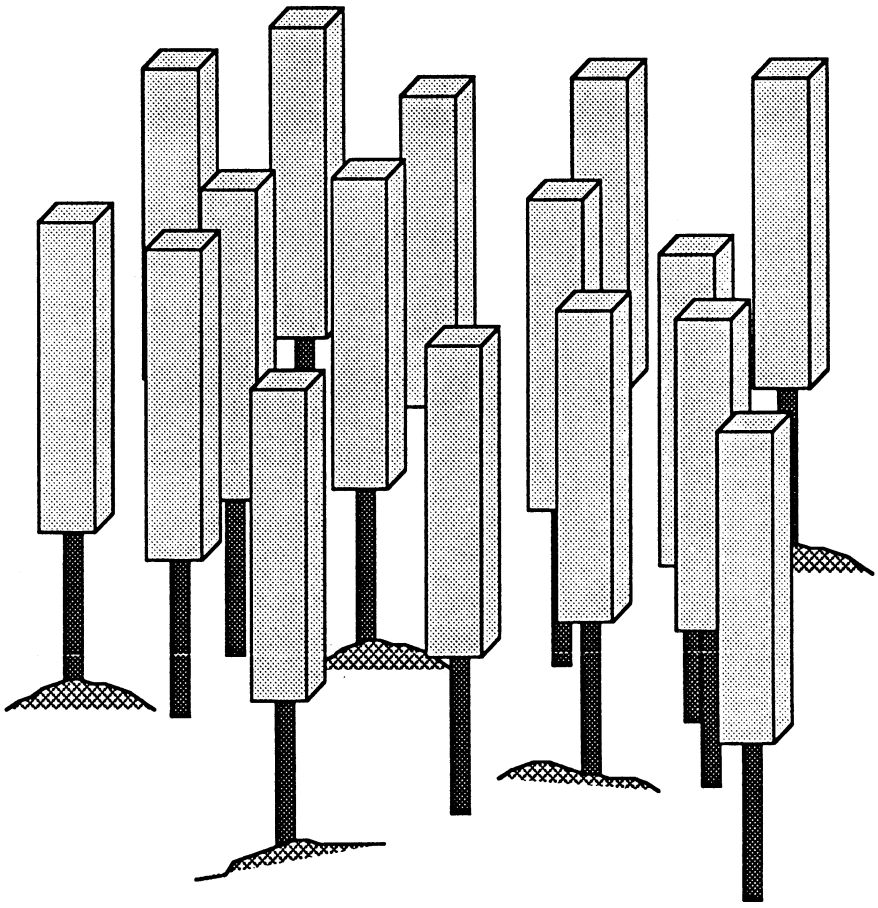

Figure 6.27: Canopy geometry used in MIMICS II simulation of black spruce stand BS-1.

meters. The crown height was chosen to correspond to the average tree height and is identical to the average trunk height. The tree-level parameters are summarized in Table 6.17. The number densities of the constituents in the crown layer were

Table 6.17: Tree level parameters for black spruce stand BS-1.

Constituent	Mean Length	Mean Diameter	Number Density	Orientation
Primary Branches	0.81 m	2.37 cm	1.0 m^{-3}	$\sim \sin^9(\theta - 30°)$
Secondary Branches	0.51 m	1.06 cm	6.55 m^{-3}	$\sim \sin^9(\theta)$
Needles	0.8 cm	0.1 cm	91,700 m^{-3}	$\sim \sin(\theta)$
Trunks	7.8 m	8.9 cm	0.2 m^{-2}	Vertical

obtained by increasing those applied in the continuous canopy model in such a way as to keep a constant total number of constituents in the canopy. For a continuous canopy with number density 0.2 trees/m^2, the equivalent canopy area per tree is $1/0.2 = 5$ m^2/tree. If this area is condensed into a square-column crown volume with cross-sectional area 1 m^2, the number density of constituents in the crown volume increases by a factor of 5. Thus, the number densities listed in the table represent a factor of 5 increase in those used for modeling the equivalent closed-crown canopy.

Constituent dielectric properties are listed in Table 6.18. These parameters are

Table 6.18: Black Spruce Canopy Dielectric Characteristics.

Constituent	L-Band	C-Band	X-Band
Primary branches	14.3 +i 5.1	10.7 +i 4.0	8.9 +i 3.9
Secondary branches	15.7 +i 5.6	11.9 +i 4.5	9.8 +i 4.4
Needles	18.5 +i 6.4	14.1 +i 5.4	11.5 +i 5.5
Trunks	12.5 +i 4.5	9.3 +i 3.3	7.8 +i 3.2
Ground surface	5.6 +i 1.4	6.6 +i 0.9	5.8 +i 1.4

consistent with those found for thawed black spruce. The ground surface dielectric was computed by applying the dielectric models in Appendix A with a volumetric moisture of 0.1.

For a single square column crown of height c and side length a, from Equations (5.44) and (5.55):

$$p(s|1) = \begin{cases} \frac{2\cos\theta\sin\theta}{ac}s + \left(1 - \frac{a}{c\tan\theta}\right)\delta_k(s - s_m) \\ \qquad ;\theta \geq \theta_c; 0 \leq s \leq s_m; s_m = a/\sin\theta \\ \frac{2\cos\theta\sin\theta}{ac}s + \left(1 - \frac{c\tan\theta}{a}\right)\delta_k(s - s_m) \\ \qquad ;\theta \leq \theta_c; 0 \leq s \leq s_m; s_m = c/\cos\theta \\ 0 \qquad ;\text{otherwise.} \end{cases} \tag{6.6}$$

Assuming all of the crowns in the black spruce stand are of identical height and width, it follows that

$$\int_0^\infty p(s|1)\, e^{-\lambda_i s} ds = \begin{cases} \frac{2\sin\theta\cos\theta}{ac\lambda_i^2}\left[1 - e^{-\lambda_i s_m}(\lambda_i s_m + 1)\right] + \left(1 - \frac{a}{c\tan\theta}\right)e^{-\lambda_i s_m} \\ \qquad ;\theta \geq \theta_c, s_m = a/\sin\theta \\ \frac{2\sin\theta\cos\theta}{ac(\lambda_i)^2}\left[1 - e^{-\lambda_i s_m}(\lambda_i s_m + 1)\right] + \left(1 - \frac{c\tan\theta}{a}\right)e^{-\lambda_i s_m} \\ \qquad ;\theta \leq \theta_c, s_m = c/\cos\theta \end{cases} \tag{6.7}$$

for each eigenvalue λ_i. Applying this relation to the polarimetric MIMICS II model allows for determination of canopy backscatter.

Figure 6.28 shows the simulated L-, C-, and X-band backscatter from the black spruce canopy as a function of radar incidence angle for VV, HH and HV polarizations. Data are shown for the canopy modeled as a discontinuous stand (MIMICS II) and for the canopy modeled as an equivalent continuous canopy, with the crown scattering constituents distributed uniformly throughout the crown layer (MIMICS I). This figure shows that the discontinuous nature of the canopy has a negligible effect on backscatter at all three frequencies, with only a slight effect at C- and X-bands for the cross-polarized return. This phenomenon is also reflected in the one-way crown layer transmissivity, shown in Figure 6.29, where minimal difference is seen between the MIMICS I and MIMICS II models.

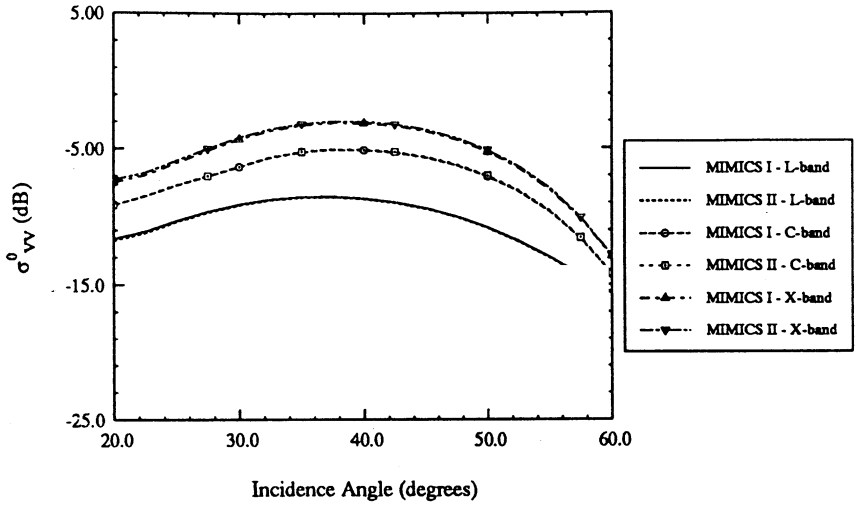

(a) VV-polarized backscatter.

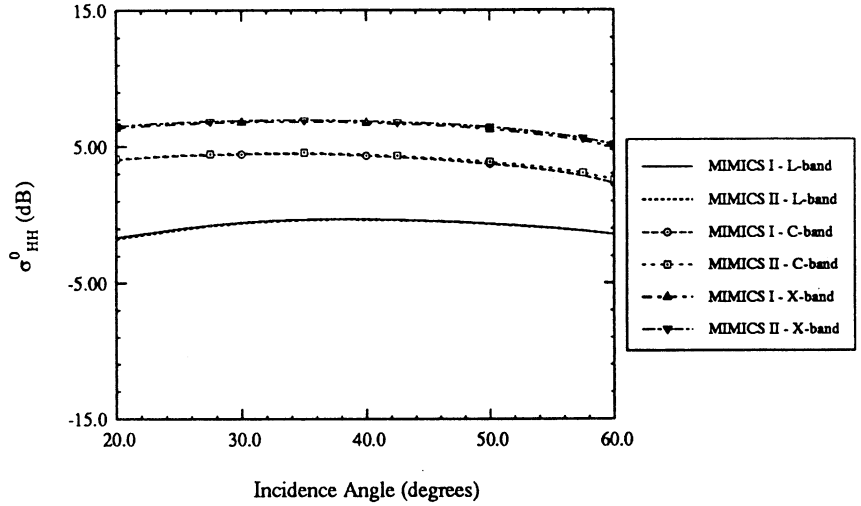

(b) HH-polarized backscatter.

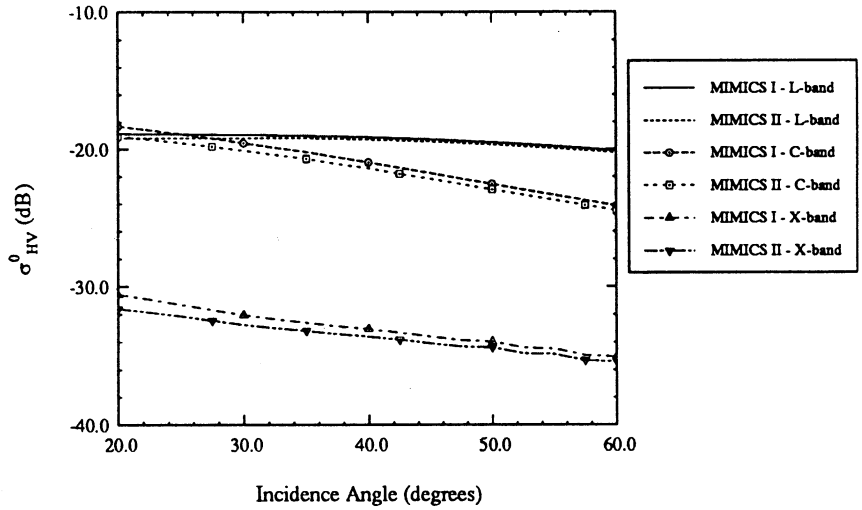

(c) HV-polarized backscatter.

Figure 6.28: Comparison of net canopy backscatter from a black spruce canopy modeled with a continuous crown layer (MIMICS I) and a discontinuous crown layer (MIMICS II) at L- C- and X-bands for (a) VV, (b) HH, and (c) HV polarizations.

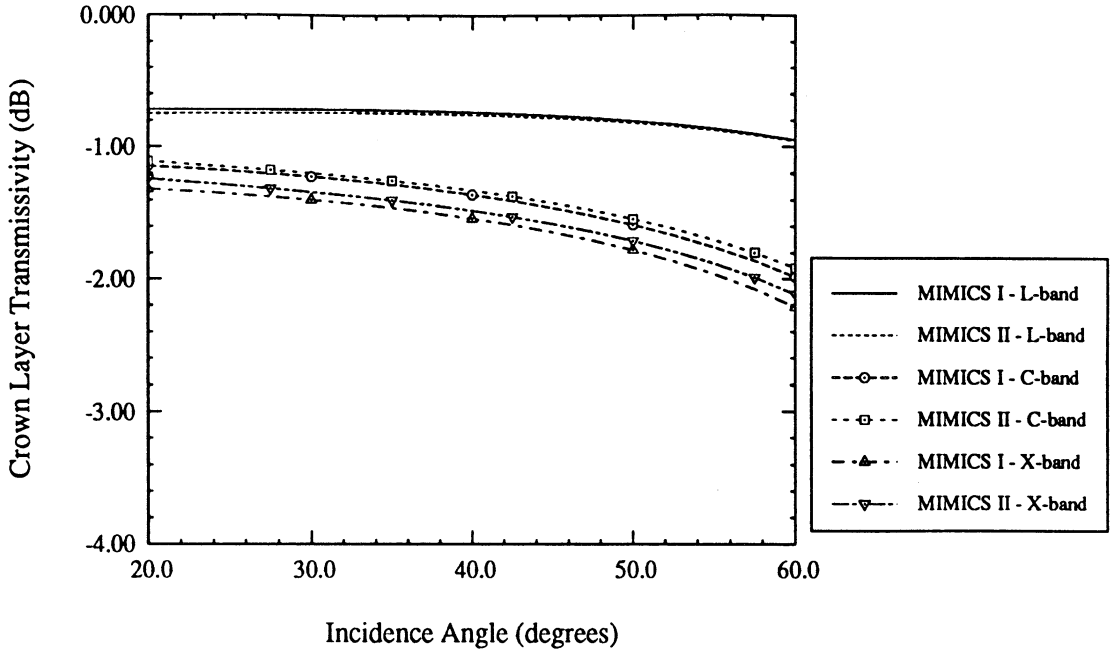

(a) V-polarized transmissivity.

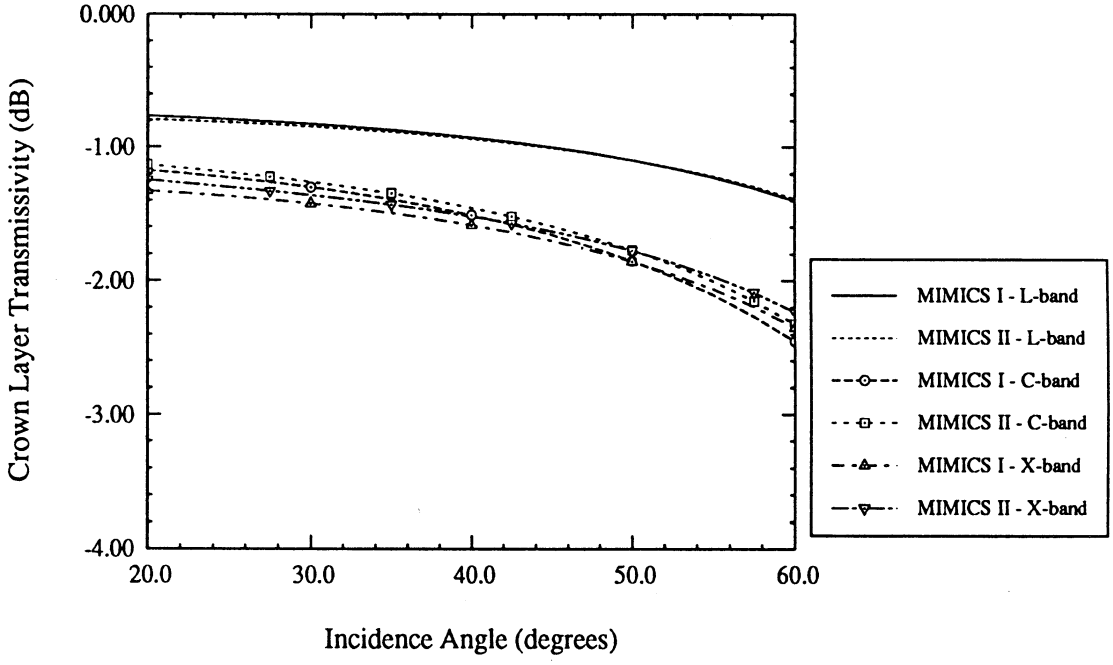

(b) H-polarized transmissivity.

Figure 6.29: Comparison of crown layer transmissivity through a black spruce canopy modeled with a continuous crown layer (MIMICS I) and a discontinuous crown layer (MIMICS II) at L- C- and X-bands for (a) V-polarization and (b) H-polarization.

Figures 6.30 and 6.31 illustrate the most dominant contributions to total canopy backscatter for L-band VV and HV polarized backscatter. Simulations are presented for both MIMICS I and MIMICS II. The VV-polarized backscatter is dominated by the ground-trunk interaction mechanism at intermediate incidence angle and by the direct crown backscatter near $\theta = 20°$ and $\theta = 60°$. The cross-polarized backscatter is dominated exclusively by direct crown backscatter.

Essentially, these figures demonstrate that the crown volumes contain such a sparse distribution of constituents that distributing the constituents in individual crown volumes has an insignificant effect on the net canopy backscatter. To demonstrate this effect further, the number density of scatterers in the crown volumes may be increased while maintaining constant crown size. A *density multiplication factor*, M_d is defined such that the volume density of scatterers in the crowns is multiplied by M_d thereby modifying scattering and extinction in the crown volumes. For example, setting $M_d = 2$ doubles the the phase matrix $\mathcal{P}_c$ while also doubling the extinction matrix κ_c. $M_d = 1$ corresponds to the reference canopy.

Figures 6.32 and 6.33 illustrate the effect of M_d at L-band for incidence angles of 20° and 60°. Figure 6.32 compares the like- and cross-polarized backscatter simulated with the open-crown canopy model with that simulated with the closed-crown canopy model. Little difference is seen between the models for low values of M_d whereas as much as 2 dB of difference is observed at higher M_d. At both incidence angles, the HH-polarized backscatter modeled with MIMICS II exhibits an enhanced backscatter over that modeled with MIMICS I. However, for VV and HV polarizations, σ^0 decreases when going from MIMICS I to MIMICS II. This occurs because the HH-polarized backscatter is dominated by the ground-trunk interaction mechanism while direct crown backscatter contributes more significantly to the VV-

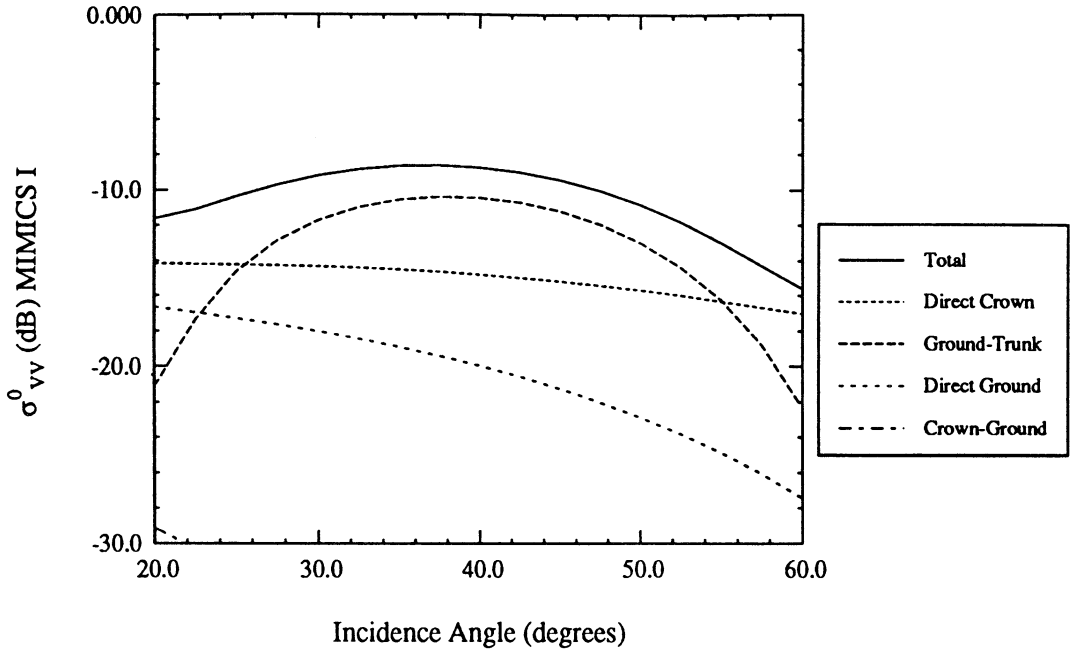

(a) MIMICS I continuous crown layer.

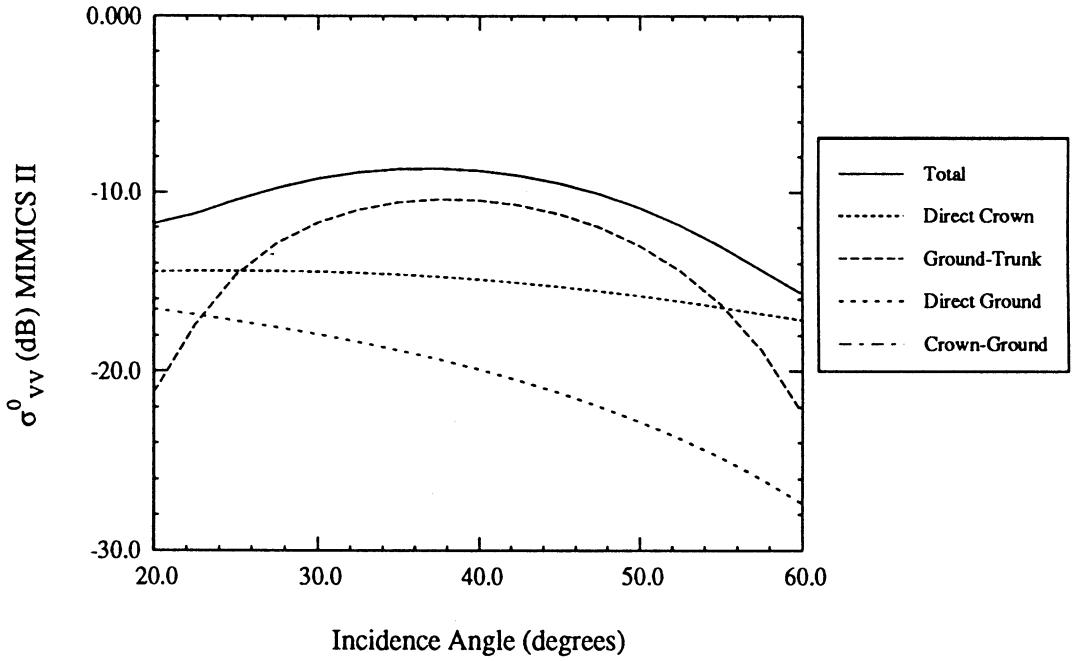

(b) MIMICS II discontinuous crown layer.

Figure 6.30: Comparison of L-band VV-polarized backscatter from a black spruce canopy modeled with (a) a continuous crown layer (MIMICS I) and (b) a discontinuous crown layer (MIMICS II).

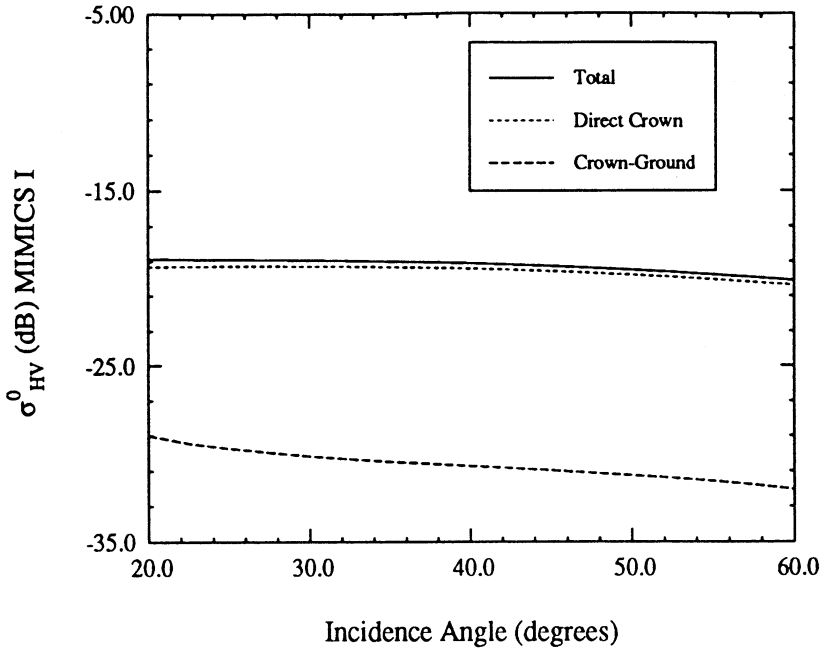

(a) MIMICS I continuous crown layer.

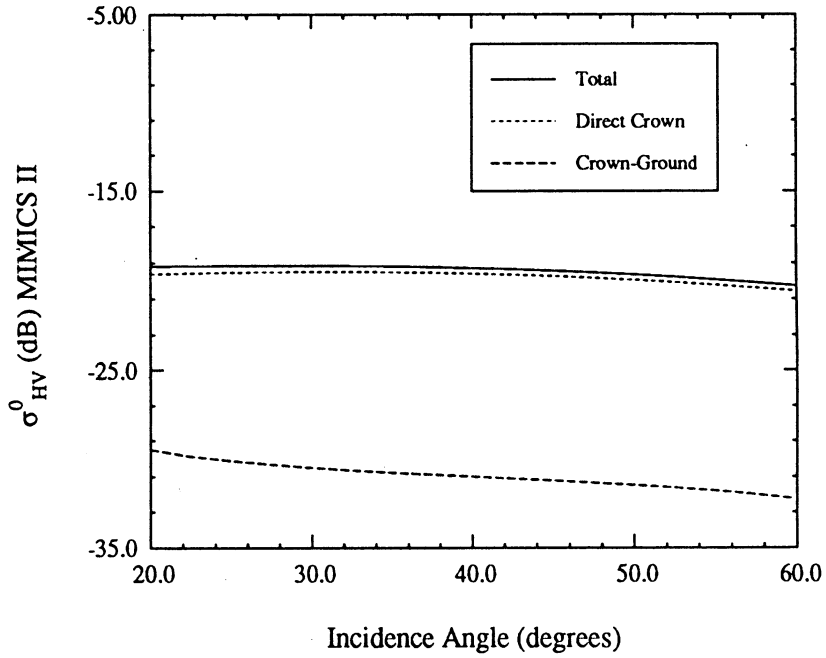

(b) MIMICS II discontinuous crown layer.

Figure 6.31: Comparison of L-band HV-polarized backscatter from a black spruce canopy modeled with (a) a continuous crown layer (MIMICS I) and (b) a discontinuous crown layer (MIMICS II).

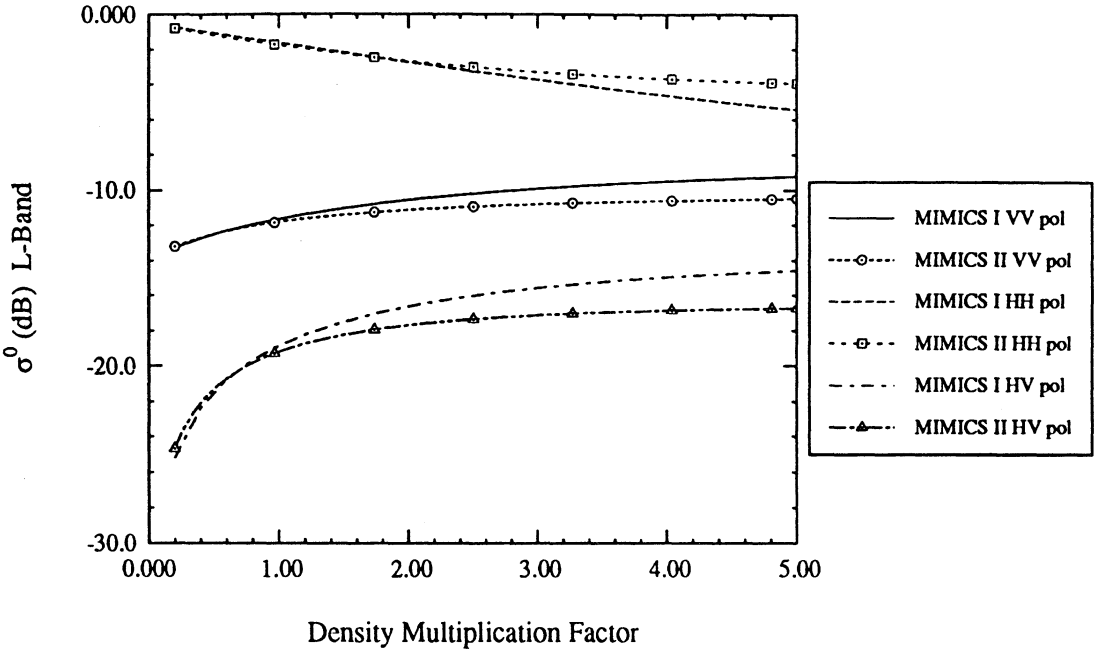

(a) Incidence angle = 20°.

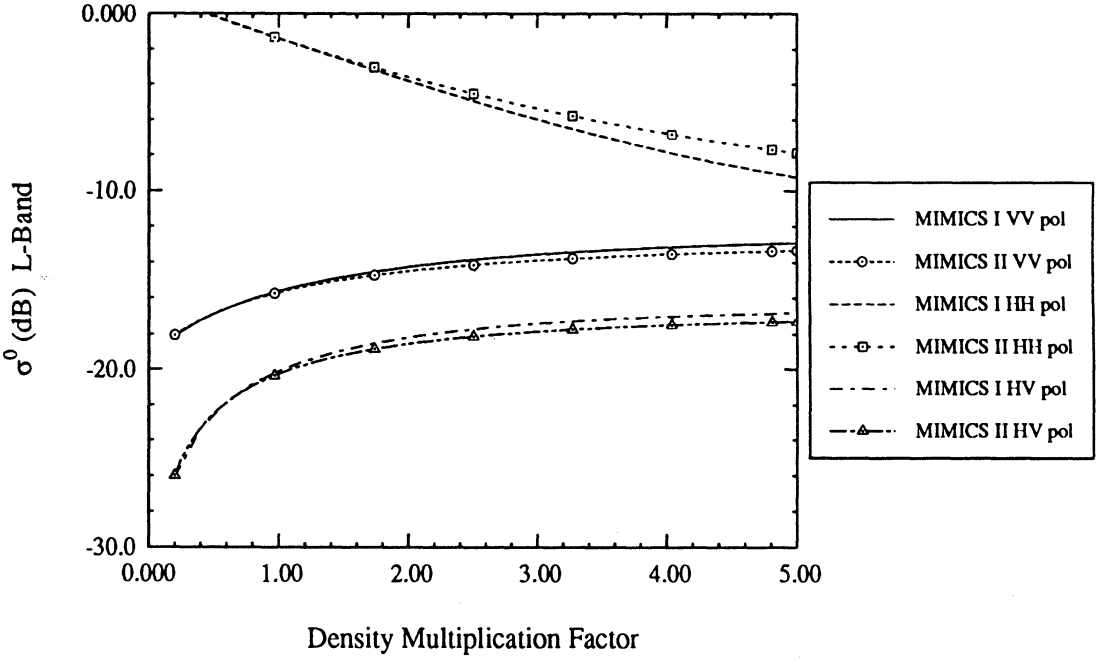

(b) Incidence angle = 60°.

Figure 6.32: Comparison of net canopy backscatter from a black spruce canopy modeled with a continuous crown layer (MIMICS I) and a discontinuous crown layer (MIMICS II) at VV, HH and HV polarizations for incidence angles of (a) 20° and (b) 60° as a function of the density multiplication factor.

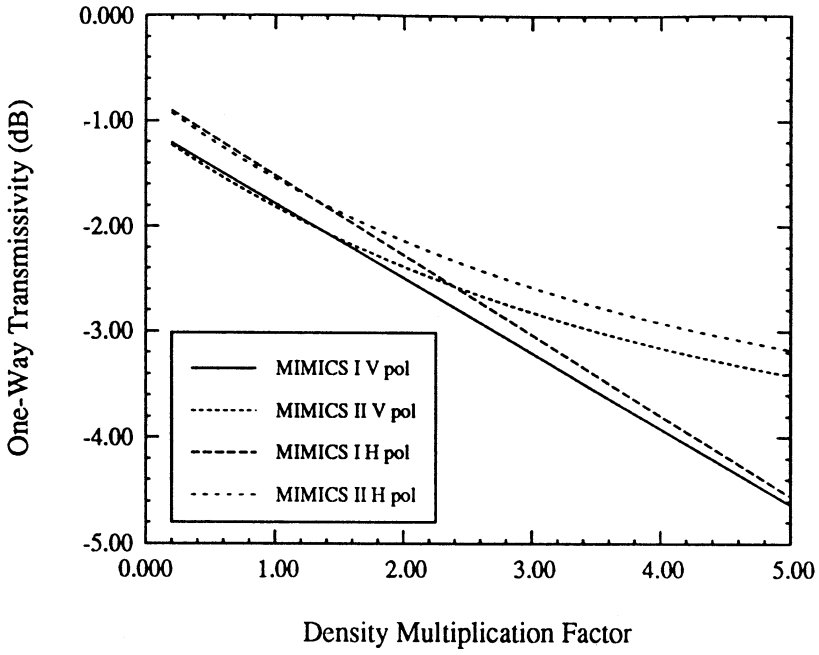

(a) Incidence angle = 20°.

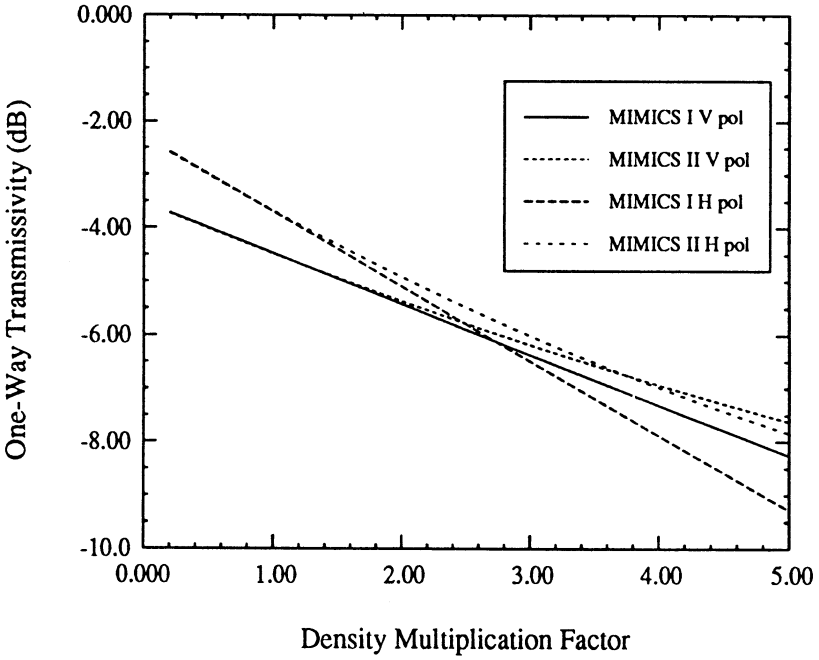

(b) Incidence angle = 60°.

Figure 6.33: Comparison of one-way transmissivity through a black spruce canopy modeled with a continuous crown layer (MIMICS I) and a discontinuous crown layer (MIMICS II) for V and H polarizations for incidence angles of (a) 20° and (b) 60° as a function of the density multiplication factor.

and HV-polarized backscatter. As the number density of scatterers in the individual crown volumes increases, the open canopy allows more radiation to penetrate the crown layer than does the closed canopy. This gives rise to a pronounced ground-trunk interaction mechanism and a decrease in the direct crown backscatter.

Figure 6.33 illustrates the effect of M_d on the canopy transmissivity. Here, the transmissivity of the closed canopy decreases linearly (on the dB scale) with M_d while that of the open canopy shows less sensitivity. For low M_d, the open and closed canopies have very similar transmissivities, while for high M_d, the open canopy allows more radiation to penetrate than does the closed canopy. This is a direct result of the gaps that are present in the open canopy crown layer. As the crown volumes become more and more opaque, the effect of these gaps becomes more pronounced. For perfectly opaque crowns, the value of crown layer transmissivity becomes $P(0)$, which corresponds to the fraction of incident radiation that intersects no tree crowns. On the other hand, for a perfectly opaque continuous canopy, no radiation penetrates the crown layer. Note that the difference between MIMICS I and MIMICS II diminishes as incidence angle increases.

In adapting canopy geometry from the closed-crown to the open-crown case, the importance of the individual crown shapes should be considered. One way which allows this question to be addressed is to examine the effect of varying crown side length, l. Figure 6.34 shows such an analysis. Here, l is varied from 0.5 m to 2.24 m while holding the total number of crown layer scatterers constant. The maximum value chosen for l yields an individual crown volume in the open canopy that is equivalent to the effective individual crown volume of the closed canopy and is given by $l_{\max} = 1/\sqrt{N_t}$ where $N_t = 0.2$ trees/m^2 is the canopy density. As seen in Figure 6.34, σ^0 of the open canopy at $l_{\max}$ is nearly identical to that of the closed

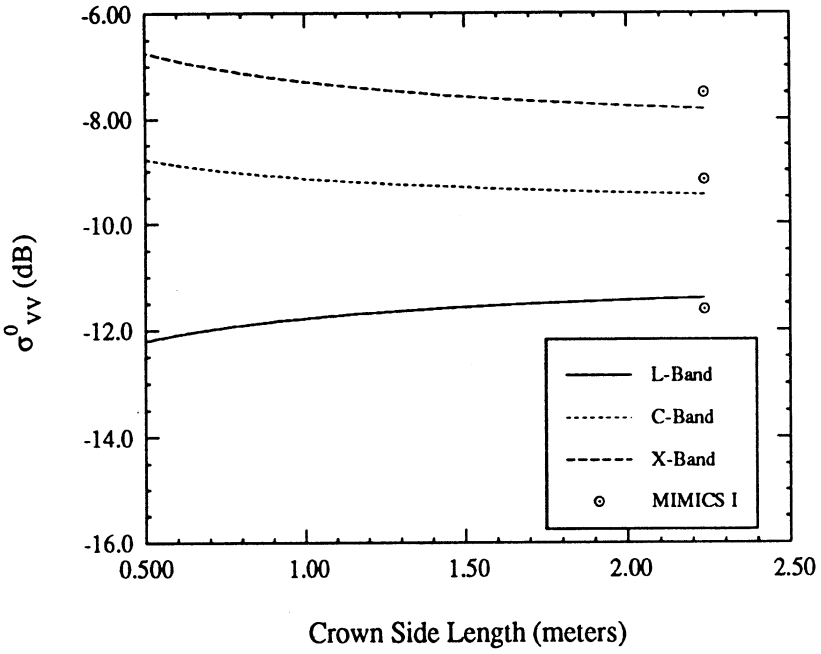

Figure 6.34: VV-polarized canopy backscatter as a function of crown side length with total crown layer biomass held constant. Results are for L, C and X bands at an incidence angle of $\theta = 20°$. Results for the equivalent closed crown canopy (MIMICS I) are also shown.

canopy. Making the crown volumes smaller by decreasing l while increasing the number density of scatterers in the individual crowns such that the total number of scatterers in the canopy remains constant then indicates the sensitivity of σ^0 to this parameter. The X-band backscatter exhibits the most sensitivity to l, with σ^0 increasing by about 1 dB as l is decreased to 0.5 m.

Canopy cover fraction, C, may be defined as the fraction of total canopy area that is seen as covered by vegetation when the canopy is viewed at an incidence angle $\theta = 0$. Applying the Poisson distribution, the fraction of ground area not covered by any crown is $P(0) = e^{-l_c^2 N_t}$ so that the fraction of covered area is $1 - P(0)$ or

$$C = 1 - e^{-l_c^2 N_t}. \tag{6.8}$$

MIMICS II provides a convenient method for modeling backscatter as a function of cover fraction. Figure 6.35 shows such an analysis at L-band for $\theta = 20°$. The crown volumes are identical to those in the black spruce canopy while canopy density is varied over $0.02 \leq N_t \leq 2$, giving $0.0198 \leq C \leq 0.8647$. Backscatter is seen to increase with cover fraction for VV and HV polarizations but decreases slightly for HH polarization. Figure 6.36 shows the components of total VV-polarized backscatter at L-band. This figure shows that for lower values of C the ground-trunk component contributes most to the canopy backscatter whereas at high values the direct crown backscatter comes more into play. The reference canopy has $N_t = 0.2$ which corresponds to $C = 0.18$.

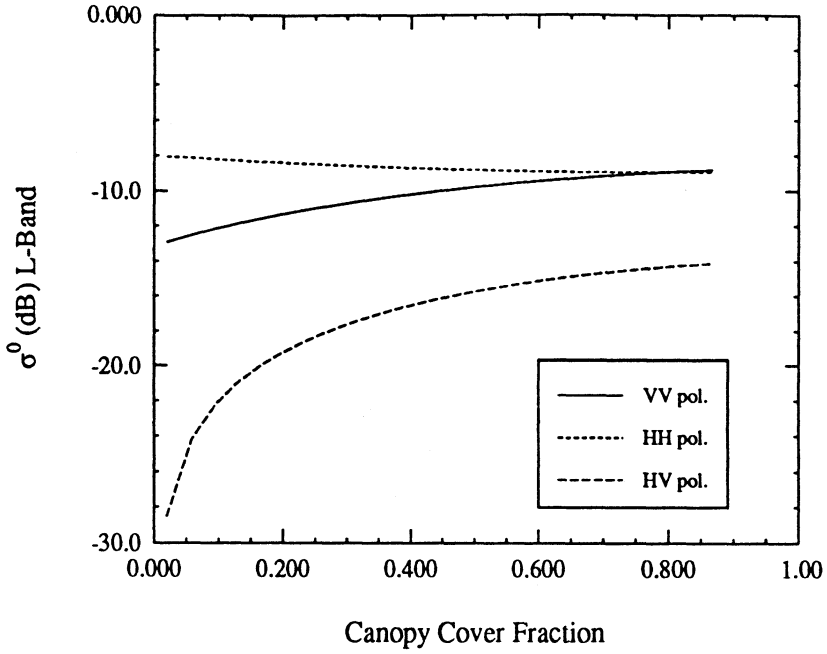

Figure 6.35: L-band backscatter from a black spruce canopy for VV, HH and HV polarizations as a function of canopy cover fraction.

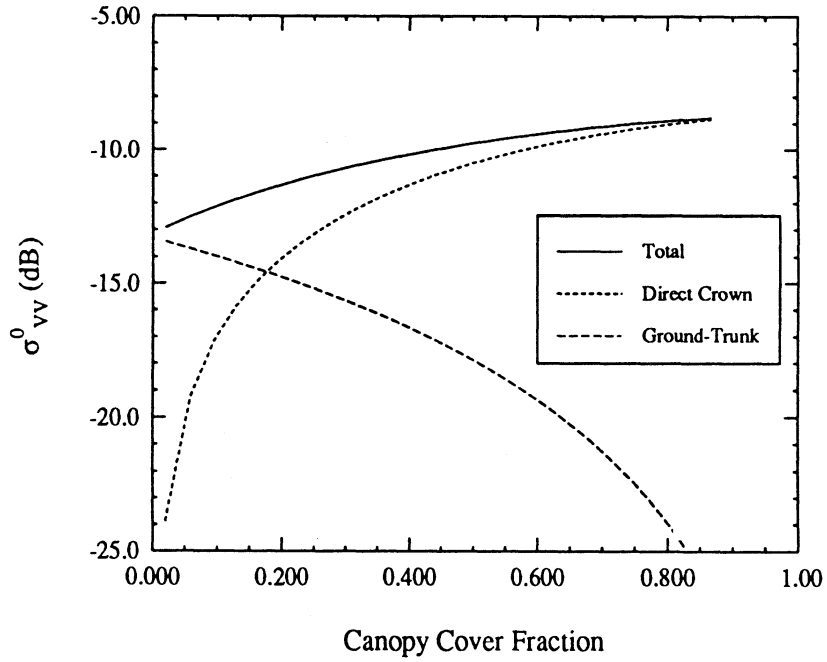

Figure 6.36: L-band VV -polarized backscatter from a black spruce canopy at an incidence angle of $\theta = 20°$ as a function of canopy cover fraction.

6.4.2 Coniferous Canopy Simulation

Having examined the effects of an open crown layer on backscatter from a sparse stand, the backscatter from a stand of more fully developed coniferous trees is now considered. Total canopy backscatter from the white spruce stand (WS-5) studied in the boreal forest analysis was dominated by the direct crown component. The tree-level parameters of the coniferous stand now simulated by MIMICS II are chosen to be similar to those of stand WS-5 and are summarized in Table 6.19.

Table 6.19: Tree level parameters for the coniferous stand.

Constituent	Mean Length	Mean Diameter	Number Density	Orientation
Primary Branches	1.13 m	2.24 cm	3.08 m^{-3}	$\sim \sin^4\theta$
Secondary Branches	0.57 m	1.04 cm	16.62 m^{-3}	$\sim \sin^9\theta$
Needles	1.6 cm	0.1 cm	86,162 m^{-3}	$\sim \sin\theta$
Trunks	17.4 m	18.0 cm	0.12 m^{-2}	Vertical

For purposes of modeling the crown layer, the crowns are assumed to be conical with identical height $h = 10$ meters an basal diameter $l = 3$ meters, yielding a volume of $V' = 23.56$ m^3. Noting that the equivalent volume per tree in the continuous canopy simulation with crown layer thickness d and canopy density N_c was $d/N_c = 17.4/0.12 = 145$ m^3, the number density of each crown constituent in Table 6.19 represents an increase of $145/23.56 = 6.15$ over the corresponding number density of the continuous canopy.

Table 6.20 lists the dielectric parameters for the coniferous stand at L-, C- and X-bands for both frozen and thawed canopy conditions. These parameters are consistent with those of the white spruce stand.

Figure 6.37 shows MIMICS I and MIMICS II simulations of vertically polarized one-way crown layer transmissivity for thawed and frozen canopy conditions at L-,

Table 6.20: Coniferous Canopy Dielectric Characteristics.

Thawed Conditions

Constituent	L-Band	C-Band	X-Band
Primary branches	34.78 +i 10.58	27.59 +i 11.34	18.82 +i 12.46
Secondary branches	19.11 +i 6.54	14.57 +i 5.63	11.88 +i 5.78
Needles	22.26 +i 7.40	17.15 +i 6.77	13.84 +i 7.09
Trunks	36.47 +i 10.99	29.01 +i 11.97	22.78 +i 13.2
Ground surface	5.6 +i 1.4	6.6 +i 0.9	5.8 +i 1.4

Frozen Conditions

Constituent	L-Band	C-Band	X-Band
Primary branches	5.12 +i 1.08	4.78 +i 0.32	4.74 +i 0.18
Secondary branches	4.34 +i 0.97	4.04 +i 0.29	4.00 +i 0.16
Needles	4.53 +i 0.98	4.22 +i 0.30	4.18 +i 0.16
Trunks	5.19 +i 1.09	4.85 +i 0.32	4.81 +i 0.18
Ground surface	7.96 +i 0.96	7.96 +i 0.96	7.96 +i 0.96

C-, and X-bands. The difference between the open-crown and closed-crown cases is more prevalent for thawed conditions. In this case, at $\theta = 20°$ the MIMICS I and MIMICS II transmissivities differ by almost 2 dB at L-band at by about 3 dB at C- and X-band with the open-crown canopy having higher transmissivity than the closed-crown case. These differences decrease as incidence angle increases. For frozen conditions, almost no difference in transmissivity is seen at L-band whereas about 2 dB of difference is observed at $\theta = 20°$ for the other frequencies. Once again, these differences diminish as θ increases.

Figures 6.38 and 6.39 show simulations of canopy backscatter for thawed and frozen conditions. MIMICS I and MIMICS II simulations are shown for like- and cross-polarized configurations at L-, C- and X-bands. For thawed conditions, the like-polarized backscatter from the open-crown canopy is as much as 6 dB higher than that of the closed-crown canopy with the greatest difference observed at X-band for shallow incidence angles. However, cross-polarized backscatter from the open-crown canopy is less than that from the closed-crown canopy. Backscatter from the frozen

canopy exhibits similar behavior but with much less difference between MIMICS I and MIMICS II. Once again, these differences decrease with increasing θ.

To gain an understanding of model behavior, the individual contributions to canopy backscatter may be examined. Figures 6.40 and 6.41 show the contributions to total X-band VV-polarized backscatter for thawed and frozen conditions. The open crown layer has been shown to contribute to a higher canopy transmissivity. Figures 6.40 and 6.41 demonstrate that this increase in transmissivity contributes directly to enhanced contributions from the ground-trunk interaction mechanism as well as from the other mechanisms that involve the lower (trunk and ground) layers of the canopy. Furthermore, the open-crown canopy exhibits less direct crown backscatter than does the closed-crown canopy.

The effect of applying MIMICS II to model changes in backscatter as a function of canopy parameters that are not directly related to the crown layer constituents is illustrated in Figure 6.42. This figure shows the MIMICS I and MIMICS II like-polarized L-band response to changes in volumetric soil moisture at $\theta = 20°$. Figure 6.42(a) shows these simulations for dry trunks with relative dielectric $\epsilon_r = 5.19 + i1.09$, which is equivalent to that applied for frozen trunks. Figure 6.42(b) shows simulations for wet trunks with $\epsilon_r = 36.4 + i10.99$. The remaining canopy dielectrics are assumed to be the same as for a thawed canopy. Soil moisture has been varied from a volumetric fraction of 0.01 which represents a very dry soil surface, to 0.5 which represents a well-saturated surface. For all cases, the increase in crown layer transmissivity has lead directly to an additional 2 dB of increased backscatter sensitivity over this range of soil moisture.

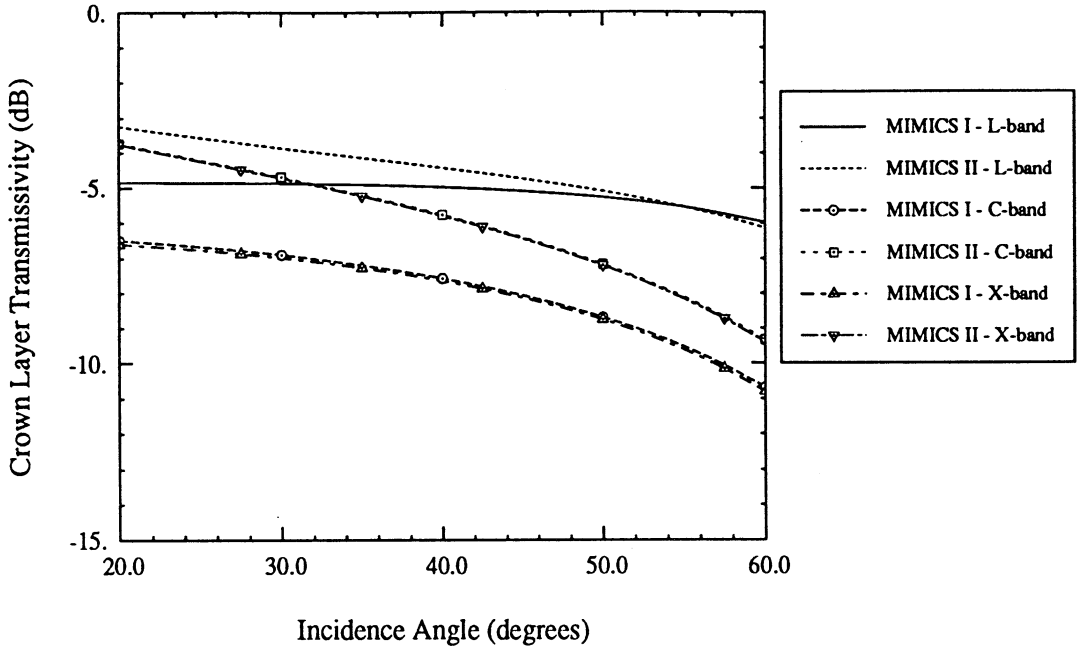

(a) Thawed conditions

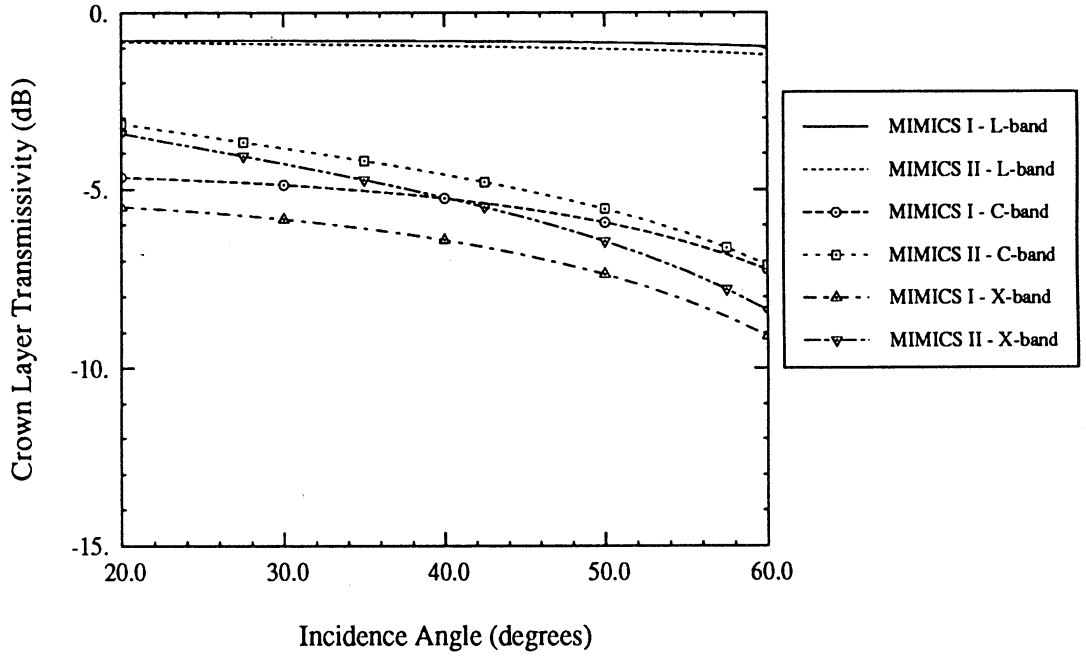

(b) Frozen conditions

Figure 6.37: One-way V-polarized transmissivity through a white spruce crown layer modeled as continuous (MIMICS I) and discontinuous (MIMICS II) for (a) thawed conditions and (b) frozen conditions.

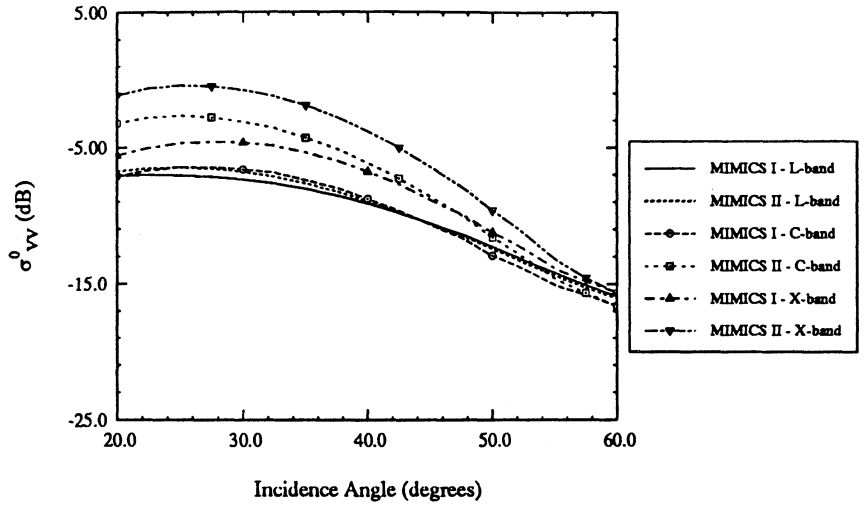

(a) VV-polarization

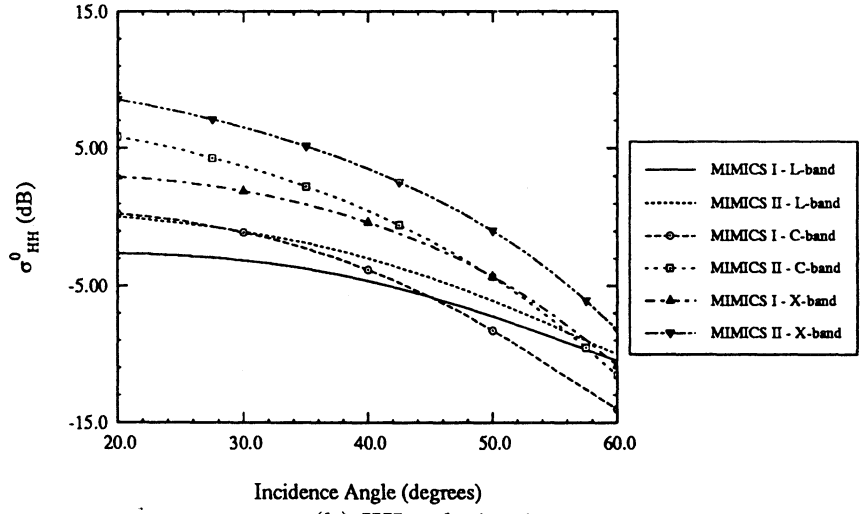

(b) HH-polarization

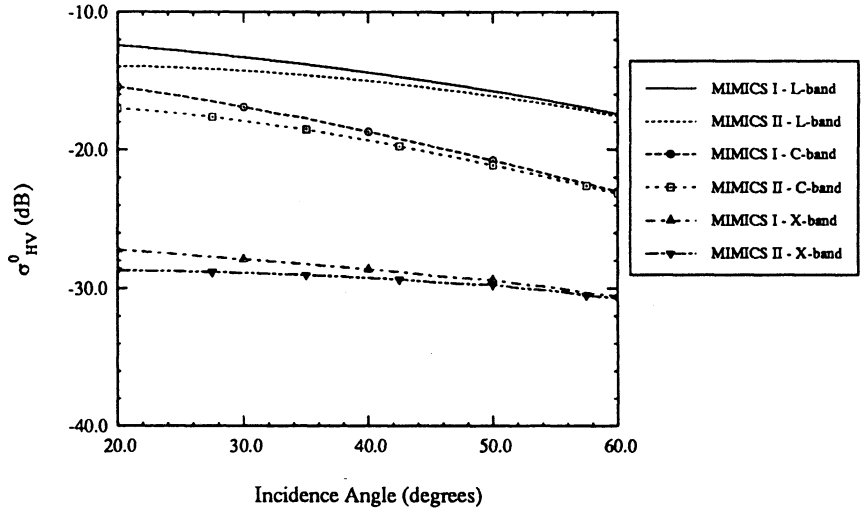

(c) HV-polarization

Figure 6.38: Backscatter from a thawed white spruce canopy modeled with a closed crown layer (MIMICS I) and with an open crown layer (MIMICS II) at (a) VV, (b) HH and (c) HV-polarization.

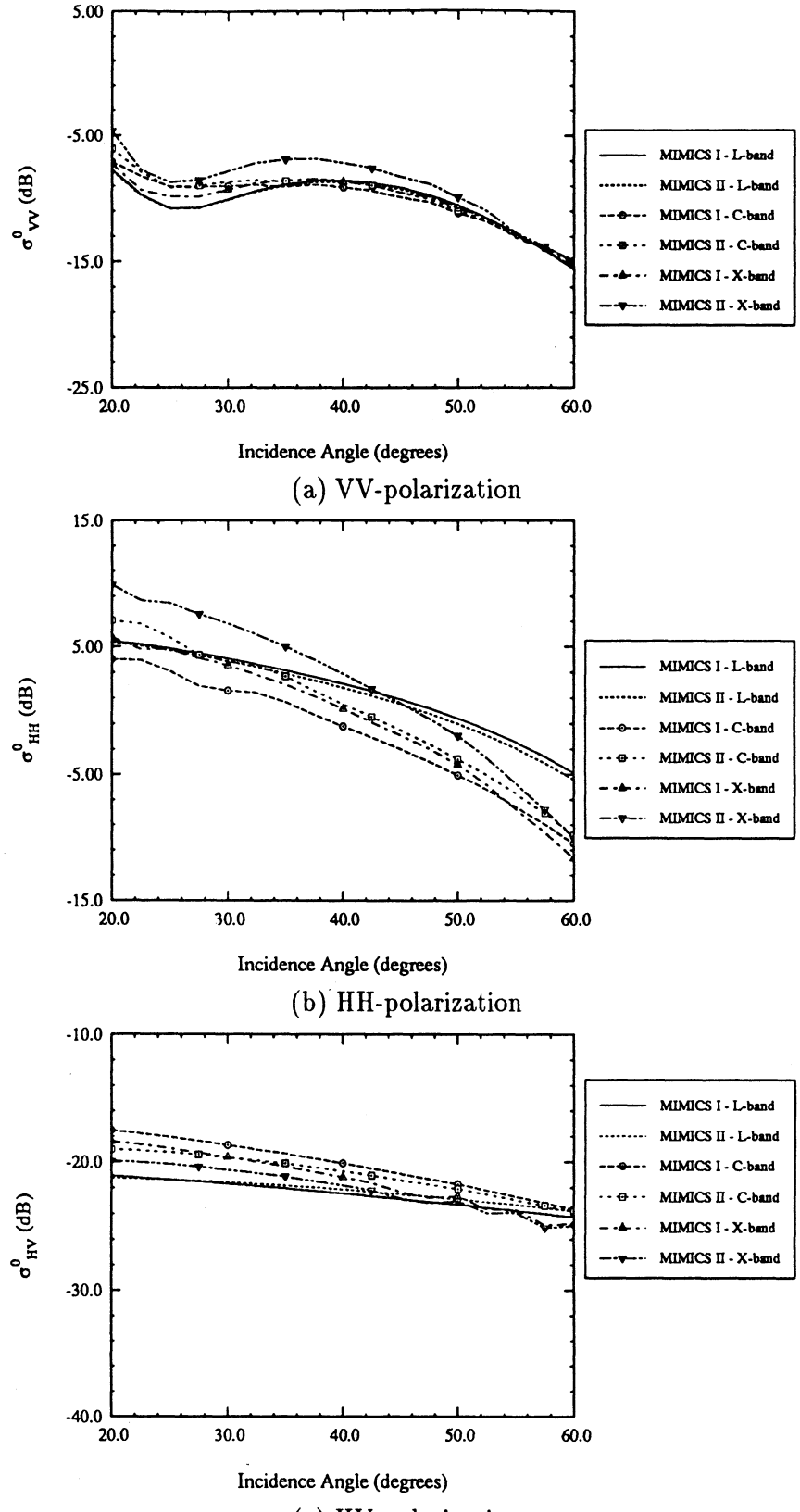

(a) VV-polarization

(b) HH-polarization

(c) HV-polarization

Figure 6.39: Backscatter from a frozen white spruce canopy modeled with a closed crown layer (MIMICS I) and with an open crown layer (MIMICS II) at (a) VV, (b) HH and (c) HV-polarization.

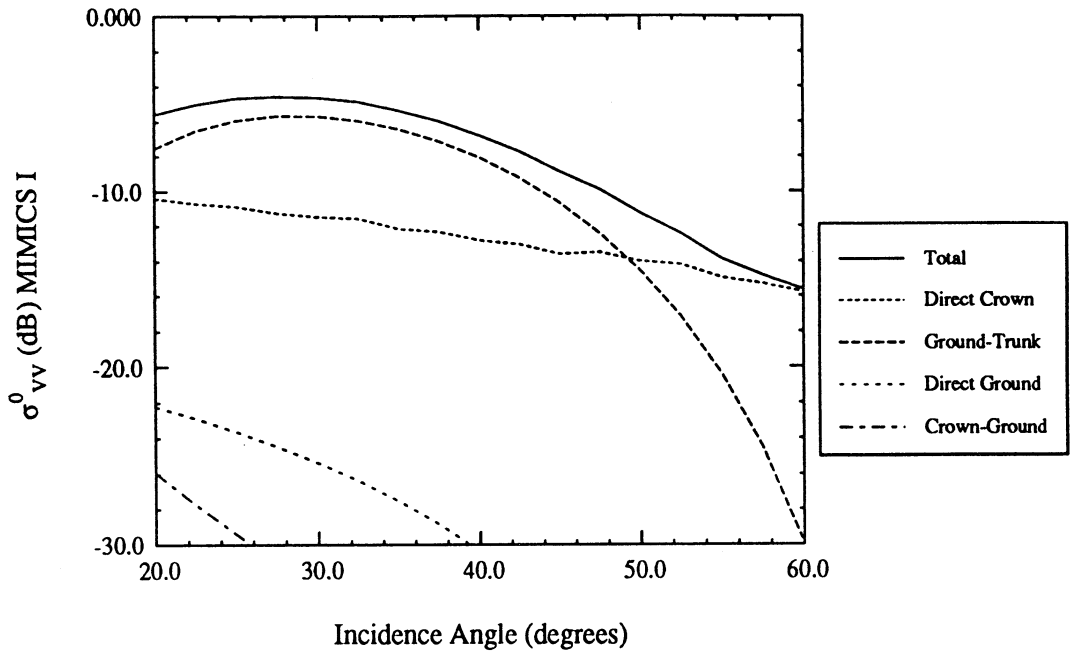

(a) Closed crown layer.

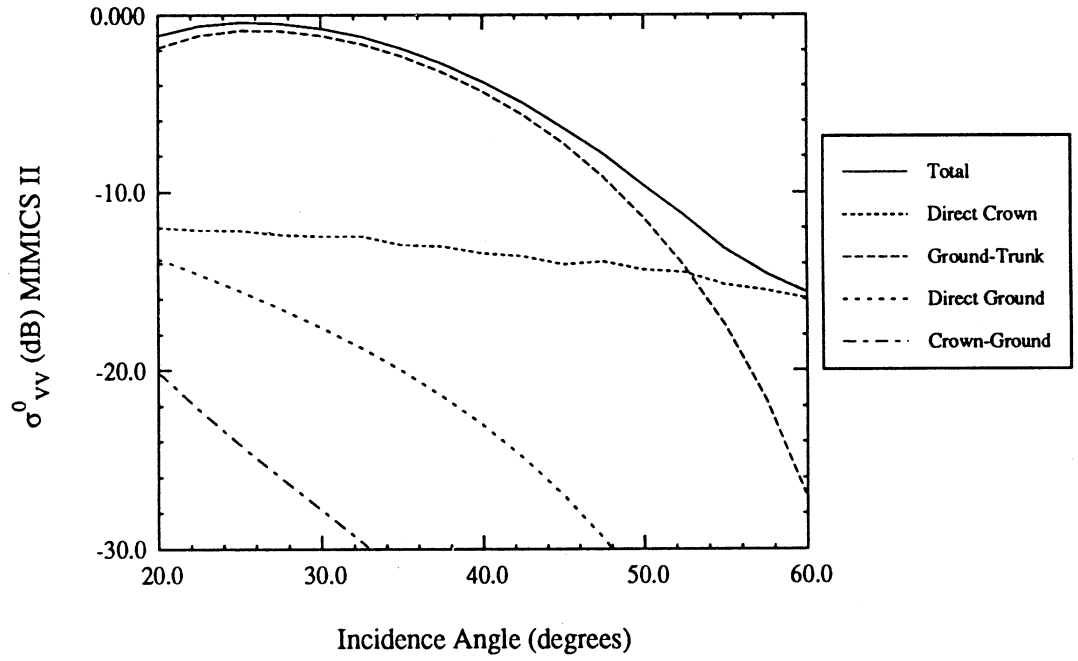

(b) Open crown layer.

Figure 6.40: Contributions to net canopy backscatter at X-band from a thawed white spruce canopy for (a) a closed-crown canopy (MIMICS I) and (b) an open-crown canopy (MIMICS II).

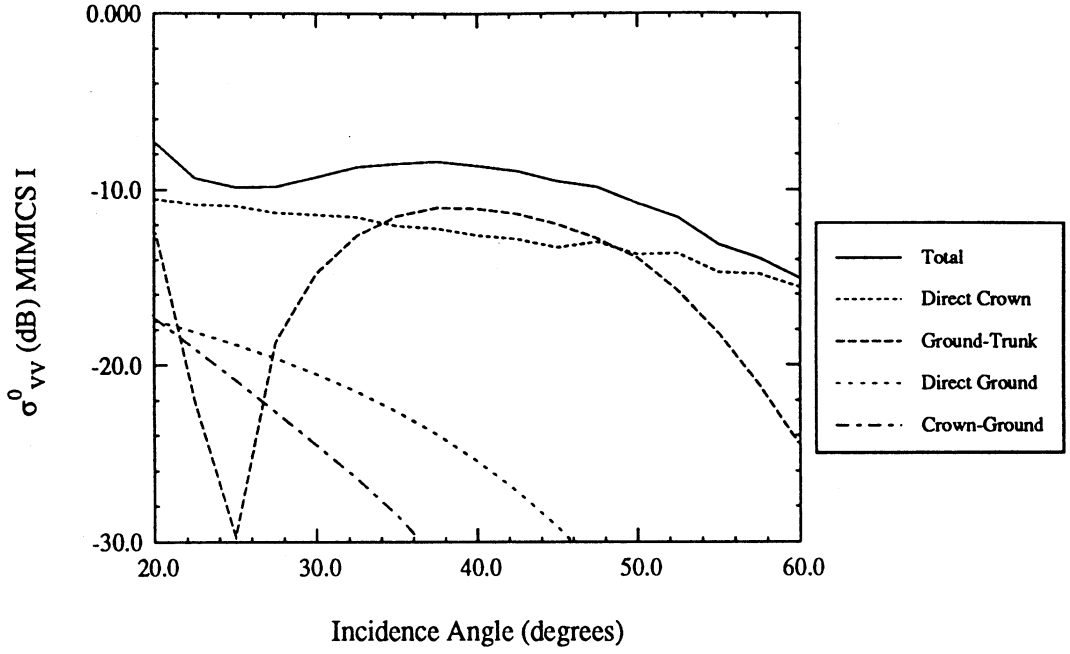

(a) Closed crown layer.

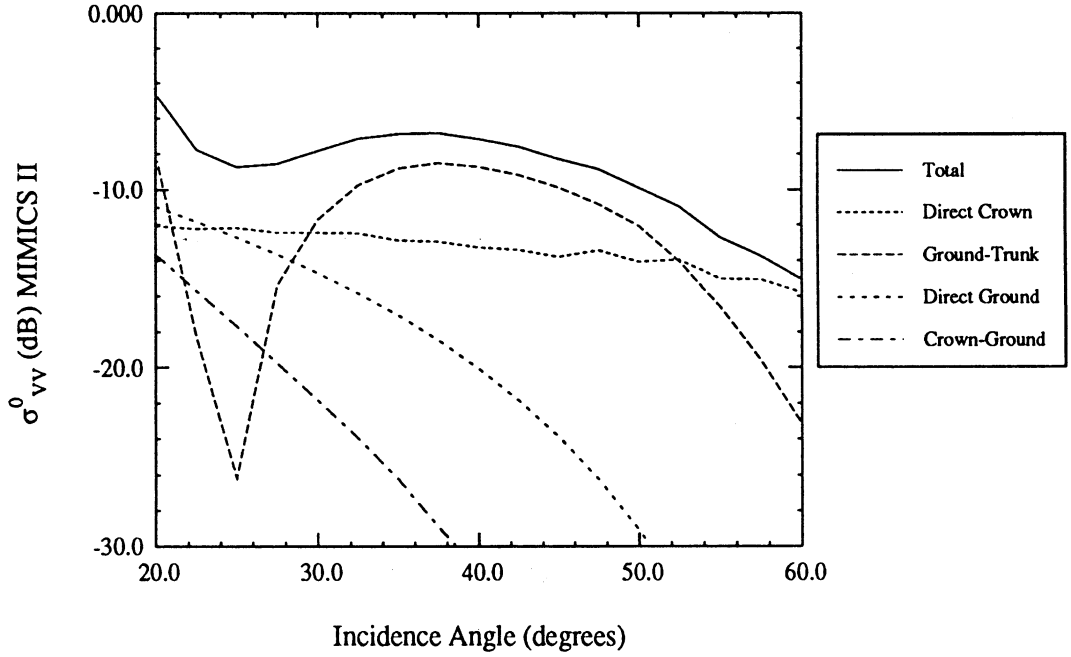

(b) Open crown layer.

Figure 6.41: Contributions to net canopy backscatter at X-band from a frozen white spruce canopy for (a) a closed-crown canopy (MIMICS I) and (b) an open-crown canopy (MIMICS II).

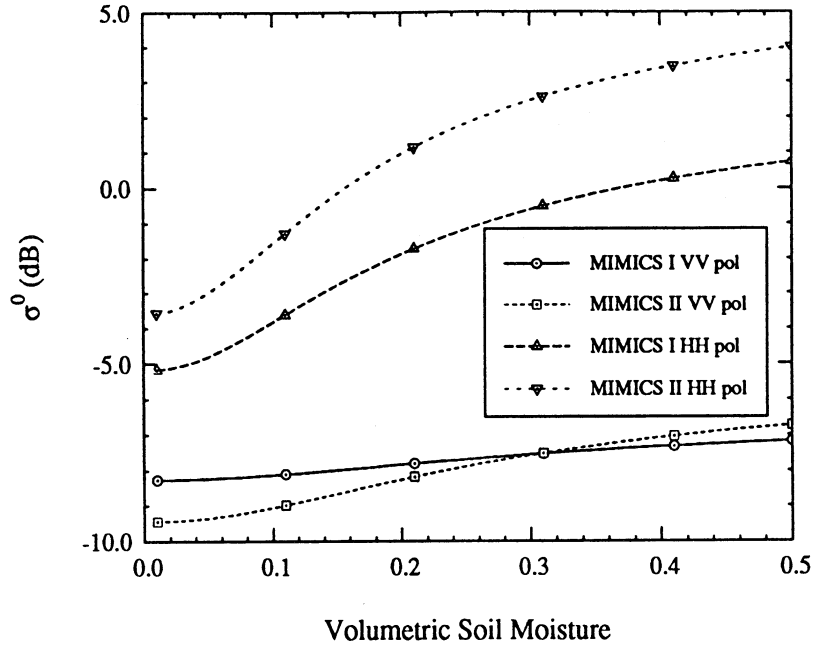

(a) Dry trunks ($\epsilon_r = 5.19 + i1.09$).

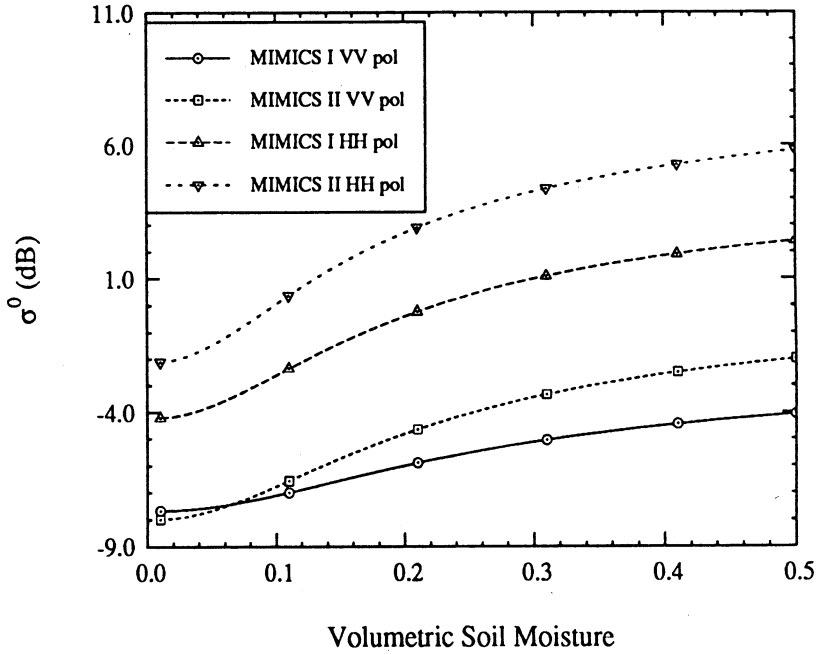

(b) Wet trunks ($\epsilon_r = 36.4 + i10.99$).

Figure 6.42: Response of L-band like-polarized canopy backscatter to changes in volumetric soil moisture for a closed-crown canopy (MIMICS I) and an open-crown canopy (MIMICS II) for a canopy with (a) dry trunks and (b) wet trunks. Simulations are for an incidence angle of $\theta = 20°$.

6.4.3 Deciduous Canopy Simulation

In Section 6.2 and in Appendix G, MIMICS I was applied to model multi-angle and multi-temporal backscatter from a walnut orchard. One conclusion of this study was that the discontinuous nature of the orchard canopy had a significant effect on backscatter at X-band. This hypothesis is now addressed by applying MIMICS II to model a deciduous canopy with tree-level parameters similar to those found in the walnut orchard. The crown volumes are assigned spherical shapes in this analysis. It should be noted that MIMICS II simulates backscatter from natural stands for which the trees are randomly distributed in location and that the orchard canopy represents a well-manicured hedgerow geometry. Therefore, a direct one-to-one comparison of MIMICS II simulations to measurement results is inappropriate.

The tree-level parameters of the open-crown canopy are summarized in Table 6.21. In addition, the leaf parameters are identical to those presented in Section 6.2 except for a number density of 308 leaves per cubic meter in each crown volume. This yields an LAI of 3.4 averaged over the canopy. Effects of leaf curvature are ignored in this analysis.

Table 6.21: Tree-level parameters for the open-crown deciduous stand.

Constituent	Mean Length	Mean Diameter	Number Density	Orientation
Primary Branches	0.38 m	2.03 cm	1.59	$\sim \sin^4 2\theta$
Secondary Branches	0.11 m	0.60 cm	1.39	$\sim \sin\theta$
Stems	18 cm	0.1 cm	308	$\sim \sin\theta$
Trunks	0.7 m	9.0 cm	308	Vertical

To simplify the modeling process, the larger size class of branches that had been placed in the trunk layer in Section 6.2 is now distributed in the crown layer, thereby leaving only the vertical trunks in the trunk layer. This yields an equivalent con-

tinuous canopy with a trunk layer 0.7 meters tall and a crown layer 4.1 meters tall. For a canopy with density 0.07 trees/m^2, the equivalent effective volume per crown in a continuous crown layer is 4.1/0.07 = 58.57 m^3 per crown. To model these as spherical crowns, let the spherical diameter $d = 4.1$ meters. Then the crown volume is $\frac{\pi}{6}d^3 = 36.09\text{m}^3$. The number density of crown constituents is then increased by 58.57/36.09 = 1.62 in going from the continuous to the discontinuous crown layer.

Table 6.22 lists the L- and X-band relative dielectric constants for the deciduous canopy. These values are consistent with those estimated for the walnut orchard.

Table 6.22: Canopy Dielectric Characteristics.

Constituent	L-Band	X-Band
Ground Surface	$25 + i2.5$	$20.2 + i7.6$
Trunk Branches	$45 + i11.2$	$35.0 + i14.8$
Primary Branches	$34 + i8.5$	$25.9 + i10.8$
Secondary Branches	$30 + i7.5$	$22.7 + i9.4$
Leaves and Stems	$28.3 + i8.5$	$21.8 + i8.8$

For spherical crowns of diameter c,

$$\int_0^\infty p(s|1)\, e^{-\lambda_i s} ds = \left(\frac{2}{c^2}\right) \frac{1}{\lambda_i^2} \left[1 - e^{-\lambda_i c}(\lambda_i c + 1)\right] \tag{6.9}$$

for each eigenvalue λ_i. Applying this relation to the polarimetric open-crown canopy model allows simulation of canopy backscatter.

Figure 6.43 shows MIMICS I and MIMICS II simulations of L- and X-band canopy transmissivity through a deciduous canopy as a function of incidence angle. The L-band transmissivity demonstrates less than 0.2 dB of difference between the open-crown and the closed-crown canopies. At X-band, however, one-way transmissivity differs by more than 1 dB between the open- and closed-crown models.

Figure 6.44 compares the like-polarized X-band backscatter simulated with MIM-

ICS I and MIMICS II. At $\theta = 20°$, there is as much as 2 dB of difference between the two models whereas at 60° there is essentially no difference. Figures 6.45 and 6.46 show the contributions to X-band canopy backscatter for VV and HH polarizations. In all cases, a significant direct ground contribution is observed. This is an artifact of a combination of the high soil dielectric ($\epsilon_r = 21.8+i8.8$ at X-band) together with the enhanced surface roughness used to account for the presence of short vegetation on the ground surface. The open-crown canopy simulations exhibit more direct ground backscatter than do the closed-crown simulations because of the increased canopy transmissivity. In addition, MIMICS II predicts less direct crown backscatter than MIMICS I. If the underlying soil surface were assumed to be as smooth as that of the walnut orchard, the net canopy backscatter for VV-polarization would in fact be dominated by the direct crown component, and MIMICS II would predict an overall decrease in the net canopy backscatter relative to MIMICS I.

Figure 6.47 illustrates the effect of varying the volume of the spherical crown while keeping the total number of scattering constituents in each crown constant. The like-polarized X-band backscatter is shown as a function of crown diameter for incidence angles of 20° and 60°. These simulations are also compared to the MIMICS I results for the continuous crown canopy. Significant differences between MIMICS I and MIMICS II are seen for the shallower incidence angle especially for small crown volumes whereas essentially no difference exists between MIMICS I and MIMICS II for $\theta = 60°$ except at crown diameters less than about 2.5 meters.

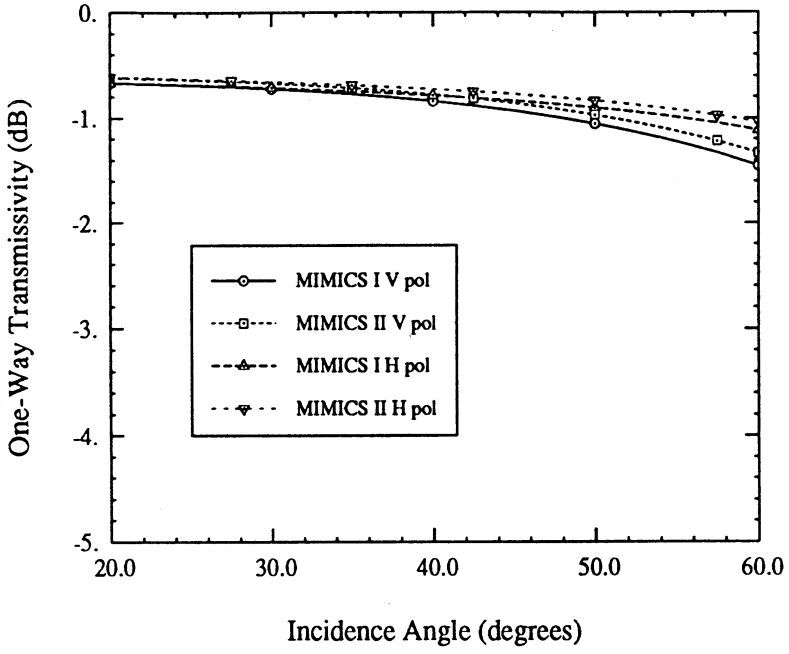

(a) L-band

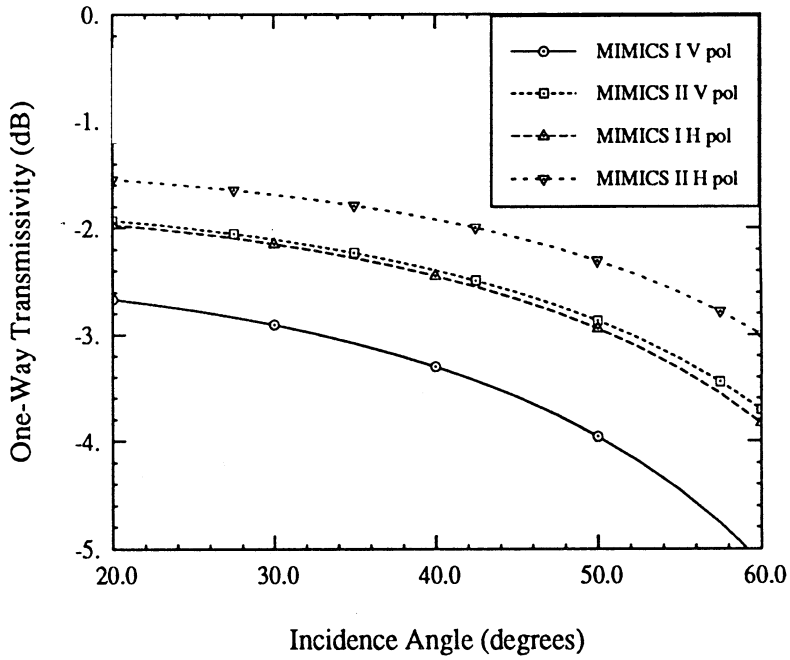

(b) X-band

Figure 6.43: Comparison of MIMICS I and MIMICS II simulations of one-way transmissivity through a deciduous canopy for (a) L-band and (b) X-band.

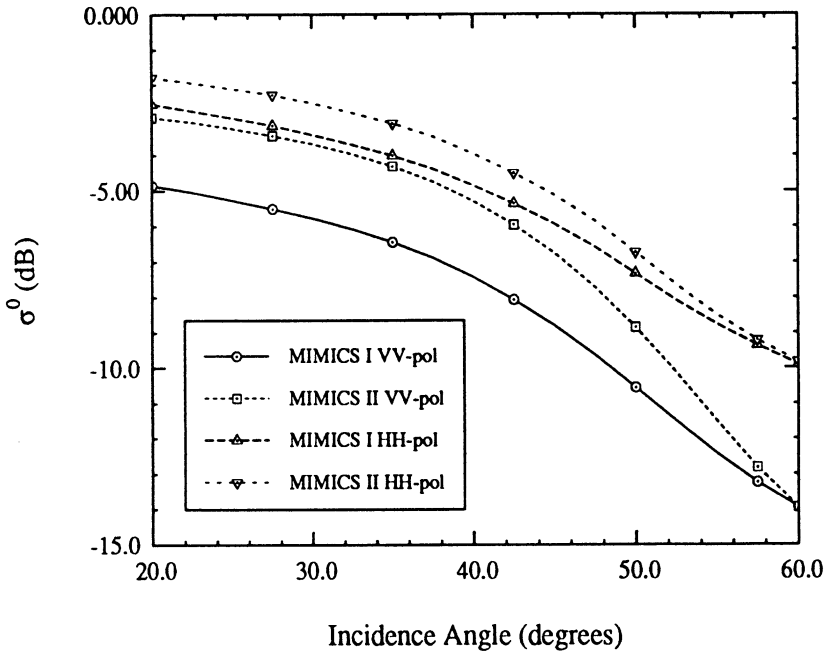

Figure 6.44: Comparison of MIMICS I and MIMICS II simulations of like-polarized X-band backscatter from a deciduous canopy.

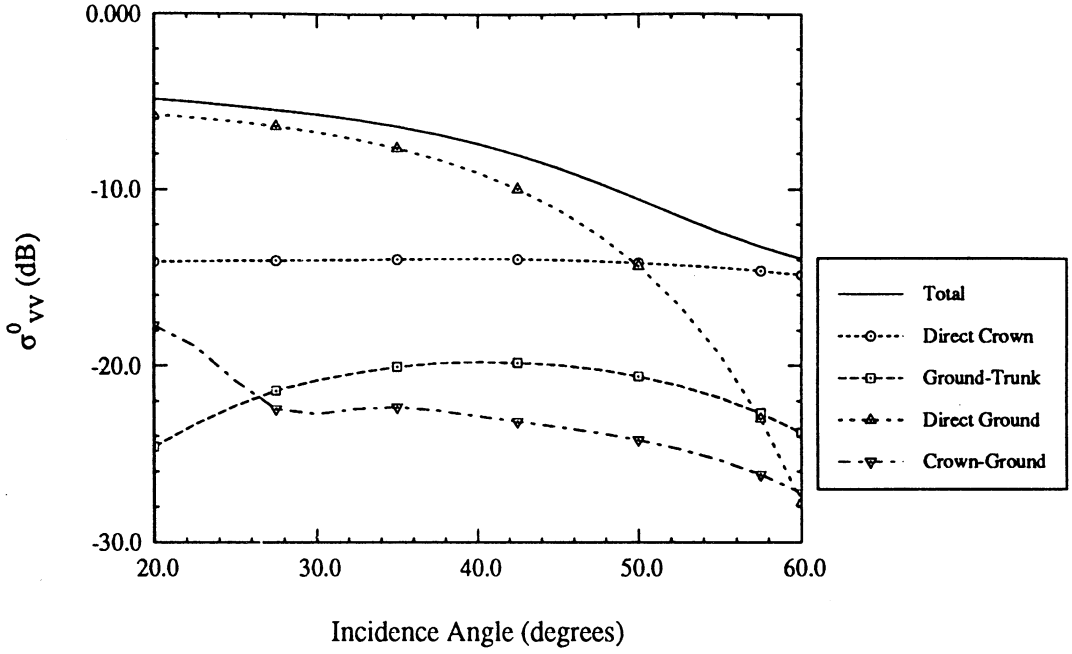

(a) Closed-crown canopy (MIMICS I)

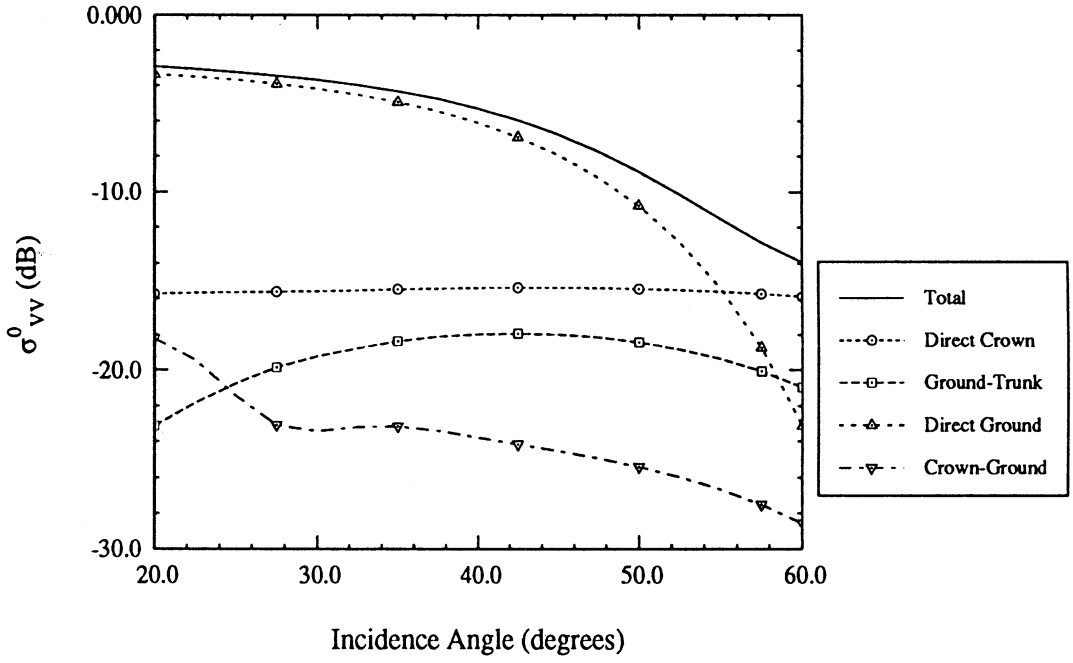

(b) Open-crown canopy (MIMICS II)

Figure 6.45: Comparison of contributions to net backscatter for (a) MIMICS I and (b) MIMICS II simulations of VV-polarized X-band backscatter from a deciduous canopy.

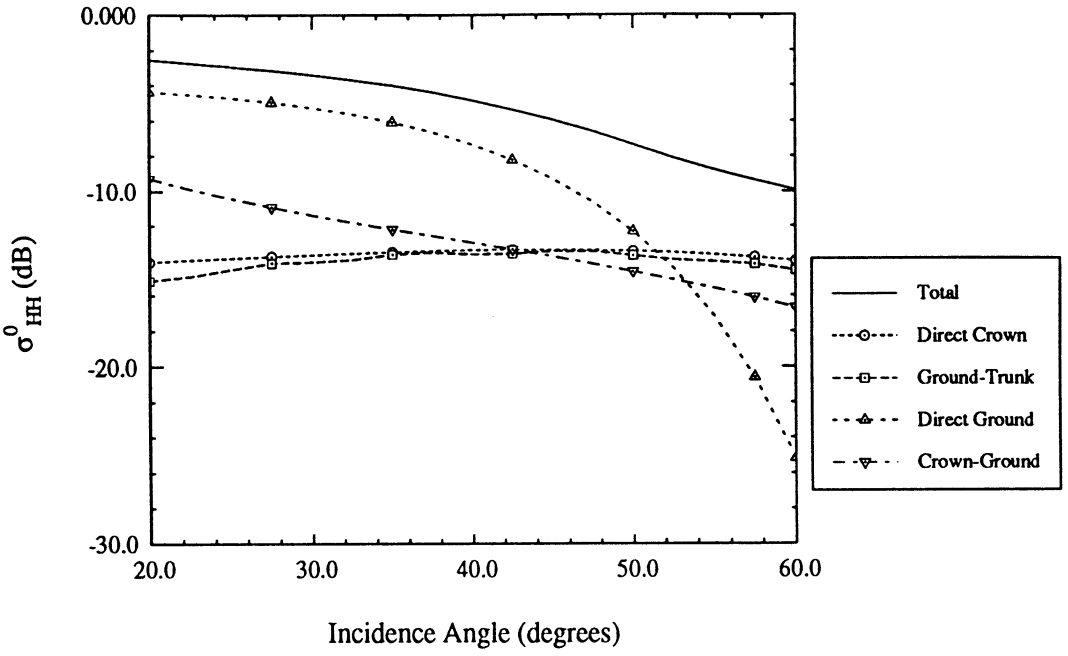

(a) Closed-crown canopy (MIMICS I)

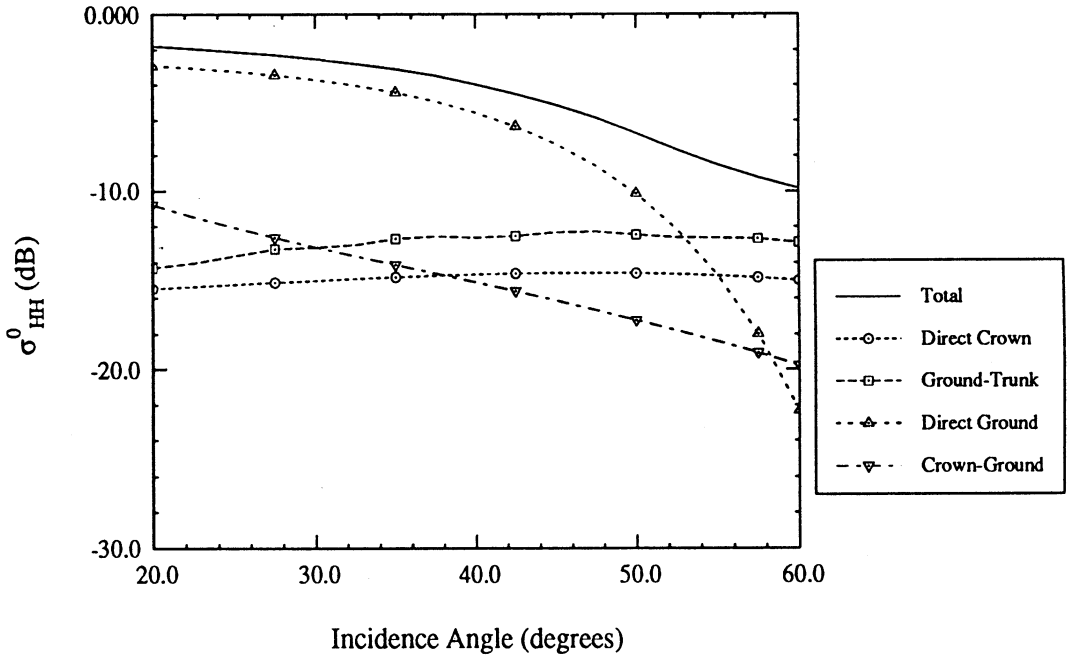

(b) Open-crown canopy (MIMICS II)

Figure 6.46: Comparison of contributions to net backscatter for (a) MIMICS I and (b) MIMICS II simulations of HH-polarized X-band backscatter from a deciduous canopy.

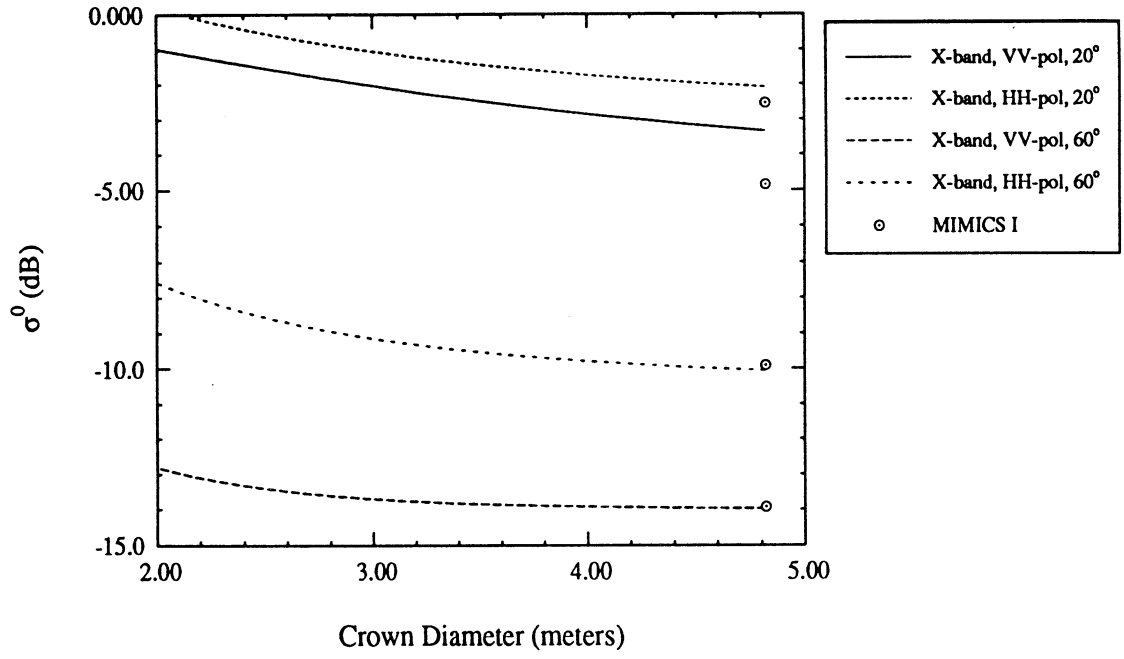

Figure 6.47: MIMICS II like-polarized X-band backscatter sensitivity to changes in crown diameter. Simulations are shown for incidence angles of 20° and 60°. The MIMICS I closed-crown canopy simulation is also shown.

6.4.4 Summary of MIMICS II Results

In this section, MIMICS II has been applied to model three different types of canopy architectures. The first represents a sparsely populated stand of black spruce trees for which the crown layer constituents contributed little to the net canopy backscatter. Accounting for the discontinuities in this canopy through the application of the open-crown canopy model demonstrated that redistributing the crown constituents into individual crown volumes had little effect on σ^0 unless these volumes were very densely packed with scatterers. The second canopy consisted of a stand of conifers which was much more fully developed. The direct crown component of backscatter from this stand was a significant contributor to the net canopy backscatter. When applying MIMICS II to account for crown layer gaps, an increase was observed in the crown layer transmissivity, and a corresponding increase in the contribution of scattering mechanisms that involve the lower canopy layers (trunk and ground) followed. A decrease in the direct crown backscatter was also observed. The third canopy represented a fully-foliated deciduous stand. Here, MIMICS II predicted a significant difference in the canopy backscatter (compared to MIMICS I) at X-band.

In general, the effects of the discontinuous crown layer geometries were found to be most prevalent at high frequencies and at low incidence angles. The canopies under study therefore appear more continuous from a radar perspective at high incidence angles, where a significant number of crown volumes are penetrated by the radar, and at low frequencies, where extinction in the crown volumes is less significant. Implications of accounting for the crown layer gaps were addressed in the analysis of the fully developed coniferous canopy, where an increase was observed in simulated backscatter response to changes in soil moisture. This is a direct result of the increase

in crown layer transmissivity which in effect allows the radar to see through to the lower layers of the canopy more easily.

As with MIMICS I, MIMICS II models tree canopies as having distinct crown and trunk layers. In this approach, the positioning of the trunks is completely uncorrelated with the placement of the individual crown volumes. While this approximation has a negligible effect on backscatter for many canopy geometries, it may overestimate trunk-ground backscatter for other geometries. Cases in which this may be a problem include coniferous canopies in which the trunks extend a significant distance into the crown volumes. Effects of this limitation may be analyzed by eliminating the trunk layer and distributing the trunks within the crown layer as vertical branches. Thus the canopy is modeled as a single layer of vegetation with one trunk per crown volume. Modeling the canopy in this way allows for the placement of the individual trunks to be directly coupled with the location of the crown volumes.

CHAPTER VII

CONCLUSIONS AND RECOMMENDATIONS

7.1 Summary

This thesis has presented the development of a first-order radiative transfer model for simulating microwave backscatter from tree canopies (MIMICS). The model is fully polarimetric and accounts for a wide variety of canopy architectures. The fundamental contribution of this work has been the presentation of a model for tree canopies that have discontinuous crown layer geometries (MIMICS II). The radiative transfer solution derived for the closed-crown canopy geometry (MIMICS I) has been extended to account for the open-crown geometry. Statistics have been developed that describe the scattering and extinction properties of individual crown volumes and these statistics have been introduced into the radiative transfer solution.

MIMICS has been very useful in coupling canopy biophysical parameters to measured radar data in a number of modeling studies. In particular, when used to model L- and X-band scatterometer measurements of a walnut orchard, the model not only successfully accounted for the variation in measured backscatter as a function of radar incidence angle, but it also accounted for the variations in σ^0 observed on 24 hour and longer time scales. Using the model, it has been possible to couple these variations in σ^0 to variations in soil moisture and canopy water status. When used

to model backscatter from and transmissivity through Alaskan boreal forest stands, MIMICS successfully accounted for variations occurring as functions of species and canopy freeze/thaw state. In both of these analyses, canopy dielectric properties have been shown to be very important parameters in modeling the canopy scattering and attenuation.

Model simulations have been performed in which results computed with the open-crown model were compared to results computed with the closed-crown model for canopies with the same total number of scattering constituents in the crown layer. Results of these analyses have demonstrated that the gaps that occur in the crown layer of a discontinuous canopy may significantly affect the crown layer transmissivity and the canopy backscatter. Generally speaking, for trees whose crowns are not well developed the crown layer has an insignificant contribution to the total canopy backscatter and the difference between the MIMICS I and MIMICS II solutions is small. However, for more well-developed canopies the crown layer constituents may contribute significantly to the net backscatter and therefore the crown layer gaps have an important effect on σ^0. This effect becomes more pronounced at shallow incidence angles and at higher frequencies. As incidence angle increases, and as frequency decreases the open-crown and closed-crown backscatter solutions become very similar.

In spite of the remarkable success obtained in applying MIMICS, there have been some difficulties in simulating some measured data. Most notably, the accuracy of MIMICS is questionable for cross-polarized configurations at X-band. This problem occurred in modeling X-band backscatter from the walnut orchard, and is attributed to the fact that MIMICS, being a first-order model, does not account for multiple scattering contributions.

7.2 Recommendations for Future Work

Several projects may be considered as natural extensions of this work. MIMICS has been shown to accurately model multi-polarized backscatter at lower frequencies (L-band). However the accuracy of results obtained for cross-polarized backscatter at X-band have been questionable. For this reason, techniques for obtaining numerically efficient estimates of second- and higher-order scattering should be explored. In addition to studying higher order scattering in the crown layer, a more general second-order model that accounts for multiple scatter between canopy layers should be explored. For example, effects of scattering interactions between the trunk and crown layers may be significant in some coniferous stands in which the trunks extend far into the crowns.

In studying sparsely populated canopies and any canopy for which scatter from the underlying ground surface becomes important, the accuracy of the ground surface scattering models comes into question. This is especially true for natural forest canopies in which the underlying surface may have a very complex structure. The characteristics of understory and litter layers should be accounted for.

In considering more varied types of forest stand geometries, it may be desirable to account for canopies that consist of more than one tree species. The techniques discussed in Chapter V may be extended to define statistical parameters over a second set of canopy- and tree-level random variables, thereby defining effective phase and extinction matrices for a mixed stand. Applications of this type become important when studying forest succession processes.

Beyond these issues of model development, the inversion problem needs to be addressed so that useful information about canopy parameters may be obtained by

coupling the model to radar measurements. MIMICS inversion algorithms should attempt to provide estimates of soil moisture, canopy water status and total canopy biomass. This final aspect will provide a significant advance in understanding the role of forest ecosystems in the global carbon cycle.

APPENDICES

APPENDIX A

DIELECTRIC MODELS FOR CANOPY CONSTITUENTS

This appendix describes the relationships of the dielectric constants of the various canopy constituents to their respective moisture contents. Section A.1 discusses the variation of vegetation dielectric with gravimetric water content. The same dielectric model is used for all vegetation material, including leaves, trunks and branches. The dielectric behavior is governed by the gravimetric moisture content m_g and the bulk density ρ, which together define the volumetric moisture content m_v. The model used to relate the dielectric constant of soil to its volumetric water content is given in Section A.2. This section also provides expressions for the dielectric constant of standing water. In all cases, the dielectric constants are assumed to have the form $\epsilon = \epsilon' - j\epsilon''$. Note that in order to apply results derived from these models as inputs to MIMICS, the complex conjugate of ϵ should be used such that the dielectric constants are of the form $\epsilon = \epsilon' + i\epsilon''$.

A.1 Dielectric Behavior of Vegetation

A.1.1 Model in Terms of Volumetric Moisture

Ulaby and El-Rayes [63] have shown that the dielectric constant of vegetation material may be modeled by a Debye-Cole dual-dispersion model. This model consists

of a free water component that accounts for the volume of the vegetation occupied by water in free form and a bound water component that accounts for the volume of the vegetation occupied by water molecules bound to bulk vegetation molecules. Based on this model, the dielectric constant for vegetation is given by:

$$\epsilon = A + B\left(4.9 + \frac{\epsilon_s - \epsilon_\infty}{1 + j\frac{f(\mathrm{Hz})}{f_o}} - j\frac{22.74}{f(\mathrm{GHz})}\right) + C\left(2.9 + \frac{55}{1 + \sqrt{j\frac{f(\mathrm{GHz})}{0.18}}}\right) \tag{A.1}$$

where f(Hz) is frequency in Hz, f(GHz) is frequency in GHz, and

$$\epsilon_\infty = 4.9 \tag{A.2}$$

$$\epsilon_s = 88.045 - 0.4147T + 6.295 \times 10^{-4}T^2 + 1.075 \times 10^{-5}T^3 \tag{A.3}$$

$$f_o = (2\pi\tau)^{-1} \tag{A.4}$$

$$(2\pi\tau) = 1.1109 \times 10^{-10} - 3.824 \times 10^{-12}T + 6.938 \times 10^{-14}T^2 - 5.096 \times 10^{-16}T^3. \tag{A.5}$$

where T is temperature in °C and (A.4) gives f_o in Hz. Given the gravimetric moisture content m_g and the bulk density of the dry vegetation material ρ, the volumetric water content m_v of the vegetation material may be found from

$$m_v = \frac{m_g\rho}{1 - m_g(1 - \rho)}. \tag{A.6}$$

The constants A,B and C are then computed using

$$A = 1.7 + 3.2m_v + 6.5m_v^2 \tag{A.7}$$

$$B = m_v(0.82m_v + 0.166) \tag{A.8}$$

$$C = \frac{31.4m_v^2}{59.5m_v^2 + 1}. \tag{A.9}$$

A.1.2 Model for Leaves

For leafy vegetation, A, B and C in (A.1) may be computed directly from the moisture gravimetric fraction. The constants become

$$A = 1.7 - 0.74m_g + 6.16m_g^2 \tag{A.10}$$

$$B = m_g(0.55m_g - 0.076) \tag{A.11}$$

$$C = \frac{4.64m_g^2}{7.36m_g^2 + 1}. \tag{A.12}$$

The dielectric model given by (A.1) has been found to give excellent agreement with experimental data over a wide range of moisture conditions and over a frequency range extending from 0.2 to 20 GHz. It is used together with (A.6) through (A.9) to model the dielectric constants of trunks and branches and with (A.10) through (A.12) to model the dielectric constant of leaves.

A.2 Dielectric Behavior of the Ground Surface

In this section, the dielectric properties for two types of ground surfaces are considered. The first is a soil surface consisting of a mixture of sand, silt and clay. The second is a standing water surface. The dielectric constant for the soil surface is determined using an empirical model whereas a semi-analytic model is used to predict the dielectric of a standing water surface.

A.2.1 Soil

Hallikainen *et al.*, [25] expressed the dielectric constant of soil consisting of a mixture of sand, silt and clay as

$$\epsilon_s = \epsilon_s' - j\epsilon_s'' \tag{A.13}$$

where the real and imaginary parts each fit a polynomial of the form

$$\epsilon = (a_0 + a_1 S + a_2 C) + (b_0 + b_1 S + b_2 C)\, m_v + (c_0 + c_1 S + c_2 C)\, m_v^2, \quad \text{(A.14)}$$

$$\epsilon = \epsilon_s' \text{ or } \epsilon_s''.$$

Here, m_v is the soil volumetric moisture content while S and C are the sand and clay textural components of the soil in percent by weight. The polynomial coefficients are listed in Table E.1 and the prediction accuracy of the model is given by Hallikainen *et al.*, [25].

Table E.1.

Coefficients of Polynomial Expressions

Frequency (GHz)	a_0	a_1	a_2	b_0	b_1	b_2	c_0	c_1	c_2
Coefficients for Computing ϵ_s'									
1.4	2.862	-0.012	0.001	3.803	0.462	-0.341	119.006	-0.500	0.633
4	2.927	-0.012	-0.001	5.505	0.371	0.062	114.826	-0.389	-0.547
6	1.993	0.002	0.015	38.086	-0.176	-0.633	10.720	1.256	1.522
8	1.997	0.002	0.018	25.579	-0.017	-0.412	39.793	0.723	0.941
10	2.502	-0.003	-0.003	10.101	0.221	-0.004	77.482	-0.061	-0.135
12	2.200	-0.001	0.012	26.473	0.013	-0.523	34.333	0.284	1.062
14	2.301	0.001	0.009	17.918	0.084	-0.282	50.149	0.012	0.387
16	2.237	0.002	0.009	15.505	0.076	-0.217	48.260	0.168	0.289
18	1.912	0.007	0.021	29.123	-0.190	-0.545	6.960	0.822	1.195
Coefficients for Computing ϵ_s''									
1.4	0.356	-0.003	-0.008	5.507	0.044	-0.002	17.753	-0.313	0.206
4	0.004	0.001	0.002	0.951	0.005	-0.010	16.759	0.192	0.290
6	-0.123	0.002	0.003	7.502	-0.058	-0.116	2.942	0.452	0.543
8	-0.201	0.003	0.003	11.266	-0.085	-0.155	0.194	0.584	0.581
10	-0.070	0.000	0.001	6.620	0.015	-0.081	21.578	0.293	0.332
12	-0.142	0.001	0.003	11.868	-0.059	-0.225	7.817	0.570	0.801
14	-0.096	0.001	0.002	8.583	-0.005	-0.153	28.707	0.297	0.357
16	-0.027	-0.001	0.003	6.179	0.074	-0.086	34.126	0.143	0.206
18	-0.071	0.000	0.003	6.938	0.029	-0.128	29.945	0.275	0.377

This model is independent of soil temperature. In general, the dielectric constant of soil changes very little with temperature for soil that is not frozen. For soil temperatures below freezing, however, the temperature dependence becomes more important. Variations in the real and imaginary parts of ϵ_s as a function of temperature and moisture content are shown in Ulaby *et al.*, [70], p. 2099.

A.2.2 Standing Water

The dielectric constant of standing water is, in general, a function of the water salinity S. At frequencies above 5 GHz, however, salinity exercises a negligible influence on ϵ and, therefore, S may be set to zero in the expressions below (Ulaby *et al.*, [70] pp. 2020-2025):

$$\epsilon_{sw} = \epsilon'_{sw} - j\epsilon''_{sw} \tag{A.15}$$

$$\epsilon'_{sw} = \epsilon_{sw\infty} + \frac{\epsilon_{sw0} - \epsilon_{sw\infty}}{1 + (2\pi f \tau_{sw})^2} \tag{A.16}$$

$$\epsilon''_{sw} = \frac{2\pi f \tau_{sw} (\epsilon_{sw0} - \epsilon_{sw\infty})}{1 + (2\pi f \tau_{sw})^2} + \frac{\sigma_i}{2\pi \epsilon_0 f} \tag{A.17}$$

where ϵ_0 is the permittivity of free space, $\epsilon_{sw\infty} = 4.9$ and f is frequency in Hz.

In general, ϵ_{sw0} varies with salinity S (parts per thousand) and temperature T (°C) as

$$\epsilon_{sw0}(T,S) = \epsilon_{sw0}(T,0) \cdot a(T,S) \tag{A.18}$$

where

$$\epsilon_{sw0}(T,0) = 87.134 - 0.1949T - 0.01276T^2 + 2.491 \times 10^{-4}T^3 \tag{A.19}$$

$$a(T,S) = 1.0 + 1.613 \times 10^{-5}TS - 3.656 \times 10^{-3}S + 3.210 \times 10^{-5}S^2 - 4.232 \times 10^{-7}S^3. \tag{A.20}$$

These expressions are based on data generated for salinities in the range $4 < S < 35$.

Similarly, the relaxation time τ_{sw} may be expressed as

$$\tau_{sw}(T,S) = \tau_{sw}(T,0) \cdot b(T,S) \tag{A.21}$$

where

$$\tau_{sw}(T,0) = \left(\frac{1}{2\pi}\right)(1.1109 \times 10^{-10} - 3.824 \times 10^{-12}T$$

$$+6.938 \times 10^{-14}T^2 - 5.096 \times 10{-}16T^3) \tag{A.22}$$

$$b(T,S) = 1.0 + 2.282 \times 10^{-5}TS - 7.38 \times 10^{-4}S$$

$$-7.760 \times 10^{-6}S^2 + 1.105 \times 10^{-8}S^3. \tag{A.23}$$

This expression is based on data for $0 \leq T \leq 40°C$ and $0 \leq S \leq 157$ for a solution of NaCl.

Finally, the ionic conductivity σ_i is

$$\sigma_i(T,S) = \sigma_i(25,S)\, e^{-\phi} \tag{A.24}$$

where

$$\sigma_i(25,S) = S\Big[0.18252 - 1.4619 \times 10^{-3}S$$

$$+2.093 \times 10^{-5}S^2 - 1.282 \times 10^{-7}S^3\Big] \tag{A.25}$$

$$\phi = \Delta\Big[2.033 \times 10^{-2} + 1.266 \times 10^{-4}\Delta + 2.464 \times 10^{-6}\Delta^2$$

$$-S(1.849 \times 10^{-5} - 2.551 \times 10^{-7}\Delta$$

$$+2.551 \times 10^{-8}\Delta^2)\Big] \tag{A.26}$$

with $\Delta = 25 - T$. These expressions are valid for $0 \leq S \leq 40$.

A.2.3 Snow Layer

Hallikainen *et al.*,[24], have modeled the dielectric constant of a wet snow layer with a Debye-like model. The relative dielectric constant of snow $\epsilon_r = \epsilon_r' - j\epsilon_r''$ is given by

$$\epsilon_r' = A + \frac{Bm_v^x}{1 + (f/f_0)^2} \tag{A.27}$$

$$\epsilon_r'' = \frac{C + (f/f_0)m_v^x}{1 + (f/f_0)^2} \tag{A.28}$$

where m_v is the snow wetness (volume %), f is frequency in GHz, f_0 is the relaxation frequency of liquid water at 0°C (GHz) and the coefficients A, B, C and x are empirically derived for $f \leq 15$ GHz as

$$\begin{aligned} A &= 1.0 + 1.83\rho_{ds} + 0.02m_v^{1.015} \\ B &= C = 0.073 \\ x &= 1.31 \end{aligned}$$

where ρ_{ds} is the dry snow density (g/cm^3).

APPENDIX B

SCATTERING MODELS FOR ROUGH SURFACES

This appendix describes three models for backscatter from rough surfaces. A rough surface may be characterized in terms of the *surface correlation length*, l, and the *standard deviation of surface height*, s. The solutions presented here are derived by Ulaby and Elachi [62], Chapter 4, and, although valid only within a limited range of l and s, may still be used quite effectively in many situations. The three models presented are (1) the Kirchhoff model under the stationary phase approximation (also known as the geometrical optics model), (2) the Kirchoff model under the scalar approximation (also known as the physical optics model), and (3) the small perturbation model. Loosely speaking, the geometrical optics model is best suited for very rough surfaces, the physical optics model is suitable for surfaces with intermediate scales of roughness, and the small perturbation model is suitable for surfaces with short correlation lengths. Model forms given here are for surfaces with correlation functions of the form $\rho(\xi) = \exp(-\xi^2/l^2)$. The validity conditions for these models are:

- Geometrical optics model:

$$kl > 6, \quad \frac{l^2}{2.76s} > \lambda, \quad ks > \frac{\sqrt{10}}{2\cos\theta_i}$$

- Physical optics model:

$$kl > 6, \quad \frac{l^2}{2.76s} > \lambda, \quad m < 0.25$$

- Small perturbation model:

$$kl < 0.3, \quad m < 0.3, \quad kl < 3.0$$

where λ is the radar wavelength, k is the wavenumber, θ_i is the radar incidence angle and $m = \sqrt{2}s/l$ is the RMS surface slope.

To define the scattering problem geometry, consider a field incident on a rough surface in direction $\hat{\mathbf{k}}_i$ and scattered in direction $\hat{\mathbf{k}}_s$. Let $\hat{\mathbf{v}}_i$ and $\hat{\mathbf{h}}_i$ denote the unit polarization vectors for the vertical and horizontal components of the incident field, and let $\hat{\mathbf{v}}_s$ and $\hat{\mathbf{h}}_s$ denote the unit polarization vectors for the scattered field. These unit vectors are given in terms of the inclination and azimuth angles for the incident and scattered fields, (θ_i, ϕ_i) and (θ_s, ϕ_s), by the following relations:

$$\hat{\mathbf{k}}_f = \hat{\mathbf{x}} \sin\theta_f \cos\phi_f + \hat{\mathbf{y}} \sin\theta_f \sin\phi_f + \hat{\mathbf{z}} \cos\theta_f \tag{B.1}$$

$$\hat{\mathbf{h}}_f = -\hat{\mathbf{x}} \sin\phi_f + \hat{\mathbf{y}} \cos\phi_f \tag{B.2}$$

$$\hat{\mathbf{v}}_f = \hat{\mathbf{h}}_f \times \hat{\mathbf{k}}_f = \hat{\mathbf{x}} \cos\theta_f \cos\phi_f + \hat{\mathbf{y}} \cos\theta_f \sin\phi_f - \hat{\mathbf{z}} \sin\theta_f, \tag{B.3}$$

where the subscript $f \in \{i, s\}$ represents either the incident or the scattered wave. For the backscattering case, $\theta_s = \pi - \theta_i$ and $\phi_s = \pi + \phi_i$.

B.1 Geometrical Optics Model

For a field with wavenumber k_1 incident on a rough surface, the correlation products of scattering matrix elements used to compute the Stokes scattering operator are given by

$$\langle S_{pq} S^*_{mn} \rangle = \frac{A|k_1|^2 q^2}{8\pi q_z^4 m^2} U_{pq} U^*_{mn} \exp\left[-\frac{q_x^2 + q_y^2}{2q_z^2 m^2}\right] . \tag{B.4}$$

The polarization dependent quantities are

$$U_{vv} = -\frac{q|q_z|}{q_z k_1 D^2}[r_v(\hat{\mathbf{v}}_s\cdot\hat{\mathbf{k}}_i)(\hat{\mathbf{v}}_i\cdot\hat{\mathbf{k}}_s) + r_h(\hat{\mathbf{h}}_s\cdot\hat{\mathbf{k}}_i)(\hat{\mathbf{h}}_i\cdot\hat{\mathbf{k}}_s)] \tag{B.5}$$

$$U_{vh} = -\frac{q|q_z|}{q_z k_1 D^2}[r_v(\hat{\mathbf{v}}_s\cdot\hat{\mathbf{k}}_i)(\hat{\mathbf{h}}_i\cdot\hat{\mathbf{k}}_s) - r_h(\hat{\mathbf{h}}_s\cdot\hat{\mathbf{k}}_i)(\hat{\mathbf{v}}_i\cdot\hat{\mathbf{k}}_s)] \tag{B.6}$$

$$U_{hv} = -\frac{q|q_z|}{q_z k_1 D^2}[r_v(\hat{\mathbf{h}}_s\cdot\hat{\mathbf{k}}_i)(\hat{\mathbf{v}}_i\cdot\hat{\mathbf{k}}_s) - r_h(\hat{\mathbf{v}}_s\cdot\hat{\mathbf{k}}_i)(\hat{\mathbf{h}}_i\cdot\hat{\mathbf{k}}_s)] \tag{B.7}$$

$$U_{hh} = -\frac{q|q_z|}{q_z k_1 D^2}[r_v(\hat{\mathbf{h}}_s\cdot\hat{\mathbf{k}}_i)(\hat{\mathbf{h}}_i\cdot\hat{\mathbf{k}}_s) + r_h(\hat{\mathbf{v}}_s\cdot\hat{\mathbf{k}}_i)(\hat{\mathbf{v}}_i\cdot\hat{\mathbf{k}}_s)] \tag{B.8}$$

$$q^2 = q_x^2 + q_y^2 + q_z^2 = 2k_1^2\left[1 - (\hat{\mathbf{k}}_s\cdot\hat{\mathbf{k}}_i)\right] \tag{B.9}$$

$$q_x = k_1(\sin\theta_i\cos\phi_i - \sin\theta_s\cos\phi_s) \tag{B.10}$$

$$q_y = k_1(\sin\theta_i\sin\phi_i - \sin\theta_s\sin\phi_s) \tag{B.11}$$

$$q_z = k_1(\cos\theta_i - \cos\theta_s) \tag{B.12}$$

$$D = \sqrt{(\hat{\mathbf{k}}_i\cdot\hat{\mathbf{v}}_s)^2 + (\hat{\mathbf{k}}_i\cdot\hat{\mathbf{h}}_s)^2}, \tag{B.13}$$

A is the illuminated area, and r_v and r_h are the Fresnel reflection coefficients of the surface for v and h polarizations, respectively.

B.2 Physical Optics Model

In this case, the correlation products of scattering matrix elements are

$$\langle S_{pq}S_{mn}^*\rangle = \frac{|k_1|^2}{16\pi^2}\,(I_c + I_i + I_s). \tag{B.14}$$

The first term, I_c, represents coherent scattering from the surface and is present only in the specular direction with respect to the mean surface. The second term, I_i, represents incoherent scattering, and the third term, $I_s = I_{sx} + I_{sy}$, represents

incoherent scattering due to the surface slopes. These terms are given by

$$I_i = \pi l^2 A a_{pq} a^*_{mn} e^{-q_z^2 s^2} \sum_{n=1}^{\infty} \frac{(q_z s)^{2n}}{n! n} \exp\left[-\frac{q_t^2 l^2}{4n}\right] \tag{B.15}$$

$$I_{sx} = -\pi A q_x K_x l^2 e^{-q_z^2 s^2} \sum_{n=1}^{\infty} \frac{(q_z s)^{2(n-1)}}{n! n} \exp\left[-\frac{q_t^2 l^2}{4n}\right] \tag{B.16}$$

$$I_{sy} = -\pi A q_y K_y l^2 e^{-q_z^2 s^2} \sum_{n=1}^{\infty} \frac{(q_z s)^{2(n-1)}}{n! n} \exp\left[-\frac{q_t^2 l^2}{4n}\right] \tag{B.17}$$

$$I_c = a_{pq} a^*_{mn} (2\pi)^2 A \delta(q_x)\delta(q_y) e^{-q_z^2 s^2} \tag{B.18}$$

where q_x, q_y and q_z are given by (B.10) - (B.12), $q_t^2 = q_x^2 + q_y^2$,

$$\delta(q_x)\delta(q_y) = \begin{cases} \dfrac{A}{(2\pi)^2} & q_x = q_y = 0 \\ 0 & \text{otherwise,} \end{cases} \tag{B.19}$$

$$K_x = q_z s^2 (b_{pq} a^*_{mn} + a_{pq} b^*_{mn}) \tag{B.20}$$

$$K_y = q_z s^2 (c_{pq} a^*_{mn} + a_{pq} c^*_{mn}), \tag{B.21}$$

$$a_{pq} = \begin{cases} r_{v0}(\cos\theta_i - \cos\theta_s)\cos(\phi_s - \phi_i) & pq = vv \\ r_{h0}(\cos\theta_i \cos\theta_s - 1)\sin(\phi_s - \phi_i) & pq = vh \\ r_{v0}(1 - \cos\theta_i \cos\theta_s)\sin(\phi_s - \phi_i) & pq = hv \\ r_{h0}(\cos\theta_i - \cos\theta_s)\cos(\phi_s - \phi_i) & pq = hh \end{cases} \tag{B.22}$$

$$b_{pq} = Z_{pq} \cos\phi_i \tag{B.23}$$

$$c_{pq} = Z_{pq} \sin\phi_i, \tag{B.24}$$

A is the illuminated area, and

$$Z_{hh} = r_{h0}[\sin\theta_s - \sin\theta_i \cos(\phi_s - \phi_i)] + r_{h1}(\cos\theta_i - \cos\theta_s)\cos(\phi_s - \phi_i) \tag{B.25}$$

$$Z_{vh} = -\sin(\phi_s - \phi_i)[r_{h0}\sin\theta_i \cos\theta_s + r_{h1}(1 - \cos\theta_i \cos\theta_s)] \tag{B.26}$$

$$Z_{hv} = \sin(\phi_s - \phi_i)[r_{v0} \sin\theta_i \cos\theta_s + r_{v1}(1 - \cos\theta_i \cos\theta_s)] \tag{B.27}$$

$$Z_{vv} = r_{v0}[\sin\theta_s - \sin\theta_i \cos(\phi_s - \phi_i)] + r_{v1}(\cos\theta_i - \cos\theta_s)\cos(\phi_s - \phi_i). \tag{B.28}$$

The Fresnel coefficients are

$$r_{h0} = \frac{\eta_2 \cos\theta_i + \eta_1 \cos\theta_t}{\eta_2 \cos\theta_i - \eta_1 \cos\theta_t} \tag{B.29}$$

$$r_{h1} = r_{h0}\frac{\eta_2 \sin\theta_i + \eta_1 \sin\theta_t}{\eta_2 \cos\theta_i - \eta_1 \cos\theta_t} \tag{B.30}$$

$$r_{v0} = \frac{\eta_1 \cos\theta_i + \eta_2 \cos\theta_t}{\eta_1 \cos\theta_i - \eta_2 \cos\theta_t} \tag{B.31}$$

$$r_{v1} = -\frac{[\eta_1 \sin\theta_i - \eta_2 \sin\theta_t - r_{v0}(\eta_1 \sin\theta_i + \eta_2 \sin\theta_t)]}{\eta_1 \cos\theta_i - \eta_2 \cos\theta_t} \tag{B.32}$$

where

$$\sin\theta_t = \frac{k_1}{k_2}\sin\theta_i \tag{B.33}$$

with k_1 being the wavenumber in the medium containing the incident field and k_2 being the wavenumber in the rough surface medium.

B.3 Small Perturbation Model

The unit polarization vectors for the incident, scattered, and transmitted fields are now defined as:

$$\hat{\mathrm{k}}_s^{\pm} = \hat{\mathrm{x}}\sin\theta_s\cos\phi_s + \hat{\mathrm{y}}\sin\theta_s\sin\phi_s \pm \hat{\mathrm{z}}\cos\theta_s \tag{B.34}$$

$$\hat{\mathrm{h}}_s^{\pm} = -\hat{\mathrm{x}}\sin\phi_s + \hat{\mathrm{y}}\cos\phi_s \tag{B.35}$$

$$\hat{\mathrm{v}}_s^{\pm} = \hat{\mathrm{h}}_s^{\pm} \times \hat{\mathrm{k}}_s^{\pm} = \pm\hat{\mathrm{x}}\cos\theta_s\cos\phi_s \pm \hat{\mathrm{y}}\cos\theta_s\sin\phi_s - \hat{\mathrm{z}}\sin\theta_s \tag{B.36}$$

$$\hat{\mathrm{k}}_f^{\pm} = \hat{\mathrm{x}}\sin\theta_f\cos\phi_f + \hat{\mathrm{y}}\sin\theta_f\sin\phi_f \mp \hat{\mathrm{z}}\cos\theta_f \tag{B.37}$$

$$\hat{\mathrm{h}}_f^{\pm} = -\hat{\mathrm{x}}\sin\phi_f + \hat{\mathrm{y}}\cos\phi_f \tag{B.38}$$

$$\hat{\mathrm{v}}_f^{\pm} = \hat{\mathrm{h}}_f^{\pm} \times \hat{\mathrm{k}}_f^{\pm} = \mp\hat{\mathrm{x}}\cos\theta_f\cos\phi_f \mp \hat{\mathrm{y}}\cos\theta_f\sin\phi_f - \hat{\mathrm{z}}\sin\theta_f, \tag{B.39}$$

where the subscript $f \in \{i, t\}$ denotes either the incident or the transmitted wave. The $+$ and $-$ superscripts denote upward and downward traveling waves, respectively. In addition, the transverse vector wavenumbers are defined as $\mathbf{k}_\perp = \hat{\mathbf{x}}k_x + \hat{\mathbf{y}}k_y$ for a general wave and $\mathbf{k}_{\perp i} = \hat{\mathbf{x}}k_{xi} + \hat{\mathbf{y}}k_{yi}$ for the incident wave. The z components of the vector wavenumbers are

$$k_{1z} = k_1 \cos\theta_s \tag{B.40}$$

$$k_{1zi} = k_1 \cos\theta_i \tag{B.41}$$

$$k_{2z} = \sqrt{k_2^2 - k_1^2 \sin^2\theta_s} \tag{B.42}$$

$$k_{2zi} = \sqrt{k_2^2 - k_1^2 \sin^2\theta_i}. \tag{B.43}$$

The correlation products of the scattering matrix elements for this model are given by

$$\langle S_{pq} S_{mn}^* \rangle = A k_1^2 \cos^2\theta_s f_{pq} f_{mn}^* W(|\mathbf{k}_\perp - \mathbf{k}_{\perp i}|). \tag{B.44}$$

The spectral density is

$$W(|\mathbf{k}_\perp - \mathbf{k}_{\perp i}|) = \frac{(sl)^2}{4\pi} \exp\left[-\frac{l^2}{4}|\mathbf{k}_\perp - \mathbf{k}_{\perp i}|^2\right], \tag{B.45}$$

where

$$|\mathbf{k}_\perp - \mathbf{k}_{\perp i}|^2 = k_1^2 \left[\sin^2\theta_s + \sin^2\theta_i - 2\sin\theta_s \sin\theta_i \cos(\phi_s - \phi_i)\right]. \tag{B.46}$$

The polarization dependent factors are

$$f_{vv} = \frac{2k_2^2 k_{1zi}(k_2^2 - k_1^2)}{(k_1^2 k_{2z} + k_2^2 k_{1z})(k_1^2 k_{2zi} - k_2^2 k_{1zi})} \left[k_\rho k_{\rho i} - \frac{k_1^2}{k_2^2} k_{2z} k_{2zi} K_1\right] \tag{B.47}$$

$$f_{vh} = \frac{2k_1 k_{2z} k_{1zi}(k_2^2 - k_1^2)}{(k_1^2 k_{2z} + k_2^2 k_{1z})(k_{2zi} - k_{1zi})} K_2 \tag{B.48}$$

$$f_{hv} = -\frac{2k_1 k_{2zi} k_{1zi}(k_2^2 - k_1^2)}{(k_{2z} + k_{1z})(k_1^2 k_{2zi} - k_2^2 k_{1zi})} K_2 \tag{B.49}$$

$$f_{hh} = \frac{2k_{1zi}(k_2^2 - k_1^2)}{(k_{2z} + k_{1z})(k_{2zi} - k_{1zi})} K_1, \tag{B.50}$$

with

$$K_1 = \frac{k_x k_{xi} + k_y k_{yi}}{k_\rho k_{\rho i}} \tag{B.51}$$

$$K_2 = \frac{k_y k_{xi} - k_x k_{yi}}{k_\rho k_{\rho i}} \tag{B.52}$$

and

$$k_{\rho i}^2 = k_{xi}^2 + k_{yi}^2 \tag{B.53}$$

$$k_\rho^2 = k_x^2 + k_y^2. \tag{B.54}$$

PENDIX C

SCATTERING MODELS FOR TRUNKS AND BRANCHES

Individual trunks and branches are modeled as homogeneous dielectric cylinders with a specified length l_c and diameter d_c. Three models are presented for modeling scattering from cylinders. Each model is valid over a specified range of cylinder dimensions. The first model approximates scattering from cylinders whose size is smaller than a wavelength ($l_c << \lambda$) by modeling them as prolate Rayleigh spheroids. This model is appropriate for many size classes of needles and stems. The second model may be applied to long, thin cylinders with length greater than a wavelength but with diameter very small compared to λ, i.e. $l_c >> \lambda$ and $d_c << \lambda$. This model is appropriate for many types of intermediate size branches. The final model is based on the exact solution for scattering from an infinitely long cylinder and is appropriate for large size classes of branches and trunks.

C.1 Scattering Matrix for Prolate Spheroids

A solution for scattering from small prolate spheroids with a prescribed orientation has been presented by Tsang *et al.*, [60], pp. 160-162. For cylinders with total length l_c and diameter d_c, the axis dimensions of the spheroid with equivalent volume

are

$$c = \frac{l_c}{2}\left(\frac{3}{2}\right)^{\frac{1}{3}} \tag{C.1}$$

$$a = \frac{d_c}{2}\left(\frac{3}{2}\right)^{\frac{1}{3}} \tag{C.2}$$

$$b = a. \tag{C.3}$$

For spheroids with $c > a$, define

$$A_c = -\frac{1}{c^3 e^3}\left[2e + \ln\left(\frac{1-e}{1+e}\right)\right] \tag{C.4}$$

and

$$A_a = A_b = \frac{1}{abc} - A_c \tag{C.5}$$

where $e = \sqrt{1 - a^2/c^2}$. For a spheroid oriented with axes specified by $\hat{x}_b$, $\hat{y}_b$ and $\hat{z}_b$ such that its surface is described by

$$\frac{x_b^2}{a^2} + \frac{y_b^2}{b^2} + \frac{z_b^2}{c^2} = 1, \tag{C.6}$$

the scattering matrix elements are

$$S_{vv} = Q\left\{\frac{(\hat{v}_s \cdot \hat{x}_b)(\hat{x}_b \cdot \hat{v}_i)}{1 + v_d A_a} + \frac{(\hat{v}_s \cdot \hat{y}_b)(\hat{y}_b \cdot \hat{v}_i)}{1 + v_d A_b} + \frac{(\hat{v}_s \cdot \hat{z}_b)(\hat{z}_b \cdot \hat{v}_i)}{1 + v_d A_c}\right\} \tag{C.7}$$

$$S_{hv} = Q\left\{\frac{\left(\hat{h}_s \cdot \hat{x}_b\right)(\hat{x}_b \cdot \hat{v}_i)}{1 + v_d A_a} + \frac{\left(\hat{h}_s \cdot \hat{y}_b\right)(\hat{y}_b \cdot \hat{v}_i)}{1 + v_d A_b} + \frac{\left(\hat{h}_s \cdot \hat{z}_b\right)(\hat{z}_b \cdot \hat{v}_i)}{1 + v_d A_c}\right\} \tag{C.8}$$

$$S_{vh} = Q\left\{\frac{(\hat{v}_s \cdot \hat{x}_b)\left(\hat{x}_b \cdot \hat{h}_i\right)}{1 + v_d A_a} + \frac{(\hat{v}_s \cdot \hat{y}_b)\left(\hat{y}_b \cdot \hat{h}_i\right)}{1 + v_d A_b} + \frac{(\hat{v}_s \cdot \hat{z}_b)\left(\hat{z}_b \cdot \hat{h}_i\right)}{1 + v_d A_c}\right\} \tag{C.9}$$

$$S_{hh} = Q\left\{\frac{\left(\hat{h}_s \cdot \hat{x}_b\right)\left(\hat{x}_b \cdot \hat{h}_i\right)}{1 + v_d A_a} + \frac{\left(\hat{h}_s \cdot \hat{y}_b\right)\left(\hat{y}_b \cdot \hat{h}_i\right)}{1 + v_d A_b} + \frac{\left(\hat{h}_s \cdot \hat{z}_b\right)\left(\hat{z}_b \cdot \hat{h}_i\right)}{1 + v_d A_c}\right\} \tag{C.10}$$

where

$$Q = \frac{k_0^2}{4\pi} v_0 (\epsilon_r - 1), \tag{C.11}$$

k_0 is the wave number, $v_0 = 4\pi abc/3$ is the spheroid volume, ϵ_r is the relative dielectric of the spheroid, and

$$v_d = \frac{abc}{2}(\epsilon_r - 1). \tag{C.12}$$

The vectors $(\hat{v}_i, \hat{h}_i)$ and $(\hat{v}_s, \hat{h}_s)$ are the directions of the vertical and horizontal polarization vectors of the incident and scattered waves, respectively.

C.2 Scattering Matrix for Long Thin Cylinders

A solution for scattering from cylinders that are long and thin relative to wavelength has been derived by Sarabandi,[50]. For circular cylinders of cross sectional area $A = \pi d_c^2/4$, the elements of th polarizability tensor $\mathcal{P}$ are

$$P_{xx} = 2A\frac{\epsilon_r - 1}{\epsilon_r + 1} \tag{C.13}$$

$$P_{yy} = P_{xx} \tag{C.14}$$

$$P_{zz} = A(\epsilon_r - 1) \tag{C.15}$$

For a non-magnetic cylinder with the direction of the incident electric field specified by $\hat{a} = \hat{a_x}\hat{x} + \hat{a_y}\hat{y} + \hat{a_z}\hat{z}$, the far field scattered amplitude is

$$\mathcal{S}(\hat{a}) = -\frac{k_0^2}{4\pi}\left[\hat{k}_s \times \hat{k}_s \times (l_c\mathcal{P} \cdot \hat{a})\right]\frac{\sin U}{U} \tag{C.16}$$

where

$$U = 0.5k_0 l_c(\hat{k}_s \cdot \hat{z} - \hat{k}_i \cdot \hat{z}), \tag{C.17}$$

the vectors $\hat{k}_i$ and $\hat{k}_s$ are the directions of propagation of the incident and scattered fields and k_0 is the wavenumber. For vertical and horizontal polarization vectors $(\hat{v}_i', \hat{h}_i')$ incident on the cylinder and vectors $(\hat{v}_s', \hat{h}_s')$ scattered from the cylinder, where

the prime indicates that the vectors are in the local coordinate system of the cylinder, the scattering matrix elements are

$$S_{vv} = \mathcal{S}(\hat{v}_i') \cdot \hat{v}_s' \tag{C.18}$$

$$S_{hv} = \mathcal{S}(\hat{v}_i') \cdot \hat{h}_s' \tag{C.19}$$

$$S_{vh} = \mathcal{S}(\hat{h}_i') \cdot \hat{v}_s' \tag{C.20}$$

$$S_{hh} = \mathcal{S}(\hat{h}_i') \cdot \hat{h}_s'. \tag{C.21}$$

C.3 Scattering Matrix for Large Cylinders

For an finite-length dielectric cylinder oriented vertically, (Ruck *et al.*,[49]):

$$\mathcal{S}'(\psi_i, \phi') = Q(\psi_i, \psi_s) \cdot \begin{bmatrix} \sum_{n=-\infty}^{\infty} (-1)^n C_n^{TM} e^{in\phi'} & i\sum_{n=-\infty}^{\infty} (-1)^n \bar{C}_n e^{in\phi'} \\ -i\sum_{n=-\infty}^{\infty} (-1)^n \bar{C}_n e^{in\phi'} & \sum_{n=-\infty}^{\infty} (-1)^n C_n^{TE} e^{in\phi'} \end{bmatrix} \tag{C.22}$$

where ϕ' is the azimuth scattering angle in the plane perpendicular to the cylinder axis, ψ_i is the angle formed between this plane and the unit vector along the direction of propagation of the incident field and ψ_s is the angle formed between this plane and the unit vector along the direction of propagation of the scattered field. The summation coefficients are the same as those for an infinitely long homogeneous cylinder with relative dielectric constant ϵ_r and diameter d:

$$C_n^{TM} = -\frac{V_n P_n - q_n^2 J_n(x_0) H_n^{(1)}(x_0) J_n^2(x_1)}{P_n N_n - \left[q_n H_n^{(1)}(x_0) J_n(x_1)\right]^2} \tag{C.23}$$

$$C_n^{TE} = -\frac{M_n N_n - q_n^2 J_n(x_0) H_n^{(1)}(x_0) J_n^2(x_1)}{P_n N_n - \left[q_n H_n^{(1)}(x_0) J_n(x_1)\right]^2} \tag{C.24}$$

$$\bar{C}_n = i\frac{2}{\pi x_0}\left[\frac{s_0 q_n J_n^2(x_1)}{P_n N_n - \left[q_n H_n^{(1)}(x_0) J_n(x_1)\right]^2}\right] \tag{C.25}$$

where

$$x_0 = \frac{k_0 d \cos\psi_i}{2} \tag{C.26}$$

$$x_1 = \frac{k_0 d}{2}\sqrt{\epsilon_r - \sin^2\psi_i} \tag{C.27}$$

$$q_n = \frac{n\sin\psi_i}{\frac{k_0 d}{2}}\left(\frac{1}{\epsilon_r - \sin^2\psi_i} - \frac{1}{\cos^2\psi_i}\right) \tag{C.28}$$

$$V_n = s_1 J_n(x_0)J_n'(x_1) - s_0 J_n'(x_0)J_n(x_1) \tag{C.29}$$

$$P_n = r_1 H_n^{(1)}(x_0)J_n'(x_1) - s_0 H_n'^{(1)}(x_0)J_n(x_1) \tag{C.30}$$

$$N_n = s_1 H_n^{(1)}(x_0)J_n'(x_1) - s_0 H_n'^{(1)}(x_0)J_n(x_1) \tag{C.31}$$

$$M_n = r_1 J_n(x_0)J_n'(x_1) - s_0 J_n'(x_0)J_n(x_1) \tag{C.32}$$

and

$$s_0 = \frac{1}{\cos\psi_i}\ ,\quad s_1 = \frac{\epsilon_r}{\sqrt{\epsilon_r - \sin^2\psi_i}}\ ,\quad r_1 = \frac{1}{\sqrt{\epsilon_r - \sin^2\psi_i}}. \tag{C.33}$$

Here, $J_n(\ )$ and $J_n'(\ )$ represent the Bessel functions of the first kind of order n and their derivatives and $H_n^{(1)}(\ )$ and $H_n'^{(1)}(\ )$ represent the Hankel functions of the first kind of order n and their derivatives.

The correction factor $Q(\psi_i, \psi_s)$ transforms the infinite cylinder solution to the finite cylinder case. In so doing, it is assumed that the length of the cylinder is such that $l_c >> \lambda$ or that the cylinder dimensions are such that the relations $0.5 < k_0\frac{d}{2} < 10$ and $l_c >> \frac{d}{2}$ hold (Ruck *et al.*,[49]). In this case,

$$Q(\psi_i, \psi_s) = \frac{i l_c \cos\psi_s}{\pi\cos\psi_i}\left\{\frac{\sin\left[k_0(\sin\psi_i + \sin\psi_s)\frac{l_c}{2}\right]}{\left[k_0(\sin\psi_i + \sin\psi_s)\frac{l_c}{2}\right]}\right\}. \tag{C.34}$$

The scattering matrix of an arbitrarily oriented cylinder may be expressed as

$$\mathcal{S} = \mathcal{R}\cdot\mathcal{S}'\cdot\mathcal{T} \tag{C.35}$$

where

$$\mathcal{R} = \begin{bmatrix} (\hat{v}_s\cdot\hat{v}_s^c) & (\hat{v}_s\cdot\hat{h}_s^c) \\ (\hat{h}_s\cdot\hat{v}_s^c) & (\hat{h}_s\cdot\hat{h}_s^c) \end{bmatrix} \tag{C.36}$$

and

$$\mathcal{T} = \begin{bmatrix} (\hat{v}_i \cdot \hat{v}_i^c) & (\hat{v}_i \cdot \hat{h}_i^c) \\ (\hat{h}_i \cdot \hat{v}_i^c) & (\hat{h}_i \cdot \hat{h}_i^c) \end{bmatrix}. \tag{C.37}$$

The unit vectors in (C.36) and (C.37) represent the directions of the polarization vectors for the scattered and incident fields, respectively. The vectors $(\hat{v}_s, \hat{h}_s)$ are directed along the scattered vertical and horizontal polarization directions in the reference coordinate system of the radar. The vectors $(\hat{v}_s^c, \hat{h}_s^c)$ are directed along the scattered vertical and horizontal polarization directions of the coordinate system local to the cylinder. The vectors $(\hat{v}_i, \hat{h}_i)$ and $(\hat{v}_i^c, \hat{h}_i^c)$ represent a similar set of directions for the incident field.

Given the previously stated constraints on the cylinder dimensions, the only region of error for this model is at angles of incidence at or near end-on ($\psi_i \simeq \frac{\pi}{2}$).

APPENDIX D

SCATTERING MODELS FOR LEAVES

Individual leaves are modeled as homogeneous dielectric disks with specified thickness τ and diameter d. Two models are presented for modeling scatter from such disks each of which is valid over a specified range of disk dimensions. The first model approximates scattering from a disk whose diameter is small compared to a wavelength ($d << \lambda$) by modeling it as an oblate Rayleigh spheroid. The second model is a physical optics approximation of scattering matrix elements. Generally speaking, the Rayleigh model is appropriate for low frequencies while the physical optics model is appropriate for high frequencies.

D.1 Scattering Matrix for Oblate Spheroids

A solution for scattering from small oblate spheroids with a prescribed orientation has been presented by Tsang *et al.*, [60], pp. 160-162. For disks with thickness τ and diameter d, the axis dimensions of the spheroid with equivalent volume are

$$c = \frac{\tau}{2}\left(\frac{3}{2}\right)^{\frac{1}{3}} \tag{D.1}$$

$$a = \frac{d_l}{2}\left(\frac{3}{2}\right)^{\frac{1}{3}} \tag{D.2}$$

$$b = a. \tag{D.3}$$

For spheroids with $c < a$, define

$$A_c = \frac{2}{(a^2-c^2)^{3/2}}\left[\frac{\sqrt{a^2-c^2}}{c} - \tan^{-1}\frac{\sqrt{a^2-c^2}}{c}\right] \tag{D.4}$$

and

$$A_a = A_b = \frac{1}{abc} - A_c. \tag{D.5}$$

For a spheroid oriented with axes specified by $\hat{x}_b$, $\hat{y}_b$ and $\hat{z}_b$ such that its surface is described by

$$\frac{x_b^2}{a^2} + \frac{y_b^2}{b^2} + \frac{z_b^2}{c^2} = 1, \tag{D.6}$$

the scattering matrix elements are

$$S_{vv} = Q\left\{\frac{(\hat{v}_s\cdot\hat{x}_b)(\hat{x}_b\cdot\hat{v}_i)}{1+v_dA_a} + \frac{(\hat{v}_s\cdot\hat{y}_b)(\hat{y}_b\cdot\hat{v}_i)}{1+v_dA_b} + \frac{(\hat{v}_s\cdot\hat{z}_b)(\hat{z}_b\cdot\hat{v}_i)}{1+v_dA_c}\right\} \tag{D.7}$$

$$S_{hv} = Q\left\{\frac{(\hat{h}_s\cdot\hat{x}_b)(\hat{x}_b\cdot\hat{v}_i)}{1+v_dA_a} + \frac{(\hat{h}_s\cdot\hat{y}_b)(\hat{y}_b\cdot\hat{v}_i)}{1+v_dA_b} + \frac{(\hat{h}_s\cdot\hat{z}_b)(\hat{z}_b\cdot\hat{v}_i)}{1+v_dA_c}\right\} \tag{D.8}$$

$$S_{vh} = Q\left\{\frac{(\hat{v}_s\cdot\hat{x}_b)(\hat{x}_b\cdot\hat{h}_i)}{1+v_dA_a} + \frac{(\hat{v}_s\cdot\hat{y}_b)(\hat{y}_b\cdot\hat{h}_i)}{1+v_dA_b} + \frac{(\hat{v}_s\cdot\hat{z}_b)(\hat{z}_b\cdot\hat{h}_i)}{1+v_dA_c}\right\} \tag{D.9}$$

$$S_{hh} = Q\left\{\frac{(\hat{h}_s\cdot\hat{x}_b)(\hat{x}_b\cdot\hat{h}_i)}{1+v_dA_a} + \frac{(\hat{h}_s\cdot\hat{y}_b)(\hat{y}_b\cdot\hat{h}_i)}{1+v_dA_b} + \frac{(\hat{h}_s\cdot\hat{z}_b)(\hat{z}_b\cdot\hat{h}_i)}{1+v_dA_c}\right\} \tag{D.10}$$

where

$$Q = \frac{k_0^2}{4\pi}v_0(\epsilon_r - 1), \tag{D.11}$$

k_0 is the wave number, $v_0 = 4\pi abc/3$ is the spheroid volume, ϵ_r is the relative dielectric of the spheroid, and

$$v_d = \frac{abc}{2}(\epsilon_r - 1). \tag{D.12}$$

The vectors $(\hat{v}_i, \hat{h}_i)$ and $(\hat{v}_s, \hat{h}_s)$ are the directions of the vertical and horizontal polarization vectors of the incident and scattered waves, respectively.

D.2 Physical Optics Model

Here, the disk is modeled as an $a \times b$ square resistive plate with area equivalent to that of the disk. For a disk of thickness τ and diameter d, the dimensions of the square plate are

$$a = \frac{d\sqrt{\pi}}{2} \tag{D.13}$$

$$b = a. \tag{D.14}$$

A physical optics solution for scattering from an arbitrarily oriented plate has been obtained by Sarabandi, [50]. The resistivity of the plate is

$$R = \frac{iZ_0}{k_0\tau(\epsilon - 1)}. \tag{D.15}$$

where k_0 and Z_0 are the propagation constant and intrinsic impedance, respectively, of free space. Let the plate be oriented such that the spherical coordinate angles (θ_j, ϕ_j) specify the direction of the unit vector normal to the surface of the plate. Furthermore, let the directions of propagation of the incident and scattered fields be specified by the spherical coordinate angles (θ_i, ϕ_i) and (θ_s, ϕ_s), respectively. Then, define the reflection coefficients

$$\Gamma_H(\phi_1) = (1 + \frac{2R}{Z_0}\sec\phi_1)^{-1} \tag{D.16}$$

$$\Gamma_E(\phi_1) = (1 + \frac{2R}{Z_0}\cos\phi_1)^{-1} \tag{D.17}$$

where

$$\cos\phi_1 = -[\sin\theta_j \sin\theta_i \cos(\phi_j - \phi_i) + \cos\theta_i \cos\theta_j] \geq 0. \tag{D.18}$$

The scattering matrix elements are

$$S_{vv} = \frac{-iab}{\lambda}\frac{\sin U}{U}\frac{\sin V}{V}P^2\{\cos\phi\cos\beta[(\sin\theta_i\sin\theta_j + \cos\theta_i\cos\theta_j\cos(\phi_i - \phi_j))$$

$$\cdot(\sin\theta_s \sin\theta_j + \cos\theta_s \cos\theta_j \cos(\phi_s - \phi_j))$$

$$+ \cos\theta_i \sin(\phi_i - \phi_j) \cos\theta_s \sin(\phi_s - \phi_j)] \cdot (\Gamma_H - \Gamma_E)$$

$$+[\cos(\phi_i - \phi_j)(\sin\theta_s \sin\theta_j + \cos\theta_s \cos\theta_j \cos(\phi_s - \phi_j))$$

$$+ \cos\theta_j \sin(\phi_i - \phi_j) \cdot \cos\theta_s \sin(\phi_s - \phi_j)] \cdot (\Gamma_H - \cos^2\beta \cos^2\phi\Gamma_E)\} \tag{D.19}$$

$$S_{vh} = \frac{-iab}{\lambda}\frac{\sin U}{U}\frac{\sin V}{V}P^2\{\cos\phi\cos\beta[-\cos\theta_j \sin(\phi_i - \phi_j)$$

$$\cdot(\sin\theta_s \sin\theta_j + \cos\theta_s \cos\theta_j \cos(\phi_s - \phi_j))$$

$$+ \cos(\phi_i - \phi_j) \cos\theta_s \sin(\phi_s - \phi_j)] \cdot (\Gamma_H - \Gamma_E)$$

$$+[-\cos\theta_i \sin(\phi_i - \phi_j)(\sin\theta_s \sin\theta_j + \cos\theta_s \cos\theta_j \cos(\phi_s - \phi_j))$$

$$+(\sin\theta_i \sin\theta_j + \cos\theta_i \cos\theta_j \cos(\phi_i - \phi_j))$$

$$\cdot \cos\theta_s \sin(\phi_s - \phi_j)] \cdot (\Gamma_H - \cos^2\beta \cos^2\phi\Gamma_E)\} \tag{D.20}$$

$$S_{hv} = \frac{-iab}{\lambda}\frac{\sin U}{U}\frac{\sin V}{V}P^2\{\cos\phi\cos\beta[(\sin\theta_i \sin\theta_j + \cos\theta_i \cos\theta_j \cos(\phi_i - \phi_j))$$

$$\cdot \cos\theta_j \sin(\phi_j - \phi_s) + \cos\theta_i \sin(\phi_i - \phi_j) \cos(\phi_s - \phi_j)](\Gamma_H - \Gamma_E)$$

$$+[\cos(\phi_i - \phi_j) \cos\theta_j \sin(\phi_j - \phi_s) + \cos\theta_j \sin(\phi_i - \phi_j) \cos(\phi_s - \phi_j)]$$

$$\cdot(\Gamma_H - \cos^2\beta \cos^2\phi\Gamma_E)\} \tag{D.21}$$

$$S_{hh} = \frac{-iab}{\lambda}\frac{\sin U}{U}\frac{\sin V}{V}P^2\{\cos\phi\cos\beta[-\cos\phi_j \sin(\phi_i - \phi_j) \cos\theta_j \sin(\phi_j - \phi_s)$$

$$+ \cos(\phi_i - \phi_j) \cos(\phi_s - \phi_j)](\Gamma_H - \Gamma_E)$$

$$+[-\cos\theta_i \sin(\phi_i - \phi_j) \cos\theta_j \sin(\phi_j - \phi_s)$$

$$+(\sin\theta_i \sin\theta_j + \cos\theta_i \cos\theta_j \cos(\phi_i - \phi_j)) \cos(\phi_s - \phi_j)]$$

$$\cdot(\Gamma_H - \cos^2\beta \cos^2\phi\Gamma_E)\} \tag{D.22}$$

where

$$P = (1 - \cos^2\beta \cos^2\phi)^{-1/2} \tag{D.23}$$

and

$$U = \frac{k_0 a}{2}(\sin\phi - \sin\phi') \tag{D.24}$$

$$V = \frac{k_0 b}{2}(\sin\beta\cos\phi - \sin\beta'\cos\phi'). \tag{D.25}$$

The angles β,ϕ,β' and ϕ' are defined through

$$\sin\phi = \sin\theta_i \sin(\phi_i - \phi_j) \tag{D.26}$$

$$\cos\phi = [1 - \sin^2\theta_i \sin^2(\phi_i - \phi_j)]^{1/2} \tag{D.27}$$

$$\sin\beta = q[\cos\theta_i \sin\theta_j - \sin\theta_i \cos\theta_j \cos(\phi_i - \phi_j)] \tag{D.28}$$

$$\cos\beta = -q[\cos\theta_i \cos\theta_j + \sin\theta_i \sin\theta_j \cos(\phi_i - \phi_j)] \tag{D.29}$$

$$\sin\phi' = \sin\theta_s \sin(\phi_s - \phi_j) \tag{D.30}$$

$$\cos\phi' = (1 - \sin^2\theta_s \sin^2(\phi_s - \phi_j))^{1/2} \tag{D.31}$$

and

$$\sin\beta' = \frac{\cos\theta_s \sin\theta_j - \cos\theta_j \sin\theta_s \cos(\phi_s - \phi_j)}{\sqrt{1 - \sin^2\theta_s \sin^2(\phi_s - \phi_j)}} \tag{D.32}$$

where

$$q = [1 - \sin^2\theta_i \sin^2(\phi_j - \phi_i)]^{-1/2}. \tag{D.33}$$

APPENDIX E

SECOND ORDER SCATTERING IN THE CROWN LAYER

This appendix presents the derivation of the second-order radiative transfer solution for specific intensity in the crown layer of a tree canopy. The coupled radiative transfer equations in this layer are

$$\mathbf{I}_c^+(\mu,\phi,z) = \mathrm{e}^{-\boldsymbol{\kappa}_c^+(z+d)/\mu}\mathbf{I}_c^+(\mu,\phi,-d) + \int_{-d}^{z}\mathrm{e}^{-\boldsymbol{\kappa}_c^+(z-z')/\mu}\boldsymbol{\mathcal{F}}_c^+(\mu,\phi,z')\,\mathrm{d}z' \tag{E.1}$$

$$\mathbf{I}_c^-(-\mu,\phi,z) = \mathrm{e}^{\boldsymbol{\kappa}_c^- z/\mu}\mathbf{I}_c^-(-\mu,\phi,0) + \int_{z}^{0}\mathrm{e}^{\boldsymbol{\kappa}_c^-(z-z')/\mu}\boldsymbol{\mathcal{F}}_c^-(-\mu,\phi,z')\,\mathrm{d}z' \tag{E.2}$$

where $\boldsymbol{\kappa}_c^+$ and $\boldsymbol{\kappa}_c^-$ are the crown layer extinction matrices for positive and negative propagating intensities, $\mathbf{I}_c^+$ and $\mathbf{I}_c^-$, respectively, and $\boldsymbol{\mathcal{F}}_c^+$ and $\boldsymbol{\mathcal{F}}_c^-$ are the crown layer source functions. Applying the canopy boundary conditions yields the solutions for the specific intensities:

$$\begin{aligned}\mathbf{I}_c^+(\mu,\phi,z) = {} & \mathrm{e}^{-\boldsymbol{\kappa}_c^+(z+d)/\mu}\mathrm{e}^{-\boldsymbol{\kappa}_t^+ H_t/\mu}\boldsymbol{\mathcal{R}}(\mu)\,\mathrm{e}^{-\boldsymbol{\kappa}_t^- H_t/\mu}\mathrm{e}^{-\boldsymbol{\kappa}_c^- d/\mu} \\ & \cdot\mathbf{I}_0(-\mu_0,\phi_0)\,\delta(\mu-\mu_0)\,\delta(\phi-\phi_0) \\ & + \mathrm{e}^{-\boldsymbol{\kappa}_c^+(z+d)/\mu}\mathrm{e}^{-\boldsymbol{\kappa}_t^+ H_t/\mu}\boldsymbol{\mathcal{R}}(\mu)\,\mathrm{e}^{-\boldsymbol{\kappa}_t^- H_t/\mu} \\ & \cdot\int_{-d}^{0}\mathrm{e}^{\boldsymbol{\kappa}_c^-(-d-z')/\mu}\boldsymbol{\mathcal{F}}_c^-(-\mu,\phi,z')\,\mathrm{d}z'\end{aligned}$$

$$
\begin{aligned}
&+ \; e^{-\kappa_c^+(z+d)/\mu} e^{-\kappa_t^+ H_t/\mu} \mathcal{R}(\mu) \\
&\qquad \cdot \int_{-(d+H_t)}^{-d} e^{\kappa_t^-(-(d+H_t)-z')/\mu} \mathcal{F}_t^-(-\mu, \phi, z')\, dz' \\
&+ \; e^{-\kappa_c^+(z+d)/\mu} \int_{-(d+H_t)}^{-d} e^{\kappa_t^+(d+z')/\mu} \mathcal{F}_t^+(\mu, \phi, z')\, dz' \\
&+ \int_{-d}^{z} e^{-\kappa_c^+(z-z')/\mu} \mathcal{F}_c^+(\mu, \phi, z')\, dz' \qquad \text{(E.3)}
\end{aligned}
$$

$$
\begin{aligned}
\mathbf{I}_c^-(-\mu, \phi, z) \;&=\; e^{\kappa_c^- z/\mu} \mathbf{I}_0(-\mu_0, \phi_0)\, \delta(\mu - \mu_0)\, \delta(\phi - \phi_0) \\
&\quad + \int_z^0 e^{\kappa_c^-(z-z')/\mu} \mathcal{F}_c^-(-\mu, \phi, z')\, dz' \qquad \text{(E.4)}
\end{aligned}
$$

The solutions for the first-order positive- and negative-going specific intensities at a depth z in the crown layer are

$$
\mathbf{I}_{c,dc}^{(1)+}(\mu, \phi, z) \;=\; \frac{1}{\mu}\left[\int_{-d}^{z} e^{-\kappa_c^+(z-z')/\mu} \mathcal{P}_c(\mu, \phi; -\mu_0, \phi_0) e^{\kappa_c^- z'/\mu_0}\, dz'\right] \mathbf{I}_0(-\mu_0, \phi_0) \qquad \text{(E.5)}
$$

$$
\begin{aligned}
\mathbf{I}_{c,dc}^{(1)-}(-\mu, \phi, z) \;&=\; \left\{ e^{\kappa_c^- z/\mu} \delta(\mu - \mu_0)\, \delta(\phi - \phi_0) \right. \\
&\quad \left. + \frac{1}{\mu}\left[\int_z^0 e^{\kappa_c^-(z-z')/\mu} \mathcal{P}_c(-\mu, \phi; -\mu_0, \phi_0) e^{\kappa_c^- z'/\mu_0}\, dz'\right]\right\} \\
&\quad \cdot \mathbf{I}_0(-\mu_0, \phi_0) \qquad \text{(E.6)}
\end{aligned}
$$

where $\mathbf{I}_0(-\mu_0, \phi_0)$ is the intensity incident on the layer in the direction $(-\mu_0, \phi_0)$ with $\mu_0 = \cos\theta_0$ and $\mathcal{P}_c$ is the crown layer phase matrix.

The first-order crown layer source functions are

$$
\begin{aligned}
\mathbf{F}_{c,dc}^{(1)+}(\mu, \phi, z) \;&=\; \frac{1}{\mu}\left[\int_0^{2\pi}\int_0^1 \mathcal{P}_c(\mu, \phi; \mu', \phi') \mathbf{I}_{c,dc}^{(1)+}(\mu', \phi', z)\, d\Omega' \right. \\
&\quad \left. + \int_0^{2\pi}\int_0^1 \mathcal{P}_c(\mu, \phi, -\mu', \phi') \mathbf{I}_{c,dc}^{(1)-}(-\mu', \phi', z)\, d\Omega'\right] \qquad \text{(E.7)} \\
\mathbf{F}_{c,dc}^{(1)-}(-\mu, \phi, z) \;&=\; \frac{1}{\mu}\left[\int_0^{2\pi}\int_0^1 \mathcal{P}_c(-\mu, \phi; \mu', \phi') \mathbf{I}_{c,dc}^{(1)+}(\mu', \phi', z)\, d\Omega' \right. \\
&\quad \left. + \int_0^{2\pi}\int_0^1 \mathcal{P}_c(-\mu, \phi; -\mu', \phi') \mathbf{I}_{c,dc}^{(1)-}(-\mu', \phi', z)\, d\Omega'\right]. \qquad \text{(E.8)}
\end{aligned}
$$

Substituting the first-order intensities into (E.7) and (E.8) and rearranging yields

$$\begin{aligned}
\mathbf{F}^{(1)+}_{c,dc}(\mu,\phi,z) &= \left\{\frac{1}{\mu}\int_0^{2\pi}\int_0^1 \frac{1}{\mu'}\boldsymbol{\mathcal{P}}_c(\mu,\phi;\mu',\phi')\right. \\
&\qquad \cdot\left[\int_{-d}^{z} \mathrm{e}^{-\boldsymbol{\kappa}_c^+(z-z')/\mu'}\boldsymbol{\mathcal{P}}_c(\mu',\phi';-\mu_0,\phi_0)\mathrm{e}^{\boldsymbol{\kappa}_c^- z'/\mu_0}\,\mathrm{d}z'\right]\mathrm{d}\Omega' \\
&\quad + \frac{1}{\mu}\boldsymbol{\mathcal{P}}_c(\mu,\phi;-\mu_0,\phi_0)\mathrm{e}^{\boldsymbol{\kappa}_c^- z/\mu_0} \\
&\quad + \frac{1}{\mu}\int_0^{2\pi}\int_0^1 \frac{1}{\mu'}\boldsymbol{\mathcal{P}}_c(\mu,\phi;-\mu',\phi') \\
&\qquad \left.\cdot\left[\int_{z}^{0} \mathrm{e}^{\boldsymbol{\kappa}_c^-(z-z')/\mu'}\boldsymbol{\mathcal{P}}_c(-\mu',\phi';-\mu_0,\phi_0)\mathrm{e}^{\boldsymbol{\kappa}_c^- z'/\mu_0}\,\mathrm{d}z'\right]\mathrm{d}\Omega'\right\} \\
&\quad \cdot\mathbf{I}_0(-\mu_0,\phi_0) \qquad\qquad (\mathrm{E}.9)
\end{aligned}$$

$$\begin{aligned}
\mathbf{F}^{(1)-}_{c,dc}(-\mu,\phi,z) &= \left\{\frac{1}{\mu}\int_0^{2\pi}\int_0^1 \frac{1}{\mu'}\boldsymbol{\mathcal{P}}_c(-\mu,\phi;\mu',\phi')\right. \\
&\qquad \cdot\left[\int_{-d}^{z} \mathrm{e}^{-\boldsymbol{\kappa}_c^+(z-z')/\mu'}\boldsymbol{\mathcal{P}}_c(\mu',\phi';-\mu_0,\phi_0)\mathrm{e}^{\boldsymbol{\kappa}_c^- z'/\mu_0}\,\mathrm{d}z'\right]\mathrm{d}\Omega' \\
&\quad + \frac{1}{\mu}\boldsymbol{\mathcal{P}}_c(-\mu,\phi;-\mu_0,\phi_0)\mathrm{e}^{\boldsymbol{\kappa}_c^- z/\mu_0} \\
&\quad + \frac{1}{\mu}\int_0^{2\pi}\int_0^1 \frac{1}{\mu'}\boldsymbol{\mathcal{P}}_c(-\mu,\phi;-\mu',\phi') \\
&\qquad \left.\cdot\left[\int_{z}^{0} \mathrm{e}^{\boldsymbol{\kappa}_c^-(z-z')/\mu'}\boldsymbol{\mathcal{P}}_c(-\mu',\phi';-\mu_0,\phi_0)\mathrm{e}^{\boldsymbol{\kappa}_c^- z'/\mu_0}\,\mathrm{d}z'\right]\mathrm{d}\Omega'\right\} \\
&\quad \cdot\mathbf{I}_0(-\mu_0,\phi_0)\,. \qquad\qquad (\mathrm{E}.10)
\end{aligned}$$

Substituting these first-order source functions into (E.3) and neglecting interactions with the ground gives the second order solution for positive-going intensity in the crown layer:

$$\begin{aligned}
\mathbf{I}^{(2)+}_{c,dc}(\mu,\phi,z) &= \int_{-d}^{z}\mathrm{e}^{-\boldsymbol{\kappa}_c^+(z-z')/\mu}\boldsymbol{\mathcal{J}}^{(1)+}_c(\mu,\phi,z')\,\mathrm{d}z' \qquad\qquad (\mathrm{E}.11) \\
&= \left\{\frac{1}{\mu}\int_{-d}^{z}\mathrm{e}^{-\boldsymbol{\kappa}_c^+(z-z')/\mu}\left[\int_0^{2\pi}\int_0^1 \frac{1}{\mu'}\boldsymbol{\mathcal{P}}_c(\mu,\phi;\mu',\phi')\right.\right. \\
&\qquad \left.\left.\cdot\left(\int_{-d}^{z'}\mathrm{e}^{-\boldsymbol{\kappa}_c^+(z'-z'')/\mu'}\boldsymbol{\mathcal{P}}_c(\mu',\phi';-\mu_0,\phi_0)\mathrm{e}^{\boldsymbol{\kappa}_c^- z''/\mu_0}\,\mathrm{d}z''\right)\mathrm{d}\Omega'\right]\mathrm{d}z'\right. \\
&\quad \left. + \frac{1}{\mu}\int_{-d}^{z}\mathrm{e}^{-\boldsymbol{\kappa}_c^+(z-z')/\mu}\boldsymbol{\mathcal{P}}_c(\mu,\phi;-\mu_0,\phi_0)\mathrm{e}^{\boldsymbol{\kappa}_c^- z'/\mu_0}\,\mathrm{d}z'\right.
\end{aligned}$$

$$+\frac{1}{\mu}\int_{-d}^{z}\mathrm{e}^{-\kappa_c^+(z-z')/\mu}\left[\int_0^{2\pi}\int_0^1\frac{1}{\mu'}\mathcal{P}_c(\mu,\phi;-\mu',\phi')\right.$$
$$\left.\cdot\left(\int_{z'}^{0}\mathrm{e}^{\kappa_c^-(z'-z'')/\mu'}\mathcal{P}_c(-\mu',\phi';-\mu_0,\phi_0)\mathrm{e}^{\kappa_c^- z''/\mu_0}\,\mathrm{d}z''\right)\mathrm{d}\Omega'\right]\mathrm{d}z'\Bigg\}$$
$$\cdot\mathbf{I}_0(-\mu_0,\phi_0) \tag{E.12}$$

The positive-going intensity emerging from the crown is then:

$$\mathbf{I}_{dc}^{s(2)}(\mu,\phi) = \mathbf{I}_{c,dc}^{(2)+}(\mu,\phi,0) \tag{E.13}$$
$$= \left\{\frac{1}{\mu}\int_{-d}^{0}\mathrm{e}^{\kappa_c^+ z'/\mu}\left[\int_0^{2\pi}\int_0^1\frac{1}{\mu'}\mathcal{P}_c(\mu,\phi;\mu',\phi')\right.\right.$$
$$\left.\cdot\left(\int_{-d}^{z'}\mathrm{e}^{-\kappa_c^+(z'-z'')/\mu'}\mathcal{P}_c(\mu',\phi';-\mu_0,\phi_0)\mathrm{e}^{\kappa_c^- z''/\mu_0}\,\mathrm{d}z''\right)\mathrm{d}\Omega'\right]\mathrm{d}z'$$
$$+\frac{1}{\mu}\int_{-d}^{0}\mathrm{e}^{\kappa_c^+ z'/\mu}\mathcal{P}_c(\mu,\phi;-\mu_0,\phi_0)\mathrm{e}^{\kappa_c^- z'/\mu_0}\,\mathrm{d}z'$$
$$+\frac{1}{\mu}\int_{-d}^{0}\mathrm{e}^{\kappa_c^+ z'/\mu}\left[\int_0^{2\pi}\int_0^1\frac{1}{\mu'}\mathcal{P}_c(\mu,\phi;-\mu',\phi')\right.$$
$$\left.\left.\cdot\left(\int_{z'}^{0}\mathrm{e}^{\kappa_c^-(z'-z'')/\mu'}\mathcal{P}_c(-\mu',\phi';-\mu_0,\phi_0)\mathrm{e}^{\kappa_c^- z''/\mu_0}\,\mathrm{d}z''\right)\mathrm{d}\Omega'\right]\mathrm{d}z'\right\}$$
$$\cdot\mathbf{I}_0(-\mu_0,\phi_0) \tag{E.14}$$

For backscatter, take $\mu=\mu_0$ and $\phi=\phi_0+\pi$. Making these substitutions and rearranging the equations gives the second-order solution for backscattered intensity:

$$\mathbf{I}_{dc}^{s(2)}(\mu_0,\phi_0+\pi) = \left\{\frac{1}{\mu_0}\int_{-d}^{0}\mathrm{e}^{\kappa_c^+ z'/\mu_0}\mathcal{P}_c(\mu_0,\phi_0+\pi;-\mu_0,\phi_0)\mathrm{e}^{\kappa_c^- z'/\mu_0}\,\mathrm{d}z'\right.$$
$$+\frac{1}{\mu_0}\int_{-d}^{0}\mathrm{e}^{\kappa_c^+ z'/\mu_0}\left[\int_0^{2\pi}\int_0^1\frac{1}{\mu'}\mathcal{P}_c(\mu_0,\phi_0+\pi;\mu',\phi')\right.$$
$$\left.\cdot\left(\int_{-d}^{z'}\mathrm{e}^{-\kappa_c^+(z'-z'')/\mu'}\mathcal{P}_c(\mu',\phi';-\mu_0,\phi_0)\mathrm{e}^{\kappa_c^- z''/\mu_0}\,\mathrm{d}z''\right)\mathrm{d}\Omega'\right]\mathrm{d}z'$$
$$+\frac{1}{\mu_0}\int_{-d}^{0}\mathrm{e}^{\kappa_c^+ z'/\mu_0}\left[\int_0^{2\pi}\int_0^1\frac{1}{\mu'}\mathcal{P}_c(\mu_0,\phi_0+\pi;-\mu',\phi')\right.$$
$$\left.\left.\cdot\left(\int_{z'}^{0}\mathrm{e}^{\kappa_c^-(z'-z'')/\mu'}\mathcal{P}_c(-\mu',\phi';-\mu_0,\phi_0)\mathrm{e}^{\kappa_c^- z''/\mu_0}\,\mathrm{d}z''\right)\mathrm{d}\Omega'\right]\mathrm{d}z'\right\}$$
$$\cdot\mathbf{I}_0(-\mu_0,\phi_0) \tag{E.15}$$

This solution represents the sum of three scattering mechanisms. The first term corresponds to the first-order solution for direct crown backscatter. The remaining

two terms correspond to second order scattering mechanisms. Each of these terms

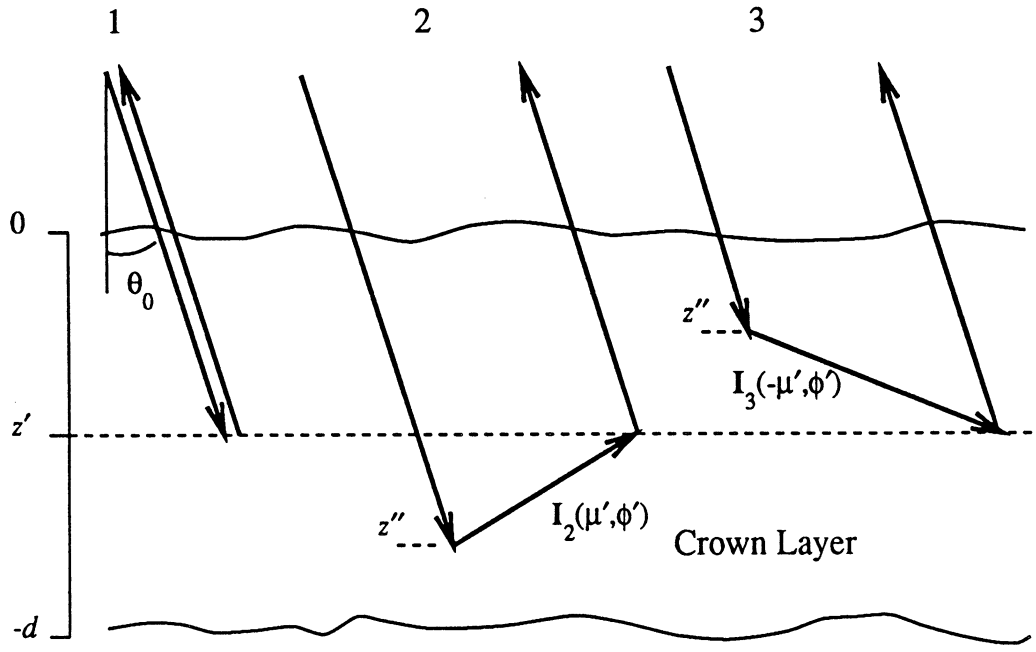

Figure E.1: Terms contributing to direct crown backscatter in the second-order solution.

is illustrated in Figure E.1. The mechanisms involved in each process are:

- Term 1: This is the first-order term that represents an intensity incident on the layer at an angle θ_0, propagating to a depth z' and scattered directly back to the radar.

- Term 2: This is a second-order term representing an intensity that is incident on the layer at an angle θ_0, propagates to a depth z'', is then scattered in an upward-going direction defined by (μ', ϕ'), propagates to a depth z', and is then scattered back toward the radar.

- Term 3: This is a second-order term similar to term 2. It corresponds to an intensity that is incident on the layer at an angle θ_0, propagates to a depth z'', is

then scattered in a downward-going direction defined by $(-\mu', \phi')$, propagates to a depth z', and is then scattered back toward the radar.

It is important to note that for a given radar incidence angle, computation of term 1 requires knowledge of the crown layer phase matrix only for a single scattering configuration. Similarly, knowledge of the extinction matrix is required only for intensity propagating in the $(-\mu_0, \phi_0)$ and $(\mu_0, \phi_0 + \pi)$ directions. However, computation of terms 2 and 3 requires knowledge of the phase and extinction matrices for scatter and propagation in all directions. For complicated phase and extinction matrices, this greatly increases the time required to compute the second order solution.

APPENDIX F

CONNECTING MODELS FOR CANOPY BIOPHYSICAL PARAMETERS

This appendix discusses some connecting models that relate fundamental canopy parameters to the parameters that drive MIMICS. Section F.1 defines the volume fractions of leaves, branches and trunks in a canopy, section F.2 defines the leaf area index of a canopy and section F.3 defines the specific and total water densities and biomasses of the canopy constituents. All three sections relate their defined parameters to MIMICS inputs.

F.1 Elemental Volume Fractions

The volume fraction of particles with an average volume $\bar{V}_p$ (cubic meters) distributed with a density N_p (particles per cubic meter) is

$$v_p = N_p \bar{V}_p. \tag{F.1}$$

Therefore, the volume fraction of leaves within the crown layer is given by

$$v_l = N_l \tau \iint ab f_d(a,b)\, da\, db \tag{F.2}$$

where N_l is the number density of leaves within the crown volume, τ is the leaf thickness, a and b are the dimensions of the equivalent flat plates that model the

leaves and $f_d(a,b)$ is the probability distribution function (PDF) of leaf sizes. Here, the leaf thickness is assumed to be constant for all of the leaves.

Similarly, the volume fraction of branches within the crown layer is given by

$$v_b = \frac{\pi N_b}{4} \iint l_c d_c^2 f_c(l_c, d_c)\, dl_c\, dd_c \tag{F.3}$$

where N_b is the number density of branches within the volume, l_c is the branch length, d_c is the branch diameter and $f_c(l_c, d_c)$ is the PDF of branch sizes.

Finally, the volume fraction of boles within the trunk layer is

$$v_t = \frac{\pi N_t}{4\bar{H}_t} \iint H_t d_t^2 f_c(H_t, d_t)\, dH_t\, dd_t \tag{F.4}$$

where N_t is the area density of trunks over the appropriate landscape patch, $\bar{H}_t$ is the average height of the trunk layer, H_t and d_t are the bole height and diameter, respectively, and $f_c(H_t, d_t)$ is the PDF that describes the distribution of bole size. Here, a landscape patch is defined as a section of land that consists of some identifiable stand that is homogeneous with respect to the spatial distribution of the canopy elements.

F.2 Leaf Area Index

The leaf area index (LAI) is defined by Ulaby *et al.*, [70], p. 1563 as the total single-side surface area of all the leaves contained in the canopy over a unit area of ground. This quantity is given by

$$LAI = \frac{d\, v_l}{\tau} \tag{F.5}$$

where v_l is the leaf volume fraction, d is the thickness of the crown layer and τ is the leaf thickness.

F.3 Biomass Parameters

F.3.1 General Definitions

The gravimetric moisture content of a specific plant part is defined as

$$m_g = \frac{M_w}{M_w + M_d} \tag{F.6}$$

where M_w is the mass of the water in the plant part and M_d is its dry mass. The dry mass for a particle with volume $V_p(\text{cm}^3)$ is

$$M_d = \rho_p V_p \qquad \text{(grams)} \tag{F.7}$$

where ρ_p is the dry density of the particle in grams per cubic centimeter. Knowing M_d and m_g, the mass of water in the particle is given by

$$M_w = \frac{m_g}{1 - m_g} M_d \qquad \text{(grams)} \tag{F.8}$$

and the specific water density within such a particle is

$$D^s_{wp} = \frac{M_w}{V_p} \tag{F.9}$$

$$= \frac{m_g}{1 - m_g} \rho_p \qquad \left(\frac{\text{g}}{\text{cm}^3}\right). \tag{F.10}$$

Knowing the density of water in a typical particle, it is of interest to find the total area density of water in the landscape patch that contains the distribution of such particles. For particles distributed with a volume fraction v_p, the total area density of water within the landscape patch is

$$D^t_{wp} = 1000\, D^s_{wp} v_p h_p \tag{F.11}$$

$$= 1000 \frac{m_g}{1 - m_g} \rho_p v_p h_p \qquad \left(\frac{\text{kg}}{\text{m}^2}\right) \tag{F.12}$$

where h_p is the vertical extent (in meters) of the particle distribution.

The specific biomass of a particle is defined in terms of mass per unit volume of the specific plant part. The total biomass is defined in terms of the total mass per unit area over the appropriate landscape patch. Both biomasses may be defined in terms of wet and dry plant material. The specific dry biomass of a particle is equivalent to its dry density. The specific wet biomass of the particle is

$$B^s_{wp} = \rho_p + D^s_{wp} \tag{F.13}$$

$$= \left[\frac{\rho_p}{1 - m_g}\right] \qquad \left(\frac{\text{g}}{\text{cm}^3}\right). \tag{F.14}$$

The total dry biomass of a class of particles is

$$B^t_{dp} = 1000\,\rho_p v_p h_p \qquad \left(\frac{\text{kg}}{\text{m}^2}\right) \tag{F.15}$$

and the total wet biomass of a class of particles is

$$B^t_{wp} = B^t_{dp} + D^t_{wp} \tag{F.16}$$

$$= 1000\,\rho_p v_p h_p \left(\frac{1}{1 - m_g}\right) \tag{F.17}$$

$$= 1000\,v_p B^s_{wp} h_p \qquad \left(\frac{\text{kg}}{\text{m}^2}\right). \tag{F.18}$$

F.3.2 Constituent Biomasses and Water Contents

Table F.1 lists the specific water contents and the specific biomasses for the three canopy constituents. Each of these parameters is given in units of grams per cubic centimeter and represents the density of water or material within the plant part itself. The variable ρ represents the dry density of the vegetation material and the variable m_g represents the gravimetric moisture of the constituent part as defined by (F.6).

Table F.2 lists the total water density and total biomasses of the indicated canopy constituents. These parameters are defined in units of kilograms per square meter

and account for the constituent mass per unit area over the appropriate landscape patch. The variable h_c represents the crown the thickness of the crown layer and d represents the thickness of the trunk layer.

The total biomass of leaves is also known as the total foliar biomass and defines the mass of leaves or needles per unit volume of canopy crown. For deciduous trees in temperate climates, this quantity is closely related to the net primary production.

Table F.1.
Specific water content and biomasses of the individual canopy constituents.

Constituent	Specific Water Content ($\frac{g}{cm^3}$)	Specific Dry Biomass ($\frac{g}{cm^3}$)	Specific Wet Biomass ($\frac{g}{cm^3}$)
Leaves	$D^s_{wl} = \frac{m_{gl}}{1-m_{gl}}\rho_l$	$B^s_{dl} = \rho_l$	$B^s_{wl} = \frac{\rho_l}{1-m_{gl}}$
Branches	$D^s_{wb} = \frac{m_{gb}}{1-m_{gb}}\rho_b$	$B^s_{db} = \rho_b$	$B^s_{wb} = \frac{\rho_b}{1-m_{gb}}$
Trunks	$D^s_{wt} = \frac{m_{gt}}{1-m_{gt}}\rho_t$	$B^s_{dt} = \rho_t$	$B^s_{wt} = \frac{\rho_t}{1-m_{gt}}$

Table F.2.
Total water content and biomasses of the canopy constituents.

Constituent	Total Water Density ($\frac{kg}{m^2}$)	Total Dry Biomass ($\frac{kg}{m^2}$)	Total Wet Biomass ($\frac{kg}{m^2}$)
Leaves	$D^t_{wl} = 1000 D^s_{wl} v_l h_c$	$B^t_{dl} = 1000 \rho_l v_l h_c$	$B^t_{wl} = 1000 B^t_{dl} v_l h_c$
Branches	$D^t_{wb} = 1000 D^s_{wb} v_b h_c$	$B^t_{db} = 1000 \rho_b v_b h_c$	$B^t_{wb} = 1000 B^t_{db} v_b h_c$
Trunks	$D^t_{wt} = 1000 D^s_{wt} v_t d$	$B^t_{dt} = 1000 \rho_t v_t d$	$B^t_{wt} = 1000 B^t_{dt} v_t d$
Total Woody Material	$D^t_{ww} = D^t_{wb} + D^t_{wt}$	$B^t_{dw} = B^t_{db} + B^t_{dt}$	$B^t_{ww} = B^t_{wb} + B^t_{wt}$
Total Crown Material	$D^t_{wc} = D^t_{wb} + D^t_{wl}$	$B^t_{dc} = B^t_{db} + B^t_{dl}$	$B^t_{wc} = B^t_{wb} + B^t_{wl}$
Total Canopy Material	$D^t_{wl} + D^t_{wb} + D^t_{wt}$	$B^t_{dl} + B^t_{db} + B^t_{dt}$	$B^t_{wl} + B^t_{wb} + B^t_{wt}$

APPENDIX G

MODELING MULTIANGLE AND MULTITEMPORAL BACKSCATTER FROM A WALNUT ORCHARD – THE EOS SYNERGISM STUDY

In this appendix, MIMICS I is used to model microwave scatterometer data that were obtained during the August 1987 EOS Simultaneity Experiment (Cimino *et al.*,[9]; Dobson *et al.*,[15]; McDonald *et al.*,[41], [42],[43], [44]). During this experiment, truck-based scatterometers were used to measure radar backscatter from a walnut orchard in Fresno County, California. Two sets of L- and X-band measurments are modeled. The first set consists of a seies of multiangle data for which a set of trees was observed at varying angles of incidence. The second set consists of a series of diurnal measurements in which this same set of trees was observed continuously over several 24 hour periods.

With *in situ* ancillary data describing canopy architecture and moisture conditions used as input, MIMICS is run at L- and X-band frequencies of 1.5 GHz and 9.6 GHz. Measured scatterometer data are compared to theoretical data generated by MIMICS. MIMICS is seen to predict the diurnal variations that are observed on 24 hour cycles. Examinations of backscatter response to changes in canopy dielectric properties are performed to determine the causes of the changes observed in the short

term trends and diurnal patterns.

G.1 Study Objectives and Test Site Description

One of the objectives of the EOS Synergism Study is to characterize short-term variations that occur in vegetation canopies as a result of processes that change on rapid temporal scales (Cimino *et al.*,[9]; Way *et al.*,[81]). To this end, a concern of this analysis is to model the diurnal variations observed in the microwave backscatter from a tree canopy. Successfully coupling the measured canopy backscatter to modeled data will significantly aid in understanding the diurnal and short-term changes in canopy properties, thereby allowing one to infer physiological processes occurring in the plant. This in turn will influence the ability to monitor changes in vegetation that occur on both seasonal and year-to-year time scales.

A field experiment was performed at the Kearney Agricultural Center in Fresno County, California during the summer of 1987 as part of the synergism study. The test site consisted of a stand of over 200 six-year-old black walnut trees. The evapotranspiration of these trees has been monitored for several years, thus providing a somewhat controlled environment in which the synergism study could be performed.

The orchard consisted of several individual water-stressed and unstressed tree plots. This analysis focuses on one individual plot of 48 unstressed trees. The average spacing between orchard rows was 6.7 meters and the average spacing between trees of a given row was 3.3 meters. These trees were irrigated in the evening with the amount of water equivalent to 100% of the water that evaporated from the canopy during the day as determined by meteorological measurements made at a nearby weather station. This experiment occurred during the trees' second year of controlled water treatment.

A hedgerow pruning technique has been used on these trees for several years. Consequently, the orchard does not represent a canopy with a true continuous crown layer. However, the tree crowns represent a significant enough fraction of the crown layer to allow for the canopy to be modeled as having a continuous crown layer. This is accomplished in the modeling analysis by re-distributing the crown layer constituents uniformly throughout the crown layer as if this layer were indeed continuous, thereby applying effective constituent volume densities in computing the phase and extinction matrices.

G.2 Scatterometer Measurement Procedure

Several sets of microwave scatterometer data were recorded over the course of the synergism experiment (Cimino *et al.*,[9]; Dobson *et al.*,[15]). The scatterometer experiments were designed to investigate the possibility of diurnal variations in radar backscatter from tree canopies. This analysis focuses on two of these data sets. The first is a set of multi-angle data in which the same set of trees were observed at incidence angles ranging from 40° to 55°. This measurement set was recorded over a time span of about two hours during the mid-afternoon. The second data set consists of a three-day measurement series during which this same set of trees was observed continuously over a three day period at a 55° incidence angle.

G.2.1 System Description and Operation

L- and X-band data were recorded using the University of Michigan scatterometer system, POLARSCAT (Tassoudji *et al.*,[58]), which was mounted on a boom platform for observation of the orchard. POLARSCAT is a calibrated polarimetric radar system capable of measuring the amplitude and phase of the signal backscat-

tered from a scene illuminated by its antenna for each of the four linear polarization configurations (HH, VV, HV, VH). The L- and X-band channels operated at 1.5 and 9.6 GHz, respectively.

An HP 8753 Vector Network Analyzer functions as the transmit source and the primary signal processor. Automatic control of the equipment is accomplished with an HP 9000 computer. The computer is interfaced with the network analyzer and peripheral equipment including a disc drive and printer to provide for real-time data reduction, hard-copy output, and data storage. Other functions of the system are controlled by a network of DC control lines which originate from a manually operated control panel. This network controls the scatterometer RF sections, the antenna positioner, the polarization switching, and boom movement.

The antennas were mounted on a rotatable positioner at the top of a rotatable boom that allowed pointing along any direction in azimuth and elevation. A video camera was mounted next to the antennas to allow the operator to view antenna pointing direction with a video monitor. The HP 9000 computer, HP 8753 Vector Network Analyzer, peripheral equipment, and other controlling instrumentation were located inside a motor home to provide for cooling and a clean working environment. The boom was elevated to a height of 12.2 meters and the system was parked next to the orchard.

Each canopy measurement was recorded for a fixed incidence angle and polarization configuration by rotating the antennas in azimuth and recording 30 independent samples over the azimuth extent of the target. The 30 samples were then averaged together to yield an average radar backscatter over the azimuth sweep. Thus, each backscatter data point corresponds to an average of thirty spatially independent backscatter measurements. This type of processing allows for the effects for signal

fading and target inhomogeneities to be accounted for.

Figure G.1 illustrates the scatterometer measurement geometry. The region probed by the scatterometer contained three rows of trees. The shaded areas representing the tree crowns correspond to estimated volumes that contain foliage. The sensed volume V shown in Figure G.1(a) may be determined at a slant range R given the radar beamwidth β and look angle θ. The volume V has a length that depends on the range resolution of the scatterometer system. Since the vegetation canopy has a deterministic row structure, the fraction of V that contains vegetation may be readily computed through geometrical analysis. Considering Figure G.1(b), as the scatterometer scans through an azimuth angle α, V traces out an arc centered at the slant range R. The *foliage fraction* may be defined as the fraction of this scanning arc volume at the slant range R that intersects the foliage volume.

Figure G.2 compares the uncalibrated backscattered power as a function of slant range for L- and X-bands to the foliage fraction computed using an X-band antenna beamwidth $\beta = 2.8°$. Through a straightforward geometrical analysis (Paris,[46]), it is possible to determine the sources of backscatter that contribute to the total backscattered power at a given slant range. Useful information exists at ranges where the power is above the noise floor. From this standpoint, useful data exist for $11 \leq R \leq 35$ at L-band and for $13 \leq R \leq 18$ at X-band. Comparing these traces to the foliage fraction indicates that significant sources of L-band backscatter exist at ranges for which the foliage fraction does not exist, thereby indicating the presence of significant scattering interactions between the canopy and ground surface. On the other hand, the X-band backscattered power contains essentially no information outside the foliage fraction region, indicating a lack of such scattering interactions. The reason for the apparent lack of backscatter interaction mechanisms

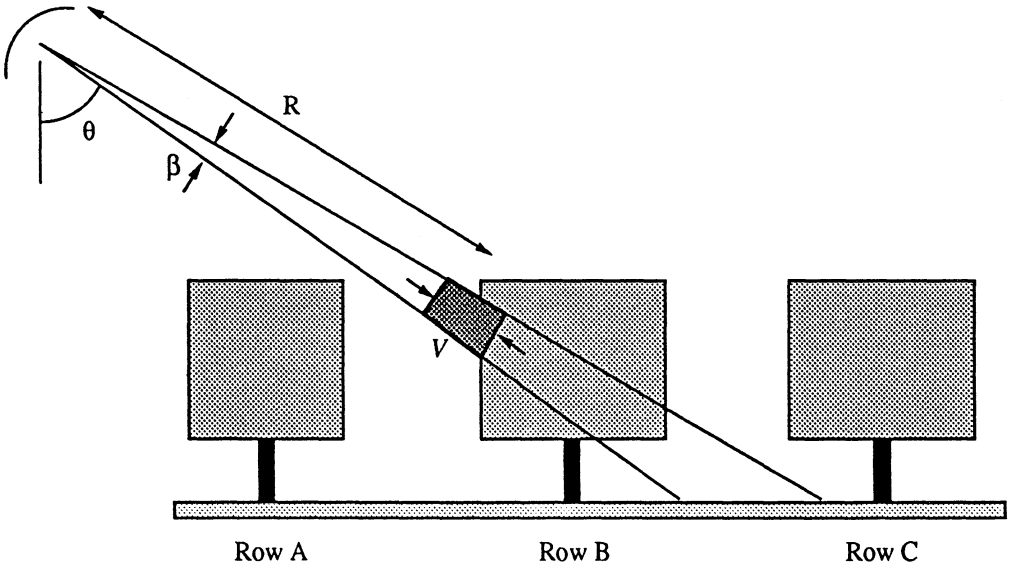

(a)

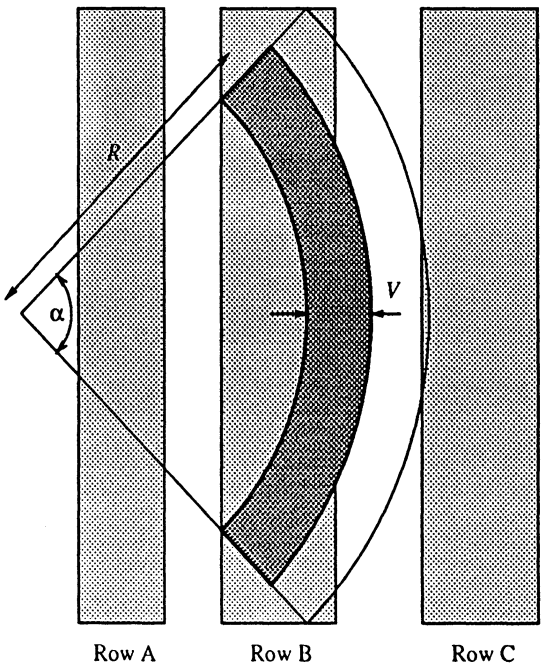

(b)

Figure G.1: Side view (a) and top view (b) of the walnut orchard showing the scatterometer measurement geometry. For a scatterometer beamwidth β, the sensing volume V is defined at a given slant range R by the pulse width and the scanning arc angle α.

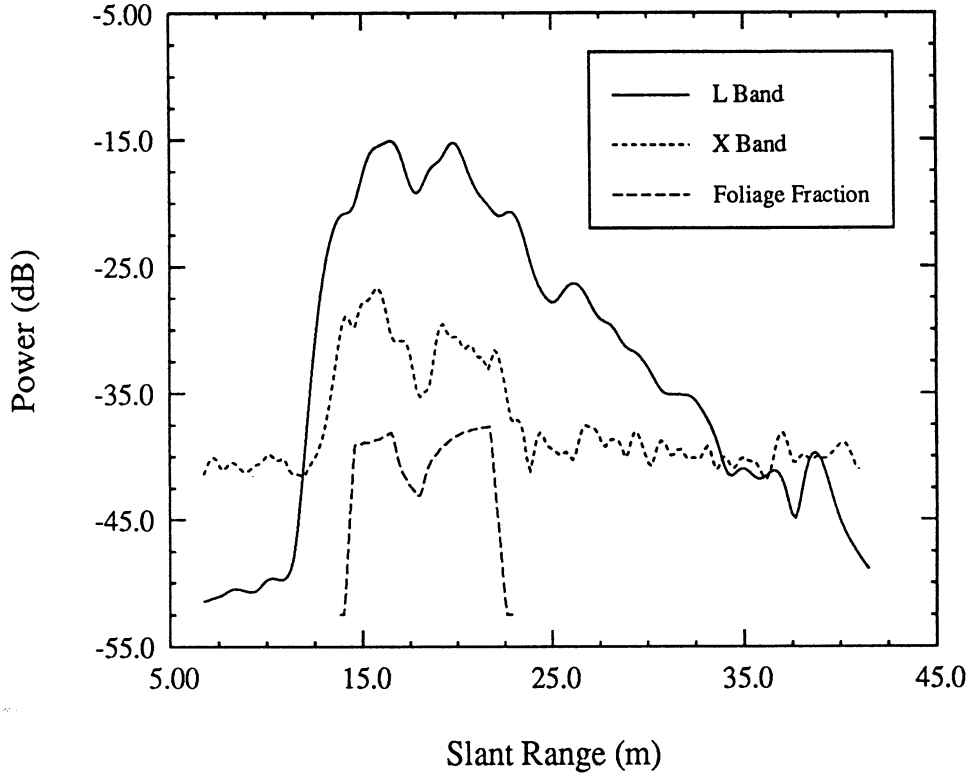

Figure G.2: Uncalibrated L- and X-band canopy backscatter *versus* slant range at $\theta = 55°$. The foliage fraction was computed for the estimated X-band sensing volume and scaled to fit on the dB axis.

at X-band is twofold. First, the occurrence of such interactions at ranges outside the immediate crown volume is masked by the system noise. That is, the signal level of these mechanisms is below -40 dB. Second, the relatively narrow X-band antenna beamwidth ($\beta = 2.8°$) limits the size of the sensing volume V to such an extent that much of these interaction mechanisms are lost simply because measurement geometry prevents them from being observed. If the scatterometer were positioned on a much higher boom, the measurement footprint within the canopy would be large enough to observe these interactions. X-band modeling in this analysis will focus on the direct crown component of canopy backscatter. It is interesting to note that the foliage fraction predicts the slight dip in backscattered power that occurs at $R \simeq 16$ m as a result of the hedgerow canopy structure and that this drop is more significant at X-band than at L-band.

G.2.2 Calibration

The scatterometers were calibrated to an absolute level using a set of wire meshes and a Luneberg lens. In order to calibrate all four polarization configurations, a polarimetric calibration target was developed. The target consisted of an array of parallel wires oriented 45° with respect to the antenna polarization vectors. This configuration generates like- and cross-polarized returns for each of the two transmit polarizations.

One calibration sequence was performed using the wire targets before the multi-angle data set was recorded. Two calibrations were performed against the polarimetric targets during the diurnal data series between August 24 - 26. One calibration was performed immediately before the beginning of the diurnal series and the other was performed immediately after the diurnal series was completed. Between these

calibrations, system stability was monitored by measuring the backscatter from the Luneberg lens several times a day.

G.3 Orchard Canopy Characteristics

As part of the synergism study, an extensive set of ancillary data was collected in order to characterize the walnut orchard. Data describing canopy architecture (Ustin *et al.*,[71],[72]), dielectric properties (Dobson,[10]) and canopy water status (Weber and Ustin, [82],[83]) were analyzed to determine canopy density, branch and leaf orientation and size distribution, constituent dielectric properties, and other gross canopy characteristics. This section describes the canopy architecture and other properties that have been adapted for input to MIMICS.

G.3.1 Canopy Architecture

Because of the row structure of the orchard and the hedge-row pruning practices, statistical sampling of the tree crown geometry was not possible. Instead, the length, diameter at mid-length and zenith and azimuth orientation angles for all branches with diameters greater than 2 cm were measured for eight trees. The number and size classes of all lateral branches were also recorded. All branch segments were numbered so that the tree skeletons could be reconstructed from these observations. In addition, the smaller branches with diameters less than 4 cm were statistically sub-sampled by class size. Four sample classes were considered (0-1, 1-2, 2-3, 3-4 cm diameters).

To adapt the branch geometry data for input to MIMICS, the orchard is divided into distinct crown and trunk layers with heights of 3.1 m and 1.7 m, respectively. These heights correspond to the observed canopy architecture. The branches are

then divided into the four size classes identified in Table G.1. Figure G.3 is a sketch of the geometry of an individual tree, showing the four branch classes and the leaves.

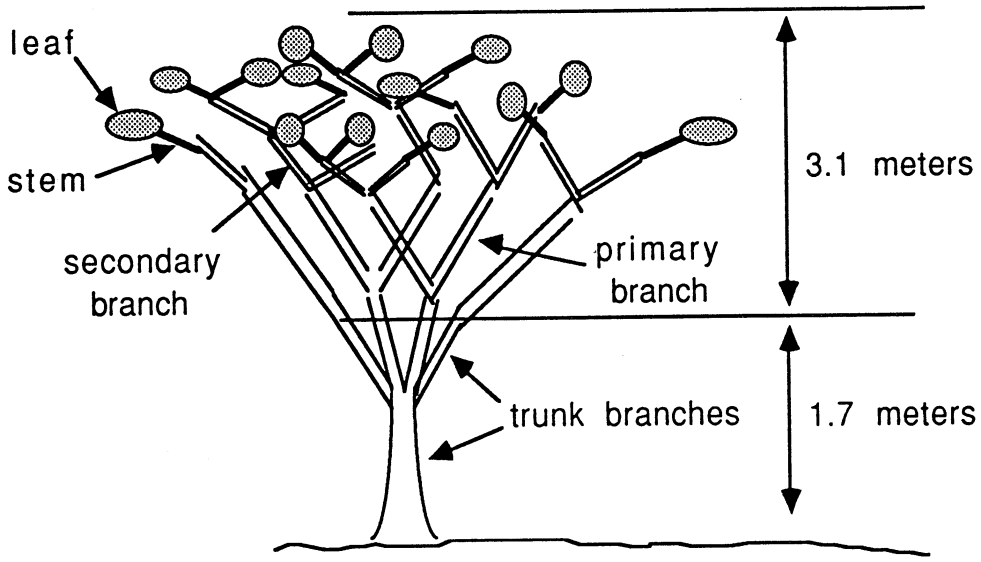

Figure G.3: Illustration of a walnut tree showing the four branch classes and the leaves.

The larger branches tend to be located in the lower portion of the canopy and are therefore considered to be part of the trunk layer. This layer consists of the trunk-branch size class and includes the tree trunks and all branches with diameters greater than 4.0 cm. The remaining three branch size classes are distributed throughout the crown layer. As shown in Table G.1, the primary branch class consists of all branches with diameters less than 4.0 cm and greater than 0.9 cm. The secondary branch class includes those branches whose diameter is less than 0.9 cm and greater than 0.4 cm. The high order stems constitute the smallest size class and have diameters less than 0.4 cm. Most of these stems represent the green petioles that are attached directly to the leaves. These size parameters, are summarized in the table along with their

average diameter and length, volume density (branches per cubic meter), and the functional form of branch orientation for each class.

In general, the larger branches tend to have mostly vertical orientations whereas the smaller branches exhibit no preferred orientation. Plots of the branch orientation PDFs are shown in Figure G.4. The branches in the trunk layer were assigned a $\cos^6\theta$

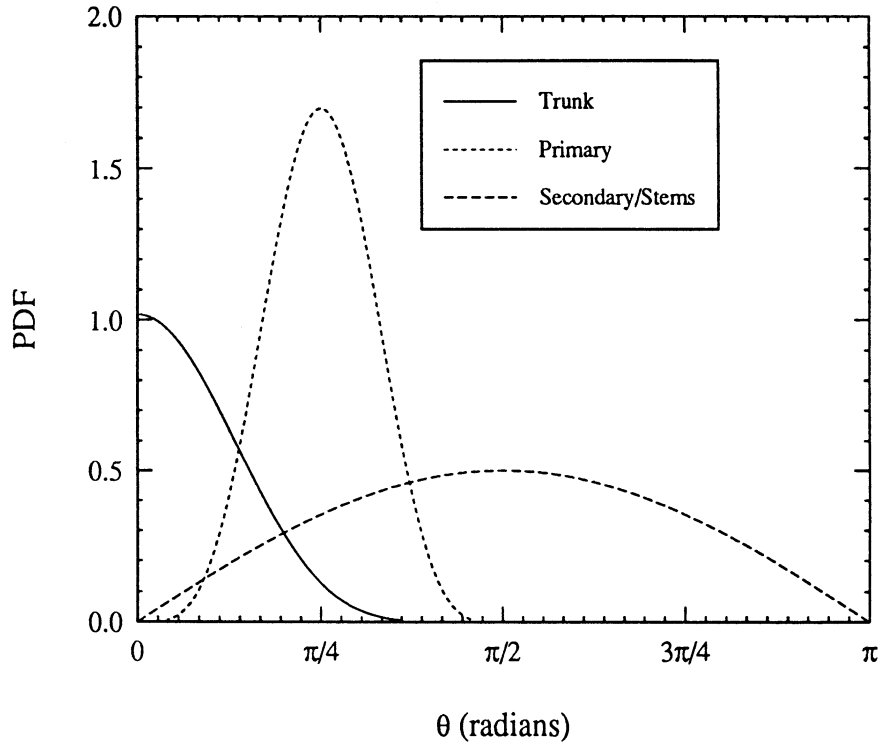

Figure G.4: Branch orientation probability distribution functions (PDFs).

distribution so that the mean value of θ is 0. The primary branches were assigned a distribution of $\sin^4 2\theta$ so that θ has a mean value of 45°. The secondary branches and higher order stems were assigned spherical distribution functions ($\sin\theta$)so that they show no preferred pointing direction in the elemental solid angle $d\Omega = \sin\theta d\theta d\phi$. This implies that these branches are oriented such that their axis directions are uniformly distributed on a spherical surface. Trigonometric functions were chosen to describe these distributions since they provide a reasonable description of canopy

architecture and their forms allow for convenient numerical integration. These functions are converted into probability distributions for use in MIMICS by dividing each by a normalizing factor given by $\int_0^\pi f(\theta)\,\mathrm{d}\theta$. Note that the PDFs describing primary and secondary branch orientations are completely described over the domain $0 < \theta < \frac{\pi}{2}$.

Table G.1: Canopy Branch Classes.

Constituent Class Characteristic	Branch Size Class			
	Trunk Branches	Crown Branches		
		primary	secondary	stems
Max. Diam. (cm)	-	4.0	0.9	0.4
Min. Diam. (cm)	4.0	0.9	0.4	-
Ave. Diam. (cm)	7.3	1.9	0.6	0.1
Ave. Length (cm)	92.8	35.8	10.9	5.0
Density ($\#/\mathrm{m}^3$)	0.13	1.25	1.14	250
Orientation $f(\theta)$	$\cos^6\theta$	$\sin^4 2\theta$	$\sin\theta$	$\sin\theta$

Characteristics of the leaves were determined from detailed leaf counts (Ustin *et al.*,[72]) and are summarized in Table G.2. Leaves were assigned a $\sin\theta$ orientation such that the direction in which the normal to the leaf surface is oriented is uniformly distributed over a spherical surface. The leaves are modeled as thin circular dielectric disks with a specified diameter and thickness. The leaf number density together with the leaf diameter and crown height yield an equivalent canopy leaf area index (LAI) of 3.4.

For purposes of defining the folding angle χ, the leaf is modeled as a square plate of area $a \times a$ equivalent to the area of the leaf modeled as a disk. The angle χ is measured along the leaf midrib as illustrated in Figure G.5(a). Knowing χ and a determines s, the distance between the opposite edges of the leaf. The leaf radius of curvature ρ is then defined as shown in Figure G.5(b). If the square plate conforms to

Table G.2: Leaf Characteristics.

Number density	250 leaves per cubic meter
Average diameter	7.47 cm
Average thickness	0.1 mm
Leaf area index	3.4
Orientation	$f(\theta) = \sin\theta$
Folding angle	$\chi = 152°$ along midrib
Radii of curvature	$\rho_1 = 7.7$ cm (along midrib)
	$\rho_2 = 10$ cm

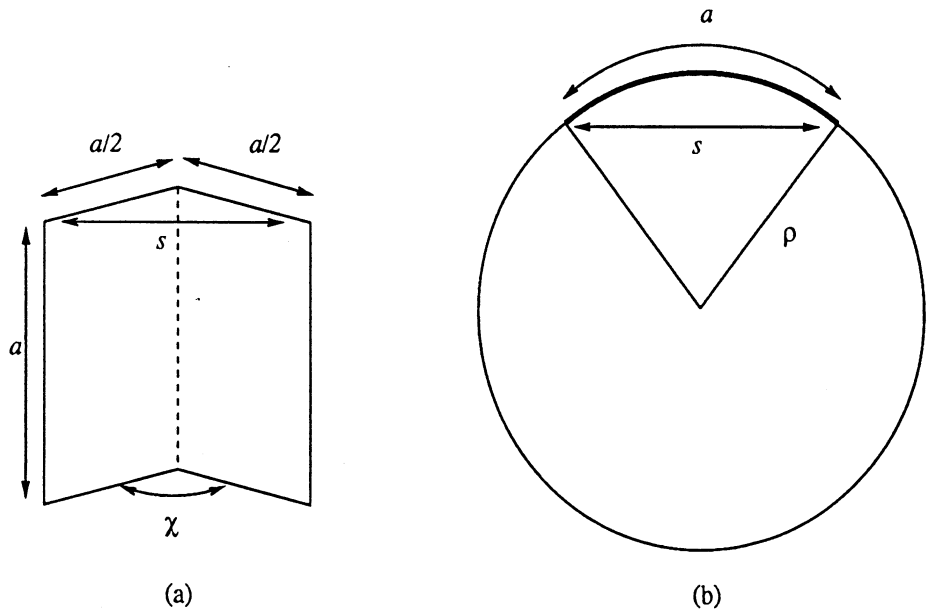

Figure G.5: Geometry used to model an $a \times a$ leaf folded along its midrib. The folding angle χ shown in (a) defines the distance s between the opposite edges of the leaf. Chord length s and arc length a define the sector of a circle with radius ρ shown in (b).

a cylindrical surface such that a now defines a circular sector with chord length s, then ρ is the radius of the cylinder. ρ_1 corresponds to the radius of curvature determined from the leaf folding angle along the midrib. ρ_2, the radius of curvature along the other leaf axis, has not been derived from measured data but rather represents an estimated value.

The effect of leaf curvature on canopy backscatter may be accounted for through an analysis based on the model for a curved leaf introduced by Sarabandi *et al.* [51]. The backscattering cross section of a curved leaf (σ_c) normalized to that of a flat leaf (σ_f) of equivalent area may be approximated by

$$\frac{\sigma_c}{\sigma_f} = \left| \frac{1}{\gamma_1} \mathcal{F}(\gamma_1) \cdot \frac{1}{\gamma_2} \mathcal{F}(\gamma_2) \right|^2 \tag{G.1}$$

where

$$\mathcal{F}(\gamma) = \int_0^{\gamma} \exp\left(iu^2\right) \mathrm{d}u \tag{G.2}$$

is the finite range Fresnel integral,

$$\gamma_1 = \frac{a}{2}\sqrt{\frac{k_0}{\rho_1}}, \quad \gamma_2 = \frac{a}{2}\sqrt{\frac{k_0}{\rho_2}} \tag{G.3}$$

and k_0 is the free space wavenumber. A plot of (G.1) as a function of frequency is shown in Figure G.6. This plot illustrates the effect leaf curvature has on backscatter from a single leaf. Normalized backscatter of a leaf conformed to a cylindrical surface with $\rho_1 = 7.7$ cm and of a leaf conformed to an ellipsoidal surface with $\rho_1 = 7.7$ cm and $\rho_2 = 10$ cm are shown. For a given curvature geometry and radar frequency, an effective leaf diameter d_e may be defined that corresponds to the diameter of a flat disk-shaped leaf having backscatter identical to the curved leaf. Since $\sigma_c \sim A_e^2$ where A_e is the effective leaf area, the effective diameter is

$$d_e = \left(\frac{\sigma_c}{\sigma_f}\right)^{1/4} \cdot d_f \tag{G.4}$$

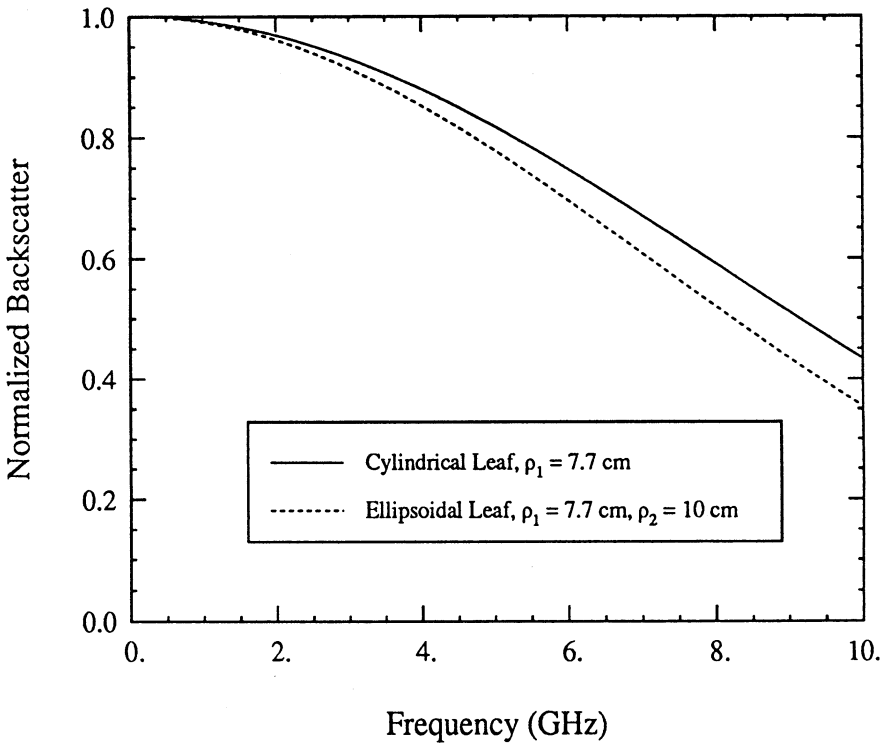

Figure G.6: Backscatter from a curved leaf normalized to a flat leaf of equal area. Backscatter is shown for a leaf curved to fit a cylindrical surface with radius of curvature $\rho_1 = 7.7$ cm and for a leaf curved to fit an ellipsoidal surface with $\rho_1 = 7.7$ cm and $\rho_2 = 10$ cm.

where d_f is the diameter of the flat leaf. The effect of leaf curvature on canopy backscatter may be approximated in MIMICS by using flat leaves with effective diameters that depend on the frequency under consideration. Table G.3 lists the normalized backscatter and corresponding effective diameters for L- and X-bands. At L-band, the effect of leaf curvature is essentially negligible.

Table G.3: Effects of Leaf Curvature at L- and X-Bands.

	Normalized Backscatter (σ_c/σ_f)		Effective Diameter (cm)
L-Band	0.972	(-0.1 dB)	7.42
X-Band	0.297	(-5.3 dB)	5.52
Flat Leaf	1.000	(0.0 dB)	7.47

A correction factor that accounts for the difference between the actual canopy LAI and the LAI observed with the scatterometer system may be determined by considering the foliage fraction together with the variation of leaf number density with height. The effective leaf area index may be computed by integrating the product of the average area of a single leaf A_l and the leaf number density per unit volume N_l over the slant range extent of the crown layer $d/\cos\theta$:

$$\mathrm{LAI}_e(\theta) = \int_0^{\frac{d}{\cos\theta}} N_l(s,\theta) A_l \cos\theta \, ds \tag{G.5}$$

The value of LAI_e represents an estimate of the leaf area actually observed by the scatterometer. The number density N_l for a given slant range s and incidence angle θ is given by $N_l(s,\theta) = f(s,\theta)N_{lc}(s)$ where $f(s,\theta)$ is the foliage fraction and $N_{lc}(s)$ is the number density of leaves at s. The correction factor $Q(\theta)$ by which the actual canopy LAI is modified is given by the ratio of the effective LAI to the actual canopy LAI, $Q(\theta) = \mathrm{LAI}_e(\theta)/\mathrm{LAI}$. By making use of canopy ground measurements and the scatterometer measurement geometry illustrated in Figure G.1, $Q(\theta)$ may be

computed over the range $40° \leq \theta \leq 55°$. The factor $Q(\theta)$ represents a slowly varying function that has a minimum of 0.35 at $\theta = 40°$, increases to a maximum of 0.6 at 51°, and then tails off to 0.55 at 55°.

G.3.2 Canopy Dielectric Characteristics

Observations of the relative dielectric constant of soil and vegetation were made *in situ* at 1.2 GHz using an Applied Microwave PDP1.2 field portable dielectric probe. Observations were made of the soil surface and tree trunks. Trunk measurements included both the exterior bark and the interior sapwood. The soil measurements were made using vendor-supplied attachments while the vegetation measurements were made using coaxial probe tips designed specifically for insertion into the tree boles. A statistically insignificant amount of dielectric data were recorded for the vegetation in the crown layer. However, the dielectric behavior of these constituents may be inferred from observations of other canopy physiological parameters, and the models applied here to predict the relative dielectric constant do in fact agree with the few recorded observations.

Dielectric Properties of Tree Trunks

To measure the relative dielectric constant of tree trunks, several probe tips were inserted at various depths into one of the tree boles in the 100% treatment plot. The probe could then be attached to any of these probe tips for observing the dielectric constant. The sensing probes were 0.141" in diameter, yielding a sensing volume for a dry medium that extends a maximum of 0.18 cm from the tip.

The dielectric properties of the tree boles were seen to vary dramatically with time and exhibit a diurnal pattern which depended upon the insertion depth of the probe

into the tree trunk. Figure G.7(a) shows a piecewise fit to the measured values of the real part of the dielectric constant. Data are shown for two insertion depths during a three day period that coincides with the time during which diurnal scatterometer data were recorded. The numbers on the time axis correspond to midnight on that day of August. The dielectric constant is seen to reach a peak near daybreak at about 6:00 am. Shortly thereafter, the values decrease rapidly until a minimum is reached at about 12:00 noon. Beginning at about 7:00 pm, the dielectric constant increases until the maximum is again reached. These trends are consistent with data observed throughout the entire coarse of the experiment.

The dielectric constant attained its highest values at about 2 cm depth inside the bole. Figure G.7(a) shows values recorded for this depth along with values observed at a 4-cm depth. In general, although the dielectric constant exhibits similar periodicity for all insertion depths, the values observed at other depths do not attain the extremely high maximum values observed at 2 cm nor do they reach the same minima. Although the maximum values obtained at the 2 cm depth approach that of water or sap, no bleeding of sap occurred around the probe tip. The piecewise fit was chosen to represent an estimate of average dielectric for the outer bole layers since these layers generally exhibit high loss and therefore limit propagation of the incident field into the inner trunk layers.

Figure G.7(b) compares this piecewise fit to the real and imaginary parts of bole dielectric constant for a 2-cm probe depth. To be consistent with measured data, a loss tangent of 0.25 was used to compute the imaginary part of the piecewise fit.

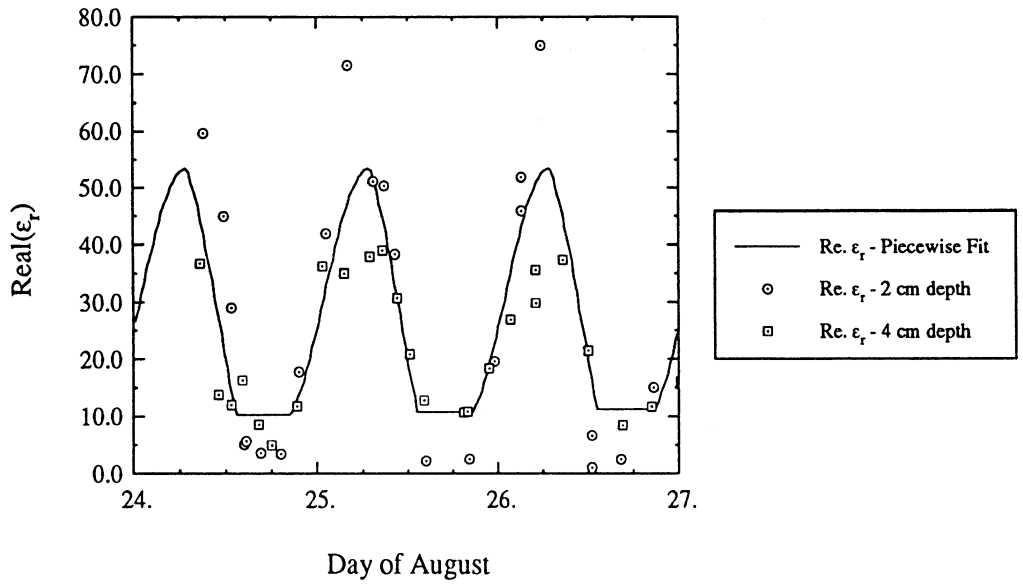

(a)

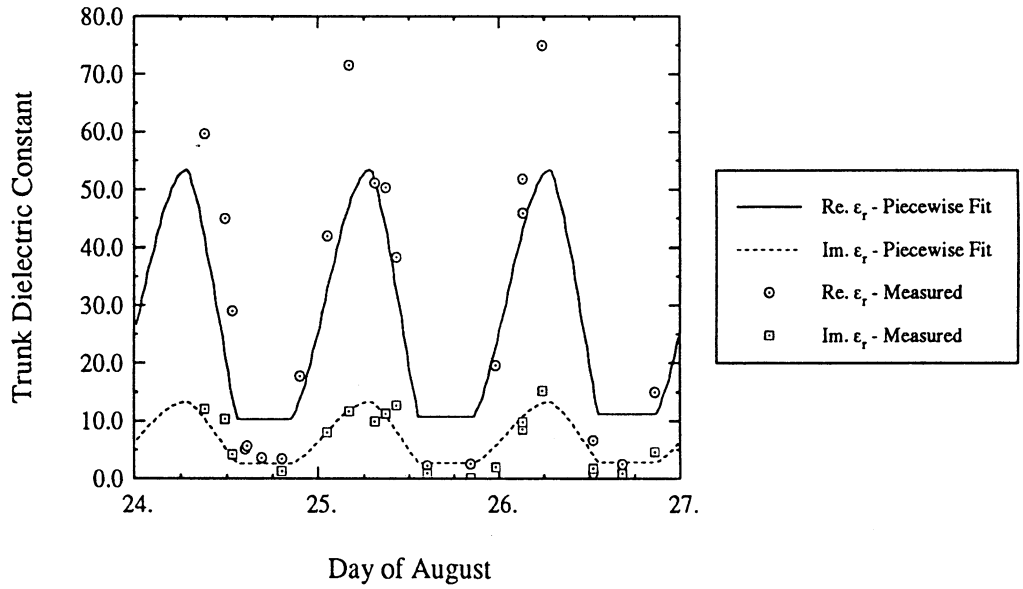

(b)

Figure G.7: Comparison of a periodic piecewise fit to measured L-band trunk dielectric constant data for (a) two insertion depths and (b) real and imaginary parts.

Dielectric Properties of Soil

The soil was monitored on an approximate hourly basis. Each observation consisted of a minimum of 15 independent, randomly selected samples used to calculate the mean ϵ_r of the surface layer. Because of spatial variations associated with the locations of the sprinkler heads used to irrigate the soil, the measured dielectric data exhibited a high degree of scatter that made it difficult to estimate an effective soil dielectric. Therefore, the soil surface area that received irrigation and remained mostly wet was analyzed separately from the area that received no irrigation and remained mostly dry. The overall effective dielectric behavior was then estimated by combining these results.

Figure G.8 illustrates the process used to estimate effective soil dielectric. Figure G.8(a) shows the real part of the measured dielectric data for the irrigated and non-irrigated areas. The fit to the measurements recorded for the irrigated areas was derived by considering the measured dielectric values together with the orchard irrigation schedule. During these three days, the orchard was irrigated 2.5 hours per day beginning at 6:00 each evening. The irrigation periods are manifest by the jumps in the dielectric constant that begin at 6 p.m. each day. The dielectric continues to increase until the irrigation shuts off. Then, ϵ_r decreases as the soil dries. The measurments of ϵ_r of the non-irrigated area were essentially constant with a real part of 3.2. The loss tangent of the soil dielectric was assigned a value of 0.1 at L-band, as was determined from the measured data.

Figure G.8(b) shows the real part of the L- and X-band effective soil dielectric used to model the combination of irrigated and non-irrigated areas. The X-band soil dielectric was estimated by applying the model developed by Hallikainen *et al.* [25]. This model expresses the real and imaginary parts ϵ_r' and ϵ_r'' of the dielectric constant

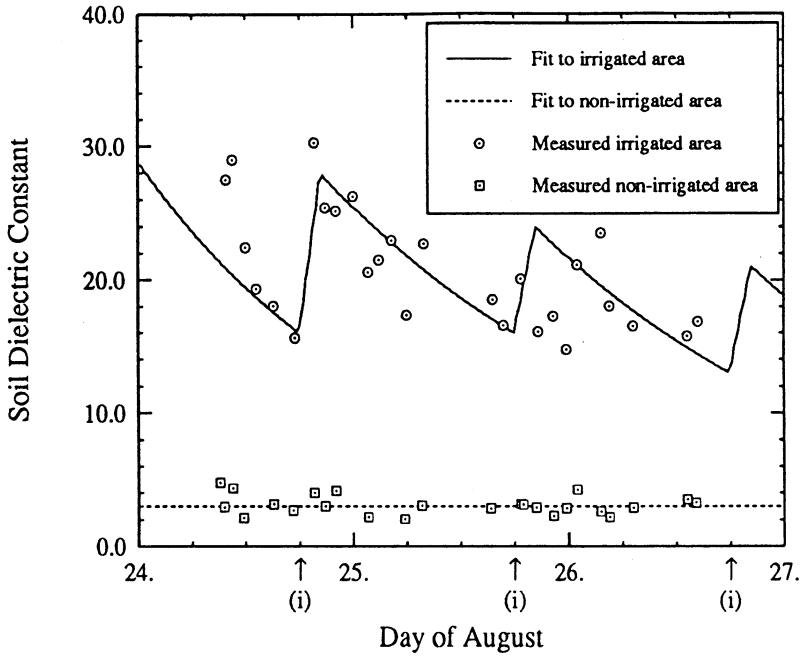

(a)

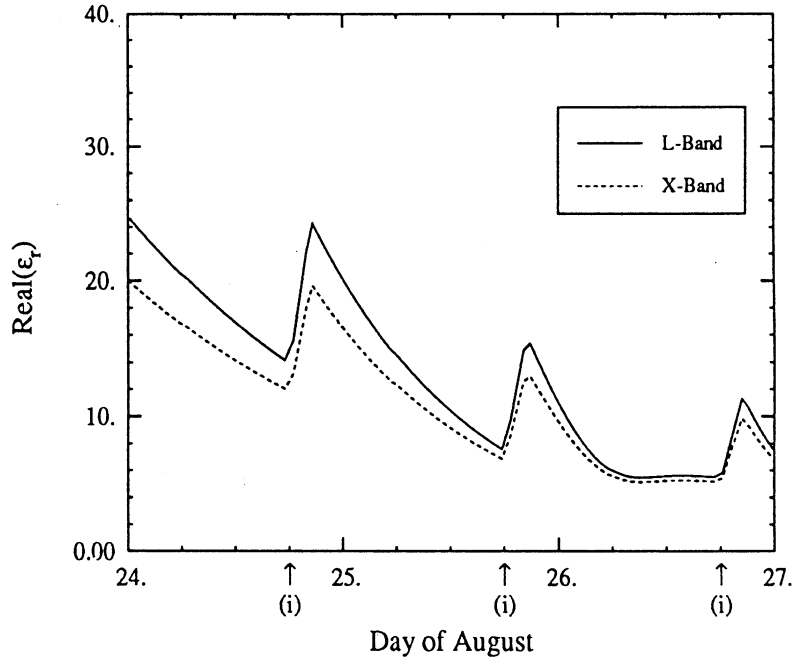

(b)

Figure G.8: Behavior of the soil dielectric constant showing (a) the fits to the measured L-band dielectric constants of the irrigated and non-irrigated areas and (b) the estimated behavior of the L- and X-band dielectric constant for the combination of irrigated and non-irrigated areas. (i) indicates the beginning of a 2.5 hour irrigation period.

of soil consisting of a mixture of sand, silt and clay in terms of the polynomial

$$\epsilon = (a_0 + a_1 S + a_2 C) + (b_0 + b_1 S + b_2 C)\, m_v + (c_0 + c_1 S + c_2 C)\, m_v^2 \quad \text{(G.6)}$$

where $\epsilon = \epsilon_r'$ or ϵ_r'', m_v is the soil volumetric moisture content and S and C are the sand and clay textural components of the soil in percent by weight. To determine the X-band soil dielectric, (G.6) was solved for m_v using the L-band dielectrics to find an effective value for m_v and then applied at 9.6 GHz to estimate the X-band dielectric.

The general decreasing trend in ϵ_r occurred because the canopy had been irrigated very heavily during the previous week. Whereas the canopy was irrigated 2.5 hours each day during the diurnal experiment, it had been irrigated 5 hours per day during the previous week. As the irrigated soil dried out form this saturated state, the total surface area of dry soil increased, thus leading to a general decrease in the effective soil dielectric over the three-day period.

By applying the wet soil dielectrics model, a correspondence may be drawn between the change in soil dielectric and the change in soil volumetric moisture. According to this dielectric model, the change in soil dielectric from a maximum of $\epsilon_r \simeq 22 + i2.2$ to a minimum of $\epsilon_r \simeq 5 + i0.5$ approximately corresponds to a decrease in soil volumetric moisture from 0.32 to 0.1, or 68%.

Dielectric Properties of the Crown Constituents

Very few dielectric measurements were obtained for tree crown constituents. However, the dielectrics of the leaves and branches may be inferred from other ancillary data. Leaf gravimetric moisture content mg_l may be used to determine the leaf dielectric constant. This quantity is defined in terms of the fresh and dry weights of the leaves, W_f and W_d, as $mg_l = \frac{W_f - W_d}{W_f}$. Analysis of wet and dry leaf weights

indicate that the average leaf gravimetric moisture was approximately 0.7. Applying the vegetation dielectric model proposed by El-Rayes, [18], and Ulaby and El-Rayes [63] at L- and X-bands, the relative dielectric constant of leaves were found to be $28.3 + i8.5$ and $21.8 + i8.8$, respectively. This value was also assigned to the dielectric of the higher order stems. No discernible variation of leaf gravimetric moisture with time was observed.

In order to assess the plant water status, a substantial amount of leaf water potential data was recorded (Weber and Ustin [82], [83]). The dielectric constants of the tree branches have been inferred by examining these leaf water potential measurements. Water potential is a complex characteristic of all plant tissue that defines the thermodynamic state of water in the plant (Bradford and Hsiao,[3]; Kramer,[34]; Passioura,[47]). Two components of water potential are of concern in this study. These are turgor pressure and osmotic potential. Turgor pressure is the pressure exerted by the cell contents on the cell walls. Osmotic potential is a measure of the ability of a solution to draw water from pure water through a semi-permeable membrane, and can be measured as the pressure that must be exerted on the solution such that no net flow of water occurs from pure water. Water potential is the sum of osmotic potential and turgor pressure. Measurement of water potential provides a sensitive means of assessing plant water status.

The movement of water through a plant is along a water potential gradient from the soil, through the roots and stems, to the leaves, and, finally, to the air. Evaporation of water from the leaf through the process of transpiration increases the concentration of solutes thereby decreasing the water potential. This leads to the movement of water from the stem to the leaf and so on down to the roots. In a steady-state situation, if the plant had adequate water, the system dynamics would

lead to a constant water potential at any point in the system. Water potential reaches a minimum when the plant reaches the period of highest water demand or when it is water stressed.

Figure G.9 shows the measured values of leaf water potential for the three day experiment duration. A periodic piecewise fit to these data is also shown. Each

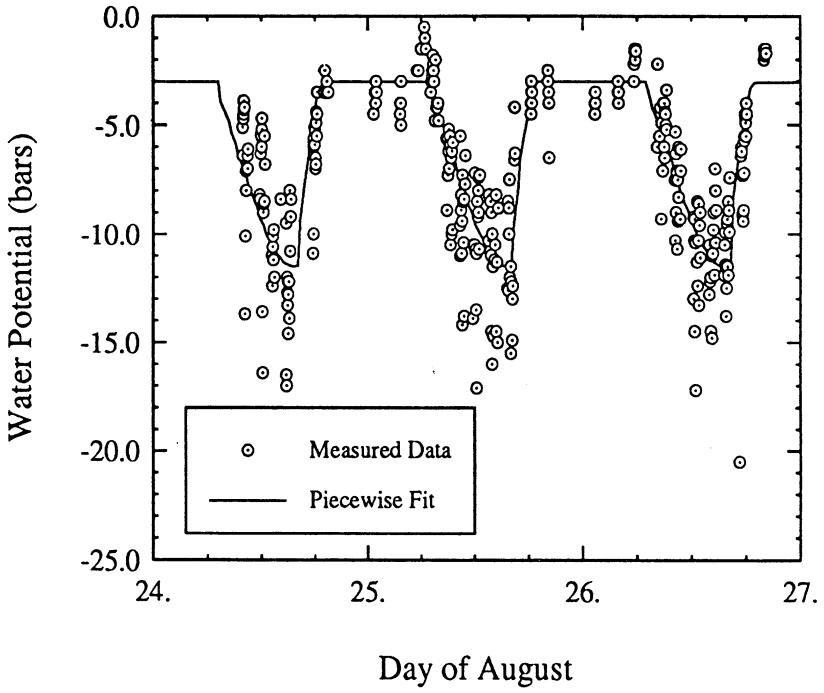

Figure G.9: Comparison of measured leaf water potential to piecewise fit.

measured data point represents the water potential measured for one individual leaf. More negative values of water potential indicate a stronger draw of water by the leaf from the plant. That is, the pressure with which the leaves are drawing water from the plant increases as the water potential becomes more negative. This phenomenon should have some effect on branch dielectric constant. Specifically, the branch di-

electric should decrease as leaf water potential becomes more negative. Similarly, as water potential becomes less negative, the leaves draw less water from the plant, and branch dielectric should increase. Therefore, the behavior of branch dielectric should be similar to that of the piecewise fit shown in Figure G.9.

Figure G.10 shows the real part of the piecewise fit to the dielectric constant for the three classes of woody vegetation. All measured values of the branch dielectric that were recorded during this time are also shown. These measured data were found by measuring the dielectric constant of a secondary branch at the point where it branched into higher order stems. The L-band piecewise fits shown for the branches were obtained by scaling the leaf water potential fit to match the measured data. Figure G.9 was first scaled to match the measured values of secondary branch dielectric. The primary branches were then assigned a dielectric function that had slightly more dynamic range than that used with the secondary branches. The maximum values of the secondary branch dielectrics were chosen to be close to the leaf dielectric. The loss tangent of all woody constituents, ϵ''/ϵ', is assigned a value of 0.25, as was measured for the bole and secondary branches.

Since all dielectric measurements of this orchard were performed at L-band, X-band dielectrics were obtained through application of the model developed by El-Rayes,[18] and Ulaby and El-Rayes [63] for estimation of vegetation dielectric constant. The vegetation dielectric is modeled with a Debye-Cole dual-dispersion model consisting of a free water component that accounts for the volume of the vegetation occupied by water in free form and a bound water component that accounts for the volume of the vegetation occupied by water molecules bound to bulk sucrose molecules.

Assuming the bulk density of the dry vegetation material $\rho = 0.4$ and a constant

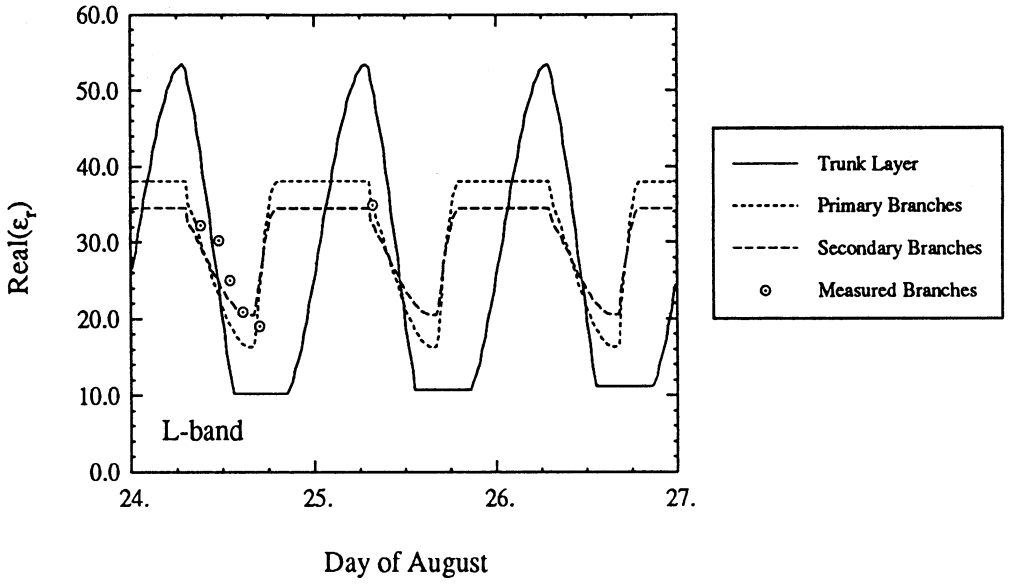

(a)

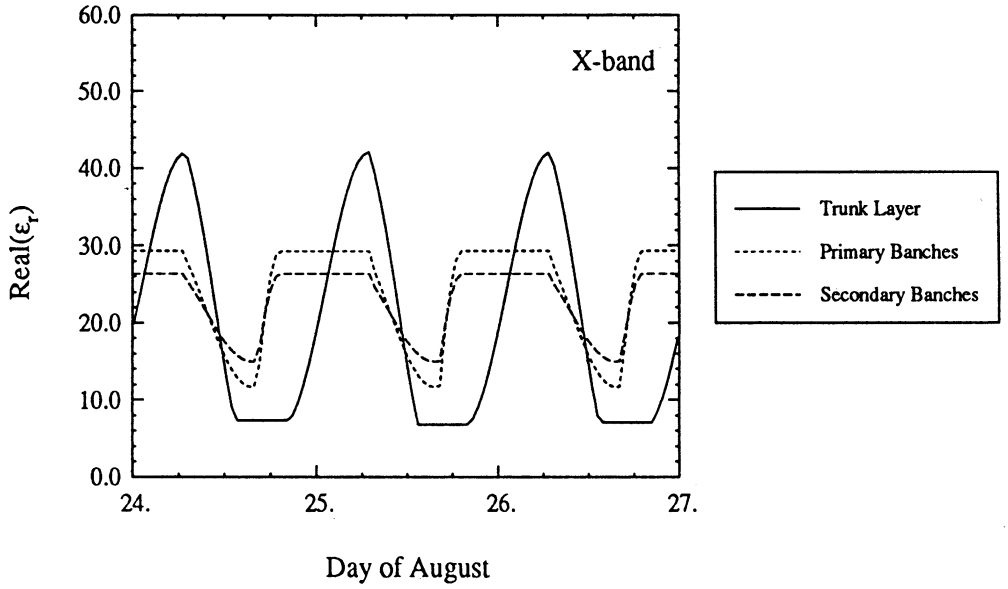

(b)

Figure G.10: Dielectric constants of woody constituents for (a) L-band and (b) X-band.

temperature $T = 13.6°$ C, the dielectrics model was numerically inverted at L-band (1.2 GHz) using the dielectric functions shown in Figure G.10(a), yielding effective values of m_g as a function of time. Given the effective m_g, the model was then applied at 9.6 GHz to obtain the real and imaginary parts of the X-band dielectrics. Figure G.10(b) illustrates the real part of ϵ_r at X-band. In general, the X-band dielectrics tend to be less than the L-band values and have less dynamic range. This frequency behavior has, in fact, been observed for other tree species (Dobson *et al.*,[11]). The diurnal variations shown in Figure G.10 are identical for all three days. That is, these functions were chosen to represent an average dielectric response of the vegetation over the duration of the diurnal experiment.

G.4 Modeling Analysis

As a first step in the modeling analysis, MIMICS was run as a function of radar look angle at L- and X-bands. Table G.4 lists the canopy dielectric parameters used in this analysis. These values correspond to measurements made at the approximate time that the multi-angle scatterometer data were recorded. Figure G.11

Table G.4: Canopy Dielectric Characteristics.

Constituent	L-Band	X-Band
Ground Surface	$25 + i2.5$	$20.2 + i7.6$
Trunk Branches	$45 + i11.2$	$35.0 + i14.8$
Primary Branches	$34 + i8.5$	$25.9 + i10.8$
Secondary Branches	$30 + i7.5$	$22.7 + i9.4$
Leaves and Stems	$28.3 + i8.5$	$21.8 + i8.8$

shows a comparison of L- and X-band modeled and measured data over the range $40° \leq \theta \leq 55°$ for like- and cross-polarized backscatter. Figure G.11(a) compares the predicted total canopy L-band backscatter with the scatterometer data. This

figure demonstrates very good agreement between MIMICS-generated data and the measured values. The like-polarized backscatter exhibit similar amplitudes with HH being slightly higher than VV in both the measured and modeled data while the cross-polarized backscatter is about 5 dB lower than the like-polarized response. Results similar to these have been obtained for like-polarized configurations by Chauhan and Lang [6] by using a distorted Born approximation to model the like-polarized backscatter from this data set.

The failure of the model to predict the cross-polarized backscatter at 40° is attributed to the inhomogeneous characteristics of the orchard canopy architecture. Whereas MIMICS I has been derived for a canopy that has a continuous crown layer, it is being used to model backscatter from a canopy with a crown layer that is discontinuous. As incidence angle becomes smaller, a larger proportion of the canopy area observed by the scatterometer consists of smooth, bare soil that is not covered by the orchard canopy. Since the model predicts backscatter for a canopy that has a homogeneous crown layer, some error will be introduced in the modeled data. We expect that the model will be more successful in predicting backscatter from this orchard at higher angles of incidence since the scatterometer observes almost no bare soil at these angles. We also expect this effect to be more pronounced for cross-polarized configurations since a smooth soil surface generates very little cross-polarized backscatter compared to that generated by the crown layer.

As has been shown in Figure G.2, measured X-band backscatter consists primarily of the direct crown contribution to the total canopy backscatter. Figure G.11(b) compares the predicted direct crown X-band backscatter with the scatterometer data. Here, MIMICS agrees with the level of the like-polarized backscatter but underestimates the cross-polarized response by as much as 10 dB. The failure of MIMICS

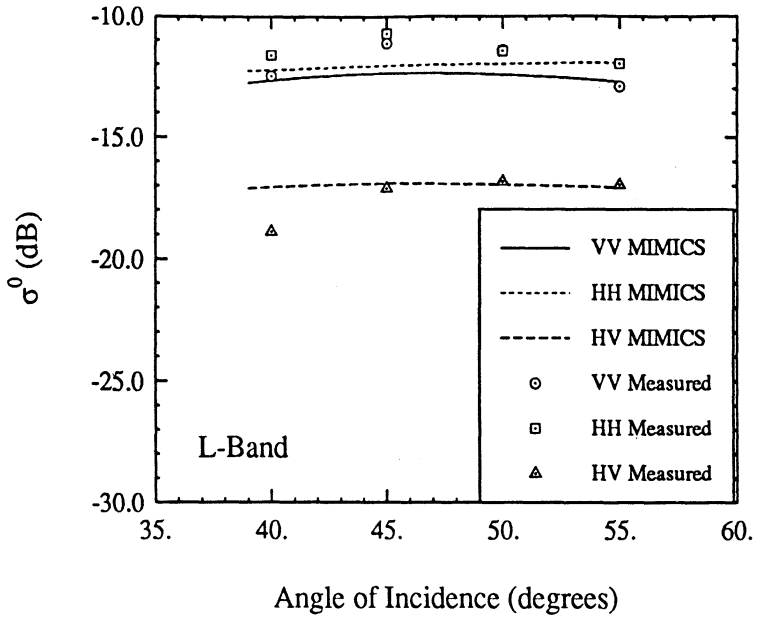

(a)

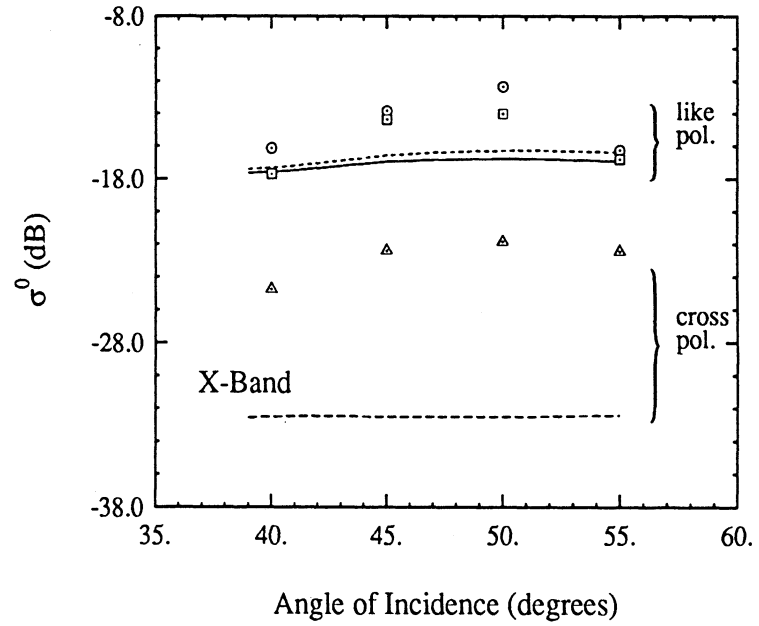

(b)

Figure G.11: Comparison of MIMICS results with measured L- and X-band multi-angle data. (a) compares L-band modeled total canopy backscatter to the scatterometer measurements for like- and cross-polarized configurations (HH, VV, HV). (b) compares X-band modeled direct crown backscatter to the scatterometer measurements for these same polarizations.

to more accurately reproduce the angular dependence of the like-polarized backscatter at 45° and 50° may be attributed to the inhomogeneous nature of the orchard canopy. Whereas MIMICS has been derived for canopies with continuous crown layer geometries, it is applied here to a canopy with a discontinuous crown layer. Furthermore, as can be seen from Figure G.1, the effective canopy geometry sampled by the scatterometer measurement volume changes with θ. This fact is further illustrated by the dip in backscattered power and in the foliage fraction at $R \simeq 16$ m (Figure G.2). As radar incidence angle changes, the canopy backscatter responds to these changes in the sampled canopy volume. The angular dependence of backscatter at X-band has been partially accounted for by applying the LAI correction factor $Q(\theta)$ in generating the multi-angle MIMICS data. However, crown layer discontinuities also affect the character of backscatter from the stems and branches. This effect is more prevalent at X-band in part because of the relatively narrow X-band beamwidth and also because the crown layer constituents that contribute most to this effect (leaves and smaller branches) contribute more to X-band scatter than to L-band.

As previously noted, the X-band cross-polarized backscatter is significantly underestimated by MIMICS. In general, the effect of higher-order multiple scattering on radar backscatter becomes more important as frequency increases. Ulaby *et al.* [65] have shown that, at millimeter wave frequencies, a numerical solution to the radiative transfer equations in which higher-order scattering is accounted for may add more than 10 dB to the predicted first-order cross-polarized backscatter while having little effect on the like-polarized backscatter. Since the numerical solution for radiative transfer requires specifying the scattering phase matrix in all incident and scattering directions, determination of the higher-order scattering contribution becomes very computationally intensive. The phase matrix of the walnut orchard

crown layer has a very complicated form and determination of the numerical solution is computationally prohibitive. Although an expression for the second-order scattering in the crown layer may be derived, analysis of these higher-order effects is beyond the scope of this study. While Ulaby *et al.* [65] derived their results at millimeter wave frequencies for which the scattering albedo for vegetation $\omega \simeq 0.6-0.9$, it is understood that ω usually increases with increasing frequency. In light of the study by Ulaby *et al.*,[65], it is expected that, as frequency increases, higher-order scattering would first be manifest in terms of its effect on the cross-polarized backscatter.

Figure G.12 shows the relative contributions of the three most important contributors to the total backscatter for the like- and cross-polarization configurations at L-band. Whereas in both like-polarized cases the same three mechanisms dominate the total backscatter, MIMICS predicts that the crown-ground and trunk-ground interaction terms are the more dominant mechanisms for the HH backscatter while the direct crown backscatter is the more dominant for VV backscatter. The major contributors to the cross-polarized backscatter are those mechanisms generated by the crown layer. This is expected since the crown layer branches are oriented such that they depolarize more than the trunk layer constituents.

Having established that MIMICS successfully predicts canopy backscatter as a function of angle, the model is now run at a constant incidence angle, $\theta = 55°$, while varying the canopy dielectric parameters so as to simulate the variations seen over the three-day diurnal experiment (Figures G.8 and G.10). Figure G.13 presents the resulting computed backscatter along with the measured values of canopy backscatter for the like- and cross-polarizations. At L-band, MIMICS successfully predicts the appropriate level of the measured data together with the decreasing trend in backscatter observed over the three day period for all three polarization configura-

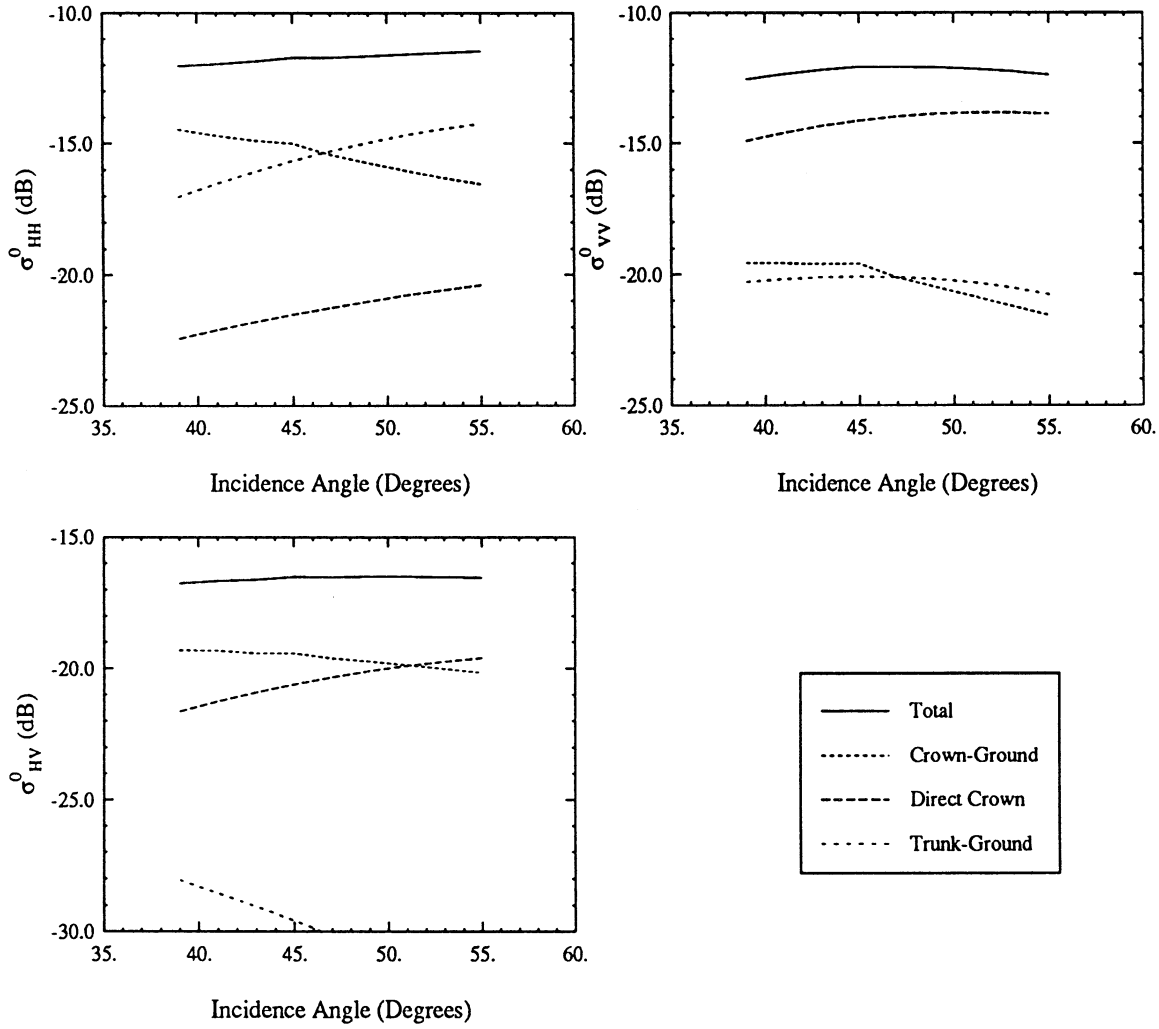

Figure G.12: Components of canopy backscatter for HH, VV and HV polarizations.

tions. Furthermore, MIMICS predicts the 1 to 2 dB dip seen in σ^0_{VV} and σ^0_{HV} in the early afternoon of each day.

The X-band MIMICS data presented here represent the direct crown component of total canopy backscatter and have been produced for a canopy with an effective leaf area index of 1.0 in order to account for the variations in effective canopy geometry as a function of incidence angle. An offset of 8 dB has been added to the cross-polarized MIMICS data to approximate the effects of higher-order scattering. Although the measured X-band data exhibit significantly more scatter than does the L-band data, the early afternoon dip in backscatter is present for all three polarizations and is predicted by MIMICS.

The variation in the measured data that is associated with the scatterometer measurement process comes primarily from two sources. The first of these is fading that arises from the coherent nature of the scatterometer. Following the analysis in Ulaby et al. [70], pp.483–486., the uncertainty due to fading is about ± 0.2 dB. The other source of variation arises from statistical sampling of the inhomogeneous orchard canopy. This is caused in large part by the partially discontinuous properties of the crown layer. Because of the azimuth scanning technique used to account for the effects of fading, each measured data point represents an average of 30 samples recorded over a single azimuth sweep. The locations sampled within the canopy by each of these 30 samples do not correspond precisely to those observed during other azimuth sweeps. Therefore, some variation will exist simply because the values of σ^0 do not represent measurements of precisely the same canopy volume. In addition, factors such as wind speed contribute to a time-varying canopy geometry. This effect is readily observed in the measured diurnal data, especially at X-band. Since X-band backscatter is a great deal more sensitive to changes in the geometry of the leaves

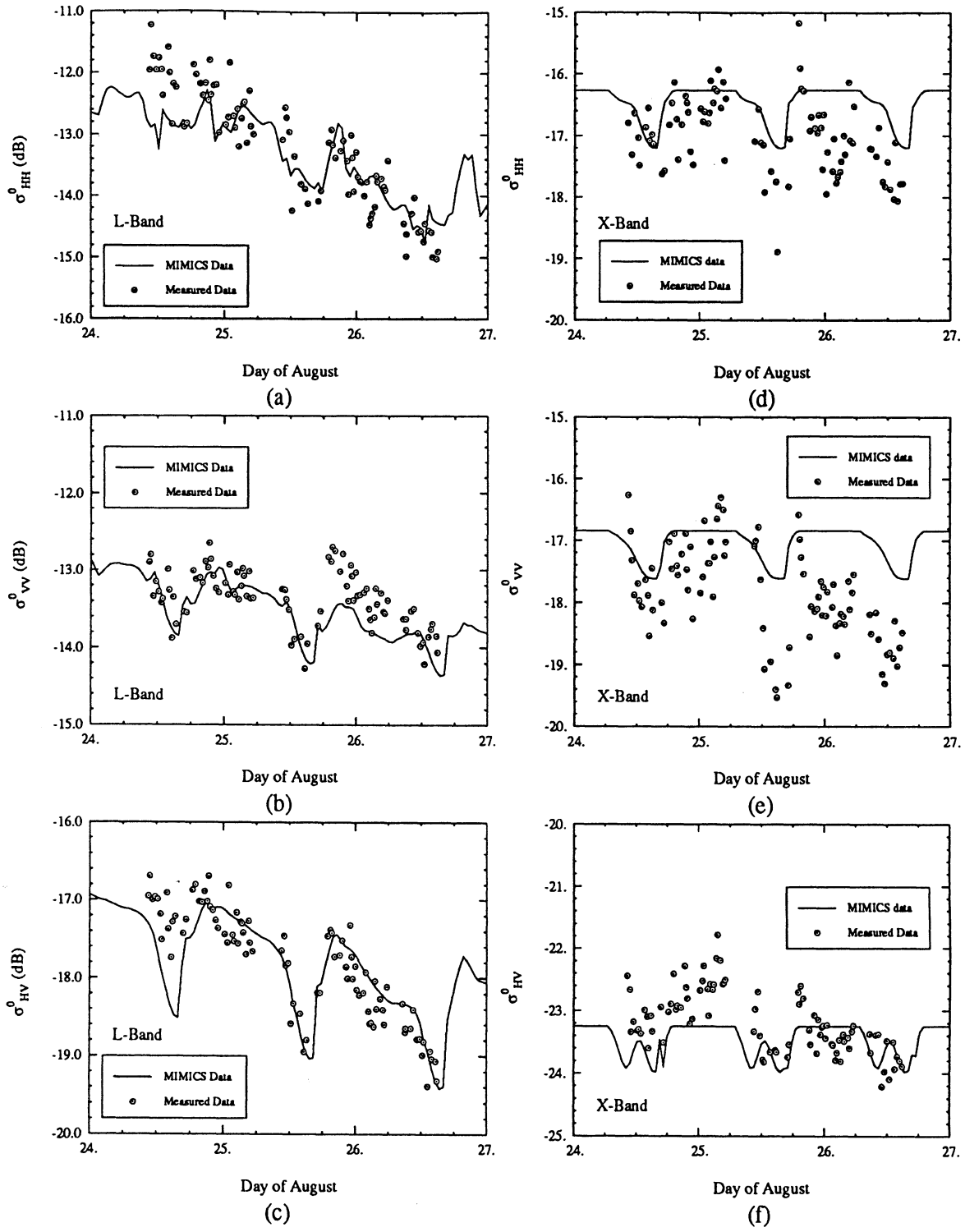

Figure G.13: Comparison of MIMICS results with measured backscatter recorded during the three day diurnal experiment for (a) HH polarized L-band backscatter, (b) VV polarized L-band backscatter, (c) HV polarized L-band backscatter, (d) HH polarized X-band backscatter, (e) VV polarized X-band backscatter and (f) HV polarized X-band backscatter. The X-band HV MIMICS data has been offset 8 dB to account for multiple scatter.

and stems than is L-band, and since these constituents exhibit more time-varying behavior than do the larger branches, a higher degree of scatter is observed in the measured X-band data. Modeling results shown here demonstrate extraordinarily good agreement between measured and predicted backscatter, especially when this measurement variability is taken into account.

Comparison of the modeled and measured canopy backscatter allows some insight into the sources of backscatter variation that are caused by changes in the physiological state of the vegetation and soil. The trends observed in L-band backscatter over this three day period may be explained in part by Figure G.12. At $\theta = 55°$, the HH polarized backscatter is dominated by the trunk-ground backscatter component. This term responds directly to changes in both trunk and soil dielectric. The VV polarized backscatter, however, is dominated by the direct crown component which should depend strongly on changes to the dielectrics of the crown layer constituents. The components which interact with the ground do have a measurable effect on σ^0_{VV}, but these effects are not as pronounced as they are with σ^0_{HH}. Therefore, σ^0_{VV} should exhibit some response to changes in soil and trunk dielectric, but not as much as σ^0_{HH}. The cross-polarized backscatter, however, is dominated by both the crown-ground and direct crown components. The trunk-ground component is more than 10 dB below these other two and should have almost no effect at $\theta = 55°$. σ^0_{HV} should therefore respond mostly to changes in both the crown and ground dielectric properties. The X-band response consists only of the direct crown component of canopy backscatter. The diurnal variations observed here are therefore attributed to changes in crown layer dielectrics.

The MIMICS simulations shown in Figures G.14 through G.15 explain how L-band backscatter responds to changes in soil and vegetation dielectric constants.

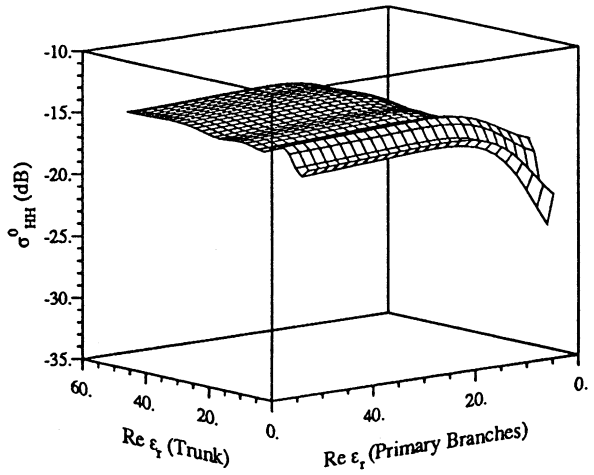

(a) HH-polarized response.

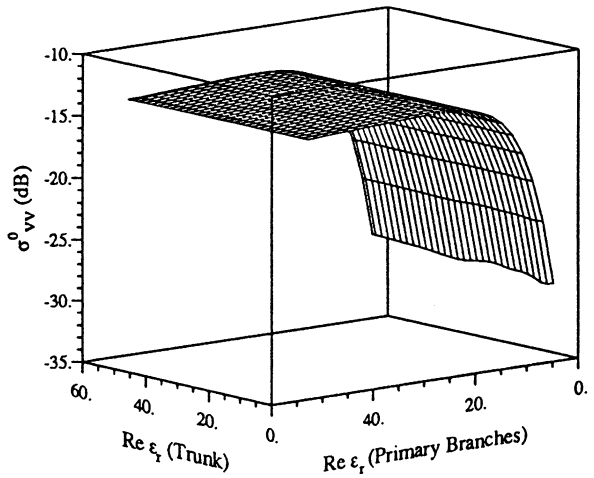

(b) VV-polarized response.

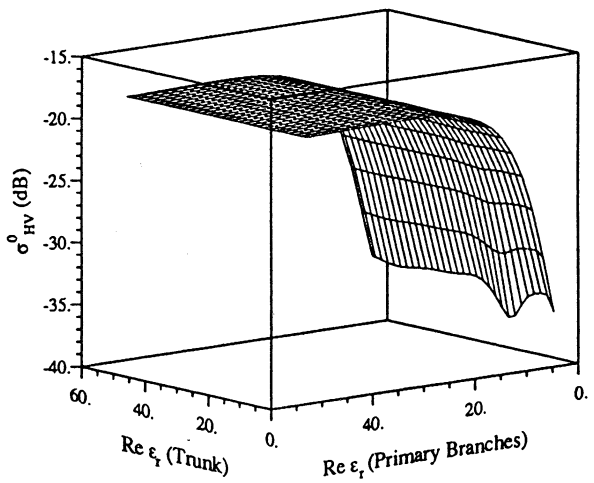

(c) HV-polarized response.

Figure G.14: L-band MIMICS response to changes in trunk and primary branch dielectric constant.

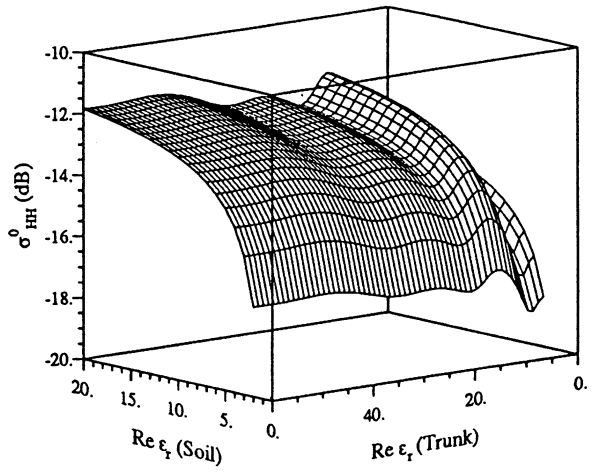

(a) HH-polarized response.

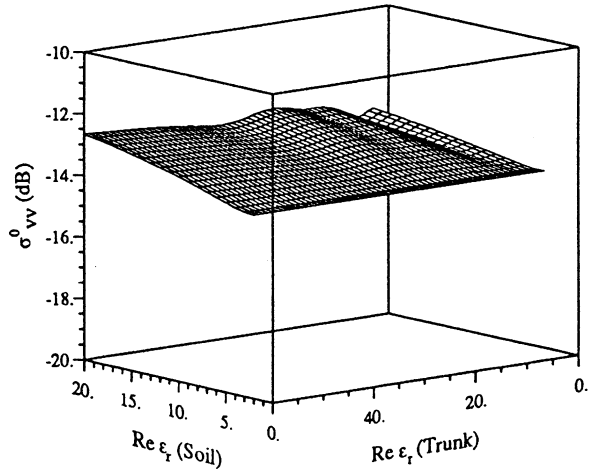

(b) VV-polarized response.

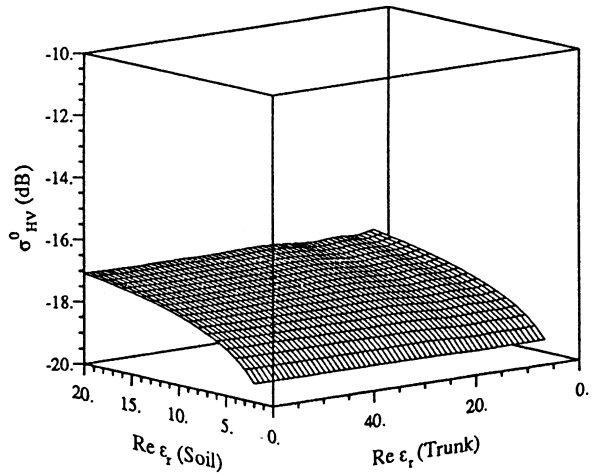

(c) HV-polarized response.

Figure G.15: L-band MIMICS response to changes in soil and trunk dielectric constant.

Each figure shows σ^0 as a function of the real part of the dielectric constant for the like- and cross-polarization configurations. Figure G.14 shows backscatter as a function of trunk and primary branch dielectrics while Figure G.15 shows net canopy backscatter as a function of soil and trunk dielectrics. The imaginary parts are varied as well, keeping a constant loss tangent for each constituent (0.25 for vegetation and 0.1 for soil). These figures give a direct indication of the sensitivity of backscatter to changes in the canopy parameters. In each case, the dielectric parameters were varied over a range appropriate to the measured dielectric data.

The HH-polarization response indicates that varying the soil dielectric constant from $20 + i2$ to $2 + i0.2$ corresponds to a maximum change of approximately 6 dB in σ^0_{HH}. Comparing this to the changes observed in σ^0_{HH} vs. trunk and branch dielectrics confirms that this quantity is most sensitive to changes in soil dielectric.

The responses of σ^0_{VV} and σ^0_{HV} seen in Figure G.14 (b) and (c) indicate almost no sensitivity to changes in trunk dielectric. However, these quantities are very sensitive to changes in primary branch dielectric over the range from $\epsilon_r = 20 + i5$ to $4 + i1$. This sensitivity gives rise to the dips in backscatter seen in the early afternoons in Figure G.13 (b) and (c). The responses of σ^0_{VV} and σ^0_{HV} to soil dielectric seen in Figure G.15 (b) and (c) show about a 2-3 dB change in σ^0 over this range of soil dielectric values, indicating some sensitivity to soil moisture.

The decreasing trend in measured σ^0 may be attributed to the decreasing soil dielectric constant. All three polarizations respond to this change but with varying degrees of sensitivity. As shown in Figure G.13, the absolute level of σ^0_{HH} decreases by about 2 dB over the three day period while σ^0_{VV} and σ^0_{VH} each change by about 1 dB. Since a 68% decrease in effective soil volumetric moisture (mv_s) has been observed, which includes the effect of irrigated as well as non-irrigated soil surfaces,

σ^0_{HH} exhibits a sensitivity to changes in soil moisture of about 2 dB/0.68 = 2.94 dB while σ^0_{VV} and σ^0_{VH} have sensitivities of about 1 dB/0.68 =1.47 dB. Since σ^0_{HH} is twice as sensitive to changes in mv_s, HH would be the the most effective polarization for determining changes in soil moisture.

The VV and HV polarizations are more sensitive to changes in the dielectric properties of the crown constituents. This is substantiated by the dips observed in σ^0_{VV} and σ^0_{HV} during the early afternoons. The VV and HV backscatter dip from between 0.5 dB to 1.5 dB each afternoon. However, σ^0_{HH} which is much less sensitive to branch dielectric (Figure G.14(a)) exhibits no such dips. It is probable that the branch dielectrics are related to the water potential via the plant water status. σ^0_{VV} and σ^0_{HV} are therefore seen to yield some indication of water status, thereby containing some information about the physiological state of the plant.

In this analysis it was found that accurate estimates of leaf parameters are important in modeling the X-band backscatter. Figure G.16(a) shows the X-band direct crown MIMICS response to changes in LAI and leaf gravimetric moisture for HH polarization. This gives a direct indication of how direct crown backscatter varies with leaf parameters. About 6 dB of sensitivity is observed over the indicated range of parameters. This underscores the importance of accurately estimating leaf dielectric, curvature and LAI in analyzing X-band radar data.

Figure G.16(b) shows HH polarized X-band direct crown backscatter response to changes in primary and secondary branch gravimetric moisture. The range of moisture values shown here corresponds to the range of effective values applied in estimating the X-band dielectric constants. σ^0_{HH} shows only about 1.2 dB of sensitivity over changes in moisture values for the primary branches. However, significantly less sensitivity is observed to changes in secondary branch moisture. This indicates

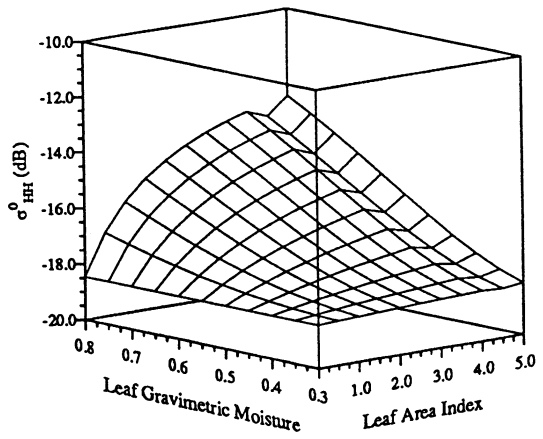

(a)

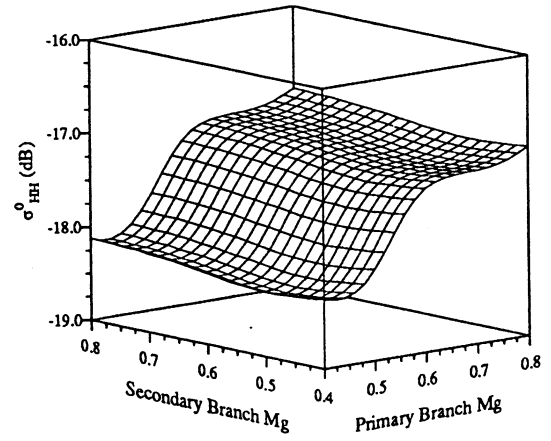

(b)

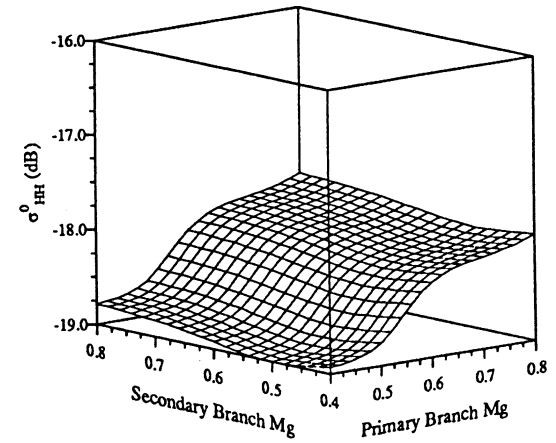

(c)

Figure G.16: X-band HH-polarized direct crown backscatter response to changes in (a) leaf gravimetric moisture and leaf area index, (b) primary and secondary branch gravimetric moisture and (c) primary and secondary branch gravimetric moisture with primary branches assigned a $\sin\theta$ orientation function.

straightaway that the dips observed in the X-band diurnal backscatter are caused by variations in the dielectrics of the primary branches.

Figure G.16(c) illustrates the effect of modifying the branch orientation on X-band HH polarized direct crown backscatter. The primary branches here have been assigned an orientation PDF of the form $\sin\theta$ which is identical to that assigned to the secondary branches and stems. Although the sensitivity to branch moisture here is similar to that shown in Figure G.16(b) where these branches had an orientation PDF of the form $\sin^4 2\theta$, there is about a 0.5 dB decrease in backscatter over the entire range of primary and secondary branch moisture. This indicates a direct response of HH-polarized backscatter to changes in branch orientation.

Figure G.17 shows the MIMICS-predicted backscatter to chnges in canopy biomass for the walnut orchard response for VV and VH polarizations. These data were generated by varying canopy height and generting σ^0 at each height. The models for canopy biophysical parameters presented in Appendix F were applied to compute the dry canopy biomass. The actual height of the canopy was 4.8 meters. Data are shown for P-band (0.5 GHz), L-band (1.5 GHz) C-band (5 GHz) and X-band (9.6 GHz). For low values of biomass, the backscatter at both like- and cross-polarizations is dominated by the direct-ground component of canopy backscatter whereas at high values the canopy itself dominates σ^0. Therefore, the σ^0 value observed at low values of biomass is determined solely from the estimate of direct ground backscatter for both polarizations. In order to achieve a reasonable estimate of both the like- and cross-polarized direct ground backscatter, measured values from Ulaby and Dobson [61] were used to simulate the direct ground backscatter. This approach was necessary because the first-order ground backscatter model implemented in MIMICS does not account for any cross-polarized return. It should also be noted that at

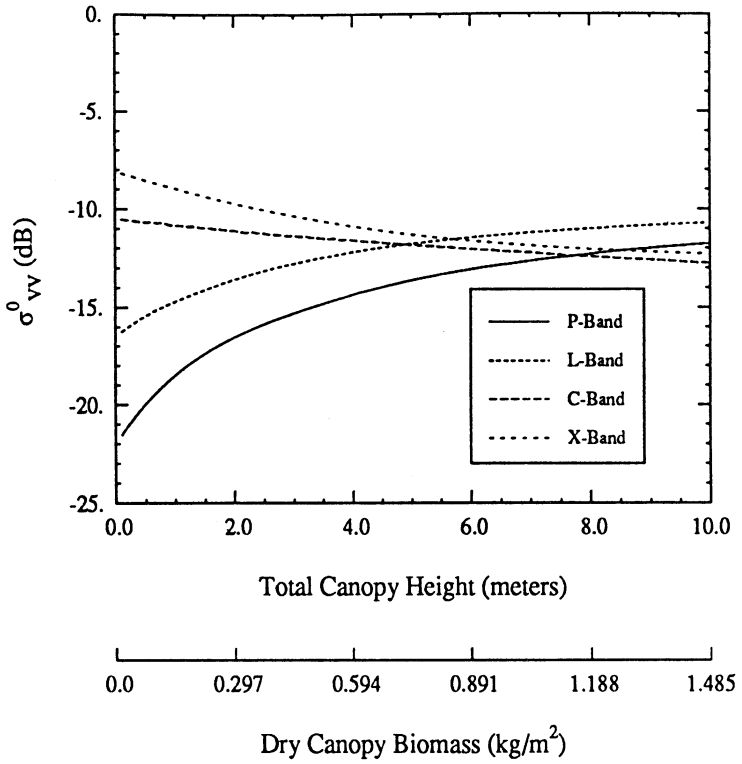

(a) VV-polarized response.

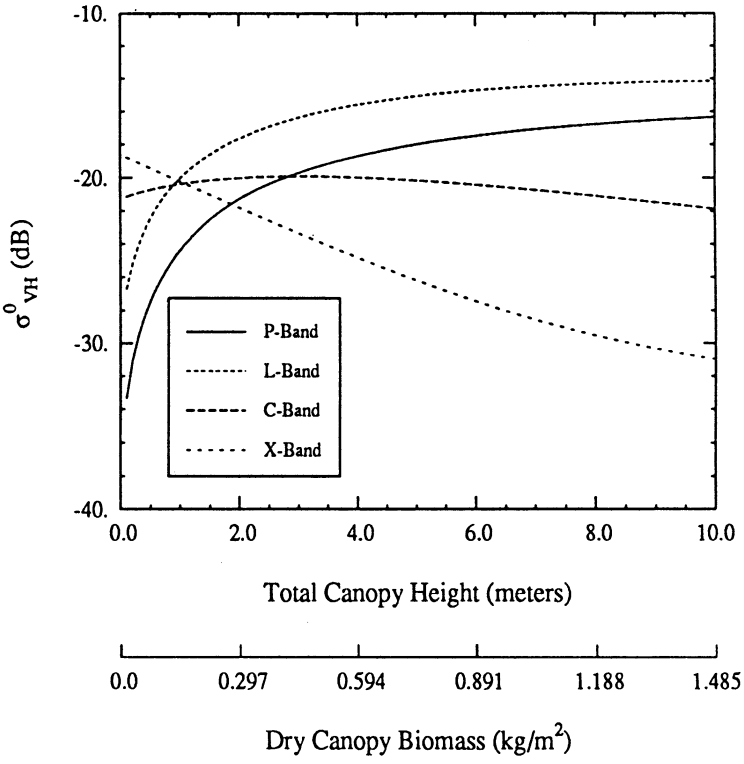

(b) VH-polarized response.

Figure G.17: Walnut orchard backscatter response to changes in canopy biomass for (a) VV-polarization, (b) VH-polarization. The incidence angle $\theta = 30°$.

high biomass values the X-band cross-polarized responce is several dB lower than anticipated because MIMICS does not account for multiple scattering in the crown layer. This analysis demonstrates that the lower radar frequencies (P- and L-bands) are more sensitive to changes in canopy biomass than are the higher frequencies (C- and X-bands).

APPENDIX H

MODELING MICROWAVE ATTENUATION AND BACKSCATTER FROM ALASKAN BOREAL FOREST CANOPIES

In March 1988, a series of airborne SAR data was acquired over the Bonanza Creek Experimental Forest near Fairbanks, Alaska (Way *et al.*, [77], [76]; Dobson *et al.*, [13], [14]). This study was the first in a series of multi-season aircraft experiments flown over selected forest sites for the purpose of understanding the kinds of biophysical properties that may be detected with spaceborne SAR systems such as the C-band SAR to be flown aboard the European Space Agency's Earth Resources Satellite (ERS-1). The purpose of this experiment was to determine if changes in plant fluid status associated with thawing and freezing result in changes in radar backscatter which could be detected by SAR and to determine if theoretical backscatter models such as MIMICS could predict these changes.

Two aircraft-mounted SAR systems were deployed during this study. The Jet Propulsion Laboratory's (JPL) P-, L- and C-band quad-polarized SAR, mounted aboard a NASA/Ames Research Center DC-8, operated at center frequencies of 450 MHz, 1.26 GHz and 5.3 GHz, respectively. The Naval Air Center/Environmental Research Institute of Michigan's (ERIM) L-, C-, and X-band quad-polarized SAR, mounted on a Navy P-3, operated at center frequencies of 1.25 GHz, 5.26 GHz and

9.38 GHz, respectively. An array of passive reflectors and active radar calibrators (ARCs) was deployed in the vicinity of the Fairbanks International Airport and imaged during the overflights to provide for external calibration of these systems.

This analysis focuses on the data obtained by the JPL SAR on March 13 at 15:03 and March 19 at 23:17 and by the ERIM/NADC SAR on March 22. All of these passes have a common look direction. These dates were selected to encompass the range of environmental conditions that occurred over the duration of the experiment. An unseasonably warm period during which thawed conditions prevailed in the forest extended through the evening of March 13. This was followed by more normal subfreezing temperatures for the remainder of the experiment. As liquid water was frozen by the subfreezing temperatures, the dielectric properties of both the vegetation and of the 20-30 cm snow layer that covered the ground were modified, thereby changing the scattering and absorption properties of these constituents.

H.1 Test Site Description and Canopy Properties

The Bonanza Creek Experimental Forest is 30,000 hectares in size and is contained within the Tanana Valley State Forest west of Fairbanks, Alaska, within a zone of discontinuous permafrost along the Tanana River. The wide diversity of forest successional stages that exist in the forest include mono- and mixed-species stands of aspen, birch, white spruce, balsam poplar, black spruce, willows and alders. To minimize the effects of surface slope on the radar backscatter, this study focuses on stands that are on the relatively flat islands along the Tanana River.

H.1.1 Stand Selection

A series of forest stands were selected on the basis of forest cover conditions and accessibility for use in canopy extinction studies using point targets (Kasischke *et al.*, [32]). For measurement of canopy transmissivity at C- and X-band, arrays of passive reflectors were deployed both in forested stands and on a nearby unforested sandbar. These stands consisted of a mono-species alder stand, along with mixed-species white spruce and balsam poplar stands.

In addition to the stand selected for the canopy extinction studies, several other stands were selected for backscatter analyses. Each of these stands is of uniform age with a single-species composition and encompasses at least 4 hectares in area. Of these stands, 19 were white spruce, 12 were balsam poplar and 11 were black spruce. Ancillary data has been obtained and summarized for seven of these stands (Jaeger, [30]). The measured and derived stand characteristics provide the basis for the MIMICS simulations of canopy backscatter and transmissivity.

H.1.2 Temperature Conditions

An unseasonably warm period prevailed in early March 1988. During this time, thawed conditions prevailed in the vegetation and a melt zone formed in the surface layer of the snow. These conditions persisted through the March 13 JPL SAR overflight. Air temperatures during this flight ranged between 2.0°C and 9.5°C. Subfreezing temperatures returned on March 14 for the remainder of the experiments. The air temperature on March 19 ranged between −14.0°C to −14.5°C and was less than −20.0°C during the flight of the ERIM/NADC SAR on March 22.

H.1.3 Ground Surface Characteristics

The ground surface was covered with a snow layer 20-30 cm deep. Below the snow layer, the upper 20 cm of the mineral soil was frozen throughout the entire experiment. Detailed measurements were made for one white spruce and one black spruce stand at the times of the overflights. These measurements included air and snow temperature profiles, snow depth, snow density profiles and snow wetness. Wetness measurements included a hydrochloric acid detection technique (Davis *et al.*, [8]) and *in situ* dielectric measurements at L- and C-bands.

The early March thaw caused the snow layer to have a complex wetness structure that varied with stand species (Dobson *et al.*, [13]). Although the average dry density of the snow pack was found to be 0.2 g/cm^3 throughout the experiment, snow wetness varied considerably with spatial location, depth, and time. The average volumetric moisture of the snow pack was found to be 2% during the SAR overflight on March 13. A Debye-like model presented by Hallikainen *et al.*, [24] was applied to estimate the dielectric properties of the snow. This model relates the snow dielectric to snow wetness (volume %), frequency and dry snow density. The modeled values of snow dielectric constant are listed in Table H.1 at L-, C- and X-bands for frozen and thawed conditions.

Table H.1: Modeled Dielectric Characteristics of Snow for Frozen and Thawed Conditions.

Frequency	Thawed Conditions (March 13)	Frozen Conditions (March 19-22)
L-Band	$1.58 + i0.024$	$1.37 + i0.0$
C-Band	$1.54 + i0.079$	$1.37 + i0.0$
X-Band	$1.49 + i0.09$	$1.37 + i0.0$

The dielectric of the frozen mineral soil was measured using portable dielectric

probes in a trench cut into the permafrost. The average L-band dielectric constant of the soil was found to be $7.96 + i0.96$.

H.1.4 Stand Geometry

Ground surveys of seven stands were conducted to determine the number of trees per unit area by species and also record their respective diameters at breast height (DBH) (Jaeger, [30]). Within each stand, a line transect was drawn along the longest stand axis. Ten sample plots were selected at random distances along the transect. Within each plot, the DBH and species were recorded for all trunks with diameter greater than 1 cm and taller than 30 cm. The status of each tree (alive/dead, broken/unbroken) was noted along with the height of at least four live trees per plot.

To estimate above ground biomass for each stand, the enumerated stand data were coupled with allometric equations. The measured DBH, heights, and status of each tree were used to estimate quantities including basal area, biomass volume, and biomass on the basis of allometric expressions drawn from the literature for each species (Kirby,[33]; Manning *et al.*,[40]; Singh,[52]; Yarie and Van Cleve,[84]). These expressions have been derived for stands in Alaska and in the Canadian Northwest Territories and Yukon. The specific equations applied here are listed by Jaeger [30]. These estimates were summed over all trees in a stand to yield the estimates shown in Table H.2 as averaged over the net areas of all sample plots in each stand. The standard deviations listed in the table are based on the plot-to-plot variance within each stand.

In addition to the six stands listed in Table H.2, the stands containing the trihedral corner reflectors were also characterized with respect to density, height and diameter (Kasischke *et al.*,[32]; Jaeger,[30]). These stands included a single species

Table H.2: Summary of Stand Biophysical Parameters.

Species	White Spruce				Black Spruce	Balsam Poplar
Stand Name	WS-1	WS-2	WS-5	WS-7	BS-1	BP-2
Density						
Mean (trunks/hectare)	1248	2073	1484	1123	1975	1615
Standard Deviation	342	576	618	654	1483	407
Basal Area						
Mean (m^2/hectare)	46	41	44	46	12	50
Standard Deviation	16.6	7.0	8.5	12.4	3.3	25.8
Basal Volume						
Mean (m^3/hectare)	442	332	392	442	51	344
Standard Deviation	169	60	100	115	12	190
Dry Biomass - Summer						
Mean (kg/m^2)	21.7	16.7	18.1	21.5	3.7	18.2
Standard Deviation	8.8	3.6	4.8	6.1	0.8	10.9
Dry Biomass - Winter						
Mean (kg/m^2)	21.7	16.7	18.1	21.5	3.7	17.9
Standard Deviation	8.8	3.6	4.8	6.1	0.8	10.7

of alder and mixed species stands of alder, balsam poplar and white spruce. Table H.3 summarizes mean DBH, height and basal area for all stands.

To characterize the trunk layer geometry in terms of parameters required for MIMICS input, DBH histograms were generated from the ancillary ground measurements and coupled with the allometric height equations listed in Table H.4. Together, these data define the PDF in size required to compute the trunk layer phase matrix for a given stand. Measurements of orientation angles were performed to characterize the PDF for characterizing trunk orientation. However, the number of non-vertical trunks in each stand was very small and the lean angles of these trunks was also small. Hence, all trunks are assumed to have a vertical orientation for purposes of MIMICS simulations.

The thickness of the crown layer for each stand was defined based on field observations. For both white spruce and black spruce, the crown layer thickness is assumed to be equal to trunk height. For alders and balsam poplars, the crown layer thick-

Table H.3: Summary of Mean DBH, Height and Basal Area for All Stands.

Stand Name	DBH (cm)	Height (m)	Basal Area (m^2/hectare)
WS-1	19.6	22.1	46
WS-2	14.5	20.1	41
WS-5	17.9	21.3	44
WS-7	21.4	24.5	46
BS-1	8.8	7.6	12
BP-2	18.0	17.6	50

Stands with trihedral reflectors:

Stand Name	Species	DBH (cm)	Height (m)	Basal Area (m^2/hectare)
Alder	alder	6.0	6.3	66.5
Balsam Poplar	balsam poplar	11.0	12.7	22.9
	alder	6.0	6.3	3.1
White Spruce	white spruce	7.8	8.6	12.4
	balsam poplar	9.4	11.6	10.0
	alder	6.1	6.3	5.4

Table H.4: Equations Defining Height-to DBH Relationship.

Species	Equation
White Spruce	$H = -1.7096 + 1.4224(\text{DBH}) - 0.016(\text{DBH})^2$
Black Spruce	$H = 0.9494 + 0.7657(\text{DBH})$
Balsam Poplar	$H = 1.0526 + 1.143(\text{DBH}) - 0.0145(\text{DBH})^2$
Alder	$H = 2.871 + 0.5666(\text{DBH})$

H = height in meters

DBH = diameter in cm measured at breast height

ness was assumed to be 25% of the average trunk height. To estimate the number density and sizes of crown layer constituents, the total biomass of each stand listed in Table H.2 was apportioned among the various constituent classes using allometric equations reported in the literature (Manning *et al.*,[40]; Singh,[52]; Van Cleve and Viereck,[73]; Yarie and Van Cleve,[84]). Typically, these equations provide a statistical breakdown of biomass apportionment for dry biomass of the trunk bark, trunk wood, the branches and the twigs and foliage. Since most of these equations were empirically derived for stands outside of the Bonanza Creek Experimental Forest, perhaps with differing local site conditions, they may produce errors in characterizing the biomass apportionment of the Bonanza Creek stands. However, they are the best available sources of information.

Additional apportionment error arises in partitioning the branches and foliage into component parts required by MIMICS (i.e. various branch size classes and foliage). In this case, apportionment of biomass was accomplished on the basis of destructive sampling undertaken at the time of the overflights. Results of the biomass apportionment are summarized for each species in Table H.5.

Table H.5: Dry Biomass Fractions of Canopy Components as Percent of Total.

	White Spruce	Black Spruce	Balsam Poplar	Alder
Trunk	85.79	86.45	90.0	90.0
Primary Branches	6.13	4.94	4.9	4.9
Secondary Branches	5.48	5.06	5.1	5.1
Foliage	2.60	3.55	NA	NA

The size and orientations of crown layer constituents have been inferred through a combination of field observations and morphology data from Nelson *et al.*,[45]. Table H.6 summarizes the geometry of the crown layer constituents. The orientation functions are specified in terms of the inclination angle θ where $\theta = 0$ corresponds

Table H.6: Geometry of Crown Layer Constituents.

Species	Constituent Class	Average Length (cm)	Average Diameter (cm)	Orientation Function
White Spruce	primary branches	113	2.24	$\sin^4\theta$
	secondary branches	57.16	1.04	$\sin^9\theta$
	needles	1.6	0.1	$\sin\theta$
Black Spruce	primary branches	81.3	2.37	$\sin^9(\theta - 30°)$
	secondary branches	51.17	1.06	$\sin^9\theta$
	needles	0.8	0.1	$\sin\theta$
Balsam Poplar	primary branches	200	1.5	$\sin^9(\theta + 60°)$
	secondary branches	100	0.75	$\sin^9(\theta + 60°)$
Alder	primary branches	200	1.5	$\sin^9(\theta + 60°)$
	secondary branches	100	0.75	$\sin^9(\theta + 60°)$

to a vertical cylinder. Each of these functions is normalized to convert it to a PDF for implementation in MIMICS.

Table H.7 lists the number density of each canopy constituent for each of the seven stands, assuming that each stand may be modeled as a continuous (closed) canopy. Under this assumption, the number density N_k of a given constituent may be computed from

$$N_k = \frac{\text{net stand biomass} \times \text{biomass apportionment fraction}}{\text{biomass of a single element} \times \text{crown layer thickness} \times \text{stand area}}$$

The biomass of a single element is computed from the size and dry density parameters of that element.

Table H.7: Number Density of Canopy Constituents.

Stand Name	Canopy Density (trees/m^2)	Primary Branches (#/m^3)	Secondary Branches (#/m^3)	Needles (#/m^3)
Alder	1.36	1.19	9.92	NA
BP-2	0.16	0.85	6.69	NA
WS-1	0.12	0.44	2.37	12,300
WS-2	0.12	0.48	2.57	13,310
WS-5	0.12	0.50	2.7	14,000
WS-7	0.12	0.48	2.6	13,490
BS-1	0.20	0.25	1.31	18,340

H.1.5 Stand Dielectric Characteristics

The dielectric properties of the trees vary as a function of frequency and canopy properties such as constituent dry density and chemistry and amount of liquids in the constituent. As environmental temperature changed from warm to sub-freezing, the chemistry and volume fraction of liquids in the canopy constituents changes dramatically between thawed and frozen states. These changes were reflected in the dielectric properties of the canopy elements. The dielectric properties of the stands were monitored with L- and C-band portable dielectric probes. The dielectric behavior of the stands was modeled by applying these *in situ* data together with dielectric models. The dielectrics listed in Table H.8 were inferred by coupling trunk dielectric profiles to dielectric models (Dobson *et al.*, [13]).

Table H.8: Relative Dielectric Constant for Tree Constituents.

Species	Frequency (GHz)	Relative Dielectric +5°C	Relative Dielectric −15°C
White Spruce	1.25	$36.47 + i10.99$	$5.19 + i1.09$
	5.3	$29.01 + i11.97$	$4.85 + i0.32$
	9.38	$22.78 + i13.20$	$4.81 + i0.18$
Black Spruce	1.25	$12.46 + i4.50$	$3.72 + i0.78$
	5.3	$9.30 + i3.33$	$3.47 + i0.23$
	9.38	$7.82 + i3.22$	$3.44 + i0.13$
Balsam Poplar and Alder	1.25	$30.71 + i9.56$	$4.95 + i1.07$
	5.3	$24.18 + i9.85$	$4.61 + i0.32$
	9.38	$19.16 + i10.69$	$4.57 + i0.17$

H.2 Boreal Forest Transmissivity Analysis

Data collected by the ERIM/NADC SAR have been applied to analyze canopy transmissivity (Dobson *et al.*, [13],[14]). These data were recorded at C- and X-bands during a total of six passes over the test site on March 22. To compute the one-way canopy propagation loss, the point target responses of the trihedrals that were placed

in the forest stands was compared to the response of those trihedrals placed in the open on the sandbar. The background clutter was removed for each target response and the image intensity was normalized to correct for known effects such as range fall-off and antenna variations. The confidence interval associated with this process and with uncertainties in trihedral alignment is estimated to be ± 1 dB (Dobson *et al.*,[13]).

Three stands were selected for the deployment of the reflector arrays. Four targets were placed in a single species alder stand, seven targets were placed in a balsam poplar stand that contained shorter alder trees, and nine reflectors were placed in a white spruce stand that contained a mixture of alders and balsam poplars. At several reflector site, ancillary data were recorded that included tree species, location relative to the trihedral, diameter and height. Table H.9 summarizes the stand statistics in the neighborhood of each target for the region of the stand toward which the reflector was bore-sited. Statistics were recorded for only six of white spruce stands. These data, together with more extensive tabular summaries (Kasischke *et al.*,[32]), show significant local variance in stand geometry, both locally within the neighborhood of individual targets and in comparing different target locations within the same stand. Not only does the within-stand variability affect the estimation of canopy extinction, but it should also be noted that in examining the measured transmissivity data there is an inherent bias toward values of low extinction due to the logistics of placing physically large reflectors in a canopy of large discrete scatterers. The measured extinction values represent realizations over only the few azimuth degrees required to construct the synthetic aperture. It would be best to have a set of infinitesimally small point targets that one could place at a statistically large number of random locations within a given stand.

Table H.9: Stand Characteristics in the Neighborhood of the Trihedral Reflectors.

Target	Species	Trees/hectare	Average DBH (cm)	Average Height (m)
T06017A	Alder	18333	6.09 (1.46)	6.32 (0.83)
T06020A	Alder	17778	7.00 (1.89)	6.84 (1.07)
T06018A	Alder	30000	5.78 (1.49)	6.15 (0.84)
T06076A	Alder	40000	5.49 (1.72)	5.98 (0.98)
T06026P	Alder	1375	8.13 (1.44)	7.47 (0.81)
	Balsam Poplar	1250	8.49 (1.60)	11.84 (1.80)
T06008P	Alder	1125	5.38 (1.46)	5.92 (0.83)
	Balsam Poplar	3125	10.64 (3.33)	12.62 (2.16)
T06006P	Alder	476	5.43 (0.29)	5.95 (0.16)
	Balsam Poplar	2540	8.86 (4.02)	11.00 (2.95)
T06021P	Alder	1665	6.59 (2.50)	6.60 (1.41)
	Balsam Poplar	1905	11.50 (5.22)	12.34 (3.60)
T12201P	Alder	606	5.63 (2.22)	6.06 (1.26)
	Balsam Poplar	1313	11.85 (4.17)	13.71 (2.18)
T12202P	Alder	2063	4.28 (0.95)	5.29 (0.54)
	Balsam Poplar	4286	11.55 (4.34)	12.95 (2.73)
T12203P	Alder	273	7.50 (0.73)	7.12 (0.42)
	Balsam Poplar	1091	14.66 (4.91)	14.45 (2.71)
T12201S	Alder	0	0.00 (0.0)	0.00 (0.0)
	Balsam Poplar	600	11.40 (3.89)	12.80 (2.26)
	White Spruce	2200	10.45 (4.72)	10.86 (3.86)
T12202S	Alder	938	6.55 (2.10)	6.58 (1.19)
	Balsam Poplar	1250	11.54 (3.32)	13.35 (2.22)
	White Spruce	469	15.60 (2.86)	15.10 (1.82)
T06005S	Alder	2333	5.66 (3.37)	6.08 (1.91)
	Balsam Poplar	778	9.29 (3.74)	11.63 (2.81)
	White Spruce	1556	8.32 (3.99)	9.17 (3.61)
T06011S	Alder	947	6.73 (4.77)	6.69 (2.70)
	Balsam Poplar	1900	8.03 (4.04)	10.30 (3.94)
	White Spruce	1700	7.28 (3.80)	8.23 (2.72)
T12203S	Alder	1375	5.77 (1.96)	6.14 (1.11)
	Balsam Poplar	750	10.85 (2.82)	12.75 (1.48)
	White Spruce	1500	7.36 (4.49)	8.25 (3.96)
T09101S	Alder	1647	6.41 (2.24)	6.50 (1.27)
	Balsam Poplar	2235	8.69 (3.52)	11.26 (2.73)
	White Spruce	4235	5.62 (2.38)	6.72 (2.15)

Numbers in parentheses are standard deviations.

To simulate one-way propagation loss for these three stands, each set of stand statistics recorded in the neighborhood of the targets was used as input to MIMICS, applying the dielectric constants for frozen vegetation constituents (Table H.8) and the trunk height *versus* DBH equations (Table H.4). For the mixed-species stands, MIMICS was run separately for each constituent species and the resultant propagation losses were added together to estimate the total net loss.

When modeling each of these stands, only extinction through the trunk layer was considered. This approach was taken because (1) the trunk layer statistics were well characterized by the ancillary ground measurements, (2) the apportionment of biomass in the crown of each species was only approximate and (3) the computation time required to model each species in the neighborhood of each reflector was prohibitively long. Furthermore, since over 85% of the dry biomass for each of these species is in the trunk layer (Table H.5), the canopy extinctions should be dominated by the trunk layer. Given the computation time constraint and in light of the limitations of the biomass apportionment for the crowns, MIMICS was run for the three stands modeled only as trunk layers.

Figures H.1 – H.3 show MIMICS simulations of the maximum and minimum one-way propagation loss for each of the three stands together with the measured values as determined for each trihedral reflector. In all cases, trunk layer extinction increases smoothly with incidence angle and the X-band extinction is generally higher than that at C-band. The maximum and minimum MIMICS simulations correspond to the maximum and minimum biomass conditions for each of the three stands. Figure H.1 shows these data for the alder stand, Figure H.2 shows data for the balsam poplar stand and Figure H.3 presents the white spruce stand simulation. In all cases, the V-polarized extinction is greater than that at H-polarization with the difference being

less than 1.5 dB.

If all extinction were indeed caused by the trunk layer, then the MIMICS simulations for the maximum and minimum biomass conditions would be expected to bound the measured propagation loss values. For the alder stand, MIMICS overestimates extinction by as much as 3 dB at each frequency. However, MIMICS does predict the general polarization and incidence angle behavior. The low values in the measured data may be related to the high variance in the tree density in the neighborhood of the target boresite direction and the natural tendency to place the reflectors in local clearings within the dense alder canopy.

The measured values observed for the balsam poplar stand are well bounded by the MIMICS simulations for both frequencies. However, the balsam poplar stand generally contained larger and fewer trees than did the alder canopy, thereby yielding individual measurements that were more dependent on the locations of fewer individual trees in front of the reflectors. This effect increased the spread in the measured data.

This same effect is observed in the white spruce canopy. In this case, MIMICS underestimated a number of observed values. This effect may be attributed to the lack of a crown layer in the modeling analysis. This is expected to have more of an effect in the white spruce canopy since these trees have a high number density of needles within the crown whereas the deciduous species were not foliated.

Figure H.4 is a plot of the MIMICS-simulated one-way propagation loss *versus* the measured loss at C-band. Data are shown for all three stands at both polarizations. Each set of stand data were fit with a straight line to help illustrate the combined effects of measurement and model error. Good correlations exist between measured data and model simulations for all three stands, with the correlation coeffi-

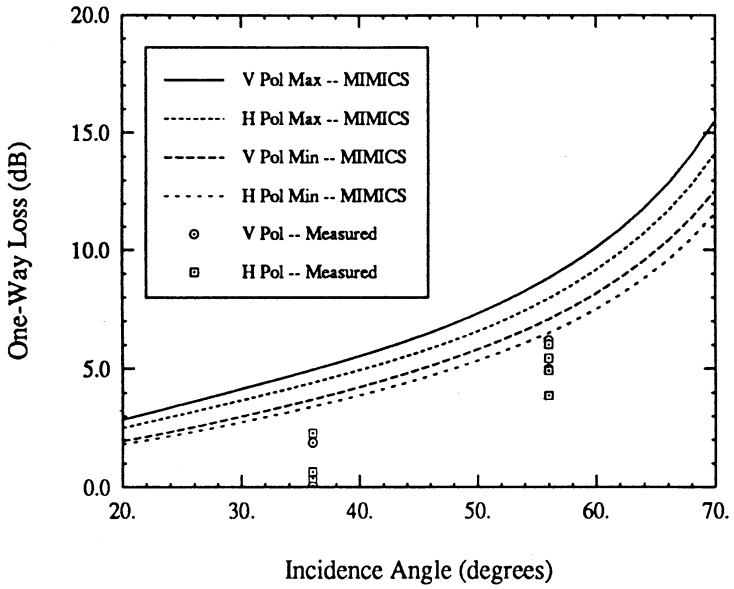

(a) C-band.

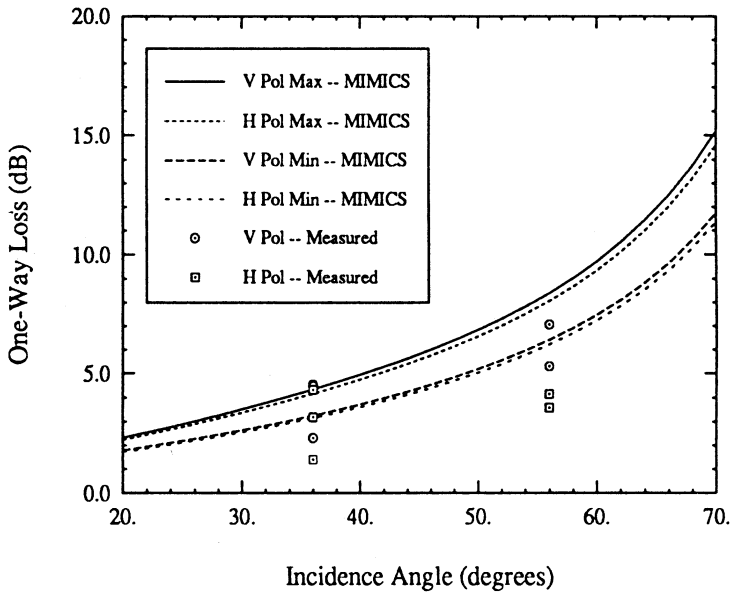

(b) X-band.

Figure H.1: Transmission loss for one-way propagation through the alder canopy. Measurements are shown for four trihedral targets at (a) C-band and (b) X-band.

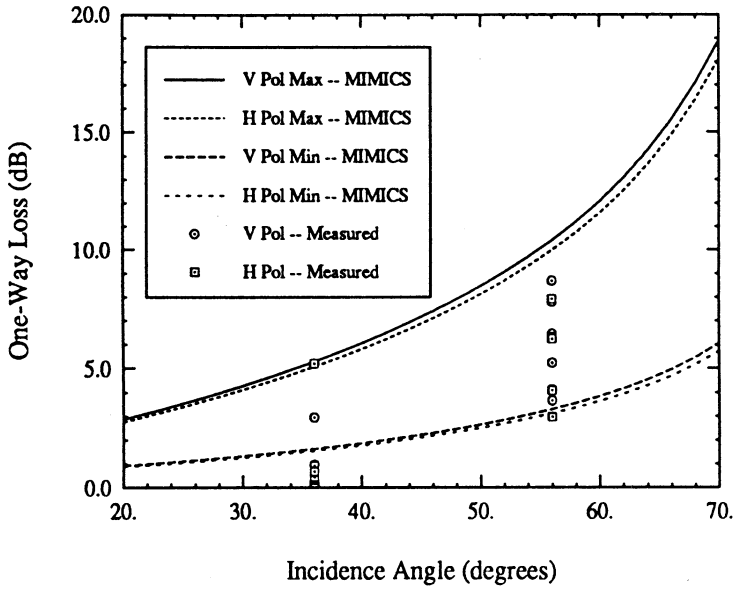

(a) C-band.

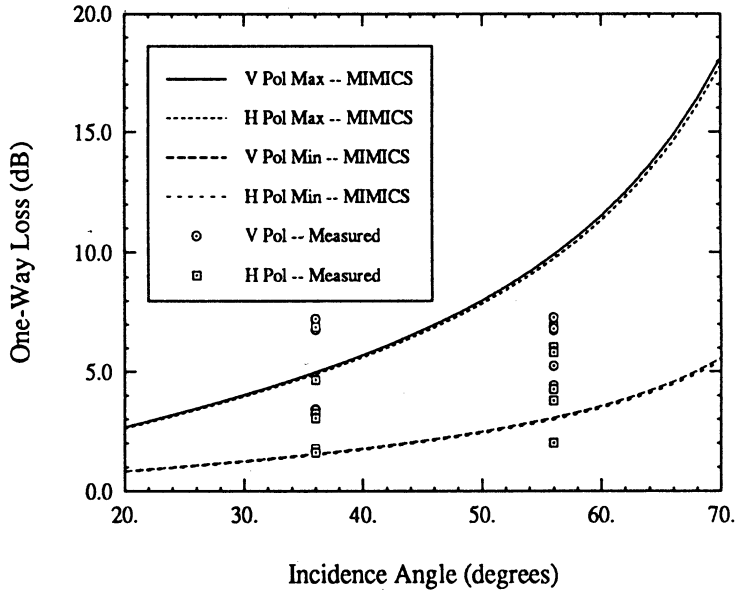

(b) X-band.

Figure H.2: Transmission loss for one-way propagation through the mixed balsam poplar-alder canopy. Measurements are shown for seven trihedral targets at (a) C-band and (b) X-band.

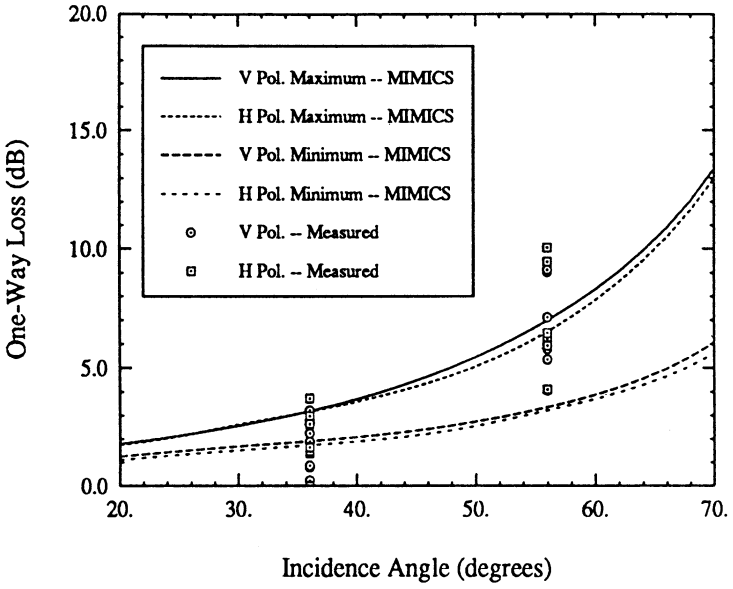

(a) C-band.

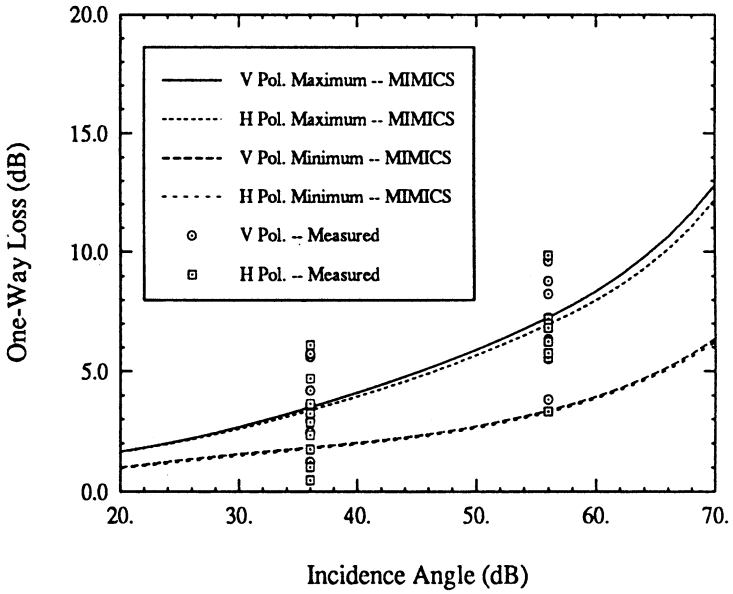

(b) X-band.

Figure H.3: Transmission loss for one-way propagation through the mixed white spruce-balsam poplar-alder canopy. Measurements are shown for nine trihedral targets at (a) C-band and (b) X-band.

cient $\rho \geq 0.75$, however MIMICS never predicts 0 dB of loss which may be measured at low values of incidence angle because of placement of the reflectors in canopy gaps. This indicates that more reflectors should be used in this type of study and more careful attention should be paid to random placement of the targets in the canopy. Furthermore, this figure illustrates the underestimation of canopy extinction by MIMICS in the white spruce stand. This illustrates the importance of including the crown layer constituents in canopy transmissivity analyses, especially for foliated species.

Figures H.5 and H.6 show MIMICS simulations of one-way canopy transmissivity at C- and X-bands for a mature white spruce stand (WS-2). This simulation is compared to the mean value observed by the trihedral reflector measurements for the young mixed-species stand. The total canopy transmissivity is shown along with the individual contributions from the crown and trunk layers for H- and V-polarizations. The total transmissivity is shown to be dominated by the transmissivity through the crown layer, which is comprised of needles and branches. This is caused in a large part by the high number density of needles in the crown layer (13,310/m^2). At the higher incidence angle ($\theta = 56°$), The MIMICS simulations agree very well with the average measured transmissivity, predicting values to within one standard deviation of the mean. However, at the steeper incidence angle ($\theta = 36°$), MIMICS underestimated the transmissivity (overestimates extinction) by at least 1 dB. In fact, the mature canopy exhibits more extinction than the mixed-species stand in nearly all cases. This is because the younger stand has a less developed crown layer than the mature stand.

Having established confidence in the ability of MIMICS to simulate extinction for these canopies, a variety of similar architectures and differing environmental condi-

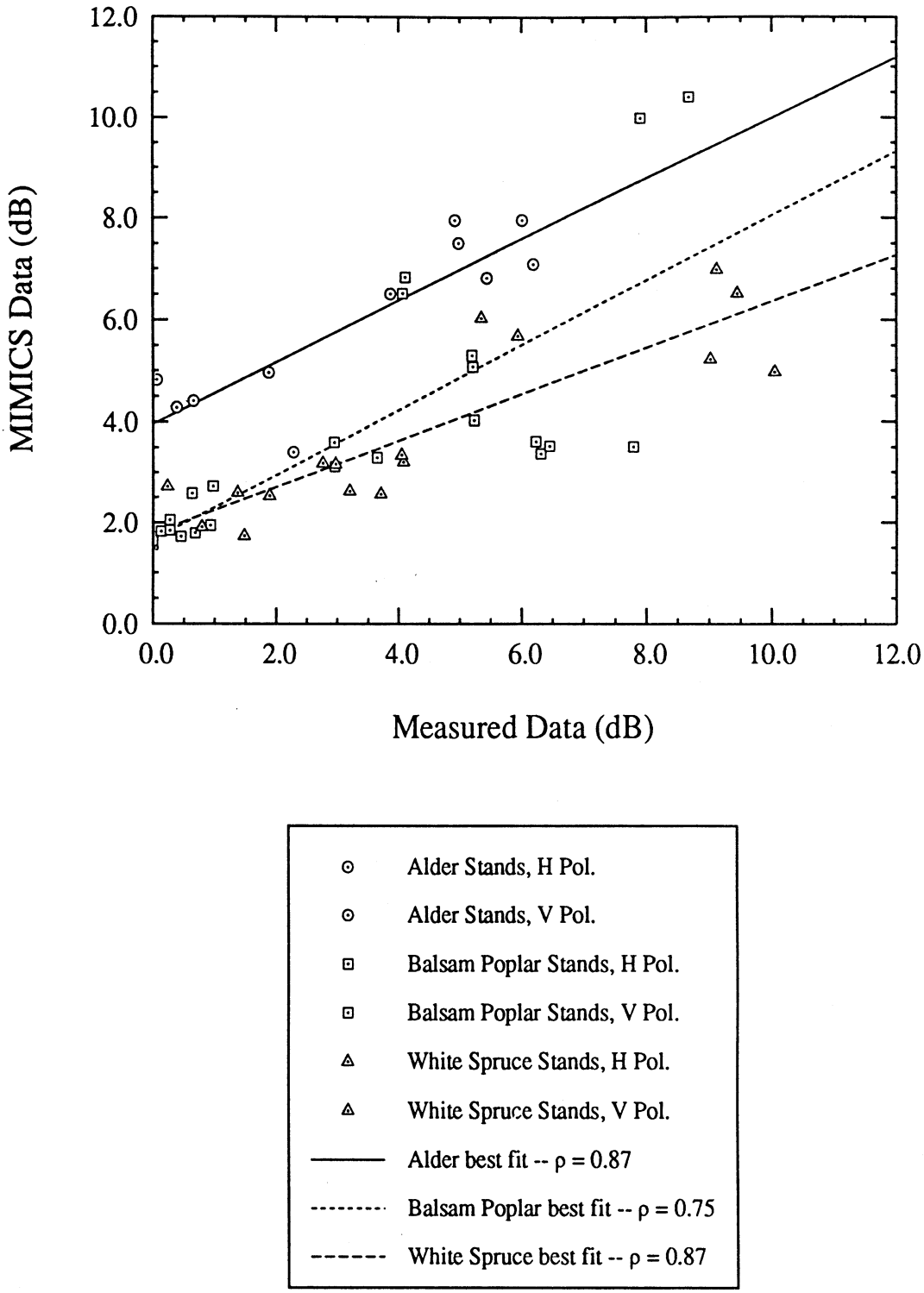

Figure H.4: Comparison of MIMICS simulated and measured transmission loss for one-way propagation through the alder, balsam poplar and white spruce canopies at C-band. The best-fit straight lines are shown for each canopy, together with their respective correlation coefficients ρ.

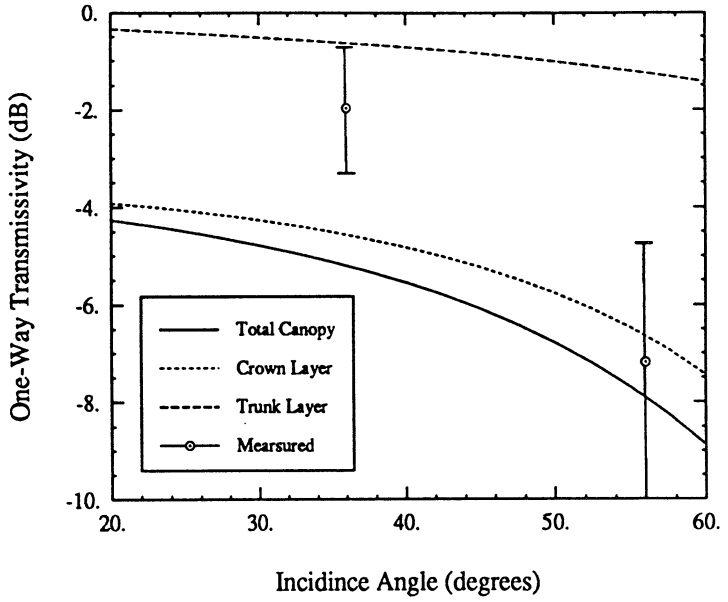

(a) H-polarization.

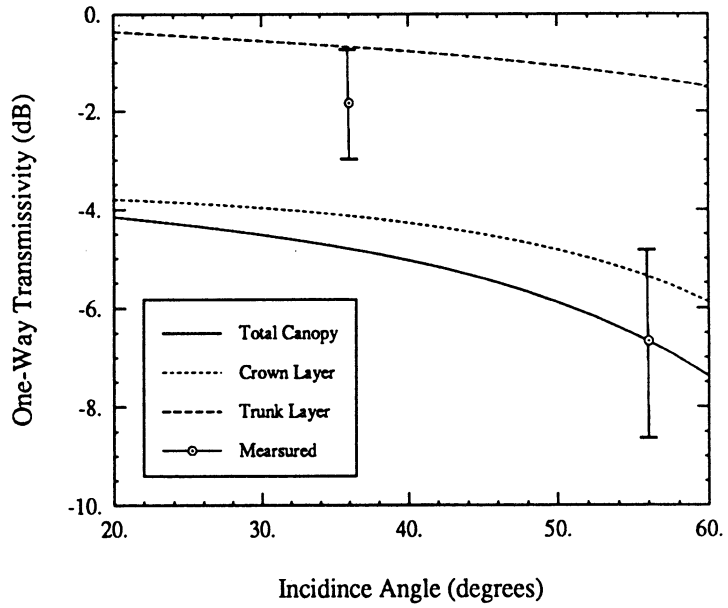

(b) V-polarization.

Figure H.5: Comparison of MIMICS simulated one-way canopy transmissivity for a mature white spruce stand (WS-2) at C-band to the average measured transmissivity of the mixed-species white spruce stands. Error bars are based on the mean value $\pm$ one standard deviation.

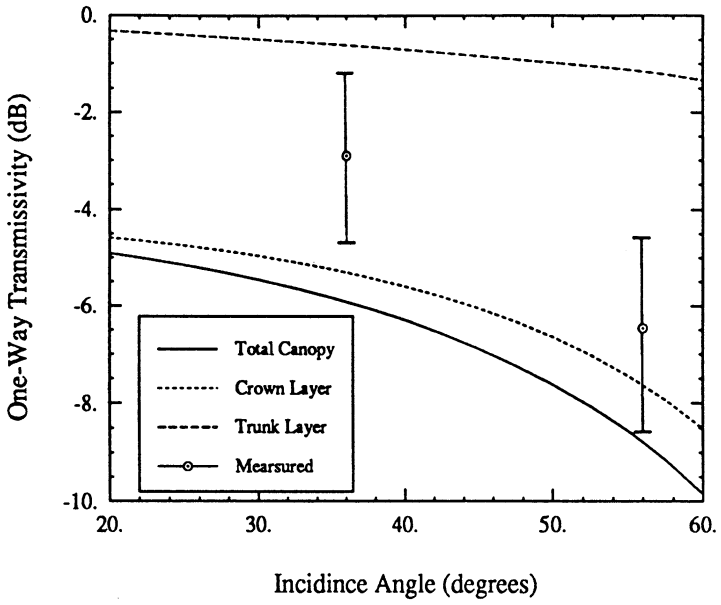

(a) H-polarization.

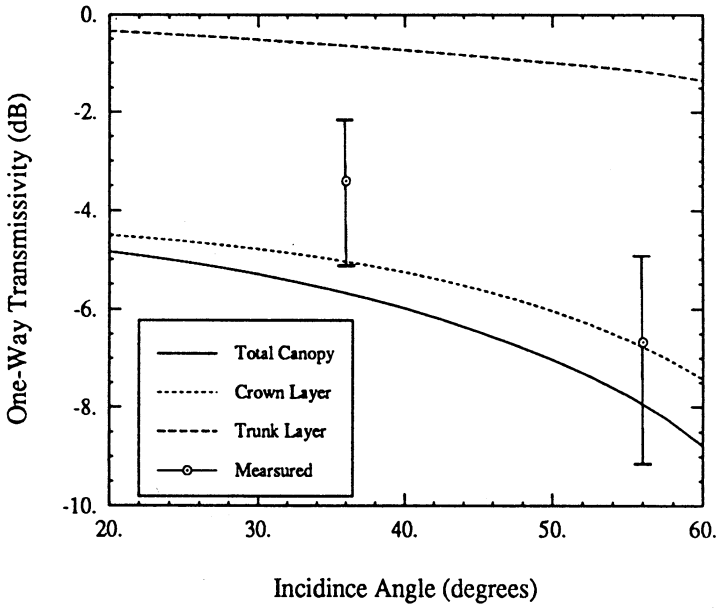

(b) V-polarization.

Figure H.6: Comparison of MIMICS simulated one-way canopy transmissivity for a mature white spruce stand (WS-2) at X-band to the average measured transmissivity of the mixed-species white spruce stands. Error bars are based on the mean value ± one standard deviation.

tions are now considered. Figures H.7 and H.8 present simulations of total one-way canopy transmissivity for mature stands of white spruce and black spruce, respectively. V-polarized data are shown for L-, C- and X-bands for frozen and thawed canopy conditions. In all cases, transmissivity decreases as the canopy changes from the frozen to the thawed states. Furthermore, transmissivity is inversely related to canopy biomass, i.e. transmissivity decreases with increasing canopy biomass. Behavior as a function of frequency demonstrates that transmissivity also decreases as frequency increases.

H.3 Boreal Forest Backscatter Analysis

Data recorded by both the JPL SAR and the ERIM/NADC SAR have been applied to analyze canopy backscatter (Dobson *et al.*, [13],[14]). Data was extracted from the SAR imagery for large single-species stands and spatially averaged to obtain the mean backscatter from a single stand. C- and X-band data were recorded with the ERIM/NADC SAR on March 22 (frozen canopy conditions) (Kasischke, *et al.*,[32]). Since the antenna gain pattern of this system contains significant ripple that is not fully characterized, the data are not fully calibrated to an absolute level. Valid data comparison is therefore limited to data recorded for stands at a common range within a given pass. Comparison of data recorded on different passes and at different incidence angles are only approximate since the passes may have different biases. Similarly, comparison of data between frequencies can only be performed on a relative scale. Therefore, MIMICS simulations of data recorded by this system are restricted to comparing those data recorded at a common range location on a given SAR pass.

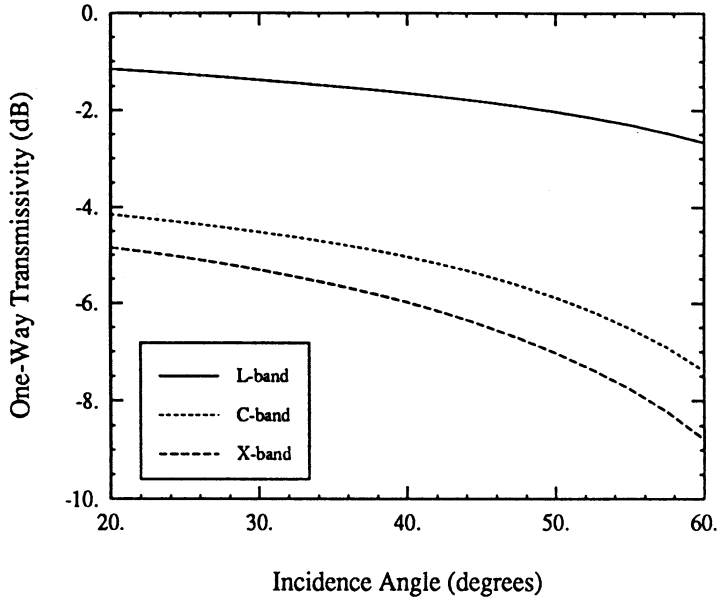

(a) Frozen conditions.

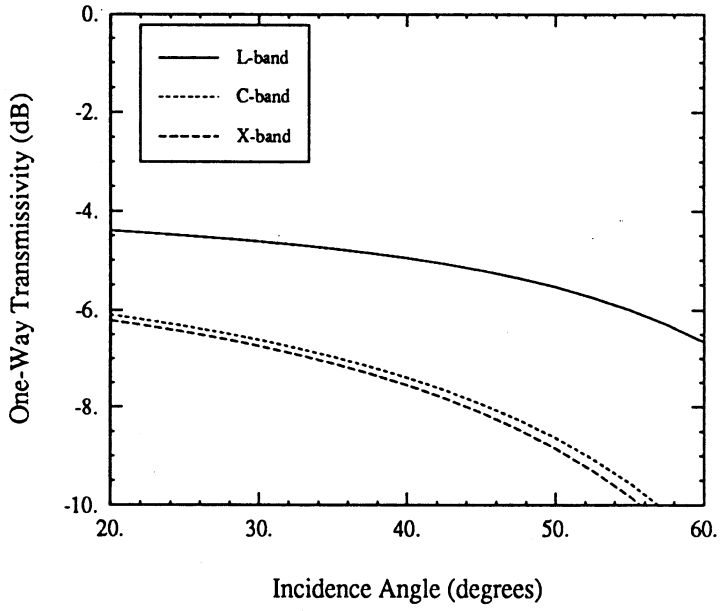

(b) Thawed conditions.

Figure H.7: MIMICS simulated one-way canopy transmissivity for a mature white spruce stand (WS-2) at L-, C- and X-bands for (a) frozen canopy conditions and (b) thawed canopy conditions.

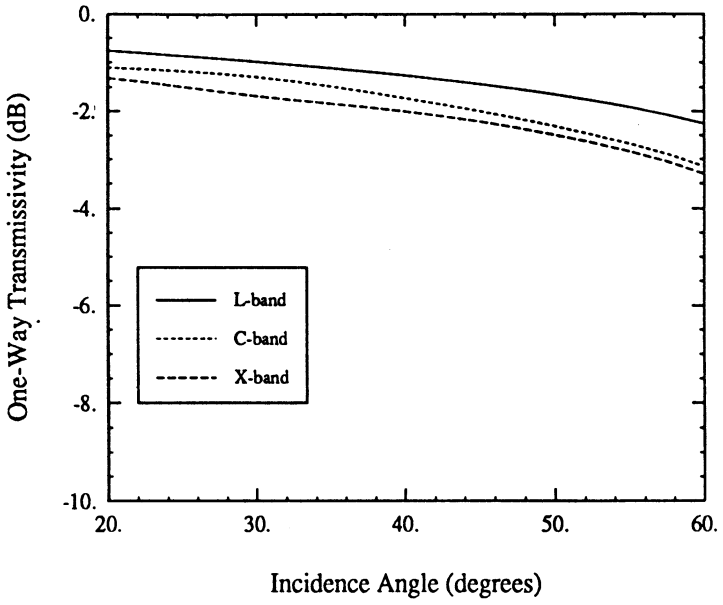

(a) Frozen conditions.

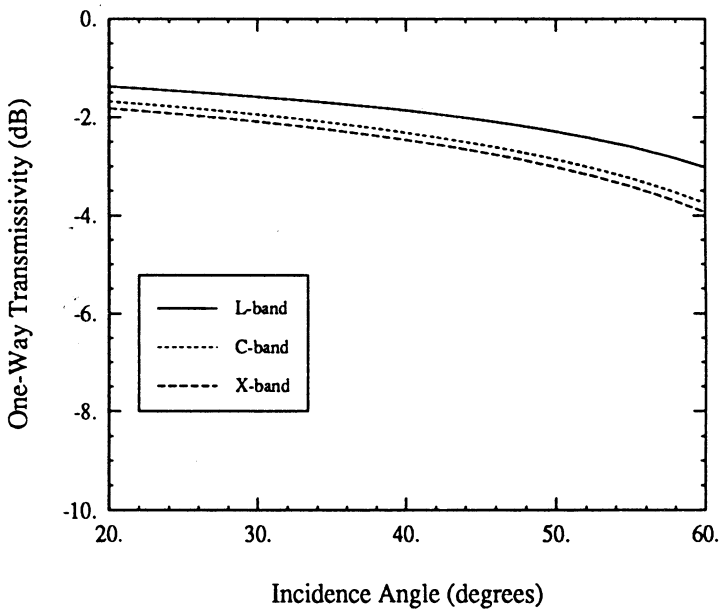

(b) Thawed conditions.

Figure H.8: MIMICS simulated one-way canopy transmissivity for a black spruce stand (BS-1) at L-, C- and X-bands for (a) frozen canopy conditions and (b) thawed canopy conditions.

L-band data were collected with the JPL SAR on March 13 (frozen canopy conditions) and on March 19 (thawed canopy conditions) (Way *et al.*,[77]). The antenna gain pattern of this system is relatively smooth and the data is easier to correct for gain variations. The two passes of L-band data were calibrated against the SAR response to several 182 cm trihedral corner reflectors located at the Fairbanks International Airport.

MIMICS simulations of canopy backscatter is limited to those stands that were characterized by on-site sampling. Since the stands considered in this study were only partially characterized by on-site sampling, information on biomass apportionment and canopy constituent size and density characteristics is only approximate. Errors introduced in the biomass apportionment analysis will have an effect on the backscatter simulated by MIMICS.

The 20-30cm thick snow layer also significantly complicated the backscatter analysis. The roughness parameters and other characteristics of the snow-ground interface were not characterized. These parameters could only be estimated by fitting MIMICS to ground backscatter measurements of open areas on sandbars that were outside the tree canopies. Since the roughness of these regions do not correspond to the roughness of a forest floor, and since the goal of this study is to examine model performance without using parameter fitting, the snow substrate was modeled as a half-space of snow with estimated RMS roughness of 1.2 cm and 24 cm correlation length. This ignores scattering at the snow-ground interface completely and in some cases reduces the effectiveness of the MIMICS simulations. A simple technique that accounts for the snow-ground interface at L-band was introduced in Section 3.2.2, however, because of lack of adequate characterization of the ground surface, its effectiveness is also somewhat limited.

H.3.1 Comparison with Measured Data

Table H.10 lists the MIMICS backscatter simulations together with the SAR backscatter observations for six stands. Measured data were recorded by the JPL SAR at L-band for both frozen and thawed conditions. A one-to-one comparison of the measured and simulated values shows very good agreement for both frozen and thawed canopy states. MIMICS, however, significantly underestimates VV-polarized backscatter from stands BS-1, BP-2 and Alder under frozen conditions. The cross-polarized backscatter from frozen BS-1 is also significantly underestimated. Figure H.9 graphically illustrates the effectiveness of MIMICS in predicting the HH- and VV-polarized backscatter. The measured SAR data are plotted against that predicted by MIMICS. Data are shown for all six stands for both frozen and thawed conditions. From here it is seen that MIMICS tends to underestimate backscatter for all stands except for white spruce. An underestimation of VV backscatter for frozen conditions

Table H.10: Comparison of MIMICS Estimates to Measured L-band SAR Data (dB).

		March 13, 1988 Thawed Conditions		March 19, 1988 Frozen Conditions	
Stand	Polarization	SAR	MIMICS	SAR	MIMICS
WS-1	HH	-10.0	-9.2	-13.1	-12.2
	VV	-10.4	-12.1	-14.9	-15.6
	VH	-15.2	-14.9	-21.0	-22.8
WS-2	HH	-8.4	-9.1	-11.4	-12.8
	VV	-9.9	-12.3	-14.5	-16.4
	VH	-14.2	-15.0	-20.4	-23.6
WS-5	HH	-8.1	-9.1	-11.1	-12.2
	VV	-9.1	-12.0	-14.8	-15.5
BS-1	HH	-12.9	-10.7	-14.9	-16.9
	VV	-14.4	-15.1	-16.4	-23.2
	VH	-20.0	-19.5	-23.7	-32.5
BP-2	HH	-9.2	-11.7	-12.7	-14.4
	VV	-10.4	-11.6	-14.8	-22.0
Alder	HH	-8.7	-9.9	-11.3	-14.6
	VV	-9.7	-11.4	-14.0	-23.2

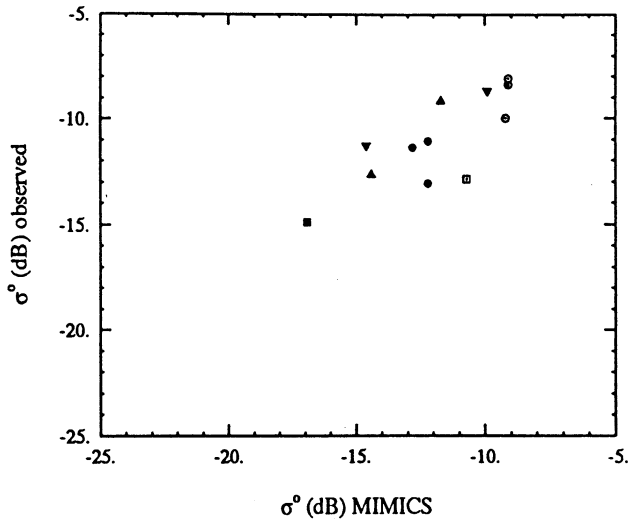

(a) HH-polarization.

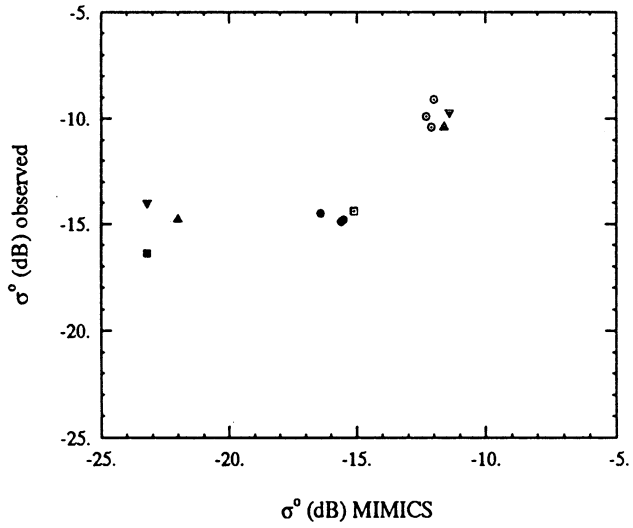

(b) VV-polarization.

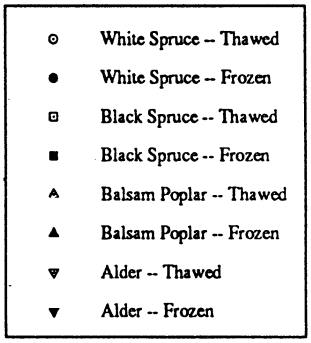

Figure H.9: Comparison of measured canopy backscatter to MIMICS simulated backscatter for (a) HH-polarization and (b) VV-polarization.

for all stands except white spruce is also clearly evident. Since the alder and balsam poplar stands have no foliage in their crown layers, and since the black spruce stand has a fairly sparse crown layer as compared to the white spruce canopies, scattering mechanisms involving interaction with the ground surface contribute more readily to the net canopy backscatter than they do for the white spruce stands, since they are fully foliated. The general underestimation of σ^0 may therefore be attributed to the modeling of the snow surface as an infinite half-space. It is expected that accounting for scatter at the snow-ground interface would increase σ^0 somewhat and may alleviate this problem.

Table H.11 compares the measured and predicted L-band polarization ratios $\sigma^0_{HH}/\sigma^0_{VV}$ and $\sigma^0_{HH}/\sigma^0_{VH}$ for the six stands under frozen and thawed conditions. Here

Table H.11: Comparison of Measured and Modeled Polarization Ratios at L-band.

	$\sigma^0_{HH}/\sigma^0_{VV}$ (dB)			
	March 13, 1988		March 19, 1988	
Stand	Thawed Conditions		Frozen Conditions	
	SAR	MIMICS	SAR	MIMICS
WS-1	0.4	2.9	1.8	3.4
WS-2	1.5	3.1	3.1	3.6
WS-5	1.0	2.9	3.7	3.3
BS-1	1.5	4.4	1.5	6.3
BP-2	1.2	-0.1	2.1	7.6
Alder	1.0	1.5	2.7	8.6
	$\sigma^0_{HH}/\sigma^0_{VH}$ (dB)			
WS-1	5.2	5.7	7.9	10.5
WS-2	5.8	5.9	9.0	10.8
BS-1	7.1	8.8	8.8	15.6

MIMICS performs nicely with the exception of frozen conditions where underestimation of VV- and VH-polarized backscatter on account of the snow/soil model becomes apparent. MIMICS successfully predicts the the polarization ratios are smaller for the thawed canopy state for all of the stands.

Table H.12 illustrates the effect of changing freeze/thaw state on the canopies. Measured and simulated L-band values of the ratio $\sigma^0_{\text{thawed}}/\sigma^0_{\text{frozen}}$ are presented for each stand. MIMICS successfully predicts the observed increase in σ^0 in going from

Table H.12: Comparison of the Effects of Freeze/Thaw State on L-band Backscatter.

	$\sigma^0_{\text{thawed}}/\sigma^0_{\text{frozen}}$ (dB)					
	HH		VV		VH	
Stand	SAR	MIMICS	SAR	MIMICS	SAR	MIMICS
WS-1	3.1	3.1	4.5	3.6	5.8	7.9
WS-2	3.0	3.7	4.6	4.2	6.2	8.5
WS-5	3.0	3.1	5.7	3.6	-	7.9
BS-1	2.0	6.2	2.0	8.1	3.7	13.0
BP-2	3.5	2.7	4.4	10.4	-	15.1
Alder	2.6	4.7	4.3	11.8	-	16.2

a frozen to a thawed state. For the white spruce stands, the MIMICS estimates are in very good agreement with the measurements. Notable discrepancies exist again at VV and VH polarizations for the more sparse stands.

Figures H.10 and H.11 present L-band polarization responses for frozen and thawed white spruce (WS-5), respectively, as simulated by MIMICS. Responses are shown for co-polarized and cross-polarized configurations. Figures H.12 and H.13 present the measured frozen and thawed L-band responses. Again MIMICS successfully recreates the behavior of the measured data. MIMICS not only correctly reproduces the shapes of each of the surfaces, but it accounts for the increase in the pedestal observed in going from frozen to thawed states. These figures demonstrate that MIMICS has successfully modeled the backscatter response of this stand for all of these polarization states. Figure H.14 shows the linear polarized response of this stand as simulated by MIMICS for frozen and thawed conditions. The character of the responses are very similar for the two environmental states, with the thawed conditions yielding slightly more cross-polarized backscatter.

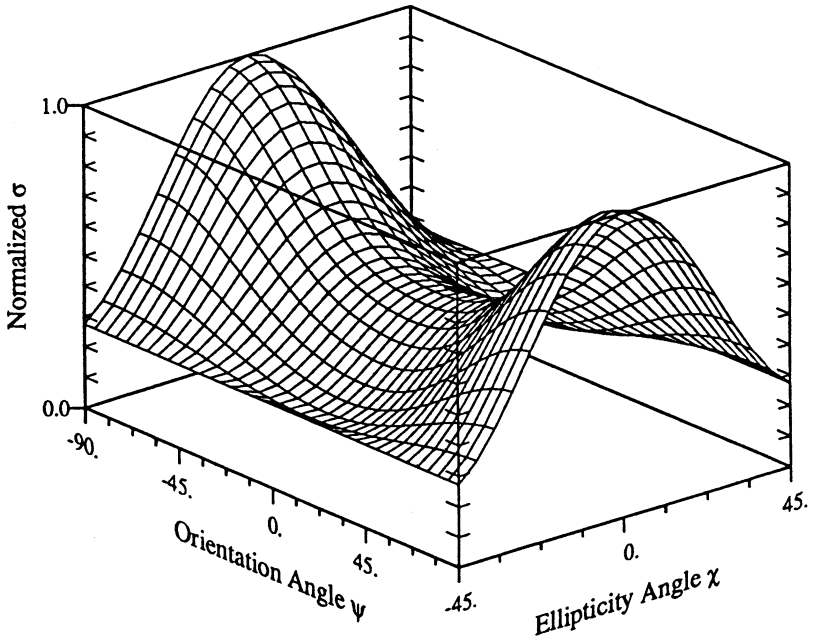

(a) Co-polarized response.

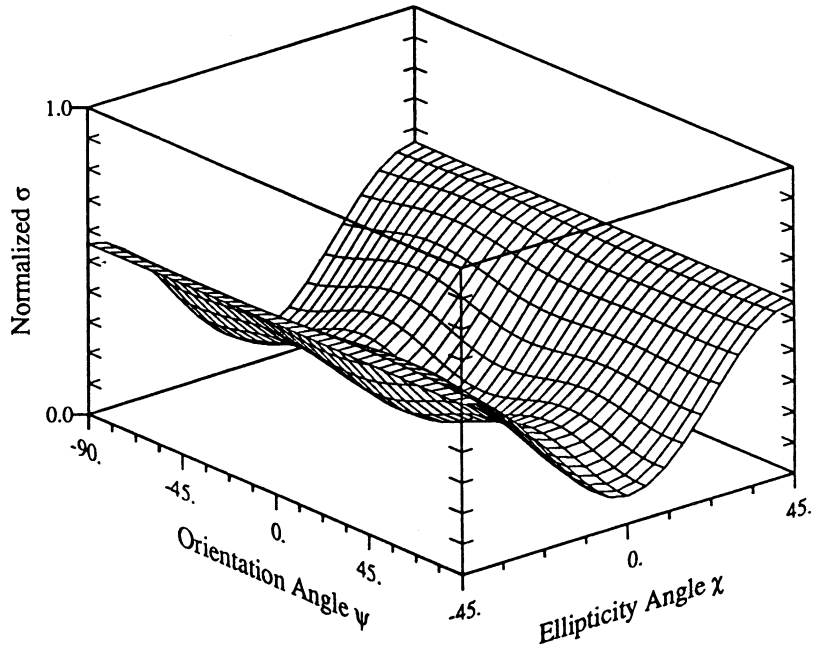

(b) Cross-polarized response.

Figure H.10: MIMICS simulated L-band polarization response of frozen white spruce stand WS-5.

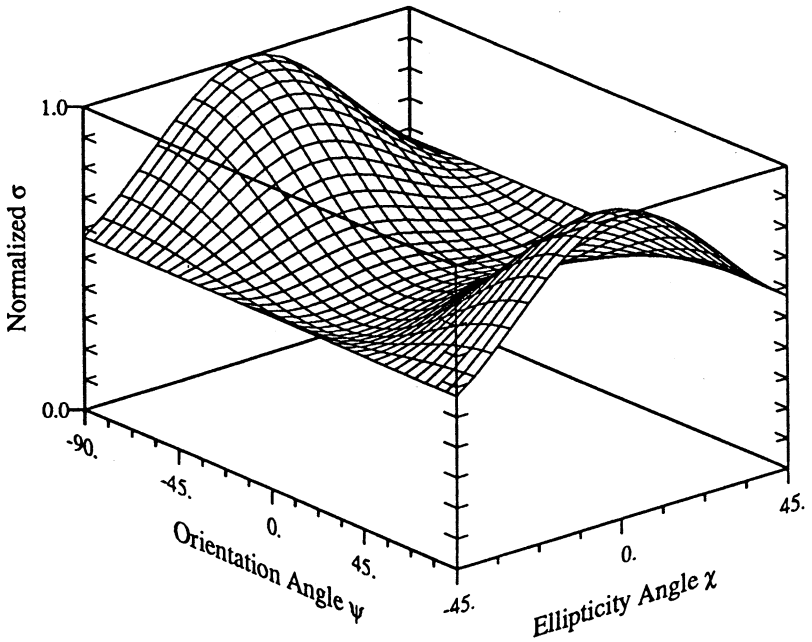

(a) Co-polarized response.

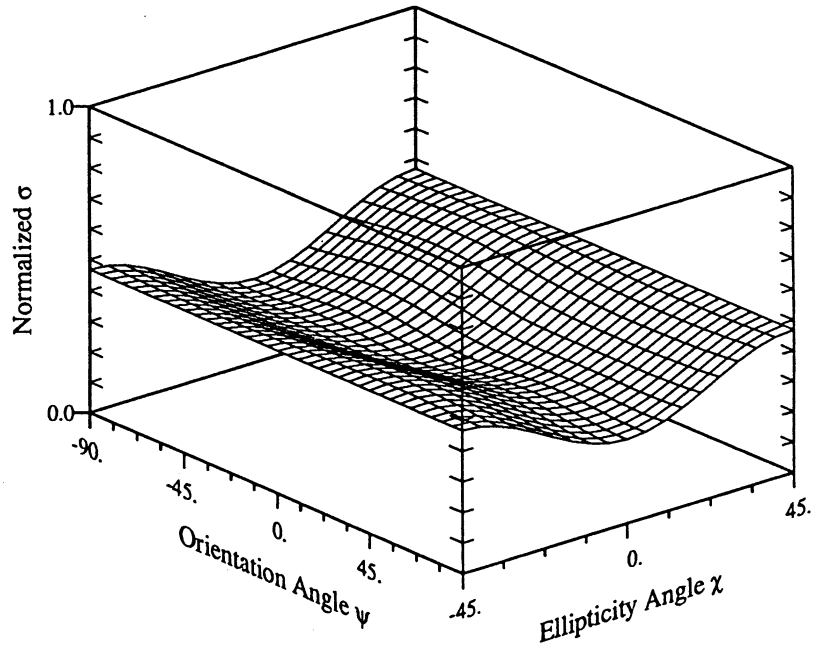

(b) Cross-polarized response.

Figure H.11: MIMICS simulated L-band polarization response of thawed white spruce stand WS-5.

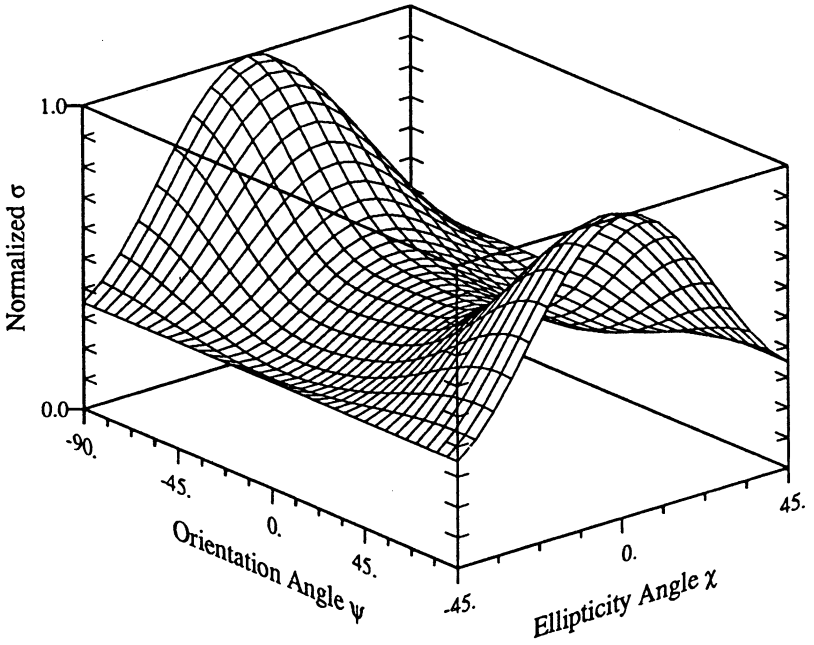

(a) Co-polarized response.

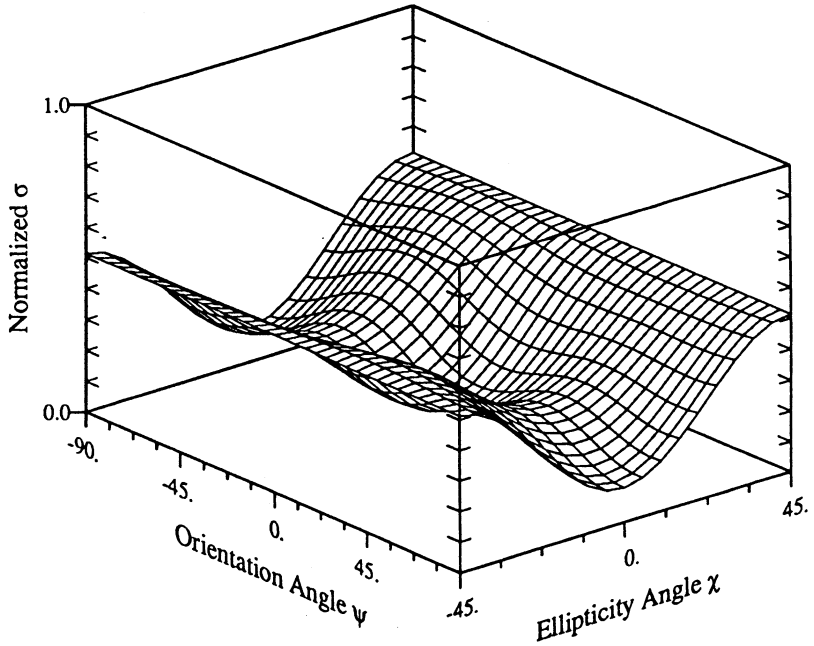

(b) Cross-polarized response.

Figure H.12: Measured L-band polarization response of frozen white spruce stand WS-5.

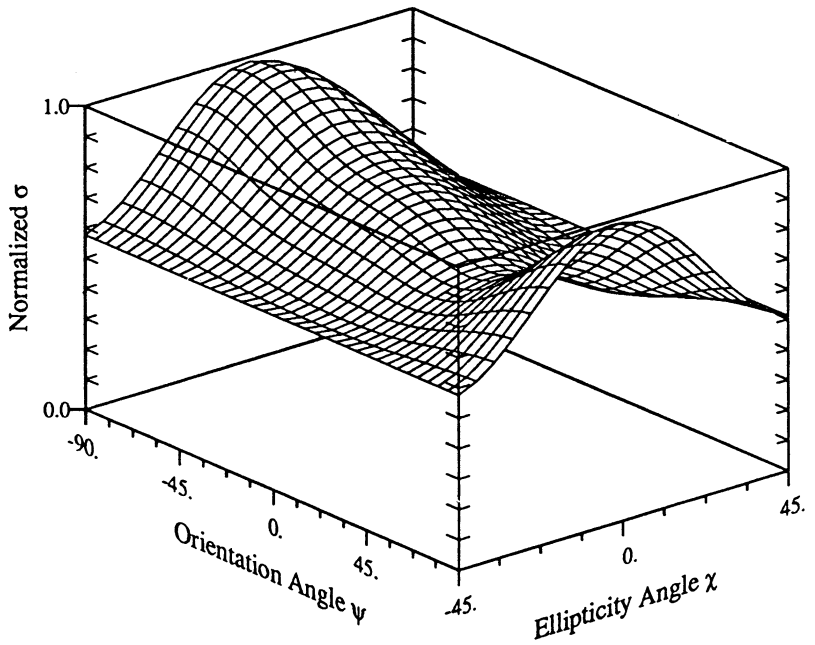

(a) Co-polarized response.

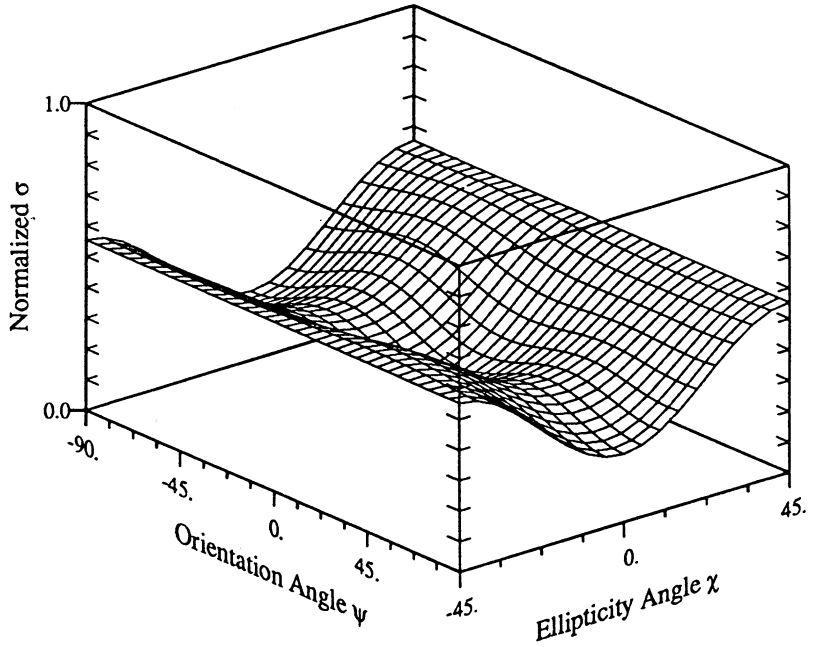

(b) Cross-polarized response.

Figure H.13: Measured L-band polarization response of thawed white spruce stand WS-5.

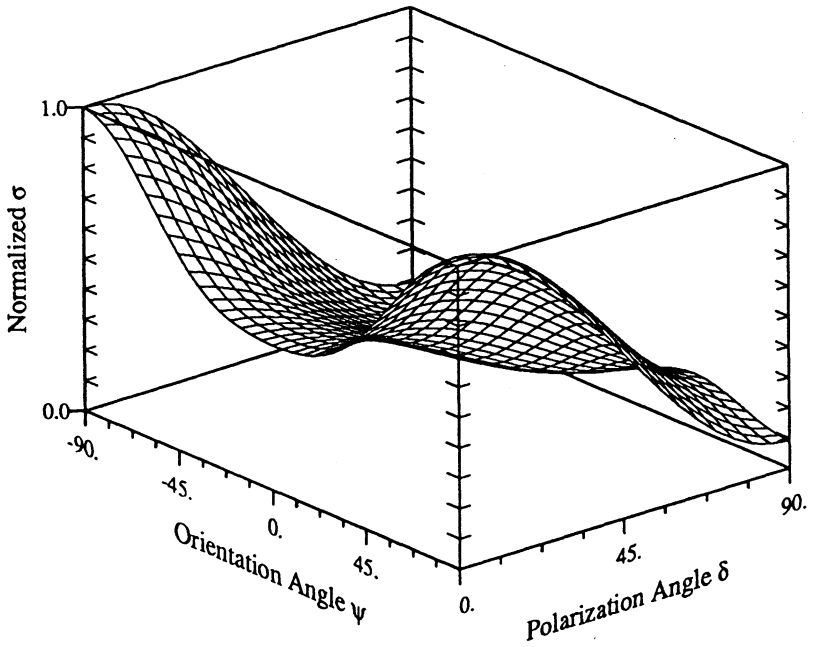

(a) Frozen Conditions.

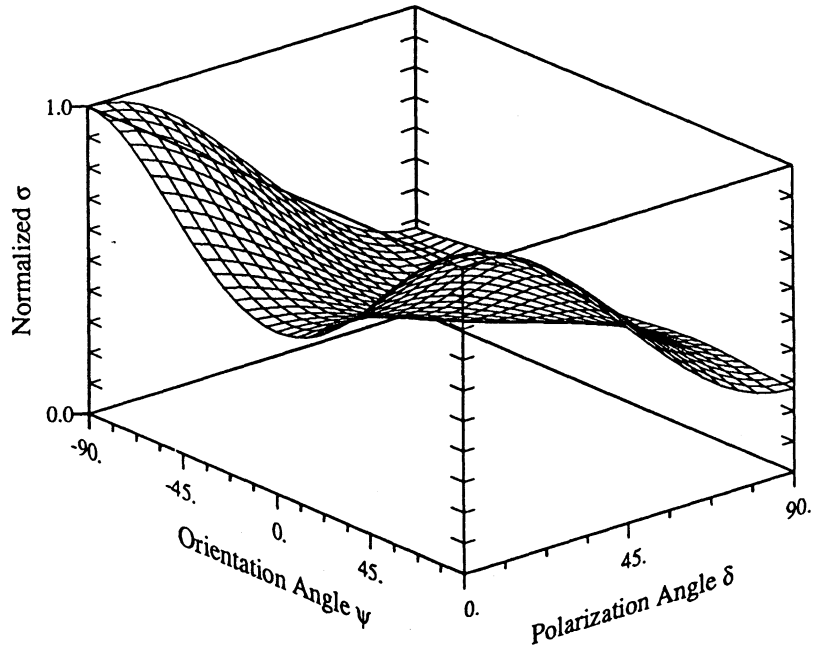

(b) Thawed Conditions.

Figure H.14: MIMICS-simulated L-band linear polarization response of thawed white spruce stand WS-5.

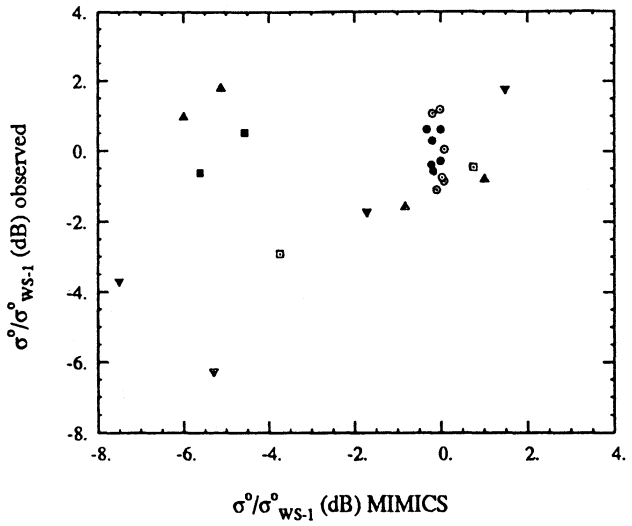

(a) C-Band.

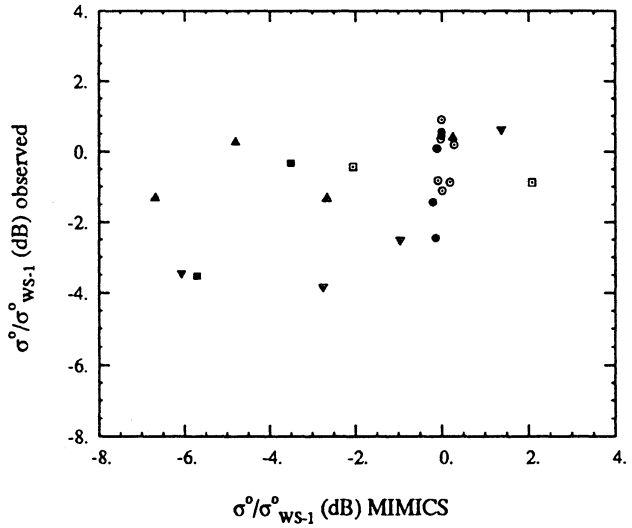

(b) X-Band.

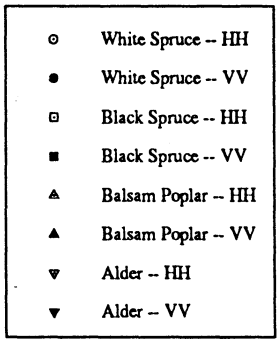

Figure H.15: Comparison of measured canopy backscatter to MIMICS simulated backscatter for (a) C-band and (b) X-band. The data have been normalized to the backscatter from white spruce stand WS-1 for each SAR pass.

Modeling at C- and X-bands has been complicated by the lack of available calibrated SAR data from the ERIM/NADC SAR. Furthermore, since this SAR flew only during times for which the canopies were frozen, only this environmental state is considered. To deal with the uncalibarted data problem, the backscatter values were normalized to that of the white spruce stand WS-1 for each SAR pass. These normalized data are presented in Figure H.15. For the most part, MIMICS predictions agree with the SAR measurements to within ± 1.5 dB. Exceptions to this include some observations of the balsam poplar, black spruce and alder stands at VV-polarization. As was the case at L-band, this is probably caused by the method used to model the snow-soil interface.

H.3.2 White Spruce Simulations

Having established the ability to model backscatter from these forest stands, MIMICS is now used to simulate backscatter over a wider range of sensor parameters and the backscatter is examined on a more detailed level. White spruce and black spruce stands are considered in these simulations. Since the best estimates of backscatter were obtained for white spruce canopies, these stands are considered first

Figure H.16 shows the simulated backscatter from stand WS-5 at L-, C- and X-bands for frozen conditions. Figure H.17 shows backscatter for thawed conditions. In general, MIMICS predicts that σ^0 increases at L-band as the canopy moves from a frozen to a thawed state. However, a decrease is observed in σ^0 at C- and X-bands for these conditions. Furthermore, for frozen conditions, σ^0 increases with frequency whereas the reverse is true for thawed conditions.

The scattering contributions to the net canopy backscatter are depicted in Fig-

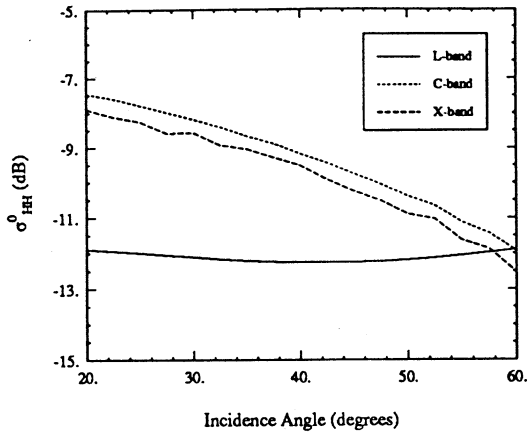

(a) HH-polarization.

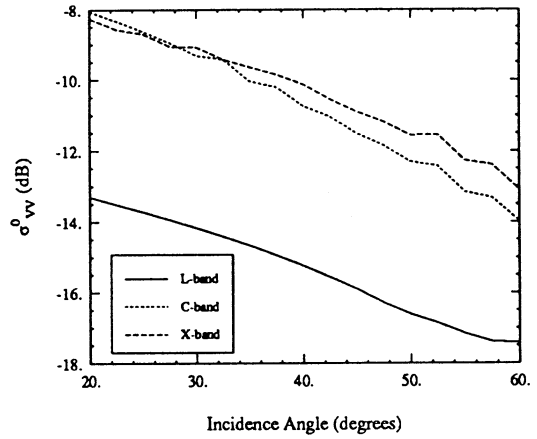

(b) VV-polarization.

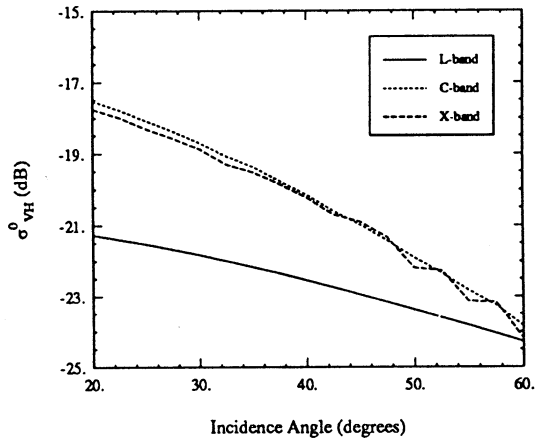

(c) VH-polarization.

Figure H.16: MIMICS simulated canopy backscatter for a white spruce stand (WS-5) at L-, C- and X-bands under frozen canopy conditions for (a) HH-polarization, (b) VV-polarization and (c) VH-polarization.

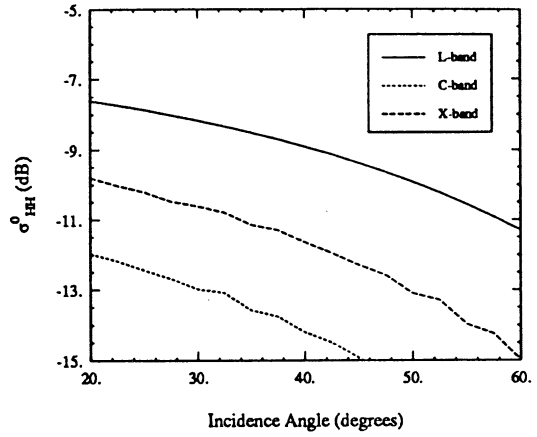

(a) HH-polarization.

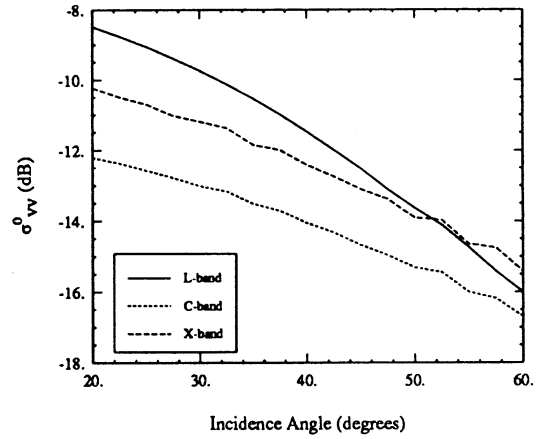

(b) VV-polarization.

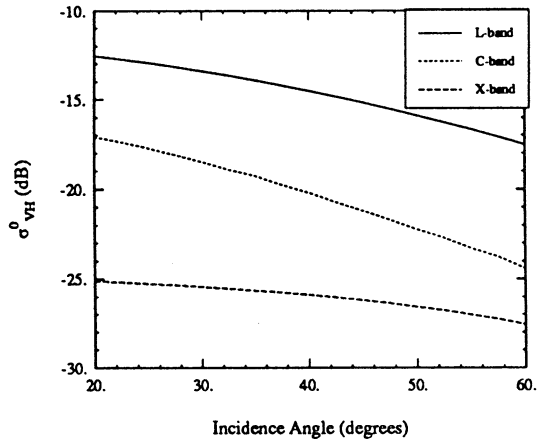

(c) VH-polarization.

Figure H.17: MIMICS simulated canopy backscatter for a white spruce stand (WS-5) at L-, C- and X-bands under thawed canopy conditions for (a) HH-polarization, (b) VV-polarization and (c) VH-polarization.

ures H.18 through H.21 for L- and C-bands for frozen and thawed canopy states. In all cases, canopy backscatter is dominated by the direct crown contributions to σ^0, thereby negating effects that the snow-covered soil may have on the net backscatter. Treatment of the ground surface becomes important only at L-band, for HH-polarization, where the ground-trunk interaction is significant at high incidence angles.

Figures H.22 and H.23 present net L- and C-band backscatter for all white spruce stands for frozen and thawed states. As expected, σ^0 is seen to respond similarly for all three canopies. At L-band, for all polarizations σ^0 increases as the canopy thaws while at C-band, σ^0 decreases. The C-band cross-polarized backscatter, however, remains relatively constant.

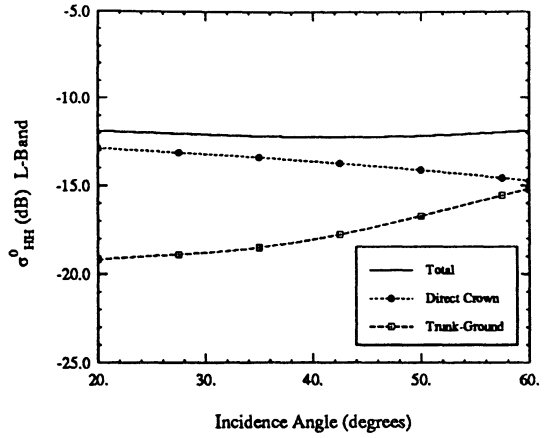

(a) HH-polarization.

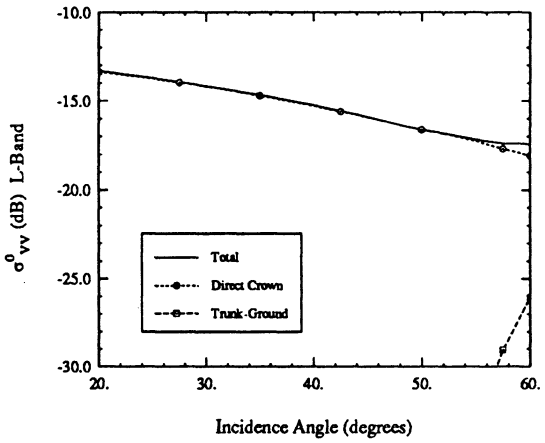

(b) VV-polarization.

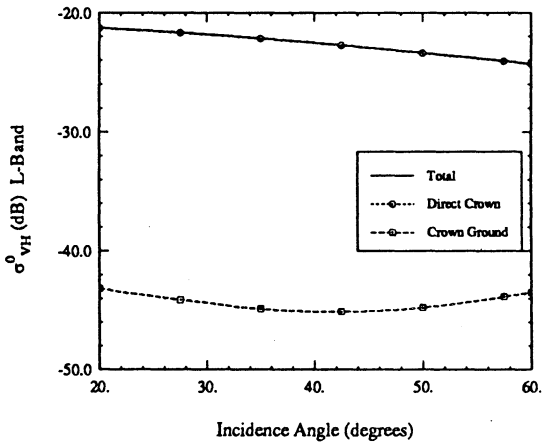

(c) VH-polarization.

Figure H.18: Canopy backscatter components for white spruce stand (WS-5) at L-band under frozen canopy conditions for (a) HH-polarization, (b) VV-polarization and (c) VH-polarization.

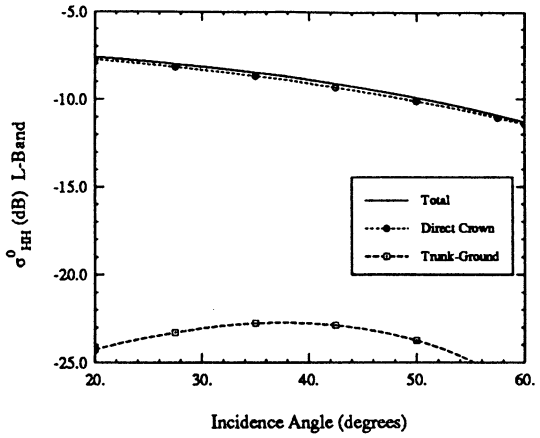

(a) HH-polarization.

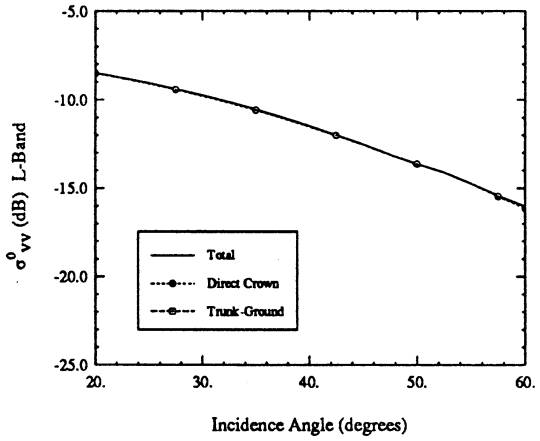

(b) VV-polarization.

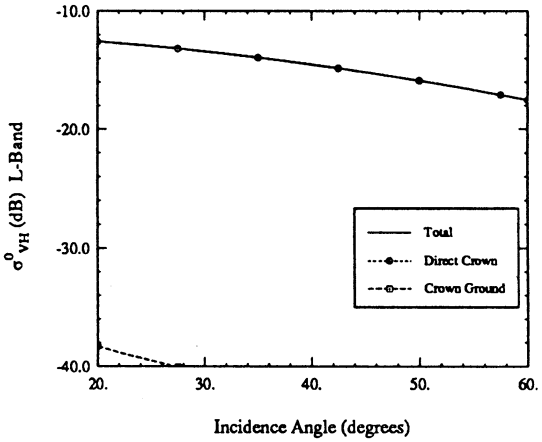

(c) VH-polarization.

Figure H.19: Canopy backscatter components for white spruce stand (WS-5) at L-band under thawed canopy conditions for (a) HH-polarization, (b) VV-polarization and (c) VH-polarization.

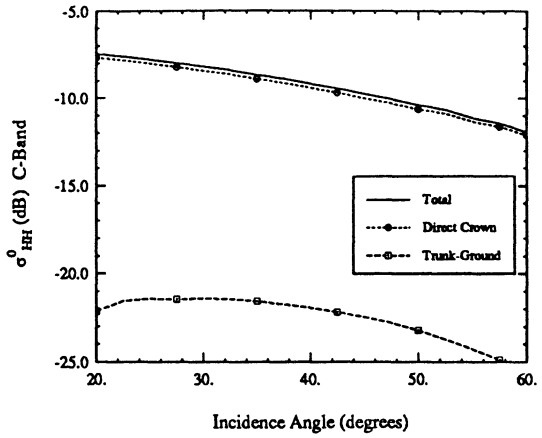

(a) HH-polarization.

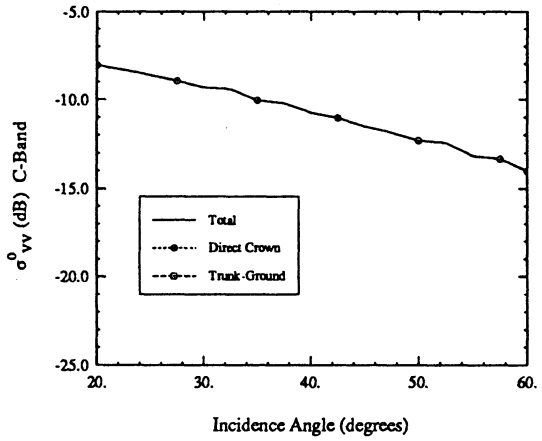

(b) VV-polarization.

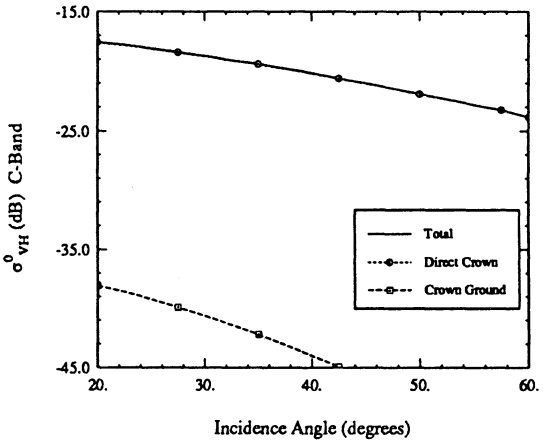

(c) VH-polarization.

Figure H.20: Canopy backscatter components for white spruce stand (WS-5) at C-band under frozen canopy conditions for (a) HH-polarization, (b) VV-polarization and (c) VH-polarization.

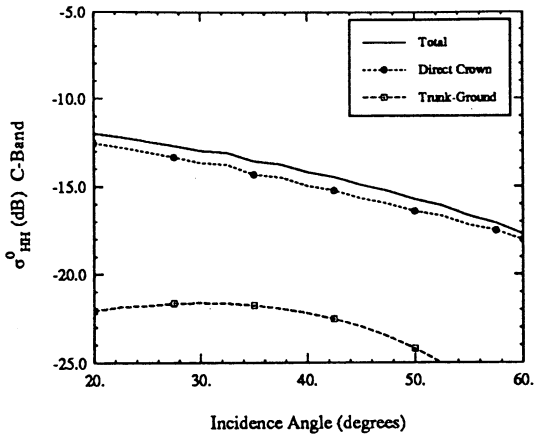

(a) HH-polarization.

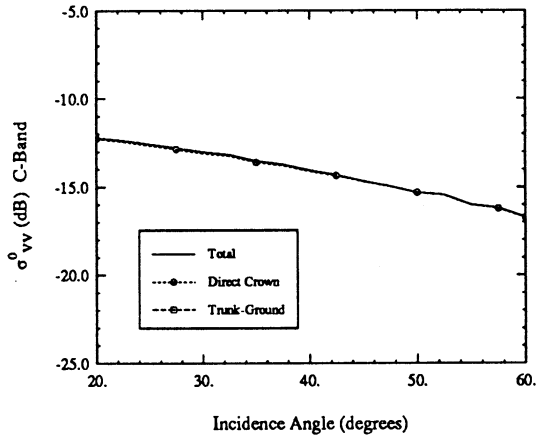

(b) VV-polarization.

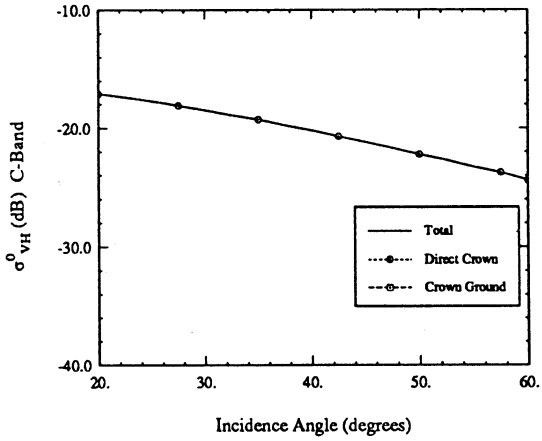

(c) VH-polarization.

Figure H.21: Canopy backscatter components for white spruce stand (WS-5) at C-band under thawed canopy conditions for (a) HH-polarization, (b) VV-polarization and (c) VH-polarization.

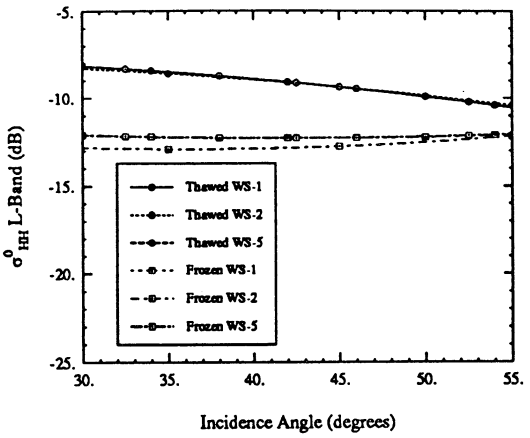

(a) HH-polarization.

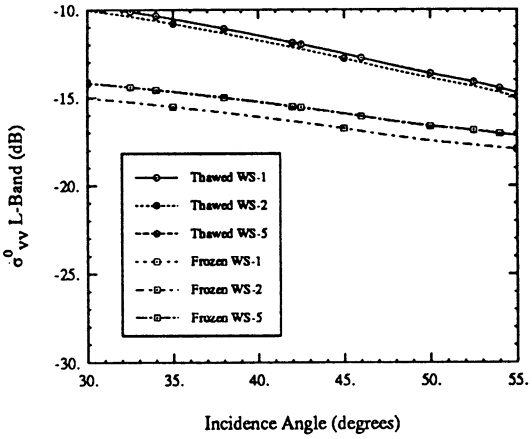

(b) VV-polarization.

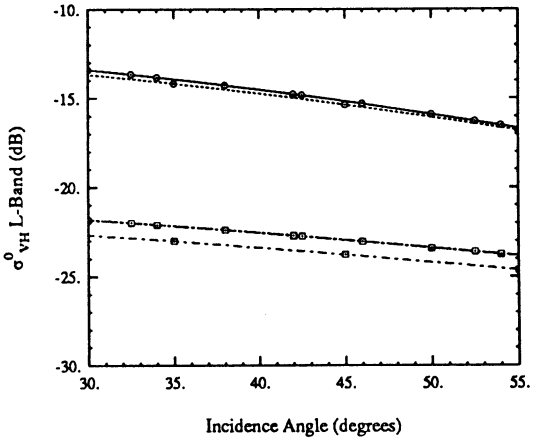

(c) VH-polarization.

Figure H.22: Total canopy backscatter for frozen and thawed white spruce stands at L-band for (a) HH-polarization, (b) VV-polarization and (c) VH-polarization.

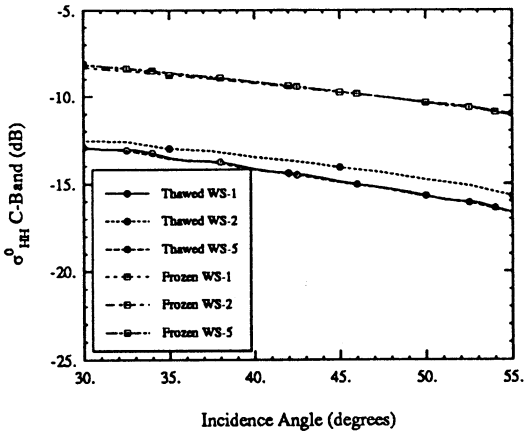

(a) HH-polarization.

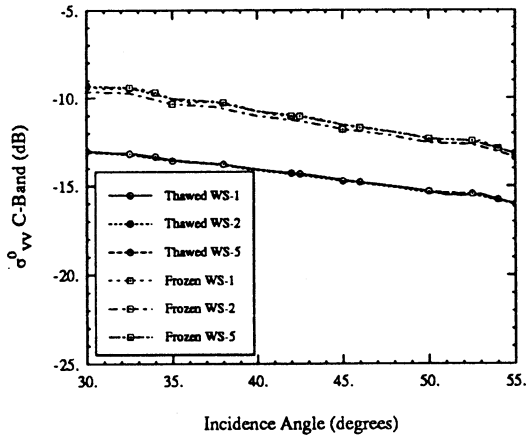

(b) VV-polarization.

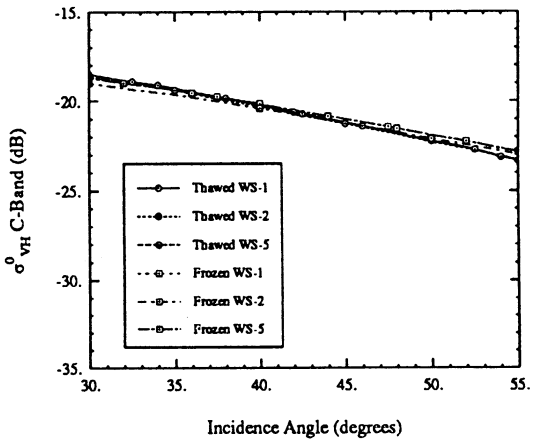

(c) VH-polarization.

Figure H.23: Total canopy backscatter for frozen and thawed white spruce stands at C-band for (a) HH-polarization, (b) VV-polarization and (c) VH-polarization.

H.3.3 Black Spruce Simulations

The black spruce stand considered here is much more sparsely populated stand than the white spruce. This stand, in fact, does not represent a closed canopy. However, to simplify this initial analysis, MIMICS I is applied to model σ^0 for the black spruce stand as if it were indeed a closed canopy.

Figures H.24 and H.25 show σ^0 at L-, C- and X-bands for frozen and thawed conditions. Backscatter from this stand exhibits more complex behavior than does that from white spruce. For frozen conditions, σ^0 shows a general increase with frequency. However, for thawed conditions, backscatter decreases with frequency for VV and VH polarizations whereas the HH-polarized backscatter increases with frequency. As the canopy moves from a frozen to a thawed state, L-band backscatter increases for all three polarizations.

Examination of the individual contributions to the net canopy backscatter lends some insight into the behavior of σ^0. Figures H.26 and H.27 show the major contributors to L-band backscatter for frozen and thawed states while Figures H.28 and H.29 show those for C-band backscatter. At L-band, the trunk-ground interaction mechanism is a significant contributor to σ^0 at HH-polarization for both frozen and thawed states. However, the direct crown mechanism is the dominant term for VV and VH polarizations. Similar trends are observed at C-band. The decrease in scattering contributions that involve the ground surface is probably responsible for MIMICS underestimating the black spruce backscatter.

To gain an understanding of the effect of the snow layer on net backscatter, the approach presented in Section 3.2.2 may be applied at L-band to model the scattering at the snow-soil interface. Figures H.30 and H.31 compare backscatter from the canopy with the ground layer modeled as a half-space of snow to this layer

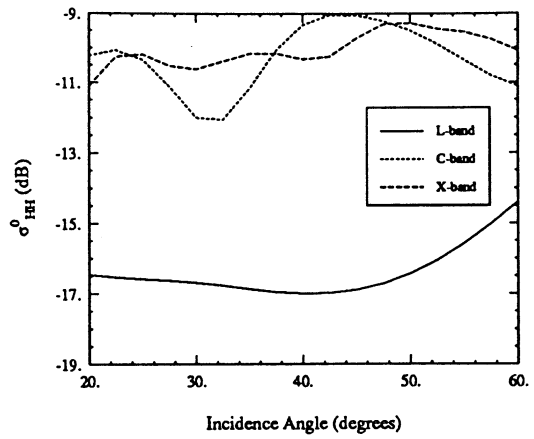

(a) HH-polarization.

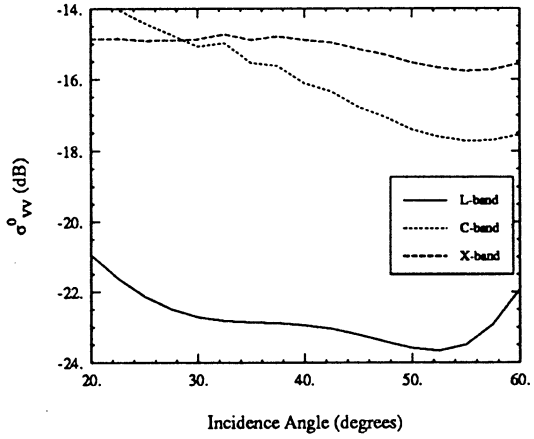

(b) VV-polarization.

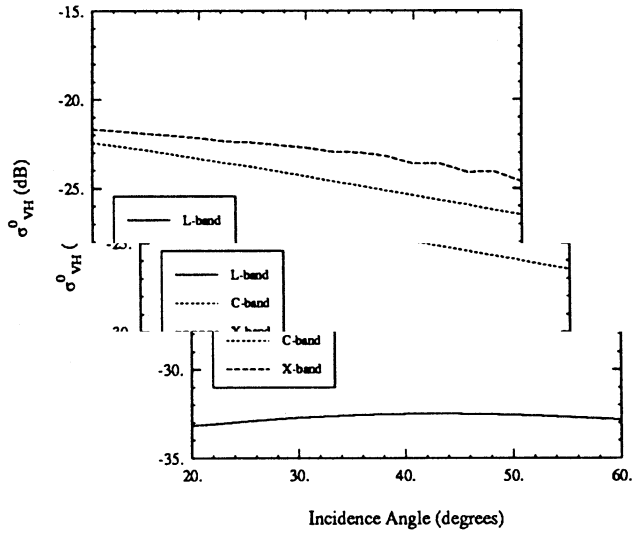

(c) VH-polarization.

Figure H.24: MIMICS simulated canopy backscatter for a white spruce stand (WS-5) at L-, C- and X-bands under frozen canopy conditions for (a) HH-polarization, (b) VV-polarization and (c) VH-polarization.

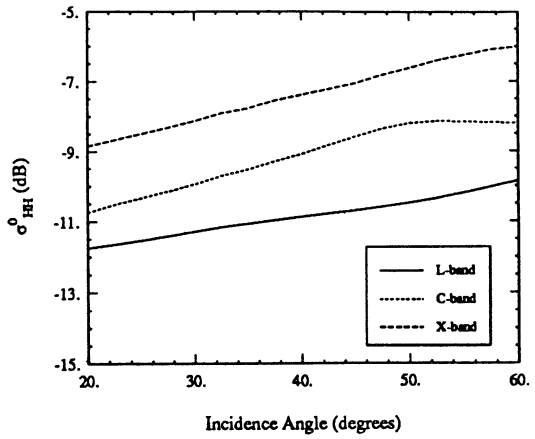

(a) HH-polarization.

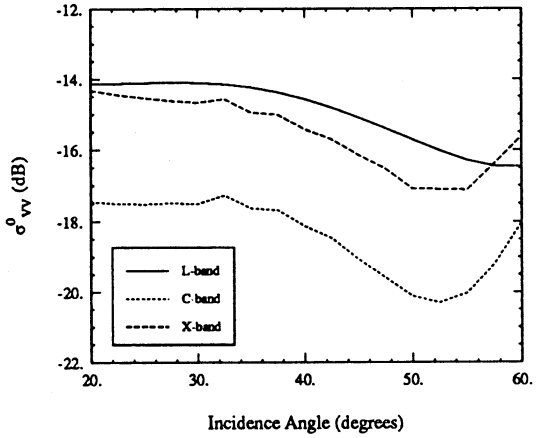

(b) VV-polarization.

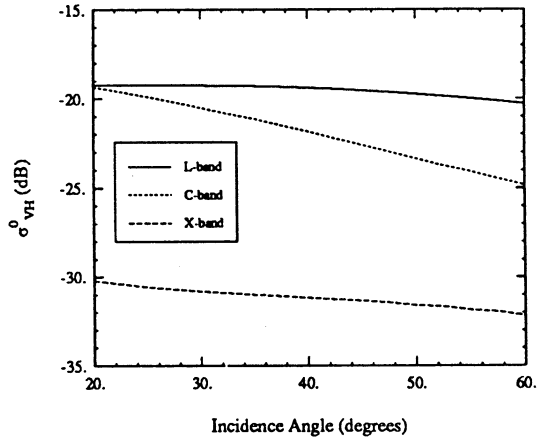

(c) VH-polarization.

Figure H.25: MIMICS simulated canopy backscatter for a black spruce stand (BS-1) at L-, C- and X-bands under thawed canopy conditions for (a) HH-polarization, (b) VV-polarization and (c) VH-polarization.

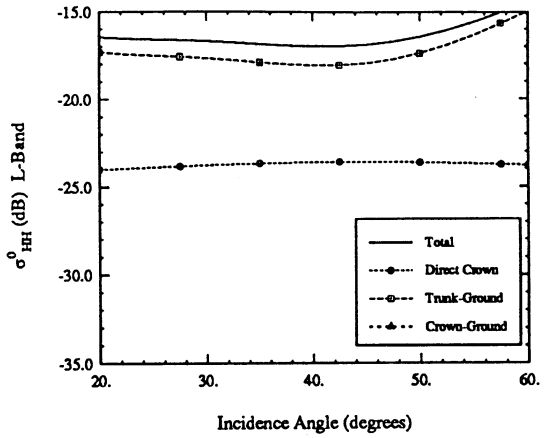

(a) HH-polarization.

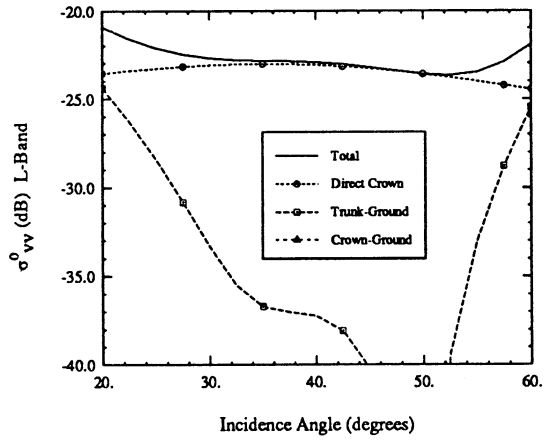

(b) VV-polarization.

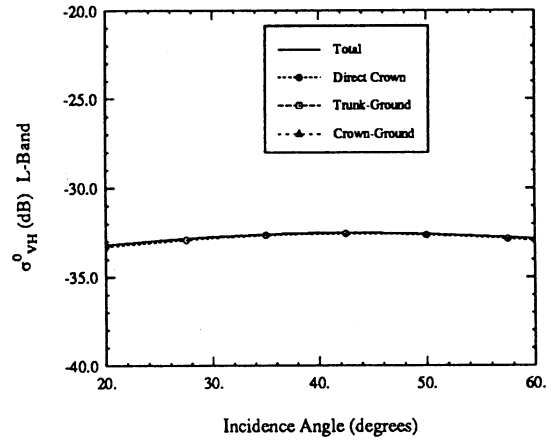

(c) VH-polarization.

Figure H.26: Canopy backscatter components for black spruce stand (BS-1) at L-band under frozen canopy conditions for (a) HH-polarization, (b) VV-polarization and (c) VH-polarization.

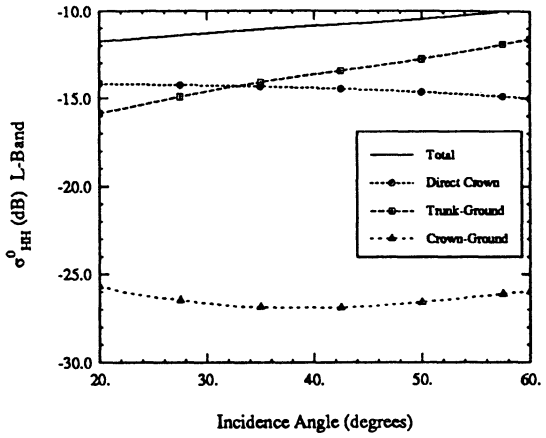

(a) HH-polarization.

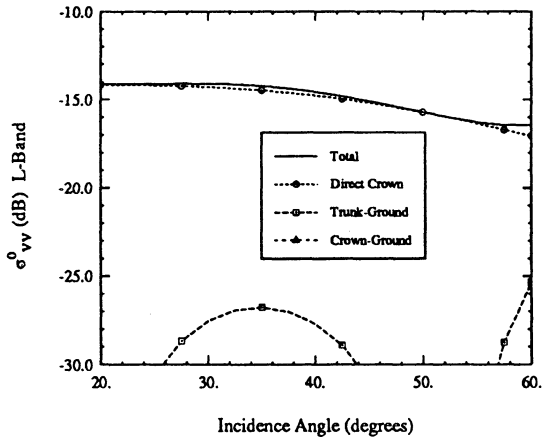

(b) VV-polarization.

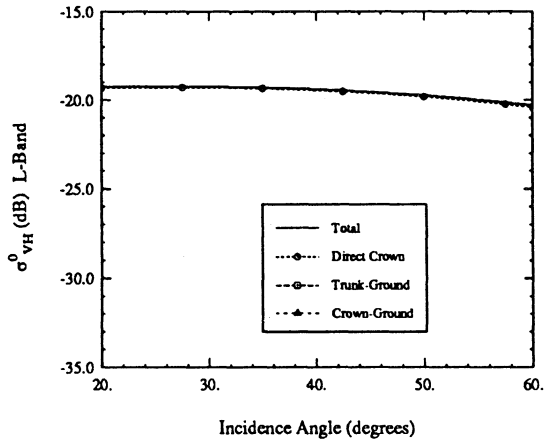

(c) VH-polarization.

Figure H.27: Canopy backscatter components for black spruce stand (BS-1) at L-band under thawed canopy conditions for (a) HH-polarization, (b) VV-polarization and (c) VH-polarization.

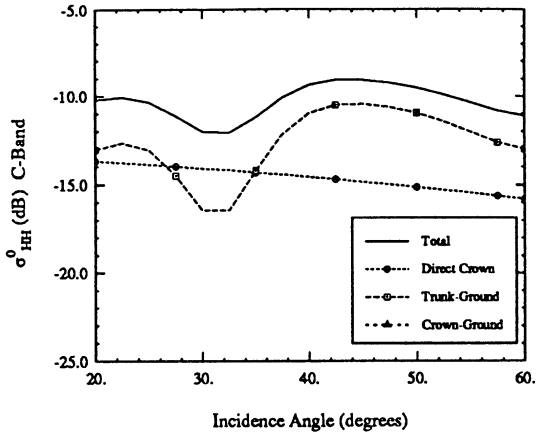

(a) HH-polarization.

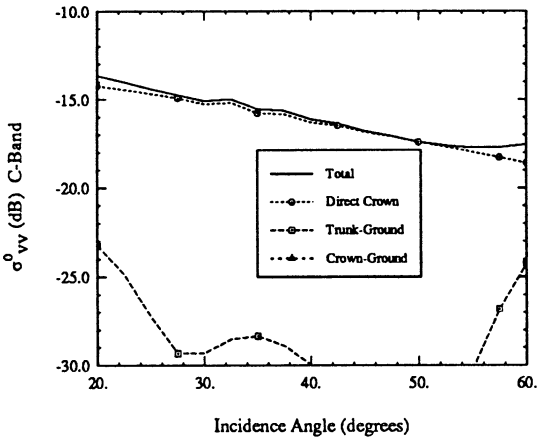

(b) VV-polarization.

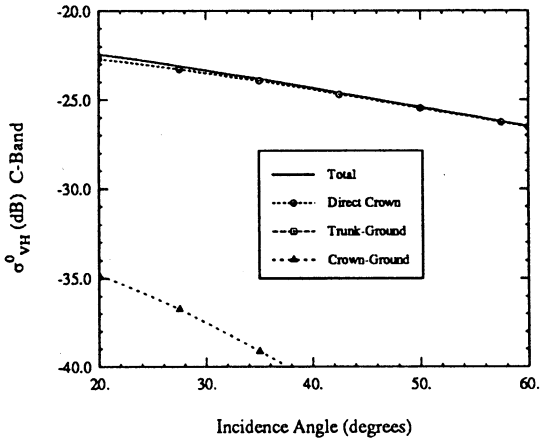

(c) VH-polarization.

Figure H.28: Canopy backscatter components for black spruce stand (WS-5) at C-band under frozen canopy conditions for (a) HH-polarization, (b) VV-polarization and (c) VH-polarization.

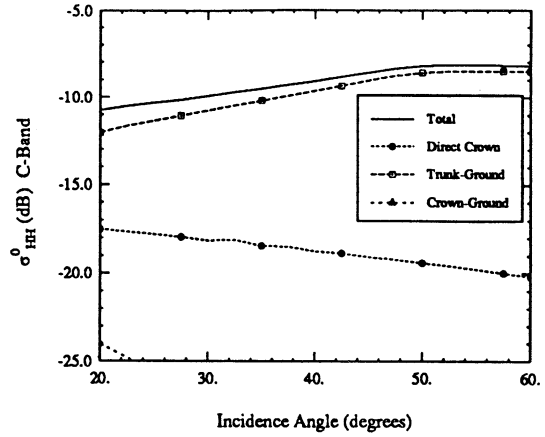

(a) HH-polarization.

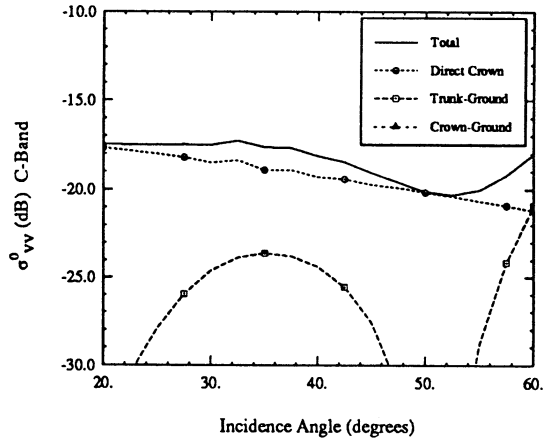

(b) VV-polarization.

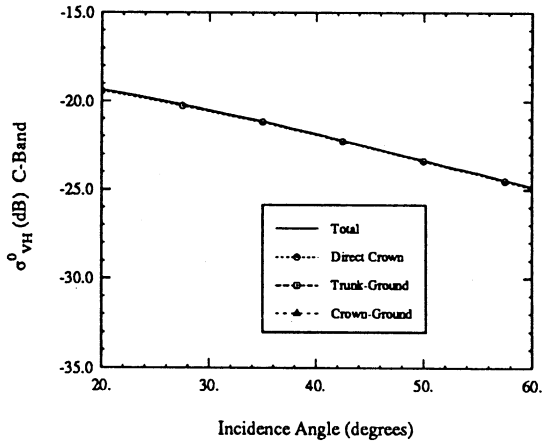

(c) VH-polarization.

Figure H.29: Canopy backscatter components for white spruce stand (WS-5) at C-band under thawed canopy conditions for (a) HH-polarization, (b) VV-polarization and (c) VH-polarization.

modeled as a 20 cm thick snow layer over a frozen soil half-space. Figure H.30 shows this simulation for frozen canopy conditions while Figure H.31 shows these data for thawed canopy conditions. In both cases, σ^0 is higher for the snow-covered soil for all polarizations. The effect is more prevalent for like-polarized backscatter with σ^0_{vv} being responding slightly more than σ^0_{hh}.

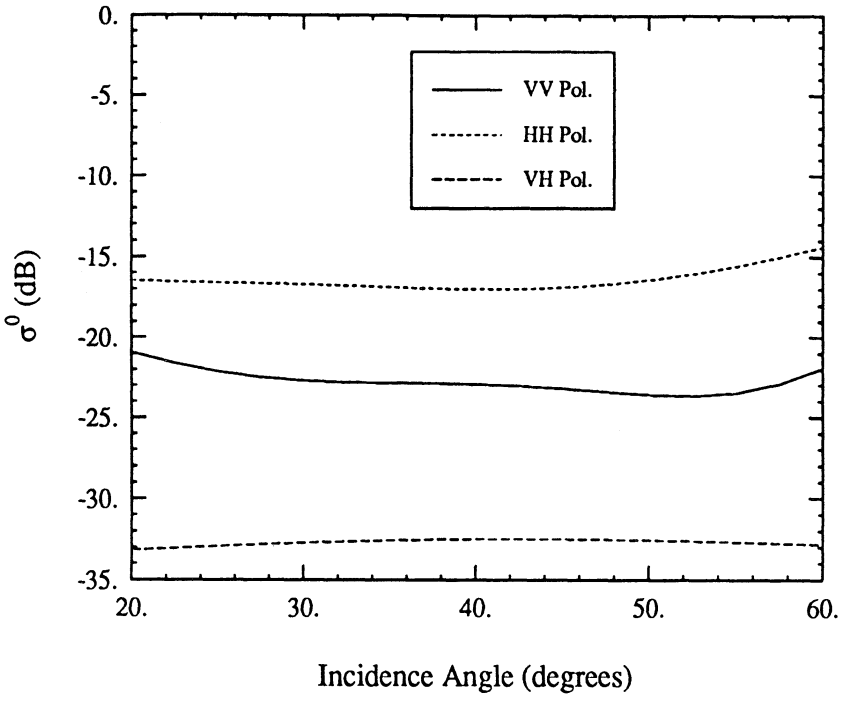

(a) Snow half-space.

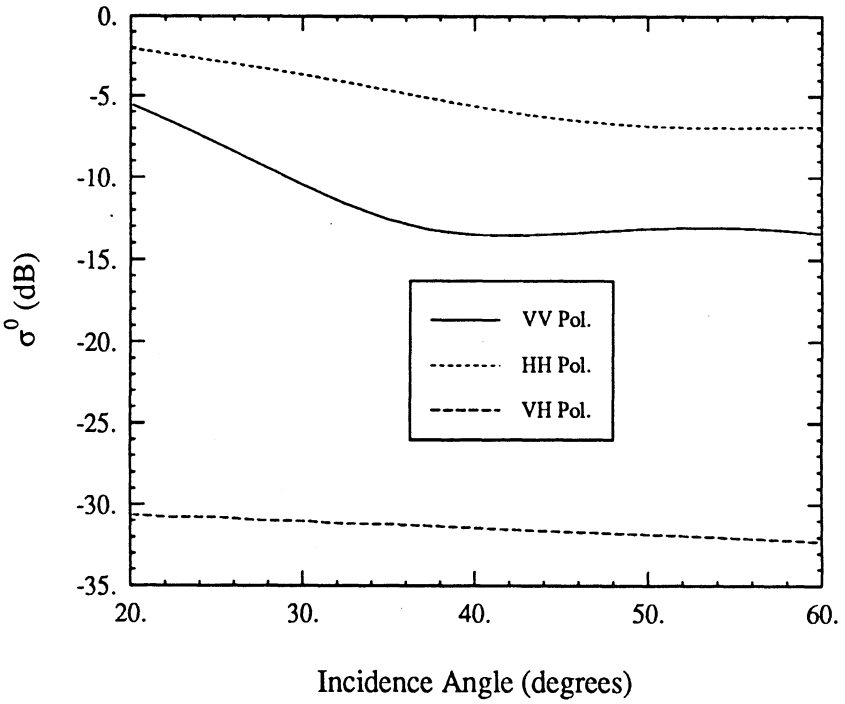

(b) Snow layer over soil half-space.

Figure H.30: Total canopy backscatter for black spruce stand (BS-1) at L-band under frozen canopy conditions for (a) ground layer consisting of a snow half-space and (b) ground layer consisting of a snow layer on top of a soil half-space.

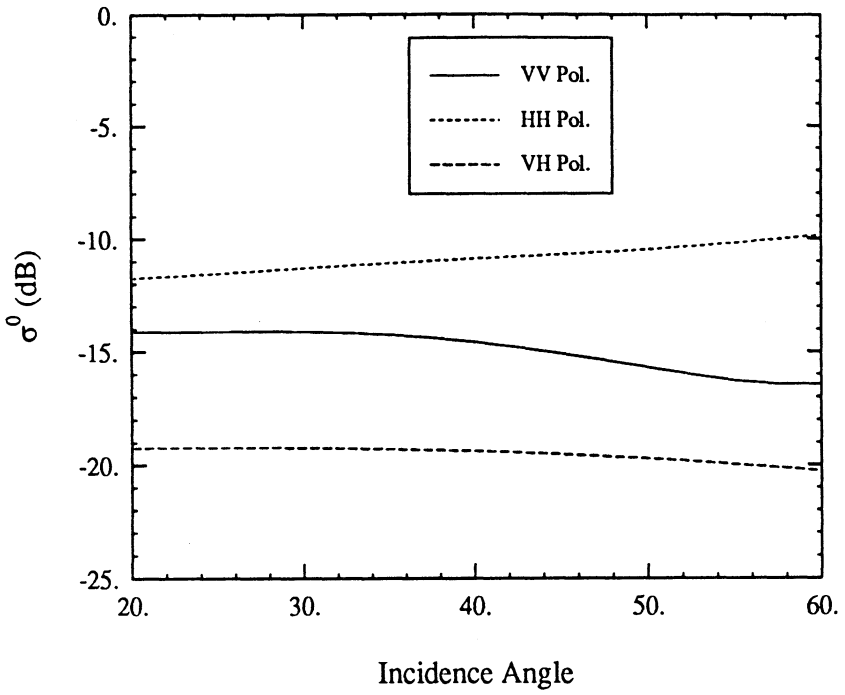

(a) Snow half-space.

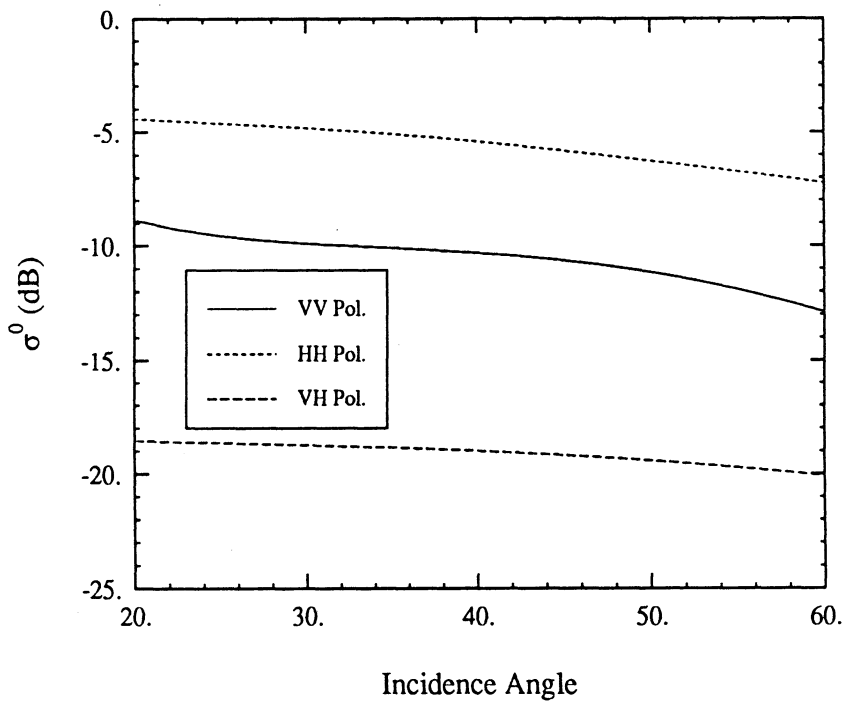

(b) Snow layer over soil half-space.

Figure H.31: Total canopy backscatter for black spruce stand (BS-1) at L-band under thawed canopy conditions for (a) ground layer consisting of a snow half-space and (b) ground layer consisting of a snow layer on top of a soil half-space.

BIBLIOGRAPHY

BIBLIOGRAPHY

[1] Agrawal, A. P., and W. M. Boerner, "Redevelopment of Kennaugh's Target Characteristic Polarization State Theory Using the Polarization Transformation Ratio for the Coherent Case," *IEEE Transactions on Geoscience and Remote Sensing,* Volume GE-27, pp 2-14, 1988.

[2] Attema, E. P. W. and F. T. Ulaby, "Vegetation Modeled as a Water Cloud," *Radio Science*, Vol. 13, No. 2, March–April, 1978, pp. 357–364.

[3] Bradford, K. J. and T. C. Hsiao, "Physiological Responses to Moderate Water Stress," In: Lange, O. R., P. S. Nobe, C. B. Osmond and H. Ziegler (Eds.), Encyclopedia of Plant Physiology NS Volume 12B, Physiological Plant Ecology II, Springer-Verlag, 1982, pp.264–324.

[4] Chandrasekhar, S., Radiative Transfer, New York, NY: Dover Publications, 1960.

[5] Charles-Edward, D. A. and M. R. Thorpe, "Interception of diffuse and direct-beam radiation by a hedgerow apple orchard," *Ann. Bot.'* Vol. 40, pp. 603-613, 1976.

[6] Chauhan, N. S. and R. S. Lang, "Microwave Modelling of Orchard Canopy," *Proceedings of International Geoscience and Remote Sensing Symposium,* 12-16 September 1988, Edinburgh, U.K., Vol. 3 , pp. 1757-1759.

[7] Cimino, J, C. Elachi and M. Settle, "SIR-B – The Second Shuttle Imaging Radar Experiment," *IEEE Transactions on Geoscience and Remote Sensing,* Vol. GE-24 No. 4 July 1986, pp. 445-452.

[8] Davis, R. J., J. Dozier, E. LaChapelle and R. Pula. "Field and Laboratory Measurements of Liquid Water by Dilution," *Water Research,* Volume 21, pp. 1415–1420, 1985.

[9] Cimino, J., M. C. Dobson, D. Gates, E. Kasischke, R. Lang, J. Norman, J. Paris, F. T. Ulaby, S. Ustin, V. Vanderbilt, and J. Weber, "Eos Synergism Study 1987 Field Experiment Data Report," JPL Technical Report, May 1988.

[10] Dobson, M. C., "Diurnal and Seasonal Variations in the Microwave Dielectric Constant of Selected Trees," *Proceedings of International Geoscience and Remote Sensing Symposium,* 12-16 September 1988, Edinburgh, U.K., Vol. 3, p. 1754.

[11] Dobson, M. C., R. de la Sierra and N. Christensen, "Spatial and Temporal Variation of the Microwave Dielectric Properties of Loblolly Pine Trunks," *Proceedings of International Geoscience and Remote Sensing Symposium,* 3-6 June 1991, Espoo, Finland.

[12] Dobson, M. C., K. C. McDonald and E. S. Kasischke, "Microwave Extinction of Boreal Forest Canopies in Winter," *Proceedings of International Geoscience and Remote Sensing Symposium,* Vancouver, B.C., 1989.

[13] Dobson, M. C., K. C. McDonald and F. T. Ulaby, "Modeling of Forest Canopies andAnalysis of Polarimetric SAR Data," Radiation Laboratory Technical Report no. 026143-1-F, December, 1989.

[14] Dobson, M. C., K. C. McDonald, F. T. Ulaby, E. S. Kasischke and J. B. Way, "Modeling the Effects of Temperature on Microwave Extinction and Backscatter from a Boreal Forest in Winter," To be submitted to *IEEE Transactions on Geoscience and Remote Sensing*, 1991.

[15] Dobson, M. C., K. C. McDonald, F. T. Ulaby and J. F Paris, "Diurnal Patterns in Multifrequency, Multipolarization Backscattering by a Walnut Orchard," *Proceedings of International Geoscience and Remote Sensing Symposium,* 12-16 September 1988, Edinburgh, U.K., Vol. 3 , p. 1755.

[16] Dobson, M. C. and F. T. Ulaby, "Preliminary Evaluation of the SIR-B Response to Soil Moisture, Surface Roughness, and Crop Canopy Cover," *IEEE Transactions on Geoscience and Remote Sensing,* Vol. GE-24 No. 4 July 1986, pp. 517-526.

[17] Durden, S. L., J. J. van Zyl and H. A. Zebker, "Modeling and observation of the radar polarization signature of forested areas," *IEEE Transactions on Geoscience and Remote Sensing,* Vol. 27 No. 3 May 1989, pp. 290-301.

[18] El-Rayes, M. "The Measurement and Modelling of the Dielectric Behavior of Vegetation Materials in the Microwave Region (0.5-20.4 GHz)," Ph.D. Dissertation, Department of Electrical Engineering and Computer Engineering, University of Kansas, Lawrence, Kansas, November, 1986.

[19] Eom, H. J. and A. K. Fung, "A Scatter Model for Vegetation up to KU-Band," *Remote Sensing of Environment*, Vol. 15, 1984, pp. 185-200.

[20] Evans, D. L., T. G. Farr, J. J. van Zyl and H. A. Zebker, "Radar polarimetry: Analysis tools and applications," *IEEE Transactions on Geoscience and Remote Sensing,* Vol. 26 No. 6 November 1988, pp. 774-789.

[21] Ferguson, J. H. A., "A comparison of two planting systems in orchards as regards the amount of radiation intercepted by the trees," *Neth. J. Agric. Sci.'* Vol. 8 , pp. 271-280, 1963.

[22] Fung, A. K. and F. T. Ulaby, "A Scatter Model for Leafy Vegetation," *IEEE Transactions on Geoscience and Remote Sensing*, Vol. GE-16, No. 4, October 1978, pp. 281–286.

[23] Gedis, A. J., and R. Jackson, "The expected proportion of a region polluted by K sources," *Geographical Analysis,* Vol.3, pp. 256-261, 1971.

[24] Hallikainen, M. T, F. T. Ulaby and M. Abdelrazik, "Dielectric Properties of Snow in the 3 to 37 GHz Range," *IEEE Transactions on Antennas and Propagation*, Vol. AP-34, No. 11, November 1986, pp. 1329–1340.

[25] Hallikainen, M. T. , F. T. Ulaby, M. C. Dobson, M.A. El-Rayes and L. -K. Wu, "Microwave Dielectric Behavior of Wet Soil - Part I: Empirical Models and Experimental Observations," *IEEE Transactions on Geoscience and Remote Sensing*, Volume GE-23, Number 1, pp. 25-34, 1985

[26] Horn, H. S., The Adaptive Geometry of Trees, Princeton, New Jersey: Princeton University Press, 1971.

[27] Ishimaru, A., Wave Propagation and Scattering in Random Media, Volumes I and II, New York, NY: Academic Press, 1978.

[28] Ishimaru, A., and R.L.-T. Cheung, "Multiple Scattering Effects on Wave Propagation due to Rain," *Ann. Telecommunication,* Volume 35, pp.373-379, 1980.

[29] Jackson, J. E., and J. W. Palmer, "Interception of light by model hedgerow orchards in relation to latitude, time of year and hedgerow configurations and orientation," *Journal of Applied Ecology,* Vol. 9, pp. 341-358, 1972.

[30] Jaeger, B., "Report on Stand Characteristics Measured in Bonanza Creek Experimental Forest for the SAR-IFIT Project (Synthetic Aperture Radar-International Forestry Investigation Team), Summer 1988," Forest Soils Laboratory Technical Report, University of Alaska, Fairbanks, Alaska, December 1988.

[31] Karam, M. A. and A. K. Fung, "Electromagnetic Scattering from a Layer of Finite Length, Randomly Oriented, Dielectric, Circular Cylinders Over a Rough Interface with Application to Vegetation," *International Journal of Remote Sensing*, Vol. 9, No. 6, June 1988, pp. 1109–1134.

[32] Kasischke, E. S., M. C. Dobson, D. Beverstock and K. C. McDonald, "X and C-Band Forest Extinction Study," ERIM Tech Report, Environmental Research Institute of Michigan, Ann Arbor, MI, April 1989.

[33] Kirby, C. L., "A Taper and Volume Table and Volume Formulae for Black Spruce in Saskatchewan," *Forestry Chronicle,* pp. 242–253, September, 1960.

[34] Kramer, P. J., "Water Relations of Plants," New York, NY: Academic Press, Inc., 1983.

[35] Lang, R. H. and J. S. Sidhu, "Electromagnetic Backscattering From a Layer of Vegetation: A Discrete Approach," *IEEE Transactions on Geoscience and Remote Sensing*, Volume GE-21, No. 1, January 1983, pp. 62–71.

[36] Lee, J. K., and J. A. Kong, "Active Microwave Remote Sensing of an Anisotropic Random Medium Layer," *IEEE Transactions on Geoscience and Remote Sensing*, Volume 23, 1985, pp. 910–923.

[37] Li, X., "Geometric-optical modeling of a coniferous forest canopy," Ph.D. dissertation, University of California, Santa Barbara, 1985.

[38] Li, X., and A. H. Strahler, "Geometric-Optical Modeling of a Conifer Forest Canopy," *IEEE Transactions on Geoscience and Remote Sensing,* Vol. GE-23 no. 5 September 1985, pp. 705-721.

[39] Li, X. and A. H. Strahler, "Modeling Gap Probability of a Discontinuous Vegetation Canopy," *IEEE Transactions on Geoscience and Remote Sensing,* Vol. 26 no. 2 March 1988, pp. 161-170.

[40] Manning, G. H., M. R. C. Massie and J. Rudd, "Metric Single-Tree Weight Tables for the Yukon Territory," Information Report BC-X-250, Pacific Forest Reasearch Centre, 1984.

[41] McDonald, K. C., M. C. Dobson and F. T. Ulaby, "Using MIMICS to Model Microwave Backscatter from Tree Canopies," *Proceedings of 1989 International Geoscience and Remote Sensing Symposium,* Vol. 4 , p. 2491.

[42] McDonald, K. C., M. C. Dobson and F. T. Ulaby, "Using MIMICS to model L-band multi-angle and multi-temporal backscatter from a walnut orchard," *IEEE Transactions on Geoscience and Remote Sensing*, Volume 28, Number 3, pp. 477-491 1990.

[43] McDonald, K. C., M. C. Dobson and F. T. Ulaby, "Modeling multi-frequency diurnal backscatter from a walnut orchard," Submitted to *1991 International Geoscience and Remote Sensing Symposium,* Espoo, Finland.

[44] McDonald, K. C., M. C. Dobson and F. T. Ulaby, "Modeling multi-frequency diurnal backscatter from a walnut orchard," Submitted to *IEEE Transactions on Geoscience and Remote Sensing*, 1991.

[45] Nelson, N. D., T. Burk and J. G. Isebrands, "Crown Architecture of Short-Rotation, Intensively Cultured Populus. I. Effects of Clone and Spacing on First-Order Branch Characteristics," *Canadian Journal of Forest Research,* Volume II, pp. 73–81, 1981.

[46] Paris, J. K., "Probing Thick Vegetation Canopies with a Field Microwave Scatterometer," *IEEE Transactions on Geoscience and Remote Sensing,* Vol. GE-24, Number 6, 1986, pp. 886–893.

[47] Passioura, J. B., "Water in the Soil-Plant-Atmosphere Continuum," In: Lange, O. R., P. S. Nobe, C. B. Osmond and H. Ziegler (Eds.), Encyclopedia of Plant Physiology NS Volume 12B, Physiological Plant Ecology II, Springer-Verlag, 1982, pp.5–33.

[48] Richards, J. A., G.-Q. Sun, and D. S. Simonett, "L-Band Radar Backscatter Modeling of Forest Stands," *IEEE Transactions on Geoscience and Remote Sensing*, Vol. GE-25, No. 4, July 1987, pp. 487–498.

[49] Ruck, G. T., D. E. Barrick, W. D. Stuart, and C. K. Krichbaum, Radar Cross Section Handbook, Vol. 1, New York, NY: Plenum Press, 1970.

[50] Sarabandi, K., "Electromagnetic Scattering from Vegetation Canopies," Ph.D. dissertation, The University of Michigan, Ann Arbor, MI, 1989.

[51] Sarabandi, K., T. B. A. Senior and F. T. Ulaby, "Effect of Curvature on the Backscattering From a Leaf," *Journal of Electromagnetic Waves and Applications*, Vol. 2, Number 7, 1988, pp. 653–670

[52] Singh, T., "Weight Tables for Important Tree Species in the Nortwest Territories," *Forest Management Note, Note Number 27,* Northern Forest Research Centre, Edmonton, Alberta, December 1983.

[53] Skelly, W. C., "Microwave Backscatter Modelling of Forested Terrain: A Theoretical Approach to Image Interpretation," Master's thesis, Department of Geography, University of Western Ontario, London, Ontarion, 1990.

[54] Skelly, W. C., F. J. Ahern, K. McDonald and C. M. Pearce, "Simulating Microwave Backscatter Sensitivity to Forest Structure and Biomass using the MIMICS Model," Submitted to *IEEE Transactions on Geoscience and Remote Sensing*, 1991.

[55] Skelly, W. C., F. J. Ahern, K. McDonald and C. M. Pearce, "Studies of Microwave Sensitivity to Balck Spruce Stand Structure with the MIMICS Model," Submitted to *14th Canadian Remote Sensing Symposium,* Calgary, Canada, 1991.

[56] Stratton, J. A., Electromagnetic Theory, New York, NY: McGraw-Hill Book Company, Inc., 1941.

[57] Sun, G., D. S. Simonett and A. H. Strahler, "A Radar Backscattering Model for Discontinuous Forest Canopies," *Proceedings of 1989 International Geoscience and Remote Sensing Symposium,* Vol. 5 , pp. 2832-2835.

[58] Tassoudji, M. A., K. Sarabandi and F. T. Ulaby, Design Consideration and Implementation of the LCX Polarimetric Scatterometer (POLARSCAT), The University of Michigan Radiation Laboratory, Report Number 022486-T-2, June, 1989.

[59] Tsang, L. and J. Kong, "Application of Strong Fluctuation Random Medium Theory to Scattering From Vegetation-Like Half Space," *IEEE Transactions on Geoscience and Remote Sensing*, Vol. 19, No. 1, pp. 62–69, 1981.

[60] Tsang, L., J. A. Kong and R. T. Shin, Theory of Microwave Remote Sensing, New York, NY: Wiley Inerscience, 1985.

[61] Ulaby, F. T. and M. C. Dobson, Handbook of Radar Scattering Statistics for Terrain, Norwood, MA: Artech House, Inc., 1989.

[62] Ulaby, F. T. and C. Elachi, editors, Radar Polarimetry for Geoscience Applications, Dedham, MA: Artech House, Inc., 1990.

[63] Ulaby, F. T., and M. A. El-Rayes, "Microwave Dielectric Spectrum of Vegetation, Part II: Dual-Dispersion Model", *IEEE Transactions on Geoscience and Remote Sensing*, Volume GE-25, pp.550-557, 1987.

[64] Ulaby, F. T., T. H. Haddock and Y. Kuga, "Measurement and Modeling of Millimeter-wave Scattering from Tree Foliage," *Radio Science*, Vol. 25, Number 3, 1987, pp. 193–203.

[65] Ulaby, F. T., T. H. Haddock and Y. Kuga, "Measurement and Modeling of Millimeter-wave Scattering from Tree Foliage," *Radio Science*, Vol. 25, Number 3, 1987, pp. 193–203.

[66] Ulaby, F. T., D. Held, M. C. Dobson, K. C. McDonald, and T. B. A. Senior, "Relating Polarization Phase Difference of SAR Signals to Scene Properties," *IEEE Transactions on Geoscience and Remote Sensing,* Vol. GE-25 no. 1 January 1987, pp. 83-92.

[67] Ulaby, F. T., K. McDonald, K. Sarabandi and M. C. Dobson, "Michigan Microwave Canopy Scattering Model (MIMICS)," *Proceedings of International Geoscience and Remote Sensing Symposium,* 12-16 September 1988, Edinburgh, U.K., Vol. 2 , p. 1009.

[68] Ulaby, F. T., K. Sarabandi, K. McDonald, M. Whitt and M. C. Dobson, "Michigan Microwave Canopy Scattering Model (MIMICS)," Report 022486-T-1, The University of Michigan, Ann Arbor, Michigan, 1988

[69] Ulaby, F. T., K. Sarabandi, K. McDonald, M. Whitt and M. C. Dobson, "Michigan Microwave Canopy Scattering Model," *Internation Journal of Remote Sensing*, Volume 11, Number 7, 1223-1253, 1990.

[70] Ulaby, F. T., R. K. Moore and A. K. Fung, Microwave Remote Sensing, Active and Passive, Volumes 1 - 3, Dedham, MA: Artec House, 1986

[71] Ustin, S. L., S. Martens, J. Norman and D. Goldhammer, "Measurement and Characterization of Tree Canopy Architecture," *Proceedings of International Geoscience and Remote Sensing Symposium,* 12-16 September 1988, Edinburgh, U.K., Vol. 3 , p. 1753.

[72] Ustin, S. L., S. N. Martens and V. C. Vanderbilt, "Canopy Architecture of a Walnut Orchard," Submitted to *IEEE Transactions on Geoscience and Remote Sensing,* 1991.

[73] Van Cleve, K., and L. A. Viereck, "Distribution of Selected Chemical Elements in Even-Aged Alders (Alnus) Ecosystems Near Fairbanks, Alaska," *Artic and Alpine Research,* Volume 4, Number 3, pp, 239–255, 1972.

[74] van Zyl, J. J., "On the Importance of Polarization in Radar Scattering Problems," Ph.D. dissertation, Caltech Antenna Laboratory Report No. 120, 152 pp., California Institute of Technology, Pasadenda, CA, 1985.

[75] van Zyl, J. J., H. A. Zebker, and C. Elachi, "Imaging Radar Polarization Signatures: Theory and Observation," *Radio Science*, Volume 22, Number 4, pp. 529-543, 1987.

[76] Way, J., R. Kwok, E. Rignot, J. Holt, M. C. Dobson, K. McDonald and F. T. Ulaby, "Monitoring Forest Freeze-Thaw Cycles with Airborne SAR," *Fourth Airborne Geoscience Workshop*, La Jolla, CA, 29 January - 1 February, 1991.

[77] Way, J. B., J. Paris, E. Kasischke, C. Slaughter, L. Viereck, N. Christensen, M. C. Dobson, F. T. Ulaby, J. Richards, A. Milne, A. Sieber, F. J. Ahern, D. Simonett, R. Hoffer, M. Imhoff and J. Weber, "The Effect of Changing Envirinmental Conditions on Microwave Signatures of Forest Ecosystems: Preliminary Results of the March 1988 Alaskan Aircraft SAR Experiment," *International Journal of Remote Sensing,* Volume 11, pp. 1119–1144, 1990.

[78] Way, J., E. Rignot, M. C. Dobson and K. McDonald, "Monitoring the Environmental and Phenologic State of Alaskan Forests using Synthetic Aperture Radar," Submitted to *Annual meeting of the Ecological Society of America*, 1991.

[79] Way, J., E. Rignot, K. McDonald and G. Bonan, "Monitoring Temporal Change in Alaskan Forests Using AIRSAR Data," Submitted to *International Geoscience and Remote Sensing Symposium*, 1991.

[80] Way, J., E. Rignot, R. Oren, R. Kwok, K. McDonald, M. C. Dobson, G. Bonan, L. Viereck and J. E. Roth, "Monitoring Temporal Change and Species in Alaskan Forest Using Imaging Radar Data," Submitted to *IEEE Transactions on Geoscience and Remote Sensing*, 1991.

[81] Way, J. B., M. Schier, M. C. Dobson, D. Gates, F. T. Ulaby, S. L. Ustin, V. Vanderbilt, J. Weber, J. Paris, E. Kasischke, R. Lang and J. Norman, "Diurnal Change in Trees as Observed by Optical and Microwave Sensors: The EOS Synergism Study," Submitted to *IEEE Transactions on Geoscience and Remote Sensing,* 1991.

[82] Weber, J. A. and S. L. Ustin, "Water Relations of a Walnut Orchard: Simultaneous Measurement with Remote Sensing," *Proceedings of International Geoscience and Remote Sensing Symposium,* 12-16 September 1988, Edinburgh, U.K., Vol. 3 , pp. 1749–1751.

[83] Weber, J. A. and S. L. Ustin, "Diurnal Water Relations of Walnut Trees: Implications for Remote Sensing," Submitted to *IEEE Transactions on Geoscience and Remote Sensing,* 1991.

[84] Yarie, J, and K. Van Cleve, "Biomass and Productivity of White Spruce Stands in Interior Alasksa," *Canadian Journal of Forest Research,* Volume 3, No. 2, pp. 767–772, 1983.

[85] Zebker, H. A., J. J. van Zyl and D. N. Held, "Imaging Radar Polarimetry from Wave Synthesis," *Journal of Geophysical Research,* Volume 92, Number B1, pp. 683–701, 1987.